Department of Electrical Engineering,
Imperial College of Science
and Technology,
University of London.

IMPROVEMENTS IN THE GRATING LOBE AND IMPEDANCE PERFORMANCE OF ARRAY ANTENNAS

BY WARWICK RODNEY BELCHER

Thesis submitted for the award of the

Degree of Ph. D. in Engineering

August, 1973

Electrical Eng.

Industrial Research Laboratory

Plessey Radar Ltd.,
Cowes,
Isle of Wight.

ABSTRACT

The performance of electronically scanned arrays is affected by the occurrence of grating lobes and the variation of impedance levels with element phasing. Both these problems can be controlled in waveguide arrays by replacing the sidewalls between adjacent elements with boundaries which behave as reactive surfaces, and consist of thin metal (or metal-dielectric) structures.

A threefold purpose has influenced the selection of individual topics as follows:

(i) To allow further development and application of the design technique, underlying concepts are emphasised. In particular, it is shown that a smooth transition is required between the field distributions in a conventional waveguide array and free space. This can be achieved when the reactance of the element boundaries is tapered from zero to infinity.

(ii) To demonstrate the potential saving in the number of elements needed in sectorally scanned arrays, the element pattern control afforded by the design technique is investigated. For linear arrays, grating lobe radiation can be eliminated in the E-plane and reduced in the H-plane, (theoretically, as much as required).

(iii) To ensure that practical design difficulties can be solved realistically, the theory is supported by experimental programmes.

The thesis is in two parts for chronological consistency.

Within Chapters 1 - 3, existing methods of phased array design are reviewed and performance limitations are identified. The current proposal is then outlined, and a feasibility investigation with a 20 element model array is described and assessed.

Within Chapters 4 - 7, multi-mode array structures with an axial discontinuity in reactance are analysed by the Wiener-Hopf technique. The analysis is verified experimentally using a waveguide simulator, and a constraint on the periodicity of practical boundaries is identified. Finally, a general method of designing an array with a set of step discontinuities in boundary reactance is presented. Numerical optimisation procedures are recommended, and design examples are included.

ACKNOWLEDGEMENTS

It is a privilege to acknowledge the guidance and encouragement received jointly from Dr. K. Milne and Professor J. Brown, who have given generously of their time to supervise and direct the work described in this thesis.

The consideration and interest shown by colleagues and staff at Plessey Radar, Cowes, is also appreciated. In particular, the support received from Dr. G. H. Bryant, Dr. A. J. Sangster, Mr. C. Wood and Mr. C. Wigmore is gratefully acknowledged. Valuable assistance with measurements was given by Mr. K. Wellstead, Mr. A. Richardson and Mr. P. Nickels as part of their industrial training.

The preparation of this thesis has been a team effort at Plessey Radar. However, the contributions made by Mrs. C. Attrill, Miss H. Perry, Mrs. M. Plumbley and Mrs. Y. Jukes have been outstanding.

Finally, the author wishes to record his appreciation of the financial support given to this work by the Plessey Company.

CONTENTS

CHAPTER		TITLE	PAGE

(Total number of pages = 332)

CHAPTER 1

A REVIEW OF PHASED-ARRAY THEORY AND PRACTICE

1.1. Introduction

The increasingly sophisticated performance required of modern radar and aerospace navigational systems has resulted in numerous applications for electronically scanned arrays. Their advantages over mechanically rotated aerials are well known, and include their scanning speed, multi-function potential and absence of movement. As array structures with many elements, it also follows that high power transmission can be achieved using solid state sources, aperture illumination can be precisely controlled, and near-normal operation can be maintained despite individual source failures or an adverse environment. Not surprisingly, the cost of such arrays is arguably their major disadvantage. Detailed economic comparisons are not attempted in this thesis, but the benefits to be gained by any significant reduction in the number of elements needed in an array, and the consequential saving in the circuitry required to establish the element phasing, will be apparent.

In this thesis, attention is confined to the design of the radiating elements. Related topics in the field of electronic scanning are discussed in standard references (e.g. 1 to 5). The following review defines the basic parameters and concepts utilised in subsequent chapters, and provides a background to existing performance problems. A summary of recent trends in the analysis of element behaviour is also included.

1.2. The Effects of Mutual Coupling on Array Performance

It is still common practice to design an electronically scanned array of moderate size and performance by relying on classical array theory, which neglects mutual coupling. (Specifically, it is assumed that the radiation characteristics of an element can be measured in isolation and are unaffected by an array environment.) Where necessary, this approach can be supported by experimental evidence that "mutual coupling is not a serious problem". In part, this can be justified by the limitations of existing theoretical models (including their complexity), and the number and variety of practical radiating elements.

This thesis is concerned with the design of arrays requiring more accurate control of their radiating properties. For operation at frequencies above 1GHz, these arrays have usually been developed from a basic structure of open ended waveguides arranged in a periodic lattice. For such structures, the question of mutual coupling has then dominated most considerations of radiating element design. Several important trends in analytical approach can be identified (Sections 1.2 to 1.2.4.), which require reference to the following parameters:

(i) The *mutual coupling coefficient* ($C_{mn,rs}$) in a doubly-periodic array denotes the amplitude and phase of the voltage coupled to the waveguide terminal of one element (say rs) when the other element (mn) is excited by a unit voltage. (In a reciprocal structure, (mn) and (rs) are interchangeable, and for linear arrays, the number of subscripts is of course halved. The double subscript representation is preferred in this section to conform with references cited.) If two elements are electrically isolated, the corresponding mutual coupling coefficient is zero. In this thesis, it is particularly important to distinguish between "mutual coupling" as defined, and the "forward - or directional - coupling" in structures whose waveguide terminals can remain isolated.

(ii) The *active reflection coefficient* ($R_a(\psi_1, \psi_2)$) is the voltage returned to a reference element when an entire array is excited by voltages of unit amplitude and uniform phase increments (ψ_1, ψ_2). In the specific case of a planar array with a rectangular element lattice, ψ_1 and ψ_2 would be associated with the element phasing along the x- and y- axes respectively. The functional dependence of R_a on ψ_1 and ψ_2 during normal scanning opera-

(ii) contd...

tions is emphasised by its description as "active".

(iii) The *element-gain pattern* ($g_e(\theta,\phi)$) defines the variations in power gain of a particular element as a function of the spherical coordinates (θ,ϕ). The gain must be measured with the element properly located in its array environment and with all the remaining elements passively terminated in their generator source impedances. The associated element (voltage) pattern, sometimes designated $\underline{\ell}_e(\theta,\phi)$, also describes the polarisation of the spatial field (2), and is often the most convenient of all the basic parameters to measure experimentally.

It should be noted that two distinct excitation conditions have been introduced in these definitions, viz. excitation of a single element and simultaneous excitation of all elements.

1.2.1. The Infinite Array Model

The above parameters are extremely difficult to calculate in small arrays (6, 7), where they are strongly influenced by the proximity of the element (or elements) to an edge. However, a number of simplifications follow if an array becomes sufficiently large for the majority of elements to be considered part of an infinite structure. Such elements must be electrically remote from an edge - i.e. their properties should remain unchanged if the size of the array is increased (by adding more elements). Despite the residual problem of deciding how many elements in a large (but finite) practical array should be excluded from representation in this way, the infinite array model has become a standard analytical tool for assessing element behaviour.

In an infinite array, $g_e(\theta,\phi)$ need only be defined for one element, while the mutual coupling coefficients can be designated simply as C_{rs}, with element (mn) as an arbitrarily chosen reference in the continuous structure. With periodic excitation $\exp(jr\psi_1 + js\psi_2)$, it also follows that the transmission and reflection characteristics (including $R_a(\psi_1, \psi_2)$) must be identical for all elements, and that

$$R_a(\psi_1, \psi_2) = \sum_{r=\infty}^{\infty} \sum_{s=-\infty}^{\infty} C_{rs} \cdot \exp(jr\psi_1 + js\psi_2) \qquad \ldots. (1)$$

The practical significance of the infinite array model is examined in Chapter 3, in connection with a modified pattern-multiplication principle for finite arrays (cf. 2,3). For analytical purposes, an infinite array is assumed throughout this thesis (see Chapter 2).

1.2.2. Basic Studies of Mutual Coupling

The nature and consequences of mutual coupling can be described in network terms. In this section, three significant studies at this basic level are discussed, to illustrate in part one of the motivating factors for the work described in Chapters 2-6.

As shown originally by Hannan (8), two fundamental relations can be derived connecting the parameters discussed above. The first relation emphasises the degradation in gain due to mutual coupling. For an infinite planar array forming a single beam, the element-gain pattern can be expressed in the form.

$$g_e(\theta,\phi) = \frac{4\pi}{\lambda^2} \cdot A \cdot \left[1 - |R_a(\theta,\phi)|^2\right] \cos\theta \qquad \ldots. (2)$$

where A is the "unit cell" area (40) associated with each element; the sperical co-ordinate θ is measured with respect to broadside;

and the functional dependence of R_a is expressed in modified form to emphasise the correspondence between the choice of element phasing and the direction of gain measurement.

Two conditions of array excitation are related by eqn.(2), which is obtained by combining the standard formula for the (directive) gain of a large, uniformly - excited aperture with the principles of gain superposition and power conservation in an array of identical elements. The expression $\left[1 - |R_a(\theta,\phi)|^2\right]$ can be regarded as a definition of *radiation* efficiency when a beam is scanned in the direction (θ,ϕ). If an array is actually matched at broadside, the difference between the measured directivity of an element and a "cos θ" pattern, in a direction (θ,ϕ), is an indication of the active impedance mismatch when a beam is steered in that direction. [When more than one beam is formed, (typically as ψ_1 and $\psi_2 \to \pi$), eqn.(2) must be modified to account for the "shared" transmitted power. This involves the replacement of the term $[1 - |R_a(\theta,\phi)|^2]$ by appropriately defined transmission coefficients, and is examined in context in Sections 1.4 and 3.3.]

The second relation due to Hannan follows from eqn.(1) and Parseval's theorem, viz

$$\frac{1}{4\pi^2} \int_{-\pi}^{\pi} \int_{-\pi}^{\pi} |R_a(\psi_1, \psi_2)|^2 \, d\psi_1 \, d\psi_2 = \sum_{r=-\infty}^{\infty} \sum_{s=-\infty}^{\infty} |C_{rs}|^2 \quad \dots\dots (3)$$

The left hand side of this equation defines the power returned to one generator, averaged over intervals of $-\pi$ to $+\pi$ in element phasing, when all elements are excited. The right hand side of eqn.(3) equals the power returned to all elements when only one element is excited. The difference expression $[1 - \sum_r \sum_s |C_{rs}|^2]$ can therefore be interpreted as the *element* efficiency, i.e. the ratio of radiated to available power for single element excitation. Taken together, eqns.(2) and (3) provide a basis for considering "conditional" and "unconditional" impedance matching of arrays (4), and the concept of an "ideal" element pattern (8). These topics, which are central to the design technique described in this thesis, are discussed in Section 1.4.

Another network approach to mutual coupling effects has been developed by Wasylkwiskyj and Kahn in a series of recent papers (9-12). Their theory is of particular interest since it demonstrates rigorously the interrelationships between the properties of an array and its isolated elements. Only a few of their results can be mentioned here.

In common with the standard techniques of circuit analysis, the characteristic of an arbitrary antenna (either an element or an array of elements) can be defined by basic properties measured at each of its "ports". Whilst transmission line terminals are easily recognised as "local" ports, an antenna also has "free-space" ports, which are infinite in number and can be identified in an ordered fashion with a complete set of cylindrical or spherical free space modes (according to geometry). For a general network specification, it is therefore necessary to establish the free-space scattering characteristics of an antenna in addition to its radiation pattern (13). Antennas with identical radiation patterns can behave quite differently as scatterers, as shown by the model in Fig.1.1. This fact can be used as a basis of classification, and an antenna can be defined as "minimum scattering" if it becomes invisible when its local ports are terminated in appropriate reactances (14). Wasylkwiskyj and Kahn have shown that the properties of an array (its radiation pattern and mutual coupling effects) can be determined directly from the radiation pattern of a (representative) *isolated* element, if the element can be described as "minimum scattering". The array can be finite or infinite in extent - in the latter case, their results for this class of elements agree with analyses of specific structures (e.g. an array of small dipoles). When the array elements are not minimum scattering, the expressions for mutual coupling involve a set of terms dependent on the scattering properties of the isolated element (11).

The theoretical techniques introduced with this form of network representation of antennas have been applied in studies of array "blindness" (12) and in the design of a wide-beam radiating element (15). [An infinite array can be defined as "blind" - i.e. unable to transmit or receive in a particular direction (θ_o,ϕ_o) - if $|R_a(\theta_o,\phi_o)| = 1$ (16) (see following sections).] For most design purposes, however, the number of measurements required to accurately establish the radiation and scattering properties of an isolated element would be excessive (15).

A basic understanding of mutual coupling effects has also been acquired from the many analyses of specific element types and array geometries (cf. Section 1.2.4). Understandably, the results of such analyses are normally more convenient to use in the design and evaluation of typical arrays than a network theory. However, one general method proposed by Diamond (17) for infinite planar arrays has been used in design studies of waveguide elements arranged in rectangular and triangular lattices (18). Using the principle that the aperture field distribution and the radiation pattern (at all real and imaginary angles) form a Fourier pair (19), Diamond calculates the complex power radiated by an element within its array environment. The derivation assumes that the electric or magnetic fields can be specified over an aperture surface - in terms of the "free space modes" and a complete set of element modes. Standard design parameters (e.g. $g_e(\theta,\phi)$) can then be obtained for a variety of element types, including dipoles, slots and open-ended waveguides within any parallelogram lattice.

A feature common to basic studies of array performance is the acceptance of element interaction as a design "problem" (requiring evaluation and some form of compensation). By contrast, any advantages afforded by closely-spaced interacting elements, particularly in relation to pattern control, have not been defined. More specifically, it seems plausible that an array of "highly directive" elements could introduce sufficient degrees of freedom to shape the element-pattern. This concept is examined in Chapter 2, where element interaction in waveguide arrays is deliberately enhanced. It is conceivable (but not established here) that a similar principle could be developed for current-carrying radiating elements.

1.2.3. Grating Lobe Series

For engineering design purposes, many different approaches have been devised to estimate the effects of mutual coupling. As analytical techniques were refined, unjustified assumptions have been clarified, and the number of recognised techniques has decreased. The "grating lobe series" for calculating the active impedance variations in large arrays is probably the most widely accredited of approximate methods. This method enables two of the principal factors determining array performance to be considered separately. One of these factors is associated entirely with the choice of radiating element, and the other with the further effect of the element lattice which is assumed to be infinite. A detailed discussion of the technique and its limitations has been given by Wheeler (21), while its application to waveguide and dipole arrays has been demonstrated by Diamond (17) and Stark (22) respectively.

To preface the summary given here, the standard results from planar array theory which can be illustrated with a "grating lobe diagram" are indicated. (Angular directions of radiation are described through the alternative co-ordinate systems shown in Fig. 1.2.)

(i) A plane wave $\exp(-j\underline{k}.\underline{r})$, with

$$\underline{k} = k_x \underset{\sim}{a}_x + k_y \underset{\sim}{a}_y + k_z \underset{\sim}{a}_z \qquad \text{.... (4)}$$

can not propagate away from the aperture plane z = o unless $k_x^2 + k_y^2 < k^2$. This condition defines a unit circle on a normalised wave number plane (axes k_x/k and k_y/k) which divides space into "visible" and "invisible" regions (or real and imaginary scan angles).

(ii) With a rectangular element lattice (unit cell dimensions a, b), the phase increments ψ_x and ψ_y are related to the direction of propagation (Fig.1.2) through the equations

$$\psi_x = \frac{2\pi a}{\lambda} . \cos \alpha_x = \frac{2\pi a}{\lambda} . \sin \theta . \cos \phi = k_x a \qquad \text{.... (5b)}$$

$$\psi_y = \frac{2\pi b}{\lambda} . \cos \alpha_y = \frac{2\pi b}{\lambda} . \sin \theta . \cos \phi = k_y b \qquad \text{.... (5b)}$$

Similar relations can be derived for other element lattices.

(iii) Periodic aperture fields create an infinite set of free-space grating waves, which occur at angles governed by the element phasing and lattice geometry. For the specific structure

(iii) contd...

considered in (ii) above, grating waves form at angles defined by

$$k_{xn} = k_{xo} + (2\pi/a)n, \quad n=\pm1,\pm2 \qquad \dots. (6a)$$

$$k_{ym} = k_{yo} + (2\pi/b)m, \quad m=\pm1,\pm2 \qquad \dots. (6b)$$

where k_{xo} and k_{yo} denote the direction of the main beam. (For symmetrical arrays, the main beam is always associated with phase increments which do not exceed 180^o in absolute value.)

These details can be brought together in a grating lobe diagram, as shown in Fig.1.3. The directions of all beams can be shown graphically with the construction based on eqns.(5) and (6), and the occurrence of any visible (i.e. radiated) grating waves can be recognised immediately.

To calculate active impedance variations through a grating lobe series, an appropriate "impedance crater" must first be derived. For a specific mode of element excitation, this function defines the effective terminal impedance associated with a single beam formed at any angle (real or imaginary) in space. Conventionally, it is assumed that the element is single-moded (e.g. only the TE_{10} mode would be considered in a rectangular waveguide), and the "crater" is plotted as a series of impedance (or admittance) contours on normalised wavenumber axes. An example of an admittance crater is given in Fig.1.4 for a rectangular waveguide element. Since an infinite number of (grating) waves are formed when an array is periodically excited, the total admittance (at a particular scan angle) can be formed by adding together the admittance values at all "beam" positions on the grating lobe diagram. This is readily accomplished if the grating lobe diagram is overlain with the admittance crater. Satisfactory engineering estimates of the active admittance can often be obtained by taking a relatively small number of terms. (An exception is the infinitesimal dipole element.) A representative number of scan conditions must be examined to provide a useful summary of the overall impedance variations.

An impedance or admittance crater is characteristic of a specific element (or, more precisely, a mode of excitation) and is unaffected by modifications to the element lattice. The consequences of changing the wall thickness or the basic arrangement of the elements can therefore be assessed by substituting a new grating lobe diagram. The calculation of the impedance crater is also straight forward, although the further concept of an infinite current sheet must be introduced to explain the technique (17).

The infinite current sheet, which is the limiting case of an array of closely-spaced small dipoles, demonstrates an impedance variation over real and imaginary angles given by

$$\frac{Z(k_x,k_y)}{Z(0,0)} = \frac{1 - k_y^2}{\sqrt{1 - k_x^2 - k_y^2}} \qquad \text{.... (7)}$$

where Z(0,0) is its radiation impedance at broadside, and the current flow is in the y-direction. This result, based on aperture projection and analytic continuation principles, was first obtained by Wheeler (21). Since a uniform current sheet does not produce any grating lobes, eqn.(7) defines the complete impedance variation. The directivity of a practical element (e.g. a waveguide horn or slot) is accounted for by multiplying eqn.(7) by the appropriate "mode pattern" i.e. the square of the transform of the mode electric-field distribution. (The possibility of cross-mode coupling is not considered here - a different impedance variation "multiplier" must then be used (17).)

The grating lobe series gives an exact result only when the elements are strictly single moded. The infinitesimal dipole (or its dual, the infinitesimal slot) is an example of such an element. This element, however, is also "minimum scattering" and it is of interest to confirm that the same results have been obtained by the two methods of analysis

(10). Although the grating lobe series offers important advantages of flexibility and numerical simplicity during design, its major limitation is its inaccuracy when higher-order element modes become significant. In particular, it gives quite unacceptable results for arrays exhibiting "blindness" within the limits for an endfire grating wave.

1.2.4. Multi-mode Analyses of Planar Waveguide Arrays

The first multi-mode analysis of an infinite waveguide array scanned at an arbitrary angle was reported by Farrell and Kuhn (23) less than 8 years ago. (Essentially, solutions are obtained for the modes existing on each side of the aperture, and the associated electric and magnetic fields are matched at the aperture plane.) In the intervening period, this method of analysis has become accepted as the modern standard (2, 4). Virtually all of the published work in this field has been carried out in the U.S.A., as part of a co-ordinated effort to develop practical, high performance planar arrays. Examples of such arrays are given in the survey papers in reference 5. Some of the advances afforded by recent work on waveguide element design are considered in this section. (Dipole arrays are affected by the stubs supporting each element, and a comparable definition of performance has not yet been achieved (2).)

Using multi-mode analyses, an arbitrarily-close approximation to the "exact" solution of the aperture boundary-value problem can be obtained. Apart from the limitations of the infinite array model, excellent agreement between theory and practice is observed. In special cases, an analytical solution can be obtained in one or two planes of scan (see Chapter 4). Generally, however, numerical techniques requiring a digital computer must be adopted. The number of modes (i.e. waveguide modes on one side of the aperture, free space (grating) modes on the other side) affecting the observed characteristics of an array depends on a complex combination of element type, size and lattice, but the convergence is normally such that about 30 modes are adequate (4). (Several of the numerical techniques are outlined in reference 4.)

As distinct from any approximate methods of analysis (including the grating lobe series), the multi-mode approach has enabled the blindness phenomenon to be predicted accurately. The results presented by Farrell and Kuhn (Fig.1.5) illustrate the significance of the higher order element modes, and the extreme consequences of blindness (within the grating-wave limits) on the coverage of an array. This effect has been interpreted in various ways, but a consistent explanation has only recently been proposed by Oliner (16). In a periodically excited array, blindness can be associated with the resonance of a higher-order mode near cut-off. The blindness effect remains a central consideration in the design of arrays with wide-angle coverage.

The basic open-ended waveguide element is normally modified to improve the array performance. In particular, a general requirement to optimise the radiation efficiency has led to the introduction of various element matching networks. Standard examples include:-

(i) dielectric plugs inserted in each waveguide (24),

(ii) dielectric sheaths forming a continuous layer over the aperture (24),

(iii) conducting fences between elements above the aperture (25),

(iv) thin irises partially sealing the waveguide ends (26),

(v) changes in waveguide cross-section near the aperture (27),

and

(vi) certain combinations of (i) to (v).

(Interelement connection within the feed structure is considered in Section 1.4.) The interaction between these matching structures and the aperture can be included in the multi-mode analysis. By assuming a specific form of network, the element design can be systemmatically "optimised" by using a more refined computer programme (39). Frequency and scanning limits can also be predicted when the minimum radiation efficiency is specified.

Recent publications indicate that the design of radiating elements for (interlaced) multi-frequency (28), broad band (29) and circularly polarised arrays (30) is now receiving support. This work extends the techniques outlined in the previous paragraphs - e.g. a dual frequency array has been analysed by multi-mode techniques, taking into account the mutual coupling between waveguides of different size.

1.3. Existing Performance Limitations

From the foregoing discussions, several performance limitations imposed, in part, by existing design emphases, can be identified. These include two problems common to all electronically scanned arrays, viz

(i) the active impedance variations caused by mutual coupling between the elements (cf. eqn.(1));

(ii) the element spacing restriction caused by the occurrence of grating waves (cf. eqns.(5) and (6));

and another two problems which can be significant in specific applications,

viz (iii) the control of polarisation;

and (iv) the constraints on bandwidth.

In the next chapter, a design principle is outlined which affords control of problems (i) and (ii). Problems (iii) and (iv) are not considered in detail, although the potential value of the design principles in respect of each should not be discounted (see Section 2.7). It is therefore pertinent to examine problems (i) and (ii) against the background of current design practice.

As already indicated, several techniques affording an improved active impedance match have been developed. Some of these have been demonstrated in planar arrays, where the achievement of solid-angle matching is more complicated than matching in a single plane of scan (see Section 2.7). Particular emphasis has been placed recently on the control of blindness at specific angles, using matching networks which tend to equalise the element efficiency at all angles. (Actual performance is related to the coverage limits; element efficiencies of 50% to 70% can be acceptable for wide-angle scanning.) However, in view of the "optimisation" procedures which are now utilised, it appears unreasonable to expect further significant improvements with present techniques. For waveguide arrays (both linear and planar), low radiation efficiency in the E-plane seems a particular problem. In addition, a general requirement exists for improved matching techniques compatible with broadband operation (2). The fundamental limits on impedance matching have not yet been approached (see Section 1.4).

The possibility of allowing grating lobes to radiate, but reducing their amplitudes to an acceptably low level, appears to have been discounted in the mainstream of research activity (2). Standard design practice is to limit the element spacing so that any grating wave remains evanescent at the maximum scan angle. For a linear array, the resultant element spacing is readily derived from eqns.(5) and (6). Taking $\phi = 0$, it follows that

$$\frac{k_{xo}}{k} = \frac{\psi_x}{2\pi} \cdot \frac{\lambda}{a} = \sin\theta_o \qquad \text{.... (8)}$$

and $$\frac{k_{xn}}{k} = \frac{k_{xo}}{k} + \frac{n\lambda}{a} = \sin\theta_o + \frac{n\lambda}{a} = \sin\theta_n \qquad \text{.... (9)}$$

Assuming array symmetry about broadside, the dominant grating wave $(n = -1)$ is then evanescent if

$$\left|\sin\theta_{-1}\right| > 1$$

$$\text{i.e. if } \frac{a}{\lambda} < \frac{1}{1 + \sin\theta_{o,max}} \qquad \text{.... (10)}$$

(The corresponding phase increment ψ_x is $< \pi$ (from eqn.8).) In the case of a planar array, the limitations on element phasing are interdependent, and can be appreciated most readily by constructing the maximum-scan locus on the grating lobe diagram about each unscanned wave (Fig.1.6).

The significance of these accepted limits on element spacing depends on the proposed coverage, which is influenced by another basic factor. Considering Hannan's general equation for element-gain, i.e.

$$g_e(\theta,\phi) = \frac{4\pi}{\lambda^2} \; A \left[1 - |R_a(\theta,\phi)|^2\right] \cos\theta \qquad \ldots\ldots (2)$$

it is apparent that the overall gain of an array is inherently limited off broadside by the "cos θ" term, even if a high radiation efficiency is maintained. This drop in gain corresponds to a reduction in the effective (or projected) aperture when $\theta \neq 0$. For most applications, this effect places an upper limit on θ_o of approximately 45°. When the wide-angle scanning performance of the array is not the determining factor, system requirements of 10° to 40° are commonly specified (e.g. in navigational systems and in tracking of missile clusters). It therefore follows that a significant spatial region remains unoccupied by the main beam or any grating lobe when the element spacing satisfies the conditions given above in expn.(10) (in the case of a linear array) and illustrated by the unshaded area within the unit circle of Fig.1.6 (in the case of a planar array). By allowing grating lobes to radiate, a considerable increase in element spacing could be achieved for scanning limits in the range just discussed. For a linear array, the theoretical limit is

$$\frac{a}{\lambda} = \frac{1}{2 \sin \theta_{o,max}} \qquad \ldots\ldots (11)$$

where the maximum phase increment of π radians is assumed between elements. For example, taking $\theta_{o,max}$ as 30°, a 30% reduction in the number of elements would be possible if this spacing were adopted in preference to that defined by expn.(10) (Fig.1.7). (A larger reduction could be made in a planar array providing comparable solid-angle coverage.) However, to realise any of this potential saving without multiple beam ambiguities, the element pattern must afford suitable amplitude discrimination between the main beam and the grating lobes.

These individual performance limitations provide a logical introduction to the principles of "ideal" behaviour.

1.4. The Properties of an "Ideal" Element

At least two concepts of an "ideal element" for an infinite planar array have been proposed (8, 31). One of these, due to Hannan (8), suggests that simultaneous control of the impedance mismatch and grating lobes should be sought. The second proposal is concerned only with impedance matching, and has been adopted exclusively in the most recently published textbook (4).

In any definition of "ideal" behaviour, two distinct questions must be considered:-

(a) What characteristics is it desirable to achieve?

(b) What fundamental constraints must be recognised?

Following the discussion of the previous section, it is argued here that Hannan's concept should be preferred.

In 1964, Hannan showed that the possibility of eliminating the active impedance mismatch and the visible grating lobes does not conflict with power conservation and maximum element-gain requirements (8).

By considering the degrees of freedom afforded by an infinite network of interconnecting circuits in the feed lines, he subsequently suggested that perfect impedance matching could actually be achieved for all real scanning angles (20). Varon and Zysman pointed out that this model ignores the interaction between the fields at the array aperture and within the connecting circuits (32). In a mathematically rigorous analysis (33), these authors established that perfect impedance matching over a continuous scanning sector is unattainable, although there is no fundamental limit on how small the residual mismatch can be made provided the initial impedance has a finite real component. This result is consistent with the limitations on broadband matching of an arbitrary impedance (34). For "engineering" purposes, however, Hannan's assumption does not lead to any inconsistencies, since the impedance match can be perfect at a denumerably infinite number of real scan angles.

The various concepts of an "ideal" element can now be identified through the network equations given in Section 1.2.2. It suffices initially to consider a linear array scanned in "two-dimensional" space. [A parallel plate structure is an obvious example.] The corresponding characteristics of a general planar array can then be illustrated through an appropriate grating lobe diagram. The linear forms of eqns.(3) and (2) become

$$\frac{1}{2\pi}\int_{-\pi}^{\pi} |R_a(\psi_x)|^2 d\psi_x = \sum_{r=-\infty}^{\infty} |C_r|^2 \quad \ldots. \ (12)$$

$$g_e'(\theta) = \frac{4\pi}{\lambda} \cdot a \left[1 - |R_a(\theta)|^2\right] \cdot \cos\theta \quad \ldots. \ (13)$$

where $g_e'(\theta)$ = element-gain per unit wavelength in the y-direction;

and a = unit cell dimension in the x-direction.

Like eqn.(3), this equation for element-gain does not apply in general when grating waves radiate (see following paragraphs). Two values of element spacing are considered.

(i) If $a/\lambda < 0.5$, no grating waves are radiated for any value of $\theta_{o,max}$ (cf. eqn.(10)) and complete angular coverage is theoretically possible (Fig.1.7). However, the main beam also becomes evanescent when $2\pi a/\lambda < |\psi_x| < \pi$. To maintain the principle of power conservation within this range of element phasing, $|R_a(\psi_x)|$ must then be unity. Referring to eqn.(12), it follows that mutual coupling between the array elements can not be avoided. This is true of any infinite linear array if $a/\lambda < 0.5$. For an "ideal" array, in the absence of visible grating waves, the one requirement therefore is to eliminate the active impedance

(i) contd...

mismatch for all the remaining values of ψ_x - i.e. $0 \leq |\psi_x| \leq 2\pi a/\lambda$. Such an array is said to be conditionally matched, and its element-gain pattern is given by

$$g_e(\theta) = \frac{4\pi}{\lambda} a \cos\theta, \; 0 \leq |\theta| \leq \pi/2 \qquad \ldots\ldots (14)$$

This "ideal" requirement creates a situation in which the *radiation* efficiency of the array (all elements excited) is unity when a beam is formed in the visible region, although the *element* efficiency must be less than unity, since power is coupled to adjacent elements if a single element is excited. The desired performance can only be obtained if the individual mutual coupling coefficients C_r take a specific set of values which satisfy the equations

$$\sum_{r=-\infty}^{\infty} C_r.\exp(jr\psi_x) = 0 \text{ for } 0 \leq |\psi_x| \leq 2\pi a/\lambda \qquad \ldots\ldots (15a)$$

$$\sum_{r=-\infty}^{\infty} C_r.\exp(jr\psi_x) = 1 \text{ for } 2\pi a/\lambda \leq |\psi_x| \leq \pi \qquad \ldots\ldots (15b)$$

This definition of "ideal" behaviour is generally not disputed.

(ii) If $a/\lambda > 0.5$, at least one beam is formed in the visible region for any element phasing (cf. eqn.(8)), and it follows from eqn.(12) that there is no fundamental reason preventing a vanishing active reflection coefficient for all element phasing. Under this condition, the elements must be electrically isolated - i.e. $C_r = 0$, $r = 0, \pm 1, \pm 2, \cdots$ .... (16)

An array with this property is unconditionally matched, and its element efficiency is unity. The distinction between the two concepts of "ideal elements" arises when $2\pi(1 - a/\lambda) < |\psi_x| < \pi$ if $0.5 < a/\lambda < 1$, or for all ψ_x if $a/\lambda > 1$, since the presence of one or more visible grating lobes must be considered. In the

(ii) contd....

absence of any accepted techniques for controlling the formation of grating waves, one concept requires that the radiated power should simply be shared between the main beam and the grating lobes (4). The corresponding "ideal" element-gain pattern has a "cos θ" shape over the range $0 \leq |\theta| \leq \sin^{-1}(\lambda/a - 1)$ if $a/\lambda < 1$, but is otherwise undefined. By contrast, Hannan suggests that all the incident power should pass into the main beam. This idea demands a sectoral element-gain pattern of the form

$$g_e'(\theta) = \frac{4\pi}{\lambda} a \cos\theta \quad \text{for } 0 \leq |\theta| \leq \theta_{o,max} \qquad \text{.... (17a)}$$

$$= 0 \qquad \text{for } \theta_{o,max} \leq |\theta| \leq \pi/a \qquad \text{.... (17b)}$$

where $\theta_{o,max} = \sin^{-1}(\frac{\lambda}{2a})$, the angle for which the phase increment $\psi_x = \pi$.

It is believed that the design technique described in this thesis provides the first specific example of an array structure in which this behaviour can be accurately approximated. Consequently, it follows that the main argument against Hannan's concept - viz its suspected unrealisability - should be reconsidered.

In the case of planar arrays, three separate conditions must be recognised. These can be illustrated on the grating lobe diagram assuming a square element lattice (Fig.1.8):

(i) If $a/\lambda < 0.5$, a single beam without grating lobes is formed, but the match is conditional (i.e. mutual coupling is unavoidable).

(ii) If $0.5 < a/\lambda < 1/\sqrt{2}$, grating waves can now form for some values of element phasing, whilst the impedance match remains conditional.

(iii) If $a/\lambda > 1/\sqrt{2}$, the mutual coupling coefficients can theoretically be zero.

Equivalent results have been derived for other element arrangements (20), and an "ideal" element-gain pattern for a potential rectangular lattice is sketched in Fig.1.9.

To conclude this section, two examples of work which can be associated with these principles should be noted.

In a recent paper, Phelan and Harrison claim significant pattern control using radiating elements which they describe as "diskpoles" (35). The elements, which were developed experimentally, consist of dipoles mounted above a conducting plane, and loaded reactively by a surmounting disc. Using these "diskpoles" in a planar array, the authors suggest that a 30% - 50% reduction in the number of array elements is possible by allowing grating lobes to radiate. (The saving for the example shown in their paper appears to be substantially smaller - possibly about 10% - with a minimum grating lobe suppression of 20dB for main beam scanning limits of 10°.) Whilst the "diskpole" has several important features (e.g. mechanical simplicity and optional linear or circular polarisation), it must be argued on present evidence that the potential element pattern control, in respect of grating lobes, is inherently limited.

In the preceding discussion of standard matching techniques (Section 1.2.4), the possible use of circuits connecting the element feedlines behind the aperture was not considered. However, this technique has been recognised, and assessed theoretically and experimentally (20, 36, 37, 38). Its principal advantage over other techniques is the scan-dependent effect of such circuits on element impedance (Fig.1.10). A limiting case, of course, is the theoretical model used by Hannan to establish the possibility of "perfect" matching (20). The use of transmission lines behind a conventional array aperture is postulated as a method of interconnecting remote elements. This format has been investigated for dipole arrays with coaxial feed-lines (36). By restricting interconnections to adjacent elements only (Fig.1.11a), Amitay has demonstrated that a very significant improvement in active match can be obtained by assuming lumped reactances at a single point in the feed lines (Fig.1.11b) (37). For a planar array of square waveguides, the calculated radiation efficiency exceeds 95% over a substantial portion of a 45° conical scan sector if all the parameters shown in Fig.1.11 are optimised through a computer programme. (This figure drops rapidly, however, to < 70% in the E-plane.) Sidewall coupling using a single tuned Bethe-hole between the central element and each of its immediate eight neighbours has been investigated experimentally at Bell Telephone Laboratories (38). Measurements were made on square grid arrays with as many as 19 X 19 elements. Assuming that the coupling between neighbours can be altered without affecting the rest of the elements, the measured radiation efficiency exceeds 95% over most of a conical scan region with $\theta_{o,max} = 45^{\circ}$, and 80% in the E-plane.

The design technique discussed in this thesis can also be interpreted as a method of providing element interconnection with reactive circuits. For comparative purposes, two important aspects of the work in references 20, 36, 37 and 38 should be noted.

(i) The essential character of the radiating elements remains unaltered, and the matching circuits are actually used to create a second discontinuity in the feed lines to cancel the effects at the aperture plane. This affords no control of the element pattern, and the inherent separation of the two discontinuities leads to bandwidth limitations.

(ii) The interconnecting circuits have been represented as lumped reactances or transmission lines. The possibility of continuously distributed element coupling has not been discussed.

It is considered that these factors may have affected the viability of the connecting circuit technique and it has yet to gain practical acceptance.

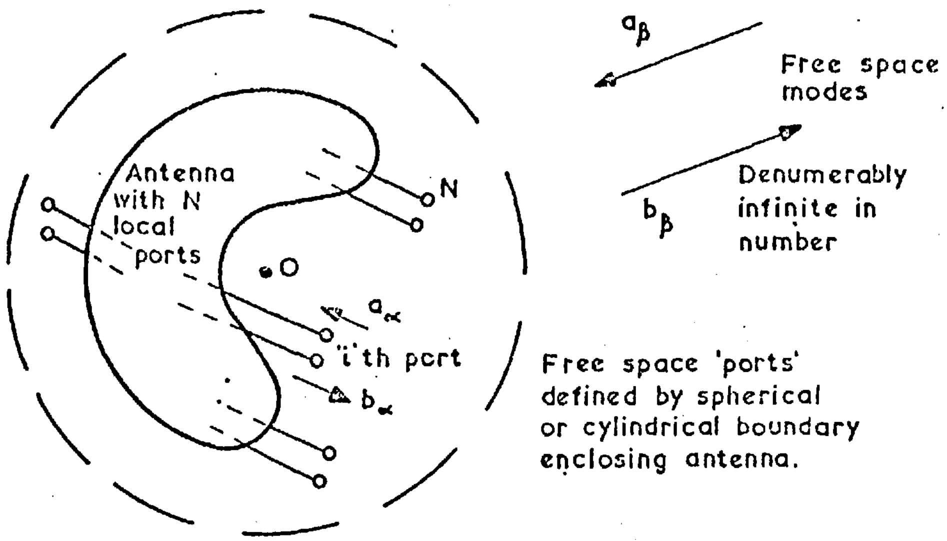

In general

$$\begin{bmatrix} b_\alpha \\ \hline b_\beta \end{bmatrix} = \left[\begin{array}{c|c} S_{\alpha\alpha} & S_{\alpha\beta} \\ \hline S_{\beta\alpha} & S_{\beta\beta} \end{array}\right] \begin{bmatrix} a_\alpha \\ \hline a_\beta \end{bmatrix}$$

In transmission : $[a_\beta] = 0$

$$[b_\alpha] = [S_{\alpha\alpha}][a_\alpha]$$

$$[b_\beta] = [S_{\beta\alpha}][a_\alpha]$$

$[S_{\alpha\alpha}]$ describes the mutual coupling among local ports

$[S_{\beta\alpha}]$ describes the modal radiation pattern

In reception : $[a_\alpha] = 0$ if all local ports are matched.

$$[b_\alpha] = [S_{\alpha\beta}][a_\beta]$$

$$[b_\beta] = [S_{\beta\beta}][a_\beta]$$

$[S_{\alpha\beta}]$ describes the modal receiving pattern

$[S_{\beta\beta}]$ describes the modal scattering pattern

Fig. 1.1 Network representation of an arbitrary antenna

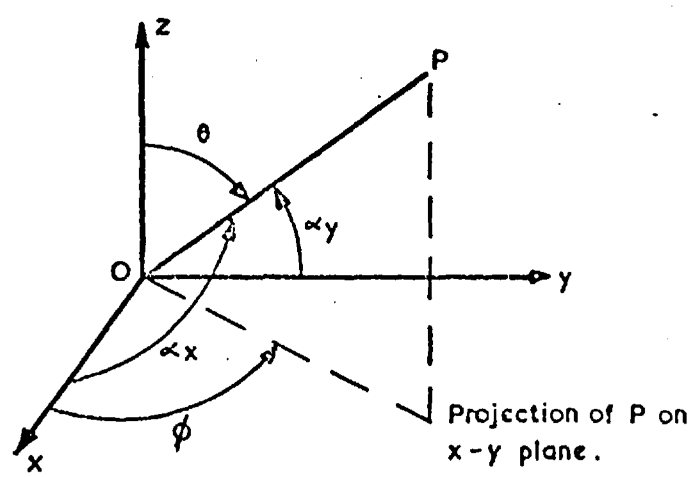

Fig. 1.2 Alternative co-ordinate systems

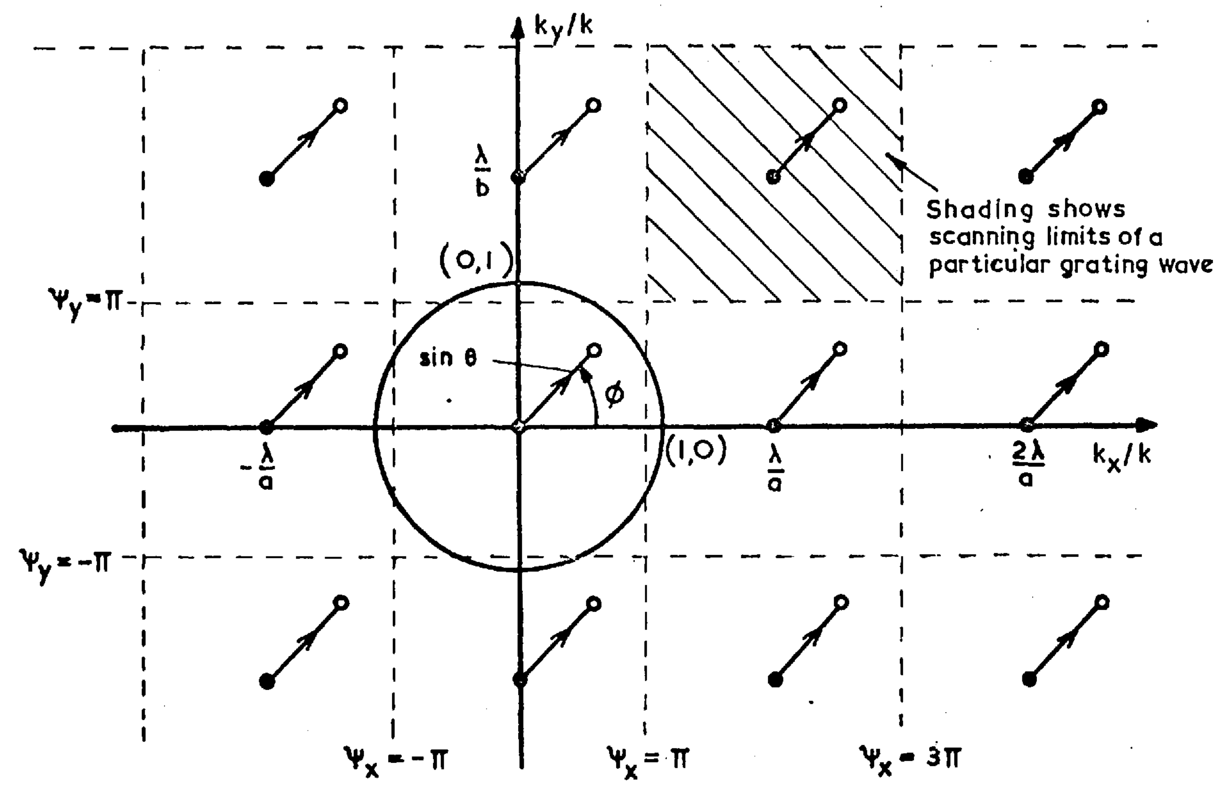

Code :- Unit circle defines visible region of space.
Chain lines define limits of scan for individual waves.
● = beam directions for unscanned array
O = beam directions for scanning at θ,φ
(Only the main beam is visible for example illustrated)

Fig.1.3 Grating lobe diagram assuming a = b = 0.573λ, showing a scanning condition off broadside

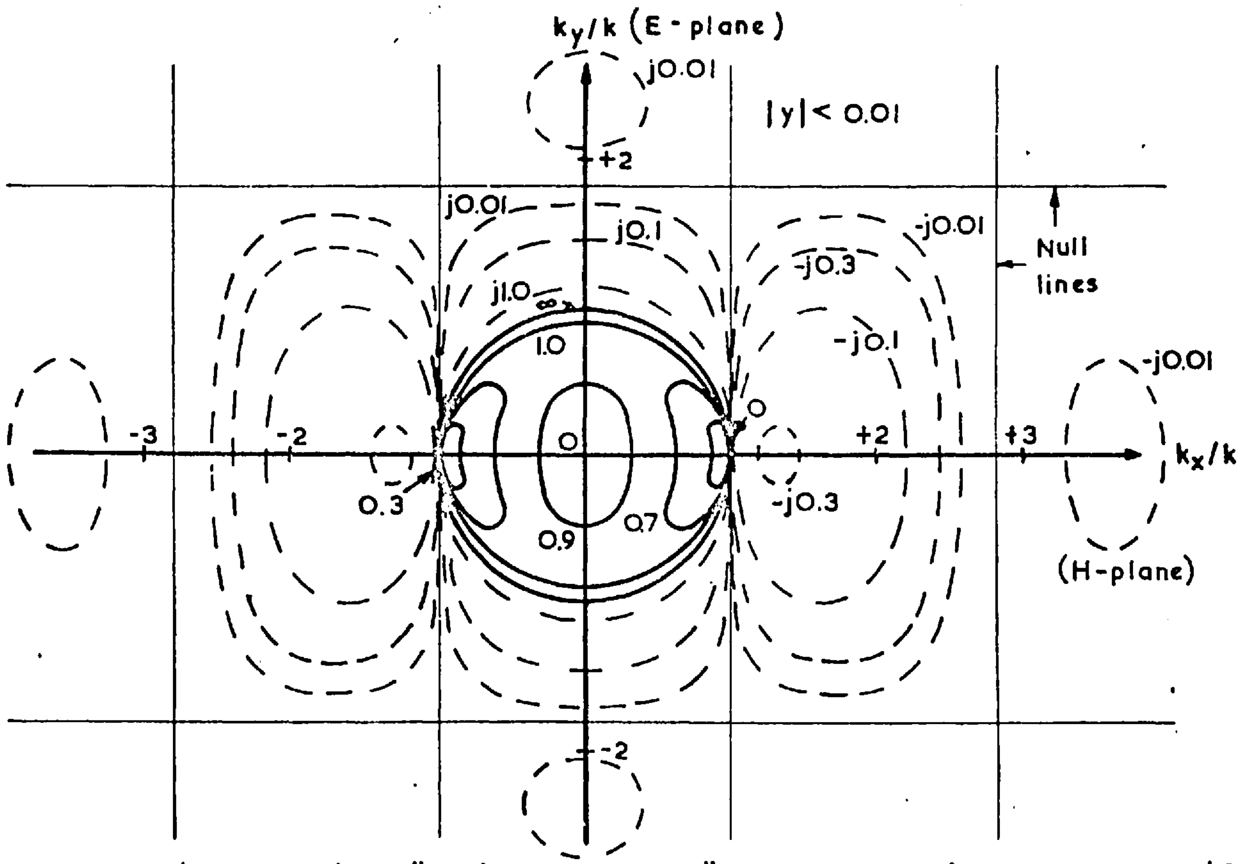

Fig. 1.4 Normalised "Admittance crater" for TE_{10} mode in square waveguide of dimensions 0.535λ (Diamond, reference 17)

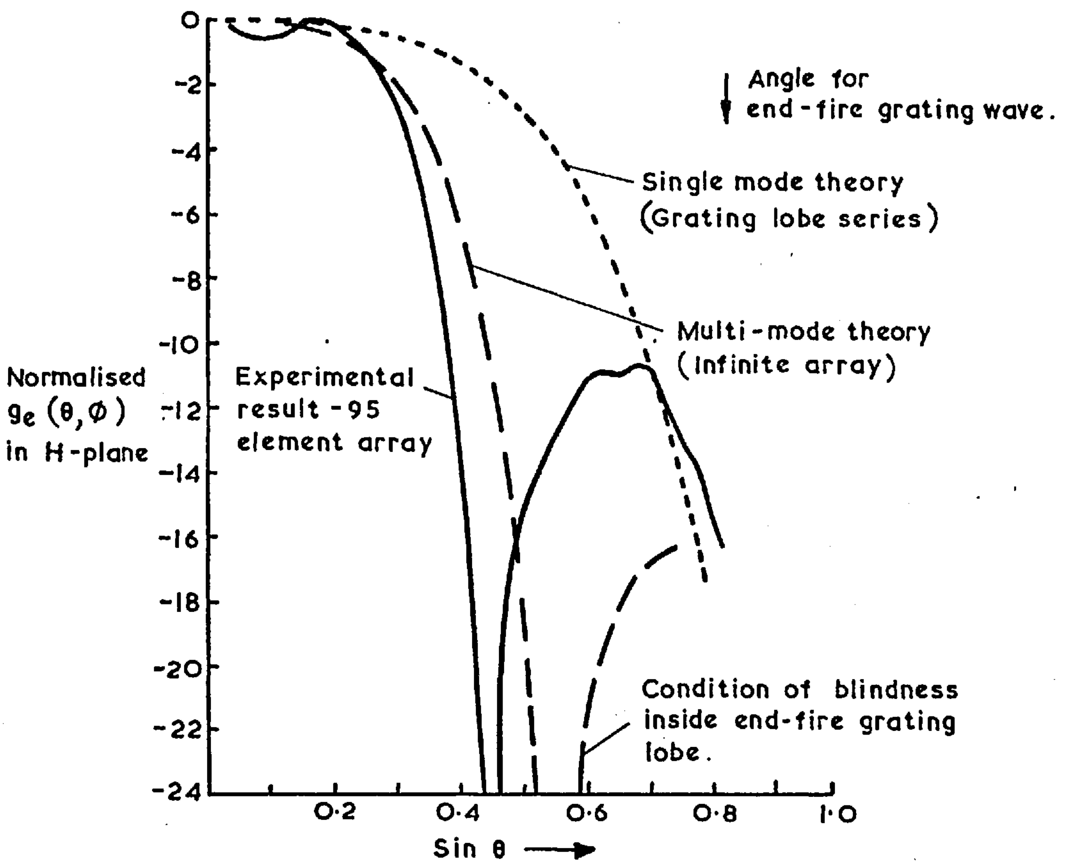

Fig. 1.5 Comparison of single and multi-mode analyses with experimental results in a waveguide array (Farrell and Kuhn - reference 23)

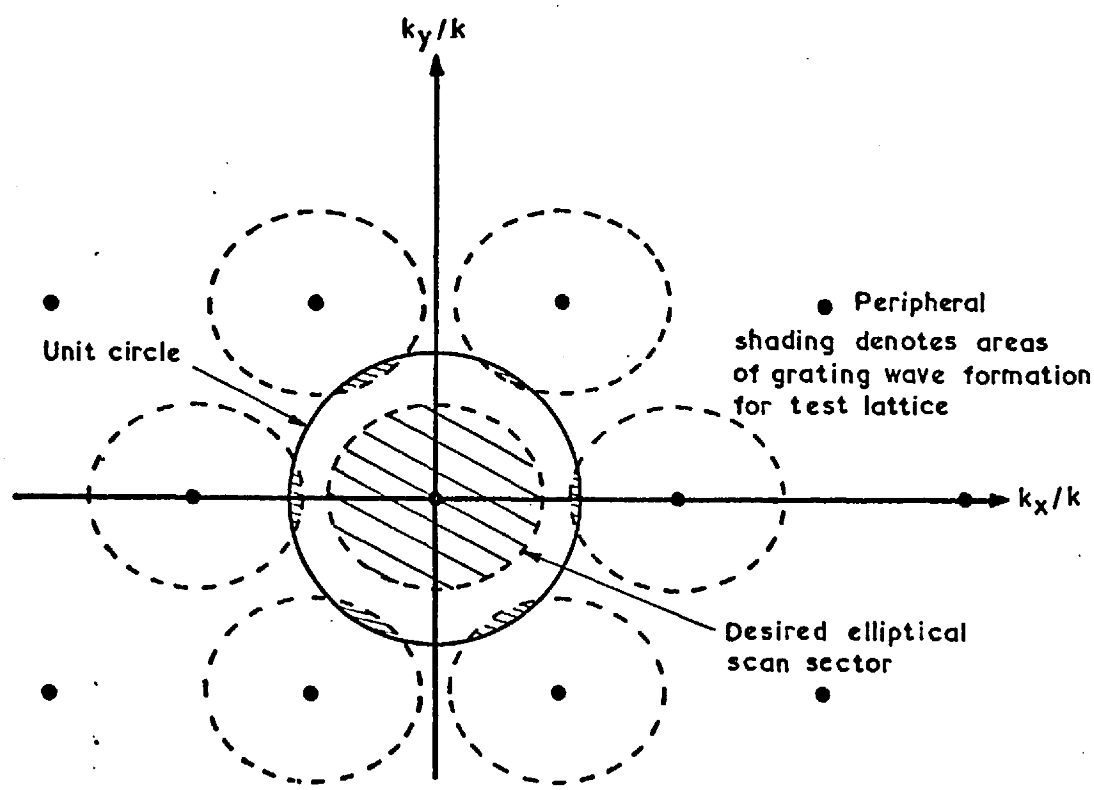

Code: ● = unscanned beam directions for a triangular lattice

Fig. 1.6 Modified grating lobe diagram for triangular element lattice showing grating wave radiation

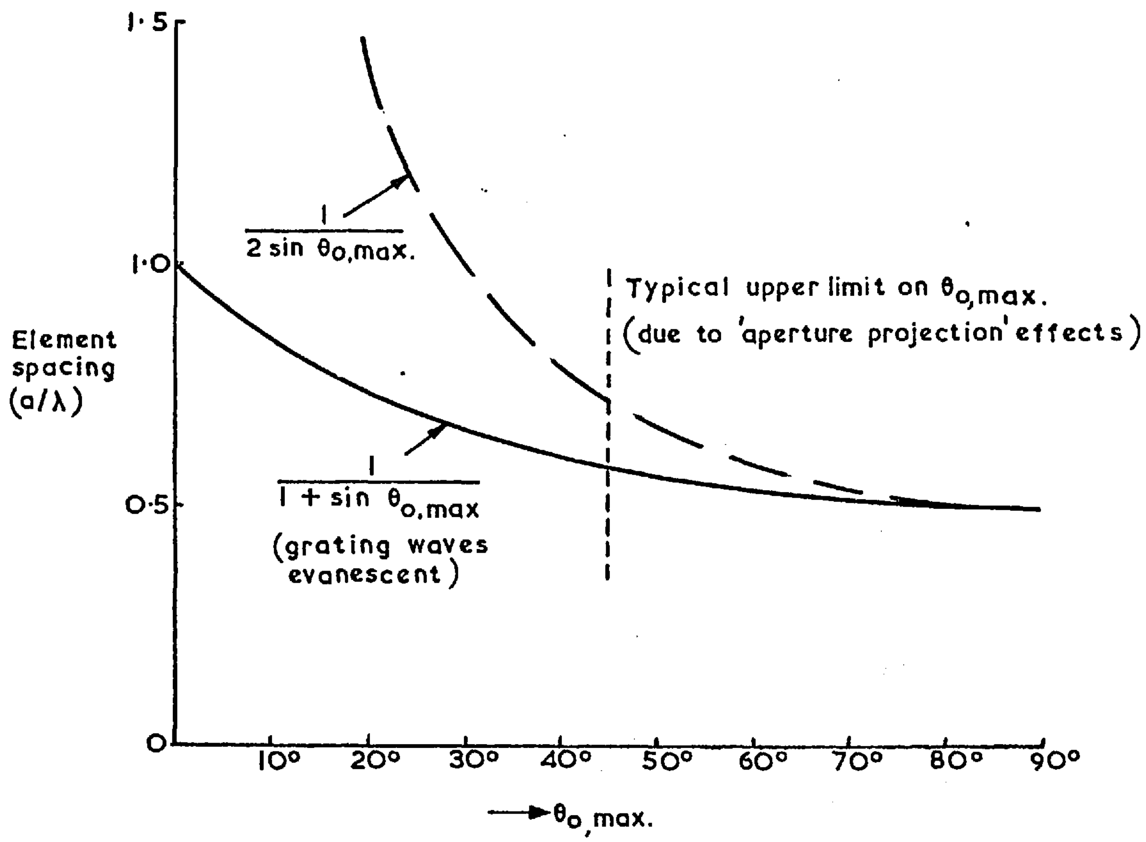

Fig. 1.7 Potential element saving with visible grating waves (for a linear array). For example, if $\theta_{o,max} = 30^{\circ}$, a/λ could be increased from 0.67 to 1.0.

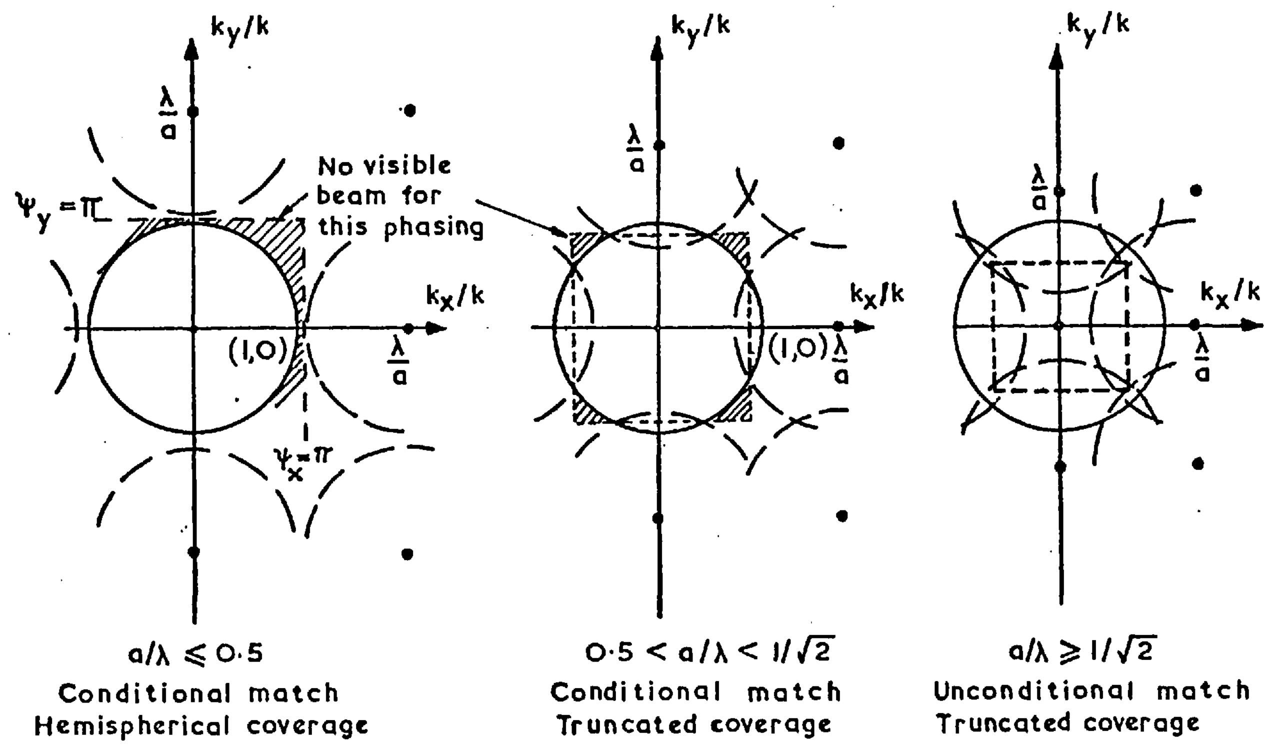

Fig. 1.8 Properties of an "ideal" planar array element in a square lattice

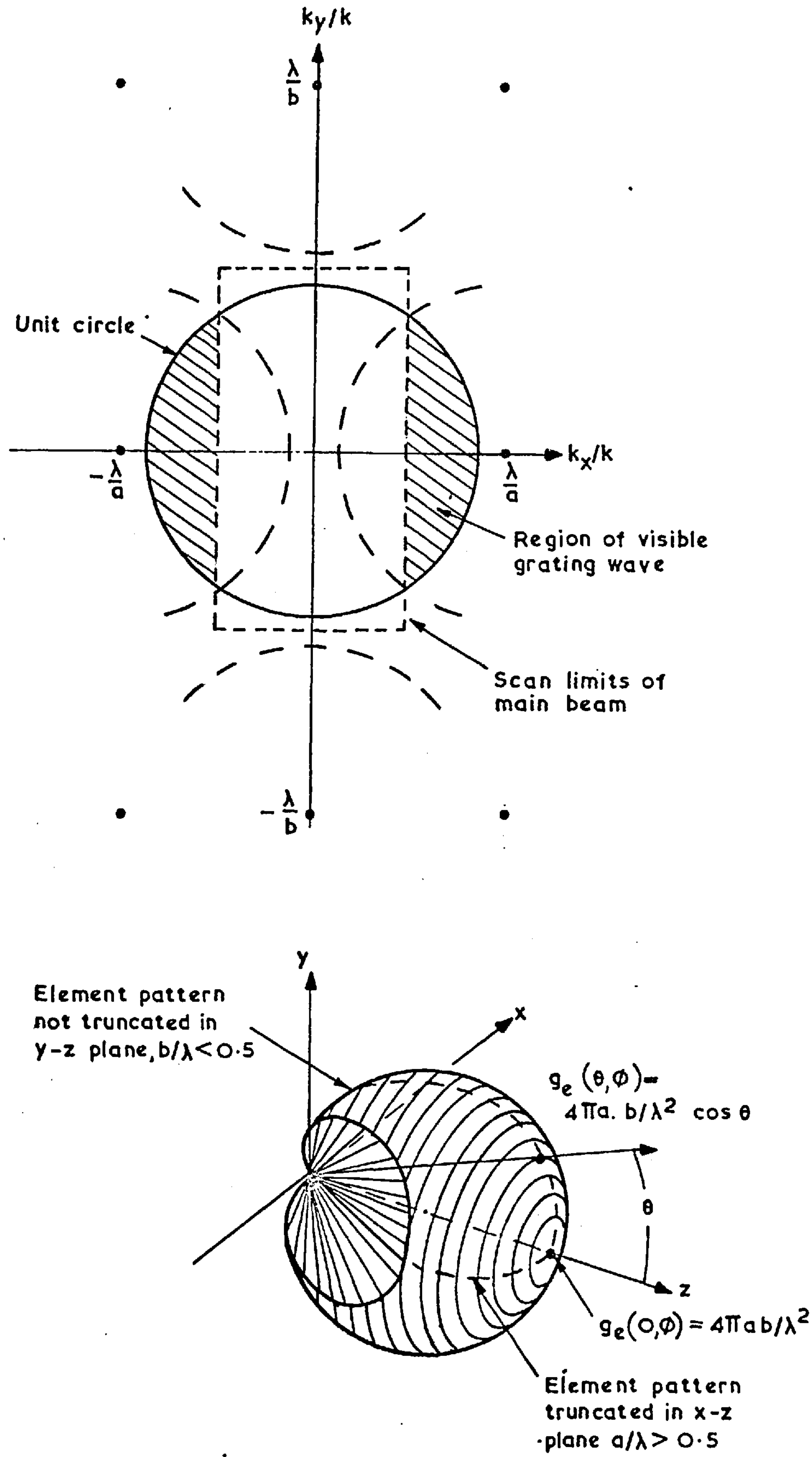

Fig. 1.9 "Ideal" element-gain pattern for specified rectangular array lattice ($b/\lambda < 0.5$, $a/\lambda > 0.5$)

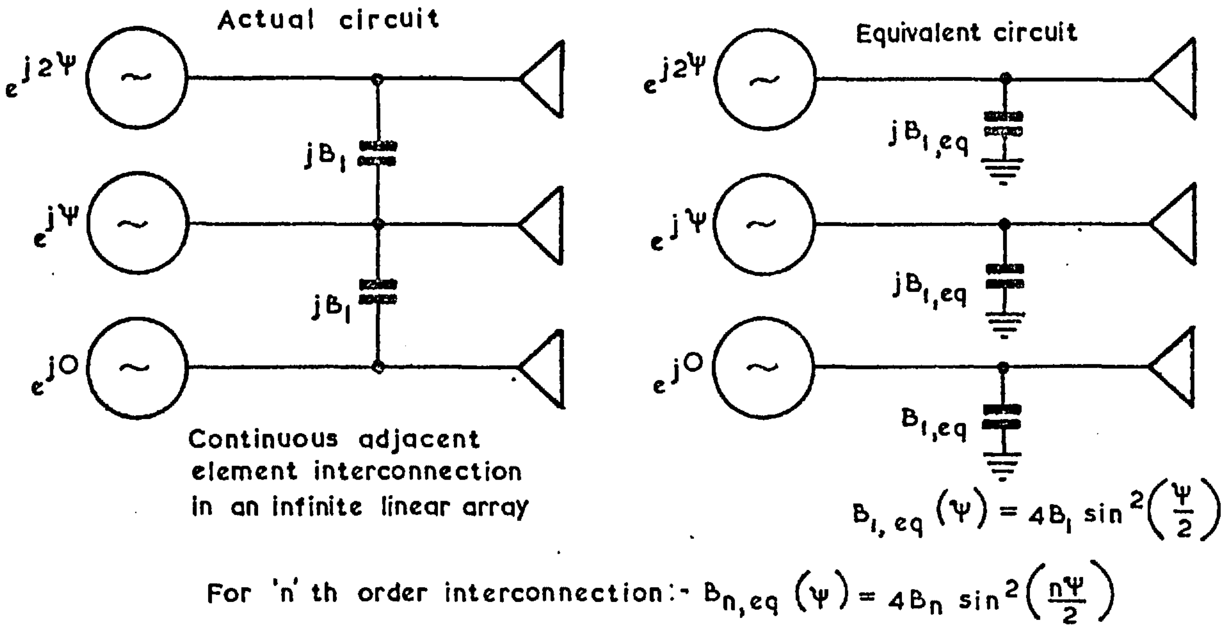

Fig. 1.10 Actual and equivalent connecting circuits in an infinite array (Hannan - reference 20)

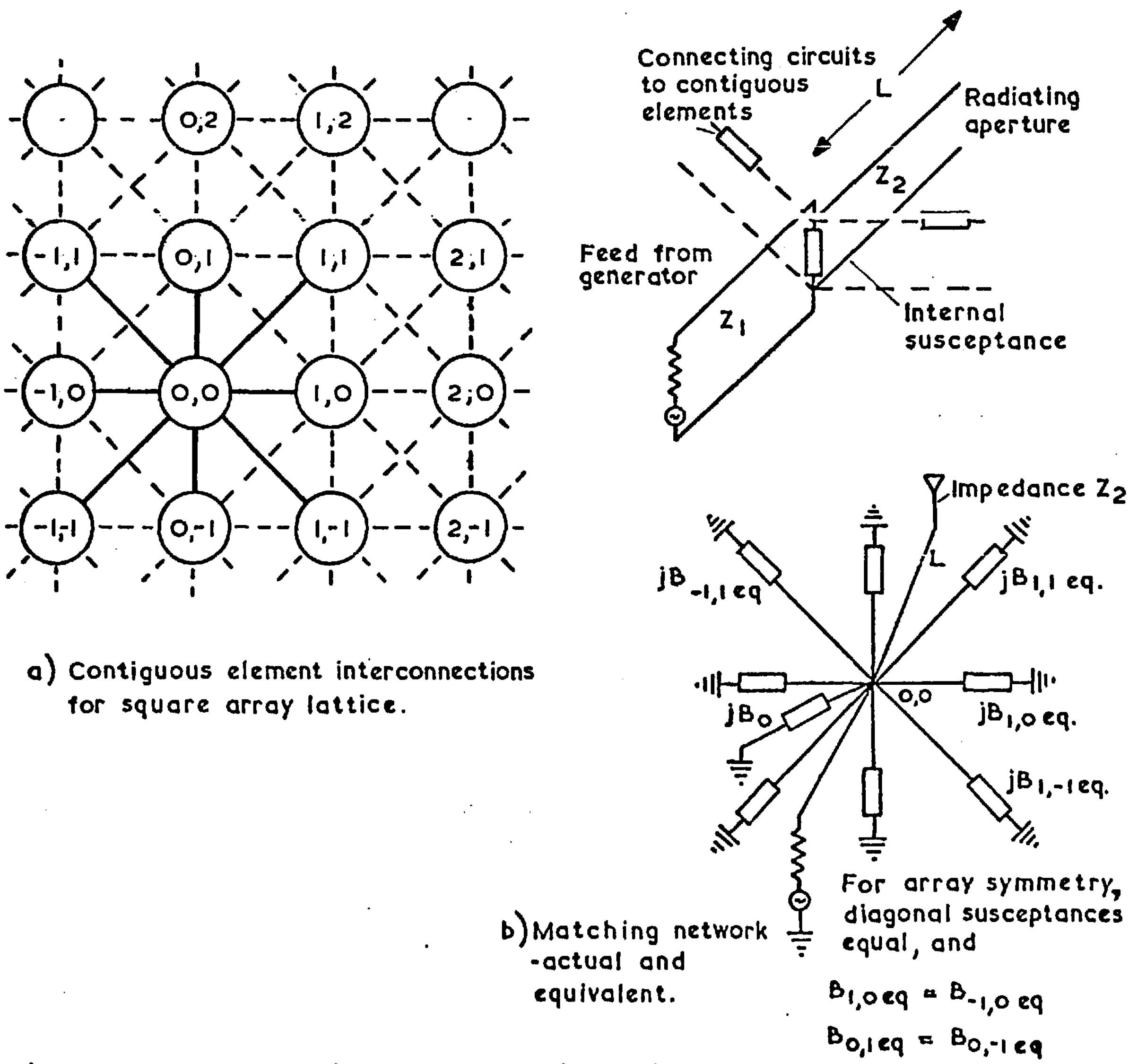

Fig. 1.11 Model for impedance matching using contiguous element coupling (Amitay - reference 37)

CHAPTER 2

PROPAGATION IN INFINITE ARRAYS WITH REACTIVE ELEMENT BOUNDARIES

2.1 Introduction

In this chapter, a theoretical study is made of propagation in large array structures with reactive element boundaries. For the purpose of this thesis, it is valid to regard these boundaries as extensions of the conducting sidewalls between the waveguide elements of conventional array feeds. This interpretation does not restrict the generality of the analysis, but simply anticipates the proposed applications. The potential advantages afforded by the use of these structures in electronically scanned arrays is illustrated by considering array performance in the two principal planes of scan - viz the H- and E-planes.

A number of assumptions are made to facilitate the analysis.

(i) The array structure is considered to be of infinite size and periodically excited (e.g. by a set of coherently phased oscillators) to permit the application of Floquet's theorem in the transverse plane. For practical arrays of finite dimensions, the analysis becomes invalid near an "edge", but otherwise approximates the nearly uniform behaviour of the bulk of the elements in a large array (cf. Chapter 1). The problem of "edge behaviour" is considered in Chapter 3 as part of the feasibility investigation.

(ii) The element boundaries are assumed to be uniform reactive surfaces of zero thickness. In later work, it is shown that practical reactive boundaries (e.g. metallic structures which modify the fields in their immediate vicinity) are periodic in the axial direction, and the presence of axial space harmonics must be considered. At this stage, it is sufficient to note that similar assumptions of uniformity have been made previously in the analyses of corrugated waveguides (41) and artificial dielectrics (42). The close relationship between studies in the latter topic and the current work is demonstrated in Section 2.4.

(iii) The properties of each reactive boundary are assumed invariant as the element spacing is modified. This can only be achieved when the reactive coupling between adjacent boundaries is negligible. An element spacing of the order of half a wavelength or more would normally be satisfactory. For practical structures, this assumption is closely linked with (ii) above.

(iv) Only those problems which can be solved assuming scalar fields are analysed in detail in this chapter. For linear waveguide arrays, the analyses are strictly appropriate to parallel plate structures only, although the conditions under which this can be relaxed in each polarisation are explained in the following sections and in Chapter 3. For planar waveguide arrays with zero wall thickness, the assumptions correspond to excitation in the H- and quasi E-planes (43).

(v) In the basic analysis of Sections 2.2 and 2.4, axial discontinuities are assumed to be remote from the region in which the field solutions are obtained. The problem of an axial discontinuity in the boundary reactance is analysed in Chapter 4.

(vi) The structures are assumed to be lossless.

In relation to Chapter 1, this theoretical model immediately introduces an array structure with inherent element to element coupling. The following analysis also demonstrates a fundamental relationship between several performance parameters which are often taken to be independent (e.g. as described in Section 1.3). This relationship covers impedance matching, grating lobe formation, polarisation control and even bandwidth.

2.2 Propagation in a Region of Constant Boundary Reactance - H-plane Scan

2.2.1 Derivation of the Characteristic Equation

The theoretical model in Fig. 2.1 shows part of the infinite two-dimensional uniformly excited array with co-ordinate axes as shown and the electric field restricted to the y-direction.

$$\text{i.e. } \underset{\sim}{E} = E_y \hat{a}_y \qquad \ldots.(1)$$

The phase increment ψ_h between array elements can be assumed positive without any loss of generality in view of the symmetry of the field solutions about the broadside scanning condition (when $\psi_h = 0$). As stated in Chapter 1, it is necessary to restrict ψ_h to the range $|\psi_h| < \pi$ to ensure consistent definition of the dominant and higher order "modes" of propagation (yet to be described).

The reactive surface between adjacent elements ensures that the tangential electric field is continuous and, in general, finite across the boundaries of each unit cell of the array. It is convenient to characterise the reactive boundaries in terms of their susceptance (b_h) normalised with respect to the plane wave admittance $(\varepsilon|\mu)^{\frac{1}{2}}$ of the medium in which the surfaces are located. This susceptance can be related to the magnitudes of the tangential electric and magnetic fields as shown below.

The general vector wave equation for the electric field within any unit cell of the structure in Fig. 2.1 can be reduced to the scalar form

$$\frac{\partial^2 E_y}{\partial x^2} + \frac{\partial^2 E_y}{\partial z^2} + \omega^2 \mu\varepsilon E_y = 0 \qquad \ldots.(2)$$

Since the field E_y is also periodic in the overall structure, separated solutions of the general form

$$E_y = \{A\exp[-jk_x(x-ra)] + B\exp[+jk_x(x-ra)]\}.\exp(-jk_z z).\exp(-jr\psi_h) \ldots.(3)$$

can be expected in the unit cell defined by $(2r-1)a/2 < x < (2r+1)a/2$, where r is any integer. To satisfy eqn.(2), it is necessary that

$$k_x{}^2 + k_z{}^2 = k^2 = \omega^2\mu\varepsilon \qquad \ldots.(4)$$

At this stage, either k_x or k_z can take an imaginary value, although complex values (requiring exponential growth in either the positive or negative x-direction) are precluded by the principles of power conservation within an infinite lossless structure. A and B are unknown amplitude factors which are not independent of each other, and can be normalised on the basis of power flow (as shown later).

The only other field components in the structure are H_x and H_z, which can be obtained directly from Maxwell's equations:

$$H_x = \frac{1}{j\omega\mu}\frac{\partial E_y}{\partial z} \quad ; \qquad \ldots.(5a)$$

$$H_z = \frac{-1}{j\omega\mu}\frac{\partial E_y}{\partial x} \qquad \ldots.(5b)$$

Discrete values for k_x, k_z and B/A can be obtained by applying the boundary conditions to the general solution given by eqn.(3), and solving the resulting equation in one of the unknowns (which is chosen to be k_x). The main steps in this procedure are supported where necessary by the detailed analyses given in Appendix 2A.

In the transverse (or x-) direction, the overall structure can be regarded as a periodically loaded transmission line. The effective (or composite) propagation constants k_{xc} (44) in this direction are determined by the imposed excitation of the structure, and are given by

$$k_{xc} = (\psi_h + 2n\pi)/a \quad ; \quad n = 1,2,3,\cdots \qquad \ldots.(6)$$

(It must be emphasised that k_x, as defined in eqn.(3), does not represent a composite propagation constant within the overall structure, since it is a quantity defined only within a unit cell. By contrast, k_z does represent the overall propagation constant in the z-direction.) With respect to the x-direction, "transverse" field components E_y and H_z can be compared directly with voltage and current respectively on a periodically loaded parallel-wire line (Fig. 2.2).

Continuity of the transmission line voltages at each shunt susceptance in Fig. 2.2 is directly analogous to the continuity of E_y, which can be expressed explicitly as follows:

$$E_y|_{x=(2r+1)a/2-\delta} = E_y|_{x=(2r+1)a/2+\delta} \text{ as } \delta \to 0 \qquad \text{....(7)}$$

Similarly, the discontinuity in current at x = 2(r+1)a/2 in Fig. 2.2 can be compared with the boundary conditions in terms of H_z, viz

$$H_z|_{x=(2r+1)a/2+\delta} - H_z|_{x=(2r+1)a/2-\delta} = -J_y|_{x=(2r+1)a/2} \text{ as } \delta \to 0 \qquad \text{..(8)}$$

The negative sign is required to maintain consistency with vector operators. The equivalent reactance of each y-directed current sheet can then be defined in a manner consistent with the transmission line analogy as follows:

$$jX_h = \left.\frac{E_y}{J_y}\right|_{x=(2r+1)a/2} \qquad \text{....(9)}$$

(X_h is not normalised with respect to $(\mu/\varepsilon)^{\frac{1}{2}}$.)

Substituting the general solution for E_y (eqn.(3)) in eqn.(7) gives the result

$$\frac{B}{A} = \frac{\exp(jk_x a) - \exp(j\psi_h)}{\exp[j(k_x a+\psi_h)] - 1} \qquad \text{...(10)}$$

which can be reduced to the equivalent real forms

$$\frac{B}{A} = \frac{\cos\psi_h - \cos(k_x a)}{1 - \cos(k_x a + \psi_h)} = \frac{1 - \cos(k_x a - \psi_h)}{\cos\psi_h - \cos(k_x a)} \qquad \text{...(11)}$$

$$= \frac{\sin[(k_x a - \psi_h)/2]}{\sin[(k_x a + \psi_h)/2]} \qquad \text{...(12)}$$

as shown in Appendix 2A, Section (i) if $k_x a$ is real.

Substituting the general solution in eqn.(8) and utilising eqns.(5b),(9) and (10), the characteristic equation governing propagation within any unit cell of the structure can be obtained. Retaining the same parameters, it can be shown after some manipulation (Appendix 2A, Section (ii)) that

$$\frac{\omega\mu}{2X_h} \cdot \frac{\sin(k_x a)}{k_x} + \cos(k_x a) - \cos(\psi_h) = 0 \qquad \ldots(13)$$

By multiplying the first term by $a\sqrt{\varepsilon}$ on the top and bottom lines, it follows that the characteristic equation can be expressed in the form

$$K_h \cdot \frac{\sin(k_x a)}{k_x a} + \cos(k_x a) - \cos(\psi_h) = 0 \qquad \ldots(14)$$

where $K_h = \pi \cdot \frac{a}{\lambda} \cdot -b_h$ and $b_h = -(\mu/\varepsilon)^{\frac{1}{2}}/X_h$.

The normalised susceptance b_h is shown to be a powerful unifying parameter in subsequent work. Equation (14) is valid in a free space region (where $b_h = 0$) and reduces to

$$\cos(k_x a) = \cos(\psi_h) \qquad \ldots(15)$$

which has positive solutions

$$k_x a = 2n\pi \pm \psi_h \text{ with } n = 0, 1, 2, \ldots. \qquad \ldots(16)$$

Similarly, values for $k_x a$ as $b_h \to \pm \infty$ (corresponding to a waveguide array) can be found by solving the reduced equation

$$\frac{\sin(k_x a)}{k_x a} = 0 \qquad \ldots(17)$$

which has positive solutions

$$k_x a = n\pi \; ; \; n = 1, 2, 3, \ldots. \qquad \ldots(18)$$

For other values of b_h, solutions to eqn.(14) can not be obtained analytically, and must therefore be found numerically. This is investigated in the next section. All of these forms of the characteristic equation are seen to be symmetrical in $k_x a$. The choice of positive values only in eqns.(16) and (18) resolves any ambiguity associated with negative values of ψ_h and gives all the independent solutions. In the next section, therefore, where ψ_h is always assumed positive, only positive values of $k_x a$ are of interest.

2.2.2 <u>Solutions of the Characteristic Equation</u>

Taking a/λ, b_h and ψ_h as parameters, it is now possible to find a set of discrete solutions for $k_x a$ from eqn.(14). These solutions, of course, only apply within each unit cell when all the adjacent elements of the structure are excited in a uniform periodic fashion. In particular, the solutions would not hold if only a single element were excited at some point within the structure, or if the unit cell were removed from the array environment. (These restrictions do not apply to the propagation characteristics of the conventional element in a waveguide array).

As a preliminary step, it is convenient to split the solutions of eqn.(14) into two categories, characterised respectively by real and imaginary values of k_x. In the latter case, let

$$k_x = j\gamma_x \qquad \ldots(19)$$

Then two equations in real variables have to be solved for the two cases, viz:-

$$K_h \frac{\sin(k_x a)}{k_x a} + \cos(k_x a) = F_1(k_x a) = \cos(\psi_h) \qquad \ldots(20)$$

and $$K_h \frac{\sinh(\gamma_x a)}{\gamma_x a} + \cosh(\gamma_x a) = F_2(\gamma_x a) = \cos(\psi_h) \qquad \ldots(21)$$

For eqn.(21), B/A is complex, and is given by a relation readily derived from eqn.(11), viz

$$\frac{B}{A} = \frac{1 - \cos(\psi_h).\ \cosh(\gamma_x a) - j\sin(\psi_h).\ \sinh(\gamma_x a)}{\cos(\psi_h) - \cosh(\gamma_x a)} \qquad \ldots(22)$$

Solutions to eqns.(20) and (21) depend on the value assigned to the phase increment ψ_h, which takes continuously adjustable values within the range

$$|\psi_h| \leqslant 2\pi.\frac{a}{\lambda}.\sin\theta_{o,max} \qquad \ldots(23)$$

for electronic scanning applications, where $\theta_{o,max}$ is the maximum main beam scan angle with respect to broadside. Although it is not necessary to restrict the values of a/λ in this section, it can be assumed, however, that attention will eventually be focussed on the range $0.5 < a/\lambda < 1.0$, where the limits correspond to the TE_{10} and TE_{20} cut-off conditions respectively in a conventional waveguide feed element. In Fig. 2.3., standard graphs have been plotted showing the variation of θ_o with ψ_h for different values of a/λ in this range. Following the discussion in Chapter 1, symmetrical scan limits $\theta_{o,max}$ of less than 45^o from broadside will be important in later work.

In Figs. 2.4. and 2.5., the functions $F_1(k_x a)$ and $F_2(\gamma_x a)$ (as defined in eqns.(20) and (21)), have been plotted for representative values of K_h. It should be noted that a positive value of K_h corresponds to a negative value of b_h - i.e. inductive current sheets. Conversely, a negative value of K_h implies capacitive surfaces. In view of the inherent limits on $\cos \psi_h$, viz $-1 \leqslant \cos \psi_h \leqslant +1$, a study of Figs. 2.4. and 2.5 indicates that the type of reactive surface also sets important restrictions on the nature of the roots of eqn.(14). At this point, therefore, the analysis can be simplified by recognising that all possible solutions of the H-plane characteristic equation must fall into one of the following four categories:

(i) k_x real and b_h inductive

(ii) k_x real and b_h capacitive

(iii) k_x imaginary and b_h inductive

(iv) k_x imaginary and b_h capacitive.

These four categories are now considered separately. The particular case where $b_h = \psi_h = 0$ should be excluded.

<u>Category (i)</u>: Referring to Fig. 2.4., it can be seen that an infinite number of roots are obtained when K_h is positive. For all values of a/λ and ψ_h, the characteristic equation has discrete first order roots with one value in each range $n\pi < k_x a \leqslant (n+1)\pi$, where n can be zero or any positive integer. In common with the propagation characteristics of a closed cylindrical waveguide, not all of these

roots correspond to propagating modes in the axial direction. From eqn. (4), it follows that k_z is real only if $ka > k_x a$

$$\text{i.e.} \quad 2\pi \frac{a}{\lambda} > k_x a \qquad \ldots(24)$$

This additional information is included in Fig. 2.4., and serves to emphasise the analogy with the propagation behaviour of closed waveguides over a frequency band. In subsequent chapters, modes with k_x and k_z real will be regarded as propagating, and the remainder with k_x real and k_z imaginary will be termed evanescent. The importance of this set of modes (where b_h is inductive) will become evident as the solutions for the other three categories are examined.

If it is assumed that the value of element spacing a/λ lies within the preferred range of waveguide sizes, then at least one, and not more than two, solutions are obtained for which k_z is real. The conditions determining whether or not the second mode will propagate axially can be linked with those governing the formation of a visible grating lobe in free space. For a given value of ψ_h, a critical susceptance b_{hc} can be found which ensures that the second mode is just cut-off. From eqns.(14) and (24),

$$b_{hc} = \frac{2\{\cos(2\pi\ a/\lambda) - \cos\psi_h\}}{\sin(2\pi\ a/\lambda)} \qquad \ldots(25)$$

If $b_{hc} = 0$ (i.e. free space) then the standard condition for the formation of an end-fire grating lobe is obtained, viz

$$\cos(2\pi\ a/\lambda) = \cos\psi_h \qquad \ldots(26)$$

or, in particular,

$$\psi_h = 2\pi(1 - a/\lambda) \qquad \text{(cf. Chapter 1)}$$

For given ψ_h and a/λ, b_{hc} is always inductive if a visible grating lobe would be formed in free space i.e. if $\psi_h > 2\pi(1 - a/\lambda)$.

Further insight is afforded by considering some specific examples of the amplitude and phase distributions within the structure at any plane z = a constant. Taking $a/\lambda = 0.7$, $\psi_h = 120^\circ$ and $K_h = 1$

(i.e $b_h = -0.455$), eqn.(20) can be solved by standard numerical techniques (e.g. Newton's rule). Only a single value of $k_x a$ (= 2.4407) is obtained which satisfies the inequality condition in eqn.(24). With the possible exception (yet to be considered under category (iii)) of a solution with $k_x a$ imaginary, the structure can therefore be considered single moded under these conditions. Substituting in eqn.(11), or using a previously compiled reference chart such as Fig. 2.6, the value of B/A is found to be 0.225. The amplitude and phase distribution can then be plotted (Fig. 2.7a) since all terms in eqn.(3) have been specified.

This field distribution can be compared with the corresponding dominant mode distribution in an infinite waveguide array (Fig. 2.7b). It is evident that the peak to peak variations in both amplitude and phase are substantially smaller with the finite susceptance boundaries. Such a comparison gives the first specific indication of the connection between the analysis in this chapter and the phased array problems discussed in Chapter 1. Anticipating the results to be presented in Chapter 4, it can be appreciated at this stage that the amplitudes of the grating lobes in free space (whether propagating or evanescent) would be reduced if incident field distributions similar to that in Fig. 2.7a were obtained within a (modified) aerial feed.

A significant one-to-one relationship can also be demonstrated between the modes in a region of small inductive susceptance and the "modes" in free space. The dominant and first higher order modes in the latter case correspond to the main beam and first grating lobe respectively. The basic similarities in the amplitude and phase distributions can again be illustrated with an example.

Taking $a/\lambda = 0.695$, $\psi_h = 140^\circ$ and $b_h = -0.4$, two propagating modes are obtained having the distributions shown in Fig. 2.8. With $b_h = 0$, both free space modes, of course, have constant amplitude and linear phase. The dominant mode distributions for these two values of b_h are nearly the same, while a similar (but not as well matched) relationship is evident between the two higher order modes.

Further discussion of these modes will be suspended until the other three categories of solutions have been examined.

Category (ii): With capacitive element boundaries, it is evident from Fig. 2.4 that a solution for $k_x a$ does not necessarily exist in the range $0 < k_x a \leqslant \pi$ - i.e. in the range of the "dominant" mode using the classification above. Solutions can always be found for $k_x a$ in any other range given by $n\pi < k_x a \leqslant (n + 1)\pi$, $n = 1, 2, 3,\ldots$ If attention is restricted to values of $a/\lambda > 0.5$, and a root of eqn.(20) does exist with $k_x a < \pi$, then $k_x a \to 0$ as b_h increases to a critical value. This value does not determine a "cut-off" condition in the normal sense, but a limit on the range of b_h for which fast wave solutions (i.e. $k_z < k$) can be obtained. From eqn.(20), it is seen that

$$K_h = \cos \psi_h - 1 \qquad \ldots(27)$$

when $k_x a = 0$. This equation can be expressed as

$$b_h = \left(\frac{1 - \cos \psi_h}{\pi}\right) \frac{1}{a/\lambda} \qquad \ldots(28)$$

From eqn.(27), it is evident that no solution can be found, for any value of ψ_h, if $K_h < -2$. Eqn.(28) indicates that the normalised susceptance for this limit condition varies inversely with a/λ, assuming ψ_h is fixed. In general, therefore, solutions can be obtained with $k_x a < \pi$ if

$$b_h < \left(\frac{1 - \cos \psi_h}{\pi}\right) \frac{1}{a/\lambda} \qquad \ldots(29)$$

The amplitude and phase distributions of the two propagating modes obtained when $K_h = -1$ (with $a/\lambda = 0.7$ and $\psi_h = 120^{\circ}$) are shown in Fig. 2.9. The value of $k_x a$ for the dominant mode is always $< \psi_h$ when the current sheets are capacitive, which contrasts with a value always $> \psi_h$ (and $< \pi$) for the examples considered under category (i) above.

In view of the restriction imposed by relation (29) and further illustrated by the discussion of category (iv) solutions, H-plane propagation in aerial structures with capacitive element boundaries will not be of interest in subsequent work.

Category (iii): As shown by Fig. 2.5., no solutions of eqn.(21) can be found when b_h is inductive, since $F_2(\gamma_x a)$ is inevitably > 1 when $K_h > 1$. This result is extremely important in the proposed aerial applications and enhances the significance of category (i) solutions. It is now apparent that references to "single-moded" or "dual-moded" conditions in the discussion of category (i) solutions do not require qualification.

Category (iv): From Fig. 2.5., it is evident that a single solution for $\gamma_x a$ can be found for any value of ψ_h when $K_h < -2$. For $-2 < K_h < 0$, a solution can only be found over a restricted range of ψ_h with a limit value given by $\gamma_x a = 0$ as $b_h \to 0$. From eqn.(21), the corresponding value for K_h is given by

$$K_h = 1 - \cos \psi_h \qquad \ldots(30)$$

which is, as expected, the same as eqn.(27) occurring in the discussion of category (ii) solutions. The condition for a solution $\gamma_x a$ is different, however, since K_h here must be $< 1 - \cos \psi_h$.

Solutions for E_y obtained from eqn.(21) correspond to slow, surface-type waves supported on either side of each current surface. As K_h becomes more negative, these waves become more tightly coupled to the boundaries, and the complex expression for $B/A \to \exp(j\psi_h)$. The single solution obtained with any set of parameters a/λ, ψ_h and b_h ensures that the total number of roots of eqn.(14) is always the same.

From eqn.(30), it is evident that the occurrence of these axial slow waves cannot be avoided in a structure with capacitive surfaces when ψ_h is varied symmetrically about zero. In an aerial feed, such propagation would be undesirable, due to the matching problems with the waveguide feed elements and free space. Simultaneously, the peak to peak variations in the amplitude and phase distributions would be enhanced rather than reduced.

To conclude this discussion of the various categories of solutions, it is interesting to confirm that the possibility of T.E. - type slow waves on capacitive surfaces only is consistent with well known results (45).

2.2.3 Further "Modal" Properties

Several properties which will be utilised, either explicitly or implicitly in subsequent work, are derived below. Initially, however, the question of a standard nomenclature for identifying the modes should be considered.

In a region of low susceptance, the close relationship between the modes as defined in Section 2.2.2 and the space harmonics for an infinite linear array suggests that the same identification used for grating lobes might be adopted. The dominant mode could then be known as H_o, the next mode as H_{-1}, and the subsequent ones as H_{+1}, H_{-2}, H_{+2} ...... etc. This subscript sequence corresponds, of course, to the order in which grating lobes propagate as the element spacing in an array is increased.

As the susceptance becomes numerically large, an alternative method of classification H_1, H_2, H_3 ......, based on the similarities with conventional closed waveguides, also has merit. However, the disadvantage here lies in the fact that the mode which cuts off at $a/\lambda - \delta(\delta \to o)$ as $b_h \to -\infty$ is not strictly the same mode which cuts off at $a/\lambda + \delta$ as $b_h \to +\infty$, even though their field solutions both converge to the same result. (This is further amplified in the next section).

In general, the convention adopted in this thesis is to refer to the mode having a solution of the characteristic equation in the range $0 < k_x a \leqslant \pi$ (or with k_x imaginary if there is no solution in this range) as the "dominant" mode. A solution of eqn.(14) in the range

$\pi < k_x a \leqslant 2\pi$ then defines the second mode which, like all higher order modes, exists for any value of b_h. If attention is confined to structures with inductive current sheets, this procedure is indistinguishable from the classification of parallel plate waveguide modes.

Within any unit cell, the axial power flow (P) in a propagating mode can be found by integrating the z-directed component of the Poynting vector over the range $-a/2 < x < a/2$, assuming a dimension "b" in the y-direction. Then

$$P_n = \frac{b}{2} \operatorname{Re} \int_{-a/2}^{a/2} dx \, (\underset{\sim}{E}_n \times \underset{\sim}{H}^*_n) . \hat{a}_z \qquad \text{(n= integer defining the mode)} \qquad \ldots(31)$$

$$= \frac{b}{2} \operatorname{Re} \int_{-a/2}^{a/2} dx \, E_{yn} H^*_{xn} \qquad \ldots(32)$$

which, after substitution for E_{yn} and H_{xn} from eqns.(3) and (5a), and with $(k_x a)$ for the "n"th root given by

$$(k_x a)_n = a(k^2 - \beta_n^2)^{\frac{1}{2}}, \qquad \ldots(33)$$

gives the result

$$P_n = \frac{ab}{\omega\mu} \cdot \beta_n \cdot A_n^2 \left\{ 1 + \left(\frac{B_n}{A_n}\right)^2 + 2\left(\frac{B_n}{A_n}\right) \cdot \frac{\sin(a\sqrt{k^2-\beta_n^2})}{(a\sqrt{k^2-\beta_n^2})} \right\} \qquad \ldots(34)$$

(The subscripts indicate a particular solution). The third term within the outer brackets does not vanish unless

$$a\sqrt{k^2-\beta_n^2} = n\pi \qquad \ldots(35)$$

which would imply a conventional waveguide element. In general, therefore, the component waves $A_n \exp\left[-j(k_{xn}x + k_{zn}z)\right]$ and $B_n \exp\left[j(k_{xn}x - k_{zn}z)\right]$ of a particular mode are not orthogonal.

A normalisation can be introduced at this point which enables the independent field amplitude factor to be defined in terms of power flow.

From eqn.(34)

$$A_n = \left(\frac{\omega\mu}{ab}\right)^{\frac{1}{2}}\left\{\frac{\beta_n}{1 + (B_n/A_n)^2 + 2(B_n/A_n).\sin(a\sqrt{k^2-\beta_n^2})/(a\sqrt{k^2-\beta_n^2})}\right\}^{\frac{1}{2}} \quad ..(36)$$

for unit power flow in a cross section $-a/2 < x < a/2$, $0 < y < b$.

In lossless closed waveguides, general orthogonality relations can be demonstrated using the Lorentz reciprocity principle (46). The vanishing tangential electric field on the guide walls ensures that these results can be obtained efficiently. However, for arrays with reactive element boundaries, it can not be assumed that the tangential electric field is zero around the boundary of each unit cell. In Appendix 2B, therefore, an orthogonality condition is demonstrated for H-plane modes, from which it can be deduced that the total axial power flow in any unit cell of the structure is the sum of the power carried by each mode individually.

From energy conservation principles, it is obvious that the power flowing into the "r"th unit cell across the boundary $x=(2r - 1)a/2$ is equal to the power carried out across the boundary $x = (2r + 1)a/2$. This is assumed in Chapter 4, where the properties of an axial discontinuity in susceptance can be determined by finding the relative amplitude and phase of the modes excited on both sides of the discontinuity. The infinite set of modes form a complete set, and the tangential field can be accurately approximated in such problems by considering the first N modes (cf.23, 47).

2.3 Application to H-plane Scanning Arrays

It is now appropriate to investigate how the structures analysed in the previous section could be utilised in the feed of an electronically scanned array. To facilitate this process, two graphical aids are developed which will be referred to as "mode charts" and "velocity profiles". The discussion in this section is not restricted to structures with constant reactive current sheets. The engineering concept of a gradual transition region is introduced, in which it is assumed that the analysis of the previous section is valid if the boundary susceptance changes "sufficiently slowly" in the axial direction. A major objective in later chapters is to establish what this qualitative concept implies in terms of axial length.

2.3.1 Development and Utilisation of Mode Charts

The "mode charts" are design aids which indicate the number of propagating modes, as a function of the three effective parameters a/λ, b_h and ψ_h, in a form which is convenient for phased array applications. The completed charts can be readily appreciated, if the logic behind their development is considered for a particular mode.

In view of the various categories of solutions noted in Section 2.2.2, it is easier initially to examine the cut-off conditions for the second mode. As this mode is characterised by a value of $k_x a$ in the range $\pi < k_x a \leqslant 2\pi$, the element spacing to be considered (with $k_x a = ka$) must be $0.5 < a/\lambda \leqslant 1.0$. Choosing a/λ and b_h as the horizontal and vertical axes respectively, the locus of critical points can be plotted for a particular value of ψ_h. For inductive and capacitive element boundaries, this susceptance is defined by eqn.(25), which is repeated here

i.e $$b_{hc} = \frac{2\{\cos(2\pi a/\lambda) - \cos\psi_h\}}{\sin(2\pi a/\lambda)} \qquad \ldots(25)$$

and plotted in Fig. 2.10a assuming $\psi_h = \psi_{h,max} = 120^\circ$.

The region to the left of the locus (which includes, for example, the point P_1 in Fig. 2.10a with $b_h = -1$ and $a/\lambda = 0.6$) defines all conditions where the second mode is evanescent. Conversely, the shaded area, which extends indefinitely to the right of the locus in Fig. 2.10a, indicates the conditions for propagation when $\psi_h = 120^\circ$. In Fig. 2.10b, an alternative method of showing this region is adopted, with only a confined area of shading immediately adjacent to the locus.

For electronic scanning purposes, all values of ψ_h in the range

$0 \leqslant \psi_h \leqslant \psi_{h,max}$ should be considered. In Fig. 2.10b, a number of loci are plotted which show the variation in b_{hc} for this second mode as ψ_h is reduced in discrete steps. The locus most removed from the initial curve is obtained when $\psi_h = 0$. The two limiting cases ($\psi_h = 120^\circ$ and $\psi_h = 0$) effectively define three regions, viz

i) a region to the left of the locus L_1 in Fig. 2.10b which is always single moded,

ii) a region between the loci L_1 and L_2 which is single or dual moded as the scan condition is changed,

and iii) a region to the right to the locus L_2 which is always dual moded.

The curves L_1 and L_2 are sufficient, therefore to summarise these details in a comprehensive mode chart.

The cut-off conditions for the first mode can be obtained by restricting a/λ to values less than 0.5, and since eqn.(25) is also periodic (in increments of $a/\lambda = 1$ for a given value of ψ_h), the cut-off conditions for all the remaining modes can be deduced directly by shifting all loci, in the range $0 < a/\lambda \leqslant 1.0$ to the right by $n(a/\lambda)$, $n = 1,2,3 \ldots\ldots$ The result is shown in Fig. 2.11a, together with the dotted lines indicating the crossover conditions (eqn.(28))from fast to slow wave solutions for the first mode.

On this mode chart, a single moded region can be defined for all scan angles. In Fig.2.11a, this region has been shaded for emphasis. If a conventional waveguide array were operating with $a/\lambda = 0.65$, then the addition of an interface structure - with element boundaries of constant inductive susceptance (say $b_h = -1$) forming extensions of the sidewalls - would maintain these single mode conditions whilst reducing the fluctuations of the periodic incident field about a mean value (cf. Fig.2.7). The first grating wave would always remain evanescent, since the condition for an end fire grating lobe is given $a/\lambda = 0.667$ (when $\psi_{h,max} = 120^\circ$) as shown in Fig.2.11a. As another possibility, however, consider a/λ now increased to 0.75. Then the reduced fluctuations of the incident field (if b_h remains equal to -1) directly affects the amplitude of the grating lobe which propagates when $\psi_h > 90^o$. The extended feed (i.e. a region with $b_h = -1$) would again remain single moded. A second mode chart, with $\psi_{h,max} = 150^o$, indicates the reduction in the single moded region (for small b_h) as $\psi_{h,max} \to 180^o$ (Fig.2.11b).

Additional justification for introducing an interface region is provided by considering next the variation in axial phase velocity as a function of b_h.

2.3.2. Phase Velocity Profiles

The concept of a phase velocity profile is introduced as an interim design aid for examining the dynamic matching problem characteristic of phased arrays. In later chapters, more sophisticated methods of analysis are developed which are analogous to modern filter theory. At this stage, however, the simpler approach is preferred, partly for chronological consistency in the development of Chapters 3 and 4.

The axial phase velocity, normalised with respect to the plane wave velocity, is given by

$$\frac{v_{pz}}{v_o} = \frac{k}{k_z} \qquad \ldots(37)$$

If it is assumed that the susceptance b_h is tapered "smoothly" from a large inductive value to zero over a length $-z_o \leqslant z \leqslant 0$, with $z_o \gg \lambda$ and $a/\lambda > 0.5$, then the axial phase velocity for the dominant mode changes regularly and without any abrupt discontinuities within the transition for any value of ψ_h. For interfacing with a conventional array feed, an initial value of $b_h < -50$ is sufficient to ensure that the phase velocity is effectively independent of ψ_h and matched to the dominant mode in waveguide of the same element dimensions. A very brief review of the design of transmission line tapers is justified before this information is interpreted, since several analogies will then be emphasised.

Analytical design procedures for smoothly tapered waveguide transformers are available if the ratio of characteristic impedances at any two positions remains independent of frequency (48). Such transformers have been classified as homogeneous (49), and form a fairly restricted group since the H-plane dimension (in rectangular waveguide) must remain constant. Standard methods of design, based on linear, exponential and "continuous" binomial (or gaussian) impedance transformations, are easily applied and often acceptable. The resulting transformers are comparable in performance with the corresponding multi-section quarter wavelength devices (50). (An optimum configuration, developed from a multisection Tchebyscheff transformer, has also been derived with the reflection coefficient minimised for a specified bandwidth and length of taper (51).) No analytical methods are available, however, for designing the more general "inhomogeneous" transformers in multi-section or tapered transmission lines (see Chapter 6). One fundamental reason for this is the multiplicity of theoretical models for line impedance versus frequency.

The axial phase velocity can be identified with mode impedance in the discussion of waveguide tapers, and vice versa in the following references to arrays with reactively tapered boundaries. (It is therefore unnecessary to define a characteristic mode impedance in the latter case.) As shown in Fig. 2.12, the dynamic matching problem in each unit cell of the array can be summarised by the variation in terminal phase velocity for different values of ψ_h. In a qualitative way, it follows that the problems in developing a reactively tapered "matching transition" are similar in complexity to those encountered with a particular class of inhomogeneous transformer.

As the length of a smoothly tapered waveguide transformer is increased, the method of design gradually becomes insignificant, since an excellent impedance match is assured (Ref. 48, 50). This principle also extends to inhomogeneous transformers, and therefore suggests a method of designing reactively tapered array structures for matching the waveguide and free space modes. Figure 2.13. shows the susceptance profile required for a simple linear variation in the dominant mode phase velocity for different representative values of ψ_h, with $a/\lambda = 0.695$. Assuming that the length of a particular matching structure in Fig. 2.13 was sufficient, the non linear velocity profiles at all scan angles but one would not seriously degrade the impedance match (Fig. 2.14). For practical arrays requiring a compact transition structure, the choice of phase velocity profile would naturally become more crucial.

The occurrence of higher order modes has not been considered above, although two waveguides linked by a tapered transition are not always single - moded. If an oversize guide is excited by the lowest order mode, power transfer into other modes occurs only in the presence of discontinuities. For example, the TE_2 mode in rectangular waveguide would be generated by any asymmetrical condition, which could be introduced simply by mechanical tolerances. However, the second mode always has an extremely large phase velocity and wavelength in its initial propagating region, where its generation must be accompanied by a substantial distortion of the fields associated with the incident mode. In practice, very significant suppression of a higher order mode can usually be maintained in a waveguide or transformer over a relatively short length.

Consequently, the second order mode in a reactively tapered array structure with $0.5 < a/\lambda \leqslant 1.0$ would be suppressed by a smooth and accurately controlled phase velocity profile in the section where $b_{hc} \leqslant b_h \leqslant 0$. With only the dominant mode incident on the effective aperture plane (defined by the position where $b_h = 0$), no grating lobes would then be excited. Values of element spacing and scan angle which would normally result in the formation of a radiated grating wave could therefore be adopted, so reducing the number of elements required to fill a specified array aperture.

In a practical array, it would be impossible - and unnecessary - to completely eliminate the grating lobes. However, by significantly reducing their amplitudes, say from approximately -5dB to -25dB or less in the case of the visible grating lobe, the normal multiple beam ambiguity could be resolved in many systems. On a mode chart, the required reactive taper for this design technique can be represented by a line such as the one joining the points A, B, C in Fig. 2.11a.

2.4 Correlation with Related Work

2.4.1 The Concept of an "Ideal Element"

The discussion so far has concentrated entirely on array structures with all elements excited. In the limit, it has been concluded that an array with reactively tapered boundaries might be "perfectly" matched and free of grating lobes. These features imply a close connection with the concepts of "ideal" performance as specified by Hannan (8), and the corresponding properties of the effective "element radiator" (in an array with reactively tapered boundaries) can be deduced if such performance is assumed. (A "taper" of infinite length would be required to achieve complete impedance matching.) This theoretical equivalence between the present design proposal and the concepts of ideal behaviour as defined in Section 1.4 will now be examined.

Hannan's technique of active impedance matching (20) leads to a network requirement for an infinite number of connecting circuits. The present work defines a specific structure which, in the limit, fulfils this requirement. An unconditional match is implied, since $a/\lambda > 0.5$ (Section 1.4). In relation to element pattern control and multiple beam ambiguities, Hannan distinguished between arrays with visible grating lobes ($a/\lambda > 0.5$) and those with all grating lobes evanescent ($a/\lambda < 0.5$), and suggested finally that no design procedure appears practical for the former category (8). As stated in Chapter 1, that assessment has been endorsed, either explicitly or implicitly, by recent reviews and textbooks (2, 4, 35). However, the control of all "grating waves" (whether radiating or evanescent) is assured with the present proposals, and remains an essential property where impedance matching alone is required.

The design proposals based on the "periodic structure" analyses (Sections 2.2 and 2.3) can be interpreted quite generally. As already shown in part, the transition structure eliminates the abrupt discontinuity in boundary conditions which occurs with a conventional waveguide array at its aperture surface. The amplitude and phase distributions for the propagating wave are gradually modified within this field matching region, in the manner summarised by Fig. 2.15. Although the analysis has been restricted to a specific example, this overall design strategy is appropriate, in principle, to a broad class of arrays. It is illustrated in the next section for a linear E-plane array.

A corresponding interpretation on an "element" basis clarifies several further properties. If only one waveguide were excited in an array with "ideal" reactively tapered boundaries, progressive forward coupling to adjacent elements would occur once b_h became finite. In view of the relationship between the conventional mutual coupling coefficients (C_r) and the active reflection coefficient ($R(\psi_h)$) for a linear array, viz

$$\frac{1}{\pi} \int_{\psi_h=0}^{\pi} |R(\psi_h)|^2 \, d\psi_h = \sum_{r=-\infty}^{\infty} |C_r|^2 \qquad \ldots(38)$$

it follows that this coupling must be directional if $a/\lambda > 0.5$ with no power returned to the adjacent, passively-terminated waveguide feeds (8) (cf.Section 1.4). At the effective aperture plane, the fields due to one excited waveguide would extend over an infinite number of elements. This can be deduced from the Fourier transform relationship between the tangential aperture field and the (voltage) radiation pattern, the latter being assumed sectoral with $\sqrt{\cos\theta}$ amplitude variation between the scan limits $|\theta_{o,max}| = \sin^{-1}(\lambda/2a)$. Since this radiation pattern cannot be assumed necessarily to have constant phase, the corresponding aperture distribution is not immediately obtainable from an inverse Fourier transformation. These distributions could have general theoretical significance, however, since they would not be constant phase, in view of the different path lengths from the common feed to points on the aperture. With the array operating normally, the total field in each unit cell (which has been identified as the modal field and varies as a function of ψ_h) can be regarded as a combination of these individually orthogonal fields whose relative phasing changes periodically with the angle of scan.

The significance of the theoretical model presented in Section 2.3 is enhanced when the full range of performance possibilities is recognised. As already indicated, it is not necessary to achieve "perfect matching" or "complete elimination of grating lobes" with an operational array. Normally, the maximum impedance mismatch and the minimum grating lobe suppression would be specified as design parameters, together with the limits of scan. It is a distinctive and original feature of the present proposal that these requirements could be achieved by designing common reactive boundaries of an appropriate length and susceptance profile. In principle, the design could be "tailored" according to the specifications, with a further degree of freedom embodied in the final choice of element spacing. The various stages in this process are examined in the following chapters. For a particular element spacing, it is shown that an increasing penalty in overall complexity is incurred as the system specifications are tightened. The element spacing, of course, dictates the theoretical performance limits.

2.4.2 Visualisation as an Artificial Dielectric

After due allowance for the change in variables and the substitution of an expression for b_h, the characteristic equation derived above (eqn.(14)) corresponds with the equation given by Brown (eqn.(26) of reference 42) in his analysis of the rodded-type artificial dielectric. This emphasises the relevance of the extensive literature on the latter subject (e.g. 52, 53) and the eventual character of any practical interface structure for a waveguide array. Originally, artificial dielectrics were studied with a view to providing cheaper and/or lighter materials for microwave devices (such as lenses). Some of the more distinctive features of the present analysis are a direct consequence of the different application.

In general, the literature on artificial dielectrics has stressed the analogies with "optical" propagation. For example, effective "ray paths" can be postulated, and the properties of typical structures can be explained in terms of a composite dielectric-constant tensor. The propagation effects at an interface between an artificial dielectric and free space can then be predicted from Snell's law and transmission line theory with reasonable accuracy. Methods of impedance matching have been developed for microwave lens application (42). Whilst the distinction is not absolute, the current approach leads to a "field theory" description of propagation, with the characteristic equation derived directly from Maxwell's equations for a specified set of boundary conditions. As shown in later chapters, this approach ensures that a detailed description of the fields can be obtained throughout the structure. However, the flexibility afforded by the artificial dielectric concept is utilised in the next chapter to interpret edge effects.

In most analyses of artificial dielectric structures, the largest unit cell dimension is assumed very much smaller than the wavelength. In optical terms, this reduces dispersion to a level where it can be ignored (54). The same assumption does not apply to the present proposals. Again, the presence here of more than one propagating "mode" is novel, although the effects of evanescent modes on the propagation and matching characteristics of an artificial dielectric have been studied (55). These properties are considered later in context.

The possibility of creating additional parameters with a design approach based on artificial dielectrics should not discounted. In this thesis, for example, the reactive boundaries are assumed throughout to be coplanar with the waveguide sidewalls, and uniform (both in spacing and susceptance) in the transverse direction. These restrictions should not always be regarded as prerequisites, especially where a practical array of moderate size, or of non uniform element spacing, or with strongly tapered amplitude distribution across its aperture, would be appropriate.

2.5 Propagation in a Region of Constant Boundary Reactance - E plane Scan

2.5.1 Derivation of the Characteristic Equation

As the method of analysis here follows a similar pattern to that in Section 2.2, the same detailed explanations will not be repeated. A subscript "e" will be used to identify the parameters with the plane of scan.

The same theoretical model as shown in Fig. 2.1 can be assumed, except that $E_y = 0$ and the representative field is

$$\underset{\sim}{H} = H_y \hat{a}_y \qquad \ldots(39)$$

where H_y is a scalar quantity defining the complete magnetic field. With periodic excitation, general solutions of the form

$$H_y = \left[C\exp\{-jk_x(x-ra)\} + D\exp\{jk_x(x-ra)\}\right].\ \exp(-jk_z z).\ \exp(-jr\psi_e) \quad .(40)$$

are obtained from the reduced wave equation for the region

$(2r-1)a/2 < x < (2r+1)a/2$. The other non zero field components are

$$E_x = \frac{-1}{j\omega\varepsilon} \frac{\partial H_y}{\partial z} \qquad \text{...(41)}$$

and

$$E_z = \frac{1}{j\omega\varepsilon} \frac{\partial H_y}{\partial x} \qquad \text{...(42)}$$

The boundary conditions in each unit cell are given by

$$E_z\big|_{x=(2r+1)a/2+\delta} = E_z\big|_{x=(2r+1)a/2-\delta} \qquad \text{...(43)}$$

and

$$H_y\big|_{x=(2r+1)a/2+\delta} - H_y\big|_{x=(2r+1)a/2-\delta} = J_z\big|_{x=(2r+1)a/2}$$

$$= \frac{E_z\big|_{x=(2r+1)a/2}}{jX_e} \qquad \text{...(44)}$$

as $\delta \to 0$. As implied by the subscripts, the current flow is now in the axial direction. Substituting from eqns.(40) and (42) in eqn.(43), an analysis similar to that in Appendix 2A, Section (i) gives the result

$$\frac{D}{C} = \frac{1 - \exp[j(k_x a - \psi_e)]}{\exp(jk_x a) - \exp(-j\psi_e)} \qquad \text{...(45)}$$

which becomes

$$\frac{D}{C} = \frac{\cos(k_x a) - \cos(\psi_e)}{1 - \cos(k_x a + \psi_e)} = \frac{\sin[(\psi_e - k_x a)/2]}{\sin[(\psi_e + k_x a)/2]} \qquad \text{...(46)}$$

when $k_x a$ is real.

From the second boundary condition (i.e. eqn.(44)), the characteristic equation can then be obtained using eqns.(40), (42) and (45). The derivation is similar to that given in Appendix 2A, Section (ii), and gives the result

$$K_e.(k_x a).\ \sin(k_x a) + \cos(k_x a) - \cos\psi_e = 0 \qquad \text{...(47)}$$

where

$$K_e = \frac{1}{4\pi} \frac{\lambda}{a} (-b_e) \qquad \text{...(48)}$$

In the particular case of a two dimensional strip medium, it can be shown that the characteristic equation reduces to the result derived by Collin for oblique propagation (56).

2.5.2 Solutions of the Characteristic Equation

The possibility of both real and imaginary solutions for k_x must again be examined. Two real equations can be assumed, with

$$k_x = j\gamma_x \quad (\gamma_x \text{ real}) \qquad \ldots(19)$$

in the alternative form of eqn.(47). The equations can be written as

$$K_e.\ (k_x a).\ \sin\ (k_x a) + \cos(k_x a) = F_3(k_x a) = \cos\ \psi_e \qquad \ldots(49)$$

$$-K_e.\ (\gamma_x a).\ \sinh(\gamma_x a) + \cosh(\gamma_x a) = F_4(\gamma_x a) = \cos\ \psi_e \qquad \ldots(50)$$

The functions $F_3(k_x a)$ and $F_4(\gamma_x a)$ are plotted in Figs. 2.16 and 2.17 respectively for various representative values of K_e. A number of significant differences between the modes of propagation in the two planes of scan now become evident.

Discounting temporarily the plane wave solution when $\psi_e = 0$ and $K_e > 0.5$, it can be seen from Fig. 2.16 that a single solution for $k_x a$ is obtained in any range $n\ \pi < k_x a \leqslant (n+1)\pi$ $(n = 0, 1, 2, 3 \ldots.)$ for all values of b_e and ψ_e. (Strictly, a second equality sign is needed in the range $0 \leqslant k_x a \leqslant \pi$.) In addition, one solution corresponding to a propagating slow wave (i.e. k_x imaginary) can be found under all conditions of excitation when b_e is inductive (Fig. 2.17).

These solutions can again be grouped into different categories. One demarcation, already mentioned and apparent in Figs. 2.16 and 2.17, is encountered when $K_e = 0.5$. If $K_e < 0.5$, the slope of the function $F_3(k_x a)$ is initially negative (at $k_x a = 0^+$), and a solution of eqn.(49) with $k_x a = \delta$ (where δ is an arbitrarily small quantity) can always be found if ψ_e is sufficiently small. Such a solution corresponds to the dominant mode. However, if $K_e > 0.5$, the slope of $F_3\ (k_x a)$ is initially positive, and a solution of eqn.(49) cannot be obtained with $k_x a = \delta$, although an isolated plane wave solution still exists (with $k_x a = 0$

when $\psi_e = 0$). The dominant fast wave solution for $k_x a$ under these conditions is nonzero, continuous with ψ_e, and also in the range $0 < k_x a \leq \pi$. For consistency, therefore, the isolated plane wave solution can be regarded as the "slow" wave solution when $\psi_e = 0$ (k_x zero on an imaginary axis - cf. Fig.2.17). Further characteristics of the E-plane modes when k_x is real and imaginary can now be considered separately.

(i) Solutions with k_x real. As before, a number of numerical examples have been calculated showing the amplitude and phase distributions. In Fig.2.18, three results showing H_y for the dominant mode when $K_e = \infty$, $K_e << 0$, and $K_e \simeq -1$ are given in anticipation of the form of the reactively tapered boundaries. The magnetic field is not continuous across the element boundaries unless $b_e = 0$. However, the gradual reduction of the peak to peak variations in phase is evident in Fig.2.18. A second series of dominant mode distributions is shown in Fig.2.19, where positive values of K_e have been assumed. The result obtained in each unit cell when $K_e \to +\infty$ is simply the TM_1 waveguide mode, which propagates only if $a/\lambda \geq 0.5$. Assuming T.E.M. excitation in each waveguide element, the distributions shown in Fig.2.19. would not be appropriate in a field matching transition for a scanning array. A dominant mode reference chart showing the value of D/C for different values of ψ_e and K_e is given in Fig.2.20.

When $a/\lambda > 0.5$, the possibility of a second propagating mode must again be considered. From eqn.(49), the general cut-off condition, which applies for all values of a/λ and is defined by $k_x a = ka$, is given by

$$b_{ec} = 2\left\{\frac{\cos(2\pi a/\lambda) - \cos(\psi_e)}{\sin(2\pi a/\lambda)}\right\} \qquad \ldots.\ (52)$$

which is the same result as previously obtained for b_{hc}, although the characteristic equations in the two planes are not the same (cf. eqn.(25)). The amplitude and phase distributions for the second mode are illustrated in Fig. 2.21 for negative values of K_e. This mode becomes the first visible grating wave when K_e (or b_e) = 0. As shown below and in Chapter 3, higher order modes will not be as significant in the E-plane as in the H-plane, and will not be encountered in any practical design problems.

(ii) Solutions with k_x imaginary. It is evident from Fig. 2.17 that the solutions for $\gamma_x a$ tend to zero (for any value of ψ_e) as $K_e \to +\infty$. This is the limiting case of the slow wave solution. In the range of $0.5 > K_e > 0$, the solutions for $\gamma_x a$ increase rapidly in magnitude as $K_e \to 0$, and in the limit, approach infinity, which corresponds to a true cut-off condition in the z - direction. With $0.5 > K_e > 0$, the function $F_4(\gamma_x a)$ has a maximum at a value of $\gamma_x a$ obtained (after differentiating $F_4(\gamma_x a)$) from the transcendental equation

$$\frac{\tanh(\gamma_x a)}{\gamma_x a} = \frac{K_e}{1 - K_e} \qquad \ldots(53)$$

A complete and continuous range of solutions to eqn.(50) can be found beyond this maximum. Following the agreed convention, the solution given by $\gamma_x a = 0$ when $K_e < 0.5$ and $\psi_e = 0$ should not be associated with the current category.

The most important result, from the viewpoint of electronic scanning, is that slow waves cannot form if b_e is capacitive This is again consistent with the standard restriction on the formation of propagating TM - type surface waves (45). For large inductive values of b_e, the single slow-wave mode is loosely coupled to each current sheet. From eqn.(46), D/C can be written in the form

$$\frac{D}{C} = \frac{1 - \cos\psi_e \cdot \cosh(\gamma_x a) + j\sin\psi_e \sinh(\gamma_x a)}{\cosh(\gamma_x a) - \cos\psi_e} \qquad \ldots(54)$$

which is clearly complex in general, but tends to unity as $\gamma_x a \to 0$. Conversely, when $K_e \to 0^+$, the slow waves are tightly coupled to the current sheets and $D/C \to \exp.\,(j\psi_e)$. Further consideration of these modes is now unnecessary if it is assumed that b_e will always be capacitive.

2.5.3 Further "Modal" Properties

The idea of describing the independent field solutions within each unit cell of the periodically excited array structure as modes of propagation can be preserved in E-plane scanning structures. With capacitive current sheets, the dominant mode is a TEM (or TM_o) wave in each parallel plate waveguide (when $b_e \to +\infty$), and the main beam in free space (when $b_e = 0$). The higher order modes are the TM mode series in waveguide, and the E-plane grating lobe series in space.

"Modal" properties such as power flow, orthogonality and completeness will not be derived here. The techniques are analogous to those demonstrated in Section 2.2.3. The power flow (P_n) per unit cell of height b for the "n"th propagating mode is given by

$$P_n = \frac{ab}{\omega\varepsilon}\,\beta_n \cdot C_n^{\,2}\left\{1 + \left(\frac{D_n}{C_n}\right)^2 + 2\cdot\frac{D_n}{C_n}\,\frac{\sin(a\sqrt{k^2-\beta_n^2})}{a\sqrt{k^2-\beta_n^2}}\right\} \qquad \ldots(55)$$

This equation permits the independent amplitude factor C_n to be specified in terms of power flow.

2.6 Application to E-plane Scanning Arrays

2.6.1 Propagation in Linear Arrays of Finite Height

The dominant mode in the waveguide feed was identified in the previous section as T.E.M. However, each element in a practical array of rectangular waveguides would be excited by the TE_{01} mode - with the sinusoidal field variations in the y-direction. In a region of finite susceptance boundaries, the corresponding linear structure would still be contained between conducting planes at $y = 0, b$. A general result first published by Miles (57) simplifies the analysis of such structures if certain conditions are met. Assuming the equations

$$E_x = f_1(x,z).\sin(\pi y/b) \qquad \ldots(56a)$$

$$E_y = 0 \qquad \ldots(56b)$$

and $$E_z = f_2(x,z).\sin(\pi y/b) \qquad \ldots(56c)$$

afford a description of any allowable fields in terms of unknown functions f_1 and f_2, and the effective boundary conditions for f_1 and f_2 are the same irrespective of the waveguide height, then these functions can be found by solving the two dimensional wave equation

$$\frac{\partial^2 f_i}{\partial x^2} + \frac{\partial^2 f_i}{\partial z^2} + k^2 f_i = 0 \ (i = 1 \text{ or } 2) \qquad \ldots(57)$$

and replacing k^2 by $k^2 - (\pi/b)^2$. This result leads to the definition of an effective wavelength (λ_{eff}) given by

$$\lambda_{eff} = \frac{\lambda}{\left[1 - (\lambda/2b)^2\right]^{\frac{1}{2}}} \qquad \ldots(58)$$

for linear waveguide arrays. The significance of this result is demonstrated in Chapter 3.

Examples of structures which do not comply with the assumptions in eqns. (56a-c) should be noted. For instance, any reactive boundary which is not uniform in the y-direction could modify the sinusoidal field distribution. This is conveniently illustrated by the two broad-wall coupling structures shown in Fig. 2.22, both of which could provide fast wave coupling. Only the first structure (Fig. 2.22a) can be treated by the effective two-dimensional theory. The properties of the second structure in Fig. 2.22 are more difficult to determine, and require a variational analysis (58) or experimental measurement. As another example, it will be seen that the properties at an aperture can be deduced from the simple theory only if the parallel top and bottom plates are continuous in the "free space" region.

The more general designation λ will be retained in the following sections except when specific reference is made to an array of rectangular waveguides.

2.6.2 Interpretation of Design Aids

A typical mode chart is given in Fig. 2.23 to emphasise the single moded region which is of most significance in the E-plane. An array with capacitively-tapered element boundaries is required to provide a field-matching transition which is effective at all scan angles. It is immediately evident that a basic restriction on element spacing is dictated by the requirement for a single-moded waveguide feed. However, as shown in the next chapter, it is not necessary to contemplate waveguide feeds with mode suppressors to derive any improved performance in this polarisation. Since the mode chart does not include any allowance for finite waveguide heights, a considerable saving in the number of elements can be assured by a judicious choice of waveguide dimensions. This is considered in detail in Chapter 3.

Phase velocity profiles can be utilised again to study the impedance matching problems. Several new features are evident if a/λ is assumed to be less than 0.5 in an array with capacitively-tapered element boundaries (Fig. 2.24). In the H-plane example (Figs. 2.12 to 2.14), the element spacing automatically exceeded 0.5 and at least one beam could be formed for any value of $\psi_h < \pi$. Expressed alternatively, the terminal phase velocity for the "dominant free space mode" remained finite in the H-plane. However, with $a/\lambda < 0.5$ in the E-plane, it is clear that no beam can form in space when $\psi_e > 2\pi a/\lambda$ and the phase velocity becomes infinite. Under this condition, all the incident power supplied by a set of waveguide transmitters would be reflected, irrespective of the length of any transition region (cf.Section 1.4). One immediate consequence is that the elements can not be electrically isolated (cf. eqn.(38)).

It is also evident from the terminal phase velocity charts (i.e. Figs. 2.12 and 2.24) that the impedance matching problem is a more serious limitation in the E-plane when $a/\lambda < 0.5$, even assuming ψ_e is restricted to values less than $2\pi a/\lambda$. In later chapters, it will be shown that the major value of reactively tapered boundaries in the E-plane is their ability to minimise the active impedance mismatch over a specified scan sector where $\psi_{e,max} < 2\pi a/\lambda$. The result is anticipated at this stage simply to complete the comparison with Hannan's ideal model, which required "just the right amounts of (mutual) coupling to yield zero reflection for all scan angles" (8). A structure with smoothly tapered capacitive boundaries of infinite length would fulfil this requirement in principle, and a finite length structure would approximate it in practice.

2.7 Extension of the Design Principles - A General Assessment

Whilst the remainder of this thesis is concerned with the further development and evaluation of the concepts contained in Sections 2.2 to 2.6, it is appropriate to conclude this chapter with a general assessment of related problems involving controlled element coupling. Three important topics which might be tackled by field theory methods are considered: the possibility of analysing a planar array structure, the expectation of achieving broad-band frequency performance (say > 10%), and the question of structures with finite wall thickness. Detailed analyses are not developed, and are possibly unjustified at present in the isolated context of electronic scanning. (Selected aspects could be included in a study of propagation in "waveguides" with reactive boundaries.) The following summary is intended only as an introduction and it can not be assumed, a priori, that results leading to the definition of feasible structures would necessarily be obtained in all cases.

2.7.1 The Planar Array

A planar array consisting of thin-walled waveguide elements arranged in a rectangular lattice would appear to be a natural extension of the linear structures already analysed. However, a number of complications must be accepted if reactive boundaries are contemplated on all four sides of a rectangular unit cell. For scanning at angles θ, ϕ in a spherical co-ordinate system, all 6 field components would be present in regions of finite susceptance, and the element boundary conditions would have to allow for non-isotropic surfaces to use all the potential degrees of freedom. (Only a small number of practical "reactive surfaces" can be considered polarisation insensitive - they include sheets of high dielectric constant material, conducting plates with circular apertures in a square grid and two identical parallel wire gratings lying at right angles. The second and third are only "isotropic" when their periodic dimensions are very much less than a wavelength.) Presupposing the use of periodic boundary structures, the question of cross-mode coupling in the corners of each unit cell could become significant.

Nevertheless, the formulation of a field solution, reducing to a plane wave with predictable polarisation as the element boundaries vanish, does not appear theoretically unattainable. (From an economic viewpoint, the main requirement would be an ability to control grating lobe radiation - i.e. to reduce the number of elements). Encouragement for modest scanning requirements is provided by separating the single planar array problem into two linear array problems. For the waveguide array shown schematically in Fig. 2.25, it follows that the boundaries at $y = 0, \pm b, \pm 2b, \ldots.$ could be reactively tapered using the principles already described, while the waveguide walls at $x = 0, \pm a, \pm 2a, \ldots$ were tapered beyond the plane $z = d$. In such a structure, the z - directed reactive taper must now remain effective for wavefronts rotated by a variable angle (α_y) in the y - z plane. Over the scanning limits of $\pm \alpha_{y,max}$, the second transition would be required to maintain controlled coupling and ensure minimal reflections, although the surface currents and the direction of maximum taper would not in general be perpendicular. For modest values of $\alpha_{y,max}$ (say $< 30^o$) it seems probable that acceptable performance could be achieved with surfaces having approximately isotropic characteristics at all angles. In principle, a more sophisticated approach could eventually be adopted (if necessary) with controlled non-isotropic characteristics at selected values of α_y to optimise the scanning performance.

Finally on this topic, it should be pointed out that the attainment of a modal description of the fields in a general planar array structure would create a requirement for very extensive numerical work on boundary discontinuities. As stated in Chapter 1, the integral equations for a thin walled waveguide array scanned in an arbitrary direction can not be solved analytically (4). With finite reactive boundaries, the problem involves at least four more variables. The Weiner-Hopf technique used in Chapter 4 of this thesis would not be applicable, and a field matching technique based on numerical procedures would be needed (cf.Section 1.2.4).

2.7.2. Broadband Operation

Over a very wideband (normally at least 30%) it is found that the reactance of certain practical boundaries varies directly with frequency in the H-plane, and inversely in the E-plane. (This statement is verified by examples given in the next chapter.) Consequently, the factors K_h and K_e appearing in the characteristic equations (eqns.(14) and (47)) remain constant, and the values of k_x are the same for a given value of ψ (in either plane). The main differences in a region of finite susceptance arise from the changing value of k - both the axial velocity and the effective scan angle are affected, and possibly the number of propagating modes.

Extending the arguments developed in previous sections, it follows from the assumed susceptance property that a transition structure with reactively tapered boundaries should exhibit impedance matching and higher order mode suppression over a broad band. Without immediately specifying all the practical limits on bandwidth, this feature can be contrasted with the almost inherently narrowband characteristics of phased arrays in which the elements are impedance matched using a resonant circuit principle. For a given value of ψ, the phase velocity profile changes smoothly with frequency - e.g. from a linear to a concave or convex characteristic. To construct Fig. 2.26, it has been assumed that an H-plane array is required to operate over a wideband (say > 10%) with $\theta_{o,max} = 30^{o}$. Taking $a/\lambda = 0.695$ as the centre frequency element spacing, the variations in phase velocity profiles have then been plotted for a structure having a linear profile at midband with $\psi_h = 90^{o}$. Although the change in frequency affects the phase velocity (and impedance) more when b_h is numerically large, a sufficiently long transition structure could remain well matched.

Further evidence of the potential bandwidth is provided by the work of Carne and Brown (52), who demonstrated that the properties of an artificial dielectric structure at different scan angles (with frequency constant) and at different frequencies (with the scan angle held constant) are closely linked. Specifically, these authors show that a structure which is impedance matched over the widest possible bandwidth at normal incidence offers the best match at oblique angles of incidence. Their model consists of a periodic structure with reactive surfaces lying parallel to the interface (or effective aperture), and with unit cell dimensions assumed small with respect to wavelength. This model differs in several respects from the structures under consideration in this thesis - notably in the absence of any dispersive limitations. Nevertheless, it is considered that a corresponding relationship between frequency and scan angle might be developed for arrays with reactive boundaries to simplify the design task. In later chapters, several important results are noted which could be significant in this respect, and a general method of including frequency in the design parameters is discussed.

2.7.3 Finite Wall Thickness

As shown in Chapter 3, the question of wall thickness tends to arise as a practical mechanical detail, and not as an electrical design parameter. In a conventional H-plane array, the elements would normally be as large as practicable to minimise the impedance matching problem and (by implication) the mutual coupling. In the E-plane (and in planar arrays), thick walls might prove advantageous. Standard methods of electrical representation are given in the next chapter.

Coupling structures of finite thickness can be separated into two categories. In later chapters, it is shown that the inevitable thickness of practical boundaries does not invalidate the theory given above, even when it approaches 5% of the element spacing. However, waveguide structures with an appreciable wall thickness (say > 10%) must be considered in the second category. For field matching purposes, it is clear that a free space "mode" (i.e. a plane wave) can only be approximated within a periodic structure when its boundaries are electrically vanishing. With thick boundaries, a field discontinuity at the aperture is inevitable. This suggests that the boundary thickness should be as small as possible near the aperture, and therefore dimensionally flared if necessary within the transition region. The assumption of zero-thickness boundaries in earlier sections should correspondingly be regarded as an array feature which is essential to realise maximum gain.

The conceptual possibility of reactive structures matching waveguides of different size (or shape) to the unit cell dimensions can be regarded as the ultimate extension of the present proposals.

However, it would appear more practical for any mechanically flared region to be contained within conventional closed waveguide elements, and to concentrate on the techniques already outlined.

APPENDIX 2A

The following derivations are utilised in Section 2.2.1.

(i) Substituting eqn. (3) in eqn. (7), with $z = 0$ and $r = 0$ in the region where $x = (2r + 1)a/2 - \delta$, yields the equation

$$[A \exp\{-jk_x(a/2 - \delta)\} + B \exp\{jk_x(a/2 - \delta)\}]$$

$$= [A \exp\{-jk_x(a/2 + \delta - a)\} + B \exp\{jk_x(a/2 + \delta - a)\}].\exp(-j\psi_h)$$

and with $\delta \to o$

then $A [\exp\{-j(k_x a/2 - \psi_h)\} - \exp(+jk_x a/2)]$

$$= B [\exp(-jk_x a/2) - \exp\{j(k_x a/2 + \psi_h)\}]$$

Multiplying through by $\exp(jk_x a/2)$ and rearranging gives

$$\frac{B}{A} = \frac{\exp(j\psi_h) - \exp(jk_x a)}{1 - \exp[j(k_x a + \psi_h)]} \qquad \text{(cf. eqn. (10))}$$

$$= \frac{\exp(j\psi_h) - \exp(jk_x a)}{1 - \exp\{j(k_x a + \psi_h)\}} \cdot \frac{\exp(-j\psi_h) + \exp(-jk_x a)}{\exp(-j\psi_h) + \exp(-jk_x a)}$$

$$= \frac{1 - 1 + \exp\{j(\psi_h - k_x a)\} - \exp\{-j(\psi_h - k_x a)\}}{-\exp(j\psi_h) + \exp(-j\psi_h) + \exp(-jk_x a) - \exp(jk_x a)}$$

$$= \frac{\sin(k_x a - \psi_h)}{\sin \psi_h + \sin k_x a}$$

$$= \frac{\sin[(k_x a - \psi_h)/2]}{\sin[(k_x a + \psi_h)/2]} \qquad \text{as stated in eqn. (12)}$$

This relation is useful where $k_x a$ is real.

(ii) Examining the individual terms in eqn. (8), with $z = 0$ and $r = 0$ in the region where $x = (2r + 1)a/2 - \delta$, and omitting the common factor $\exp(-jk_z z)$, the following relations are obtained:-

From eqns. (3) and (5b)

$$H_z\big|_{x=a/2+\delta} = \frac{k_x}{\omega\mu} [A \exp\{-jk_x(a/2 + \delta - a)\}$$
$$-B \exp\{jk_x(a/2 + \delta - a)\}].\exp(-j\psi_h) \qquad \ldots\text{(A1)}$$

in the region $a/2 < x < 3a/2$.

From eqns. (3) and (5b)

$$H_{z|x=a/2-\delta} = \frac{k_x}{\omega\mu}\,[A\exp\{-jk_x(a/2-\delta)\} - B\exp\{jk_x(a/2-\delta)\}] \qquad \ldots(A2)$$

in the region $-a/2 < x < a/2$.

From eqns. (3) and (9)

$$-J_{y|x=a/2} = \frac{-1}{jX_h}\,[A\exp(-jk_x a/2) + B\exp(jk_x a/2)] \qquad \ldots(A3)$$

Combining eqns. (A1), (A2) and (A3) in accordance with eqn. (8) in text leads to the result

$$A\left[\frac{k_x}{\omega\mu}\exp(jk_x a/2).\ \exp(-j\psi_h) - \frac{k_x}{\omega\mu}\exp(-jk_x a/2) + \frac{1}{jX_h}\ \exp(-jk_x a/2)\right]$$

$$= B\left[\frac{k_x}{\omega\mu}\exp(-jk_x a/2).\ \exp(-j\psi_h) - \frac{k_x}{\omega\mu}\exp(jk_x a/2) - \frac{1}{jX_h}\exp(jk_x a/2)\right]$$

Substituting eqn. (10) for B/A after multiplying through by $\exp(-jk_x a/2)$

$$\left[\frac{k_x}{\omega\mu}\{\exp(-j\psi_h) - \exp(-jk_x a)\} + \frac{1}{jX_h}\exp(-jk_x a)\right]$$

$$= \frac{\exp(j\psi_h) - \exp(jk_x a)}{1 - \exp(jk_x a + j\psi_n)}\left[\frac{k_x}{\omega\mu}\exp(-jk_x a)\ \exp(-j\psi_h) - \frac{k_x}{\omega\mu} - \frac{1}{jX_h}\right]$$

$$\text{i.e. } \frac{k_x}{\omega\mu}\left[\exp(j\psi_h) + \exp(-j\psi_h)\right] - \frac{k_x}{\omega\mu}\left[\exp(jk_x a) + \exp(-jk_x a)\right]$$

$$+ \frac{1}{jX_h}\left[\exp(-jk_x a) - \exp(-\psi_h)\right]$$

$$= +\frac{k_x}{\omega\mu}\left[\exp(-jk_x a) - \exp(-j\psi_h) - \exp(j\psi_h) + \exp(jk_x a)\right]$$

$$+ \frac{1}{jX_h}\left[\exp(jk_x a) - \exp(j\psi_h)\right]$$

which reduces to

$$-\frac{\omega\mu}{2X_h}\;\frac{1}{jk_x}\left[\exp(jk_xa)-\exp(-jk_xa)\right]-\left[\exp(jk_xa)+\exp(-jk_xa)\right]$$

$$+\left[\exp(j\psi_h)+\exp(-j\psi_h)\right] \qquad = 0$$

i.e. $$\frac{\omega\mu a}{2X_h}\;\frac{\sin(k_xa)}{k_xa}+\cos(k_xa)-\cos\psi_h \qquad = 0$$ as stated.

APPENDIX 2B

To establish the orthogonality condition assumed in Section 2.2.3, it is necessary to prove that

$$\frac{b}{2} \mathrm{Re} \int_{-a/2}^{a/2} dx\, E_{yn} H^*_{xm} = 0 \text{ if } m \neq n$$

Substituting from eqns. (3) and (5a) in text and integrating, the problem is to prove that

$$\frac{\beta_m ab}{\omega\mu} \exp[j(\beta_n - \beta_m)z] \left\{ \frac{\sin[(a/2)(\sqrt{k^2-\beta_n^2} - \sqrt{k^2-\beta_m^2})]}{(a/2).(\sqrt{k^2-\beta_n^2} - \sqrt{k^2-\beta_m^2})} \cdot \left(1 + \frac{B_n}{A_n}\,\frac{B_m}{A_m}\right) + \frac{\sin[(a/2).(\sqrt{k^2-\beta_n^2} + \sqrt{k^2-\beta_m^2})]}{(a/2).(\sqrt{k^2-\beta_n^2} + \sqrt{k^2-\beta_m^2})} \cdot \left(\frac{B_n}{A_n} + \frac{B_m}{A_m}\right) \right\} \quad \ldots(B1)$$

$$= 0$$

where $$\frac{B_i}{A_i} = \frac{\sin[(a\sqrt{k^2-\beta_i^2} - \psi_h)/2]}{\sin[(a\sqrt{k^2-\beta_i^2} + \psi_h)/2]}, \quad i = n \text{ or } m \quad \ldots(B2)$$

(from eqn (12) in text)

and

$$a\sqrt{k^2-\beta_i^2} = K_h \frac{\sin(a\sqrt{k^2-\beta_i^2})}{\cos\psi_h - \cos(a\sqrt{k^2-\beta_i^2})} \quad \text{(from eqn. (14) in text)} \quad \ldots(B3)$$

$$= K_h \frac{\sin[(a\sqrt{k^2-\beta_i^2})/2] . \cos[(a\sqrt{k^2-\beta_i^2})/2]}{\sin[(a\sqrt{k^2-\beta_i^2} + \psi_h)/2] . \sin[(a\sqrt{k^2-\beta_i^2} - \psi_h)/2]}$$

An abbreviated form is convenient at this stage.

Let $(a\sqrt{k^2-\beta_i^2}) = 2\phi_i$

and $\psi_h = 2\psi'$

In eqn. (B1)

$$1 + \frac{B_n}{A_n} \cdot \frac{B_m}{A_m} = \frac{\sin(\phi_n + \psi'). \sin(\phi_m + \psi') + \sin(\phi_n - \psi'). \sin(\phi_m - \psi')}{\sin(\phi_n + \psi'). \sin(\phi_m + \psi')} \quad \ldots(B4)$$

Similarly

$$\frac{B_n}{A_n} + \frac{B_m}{A_m} = \frac{\sin(\phi_n - \psi'). \sin(\phi_m + \psi') + \sin(\phi_n + \psi'). \sin(\phi_m - \psi')}{\sin(\phi_n + \psi'). \sin(\phi_m + \psi')} \quad \ldots(B5)$$

From eqn. (B1), it is then necessary to prove that

$$-\frac{\sin(\phi_n - \phi_m)}{(\phi_n - \phi_m)} \cdot \Big(\text{R.H.S. of expn. (B4)}\Big) = + \frac{\sin(\phi_n + \phi_m)}{(\phi_n + \phi_m)} \cdot \Big(\text{R.H.S. of expn. (B5)}\Big) \qquad \ldots(\text{B6})$$

L.H.S. of (B6)

$$\Rightarrow \frac{\sin(\phi_m - \phi_n)}{K_h} \cdot \frac{\sin(\phi_n + \psi'). \sin(\phi_m + \psi') + \sin(\phi_n - \psi'). \sin(\phi_m - \psi')}{\sin(\phi_n + \psi'). \sin(\phi_m + \psi')} \cdot$$

$$\frac{\sin(\phi_n + \psi'). \sin(\phi_n - \psi'). \sin(\phi_m + \psi'). \sin(\phi_m - \psi')}{\left\{\begin{array}{l}\sin\phi_n . \cos\phi_n . \sin(\phi_m + \psi'). \sin(\phi_m - \psi') \\ \qquad - \sin\phi_m . \cos\phi_m . \sin(\phi_n + \psi'). \sin(\phi_n - \psi')\end{array}\right\}}$$

Substituting for ϕ_n and ϕ_m from eqn. (B3)

$$= \frac{1}{K_h} \frac{(\sin\phi_m . \cos\phi_n - \cos\phi_m . \sin\phi_n).}{T_1 - T_2} \cdot \Big\{ \sin^2(\phi_n - \psi'). \sin^2(\phi_m - \psi')$$
$$+ \sin(\phi_n + \psi'). \sin(\phi_n - \psi'). \sin(\phi_m + \psi'). \sin(\phi_m - \psi') \Big\} \qquad \ldots(\text{B7})$$

where $T_1 = \sin\phi_n . \cos\phi_n . \sin(\phi_m + \psi'). \sin(\phi_m - \psi')$

and $T_2 = \sin\phi_m . \cos\phi_m . \sin(\phi_n + \psi'). \sin(\phi_n - \psi')$

Similarly, the R.H.S. of expn. (B6)

$$\Rightarrow \frac{1}{K_h} \frac{(\sin\phi_m . \cos\phi_n + \cos\phi_m \sin\phi_n)}{T_1 + T_2} \cdot$$

$$\left\{\begin{array}{l}\sin^2(\phi_n - \psi'). \sin(\phi_m + \psi'). \sin(\phi_m - \psi') \\ + \sin^2(\phi_m - \psi'). \sin(\phi_n + \psi'). \sin(\phi_n - \psi')\end{array}\right\} \qquad \ldots(\text{B8})$$

Removing the common factors from eqns. (B7) and (B8) and multiplying through by $(T_1^2 - T_2^2)$, it is required to prove that

$$(T_1 + T_2) \quad (\sin\phi_m . \cos\phi_n - \cos\phi_m . \sin\phi_n). \Big[\sin(\phi_n - \psi'). \sin(\phi_m - \psi')$$
$$+ \sin(\phi_n + \psi'). \sin(\phi_m + \psi') \Big]$$

$$= (T_1 - T_2). (\sin\phi_m . \cos\phi_n + \cos\phi_m . \sin\phi_n). \Big[\sin(\phi_n - \psi'). \sin(\phi_m + \psi')$$
$$+ \sin(\phi_m + \psi'). \sin(\phi_m - \psi')\Big]$$

The L.H.S. can be written as

$$(F_1 - F_2 + F_3 - F_4).\ \left[\sin(\phi_n - \psi').\ \sin(\phi_m - \psi') + \sin(\phi_n + \psi').\ \sin(\phi_m + \psi')\right]$$

and the R.H.S. as

$$(F_1 + F_2 - F_3 - F_4).\ \left[\sin(\phi_n - \psi').\ \sin(\phi_m + \psi') + \sin(\phi_n + \psi').\ \sin(\phi_m - \psi')\right]$$

where $F_1 = T_1 \sin\phi_m \cos\phi_n$, $F_2 = T_1 \sin\phi_n \cos\phi_m$, etc. ...(B9)

Transposing partially to regroup similar terms gives

$$(F_1 - F_4)\ \left[+\sin(\phi_n - \psi').\ \sin(\phi_m - \psi') + \sin(\phi_n + \psi').\ \sin(\phi_m + \psi') - \sin(\phi_n - \psi').\ \sin(\phi_m + \psi') - \sin(\phi_n + \psi').\ \sin(\phi_m - \psi')\right] \quad ...(B10)$$

as the expression on the L.H.S., which should equal

$$(F_2 - F_3)\ \left[+\sin(\phi_n - \psi').\ \sin(\phi_m - \psi') + \sin(\phi_n + \psi').\ \sin(\phi_m - \psi') + \sin(\phi_n - \psi').\ \sin(\phi_m + \psi') + \sin(\phi_n + \psi').\ \sin(\phi_m + \psi')\right] \quad ...(B11)$$

$$\begin{aligned}\text{Expn.(B10)} &= (F_1 - F_4).\ \left[\sin(\phi_n - \psi') - \sin(\phi_n + \psi')\right]\left[\sin(\phi_m - \psi') - \sin(\phi_m + \psi')\right] \\ &= (F_1 - F_4).\ 4\cos\phi_n.\ \sin\psi'.\ \cos\phi_m.\ \sin\psi'\end{aligned}$$

$$\begin{aligned}\text{where } (F_1 - F_4) &= \sin\phi_n.\ \sin\phi_m\ \left[\cos^2\phi_n.\ \sin(\phi_m + \psi').\ \sin(\phi_m - \psi') - \cos^2\phi_m.\ \sin(\phi_n + \psi').\ \sin(\phi_n - \psi')\right] \\ &= \tfrac{1}{4}\sin\phi_n.\ \sin\phi_m \left\{[\cos(2\phi_n) + 1][\cos(2\psi') - \cos(2\phi_m)] - [\cos(2\phi_m) + 1][\cos(2\psi') - \cos(2\phi_n)]\right\} \\ &= \tfrac{1}{2}\sin\phi_n.\ \sin\phi_m\ [\cos(2\phi_n) - \cos(2\phi_m)].\ \cos^2\psi'\end{aligned}$$

$$\begin{aligned}\text{i.e. Expn.(B10)} &\Rightarrow 2.\ \cos\phi_n.\ \sin\phi_n.\ \cos\phi_m.\ \sin\phi_m.\ \cos^2\psi'.\ \sin^2\psi'.\ [\cos(2\phi_n) - \cos(2\phi_m)] \\ &= \tfrac{1}{8}\sin(a\sqrt{k^2 - \beta_n^2}).\ \sin(a\sqrt{k^2 - \beta_m^2}).\ \sin^2\psi_h.\ [\cos(a\sqrt{k^2 - \beta_n^2}) - \cos(a\sqrt{k^2 - \beta_m^2})]\end{aligned}$$

By a parallel procedure, expn.(B11) can be proved equal to this last expression, with

$$(F_2 - F_3) = \tfrac{1}{2}\cos\phi_n.\ \cos\phi_m\ [\cos(2\phi_n) - \cos(2\phi_m)].\ \sin^2\psi'$$

and the remaining factor in expn (B11)

$$\Rightarrow 4\sin\phi_n.\ \cos\psi'.\ \sin\phi_m.\ \cos\psi'$$

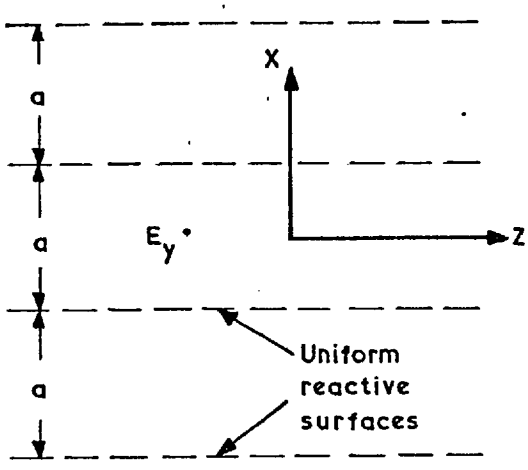

Fig. 2.1 Geometry of infinite array with reactive boundaries

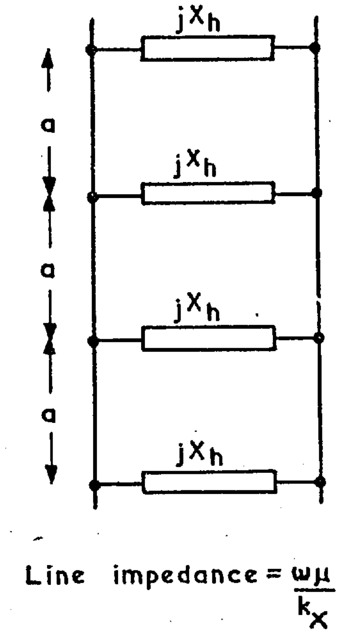

Fig. 2.2 Periodically loaded transverse line

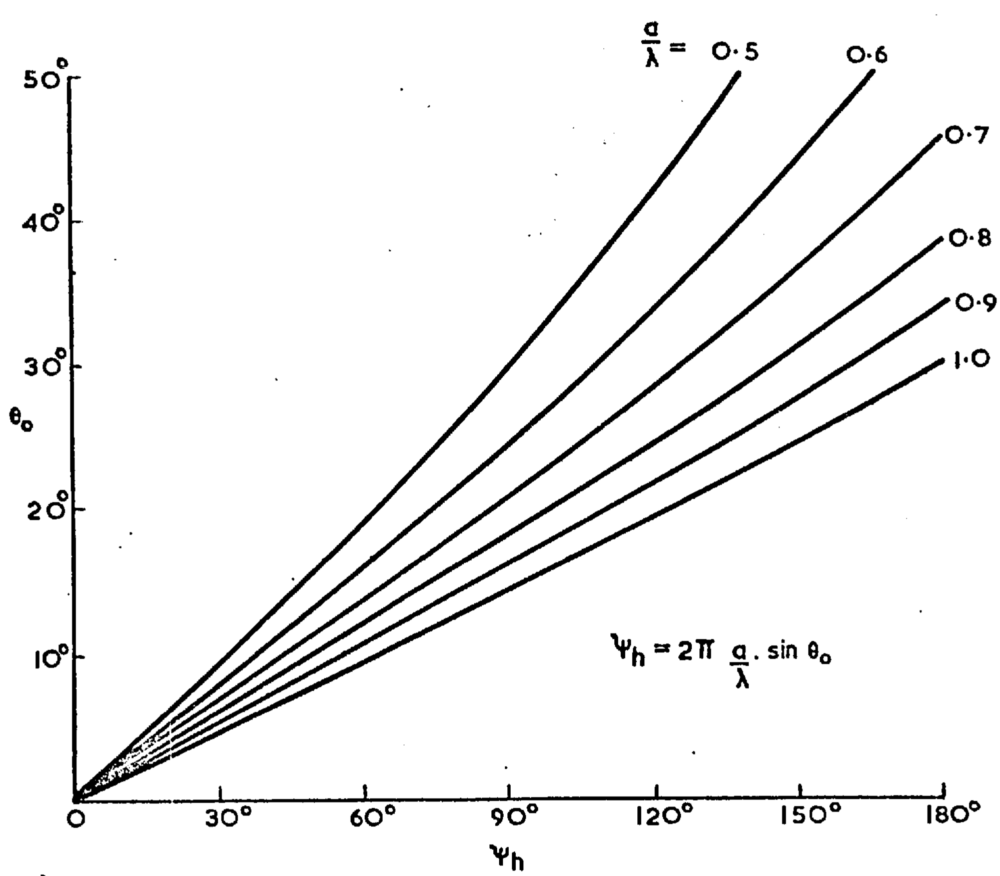

Fig. 2.3 Variation of scan angle with phase increment

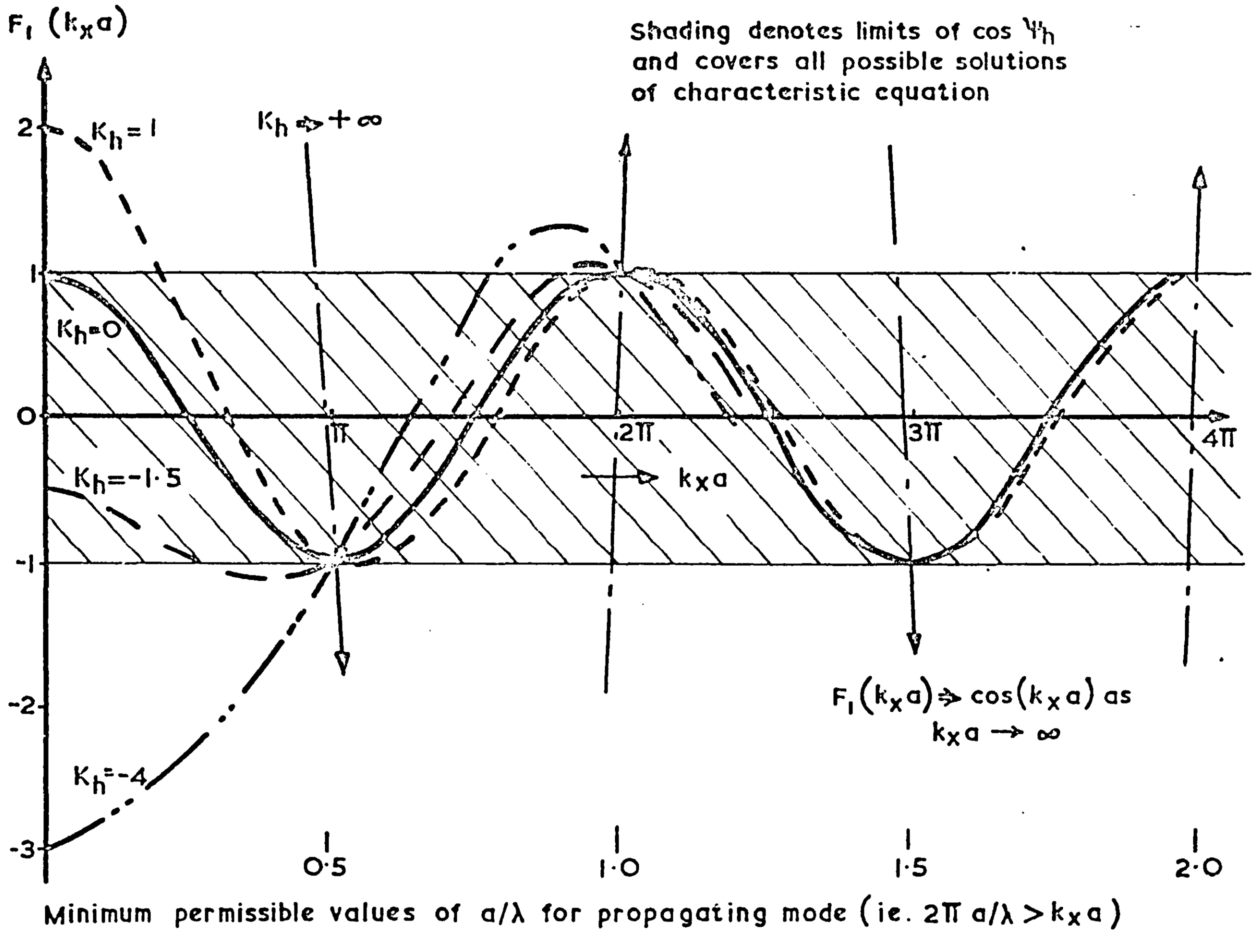

Fig. 2.4 The function F_1 $(k_x a)$, assuming k_x real

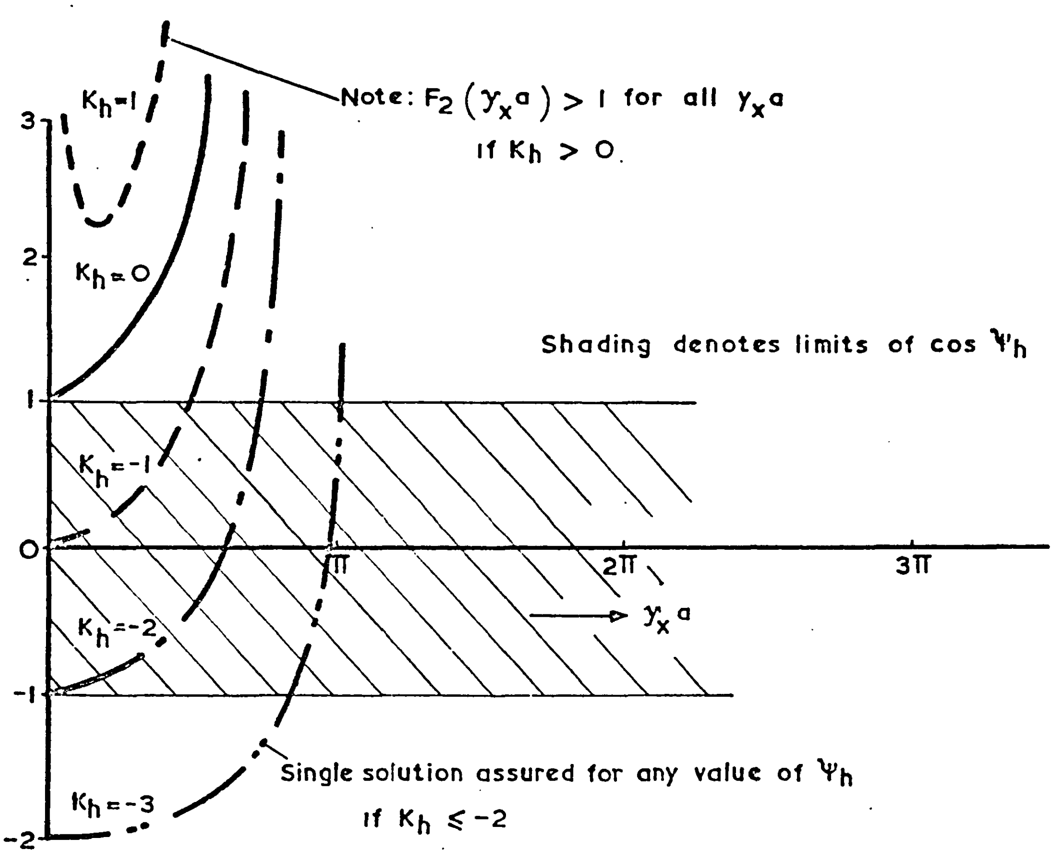

Fig. 2.5 The function F_2 $(\gamma_x a)$, assuming k_x imaginary

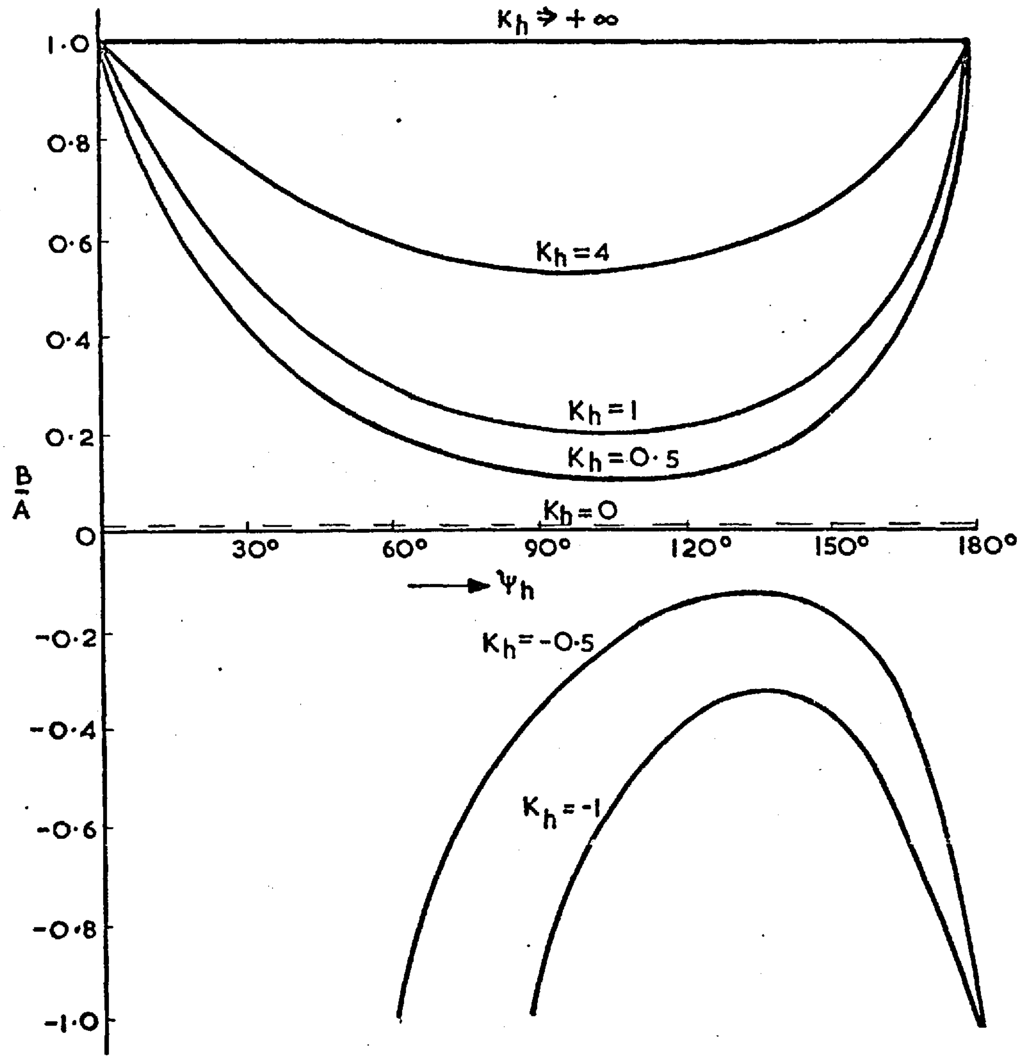

Fig. 2.6 Chart showing B/A as a function of phase increment ψ_h for dominant mode.

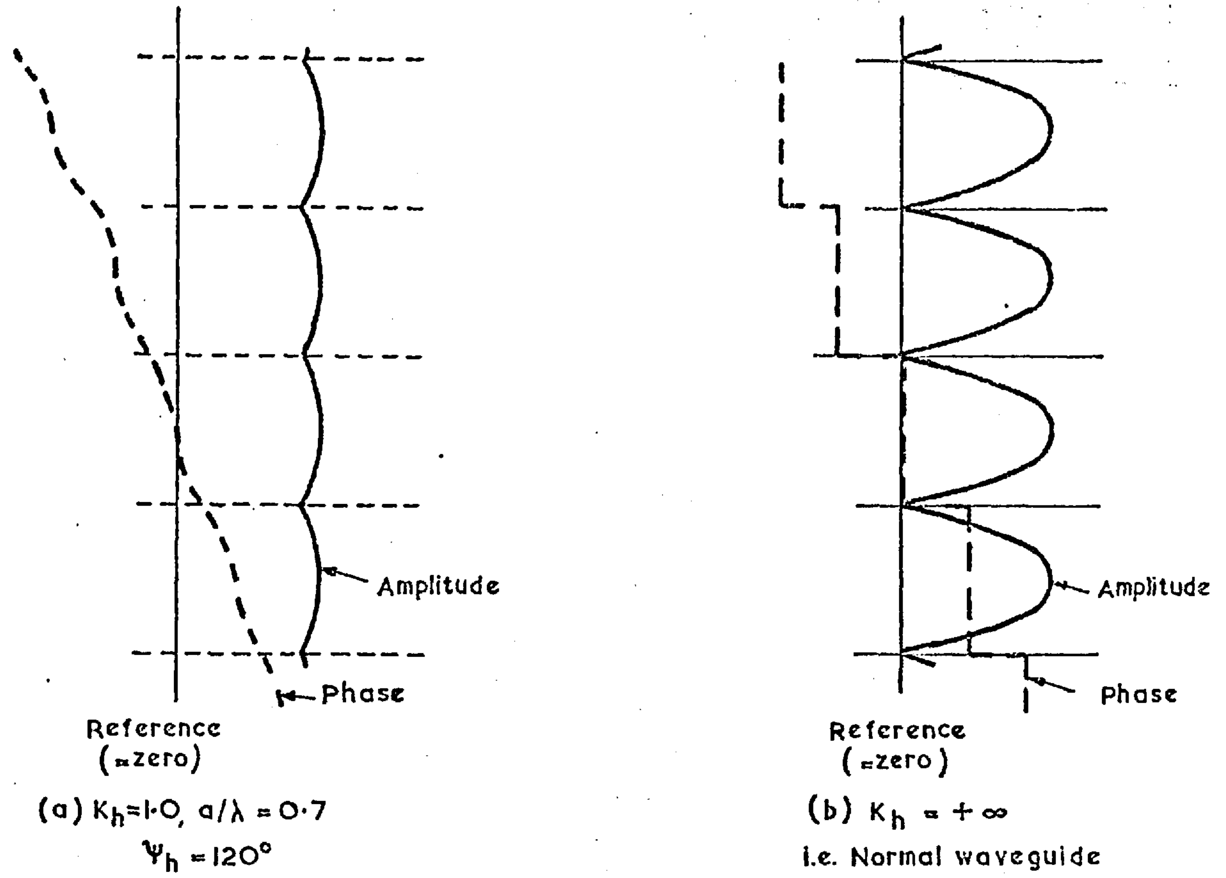

Fig. 2.7 H-plane amplitude and phase distributions - dominant mode

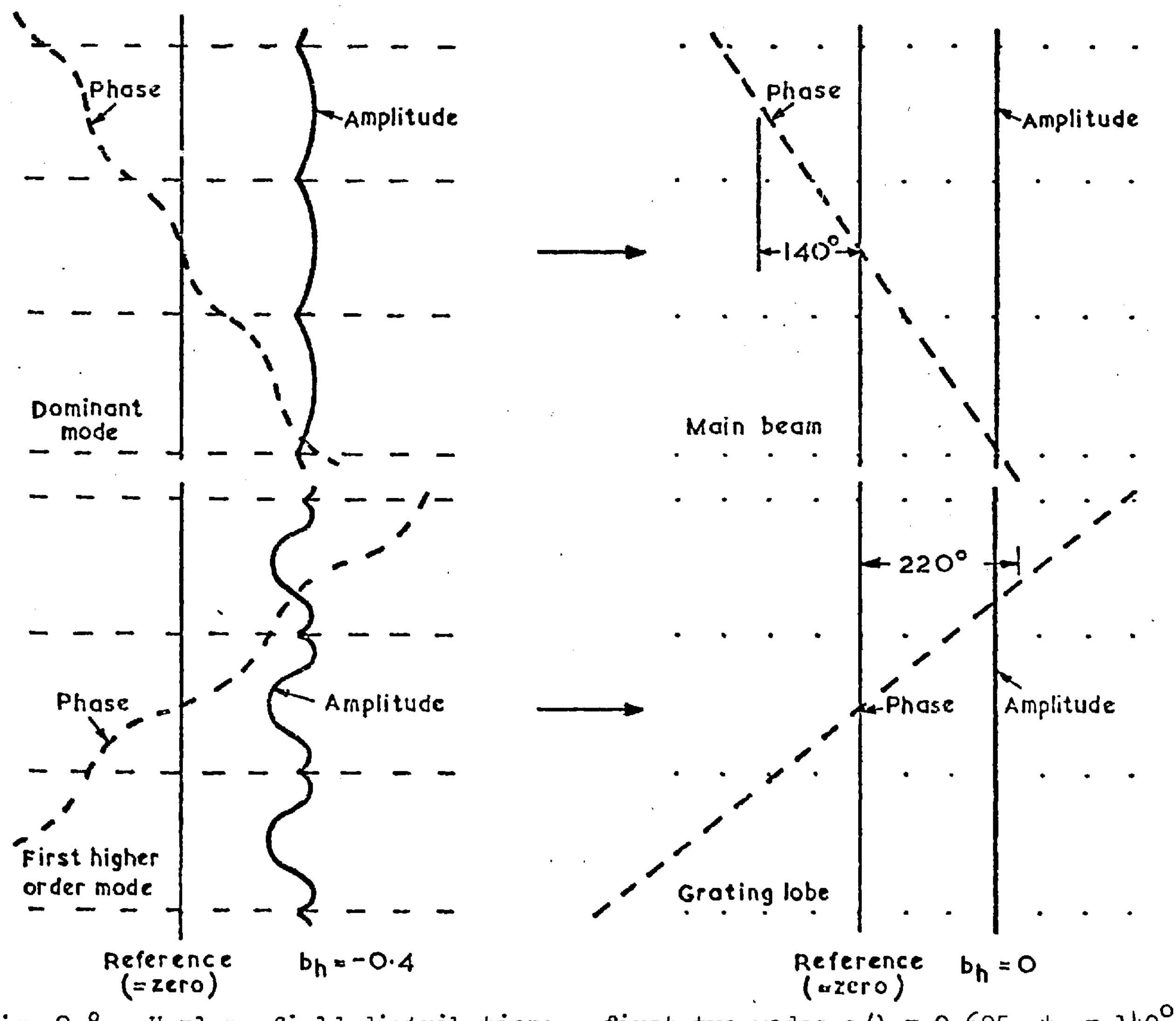

Fig. 2.8 H-plane field distributions - first two modes, $a/\lambda = 0.695$, $\psi_h = 140°$

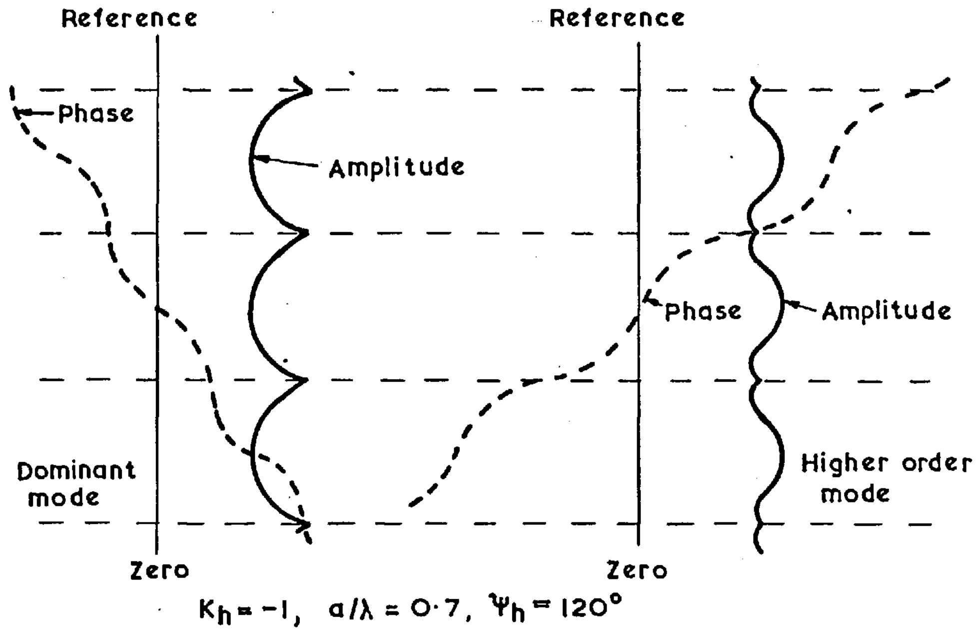

Fig. 2.9 H-plane field distributions for structure with capacitive element boundaries

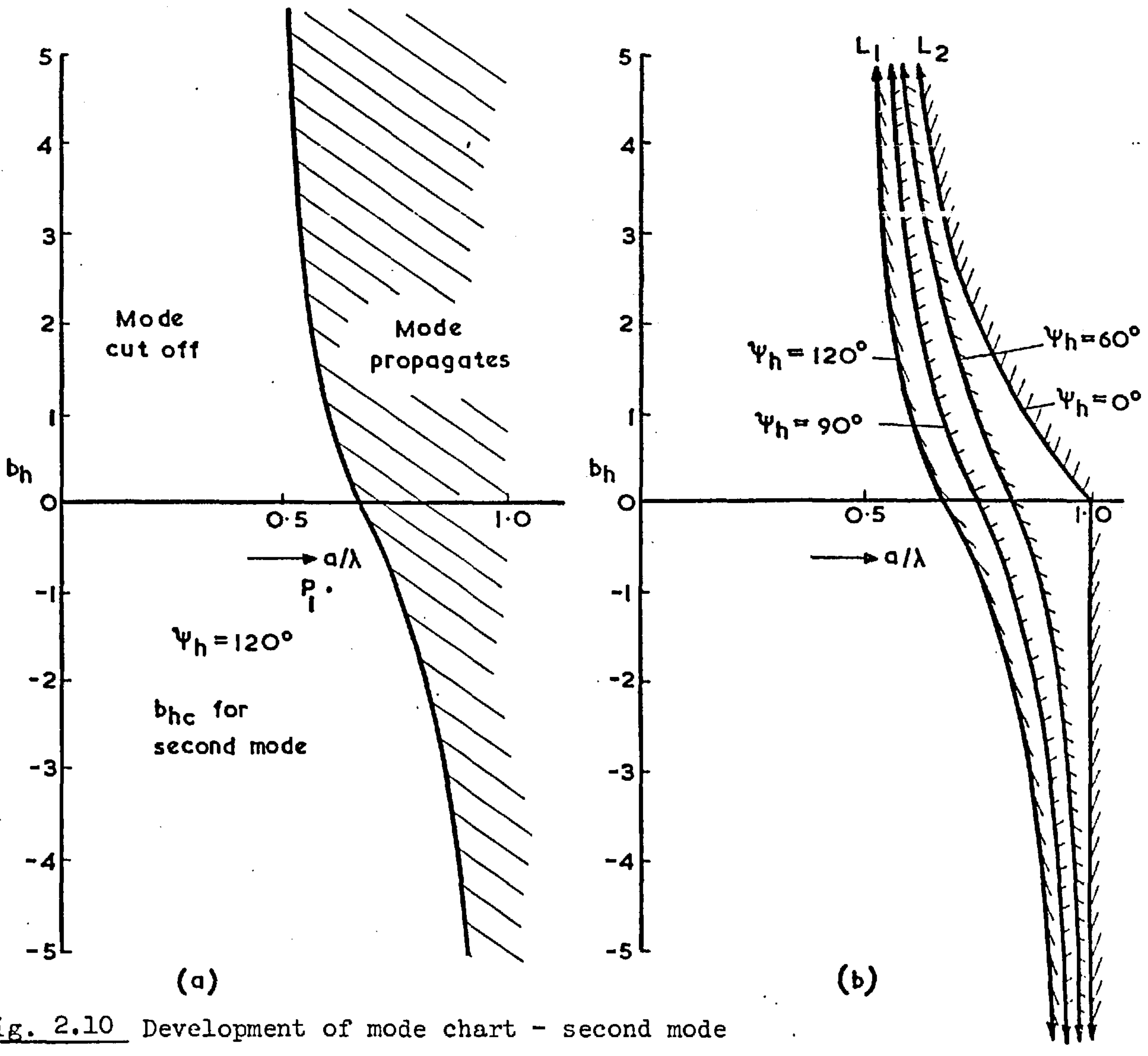

Fig. 2.10 Development of mode chart - second mode

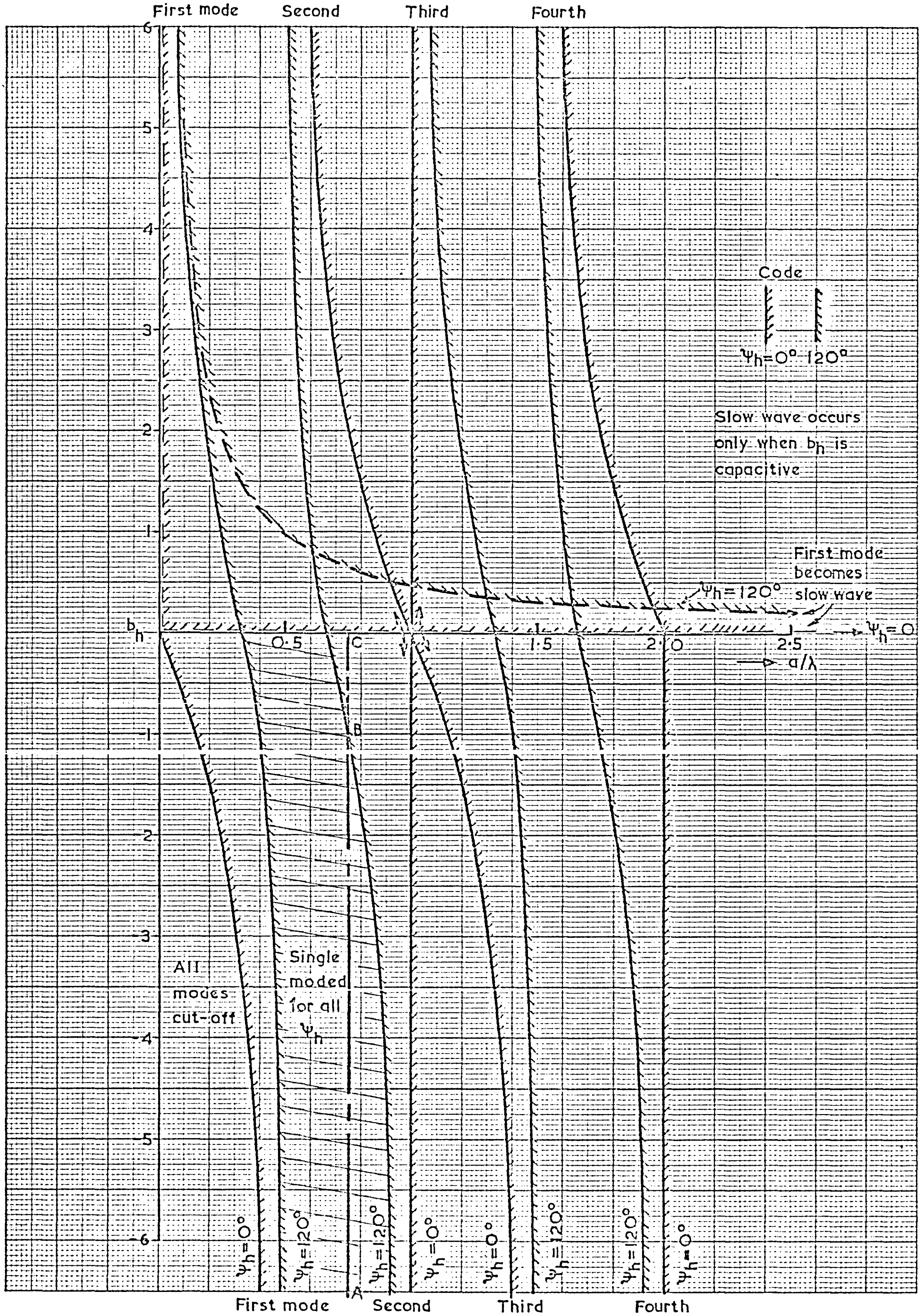

Fig. 2.11a H-plane mode chart - $\psi_{h,max} = 120^{\circ}$.

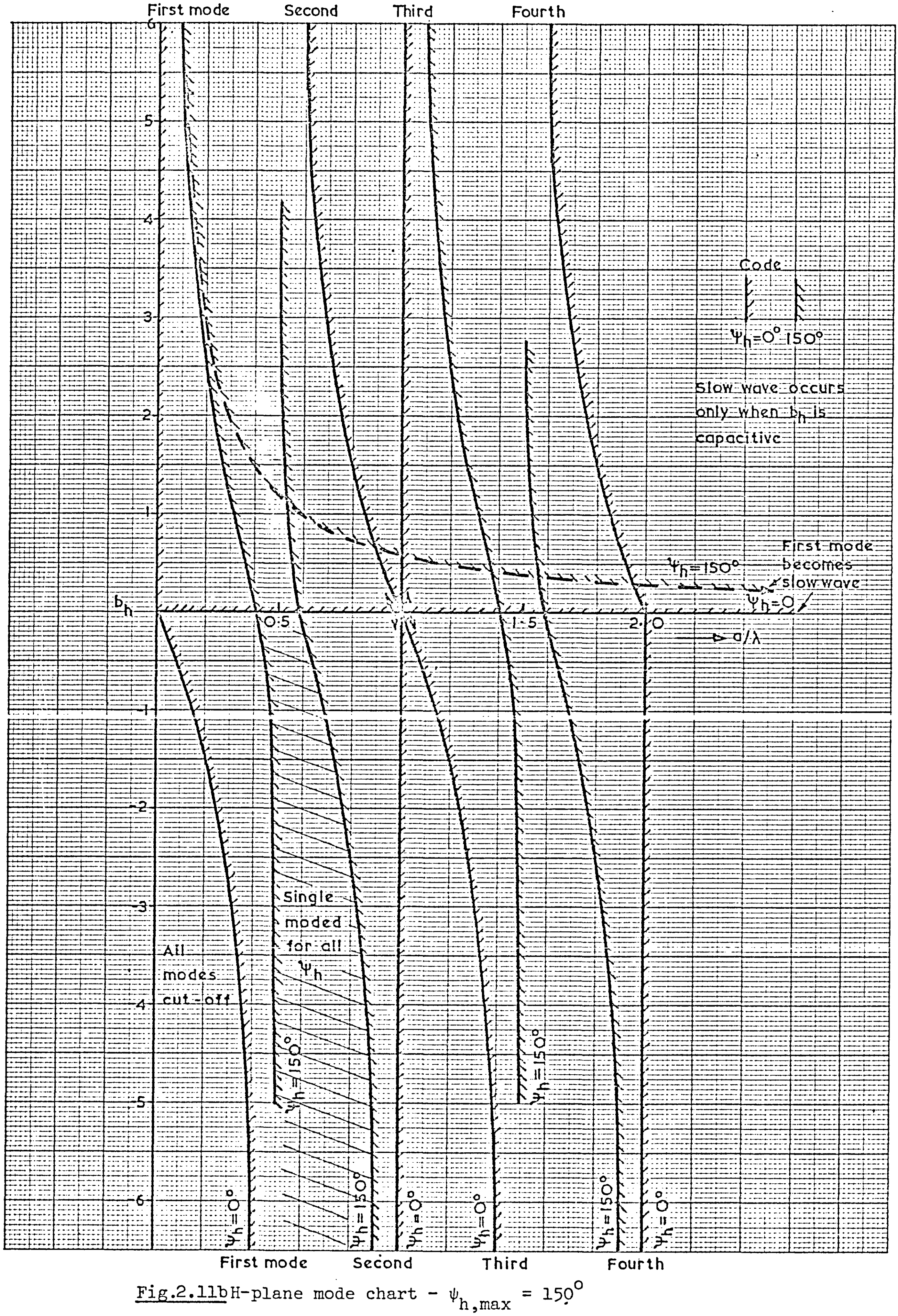

Fig.2.11b H-plane mode chart - $\psi_{h,max} = 150^{\circ}$

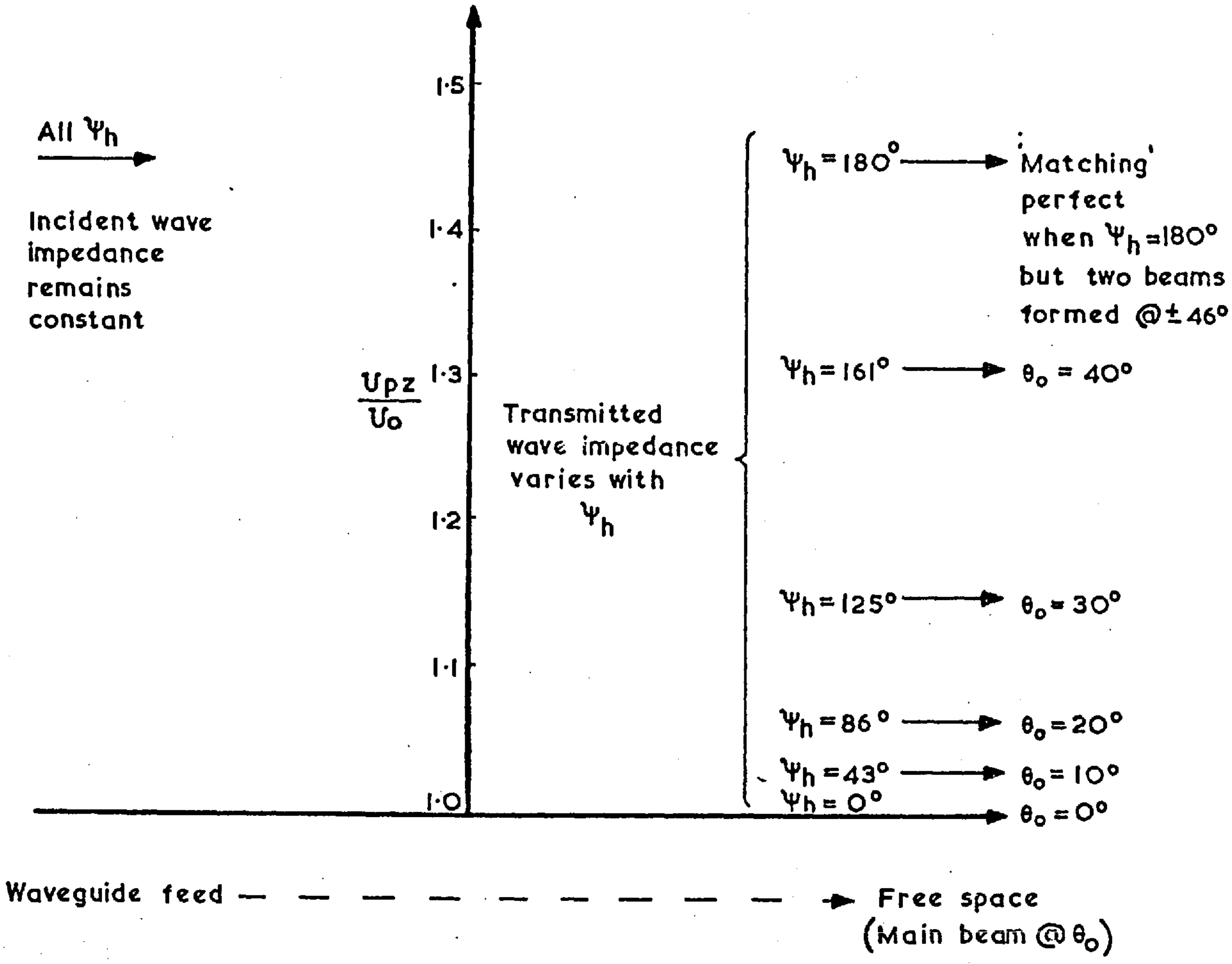

$a/\lambda = 0{\cdot}695$ assumed

Fig. 2.12 Impedance matching problem between waveguide and free space dominant "modes" - H-plane

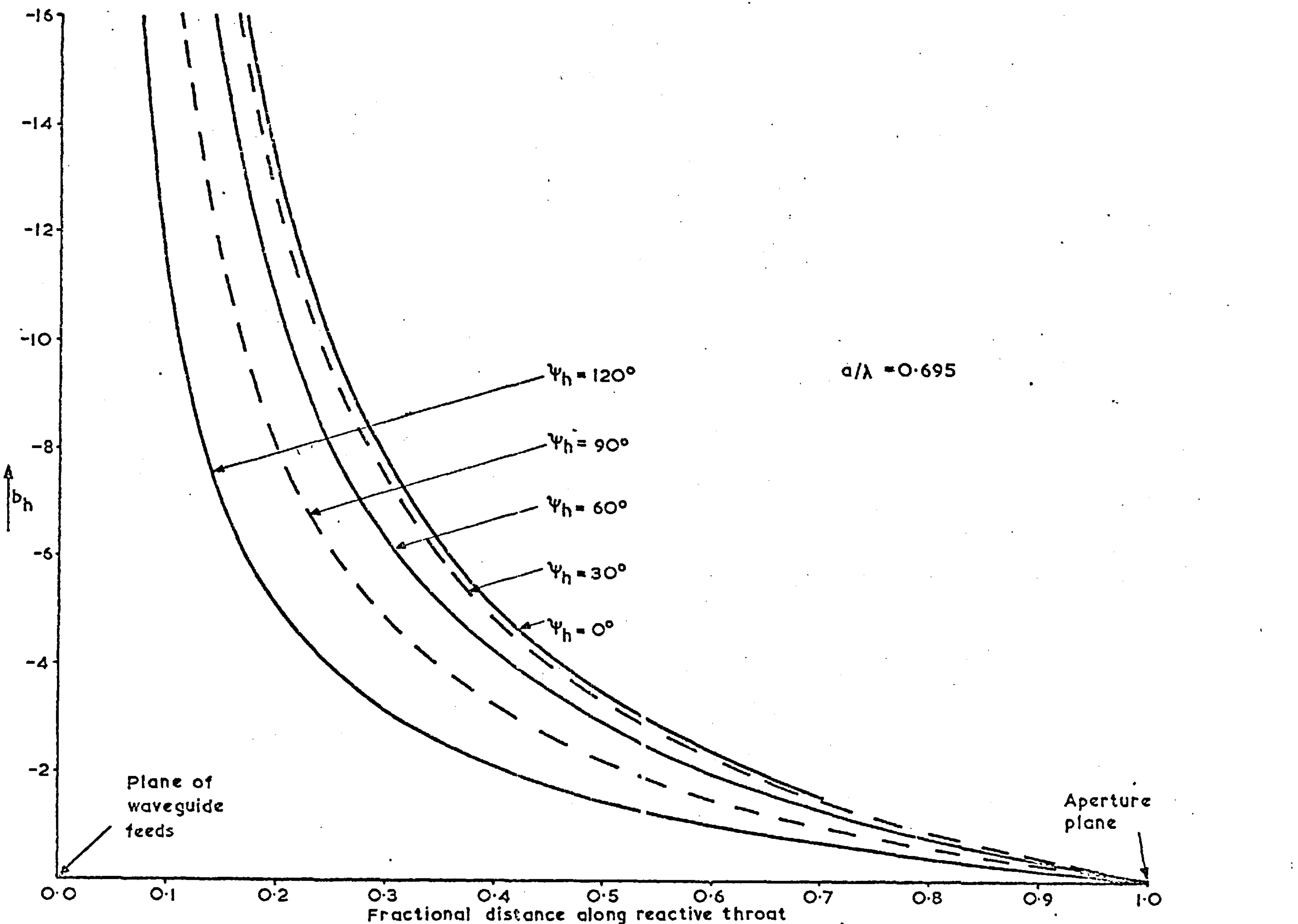

Fig.2.13 Required susceptance profiles for a linear change in phase velocity between the waveguide feed and freespace.

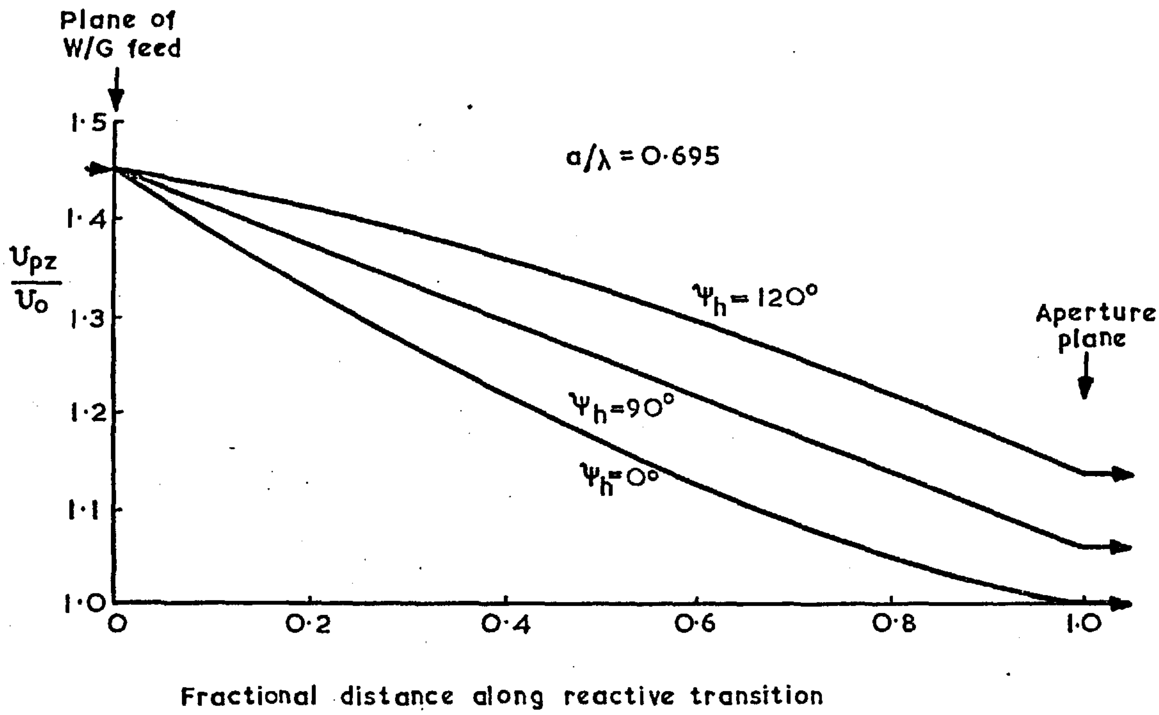

Fig. 2.14 Phase velocity profiles for a specified reactive taper (structure with linear profile when $\psi_h = 90^{\circ}$)

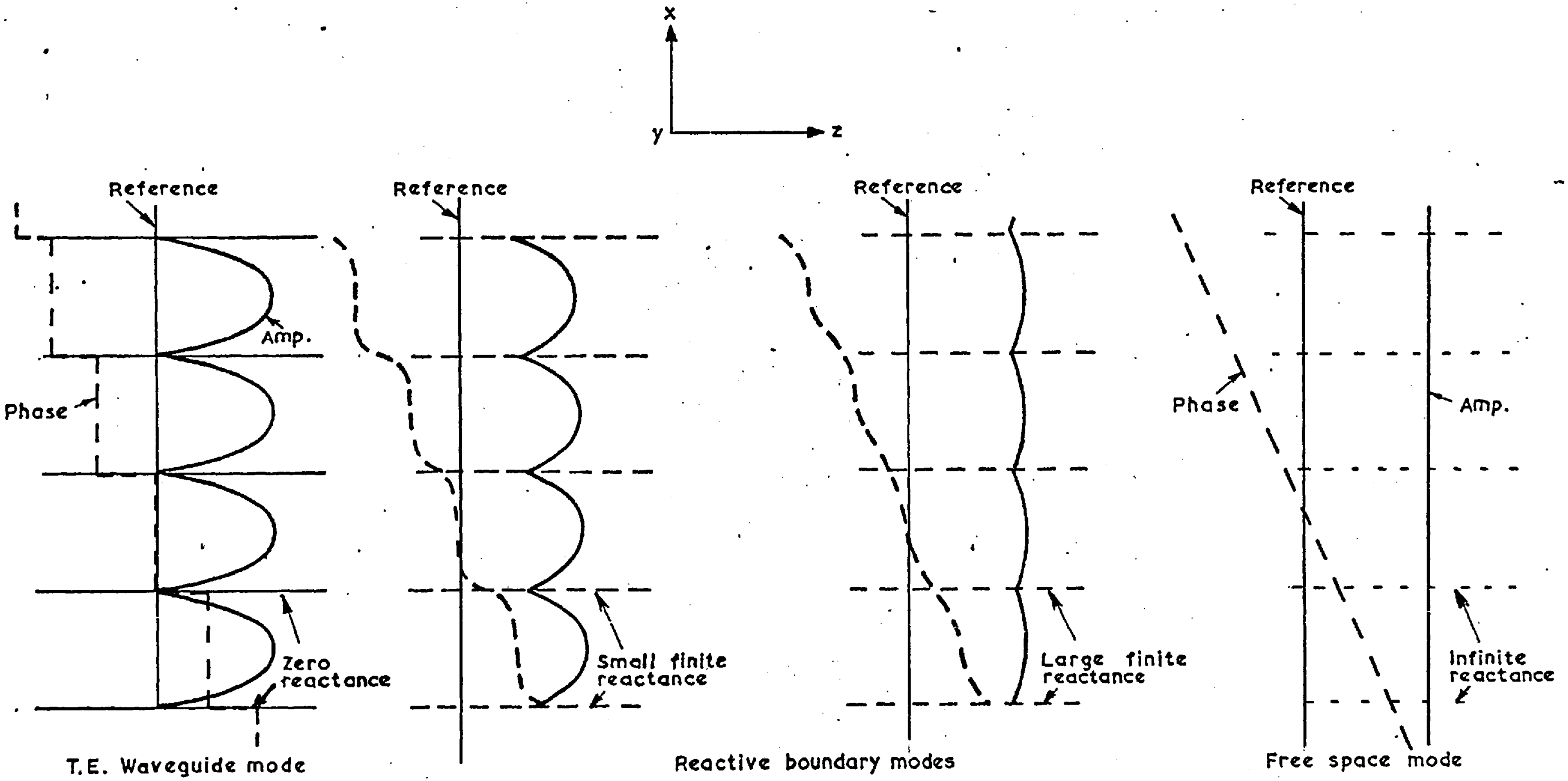

Fig. 2.15 Modification of the amplitude and phase characteristics of the incident field E_y within a reactively tapered structure (H-plane scan).

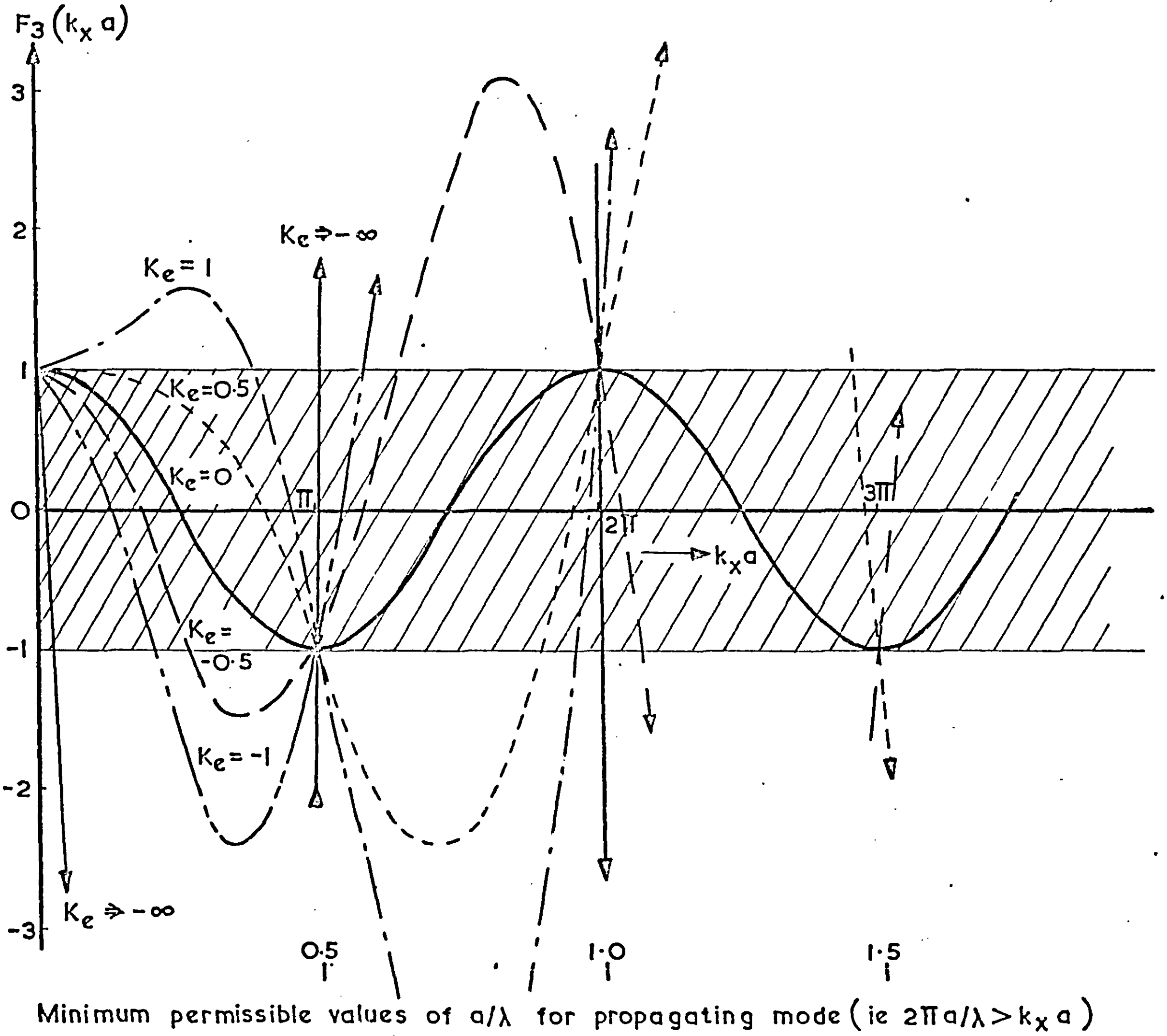

Fig. 2.16 The function $F_3(k_x a)$, assuming k_x real

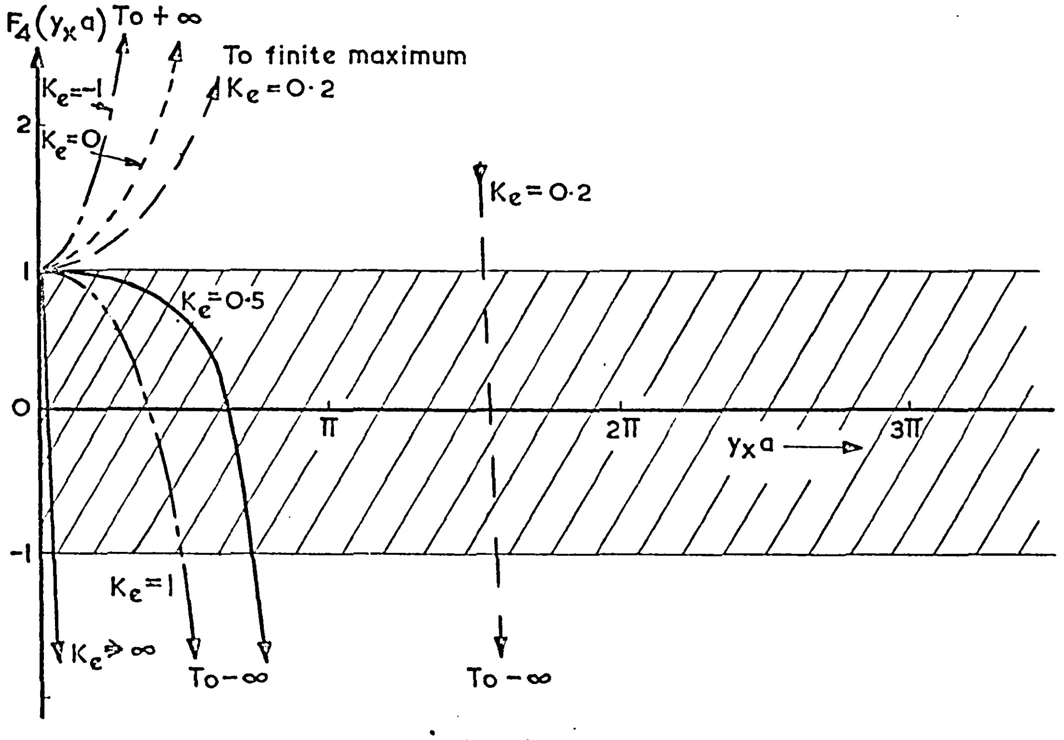

Fig.2.17 The function $F_4(\gamma_x a)$, assuming k_x imaginary

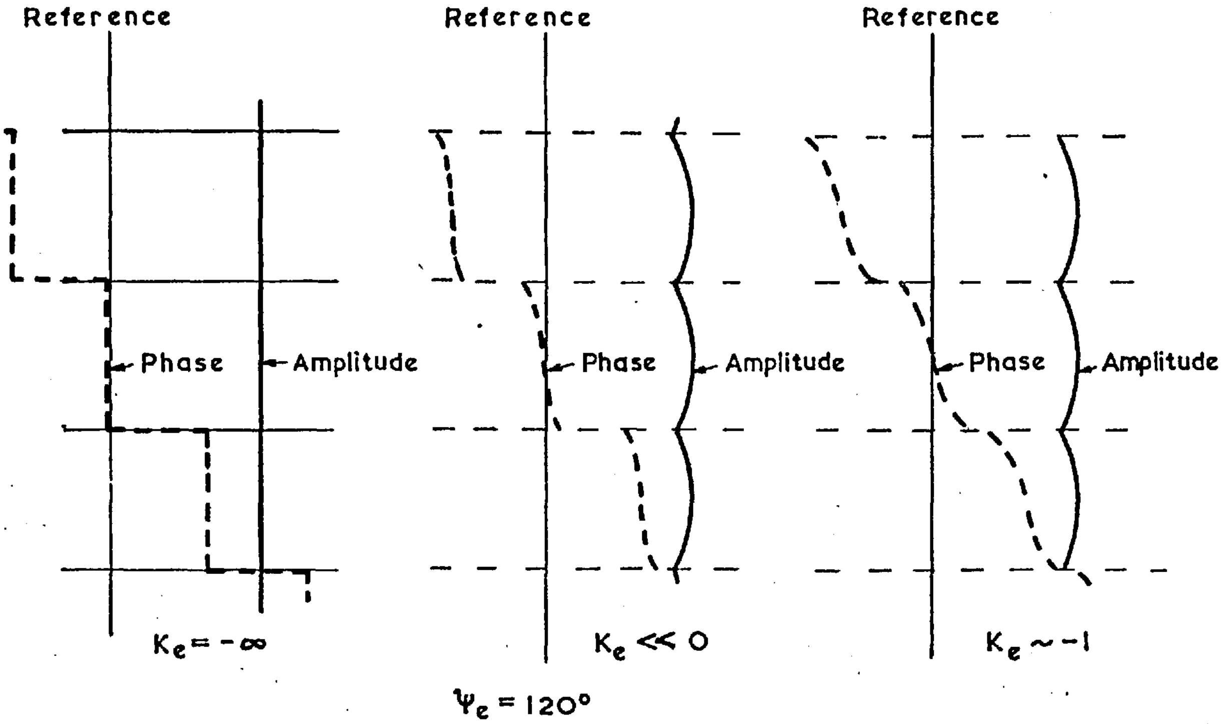

Fig. 2.18 E-plane field distributions for dominant mode (b_e capacitive)

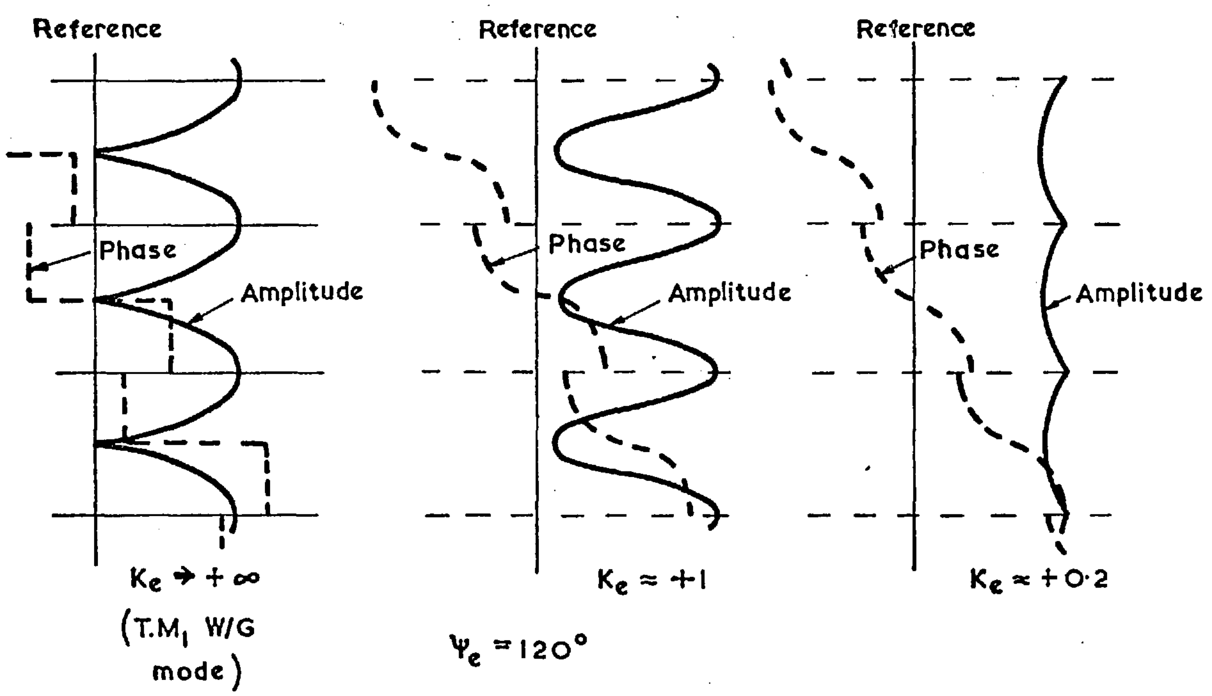

Fig. 2.19 E-plane field distributions for dominant mode - b_e inductive

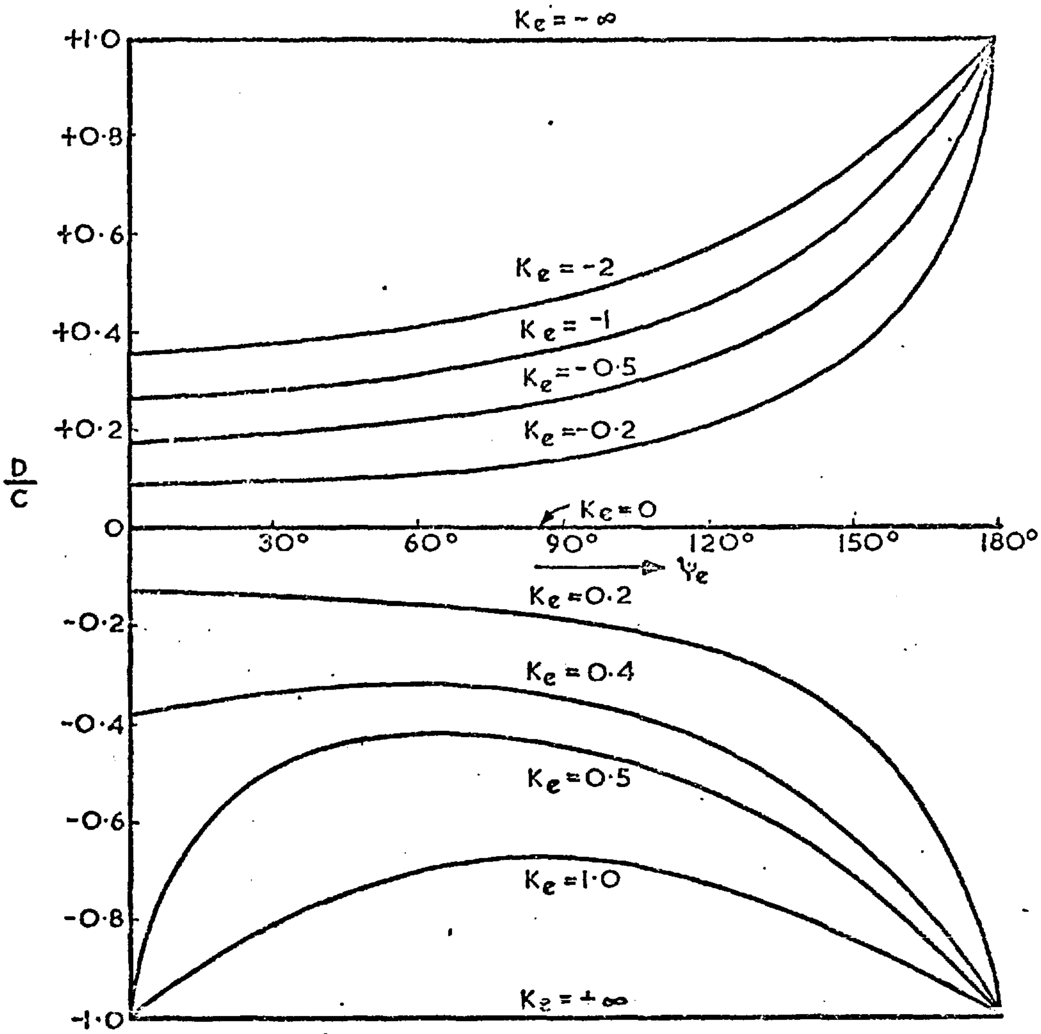

Fig. 2.20 Chart showing D/C as a function of phase increment ψ_e for dominant mode

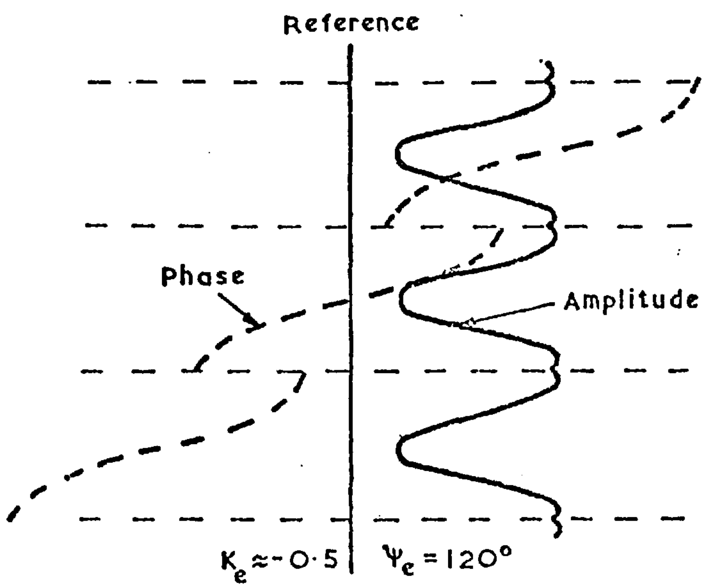

Fig. 2.21 E-plane field distributions for second mode

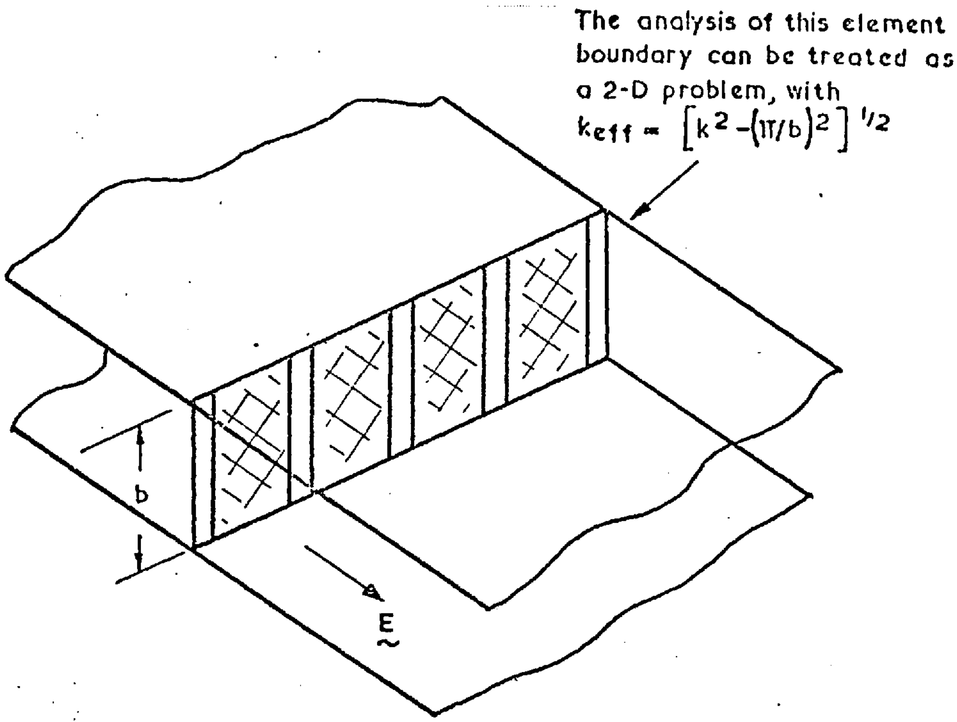

(a)

0·5 < b/λ < 1·0
assumed

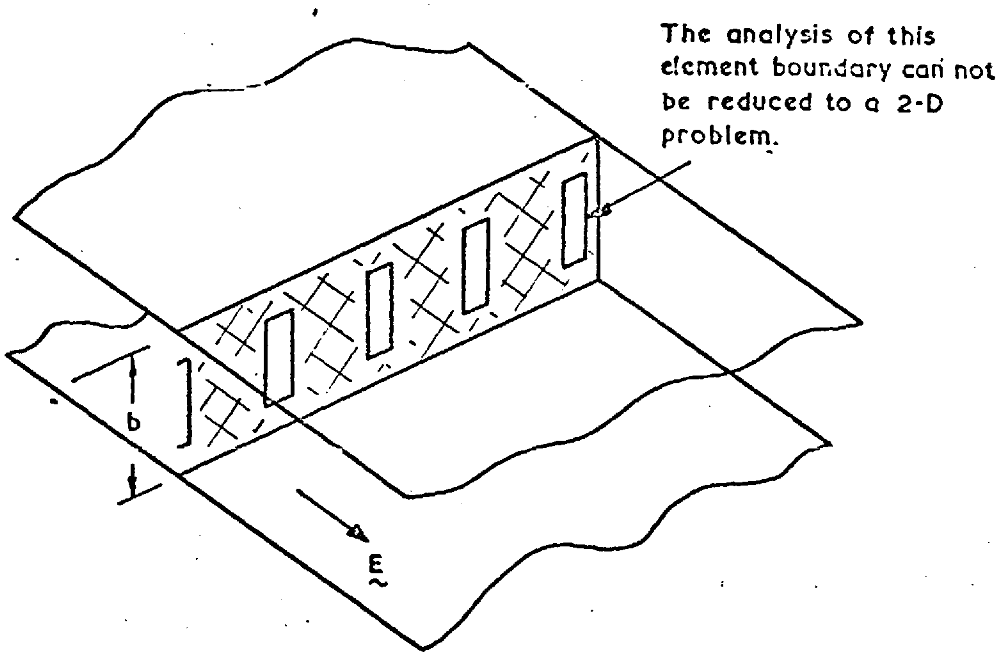

(b)

Fig. 2.22 Examples of fast-wave coupling structures in finite "height" waveguide.

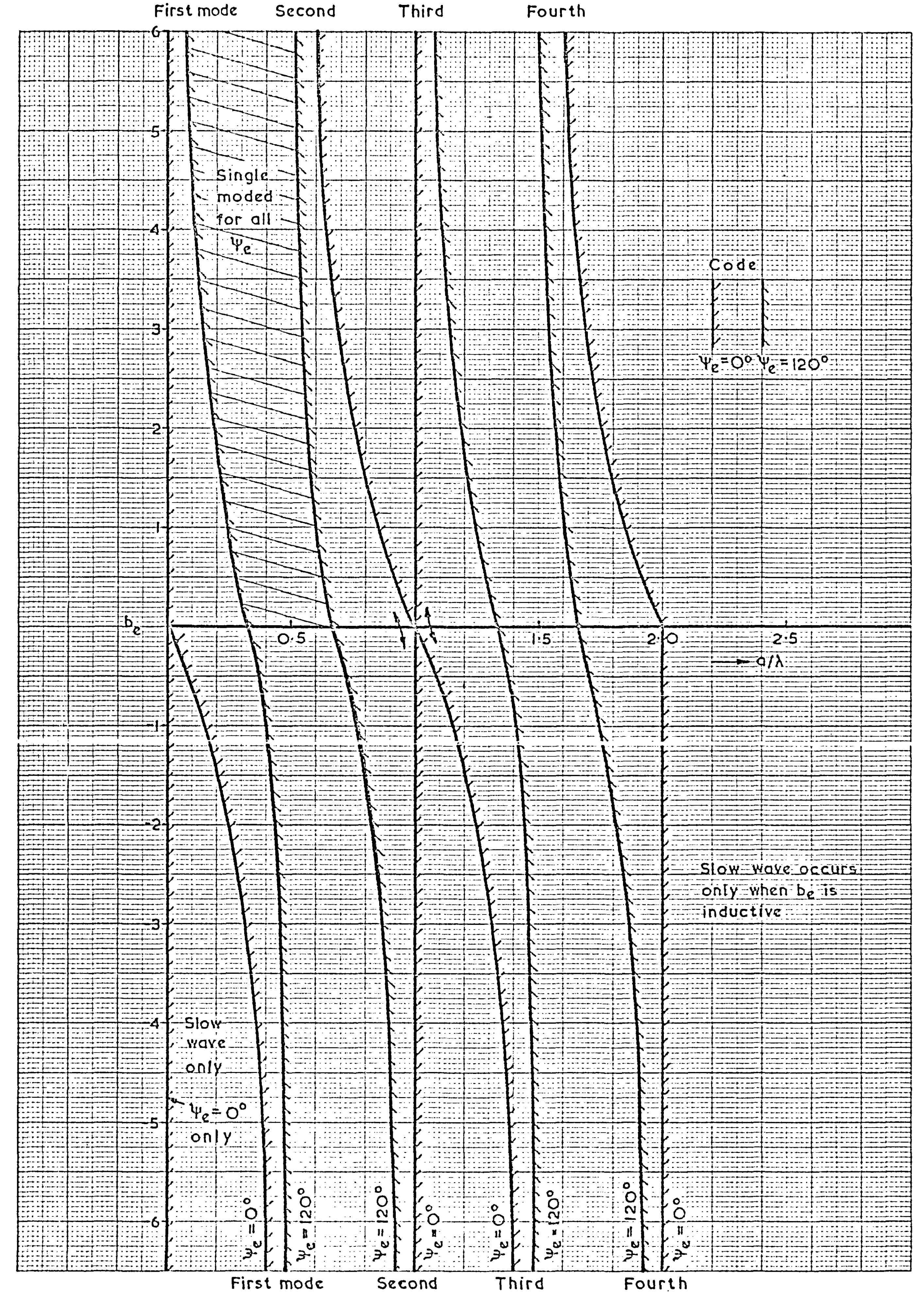

Fig.2.23 Mode chart, E-plane scan - $\psi_{e,max} = 120^o$

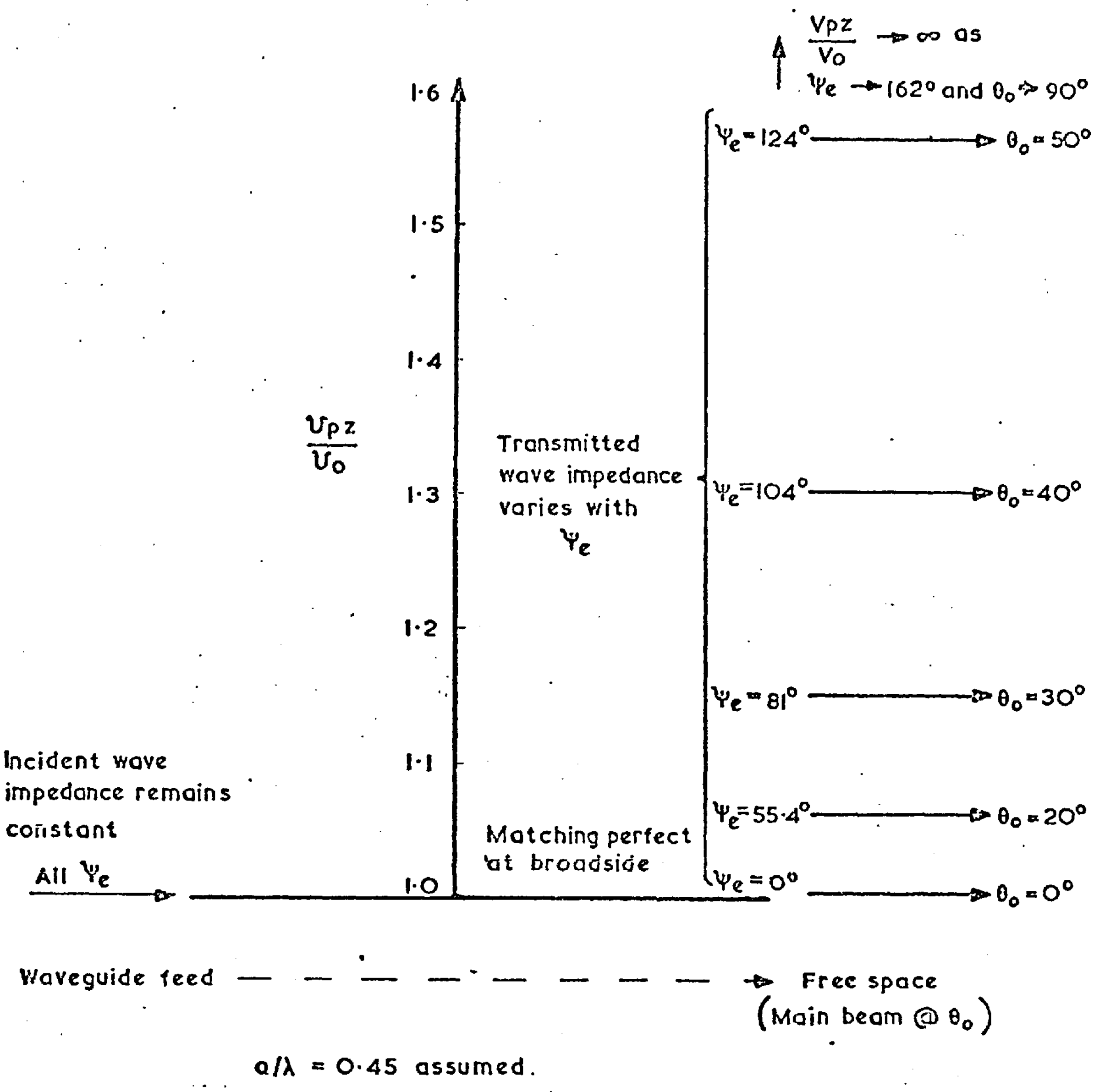

Fig. 2.24 Impedance matching problem between waveguide and free space dominant "modes" - E-plane.

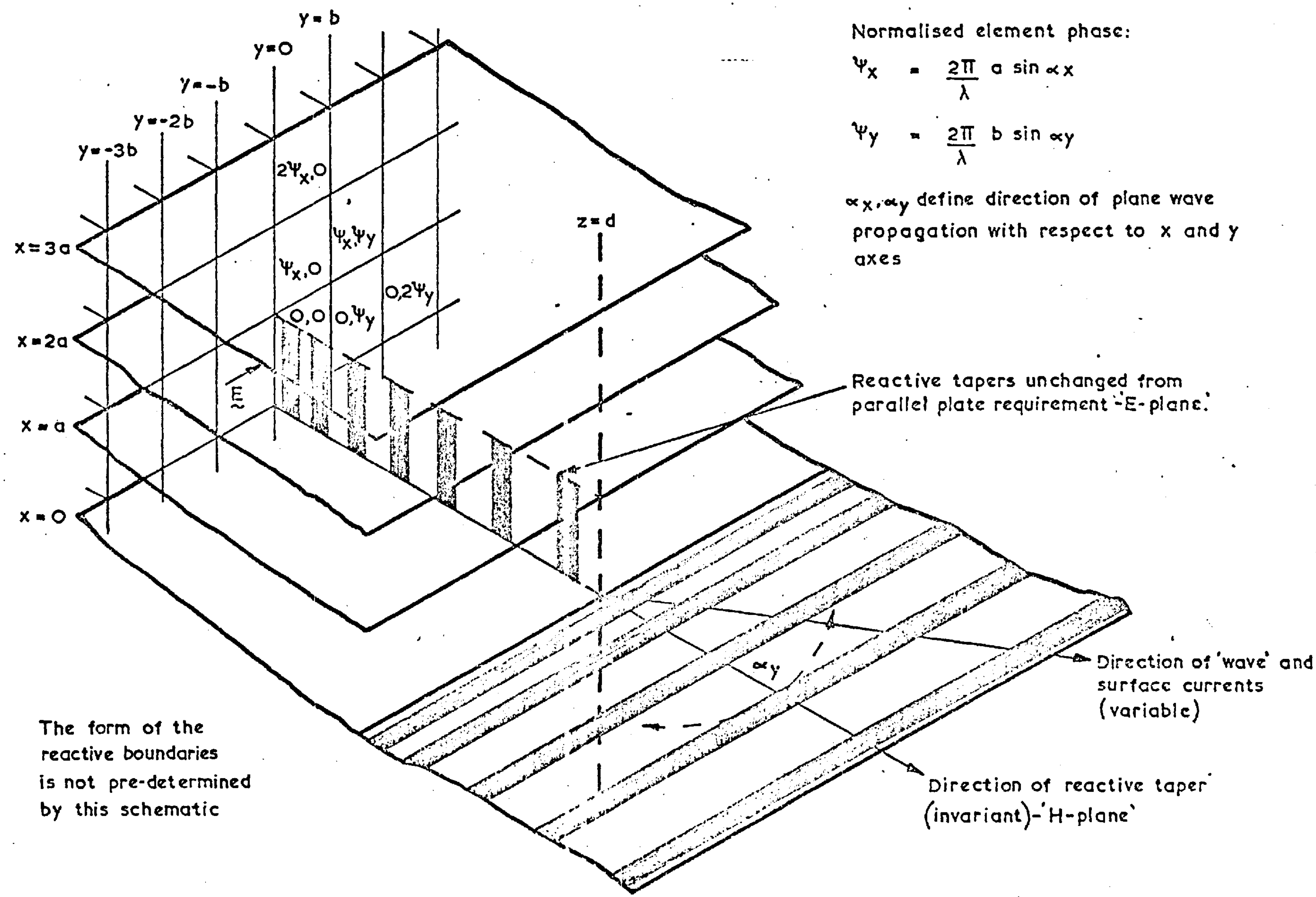

Fig. 2.25 Schematic suggestion for a planar array with reactive element boundaries (The variation of surface current direction with scan angle α_y should be noted.)

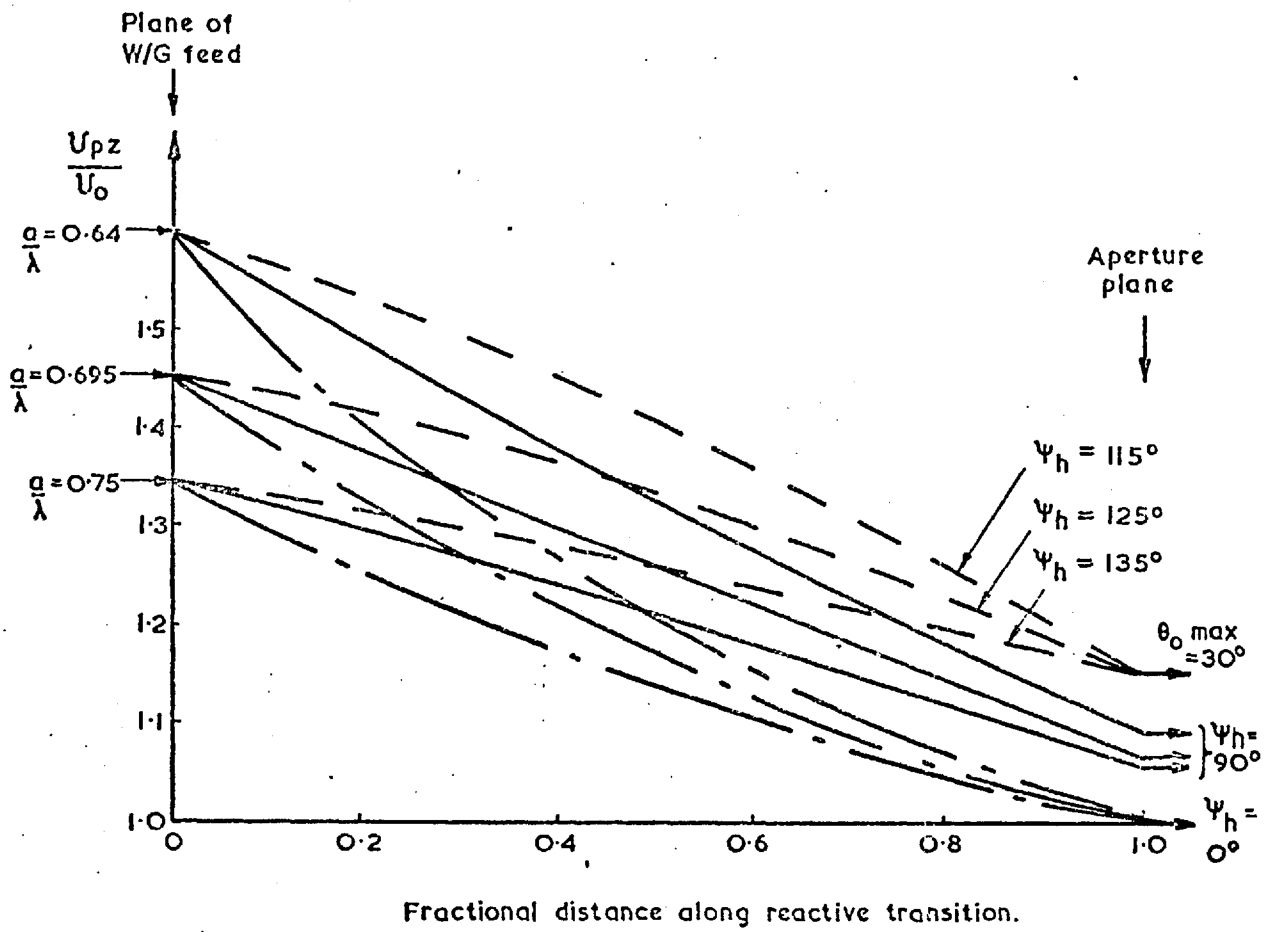

Fig.2.26 Variation in H-plane dominant mode phase velocity profiles over 16% bandwidth, assuming b_h proportional to frequency and a linear profile at centre frequency with $\psi_y = 90^{o}$.

CHAPTER 3

EXPERIMENTAL INVESTIGATION WITH A LENS-EXCITED ARRAY

3.1. Introduction

This experimental evaluation of linear array structures had two major objectives. Firstly, experimental confirmation was required of a reduction in the periodic fluctuations of the aperture fields with reactive element boundaries. Secondly, an appreciation was required of the essential problems to be solved prior to any development of a practical array with "reactively tapered" boundaries.

Considerable freedom could be exercised in planning a suitable approach. As implied by the experimental objectives, however, a number of key parameters had to be decided empirically to conclude an initial design. For example, a conceptually simple form of "reactive taper" was adopted, although it was recognised at the time that the detailed properties of the boundary must prove significant. Similarly, it was considered logical to regard more searching questions about the permissible "rates of taper" in a practical transition, the most appropriate form of the element boundaries, and the "edge effects" associated with an array of finite size, as separate design topics to be assessed partly in the light of initial experimental results. A waveguide model operating at X-band offered advantages of economy and convenience of mechanical design. However, as two distinct experimental methods have evolved for studying the performance of phased arrays, it was first necessary to decide which was more appropriate to a feasibility investigation.

The first experimental method utilizes a relatively small array and depends on the assumption that any element in a practical array is affected significantly only by its immediate neighbours. The central element of the model can therefore be regarded as typical of the bulk of the elements in a larger array. Edge effects can be investigated directly and only a single model is required for a comprehensive assessment of the performance of a larger practical array.

However, basic difficulties arise in determining a priori the minimum number of elements to ensure valid measurements. The mutual coupling between waveguide horn elements (59) and the active impedance at moderate scanning angles (60) have been predicted accurately with models of 10 elements or fewer, whereas the measurement of element patterns and polarisation effects have required more elements to be satisfactory (in one case (61), at least 20). For wide angle scanning, the method is not necessarily accurate (62), and in particular, the existence of "blindness" conditions (16) associated with more complex radiating elements and/or lattice arrangements cannot be recorded, although finite element pattern "dips" are normally observed (7).

By contrast, the second technique, using closed waveguide structures, accurately simulates conditions in an infinite array (62). It was adopted to demonstrate a condition of total "blindness", within the grating lobe limits, for an array with its aperture covered by a dielectric sheet (63), and has been employed extensively to devise matching circuits for wide-angle scanning (64). Each model requires a very small number of elements (or partial elements) and permits the simulated array to be characterised at a single scan condition (for a given frequency) usually by the excitation of one waveguide only. Several models are therefore required to obtain a representative picture of the overall array performance. The method is applicable to arrays exhibiting planes of lattice symmetry, and is developed from the principle of images (62). The measurement procedure usually requires that the array structures be reciprocal, and many scanning conditions cannot be examined unless the simulation waveguide is operated in a higher order mode (for E-plane scanning, a T.M. mode must be used). Conditions corresponding to a propagating grating wave can be investigated when two separately measurable waveguide modes are present in the simulation waveguide (see Chapter 5).

As implied in the title, the first method was preferred, with the choice of a 20 element linear array formed by a plano-concave metal-plate lens (Fig.3.1). In view of the enhanced coupling sought between radiating elements, it was considered that an early estimate of edge effects could prove particularly significant. Secondly, as demonstrated in the following sections, this method ensured that maximum flexibility could be maintained, although not without a corresponding increase in complexity and technical risk.

To minimise development costs, existing equipment and facilities were used exclusively. In addition, it was necessary to restrict the manufacturing technique for the lens to fabrication processes available in an experimental workshop (i.e. standard machine operations). However, this afforded one significant advantage, as the replacement of element "walls" could be contemplated whilst retaining the same lens structure. A two-stage programme requiring *comparative* measurements was therefore adopted. The lens was fitted initially with conducting walls to check its operation. In this form, the "reactive taper" can be considered infinitely abrupt. Subsequently, reactively tapered boundaries of finite length were substituted, to demonstrate the difference in performance.

Although several practical problems arose from the specific choice of a lens as the means of exciting the model array (see following sections), the advantages afforded by this method were considerable and included:

(i) overall flexibility,

(ii) convenience when repetitive measurements at different scanning angles were required, and

(iii) simplicity of excitation.

An analysis of the design and performance of an asymmetrical dual-polarised waveguide lens producing two beams (a main beam and a grating lobe) is given in Section 3.2.

The experimental results for the waveguide model array are presented in Section 3.3. The H-plane results are shown to be in close agreement with predictions based on an infinite array element pattern, while the grating lobe attenuation in the E-plane depends on the included angle between continuous conducting flares. The control of E-plane element patterns afforded by flares is examined in Section 3.4.

Disregarding the finite size of the model array, a design procedure for determining the reactive boundary dimensions is outlined in Section 3.5. Limitations imposed by experimental factors and theoretical uncertainties illustrate several of the design problems.

The measured performance in both polarisations is given in Section 3.6. Detailed control of the sectoral element pattern is demonstrated in the E-plane and techniques for reducing edge effects are discussed. Results in the H-plane reveal a reduction in grating wave level at large scan angles, but the overall performance does not demonstrate the viability of the design concept.

The significance of the experimental programme is assessed in the final section, with two topics identified for further investigation.

3.2. Lens Development

3.2.1. General Features

A general appreciation of the experimental model is conveyed by the schematic diagram given in Fig.3.2. The following features should be noted:

(i) The lens was not designed to permit symmetrical scanning about broadside. To provide a direct test of the reactive boundary proposal, the first requirement was for operation of the "lens" consistent with the formation of a visible grating lobe over a portion of its useful scanning range. For design parameters within the normal limits for a metal plate lens (65, 66, 67), satisfactory broadside radiation could not be expected. However, results for wide angle scanning, coupled with element pattern measurements, were sufficient for evaluation purposes.

(ii) A standard waveguide horn was used to feed the lens. The very low efficiency of this simple method of excitation was not significant. By isolating the concave surface of the lens and the feed horn within a suitable r.f. sealed "anechoic" enclosure, external interference and reflections within the feed could be suppressed. Measurement of the required radiation pattern involved rotation of the entire rig shown in Fig.3.2. A more efficient arrangement might have utilised a parallel plate feed horn forming an integral section of a single overall device. Apart from the more serious tolerancing requirements, this approach would have limited the scanning flexibility and access to the individual waveguide elements.

(iii) The lens was constructed with square waveguide elements to permit measurements in both E and H planes. In addition, only one set of reactively tapered structures were developed. To utilise these structures in both polarisations, a number of design restrictions were accepted without compromising the experimental objectives (see Section 3.5). The economy resulting from this approach was significant.

(iv) The general configuration of the lens and feed provided a basis for a comprehensive set of measurements. The frequency, the number of excited elements and the effective amplitude tapering of the aperture fields (by attenuators in the elements) could be readily varied in addition to the key parameters indicated above (viz. scan angle and polarisation). Furthermore, it was intended that direct and indirect estimates of the impedance match and the mutual coupling between elements should be obtained, although, as already stressed, the lens was not intended as a model for the accurate measurement of major design parameters.

3.2.2. Details of Electrical Design

The lens surface was designed by geometrical optics. Overall, this simplified approach was considered adequate in spite of the unusual limitations illustrated by the following summary.

A suitable ray path geometry for determining the surface is shown in Fig.3.3. For either polarisation, the refractive index (η) of the metal plate region is given by

$$\eta = \left[1 - (\lambda/2a)^2\right]^{\frac{1}{2}} \qquad \text{.... (1)}$$

where λ = free space wavelength;

and a = square waveguide element dimensions, which was required to be <0.707 to prevent propagation of higher order waveguide modes. The other parameters, viz. the ratio of focal distance to aperture size (f/D) and the surface curvature, are constrained by the relation (from Fig.3.3).

$$OA + BC = OP + \eta PE \qquad \text{.... (2)}$$

with the point P(x, y) given by

$$(u^2 + v^2)^{\frac{1}{2}} + (y - v)\sin\theta = (x^2 + y^2)^{\frac{1}{2}} + \eta(u - x) \qquad \text{.... (3)}$$

Taking $v \simeq u \sin\theta$, sets of curves for P were obtained in terms of η and u.

The requirement in the experimental lens for a visible grating wave effectively eliminates the standard design "trade-off" between the surface curvature and the refractive index for broadside radiation (Fig.3.4). As shown in Fig.3.5, any decrease in η immediately requires an increase in θ, since

$$\frac{a}{\lambda} > \frac{1}{1 + \sin\theta_o} \qquad \text{.... (4)}$$

is equivalent, from eqn.(1), to

$$\sin\theta_o > 2(1 - \eta^2)^{\frac{1}{2}} - 1 \qquad \text{.... (5)}$$

A clear distinction between the main beam and the grating lobe was preferable for evaluation of the reactive boundaries. This implied that the phase increment ψ should remain substantially less than 180°. (Whenever ψ = 180°, a symmetrical dual-beam radiation pattern becomes inevitable). With the grating lobe at $\sim -70^\circ$, and the main beam at $\sim +30^\circ$, two further requirements were fulfilled. Firstly, the grating lobe was sufficiently remote from end-fire to limit the effects of aperture projection on its amplitude (cf. Chapter 1). Secondly, since the critical susceptance for the second H-plane mode would be small, moderate grating lobe suppression could be expected with a transition structure (cf. Section 2.3).

The value of η was therefore set at 0.67 (i.e. just less than the practical upper limit of 0.707 for square waveguide) and the corresponding aperture dimension D became 13.5λ for 20 elements, with an allowance for wall thickness.

Selection of a suitable value for u was another compromise. To maintain an acceptable operating efficiency within the anechoic enclosure and an overall rig of manageable proportions, an upper limit was clearly necessary. In conflict with these requirements, satisfactory operation of the lens required u as large as possible to minimise higher order reflections at the lens surface. This effect is illustrated in Fig.3.6, where the useable aperture dimension reduces approximately in proportion to u. Final design details for a lens operating at a frequency of 9.00 GHz are given in Fig.3.7 together with the "optimum" scanning arc for the feed horn. The arc was determined graphically and effectively suppressed quadratic phase errors (65).

All the practical degrees of freedom were utilised by this design procedure. (In view of the severe surface curvature, zoning was considered impractical). Coma aberration (68) was not expected to be serious with the angular offset of the main beam limited to approximately one beamwidth (cf. (65)). By ray tracing techniques, a maximum phase error of $\pi/6$ across the array aperture was estimated for a main beam scanned towards broadside by 8° (i.e. from 32° to 24°). Near the limit of this scanning range, complete grating lobe suppression was ensured, while the "peak" of the grating lobe became invisible for a main beam at 26.2°. It was estimated that the maximum phase error due to a 4% increase in frequency ($\eta = 0.700$) would be quadratic and between 45° and 60° at the aperture edges. Although more accurate methods of analysing the scanning and frequency limitations of lenses have been developed (65), their application to this design exercise was not warranted.

The problem of secondary reflections at the concave surface of the lens (Fig.3.8) was inevitable for practical f/D ratios, in view of the severe periodicity requirements across the plane radiating aperture. For the H-plane scan, a better estimate of lens performance can be obtained directly from published curves of the transmission coefficients for a plane wave incident on an infinite array of parallel plates (69). (The theoretical solutions for this problem have been obtained for both polarisations (70), but these classical papers do not develop the solution under conditions permitting propagating secondary waves (cf. Chapter 4)). In reference 69, it is shown that satisfactory operation can be expected (for a single surface lens) in the double reflection region, with a modest increase initially in the phase error and a more severe discontinuity in the amplitude distribution across the plane aperture. However, it must also be concluded that geometrical optics provide, at best, only a first order estimate of the performance of metal plate lenses under these conditions. On this basis, it could be argued that a more accurate approach to the "lens" design was appropriate. This argument was rejected, however, for the following reasons:

(i) With multiple reflections from both surfaces of the lens, accurate prediction of the overall aperture field would be very difficult.

(ii) A modified concave surface, improving the phase distribution across the array, would be appropriate to one polarisation only.

(iii) In view of the severe curvature of the lens surface, significant errors would be expected from application of parallel plate theory for infinite structures.

(iv) The overall performance of the lens was governed in part by other

(iv) contd...

factors (e.g. mechanical tolerances). It was more appropriate, therefore, to plan for control of the amplitude and phase within each individual element.

Subsequent experience justified this strategy.

Apart from transmission and reflection effects at each surface of the lens, the basic amplitude distribution was governed by the feed horn and its orientation. An available X-band horn providing E and H plane 3dB beamwidths of 11° and 13° respectively was utilised. For "symmetrical" illumination of the lens, with this horn, the fields incident on the extreme elements were down by 4 to 6dB. Phase centre measurements were taken to confirm the validity of the "point source" principle over the angular limits subtended by the lens. Relative phase constancy of $\pm 5^{\circ}$ was demonstrated with a microwave bridge, after a sequence of convergent adjustments to determine an optimum phase centre. For both polarisations, the experimental results were in satisfactory agreement with recent theoretical analyses (71).

3.2.3. Details of the Mechanical Design

The basic principles of the mechanical construction are evident in photographs of the partially assembled unit (Figs.3.9, 3.10). Channels with a side clearance of less than 0.1mm were milled in the top and bottom plates to accommodate the element walls. Although the theoretical model assumes zero thickness boundaries between elements, practical considerations dictated a minimum thickness of 0.02λ (i.e. S.W.G.22 plate). The significance of this finite wall thickness on the properties of a reactive grating is examined in Section 3.5. Electrical continuity in the corners of each element was obtained by partially filling the channels with silver loaded resin prior to assembly. The excess resin forced from the channels by entry of the element boundaries was removed after hardening, and, as a final precaution, a coat of conducting paint was applied along all joints. To remove the element walls, the resin was first dissolved in a trichlorethylene bath over a period of several days.

As shown in Fig.3.9, the boundaries were made in two sections. The conducting walls required to achieve the basic lens action were not removed, and their lengths were sufficient to fit attenuating pads and phase-shifters. The major mechanical factors governing the length of the reactive tapers were their high cost, the difficulties of assembly and accumulative tolerances. The method of fabricating the reactive boundaries was applicable to a custom requirement only, and was realised to be inappropriate for batch production. To maintain the required uniformity, in the transverse sense, each of the reactive septa was separately machined in a special jig and all corner fillets were removed by hand (Fig. 3.11). The design was governed by the narrowest widths of a practical slit saw (for the maximum finite susceptance) and a residual metal strut (for minimum non zero susceptance near the aperture).

A throat length of 6λ was adopted for the reactively tapered septa (see Section 3.5).

Supporting ribs of passivated mild steel angle were used to minimise deformation of the top and bottom plates. The vertical flare and the extension plates were made optional to permit measuring flexibility with respect to edge effects, matching and vertical plane directivity. Their significance is examined in subsequent sections. Mechanical joints were made electrically conducting wherever necessary by using adhesive r.f. metal tape.

3.2.4. Initial Characterisation

Preliminary evaluation of the lens, as a linear array of radiating waveguides, proved quite disappointing. The amplitude and phase distributions were measured with a network analyser by clamping a suitable transition (Fig.3.11(g)) to each radiating aperture in turn, and terminating all the remaining elements in matched loads. This technique was not an exact basis for predicting the radiation pattern, since it implies an array factor unaffected by mutual coupling variations due to edge effects and multiple reflections between the two faces of the lens. However, it was a valid method for assessing tolerances, cross-polarisation and transmission characteristics of the elliptical surface.

The results for these E and H plane measurements are given in Figs.3.12 and 3.13 respectively. Superimposed on a systematic phase error caused by transmission effects at the elliptical surface, random errors (of 80° maximum in phase) due to waveguide tolerances were almost an order higher than expected. Dimensional checks revealed variations in the milled channels exceeding ± 0.3mm, while their misalignment (between top and bottom plates) introduced slight twists in the conducting walls, so compounding the differences in propagation characteristics of the waveguide elements. The degree of mode conversion to the cross-polarised dominant mode was also significant, varying between -25dB and -8dB in an irregular manner. This effect was attributed to the tolerances and the residual resin in the corners of the waveguide elements, and explained anomalous differences in element "losses" suggested by single polarisation measurements. Leakage between elements, for measurements of both polarisaticns, was satisfactory, in the worst case being -37dB total. At this level, amplitude and phase errors due to an arbitrary signal are less than ± 0.12dB and $\pm 0.8^\circ$ respectively. Although leakage measurements alone did not prove the electrical continuity of the waveguide corners, the experimental evidence implied that the construction method was satisfactory in this respect.

3.2.5. Control of the Aperture Distribution

To improve the aperture field distribution, it was necessary to develop simple, non-interacting attenuators and phase-shifters to fit in each element. Initial tests with slabs of cross linked polystyrene ($\varepsilon_r \sim 2.5$) revealed complex cross polarisation effects which were very sensitive to tolerances (even for balanced configurations of dielectric), while the amplitude of the transmitted mode varied unpredictably. For both devices, it was essential to achieve broadband matching and positive location by means of a sliding fit. The devices illustrated in Fig.3.11(c) and 3.11(d) fulfilled these requirements.

A standard 6dB attenuator was developed prior to the lens evaluation as a means of buffering unwanted reflections between the ends of each waveguide element. (Subsequent tests showed that this effect was not significant by comparison with other limitations of the lens.) Complete control of the amplitude distribution was obtained by varying the length of resistive card in this standard design. Each card was sealed with a thin layer of fibre glass (thickness <0.1mm) to prevent moisture penetration and warpage. As a compromise between the effect of tolerances and the requirement to prevent excessive attenuation, the card was supported near the "side wall" of the waveguide parallel to the electric field. Short lengths of proprietary polyurethane foam, with accurately milled slots to define the separation between the wall and the card, were used as supports. In view of the dimensional variations in the waveguide elements, the net attenuation could be guaranteed only to the nearest dB. Apart from a small and predictable increase in phase delay proportional to the length of the resistive card, the relative phasing between elements was not affected.

Several methods of achieving phase control were investigated. As already indicated, the use of compact dielectric slabs was impractical. Attempts to provide variable "phase advance" (e.g. with reduced guide dimensions) were also unsuccessful, in view of electrical contact problems and the high V.S.W.R. at resonant lengths. It was therefore decided that only "phase delay" control was practicable, with the dielectric material completely filling the guide. For ease of matching and the avoidance of higher order modes, a low dielectric constant was essential. The polyurethane foam (72) used for the attenuator supports appeared most suitable. Its consistent density, non porosity, low loss tangent and ease of shaping by machine or hand were all advantages. The phase control per unit length was obviously limited, being 1.3°/mm of guide for the densest material available. Single stage $\lambda/4$ impedance transformers at each end, easily filed by hand to an acceptable accuracy, provided a measured broadband return loss of less than -25dB, independent of the overall dielectric length. By trimming the phase-shifters during final tests of the amplitude and phase distributions, control of the incident fields to within a $\pm 10^\circ$ maximum phase error was achieved (cf. Fig.3.14). These phase-shifters had no significant effects on the amplitude distribution or the frequency sensitivity of the lens, and were regarded as satisfactory.

3.3. Waveguide Array Field Measurements

The results given in this section and Section 3.4 were recorded during the first phase of measurements with the lens forming a linear array of thin-walled, open-ended waveguide elements. In addition to recording the lens performance, mutual coupling effects were studied where practicable, although meaningful V.S.W.R. measurements were not possible in view of the cross polarisation effects. Details of the measuring system and an assessment of the experimental accuracy are given in Appendix 3A.

A 10dB cosine-on-pedestal envelope was adopted as the target amplitude illumination for the array. The repetitive array factor obtained in 'sin θ' space, assuming isotropic radiating elements, then has -20dB first sidelobe levels for any constant phase difference between the elements (77). Applying the theory of random errors for assumed deviations of 1dB in amplitude and 0.1 radian in phase, corresponding to the repeatability observed with the attenuators and phase shifters, it is readily shown that the mean interference power is 9.5dB below the desired first sidelobe level (78). The corresponding probability of this sidelobe being degraded by more than 1.5dB is only 16% (79), which was considered satisfactory.

To ensure adequate isolation between the two surfaces of the lens, the minimum attenuation in the centre elements was adjusted to be approximately 6dB (i.e. the edge element attenuation became 16dB).

3.3.1. H-plane Measurements

For the corrected H-plane amplitude and phase illumination tabulated in Fig.3.14 (Part A), the pattern shown in Fig.3.15 was obtained. With the main beam at 32° off broadside, the broader grating lobe (at -65° in azimuth) is seen to be approximately 8dB down in relative level, and substantially higher than the worst sidelobe levels (at -16 dB). As the main beam was scanned towards broadside, the relative level of the grating lobe decreased steadily, being -15dB with a 27° main beam. It will be noted, however, from Fig.3.16, that the angle of the grating lobe maximum (approximately -72°) did not agree with elementary predictions (of -84°).

The 'discrepancy' can be readily explained. Qualitatively, the characteristic was due to the effects of the relatively small aperture and the directivity of the individual radiating elements. Quantitatively, it was found that the details of the grating lobe structure (relative level, beamwidth, and angle of formation) could be predicted accurately by applying pattern multiplication concepts (2), with all the element patterns approximated by the invariant result obtained from infinite, planar array analyses (43). As several assumptions were built into this prediction, the method and its validity will be reviewed.

For an infinite, planar array of thin-walled single-mode waveguide elements scanned in the H-plane, Wu and Galindo (43) have derived exact results for the active reflection and transmission coefficients under conditions permitting a visible grating lobe, by means of a residue calculus approach (see Chapter 4). For the geometry and parameters defined in Fig.3.17, the power transmission coefficients for the main beam (T_o) and the grating lobe (T_{-1}) are given by:

$$T_o = 2\alpha_o |A_o|^2/\beta_{10} \qquad \text{.... (6)}$$

$$T_{-1} = 2\alpha_{-1}|A_{-1}|^2/\beta_{10} \qquad \text{.... (7)}$$

The factor of 2 arises from the integration of the sinusoidal incident illumination across the element. (The voltage transmission coefficients A_o and A_{-1} are given in Fig.3.17.) The symmetrical element gain pattern $g_e(\theta)$ can be obtained (6) as:

$$g_e(\theta) = T_o \cos\theta, \text{for } 0 \leq \theta \leq \arcsin(\lambda/2a);$$

$$= T_{-1} \cos\theta, \text{ for } \arcsin(\lambda/2a) \leq \theta \leq \pi/2; \qquad \text{.... (8)}$$

(Since the scan angle $\theta = \arcsin(\lambda/2a)$ corresponds to the condition when $\psi_h = \pi$, it will be appreciated that the expression for A_o in eqn.(6) should be chosen according to the value of ψ_h (cf. Fig.3.17).)

Substituting the lens value of 0.693 for a/λ, the element pattern given in Fig.3.18 is obtained. (For comparison, this figure also shows the radiation pattern for an "ideal" element (as discussed in Chapter 1) when $a/\lambda = 0.693$.) By combining this result, with the numerically calculated array factor (using data from Fig.3.14A), the predicted pattern is as shown in Fig.3.19. The prediction is seen to be in good agreement with the measured pattern at all signal levels above -20dB. Using the same technique for the excitation giving a 27° main beam, it can be shown that the element pattern taper, at angles close to endfire, causes the peak of the grating lobe to be displaced towards broadside by $|\Delta \sin\theta| \simeq 0.0.35$, i.e. from $\theta = -84^\circ$ to $\theta \sim -74^\circ$ (cf. Fig.3.16).

Several details of the lens have been neglected in the derivation of Fig.3.19 apparently without any significant loss in accuracy. In particular, the assumption of an infinite planar array environment should be examined. Wu and Galindo (43) suggest that an infinite array environment can be simulated in the H-plane when an element has nine further elements between it and an edge, although their analyses assume $a/\lambda = 0.57$. For larger values of a/λ, satisfactory agreement should therefore be expected for a smaller number of elements, since the coupling between elements becomes weaker. (In magnitude, the coupling becomes asymptotic to $s^{-3/2}$, where s is the separation (43)). For the same magnitude of extreme coupling coefficient, it is found that 6 elements on either side of the central element would be adequate for $a/\lambda = 0.693$. The difference between the centre element patterns of an infinite and a finite array is the ripple perturbation which reduces in significance as the array size increases (43). Experimental results obtained with the 20 element array are described in Section 3.4, but at this point it is sufficient to note that the perturbations, of less than 1dB at any angle, enhance slightly the agreement between Fig.3.15 and a modified Fig.3.19.

In other studies of a 91-element planar array (80), the prediction of H-plane scanning performance assuming an invariant element pattern has been very accurate to beyond the first sidelobe level. However, in common with the lens, the illumination at the edge was 10dB down. From the analyses in reference 43, the validity of the pattern multiplication procedure does not extend, in general, to a small array with strong edge illumination. (For the lens, satisfactory agreement was also obtained with a nearly uniform amplitude function, suggesting that the patterns for the edge elements were substantially similar.)

In the above assessment, the diffraction effects for the linear structure (as distinct from a planar one) have also been ignored. Most of the experimental results were taken with the vertical aperture formed by $\pm 15^{\circ}$ flares to improve the signal level in the receiver, but the array patterns were virtually unchanged without flares. The validity of the planar array analyses for the linear structure in the corresponding plane of scan is consistent with the engineering assumption that the pattern function can be separated to give $F(x,y) = F_1(x) \cdot F_2(y)$. It should also be noted, however, that the incident fields are invariant in the vertical dimension within standard waveguide, which corresponds with the free space conditions required beyond the aperture plane.

Theoretical confirmation that the thickness (t) of the element boundaries ($t \approx 0.02\lambda$) can be disregarded, is provided by the numerical results obtained from the analysis of rectangular waveguide arrays with thick walls (81). For the required normalised wall thickness of 0.03 (with respect to the waveguide dimension) the absolute change in the active reflection coefficient is $\leqslant 0.02$ at all angles of scan for $a/\lambda = 0.67$.

On the basis of the measurements described above, it was concluded that the action of a linear waveguide array can be accurately predicted in the H-plane with existing planar array analyses for $a/\lambda \approx 0.7$, and that the edge effects, even for a small array, are of secondary significance when moderate sidelobe levels (say > -30dB) are required. The complementary expectation that the active reflection coefficient was small was confirmed qualitatively by the insensitivity of the array factor to multiple reflections between the two surfaces of the lens in the absence of isolating attenuators.

3.3.2. E-Plane Measurements

The effects of mutual coupling on the E-plane scanning characteristics of the lens-array could not be predicted in detail with existing theories. Although no exact, closed form solution has been developed for the E-plane radiation properties of infinite waveguide arrays (82), the real difficulties were a consequence of the finite size of the array, and can be appreciated from known results. For an infinite planar array, the E-plane element patterns predicted by any of the recognised theories (cf. Chapter 1 and references 17, 21, 23, 83) exhibit a complete radiation null in the direction of the main beam when the grating lobe is near end-fire. Even in a very large array, the exact angle for this condition of 'blindness' is not easily calculated. The approximate 'grating lobe series' (Section 1.2.3) predicts a radiation null with the grating lobe exactly at end-fire, but the multi-mode field matching technique (23) indicates that it can occur inside the grating lobe limits even for relatively simple structures. (As noted in Section 3.1, this same effect becomes particularly significant in arrays with dielectric loading or complicated element lattices (16), but the specific structure analysed in reference 23 has open-ended square waveguides arranged in a square grid with a wall thickness of only 0.05λ.) However, in a small array, further difficulties are encountered as 'deep nulls' (e.g. a 30dB loss of signal) are seldom observed in any plane of scan. The magnitude of the finite trough in the central element pattern, and the related asymmetry of the edge effects for the other elements, are analytically indeterminate at present for practical structures.

Furthermore, it should be emphasised that all the infinite array analyses apply to planar or two dimensional parallel plate structures. The special conditions which permitted the extension of the H-plane theory to the linear model did not apply in the E-plane, where an essential vector problem was encountered (43). With the separation of the top and bottom plates controlling the effective dielectric constant of the lens, the resulting discontinuity at the aperture plane (in the third dimension) had to be recognised as another parameter of unknown significance. In previous experimental studies with linear arrays (59), individual waveguide horns were incorporated in the design to improve the match of the isolated elements. For the E-plane measurements with the lens, the detachable flares (Fig.3.1) afforded a simple method of improving the match and assessing any resulting effects on the coupling between elements.

Experimental tests with the corrected lens (see Fig.3.14, Part B) revealed a significant effect which does not appear to have been reported previously. In the initial set of results, recorded with the waveguide flares inclined at $\pm 15^{\circ}$, relative suppression of the grating lobe exceeded 35dB near end-fire (e.g. in Fig.3.20a, an expected grating lobe around -80° was non existent). Scanning the main beam further from broadside, the grating lobe increased in relative level to become -13dB for a 35° main beam (Fig. 3.20b). When the measurements were repeated without the flares, the grating lobe was very much enhanced. Typical patterns, shown in Figs.3.21a and b, be compared directly with the results in Figs.3.20a and b, as the main beam angles correspond in both cases. From these results, it was evident that useful control of the element radiation pattern could be introduced in a simple practical manner which required further investigation. For convenience, subsequent element pattern measurements were made in the laboratory anechoic chamber, following direct experimental confirmation that such results, taken in the 'near field' of the *entire* array (at a separation of 6m), were still valid. Details of this work are given in the next section.

The other characteristics observed in the E-plane were not in any way unusual. After the measurements of the centre element patterns, it was demonstrated that the pattern multiplication principle could not be applied with the same degree of accuracy in this polarization. Apart from the differences between the predicted and measured first side lobes (in both level and angle) the shape of the grating lobe beam (e.g. in Fig.3.20b) could not be interpreted in detail. These differences were attributed qualitatively to edge effects, which become more significant in the E-plane in view of the stronger mutual coupling between elements (59). (In passing, it must therefore be recognised that detailed control of the sidelobe structure in a small to moderate sized E-plane array would not be achieved without separate analyses of edge behaviour cf. Section 3.6.1.) No substantial loss of signal (corresponding to severe reflections at the aperture) was observed at angles near the condition for an end-fire grating lobe.

3.4. Element Pattern Measurements

The measurements in the E-plane are considered first.

The differences between the results shown in Figs.3.20 and 3.21 can be largely explained by the contrasting centre-element patterns measured with and without the flares (Fig.3.22). The remaining elements were terminated in matched loads for both of these measurements. Without the flares, the element pattern was not highly directive, and exhibited mutual coupling ripples characteristic of a small array. With the flares, however, a much sharper pattern was obtained, although the 3dB beamwidth was actually greater by approximately 17°.

In pattern (A) of Fig.3.22, the angles for an end-fire grating lobe ($\pm 26.2^{\circ}$) and the lowest points of the shallow "dips" do not correspond exactly. In contrast with previous measurements on a 13 element E-plane array of waveguide elements (59), the minimum occurs inside the grating lobe condition. However, by examining the results given in Fig.3.23, it is apparent that the relative angle of the trough is a function of frequency. With a smaller element spacing (e.g. $a/\lambda = 0.578$ for the lens, f = 7.5 GHz), a more distinct trough of 5 to 6dB occurs at approximately $\pm 50^{\circ}$, which is outside the 47° grating lobe condition. (A degree of asymmetry which is present at all frequencies in Fig.3.23 may have been due to an effective misalignment of the lens (including any element tolerances) or to the unequal numbers (9 and 10) of passively terminated elements either side of the test element.) Increasing the frequency from 7.5 GHz, it is seen that the angle of the main element pattern "dip" moves towards broadside more rapidly than the angle for the end-fire grating wave. At 8.5 GHz, with $a/\lambda \simeq 0.65$, the angles become equal. It will also be observed in Fig.3.23 that the magnitude of the trough reduces with increasing frequency, and at 9.5 and 10 GHz, is almost imperceptible. Qualitatively, this variation can be attributed to a decrease in element coupling with increasing wavelength separation (cf. 43). Theoretically, it focuses further interest on the unresolved questions about the overall effect (in particular its final magnitude) in an infinite linear array, as distinct from the planar array discussed in the previous section. From the results it seems reasonable to conclude that the trough would only become infinite (for an array of square waveguide elements) when a/λ approached 0.5, which is also the cut-off condition in square guide; while the trends in Fig.3.23 would be representative of those in a larger array (cf. 59). (It must be emphasised that the results in Fig.3.23 apply to square waveguide elements, which possibly limits their generality.)

However, the major effect highlighted by the results in Fig.3.22 is the dependence of the E-plane characteristics on the dimensions and details of the array normal to the plane of scan. In this context, the conditions under which two-dimensional E-plane analyses (e.g. reference 84) can be applied to linear arrays should be recognised (cf. Section 2.6.1). To clarify this dependence an early check was made on the mutual coupling effects in the flared structure. With the "non-radiating" elements short-circuited by conducting tape to eliminate all coupling, the pattern remained substantially unchanged. In Fig.3.24, the experimental result for $\pm 22.5^{\circ}$ flares shows that the only observable differences (of less than 2dB) occurred in the angular range 25° to 55° off broadside. The third result in Fig.3.24, taken with adjacent elements terminated in dominant mode "open circuits" at the aperture plane, served to emphasise that the major effect leading to grating lobe suppression could be regarded simply as a radiation property of the flare.

(A second interpretation, based on mode theory (Section 2.6), is developed in Sections 3.5.2 and 3.6. In the remainder of this section, however, the characteristics of flares are examined without reference to infinite arrays, to illustrate a number of significant properties for scanning applications. Considerable emphasis is placed on the element pattern control afforded by this relatively simple technique.)

The experimental results, which contravene the common assumption about the separability of the pattern function in its principal planes, prompted a theoretical analysis by Chappas (85). The essential problem was to predict the radiation pattern of a long conducting wedge excited from a single waveguide feed, with the electric field parallel to the axis of the wedge. To complete the analysis, it was required to calculate the radiation pattern due to an aperture field which is specified by its tangential component over a cylindrical surface. This step was accomplished numerically using a newly developed technique, applicable to more general Kirchhloff-Hugyens radiation problems and based on the reciprocity theorem (85). The pattern predicted from this work for flares set at $\pm 15^\circ$ is given in Fig.3.25 together with the appropriate experimental result. The small difference in beamwidth is not significant considering the experimental tolerances on the measurement of the flare angle.

Further experimental results, showing the variation in element pattern with the angular setting of the flares, are shown in Fig.3.26. For modest main-beam scanning limits, say $\pm 30^\circ$, it is clear that the most useful suppression of the grating lobe would be obtained with flares set at angles between $\pm 10^\circ$ and $\pm 15^\circ$. For large flare angles, the element pattern "cut-off" beyond the $\pm 30^\circ$ scanning limits would not be sufficient to maintain reasonable suppression of the grating lobe (e.g. 20dB minimum). At smaller flare angles, the "cut-off" rate is satisfactory, but the presence of prominent sidelobes with peaks approximately 9dB down for flares set at 0°, initially suggests strong grating lobe radiation for some scanning conditions. Further comment on this result will be reserved for the discussion in Section 3.6, where the characteristics of the open, parallel plate radiator will be of particular interest. For flare angles exceeding $\pm 10^\circ$, the centre element pattern was insensitive to edge conditions (e.g. to an increase in flare length from 14λ to 25λ, or to the presence of conducting tape at each end). In a practical array, it would be necessary, of course, to consider the radiation characteristics of the edge elements, which must become asymmetric unless the flare is extended by several wavelengths.

Two other results are presented in Figs.3.27 and 3.28 to illustrate the radiation properties of an aperture formed by simple flares.

In Fig.3.27, the variation in element pattern as a function of frequency is seen to be quite small. The ripples on the 8.5 GHz measurement were found at a later stage to be the result of resonant leakage from the flexible waveguide feed, and should be discounted. As expected, the improvement in the element pattern was a broadband effect, although the useful scanning limits would require consideration in any practical application. In Fig.3.28, the experimental result is given for the flares reduced to 22mm strips. For all of the measurements so far described, the flares were 150mm wide (cf. Fig.3.1), but as a final test, this dimension was reduced in 25mm increments for a constant flare angle of approximately 30°. The changes in the pattern were marginal for widths exceeding 50mm. (In the theoretical analysis (85), reflection and diffraction effects due to the finite width of the flares were not considered.)

In the above discussion, it has been stressed that the improvement in element pattern was not a consequence of mutual coupling effects in an array environment. However, special significance can still be attached to the result for scanning array applications. The conventional method of avoiding grating lobe anomalies is to restrict the element spacing, which in turn leads to mutual coupling problems (see lower frequency measurements in Fig.3.24). By reducing the level of grating lobe radiation with flares, it is possible to reduce not only the number of elements required in the array, but also the mutual coupling problems. From the results given above, the improvement in a large linear array can be readily estimated. Consider an E-plane requirement for main beam scanning to 33.5° limits ($\sin\theta_o = 0.55$), where any anomalous radiation must be kept 20dB below the main beam at all angles. Without the use of flares, an element spacing of less than 0.645λ would be needed to ensure that the grating lobes remain evanescent (cf. expn.(10), Chapter 1).

Near the limits of scan, however, the active reflection coefficient would become quite large, with the beam formed through the element pattern trough. From Fig.3.24, the difference in received signal strength for identical radar targets at broadside and at 33.5° would be 14dB, which might not be acceptable. An element spacing of 0.62λ would be required to reduce this difference to around 8dB. By contrast, an element spacing of 0.693λ could be used in conjunction with flares set at approximately 18° (Fig.3.26). The reduction in received radar signal, for a target moved from broadside to the angular scanning limit, would still be 8 to 9dB.

An interesting analogy between the proposals for reactively tapered element boundaries and the effects of the linear flare can be developed qualitatively (without reference to mode theory). For both approaches, grating lobe suppression is obtained by causing the aperture field excited by a single element to extend over many elements. When all the elements are then excited, the periodicity of the resultant aperture field, obtained in any unit cell by combining the orthogonal element contributions, is reduced significantly (cf. Section 2.4.1). This interpretation immediately precludes the use of individual waveguide horns to reduce grating lobes. Another common feature is the use of interface structures which can be regarded conceptually as tapered artificial dielectrics. The axial phase velocity is modified gradually from a value matching the waveguide feed to a value which minimises the discontinuity into free space. However, the analogy cannot be completely consistent unless the effects of element coupling can be reduced with the linear flare. Since the discontinuity in the walls dividing the elements is abrupt, (active) impedance matching problems must still be expected, with the mutual coupling coefficients probably unchanged in amplitude. The experimental measurements suggested, however, that a useful effect could be obtained, and an explanation primarily dependent on phase relationships was therefore required.

In the previous section, the element pattern trough was associated with increased reflection "losses" in the fully excited array. This mismatch occurs in each element when the signals coupled from the other elements add constructively. For arrays of open-ended waveguides, the asymptotic phase of the coupling coefficients suggests propagation along the aperture surface at approximately the free space velocity (86). For the lens this was essentially confirmed by element pattern measurements without the flares (Fig.3.29). Over the angular range of 0° to 70°, the differences in the pattern due to mutual coupling influences were largest between 20° and 40°. With the flares, it will be seen from Fig.3.24 that the corresponding effects were largest at angles between 30° and 50°. Without the proof afforded by actual measurements, this result suggests that the asymptotic phase change corresponds to "fast wave" propagation between elements, dependent on the dominant mode propagation constant between the flares (cf. Section 2.6.1). In measurements at lower frequencies with the flares and matched terminations, the sharp element pattern troughs shown in Fig.3.23 were not observed. This might be accounted for by increasingly fast propagation between the elements, which would force the mutual coupling troughs beyond the "visible region of space".

To conclude this discussion of the E-plane measurements, the following possibilities should be noted:

(i) As any solution to the matching problem in a linear waveguide array must take account of the T.E. incident field distribution, the use of flares in conjunction with reactively tapered element boundaries might afford an overall solution (see Sections 3.5.2 and 3.6.1).

(ii) By using smoothly curved flares, the properties of the "transition" could be controlled in a more flexible manner to further improve the element pattern. This might be considered analogous to finding the optimum reactive taper.

(iii) In non-scanning arrays where very low wide angle sidelobes are required, the directivity of the element pattern using flares

(iii) contd...

could permit a useful reduction in random error tolerances.

Turning briefly to measurements in the H-plane, the small element pattern ripples associated with a finite-sized array can be seen in Fig.3.30. The grating lobe condition can be recognised immediately, and, as implied by the discussion in Section 3.3.1, the pattern agrees closely with the theoretical result for an infinite array (Figs.3.18 and 3.19). Similar agreement with planar array theory was observed at other frequencies between 8 GHz and 9.4 GHz. With the flares set at $\pm 15^{\circ}$, the ripples in the element patterns were not as pronounced.

3.5. Design of the Reactive Boundaries

In this section, the major details considered in the design of the reactive boundaries are outlined. The associated analysis provides a background for interpreting the experimental performance of the lens. However, the section is more significant as an introduction to basic design problems (see following chapters).

The parallel-strip grating was adopted as the practical approximation to a continuous, reactive current sheet. The effective transmission and reflection coefficients for structures of this form have been known for many years (87, 88). (A recently published paper contains even more general results for gratings formed by cylindrical posts (89).) Slow wave propagation was automatically precluded by this choice of structure (as required), since the boundary susceptance remained inductive in the H-plane and capacitive in the (quasi) E-plane (cf. Sections 2.2 and 2.5).

The development of a tapered reactive boundary, from the data on uniform gratings, involved several compromises and assumptions. Conceptually, the basic objective was to avoid any abrupt discontinuities in boundary conditions. However, the implementation of this qualitative "concept" was governed by the following factors:

(i) The same physical boundaries could not provide equivalent electrical characteristics in both polarisations.

(ii) The fabrication technique severely limited the range of susceptances which could be achieved (Section 3.2.3).

(iii) The basis on which an "optimum" coupling profile should be developed (assuming a large array) was not rigorously defined.

(iv) The length of the reactive taper was limited to approximately 6λ, since the possible dominance of "edge effects" in a small array (aperture dimension 13.5λ) could not be completely discounted. Structural rigidity and manufacturing costs were also considered.

The significance of these factors on the design and potential performance of the lens is examined in the following sections.

3.5.1. Properties of Uniform Gratings

In reference 87, the properties of uniform gratings formed by metallic strips are given in terms of equivalent transmission line circuits. These circuits describe the effects of the structure on propagating modes only. For the electric field parallel to the strips, the normalised inductance obtained by variational techniques is given by the relation:

$$\frac{X_h}{Z} = \frac{d}{\lambda}\cos\theta' \left\{ \ln\left(\operatorname{cosec}\frac{\pi w_h}{2d}\right) + \frac{\frac{1}{2}(1-\beta^2)^2\left[(1-\frac{\beta^2}{4})(A_+ + A_-) + 4\beta^2 . A_+A_-\right]}{(1-\frac{\beta^2}{4}) + \beta^2(1+\frac{\beta^2}{2}+\frac{\beta^4}{8})(A_+ + A_-) + 2\beta^6 A_+A_-} \right\}$$

$$= \frac{d}{\lambda}\cos\theta' \left\{ F\left(\frac{d}{\lambda}, \frac{w_h}{d}, \theta'\right) \right\} \qquad \dots\dots (9a)$$

$$\text{where } \beta = \sin\frac{\pi w_h}{2d} \qquad \dots\dots (9b)$$

$$\text{and } A_\pm = \left[1 \pm \frac{2d\sin\theta'}{\lambda} - \left(\frac{d\cos\theta'}{\lambda}\right)^2\right]^{-\frac{1}{2}} - 1 \qquad \dots\dots (9c)$$

The parameters in these equations are defined in Fig.3.31. Since the effective transmission line impedance Z is given by $Z_o \sec\theta'$ ($Z_o = \sqrt{\mu_o/\varepsilon_o}$) for this polarisation, the normalised susceptance (b_h) introduced in Chapter 2 becomes

$$b_h = -\frac{\lambda}{d}\left\{F\left(\frac{d}{\lambda}, \frac{w_h}{d}, \theta'\right)\right\}^{-1}. \qquad \text{.... (9d)}$$

By maintaining $d/\lambda \ll 1$, say < 0.2, the residual dependence of b_h on the value of θ' (i.e. within the terms for β and $A_\pm$) almost disappears. This simplification is essential to retain the overall significance of the boundary susceptance as a unifying design parameter. However, the same condition also restricts the range of b_h to values exceeding unity unless $w_h/d < 0.02$; i.e. if $\lambda = 30$mm, unless $w_h < 0.12$mm, which borders on being unrealistic, regardless of manufacturing technique. In view of the fabrication limits (Section 3.2.3) and the mechanical role of the element boundaries within the assembled lens, the minimum practical value for w_h was 0.7mm.

Conversely, the major difficulty arising from the use of strip gratings in the E-plane was the limitation on the maximum value of b_e. The normalised susceptance in a two-dimensional equivalent transmission-line circuit (Fig.3.32) is given by the relation:

$$\frac{B_e}{Y} = \frac{4d}{\lambda}\cos\theta'\left[F\left(\frac{d}{\lambda}, \frac{w_e}{d}, \theta'\right)\right] \qquad \text{.... (10)}$$

where $F(\frac{d}{\lambda}, \frac{w_e}{d}, \theta')$ is the same function defined in eqn.(9) except for w_e replacing w_h. After substituting $Y_o \sec\theta'$ for the line admittance Y, the normalised susceptance b_e takes the form:

$$b_e = \frac{4d}{\lambda}\left[F\left(\frac{d}{\lambda}, \frac{w_e}{d}, \theta'\right)\right] \qquad \text{.... (11)}$$

As shown in previous work, the three-dimensional field problem can be reduced to a two-dimensional form when all field variations in the third dimension (e.g. between single moded parallel plate structures) remain constant for all components of $\underset{\sim}{E}$ or $\underset{\sim}{H}$ (Section 2.6.1). Consequently, the equivalent two-dimensional susceptance of the grating within the parallel plate lens structure was obtained by taking the effective wavelength (λ_{eff}) as:

$$\lambda_{eff} = \frac{\lambda}{\sqrt{1-(\lambda/2a)^2}} \qquad \text{.... (12)}$$

where a = the parallel plate separation and element spacing in square waveguide.

(It was necessary to apply the same scaling factor to all two-dimensional results - e.g. when checking performance by means of the mode charts.)

$$\text{Taking } \frac{d}{\lambda_{eff}} = \left[1 - (\lambda/2a)\right]^{\frac{1}{2}} . \ \frac{d}{\lambda} \qquad \text{.... (13)}$$

$$= 0.67 \times 0.2 \simeq 0.14$$

at 9 GHz to ensure the susceptance was virtually independent of θ', it was found from the data in reference 87 that the value of b_e would not exceed unity unless w_e/d were very small (say <0.05). The minimum value of w_e which could be cut and filed reliably was found during tests to be 0.5mm (corresponding to $w_e/d = 0.08$).

Drawing together the mechanical constraints for both polarisations, it was clear from these initial design estimates that the basic form of the reactive boundaries would impose the first limitations. In the H-plane, the discontinuity in the inductive susceptance at the aperture plane would be a significant problem since suitably small conducting posts were impractical. In the E-plane, a major discontinuity at the start of the reactive taper would be inevitable, in this case because the width of the slots could not be made sufficiently small.

In the analyses given above, no allowance has been made for the small, but finite, wall thickness of any practical boundary. Although the wall thickness could possibly prove a useful parameter in the control of coupling between elements in more complicated arrays (see Section 3.6.2) the use of a finite thickness boundary in the lens was dictated solely by mechanical considerations. The complementary electrical properties of the ideal "zero thickness" boundary are not retained, and in the general case, at least one extra reactive component must be introduced in the equivalent circuit representation to compensate for the additional variable (Fig.3.33). As the grating does not lose its symmetrical properties, the standard equivalent circuits become T or Π networks (87).

With a small thickness (t) of 0.02λ, only a small variation in properties would be expected unless the values of w_h or w_e were comparable with t. Using the numerical data in reference 87, this could be tested in one polarisation. (For the capacitive grating, only normal incidence appears to have been considered.) The two circuits elements in Fig.3.33 (X_{h1} and X_{h2}) are given by the following approximate relations:

$$\frac{X_{h1}}{Z} = \frac{d}{\lambda} \cos\theta' \left[\ln\left(\frac{d}{2\pi r_o}\right) + 0.601(3 - 2\cos^2\theta')\left(\frac{d}{\lambda}\right)^2\right] \quad \text{for } d/\lambda \ll 1 \qquad \ldots. (14)$$

$$\frac{X_{h2}}{Z} = \frac{d}{\lambda} \cdot \cos\theta' \left[\frac{2\pi r_1}{d}\right]^2$$

where r_o, r_1 are the equivalent radii of posts which need not be circular (when, of course, $r_o = r_1 = r$). Their values for the rectangular posts shown in Fig.3.33 can be obtained from the complete elliptic integral functions (87). The formulae for X_{h1} and X_{h2} only apply with reasonable accuracy to the range r_o, $r_1 \leqslant 0.2$ d.

As a limiting case, the properties of a grating with $t = w_h$ and $d/\lambda = 0.2$ illustrated the significant features. Firstly, it was found that $X_{h2} \ll X_{h1}$ (by 15 times in the above calculation) and could be ignored without serious errors arising. Secondly, the value of 0.18 obtained for X_{h1}/Z_o (r_o = 0.45mm) was substantially smaller than the value of ~ 0.4 for X_h/Z_o found by substitution in eqn.(9). This result represented a further limitation on the achievable range of inductive susceptance which is independent of θ'. With r_o fixed, it was therefore necessary to consider the more general results for susceptance with $d/\lambda > 0.2$. Adopting the expressions used in reference 88, the normalised susceptance becomes

$$b_h = -\frac{\lambda}{d}\left[\ln\left(\frac{d}{2\pi r_o}\right) + \frac{1}{2}\{f(\theta') + f(-\theta')\}\right]^{-1} \qquad \dots. (16)$$

$$\text{where } f(\theta') = \sum_{n=1}^{\infty} \frac{1}{n}\left[(n\lambda/d)\{(\sin\theta' + n\lambda/d)^2 - 1\}^{-\frac{1}{2}} - 1\right] \qquad \dots. (17)$$

With $w_h = t$ and $d/\lambda \leqslant 0.4$, changes in b_h of less than 15% are obtained for variations of θ' over the range $0 \leqslant \theta' \leqslant 90^o$. Over the reduced range of θ' corresponding to scanning the sector 25^o to 40^o off broadside, the variation in b_h is less than 10%.

In an attempt to overcome the inadequate E-plane data, the properties of capacitive waveguide obstacles of finite thickness were reviewed using reference 87. For an obstacle thickness about 1.5 times the slot width, increases in capacitance of 10 - 15% were obtained. These results suggested that a minor increase in the maximum finite susceptance b_e could be expected. For design purposes, a figure of 15% was assumed. The uncertainty associated with this assumption was not a serious limitation, however, as the maximum susceptance still remained very small (i.e. 0.9).

Finally it was necessary to check whether the effective properties of an isolated grating would be affected in the array environment. Since the attenuation coefficient α_x of the "n"th Floquet mode for any of the periodic gratings shown in Figs.3.31 to 3.33 is given by (cf. reference 42)

$$\alpha_x = \frac{2\pi}{\lambda}\left[(\sin\theta' \pm n\lambda/d)^2 - 1\right]^{\frac{1}{2}}, \qquad \dots. (18)$$

the minimum attenuation between reactive sheets became

$$\exp(-\alpha_x a) = \exp\left[-2\pi\left(\frac{a}{\lambda}\right)\{(\sin\theta' - \lambda/d)^2 - 1\}^{\frac{1}{2}}\right] \text{ with } n = 1\,. \qquad \dots. (19)$$

With $a/\lambda = 0.693$ and $d/\lambda = 0.2$, $\exp(-\alpha_x a) << 0.001$ for all θ', and the coupling could be ignored (cf. reference (42)). Applying the same attenuation criteria adopted in reference 42, (i.e. minimum attenuation of 46dB) it was found that d/λ should be <0.4 for $\theta'_{max} = 90^\circ$, and <0.45 for $\theta'_{max} = 60^\circ$, to prevent any significant change in susceptance. The former condition would apply in the design of an array scanning through broadside. For the offset scanning lens, the larger spacing of 0.45 could be taken as the upper limit. Further details on this problem can be found in the standard literature on artificial dielectrics (e.g. (42, 53)).

3.5.2. Characteristics of the Element Boundaries

Initial studies of the final boundary requirement were dominated by the susceptance limits outlined in Section 3.5.1. Representative mode charts and axial phase velocity profiles (cf. Sections 2.4 and 2.6) were developed to provide the design link between array performance and boundary susceptances b_e and b_h. Estimates of grating wave suppression were based on information taken from the mode charts, while the phase velocity profiles were used to assess the impedance matching problems. A phase difference of 132° between array elements, corresponding to the main beam formed at 32° off broadside, was assumed in all calculations. The use and limitations of these design aids (reproduced in Figs.3.34 and 3.35) are illustrated in this section. (The procedure ignores the finite size of the model array.)

In the E-plane, with the effective wavelength reduced in accordance with eqn.(12), the element spacing a/λ_{eff} becomes 0.465. The full line BC in Fig.3.34a indicates the range of achievable susceptances (as calculated in Section 3.5.1), and the dotted line AB shows the initial discontinuity in susceptance at the interface with the waveguide feed. The second mode is cut off for all values of b_e, in particular $b_e = 0$. It therefore follows that the grating wave can be eliminated in the E-plane by using a parallel plate region to increase the effective wavelength at the "array" aperture - i.e. at the plane where the sidewalls disappear. As this can be achieved with a conventional waveguide array, the significance of a distributed reactive taper can only be established by considering the impedance matching problem.

In the parallel plate region, with $b_e = 0$, the effective angle of propagation (ϕ) was given by:

$$\phi = \arcsin\left(\frac{\psi_e}{2\pi}\cdot\frac{\lambda_{eff}}{a}\right) \qquad \text{.... (20)}$$

which equals 52° for $a/\lambda_{eff} = 0.465$. Recognising that the capactive susceptance of strip gratings with $w_e \to d$ was virtually zero, the distinctive characteristics of the velocity profile could then be brought together, as shown in Fig.3.35a. The domination of the impedance problem by the two abrupt discontinuities was immediately apparent. As shown in Fig.3.35a, values of $b_e > 5$ would have been required to achieve a satisfactory reduction of the step from A to B. The change in phase velocity shown at z = 0 was calculated for free space propagation in the x - z plane (y = 0) at 32°. However, by fitting conducting flares to the lens, this sudden discontinuity could obviously be avoided.

An important condition must be emphasised at this point of the discussion. The elimination of grating lobes in any E-plane linear array depends on the provision of an adequate parallel-plate single mode region with b_e tending to zero. Therefore, if an effective reactive taper is not used, the plane $z = z_c$ (at which b_e disappears) should be remote from the plane z = 0, to ensure sufficient attenuation of all evanescent modes. This effect is directly relevant to the experimental results already discussed in Section 3.4. In addition, the vector field problem created by abrupt discontinuities in element boundaries parallel to the x - z and y - z planes can now be tackled in two stages, with the possibility of complete analytical solutions (cf. Section 3.3.2). Near $z = z_c$, all field variations in the y-direction remain constant as the boundaries at $x = \pm(2r + 1)a/2$ are modified to eliminate the field periodicity in the x-direction. As already indicated, this is a scalar problem (43), with $z = z_c$ defining an effective aperture plane. At $z = 0$, the edges of the parallel plates can be treated as semi-infinite 270° corners, or in the case of very thin plates, as knife edge discontinuities. For the general scan condition ($\phi \neq 0$), the diffraction effects associated with oblique incidence can then be specified in terms of the radiation properties of a two-dimensional parallel plate structure (57). This diffraction problem can be solved analytically using the Wiener-Hopf technique (93).

Returning to the discussion of design procedures, the dotted line options shown in Fig.3.35a summarise graphically the degrees of freedom which were available. As an E-plane boundary with b_e approaching zero and $d/\lambda = 0.2$ corresponded to an H-plane boundary with $-b_h \gg 1$, it was necessary to locate z_c at least 3λ from the lens aperture. The final design step, viz the detailed specification of conductor dimensions in the region $-6\lambda < z < -3\lambda$, was governed by two requirements, viz

(i) to "minimise" the active impedance mismatch within a specified transition length;

and

(ii) to minimise the uncertainty in calculated susceptance "at any point z".

Both of these requirements created further design problems. In Sections 2.4 and 2.6, it was suggested that the first requirement could be realised with an "optimum" phase velocity profile which allowed for the inhomogeneous character of the required transition. (A general approach to this problem of numerical "optimisation" is given in Chapter 6.) For initial design purposes, however, a linear profile at $\psi_e = 132^\circ$ was considered a reasonable "target", with the significance of this choice masked by the initial discontinuity AB in Fig.3.34a. Proceeding on this basis, the dimensions appropriate to a uniform grating could be calculated at regular intervals of z. With the limitation on throat length of 3λ, however, significant changes in slot width were implied within distances comparable to the grating periodicity. Several approaches to this problem were considered, including the possibility of a "linear susceptance" taper or constant increases in slot width "w_e" adjust~~ ~~ed at regular intervals of z. As all procedures had ambiguities, the supporting arguments for any of these variations were inconclusive.

It was decided to check whether an appropriate increase in slot width could be spread uniformly over a distance of 3λ. For an axial phase velocity of 2.21 v_o (shown by the point G in Fig.3.35a), the calculated boundary susceptance was 0.4 corresponding to $w_e/d \approx 0.3$ or w_e = 2mm. To maintain a linear change in axial phase velocity, this value of w_e was required at $z = -4.5\lambda$. By increasing each slot width by an average increment of 0.25mm (depending initially on the cutting widths of available slit saws) the nominal value of w_e at $z = -4.5\lambda$ averaged 2.2mm, which was considered satisfactory. At $z = -3\lambda$, the slot width had increased to 4.5mm, corresponding to a very small value of b_e. These details can be recognised in Fig.3.11a.

The set of dominant mode loci shown in Fig.3.36a illustrate the basic limit on element phasing to avoid complete internal reflection, i.e. $\psi_e < 2\pi a/\lambda_{eff}$. The corresponding freespace scan angle, given by

$$\theta_{o,max} = \arcsin\left[\sqrt{1-(\lambda/2a_y)^2}\right] \qquad \ldots.\ (21)$$

was 42^o for $a_y/\lambda = 0.672$, i.e. outside the scanning region obtainable with the experimental rig (cf. Fig.3.2).

The same general technique was used to design the remainder of the boundaries for H-plane operation. The salient features of the design problem are illustrated by Fig.3.34b and 3.35b. The most important in the mode chart was the expection of two propagating waves when $-b_h$ was less than 0.75. To achieve the minimum theoretical improvement in grating wave suppression afforded by the design concept, it was necessary to reduce the inductive susceptance to this critical value for the second mode. However, by virtue of the discussion in Section 3.5.1, this could only be attempted by accepting average values of $d/\lambda > 0.2$.

The point D in Fig.3.34b indicates the minimum realisable value of $-b_h$ with $d/\lambda = 0.2$, assuming $w_h = t = 0.7$mm. Calculations of the incident field distribution and axial phase velocity for this value suggested that an abrupt discontinuity in susceptance corresponding to DE would not afford any meaningful improvement in performance over a standard waveguide array. The decision to use larger values of d/λ was therefore inevitable, although the accompanying complications (in addition to those already discussed for the region $-6\lambda < z < -3\lambda$) led to considerable uncertainty about performance. These can be summarised as follows:

(i) Assuming a boundary with $d/\lambda > 0.2$ could be designed which afforded a suitable susceptance taper between D and E for $\psi_h = 132^o$ (Fig.3.34b), its effectiveness for other values of ψ_h could not be assumed. The variation in b_{hc} for the second mode (represented by the locus of F in Fig.3.36b) implied a specific, but experimentally unattainable, requirement for accurate control of the susceptance "taper" to guarantee a significant reduction in grating lobe radiation at all angles.

(ii) By increasing the "periodicity" of the boundary from $d/\lambda = 0.2$, to $d/\lambda \simeq 0.45$, any ability to control the axial velocity profile was seriously impaired. With an effective throat length of only 3λ, analyses of performance based on eqns.(16) and (17) for uniform gratings appeared unrealistic.

In terms of impedance matching, the second problem did not appear especially serious. Judging from the axial phase velocity profile (Fig.3.35b), it was argued that large deviations from linearity in the region $-3\lambda < z < 0$ would be unlikely if a small enough value of b_h was achieved near the aperture. Further, on comparison of Figs.3.35a and

3.35b, the small overall change in phase velocity in the H-plane (from 1.5 v_o to 1.18 v_o) suggested a matching problem of smaller magnitude than in the E-plane. (This observation is substantiated by theoretical results (43).)

Consequently, it was decided to increase the spacing between the conducting posts from 0.2λ at the point D (Fig.3.35b) to a maximum value of 0.45λ (which was consistent with limits derived from eqn.(19) in the vicinity of the aperture. Assuming $\psi_h = 132^o$ and the validity of eqns.(16) and (17), the nominal susceptance around $z = -\lambda/2$ became -0.5. However, little confidence could be placed in this calculation, and it was concluded that the measurement of performance would afford the only realistic means of evaluation.

3.6. Evaluation of the Modified Array

Initial measurements following the replacement of the lens waveguide walls with reactive boundaries showed the grating wave completely eliminated in the E-plane and moderately reduced in the H-plane. However, it was evident that the overall radiation characteristics in the E-plane were sensitive to edge conditions. (As previously indicated, the finite size of the array was disregarded in the design of the element boundaries.) The results analysed in this section provide experimental support for a design proposal to minimise edge effects in a practical array.

3.6.1. E-plane Results

The absence of grating lobes in the E-plane is illustrated by the radiation patterns given in Figs.3.37 and 3.38. The contrast with earlier results is evident by reference to Figs.3.21a and b. As distinct from other pattern details, elimination of the grating wave was not affected by test conditions. However, experimental results similar to those in Figs.3.37 and 3.38 were not obtained until suitable control of edge effects had been devised. This was provided by the triangular extension plates shown in Figs.3.1 and 3.10. The experimental justification for their use is examined in the following paragraphs.

Preliminary tests without these extension plates demonstrated the consequences of uncontrolled edge effects. A typical pattern is given in Fig.3.39, which shows a major unwanted lobe with its peak at ~ $+60^{\circ}$ and various smaller lobes (with peaks 10dB to 15dB below the maximum signal) between -10° and -80°. These features can be interpreted with a simple model.

Consider a semi-infinite parallel plate structure, with two edges at right angles, which supports a propagating T.E. mode incident at an angle ϕ to the z - axis (Fig.3.40). Its effective refractive index η is given by standard relation (cf. eqn.(1).

$$\eta = \left[1 - (\lambda/2a)^2\right]^{\frac{1}{2}} \qquad \ldots. (22)$$

Applying optical principles of refraction and reflection, it can be shown that two principal waves and two secondary waves would be transmitted (Fig.3.40). With a vanishing boundary susceptance between elements within the modified lens, this theoretical model becomes sufficiently representative of edge conditions to predict the formation of the two lobes at $+30^{\circ}$ and $+63^{\circ}$ when $\phi = 48^{\circ}$ and $\eta = 0.67$. A smaller lobe at -30°, resulting from internal reflection at the edge and refraction at the aperture of the array, would also be expected. However, the control of the aperture fields within the array feed was not sufficient for this lobe to be evident under all scan conditions, although it can be recognised in Fig.3.39. By modifying the scan angle or the amplitude distribution across the lens, a deep null (<-30dB) could also be obtained. This effect cannot be predicted, of course, with the semi-infinite model in Fig.3.40. The finite lengths of the edge and the aperture must also be recognised to explain other pattern details, such as the beamwidth of the $+60^{\circ}$ lobe or the presence of the interference lobes between -50° and -70°.

To extend the investigation of edge effects, tests were then conducted with microwave radar absorbent material (r.a.m.) along the strongly illuminated edge of the array, as shown in Fig.3.41. (Complete absorption of incident radiation could not be assumed, but a reduction in reflected power of 10dB could be achieved by careful positioning of the r.a.m. (cf. 91). With no other modifications, the characteristic edge effects were substantially reduced, whilst the required main beam and its near sidelobes were unaffected. A typical result is shown in Fig.3.42, which, apart from the r.a.m., was measured under the same conditions as Fig.3.39. As a first-order approximation, further tests with r.a.m. along both edges of the array confirmed that the second edge (see Fig.3.41) could be disregarded as a source of interference when scanning over the range $20^{\circ} < \theta_{o} < 40^{\circ}$. (In the preceding paragraph, this experimental observation has been assumed.)

As the main beam was scanned from 30° to 20°, the edge effects became less significant. For example, at $\theta_{o} = 20^{\circ}$, it was found that all spurious lobes were below the -17dB level with the edge allowed to radiate. From the experimental trend, it appeared that broadside patterns would have been insensitive to edge conditions, assuming that attention was confined to effects above -25dB. To reach any conclusions about effects below this level, it was necessary to examine element pattern characteristics (see below). However, the basic method adopted for the control of edge effects could be devised directly from an assessment of the initial array measurements.

The use of passively terminated (or dummy) elements around the aperture periphery is a possible method of containing edge effects in existing high-performance arrays. However, the provision of such elements in an operational array with reactive boundaries becomes essential if two basic characteristics of the lens are retained. These are, firstly, an amplitude distribution with non-zero edge illumination, and secondly, the use of a common reactive boundary across the array. Clearly, the number of such elements would be an important design parameter. As a logical extension of optical principles, it is considered that the minimum number could be determined approximately by the "extreme ray path" locus within the reactively tapered region (Fig.3.43). The "extreme ray path" as indicated in Fig.3.43 is defined as the vanishingly small tube in which "main beam" power from the edge of the waveguide feed is propagated through an extended reactive region at maximum scan angle. For the purpose of this geometrical optics calculation, the extended reactive boundary region can be considered as an inhomogeneous dielectric, with effective refractive index $\eta(z)$ given (in the E-plane) by the inverse of the normalised axial phase velocity. For the path geometry shown in Fig.3.43, the minimum number of dummy elements becomes the smallest integer N where

$$N \geqslant \frac{x_{max}}{(a/\lambda)} = \frac{\lambda}{a} \int_{z=-L}^{z=0} \tan\phi \; dz. \qquad \ldots . \; (23)$$

By applying Snell's Law, viz

$$\eta(z) . \sin\phi = \sin\theta_o \qquad \ldots . \; (24)$$

eqn.(23) can be reduced to

$$\frac{x_{max}}{(a/\lambda)} = \frac{\lambda}{a} \sin\theta_{o,max} \int_{z=-L}^{z=0} \frac{dz}{\left[\eta^2(z) - \sin^2\theta_{o,max}\right]^{\frac{1}{2}}} \qquad \ldots . \; (25)$$

which can be evaluated analytically - if $\eta(z)$ is approximated by a quadratic (or lower order) function - or numerically. It will be noted that this model imposes a condition on the assumed direction of propagation at the beginning of the finite susceptance boundary. In the E-plane, this direction is normal to the aperture, and the model is consistent with the restrictions imposed by conducting (waveguide) walls. If a relatively small array was proposed, it might be more realistic to take a slightly larger value of θ_o (e.g. θ_o plus the 10dB beamwidth).

Using this "ray-optics" model, it becomes apparent that several parameters must be specified before the number of dummy elements can be estimated. These include the maximum scan angle ($\theta_{o,max}$), the length of the reactive taper (L) and the effective susceptance profile. A potential simplification of these extra elements is afforded by the presence of a nominally unutilised region, as shown in Fig.3.43. In the correction of the model array, for example, it was convenient to use the open-edged triangular extensions instead of complete elements. (Recognising in addition the limited significance of the reactive boundaries in the E-plane, it was considered adequate to form a simple parallel-plate region.) As already indicated at the beginning of this section, these plates were effective in controlling edge effects over the complete scanning range of the lens.

For the measurement of Figs.3.37 and 3.38 attenuators and phase-shifters were incorporated in each waveguide feed. However, some ambiguity was inevitable using a waveguide adaptor at the aperture plane to measure amplitude and phase, despite the extensive use of r.a.m. to minimise unwanted reflections within the open array structure. By implication, the method of correction assumed that all errors in the aperture field distribution were caused by the lens surface and the waveguide feeds. An amplitude taper of approximately 10dB was adopted for the final measurements (e.g. Figs.3.37 and 3.38), while the nominal deviations from linear phase across the array were $\leq 7^{\circ}$ for the result in Fig.3.37. The net control of the radiation pattern was significant, with the elimination of a main beam coma lobe and the reduction of the first sidelobe level from -10dB to -15dB. However, the final levels remained substantially higher than any theoretical estimates based on an invariant element pattern.

For future design purposes, the two basic limitations of this method of pattern prediction must be recognised. Firstly, as shown below, the assumption of invariant element patterns - despite the compensation for gross edge effects - could be quite unjustified. (The contrast with the earlier discussion of the waveguide array (Section 3.3) is one of degree rather than principle.) A key parameter in a linear array is the ratio of the aperture length to the reactive taper length. Secondly, although a practical array would be built to tolerances consistent with the required performance, the use of long reactive tapers would introduce random errors in the aperture distribution which could be difficult to identify with a particular element. It was not practicable to determine the relative significance of these separate factors in the experimental results.

As a final note on the array tests with all elements excited, it should be recorded that the use of flares did not significantly modify the radiation patterns in the plane of measurement (cf. Section 3.3).

Element pattern tests in the E-plane provided further insight on edge behaviour particularly in relation to the "parallel plate flare" (cf. Section 3.4 and Fig.3.26). The central element pattern shown in Fig.3.44 illustrates several important features. For electronic scanning over a limited angular range, the essentially sectoral shape of the result offers, in an enhanced form, the potential advantages already ascribed to the flares (Section 3.3). The pattern shown in Fig.3.44 was measured with the triangular extension plates fitted to the lens and r.a.m. placed along their back edges. Without the r.a.m., the pattern was virtually unaffected within $\pm 80^\circ$ limits, whilst -18dB peaks, as indicated in Fig.3.44, were obtained at approximately $\pm 85^\circ$.

It was noted that the basic features of this element pattern were similar to those for a slot radiating into a finite, parallel-plate region. A numerical solution of the latter problem has been developed by Wood (92), and confirmed by tests on various single-element models with ends sealed by r.a.m. In view of the limited significance of the E-plane susceptance taper, it seemed reasonable to compare experimental results for the lens with patterns predicted by this analysis. A virtual waveguide source, 5λ from the aperture plane, was assumed to calculate the results shown in Fig.3.45. The agreement clearly demonstrated that the major characteristics of the experimental results, (over angular limits of $\pm 50^{\circ}$), could be attributed to the parallel plate effect. The smaller diffraction ripples and enhanced cut-off for the larger aperture (Figs.3.45(a) and (b)) reveal the control of radiation characteristics afforded by parallel plate structures. Lens measurements at other frequencies (Fig.3.46) highlighted the control of beamwidth which can be obtained with the parameter a_y/λ (a_y = parallel plate separation).

A more detailed examination of edge effects was possible following the construction of a parallel plate model with dimensions equal to the reactive boundary portion of the lens. With symmetrical excitation of this model, wide angle sidelobes, similar to those noted during discussion of results in Fig.3.26, were evident as expected (Fig.3.47). By sealing the edges with r.a.m., the sidelobes were "eliminated", although the remainder of the pattern was virtually unaffected. On repeating these tests with the lens, it was found that the edge radiation, at frequencies above 9 GHz, was down by 5 to 7dB (Fig.3.48). (At lower frequencies, the reactive boundaries became transparent, due to the decreasing magnitude of a/λ_{eff}, and no difference was evident at 8 GHz.) For practical purposes, this reduction in edge radiation, due to the presence of reactive boundaries, was too small, of course, to be useful. However, in a practical E-plane array, with a more efficient susceptance taper, this experimental trend should develop into a significant factor in the reduction of edge radiation. Element pattern control would be achieved with a smaller aperture dimension.

Conversely, it was concluded that a parallel plate structure afforded an opportunity to study the worst possible edge effects. The following results illustrate some of the factors which would require investigation if the "extreme ray path" concept were an inadequate design approximation. A series of tests were conducted with the parallel plate feed located near one edge (Fig.3.49). With the edge radiating, complex diffraction effects were evident at all angles due to the presence of the virtual line source at right angles to the aperture. By placing r.a.m. along the edge, the interference was substantially reduced with an accompanying reduction in gain (over much of the scanning sector) for the extreme element positions. At broadside, the apparent reduction in element pattern gain remained <1dB with the feed only 1.5λ from the edge. Although this model (with or without r.a.m.) nominally complied with the geometrical-optics requirement for broadside radiation, it was clear from the results that the detailed calculation of side lobe levels (say for a fixed beam array of moderate length) would be extremely difficult. For a broadside array designed to meet a sidelobe specification (e.g. -40dB at wide angles) a statistical analysis could be considered. By assigning "random errors" to the array factor (the "errors" increasing with element proximity to an edge), the minimum required extension of the parallel plate region beyond the extreme element might be estimated. A similar procedure could also be envisaged for a scanning array, provided the "extension" was regarded as additional to the dummy elements required by the ray-optics argument. (The problem of edge effects is reconsidered in Chapter 6 for "multi-section" structures, where each section has constant susceptance.)

Regardless of the number of dummy elements in a practical array, it is considered that the use of a suitable absorbent material along the edges of the parallel plates would be advantageous in most applications. Control of unwanted leakage would be ensured. (This leakage was not identifiable in the experimental results (e.g. Figs.3.37 and 3.38) for which the edges were deliberately left open.) As shown by the experimental results (e.g. Fig.3.49), the reduction in array gain would not be significant (provided of course dummy elements were included in scanning arrays). Tests on the lens revealed severe resonance conditions when conducting tape was applied to the sides (Fig.3.50), and implied that solid conducting walls should not be contemplated as a method of minimising leakage.

To complete this section, it is appropriate to interpret the action of the E-plane flare in the light of the above results (cf. Section 3.4). For the measurements discussed in Section 3.4, the flare length corresponded to the array aperture. Clearly, the pattern shown in Fig.3.39 indicates the basic effects which would occur if the flare angle were reduced almost to zero without compensating for edge effects. However, as already noted in Section 3.4, the radiation characteristics with modest flare angles (say $\pm 10^{\circ}$) were not significantly affected by edge conditions. The essential "trade-offs" can be clarified by considering an infinite waveguide array fitted with continuous flares (Fig.3.51). Due to the increasing plate separation, the cut-off region (and consequently the attenuation) for the higher order mode - i.e. the grating wave - is governed by the flare angle. Within a parallel plate structure, this region normal to the aperture is unbounded and attenuation is infinite. However, using a flare, the "ray paths" from each waveguide element are refracted towards the aperture by an amount dependent on the included angle. Treating the flare as an inhomogeneous dielectric region, ray path loci can be estimated by the method explained above (eqns.(23) to (25)). (Since the flare causes a reduction in phase velocity normal to the aperture, the ray path loci curve in the opposite sense to that shown in Fig.3.43.) This effect makes the flare less sensitive to edge effects, and means that the length of a practical array (with edge compensation) could be smaller. The reduction in length would be governed (through the flare angle) by the allowed grating wave levels.

It would not always be necessary, of course, to use a constant flare angle. In this event, the performance possibilities afforded by a combination of parallel plates, flares and reactive boundaries could be examined from whichever practical aspect was most important. Questions of match, grating wave suppression, scanning limits, gain reduction at $\theta_{o,max}$, number of active elements and required edge compensation would be involved. As already indicated in Section 3.4, the use of reactive boundaries within the initial portion of the flare could be advantageous. Referring to the mode chart, shown in Fig.3.34a, the "unutilised" region between the line ABC and the second mode boundary would then be eliminated, since a/λ_{eff} would be increasing as b_e decreased. As an alternative method of utilising this single moded region, it is interesting to speculate whether the dimension "a" could be increased as b_e decreased. This might be achieved if the waveguide walls were initially thick, and coupling between elements was amplitude (but not phase) sensitive to wall thickness. As an initial step, it would be necessary to develop the characteristic equations for an infinite array with suitably defined thick reactive boundaries (cf. Section 2.7.3).

3.6.2. H-plane Results

The measured grating wave suppression in the H-plane is summarised in Fig.3.52. With the main beam at 32°, the improvement over the waveguide array was only 3dB. (At the time of design, considerably higher attenuation was anticipated, despite the susceptance limitations discussed in Section 3.5.2. However, theoretical "estimates" were based on a Fourier analysis of the incident reactive-boundary mode. They were subsequently recognised as unduly optimistic and inconsistent with results for a waveguide array (43).) The best result, with the main beam scanned to $\theta_o = +39^\circ$, is shown in Fig.3.53. However, the failure to achieve any measurable improvement in relative grating lobe suppression at angles between -70° and -90° (i.e. $26.2^\circ < \theta_o < 30^\circ$) precludes a general interpretation of performance based entirely on Chapter 2.

Measurement of the centre element pattern revealed the presence of unexpected "sidelobes" at angles between 65° and 90° (Fig.3.54). These sidelobes were not affected by the addition of extension plates or r.a.m. along the edges of the array. The pattern details (slightly different for other elements in view of the mechanical tolerances) were therefore attributed to the element boundaries. A satisfactory explanation of this result must take account of the design approximations described in Section 3.5.2, in particular the variation of 'b_h' with scan angle and the finite length of the taper. Drawing to some extent on results given in Chapters 5 and 6, it is considered that the first of these approximations imposed the more fundamental limits on performance. In effect, the result in Fig.3.54 corresponds to a waveguide element pattern perturbed by a "resonant dip" outside the end-fire grating lobe condition. As the element boundaries near the lens aperture can be regarded as a set of non-uniformly spaced inductive posts, the possibility of a phase-sensitive increase or decrease in the net forward-scattered grating wave is at least plausible, if not probable. The suggestion of a sectoral pattern, as distinct from a resonant effect contained within a few degrees of scan, was a more encouraging feature of Fig.3.54. In this respect, an underlying performance similarity with the 'diskpole' radiator discussed in Section 1.4 is evident.

Further tests showed that the three extreme elements were affected discernibly by edge conditions, but only one pattern was severely distorted, possibly by leaky wave radiation (cf. structures shown in reference 120). The results, with and without r.a.m. to absorb the edge radiation, are shown in Fig.3.55. The major effect of the r.a.m. was to reduce radiation in a direction about 15° off broadside in the region where leaky waves could propagate. However, the very limited coupling over most of the taper prevented any conclusive definition of edge behaviour. The extreme "ray path" concept can not be applied, because of the anomoly as $b_h \to -\infty$ (Fig.3.56). However, the element pattern results implied that a single dummy element with its "free" edge sealed with r.a.m. would have been adequate compensation for edge effects.

Overall, it is considered that the combination of design problems, limited grating wave reduction and uncertain edge behaviour left questions about the practicability of the design concept in the H-plane largely unanswered. In the next section, specific topics for further investigation are suggested.

3.7. Conclusions

The overall significance of the experimental programme can be reviewed in terms of the experimental objectives.

3.7.1. Assessment of Results

The first of the objectives was to demonstrate that a reduction in the periodic fluctuations of the aperture field could be achieved in both polarisations with reactive element boundaries.

In the E-plane, the results illustrated how an element spacing (a/λ) exceeding the normal limit of $(1 + \sin \theta_{o,max})^{-1}$ can be adopted without any grating lobe anomalies, by employing a sufficiently small parallel plate separation leading to $a/\lambda_{eff} < 0.5$. The reactive boundaries are used to reduce the impedance mismatch. In addition, the essential parameters in shaping the element pattern with conducting flares have been defined, and an efficient method of containing edge effects, using the minimum number of dummy elements, has been proposed and experimentally confirmed. However, the size of a practical array (scanning typically to $\theta_{o,max} \sim 35^{o}$) would still be increased significantly unless the length of the reactively tapered boundary remained much smaller than the uncompensated aperture dimension. The design technique appears most appropriate to large arrays (say 50 elements or more) with a tapered amplitude illumination.

In the H-plane, discernible grating wave suppression was only achieved at scan angles exceeding 30^{o}. From the results, it was evident that a useful reduction in grating wave level (to at least -20dB with respect to the main beam) would not be achieved without more rigorous design procedures. The fundamental difference between the E and H-plane problem is implicit in this comment. Whereas the element pattern control in the E-plane can be guaranteed by a "one mode" condition at the aperture, satisfactory control in the H-plane depends on the effectiveness of the reactive taper.

Although numerous approximations were required to follow through the experimental procedure, it is not considered that any single factor can be isolated as a fundamental limitation on the value of the programme. For example, the range of susceptance values was restricted by the fabrication process, but in the light of experimental results, it is apparent that the real limitations were imposed by the use of the standard parallel-strip grating. Again, the performance in both polarisations was affected by the compromise design of the reactive boundaries. However, the basic questions raised by the design procedure would not have been altered by the use of separate E and H plane boundaries. The results did not conflict with previously formulated theory (Chapter 2) except on the question of grating wave attenuation in the H-plane, as explained in Section 3.6.2.

3.7.2. Identification of Problems

The second objective of the experimental programme was to define specific problems requiring further study. It is considered that the problems described in Section 3.5 can be summarised under two principal headings:

(i) Assuming the continued use of b_e and b_h as the unifying design parameters, the intrinsic periodicity of a practical "reactive boundary" (equivalent to d/λ in Section 3.5) should be very much smaller than the waveguide dimensions (i.e. a/λ). In the first instance, this is necessary to ensure that the properties remain independent of the angle of "wave incidence" within the structure (cf. Section 3.6.2). The development of a reactive surface with low inductive susceptance appears to be the most difficult requirement. This problem is examined in Chapter 5. In the E-plane, larger *effective* values of b_e could possibly be achieved

(i) contd...

with narrow slots of reduced length, similar to those in commercial directional couplers (cf. Fig.2.22b). These could be confined to an area remote from the aperture, and used specifically to reduce the active impedance variations.

(ii) In view of the experimental results, a "design procedure" based largely on the use of mode charts and velocity profiles can not be considered adequate for practical purposes. (This does not invalidate, of course, the general design "principles" embodied in Chapter 2.) In particular, the performance limits imposed by finite length tapers require rigorous definition. This implies an ability to minimise the active impedance mismatch in an E-plane array, and the grating lobe radiation in an H-plane array, subject to constraints on the length of the transition, for operation over scan limits of $\pm\theta_{o,max}$. Assuming an infinite array, these requirements are equivalent to minimising the "backward-scattered" dominant mode in the E-plane, and the "forward-scattered" second mode in the H-plane.

As an extension of Chapter 2, it is logical to examine a transition in which the susceptance is changed at a finite number of discrete discontinuities. The analogy with standard waveguide transformers can be preserved, although the section lengths should not be assumed quarter-wavelength (see Chapter 6). The constraint on length can be associated with a limit on the number of sections of constant boundary susceptance, with $-b_h$ or b_e decreasing monotonically. As a first step, therefore, a Wiener-Hopf analysis for an isolated discontinuity is developed in Chapter 4.

Other problems requiring a basic shift in emphasis can be specified. In the H-plane, the performance of the modified lens could not be predicted in detail unless each boundary were analysed as a set of closely spaced scattering posts. It is not immediately apparent, however, whether any structure with posts separated by 0.3λ to 0.5λ could provide a satisfactory solution. A quantitative approach to edge behaviour would also be valuable, possibly on the basis of leaky wave radiation. (For future development purposes, it is considered that the performance of an array designed in accordance with the present proposal could be controlled satisfactorily with one or more dummy elements and r.a.m.) Generalisation of the artificial dielectric concept to structures tapered in more than one direction could become significant if power absorption along the sealed edges has to be reduced.

APPENDIX 3A

DETAILS OF THE MEASURING SYSTEM USED FOR THE FIELD TESTS

For a valid comparison of the array performance with and without reactively tapered boundaries, appropriate control of the measuring accuracy was essential. For tolerancing purposes, a rigorous requirement for "one-to-one" comparisons was assumed initially, although the constraints on some parameters were subsequently relaxed, to save time, without jeopardising the overall assessment. The following summary outlines the major considerations, but detailed analyses relevant to all testing facilities are not reproduced (e.g. 65, 73, 74, 75).

Suitable positioning of the feed horn was achieved with a simple cantilever support providing for adjustments in plan and height and rotational freedom about two axes through the phase centre (Fig. 3.A1). Using a plumb-line and a builder's level, the cumulative positional error, along any axis, could be limited to an estimated ± 6mm when required. With this control, potential phase variations in the aperture plane of the array were not serious. (An error of 6mm tangential to the scanning arc produced a beam squint of approximately 0.25°.)

Within the restricted dimensions of the "anechoic" enclosure, it was not possible to suppress all significant reflections with standard blocks of radar absorbent material (latex foam or polystyrene). After correction of the amplitude and phase distribution, it was therefore necessary to leave all the blocks undisturbed. To avoid variations in surface properties from moisture absorption, each block was sealed in polythene. The effectiveness of the r.f. screening, formed from continuously bonded sheets of aluminium foil, was checked over the angular limits of $\pm 100^{\circ}$ in azimuth with the array elements sealed. A complete loss of detectable signal was achieved with the walls of the enclosure high enough (≥ 1.5m) to suppress edge diffraction interference.

In accordance with reciprocity principles and conventional practice, the test array served as the receiving aerial during tests, with the receiver installed in the supporting cabin (Fig. 3.A2). A klystron providing a maximum C.W. output of +22dBm at 9.0 GHz was utilised as the transmitter source, while the mixer and logarithmic i.f. amplifier from a small commercial radar were the crucial receiver components. At its design frequency of 9.4 GHz, the minimum detectable signal for this receiver unit was typically -95dBm with an i.f. bandwidth of 12 MHz. This performance was not available at 9.00 GHz, due to the use of inherently narrowband adaptors in the r.f. head, but a potential dynamic range of 70dB below -15dBm (effective logarithmic saturation level) was achieved. With the i.f. amplifier modified for C.W. operation, the detected output was applied directly to the Y input of a laboratory pen recorder with d.c. offset facilities, while an X input proportional to the azimuth bearing, was derived from a potentiometer controlled by the cabin turning gear. The relatively wide bandwidth of 12 MHz eliminated any serious problems due to differential frequency drift, without the provision of a.f.c. to the local oscillator (a small X-band klystron).

The main sources of receiver inaccuracy were the receiver noise and interference at low signal levels, and cabin flutter during rotation. By trimming the local oscillator before each measurement and calibrating all results individually with a rotary vane attenuator, side-lobe peaks at -20 to -25dB could be reproduced to within 0.25dB, provided the peak signal was 35dB above the minimum detectable signal. Both absolute and differential azimuth bearings could be determined to within 0.5° of arc where required, by avoiding tests under windy conditions and compensating for backlash errors in the turning gear. With an additional penalty of $\leq$10dB in sensitivity, the receiver could be operated over a wide frequency range at X-band.

In common with all conventional test facilities, further limitations on accuracy were imposed by the finite aerial separation and site reflections (75, 76). For the site geometry shown in Figure A3, the requirement for substantially uniform amplitude and phase illumination of the test aerial (i.e. maximum variations of approximately 0.25dB and $\lambda/16$ respectively) leads to the following minimum range (R) restriction (65):

$$R_{min} = \frac{4 \cdot d_1}{\lambda} \cdot \left[(d_2 + 2u)^2 + 4v^2\right]^{\frac{1}{2}} \qquad \ldots\ldots (A1)$$

where d_1, d_2 = effective apertures of the transmitting and receiving aerials,

and u, v = dimensions defining the offset of the centre of rotation.

For the relevant example of a 10dB cosine-on-pedestal distribution, the first sidelobe level is then increased by about 0.2dB (77). This was quite acceptable in view of the increased site interference and power limitations at larger aerial separations.

A cassegrain aerial system, with a 0.9m diameter primary reflector, was utilised as the radiation source in standard elevated range configuration (Fig. 3.A4). Substituting into eqn.(A1) the values given in Fig. 3.A3, the required range was approximately 75m. This separation was used throughout except for a set of E-plane tests during the first phase of measurements, when an operating range of 20dB could not be obtained from the receiver. (A 10dB loss of sensitivity was traced subsequently and corrected in the detector circuitry, but at the time the effect was attributed incorrectly to the very low efficiency of the lens system.) Experimental results, supported by theoretical calculations of the pattern with quadratic phase errors, indicated that the relative level of the grating lobe was unchanged at this shorter range, although near field effects were expected to modify slightly the significant sidelobe structure (sidelobe peaks could be in error by approximately 0.5dB).

Both the transmitting and test aerials were mounted at a height of 3m above the ground, to achieve adequate suppression of the radiation from the "image" source (Fig. 3.A4). Tests with a standard gain horn were made to ensure that the signal incident on a 2m x 1m aperture varied essentially in accordance with the directivity of the transmitting aerial, and were used as a final method of aerial alignment. Measured patterns for a standard horn, in both polarisations, were correct to within the limits of resolution given above, and free from significant azimuth site reflections 30dB below the peak of the main beam.

Fig. 3.1 Fully assembled lens array

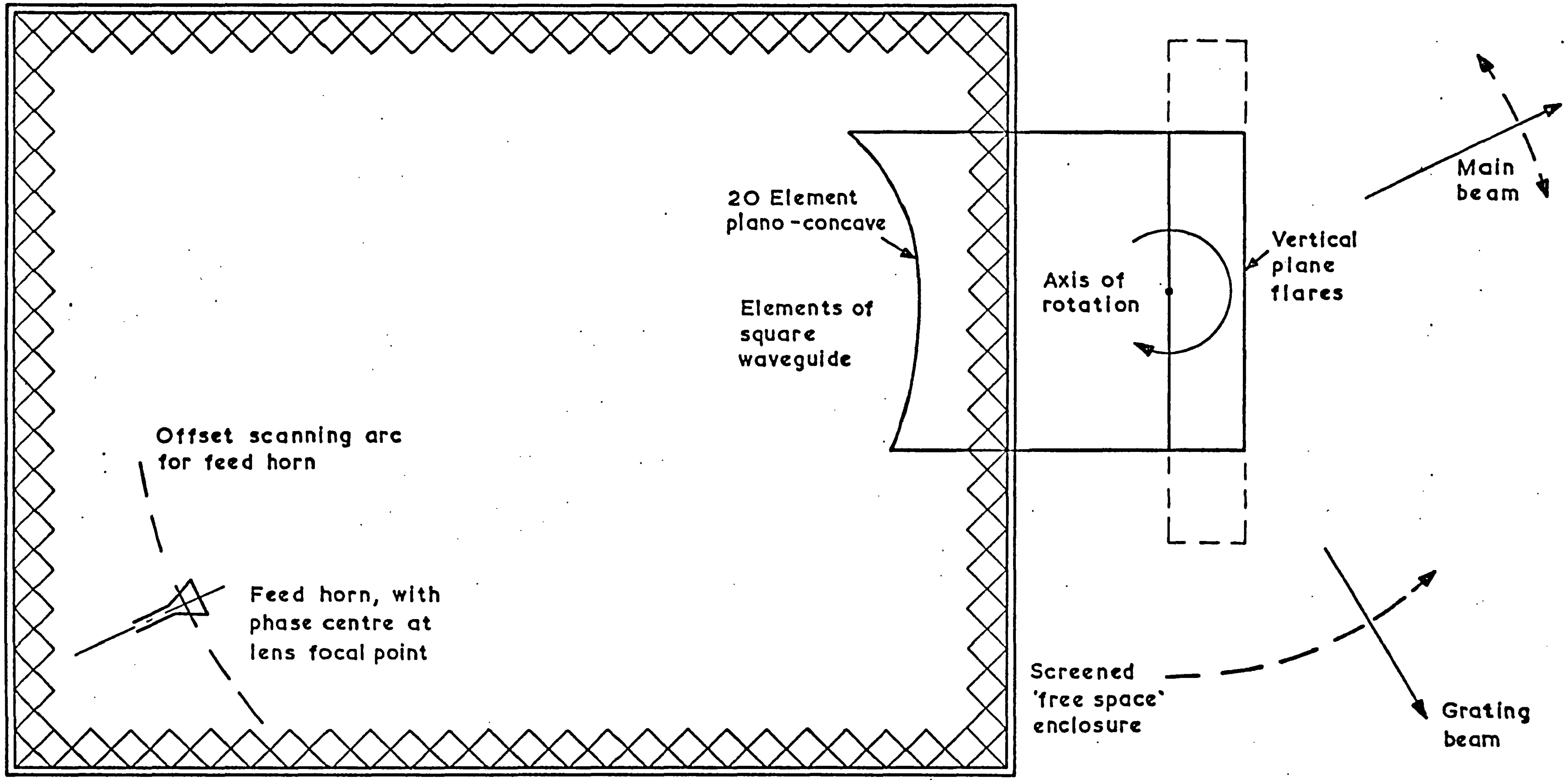

Fig. 3.2 Schematic details of the scanning array model

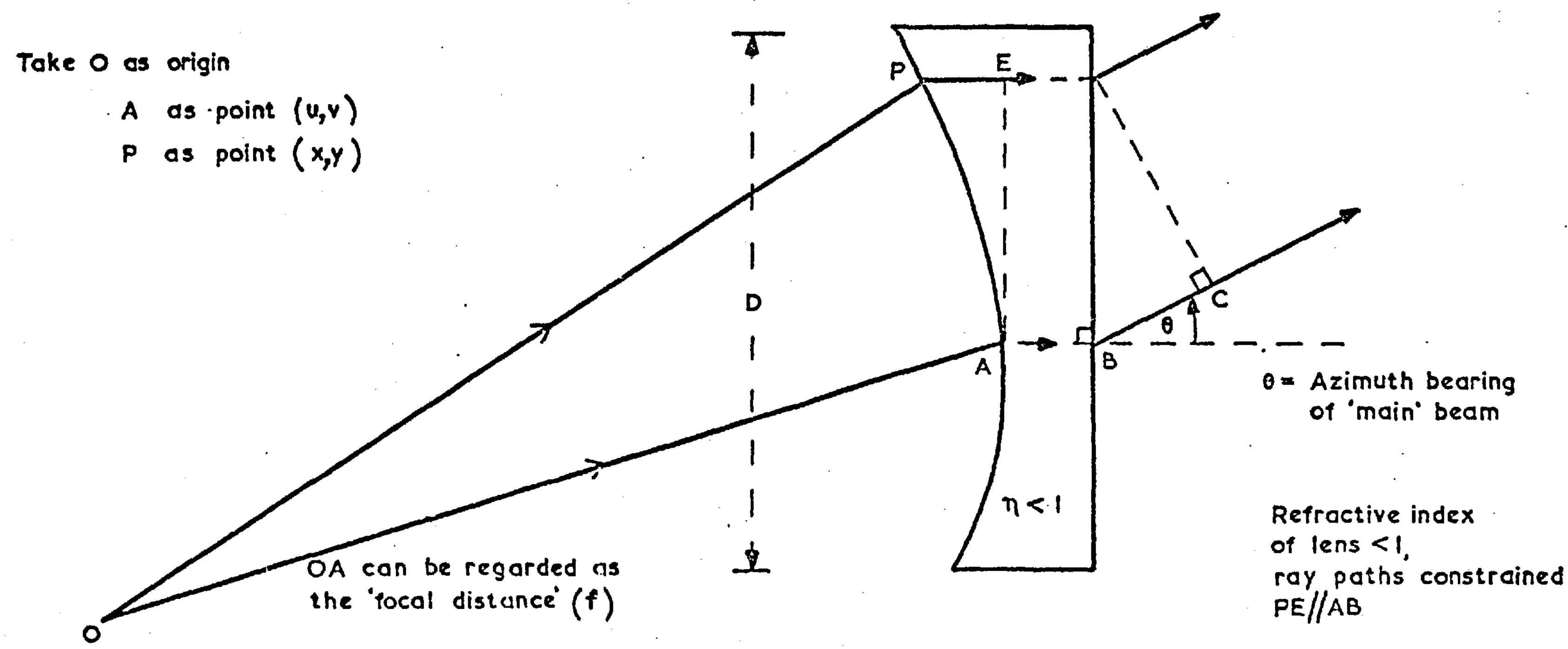

Fig. 3.3 Ray-path geometry for generation of lens surface

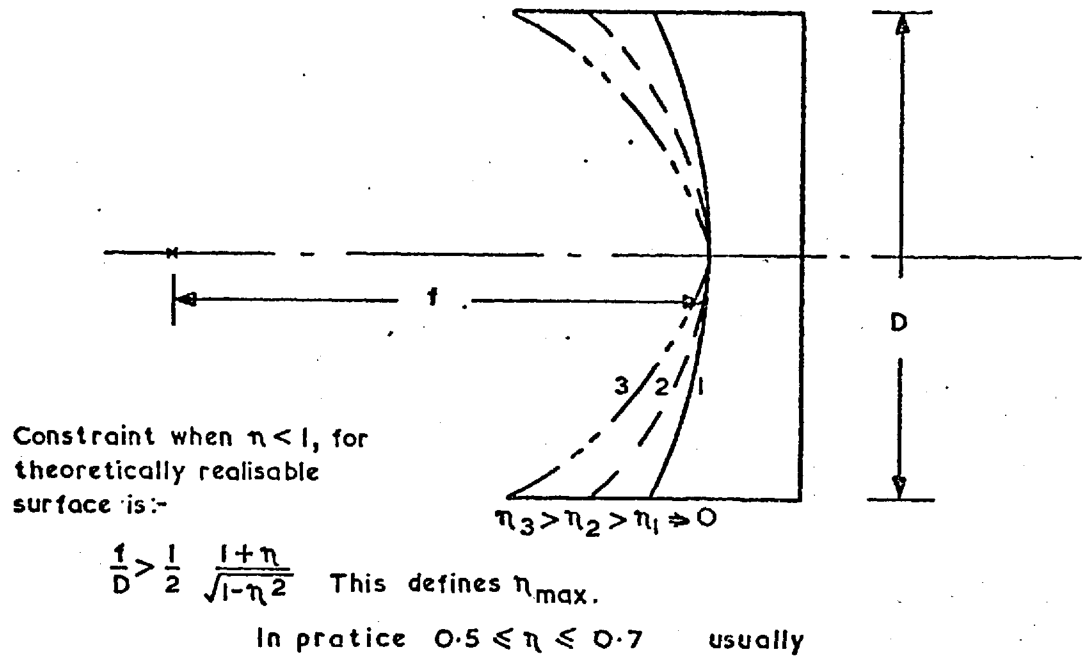

Fig. 3.4 Conventional relationship between refractive index and elliptical curvature for single surface broadside lenses.

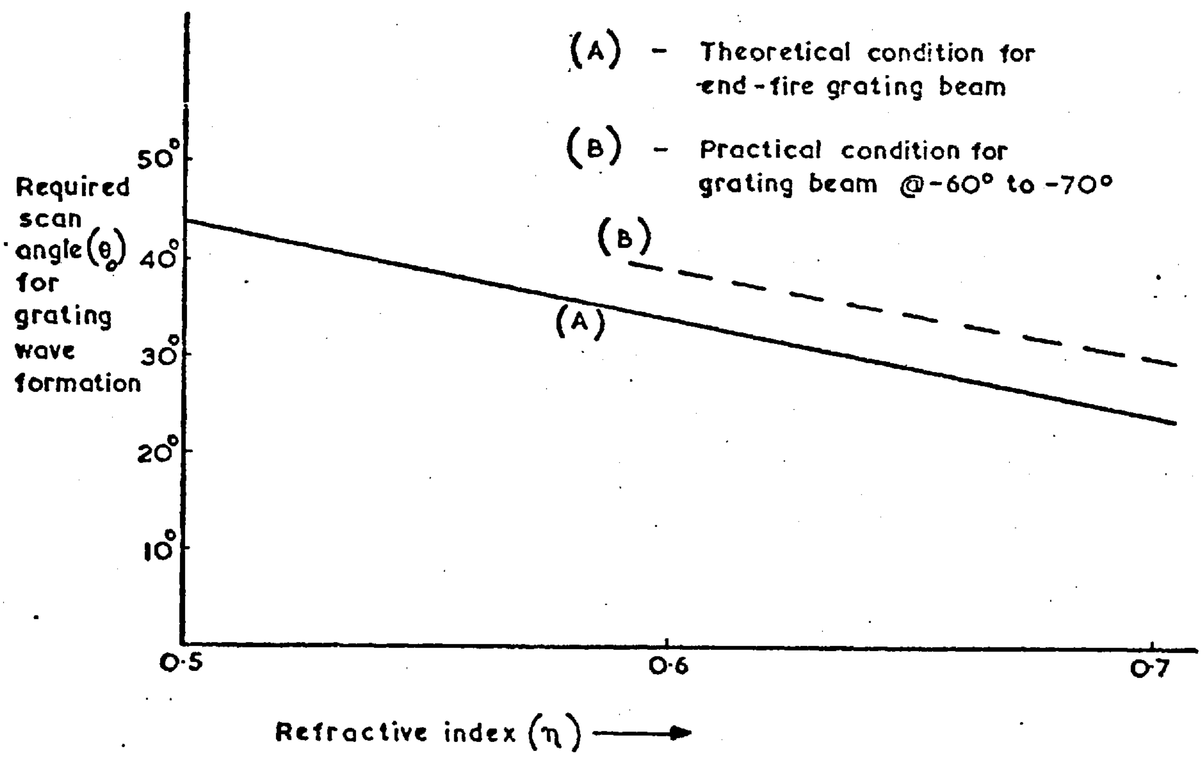

Fig. 3.5 Design constraint for offset scanning with visible grating beam for parallel-plate artificial dielectrics

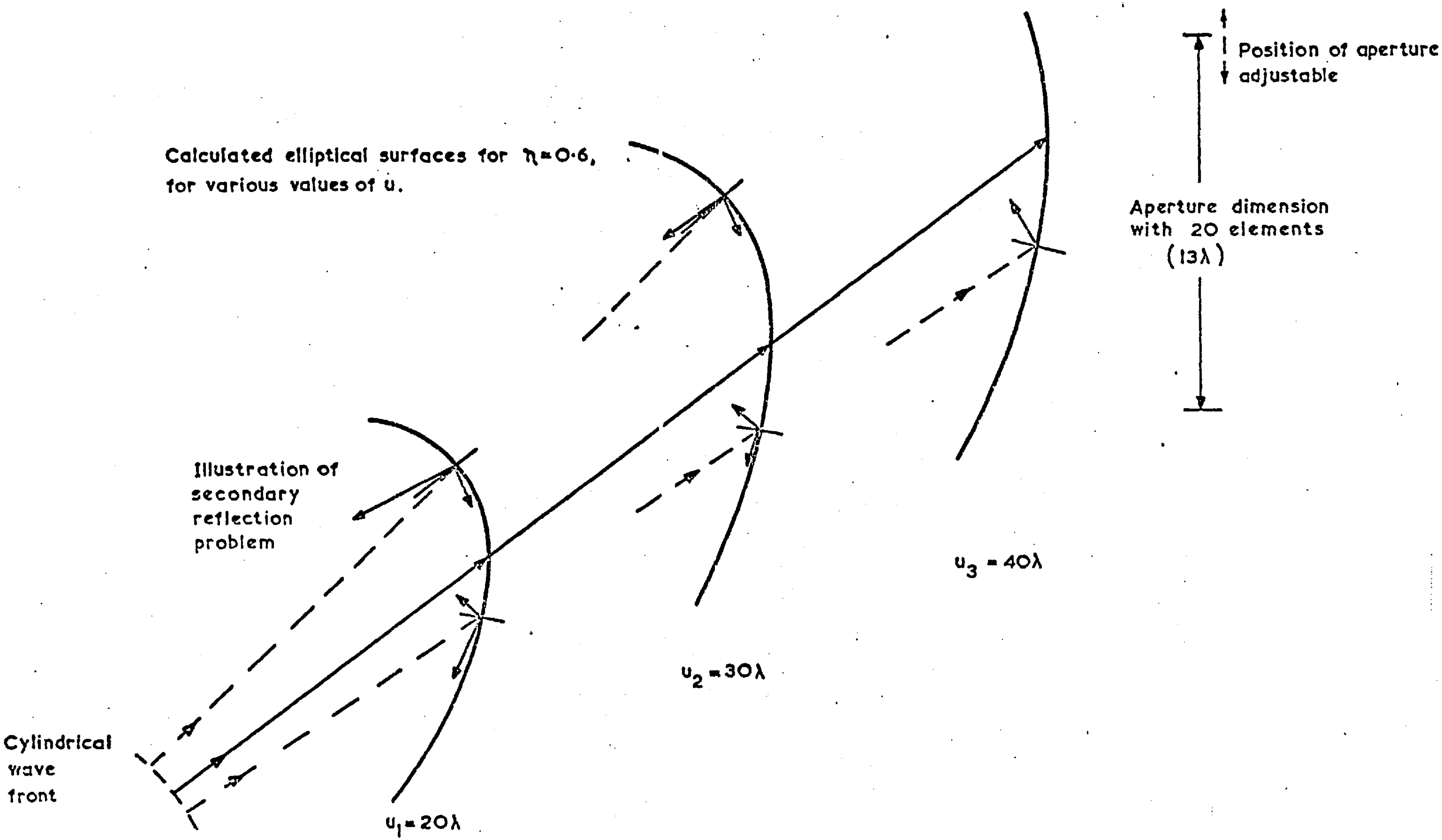

Fig. 3.6 Demonstration of requirement for large "u" to minimise secondary reflections at elliptical surface.

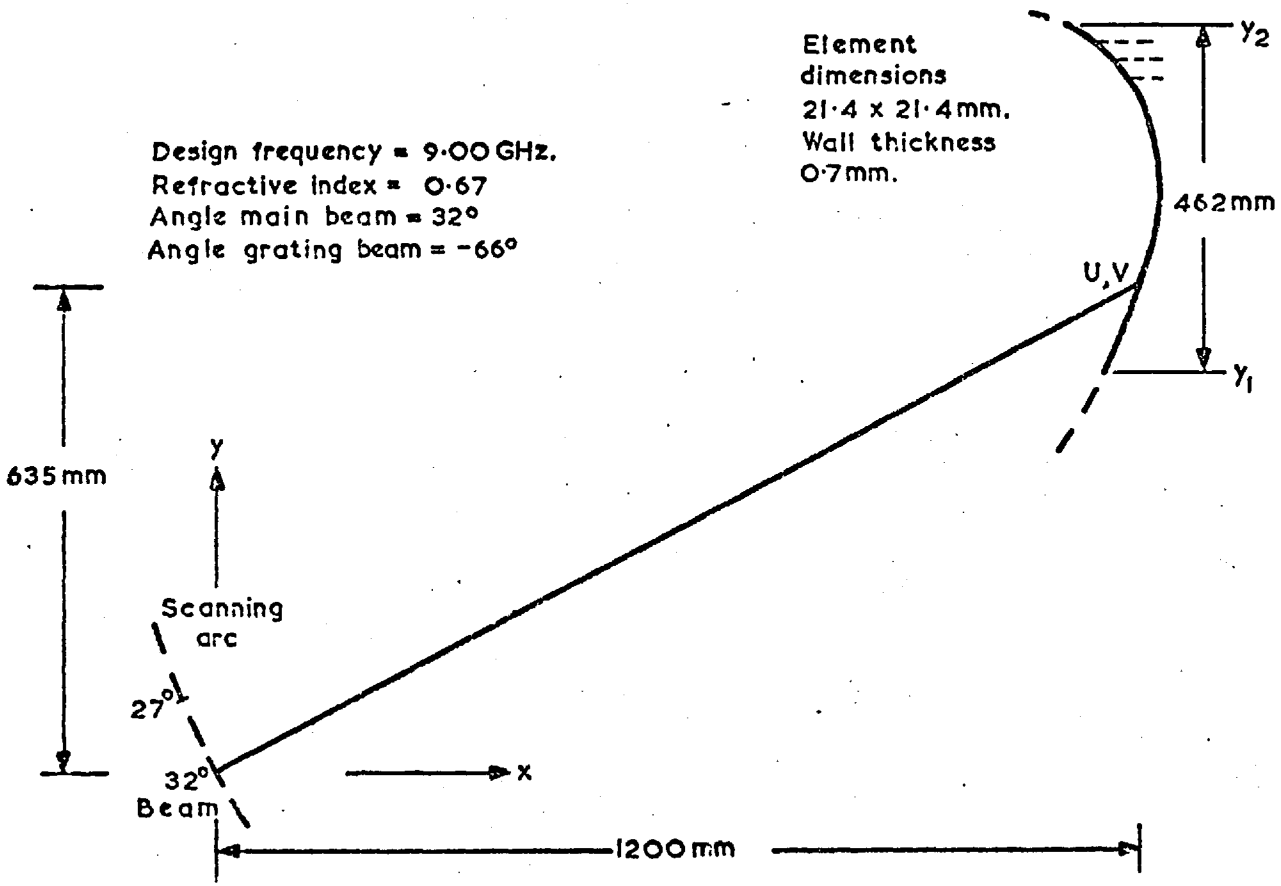

Fig. 3.7 Details of lens design based on ray optics development

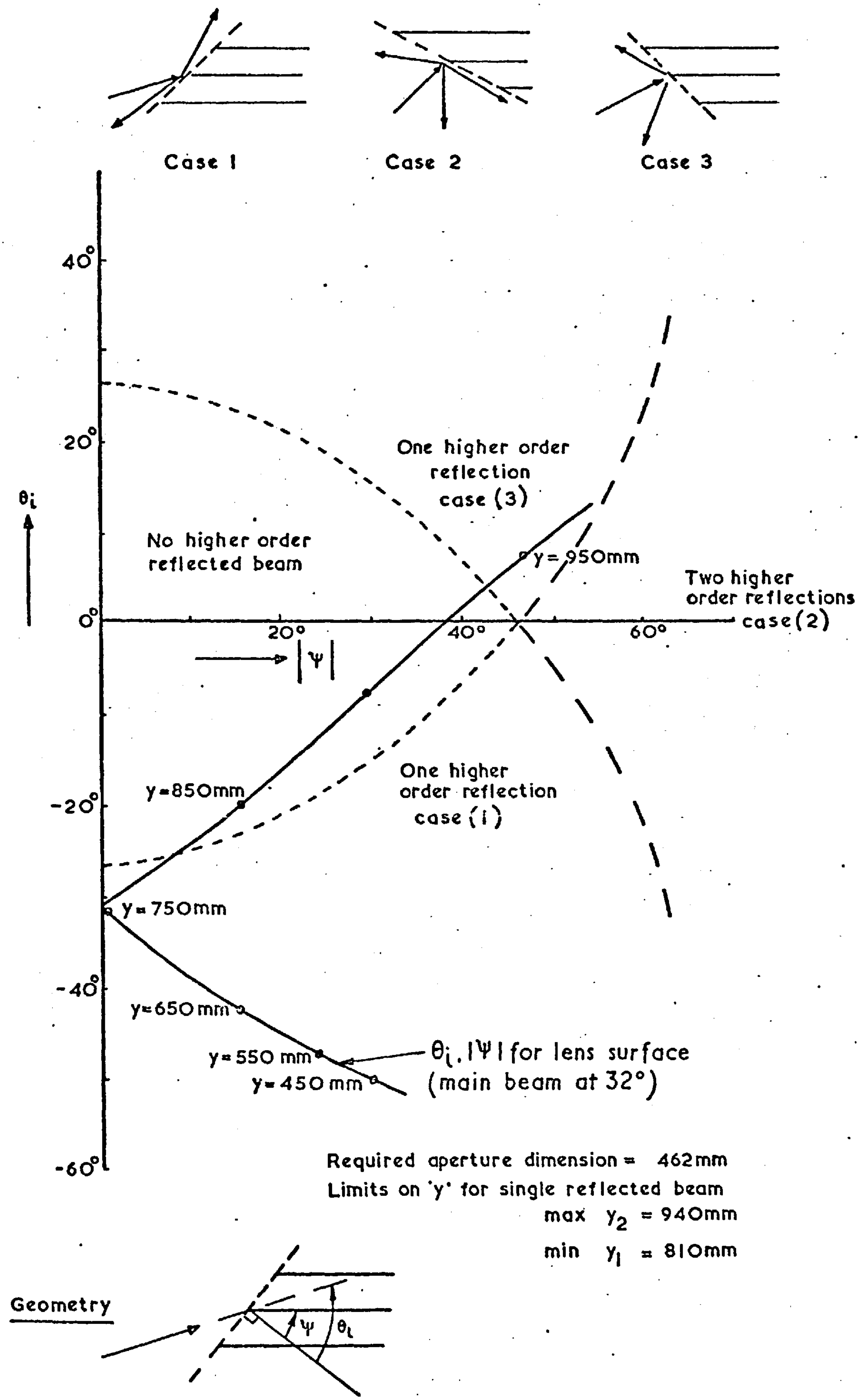

Fig. 3.8 Demonstration of secondary reflection problem at lens surface

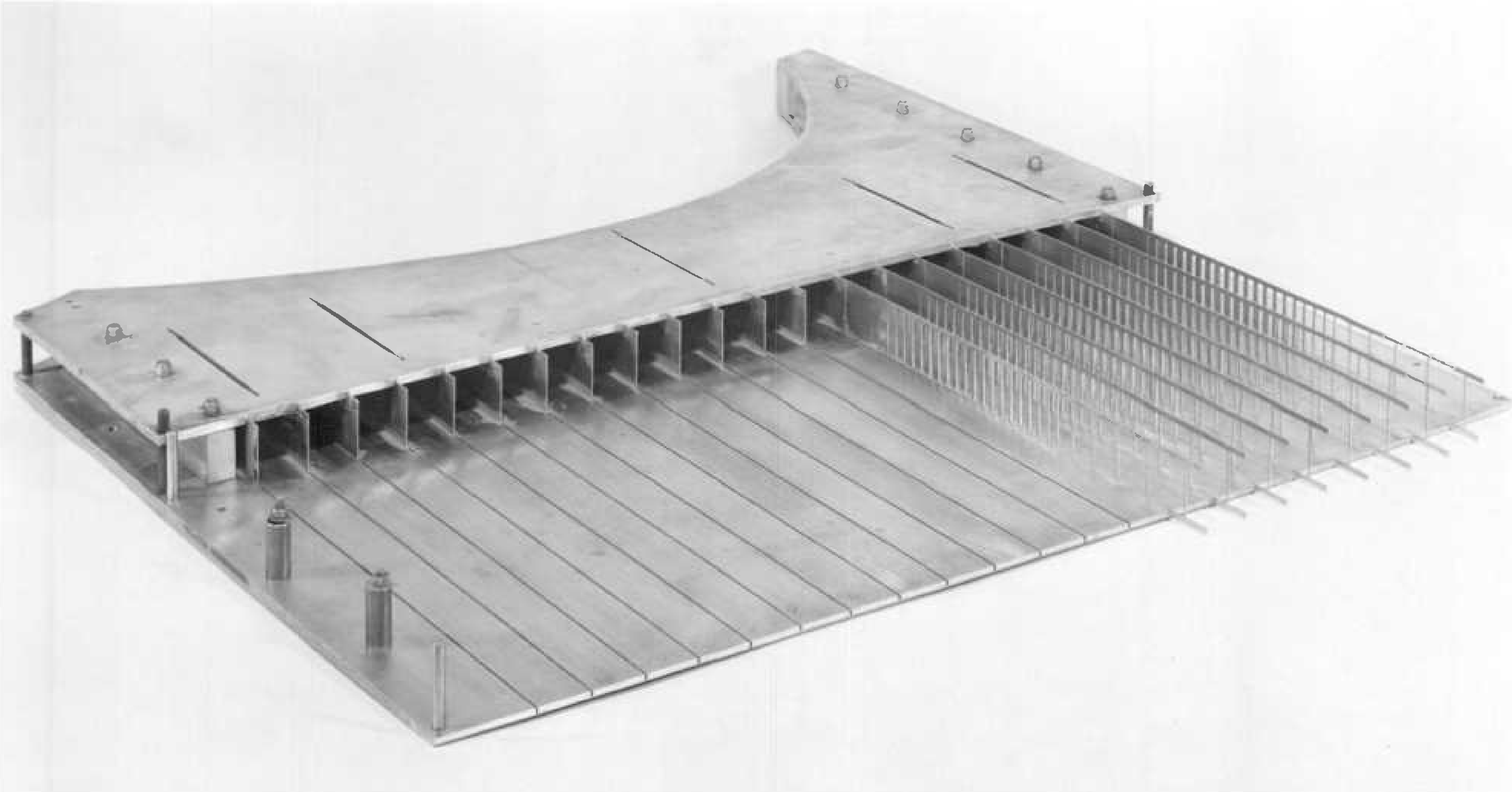

Fig. 3.9 Partially assembled lens, illustrating construction details

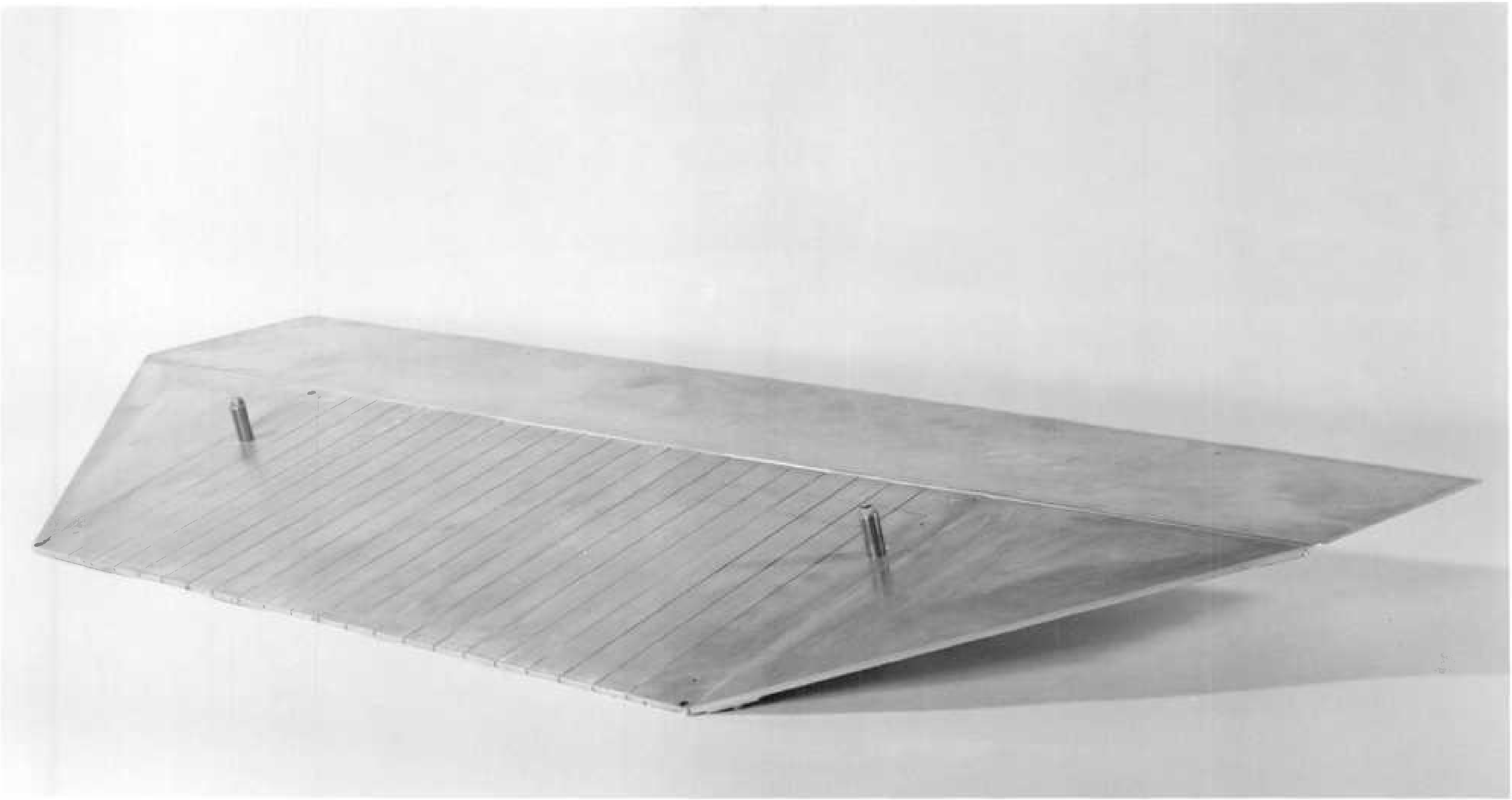

Fig. 3.10 Top plate of lens, with vertical flare and extension plates attached

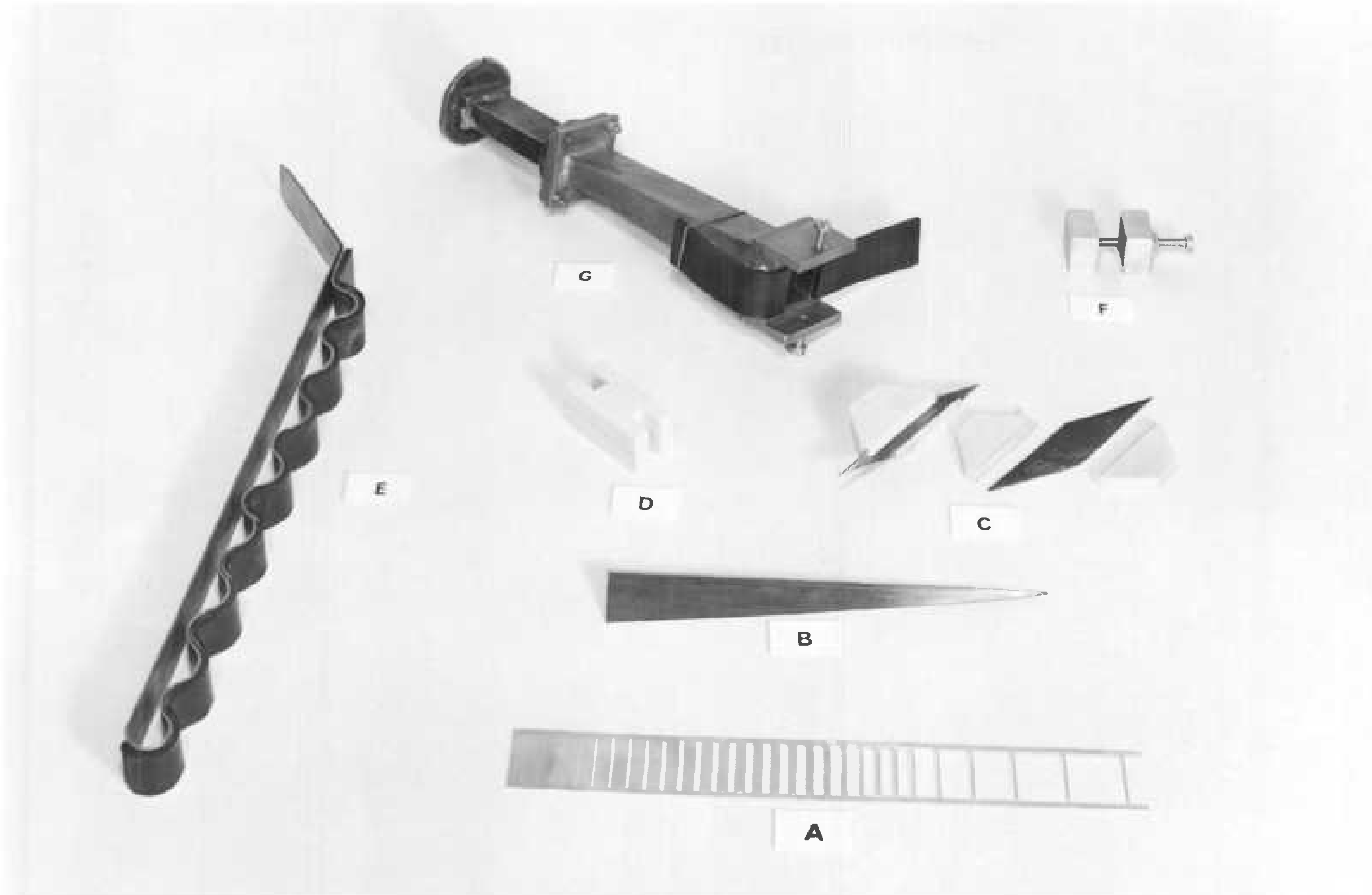

Fig. 3.11 Components developed for lens evaluation:-

(a) Reactive septum
(b) Sliding waveguide termination
(c) Waveguide attenuator
(d) Waveguide phaseshifter
(e) Load for absorbing edge radiation
(f) Sliding short-circuit
(g) Adaptor for element measurements

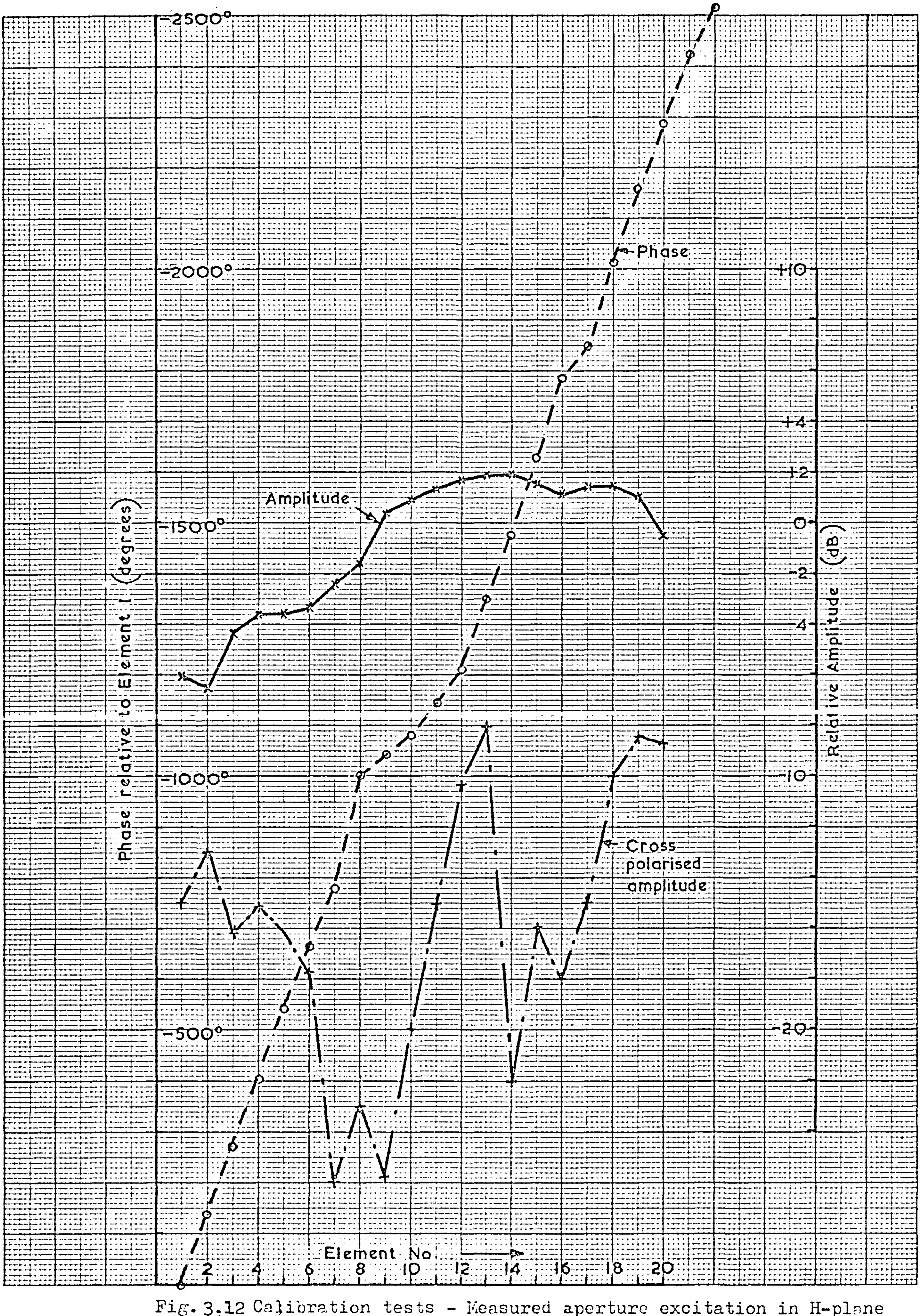

Fig. 3.12 Calibration tests - Measured aperture excitation in H-plane (for 32° beam) without attenuators or phase-shifters

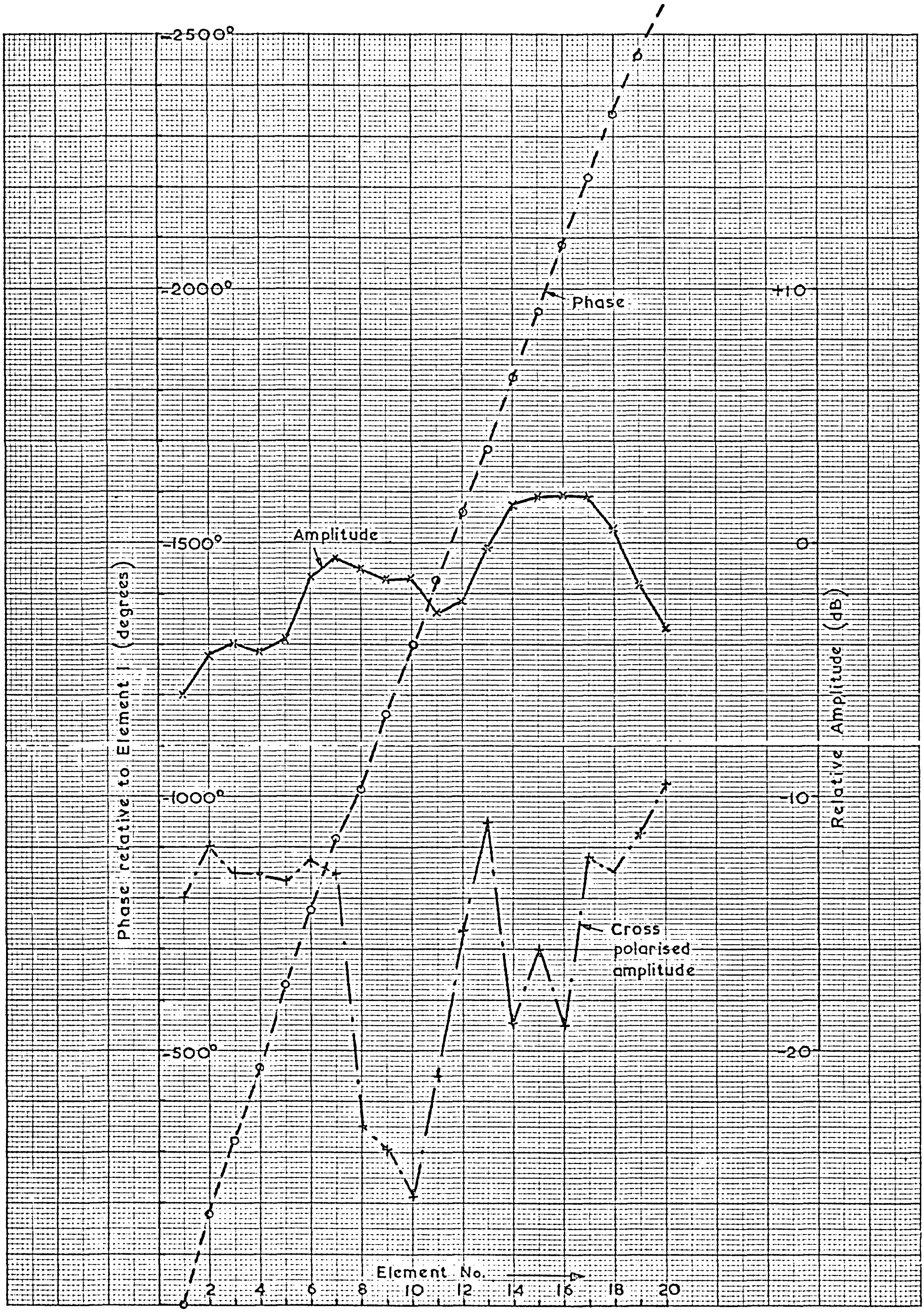

Fig. 3.13 Calibration tests - Measured aperture excitation in E-plane (for 32° beam) without attenuators or phase-shifters

(A) H-PLANE				(B) E-PLANE		
Element No.	Amplitude (dB)	Phase (degrees)	Phase difference	Amplitude (dB)	Phase (degrees)	Phase difference
1	-10.0	+13	-	-10.0	0	-
2	-8.4	-122	135°	-6.1	-134	134
3	-4.9	+105	133°	-4.5	-269	135
4	-2.3	-23	128°	-2.1	-404	135
5	-1.8	-162	139°	-0.9	-540	136
6	-1.2	+68	130°	-0.7	-680	140
7	-1.8	-70	138°	+0.4	-821	141
8	+0.7	+157	133°	+1.4	-960	139
9	+0.1	+34	123°	+1.8	-1094	134
10	+1.8	-99	133°	+3.0	-1230	136
11	+0.7	+124	137°	+3.7	-1362	132
12	+1.8	-3	127°	+3.7	-1499	137
13	+1.3	-137	134°	+1.8	-1637	138
14	+1.4	+94	129°	+1.3	-1772	135
15	+2.8	-44	138°	-1.2	-1910	138
16	+1.3	-174	130°	-1.5	-2047	137
17	+1.2	+45	141°	-4.0	-2185	138
18	-1.2	-86	131°	-6.8	-2320	135
19	-3.8	+145	129°	-9.7	-2451	131
20	-9.6	+16	129°	-12.3	-2588	137

Fig. 3.14 Measured amplitude and phase illumination of the corrected lens in the H and E planes, for the nominal horn position.

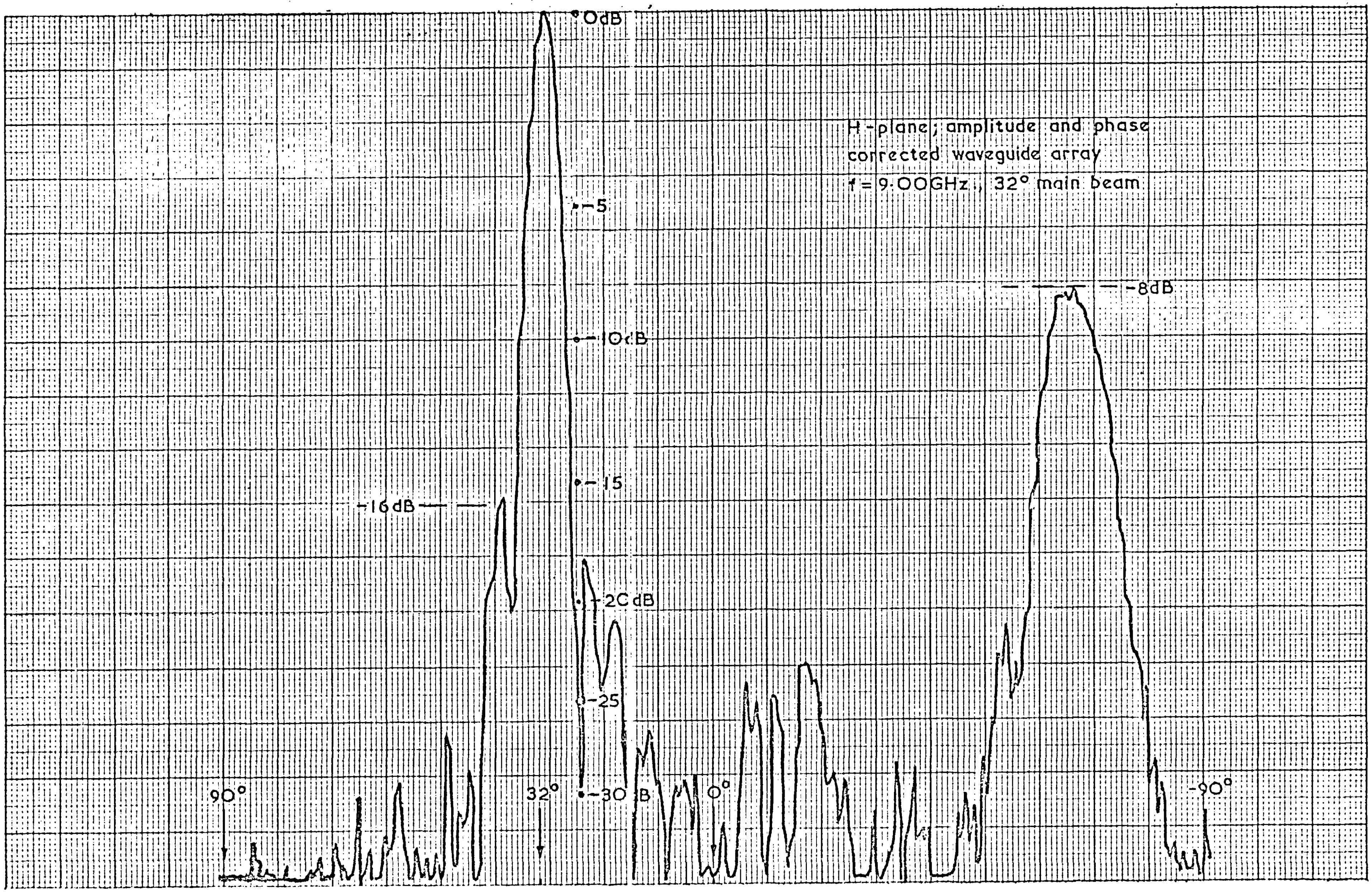

Fig. 3.15 Measured radiation pattern in H-plane for the waveguide array (32° main beam)

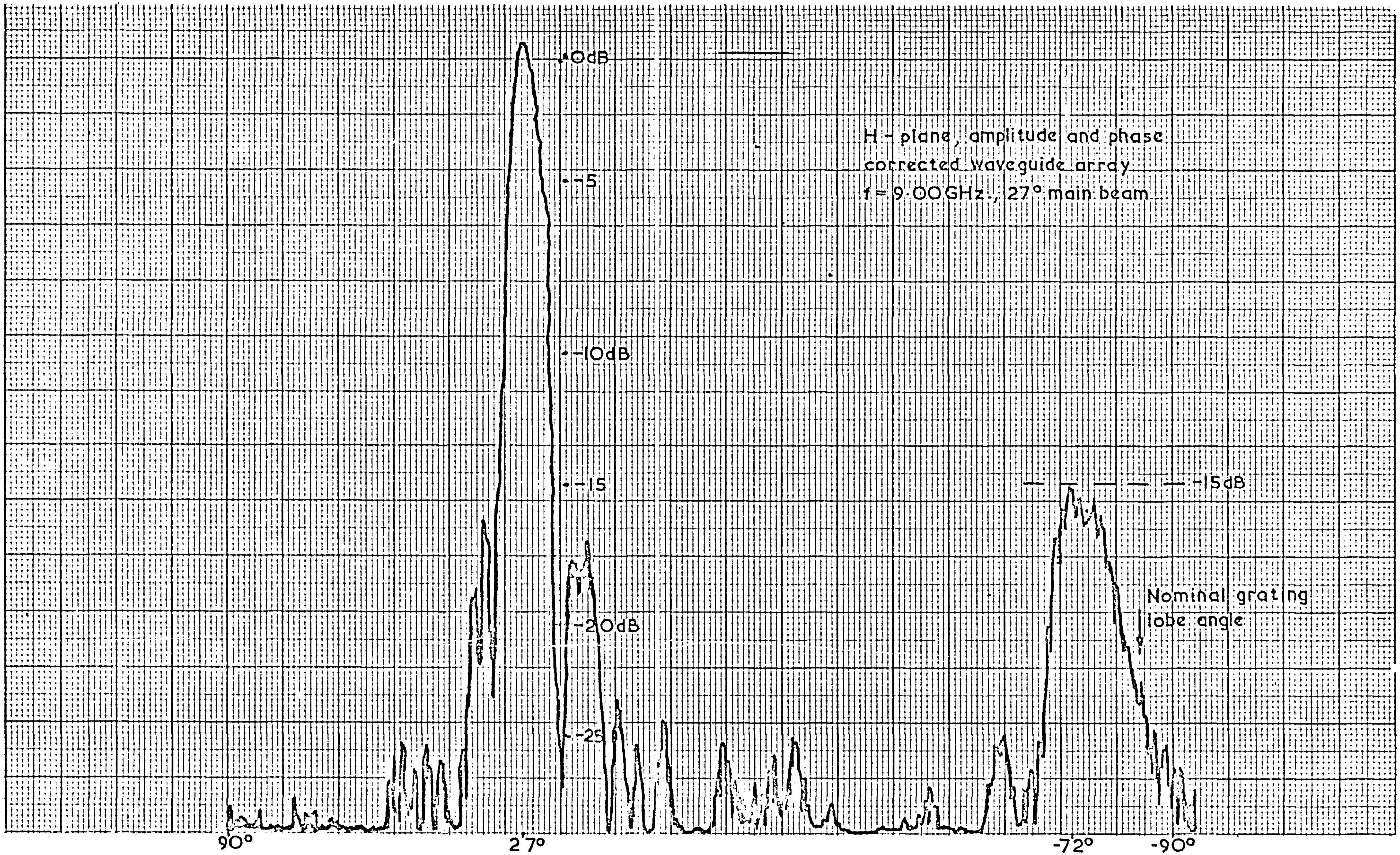

Fig. 3.16 Measured radiation pattern in H-plane for the waveguide array (27° main beam)

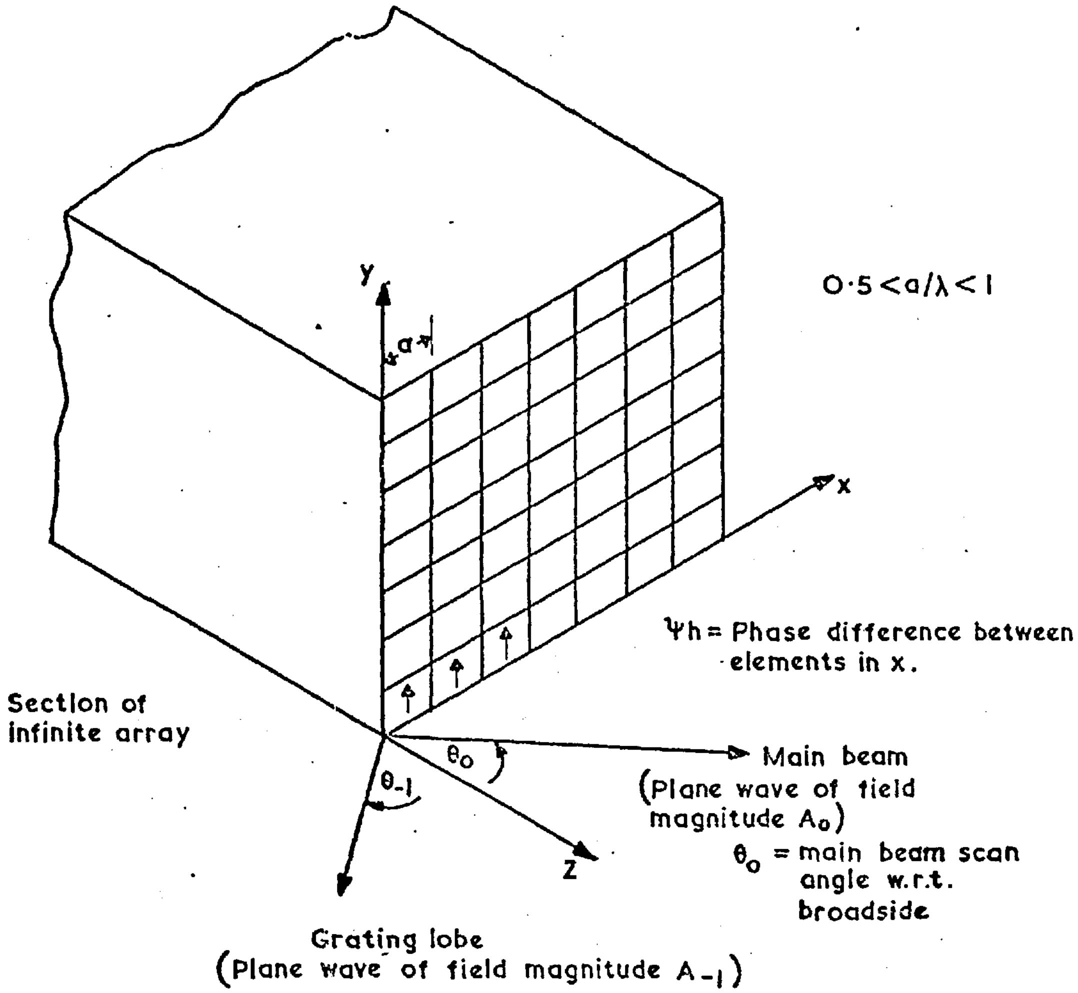

$$|A_0| = \frac{\sqrt{2}\ \beta_{10}}{\alpha_0 + \beta_{10}} \qquad \text{for } 0 \leq \Psi h \leq 2\pi\,(1 - a/\lambda)$$

$$= \frac{\sqrt{2}\ \beta_{10}}{\alpha_0 + \beta_{10}} \sqrt{\left(\frac{\alpha_0 + \alpha_{-1}}{\alpha_0 - \alpha_{-1}}\right)\left(\frac{\beta_{10} - \alpha_{-1}}{\beta_{10} + \alpha_{-1}}\right)} \qquad \text{for } 2\pi\,(1 - a/\lambda) \leq \Psi h \leq \pi$$

$$|A_{-1}| = \frac{\sqrt{2}\ \beta_{10}}{\alpha_{-1} + \beta_{10}} \sqrt{\left(\frac{\alpha_0 + \alpha_{-1}}{\alpha_0 - \alpha_{-1}}\right)\left(\frac{\alpha_0 - \beta_{10}}{\alpha_0 + \beta_{10}}\right)} \qquad \text{for } 2\pi\,(1 - a/\lambda) \leq \Psi h \leq \pi$$

$$\beta_{10} = jk\sqrt{1 - (\lambda/2a)^2}$$

$$\alpha_0 = j\sqrt{k^2 - (\Psi h/a)^2} = jk\cos\theta_0$$

$$\alpha_{-1} = j\sqrt{k^2 - [(\Psi h - 2\pi)/a]^2} = jk\sqrt{1 - (\sin\theta_0 - \lambda/a)^2}$$

Fig. 3.17 H-plane scanning characteristics of an infinite planar array, periodically excited by TE_{10} waveguide mode

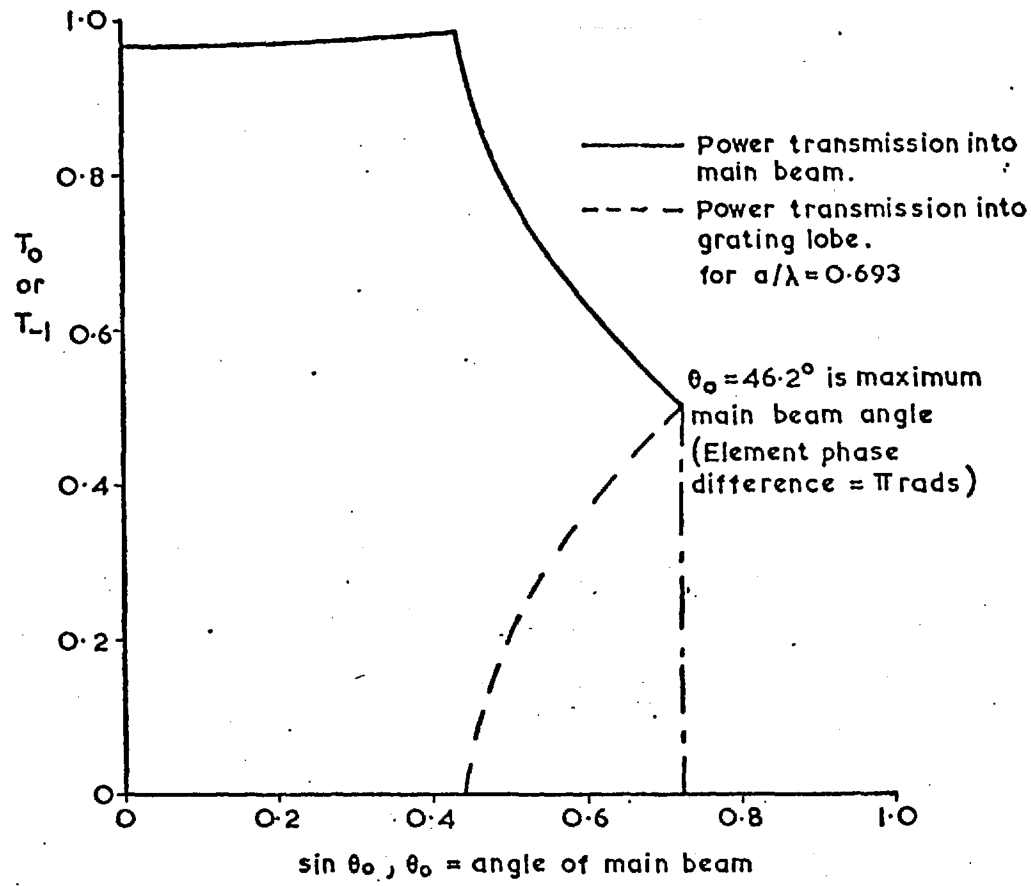

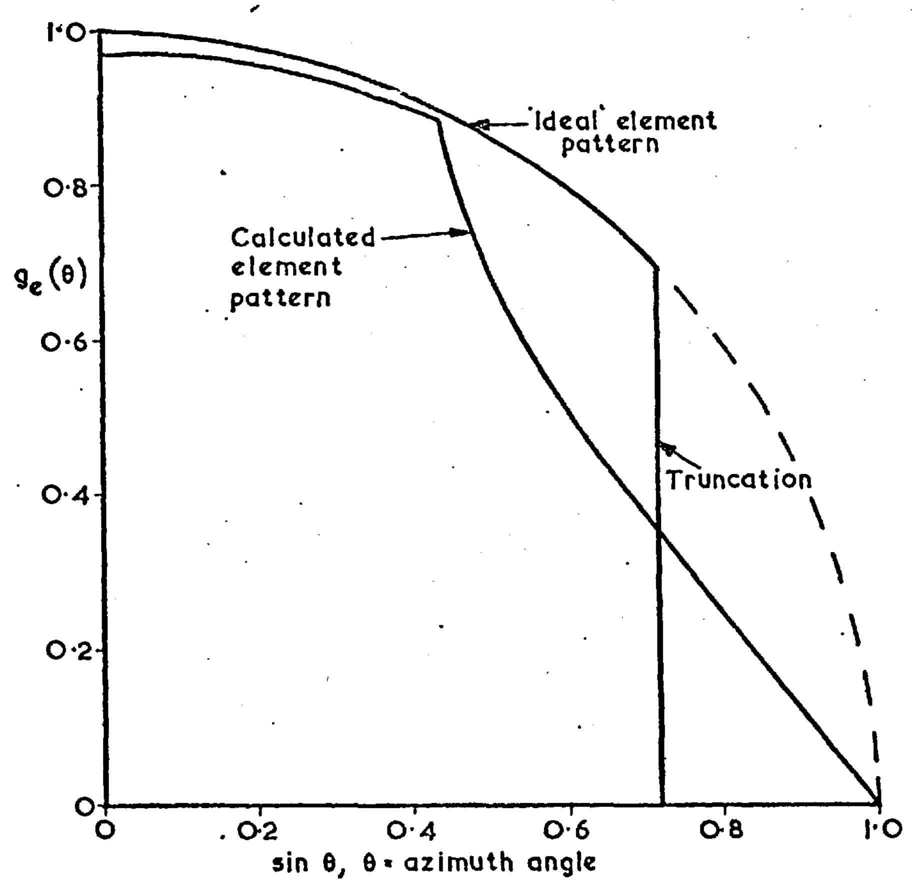

Fig. 3.18 Calculated transmission coefficients and element-gain pattern in H-plane for infinite waveguide array

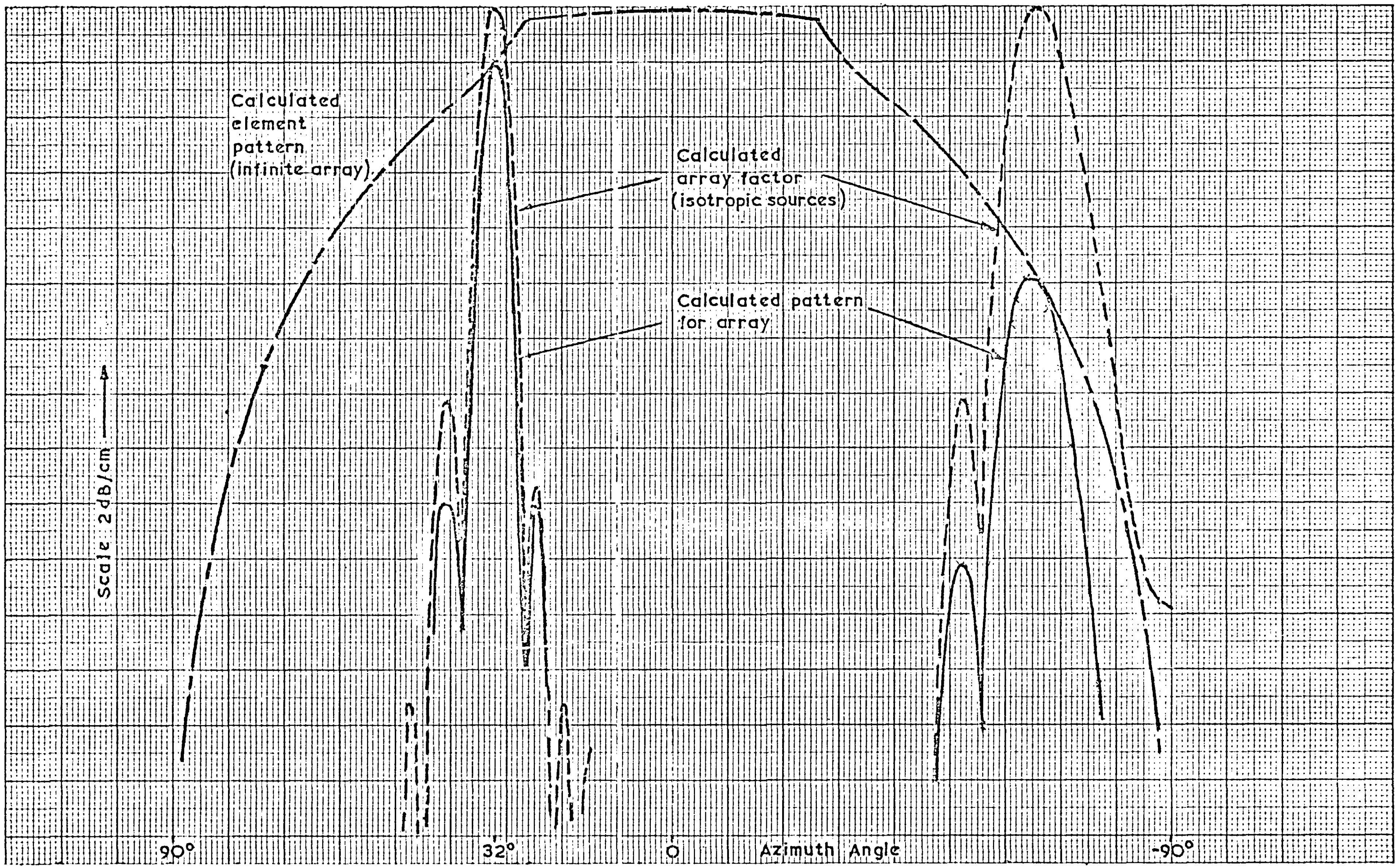

Fig. 3.19 Calculated H-plane pattern for waveguide array (32° beam)

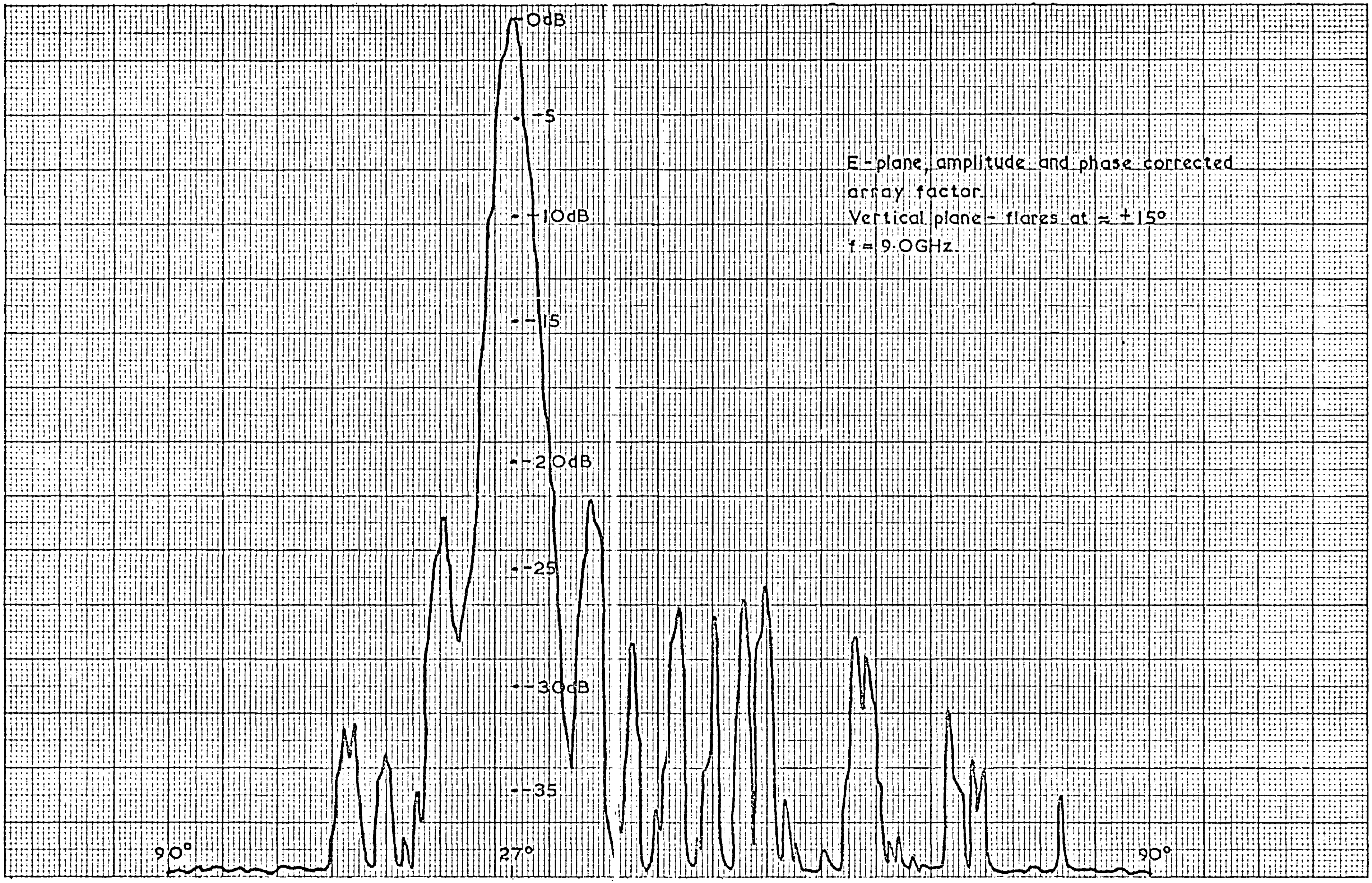

Fig. 3.20a Measured E-plane pattern for waveguide array (27° main beam; ± 15° flares)

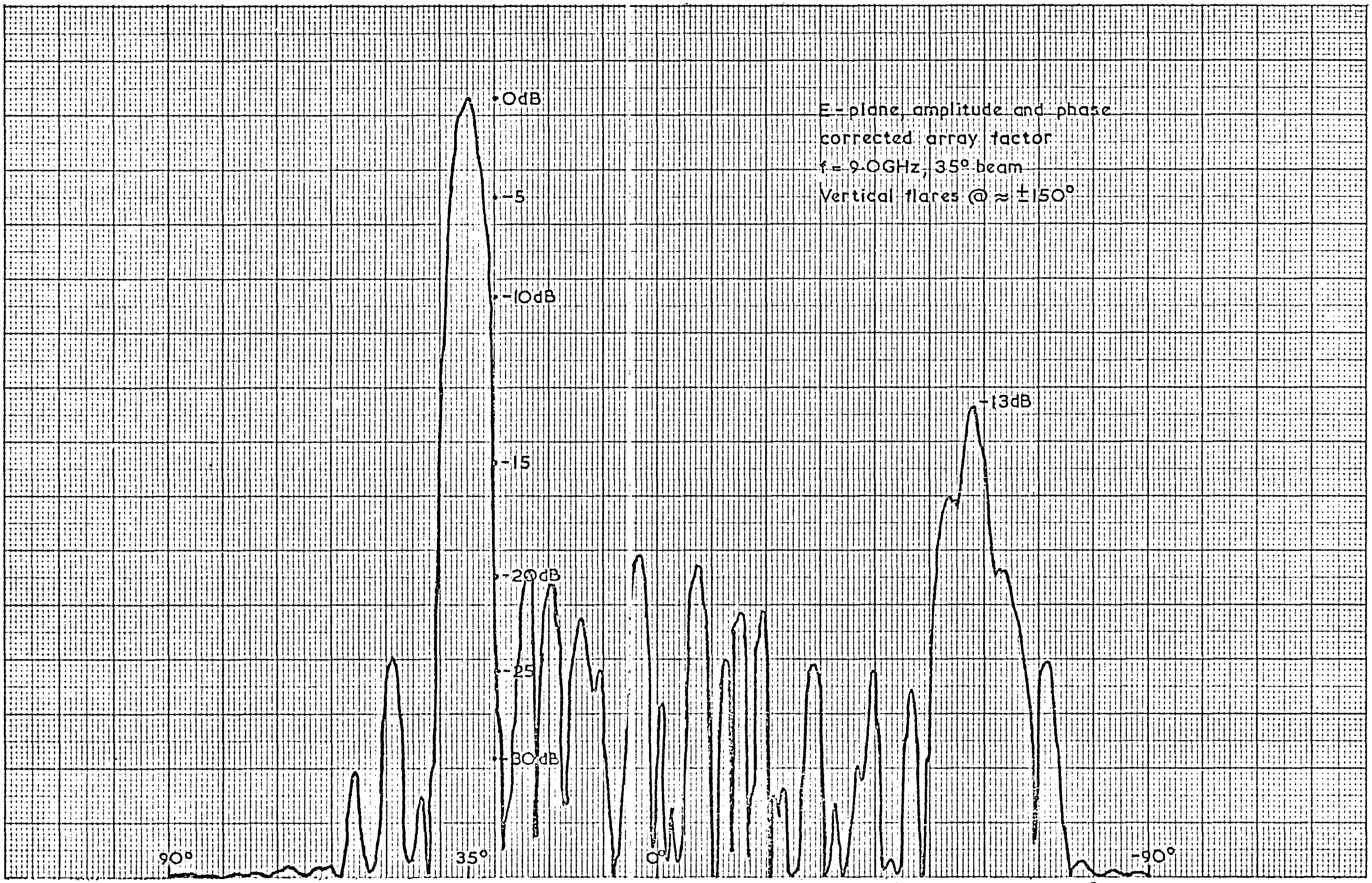

Fig.3.20b Measured E-plane pattern for waveguide array (35° main beam, ± 15° flares)

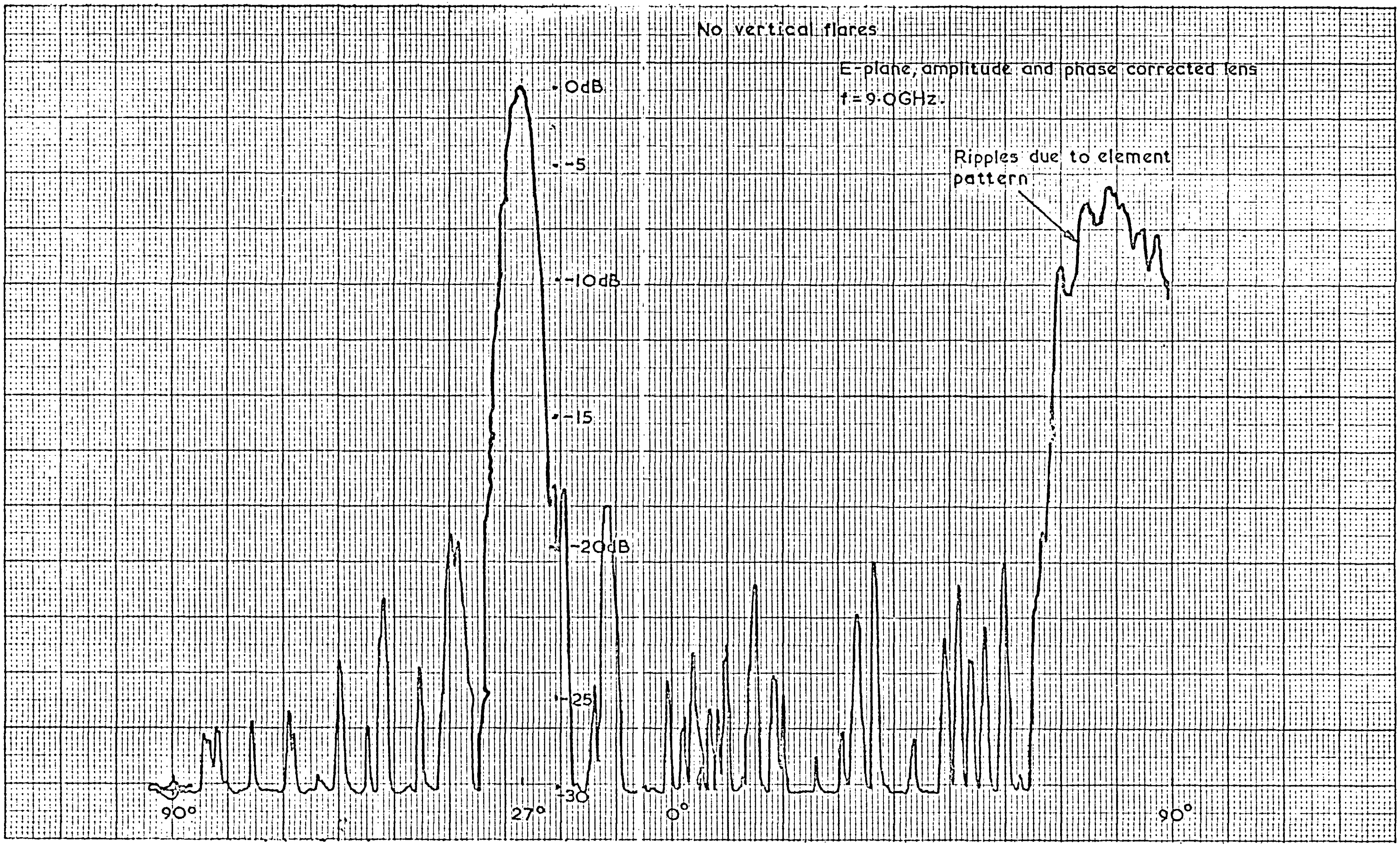

Fig. 3.21a Measured E-plane pattern for waveguide array (27^{o} main beam, no flares)

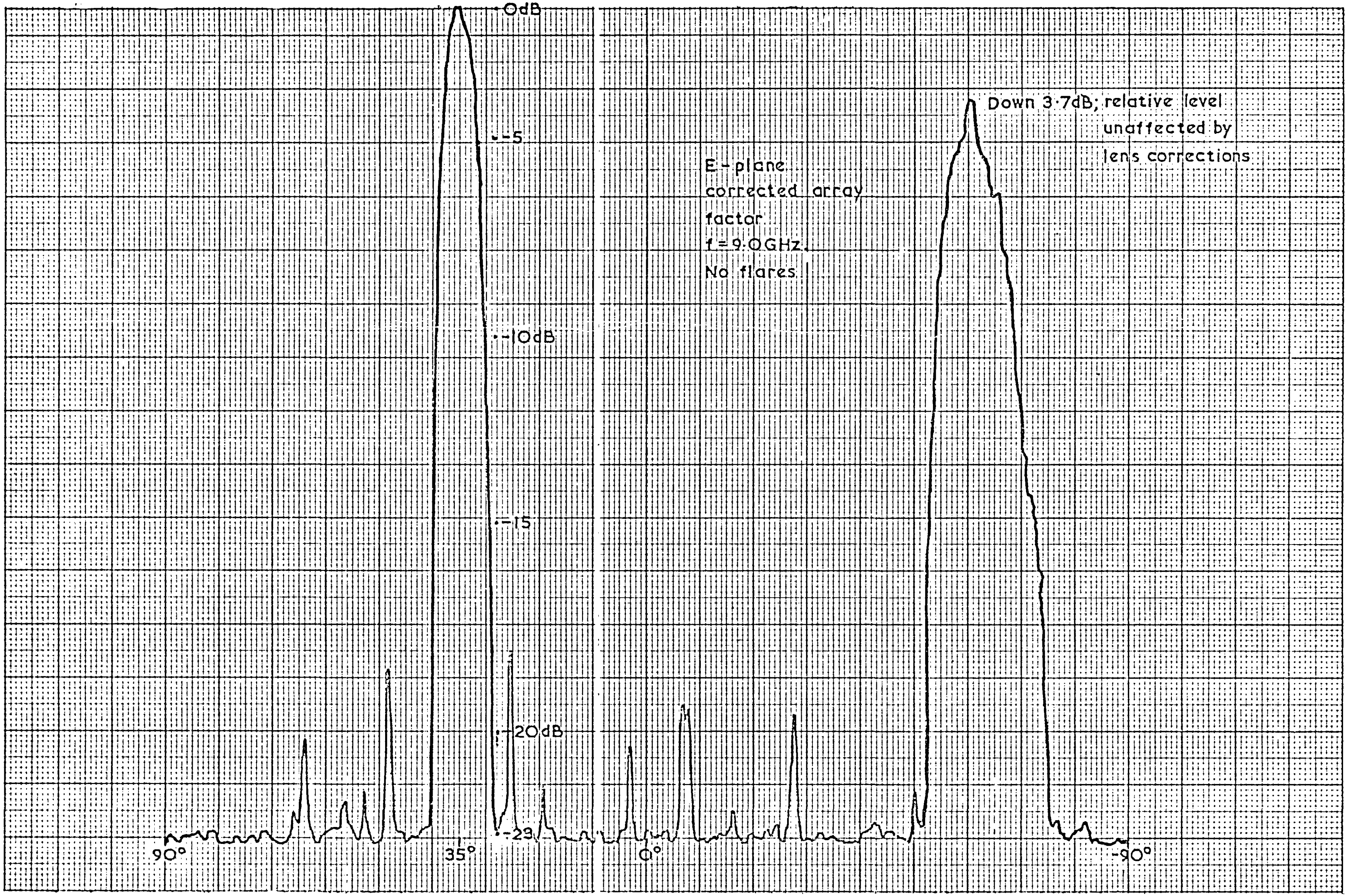

<u>Fig. 3.21b</u> Measured E-plane pattern for waveguide array (35° main beam, no flares)

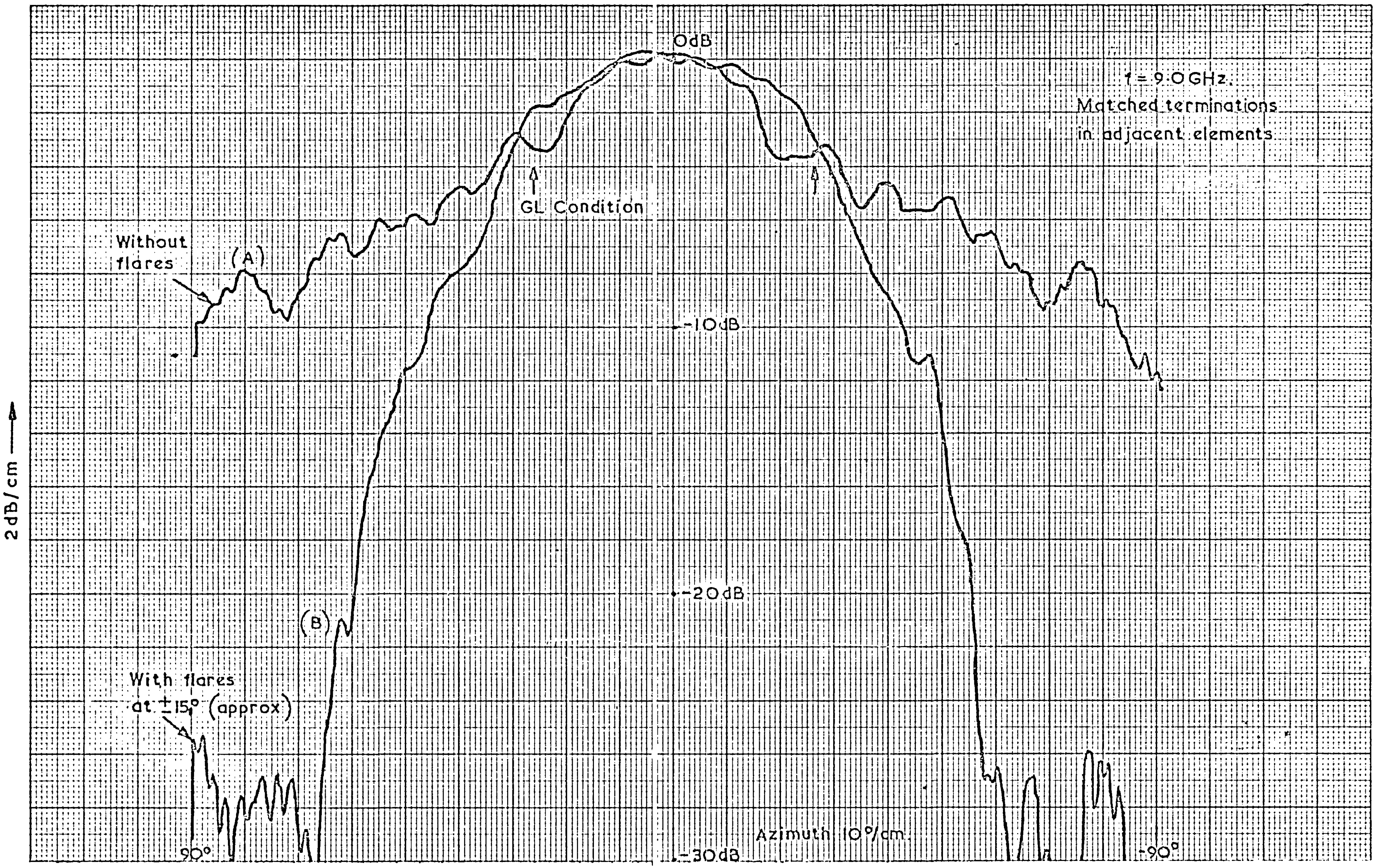

Fig. 3.22 Control of the E-plane element pattern using flares

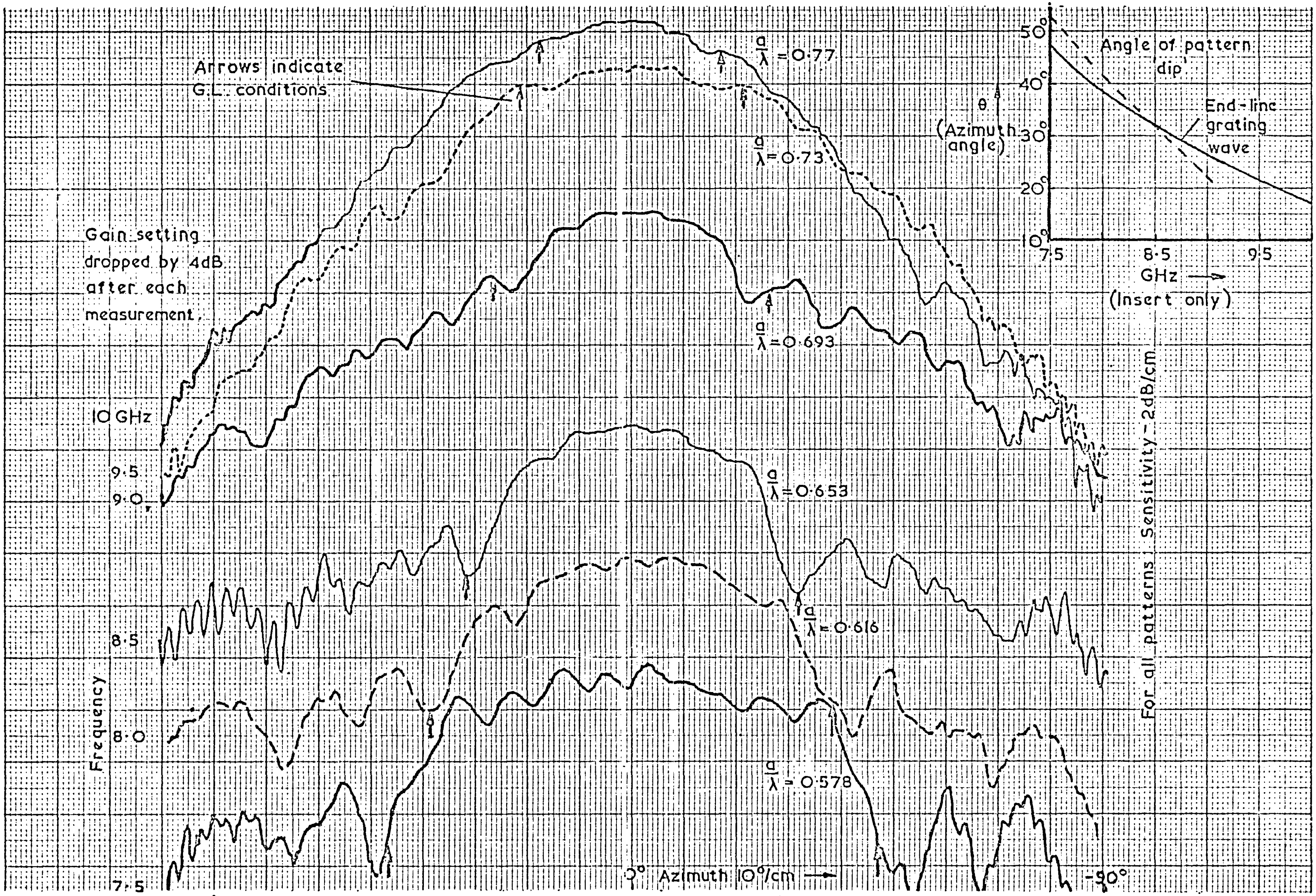

Fig. 3.23 Element pattern variation with frequency (without flares)

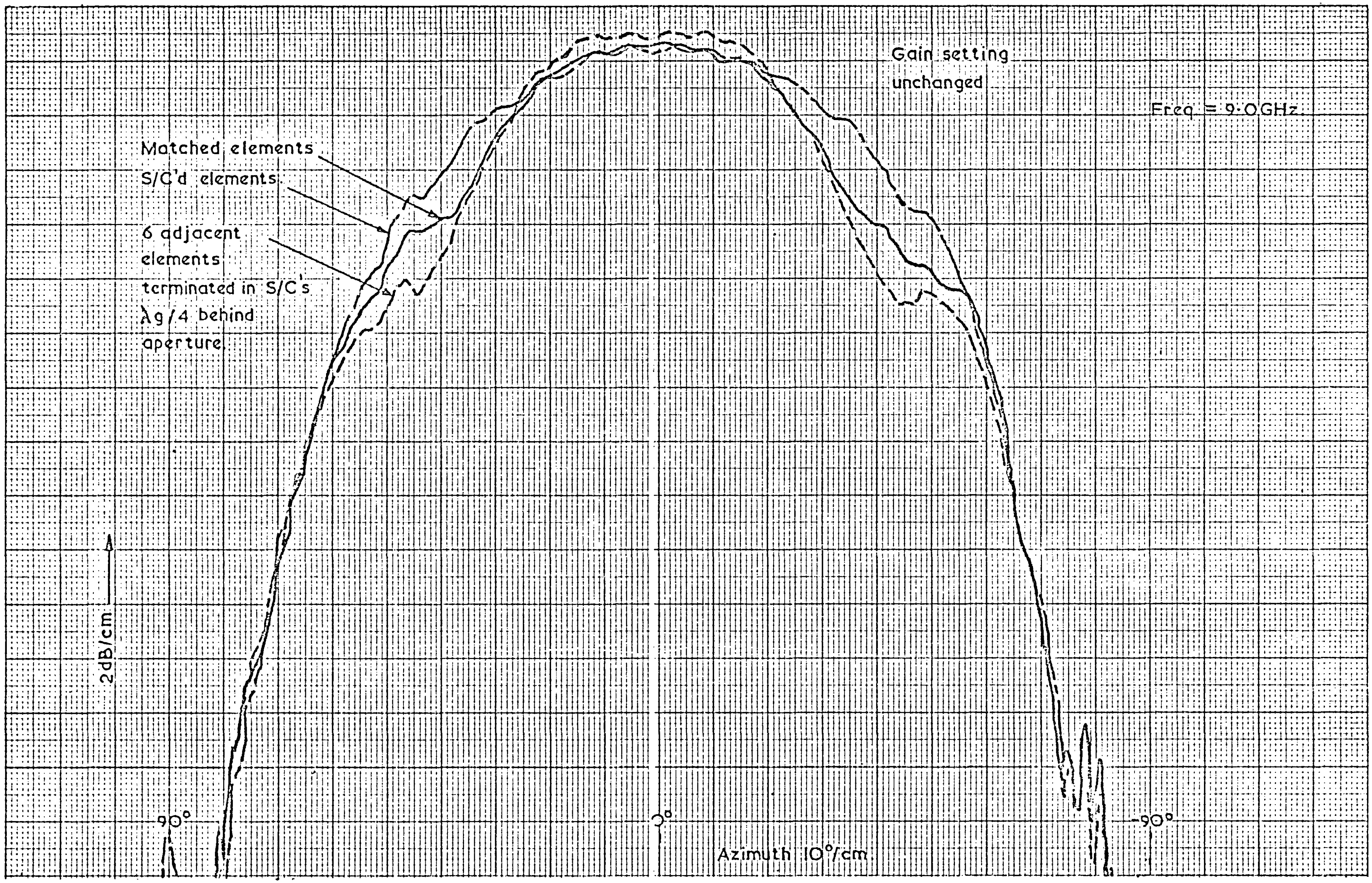

Fig. 3.24 Element patterns with ± 22.5° flares, demonstrating the dependance on mutual coupling

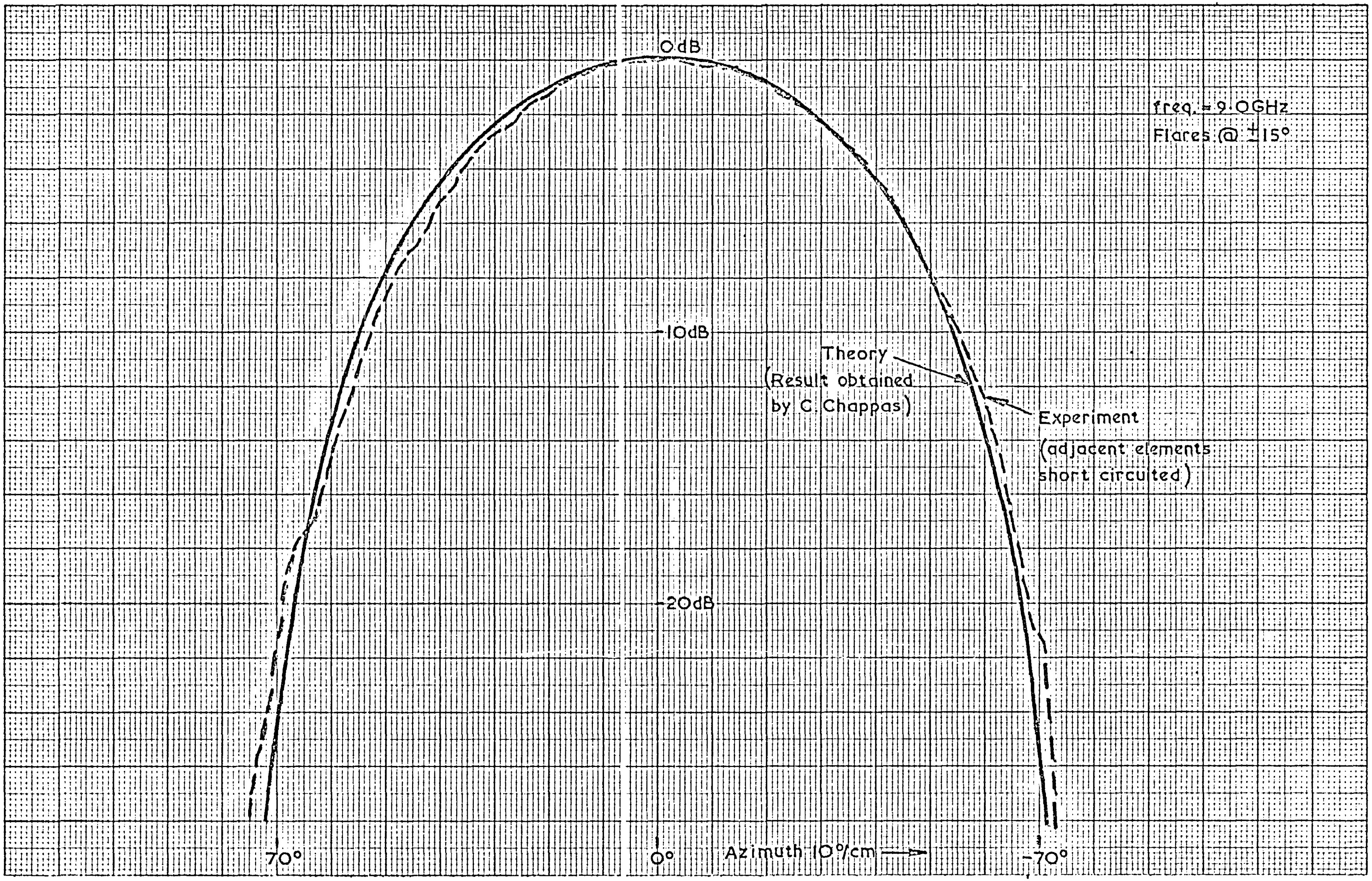

Fig. 3.25 Comparison of theoretical and experimental E-plane radiation patterns

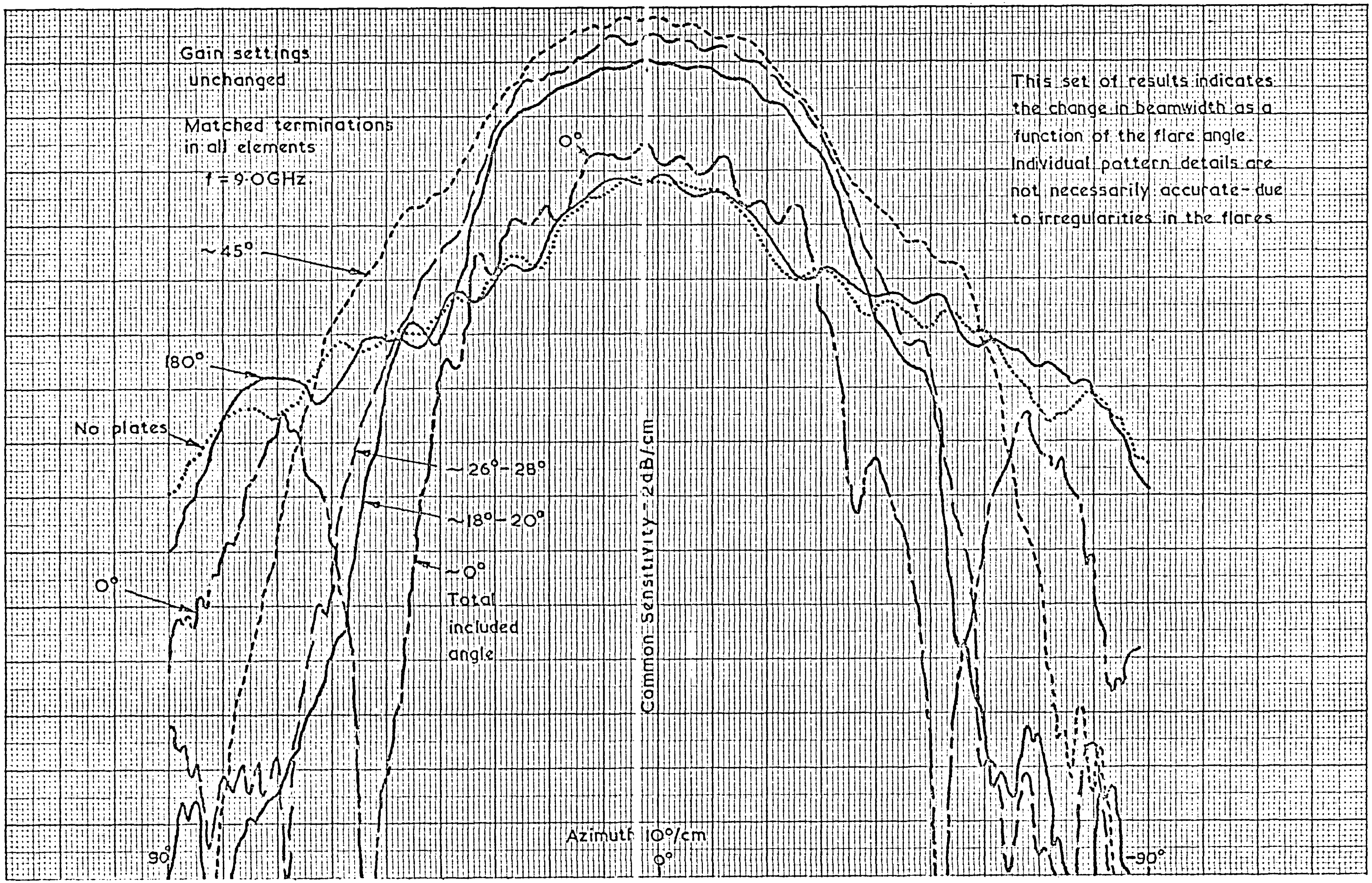

Fig. 3.26 Element patte:n dependance on the flare angle

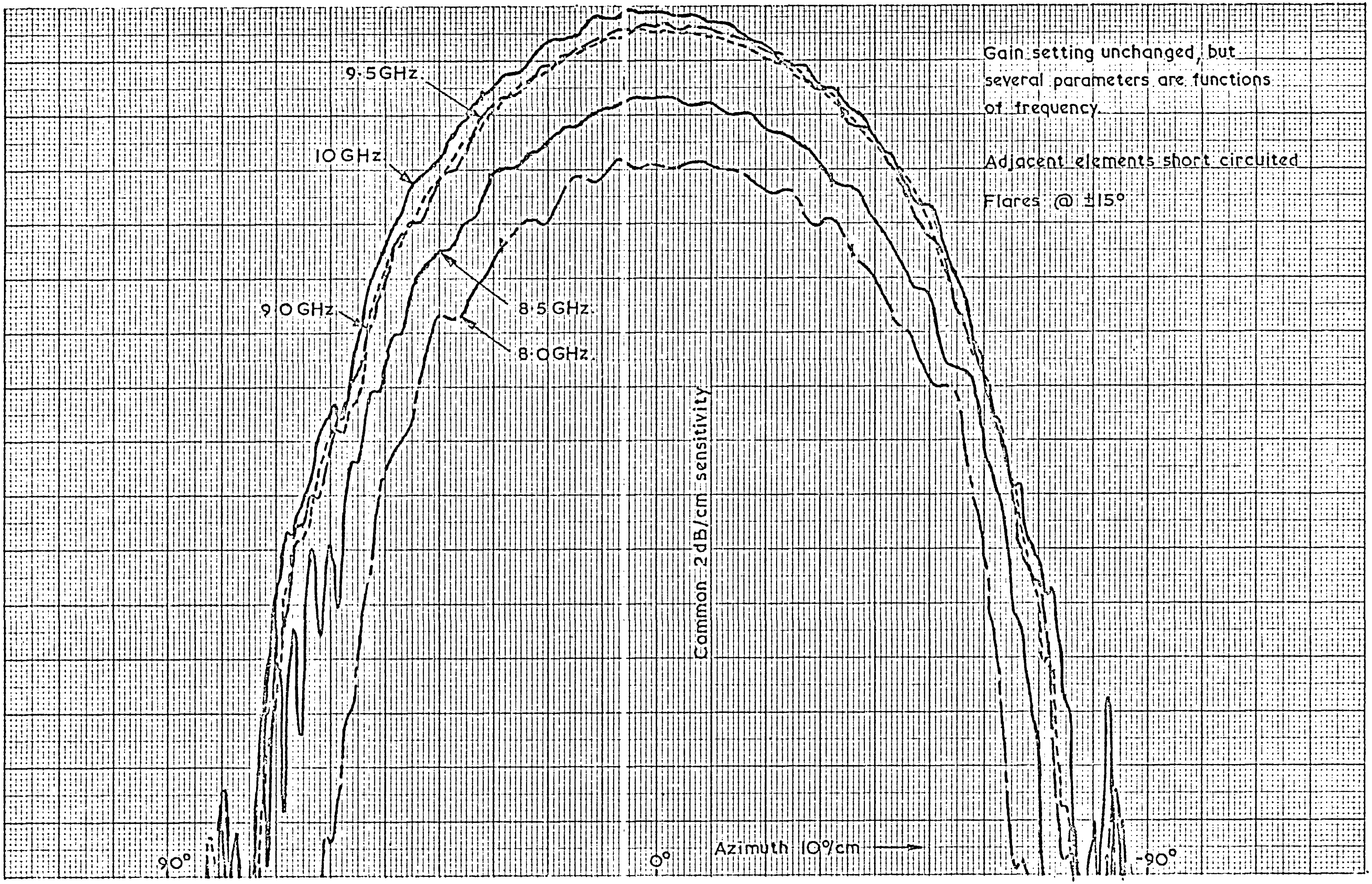

Fig. 3.27 Variation of element pattern with frequency - flares fitted

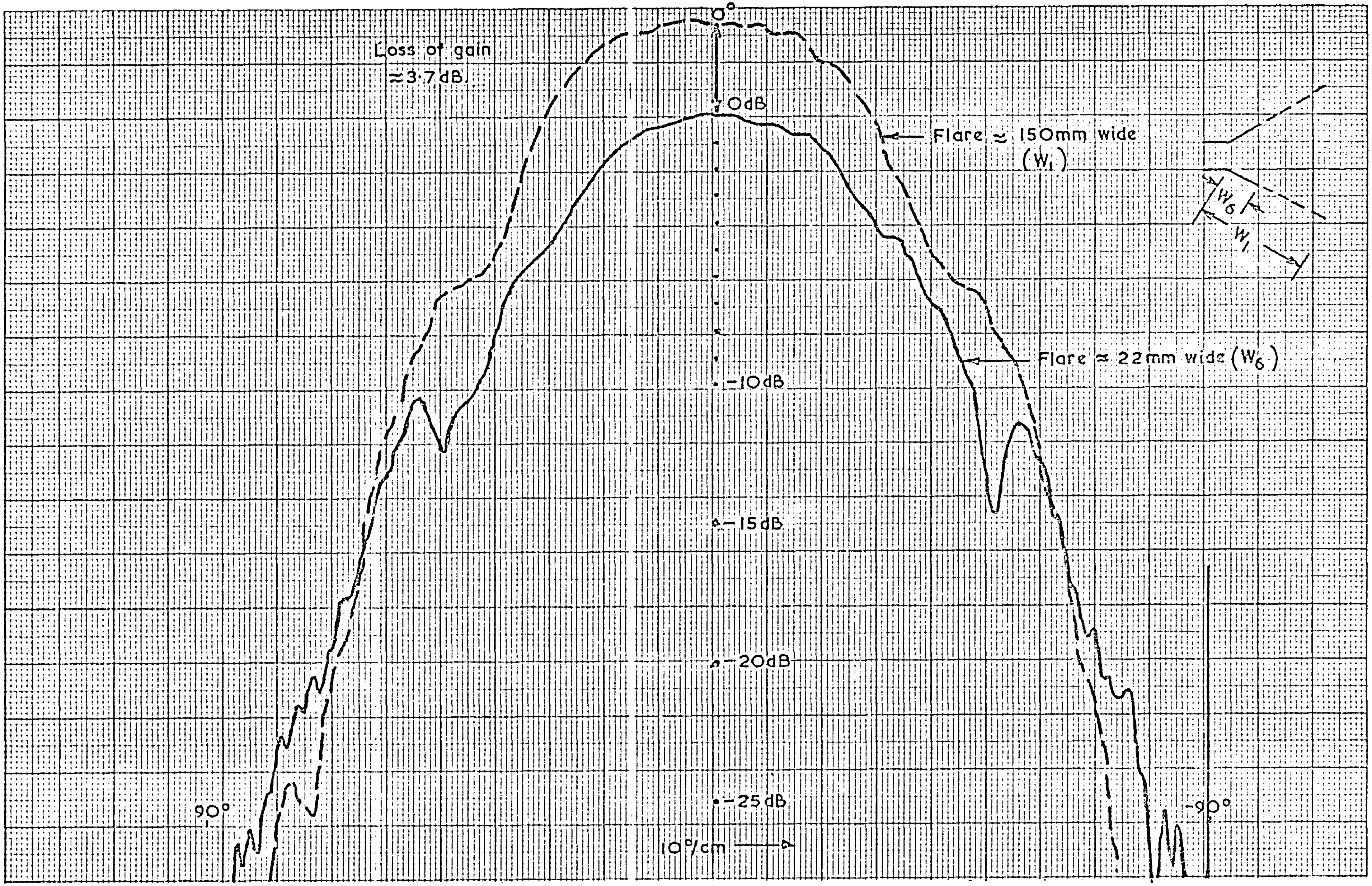

Fig. 3.28 Variation in element pattern with the width of the flare

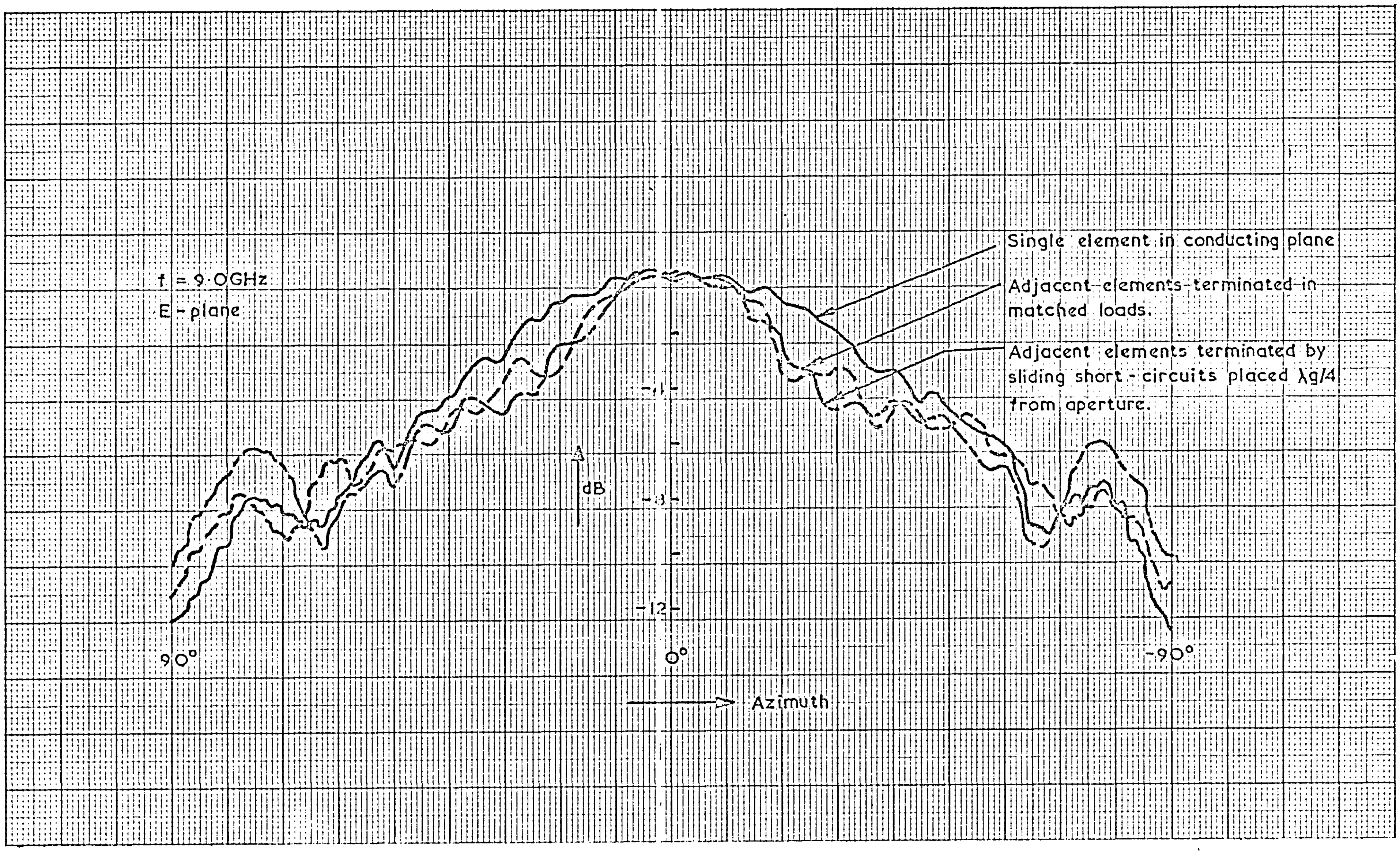

Fig. 3.29 Element pattern differences caused by mutual coupling - without flares

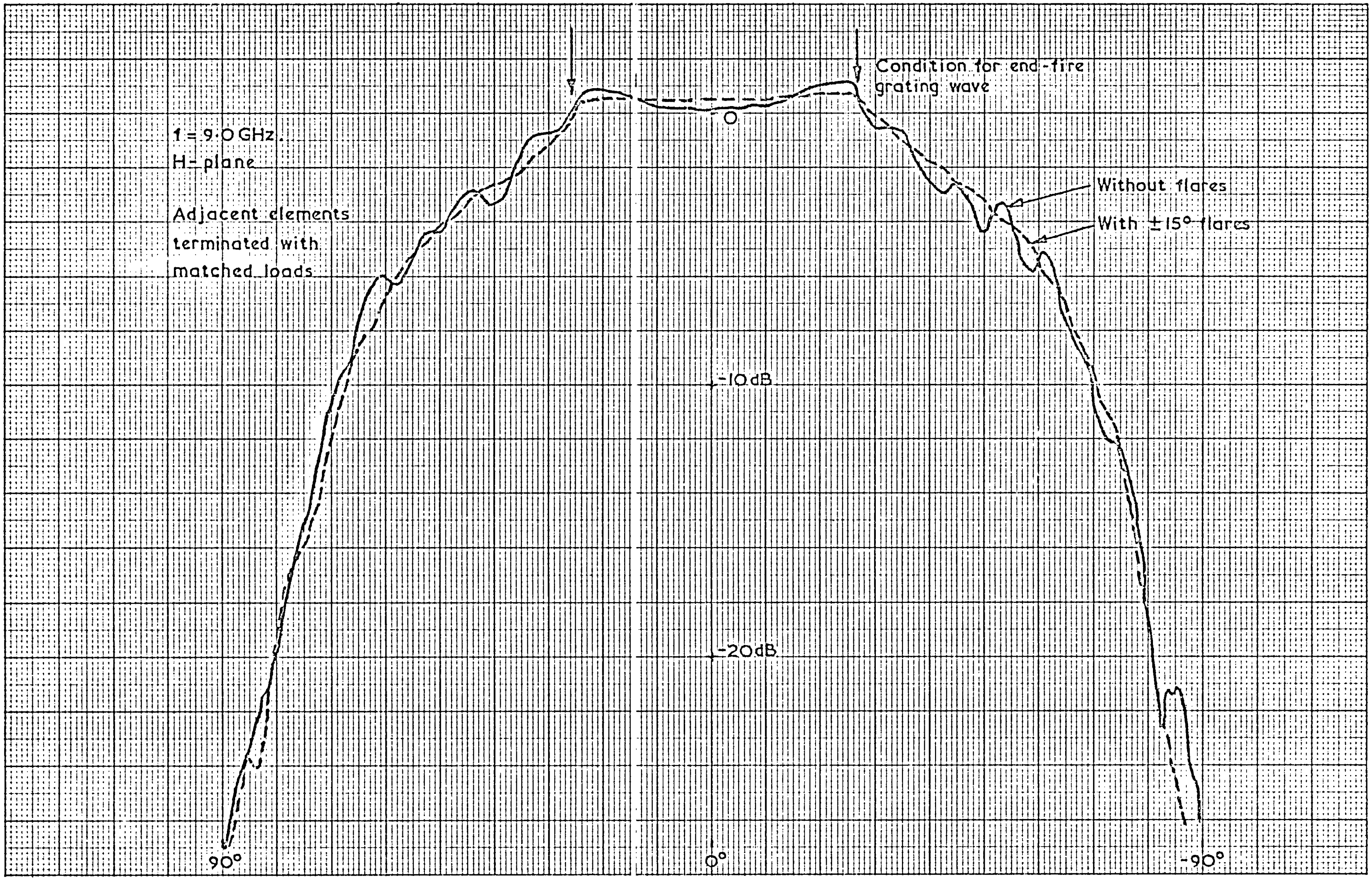

Fig. 3.30 H-plane centre element pattern for waveguide array

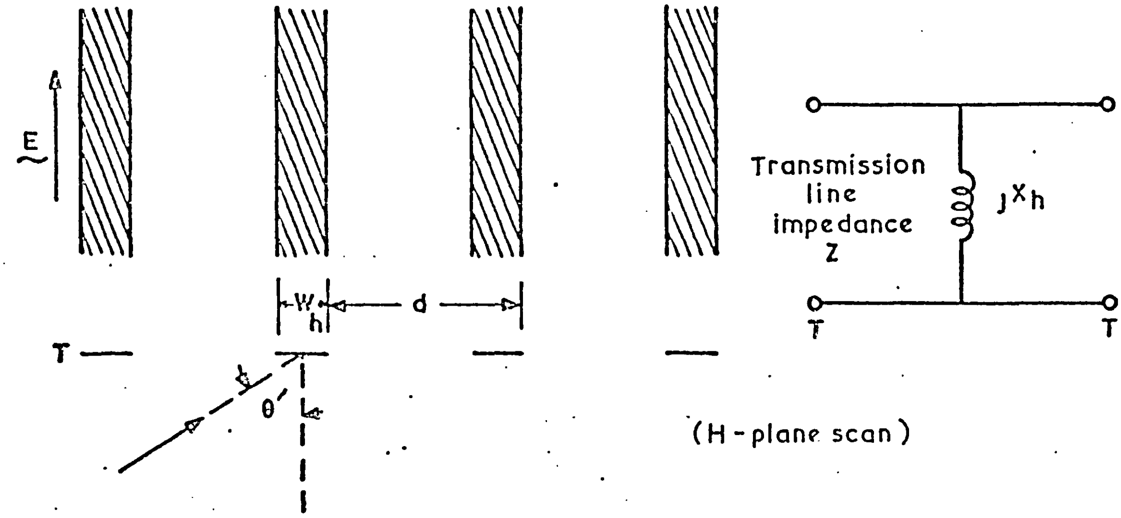

Fig. 3.31 Equivalent transmission line circuit - $\underset{\sim}{E}$// zero thickness conductors

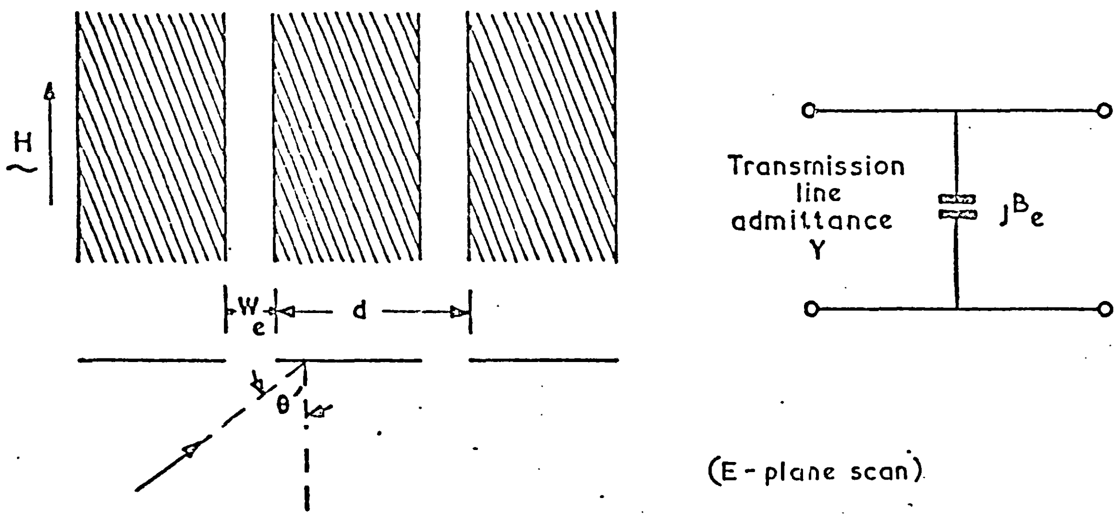

Fig. 3.32 Equivalent transmission line circuit - $\underset{\sim}{H}$// zero thickness conductors

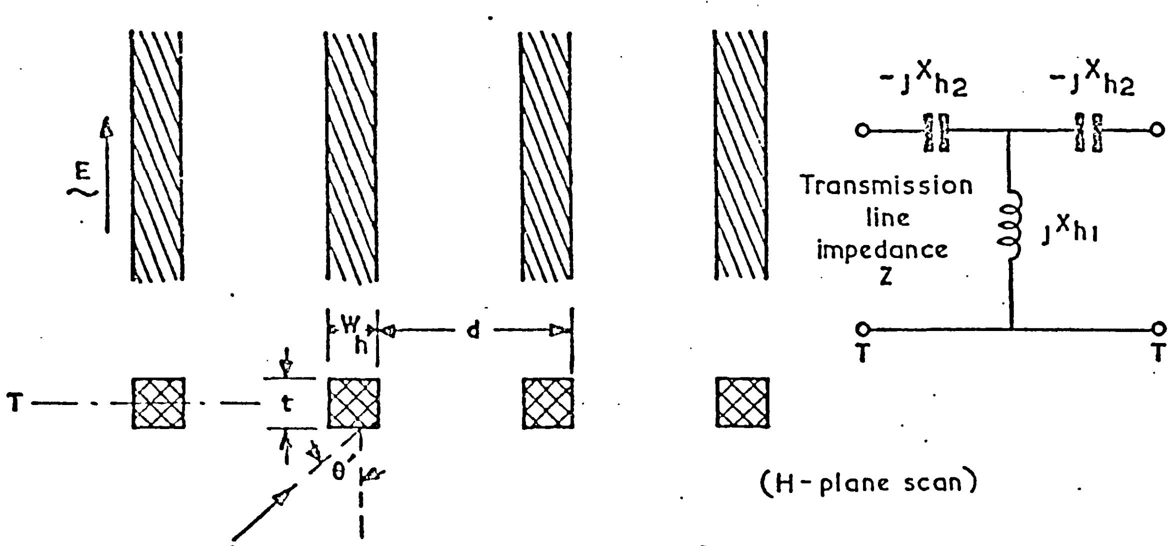

Fig. 3.33 Equivalent transmission line circuits - $\underset{\sim}{E}$// finite thickness conductors.

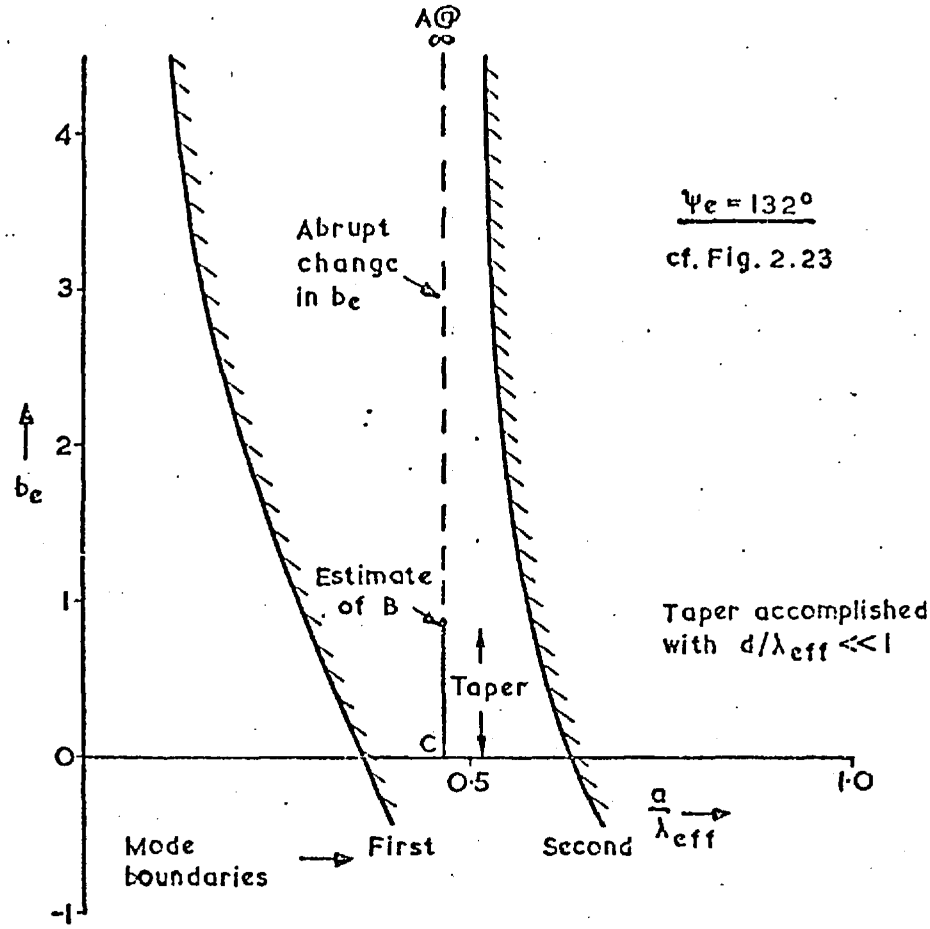

Fig.3.34a Reduced E-plane mode chart

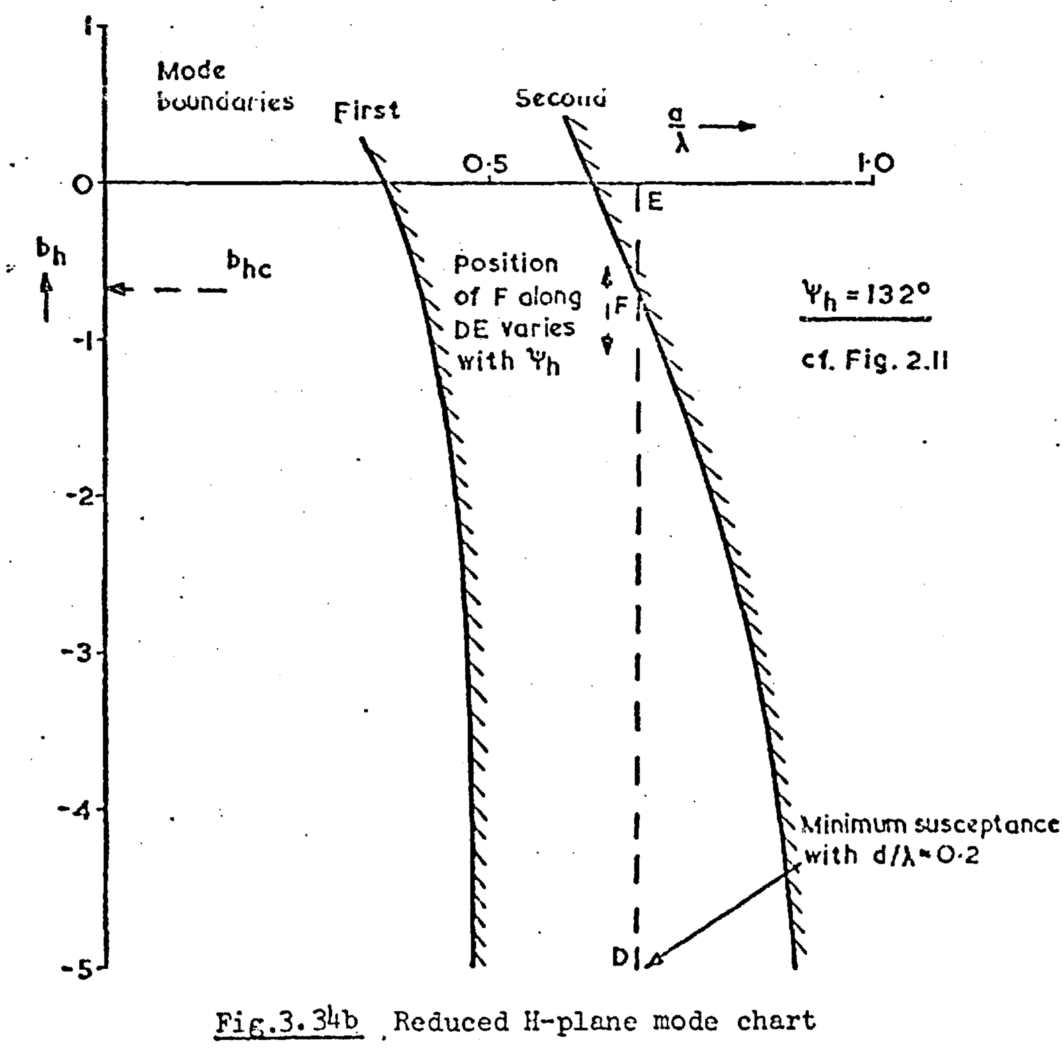

Fig.3.34b Reduced H-plane mode chart

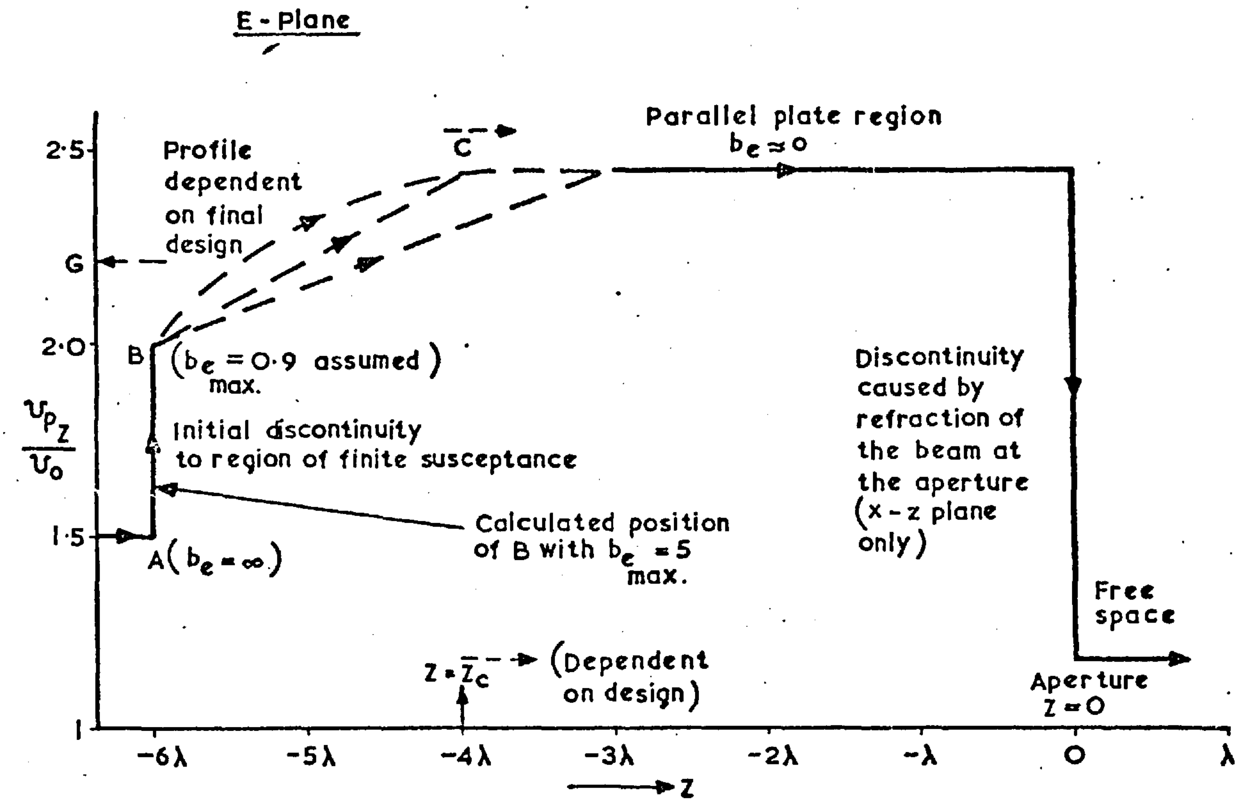

Fig. 3.35a E-plane axial phase, velocity profile $\psi_e = 132^o$

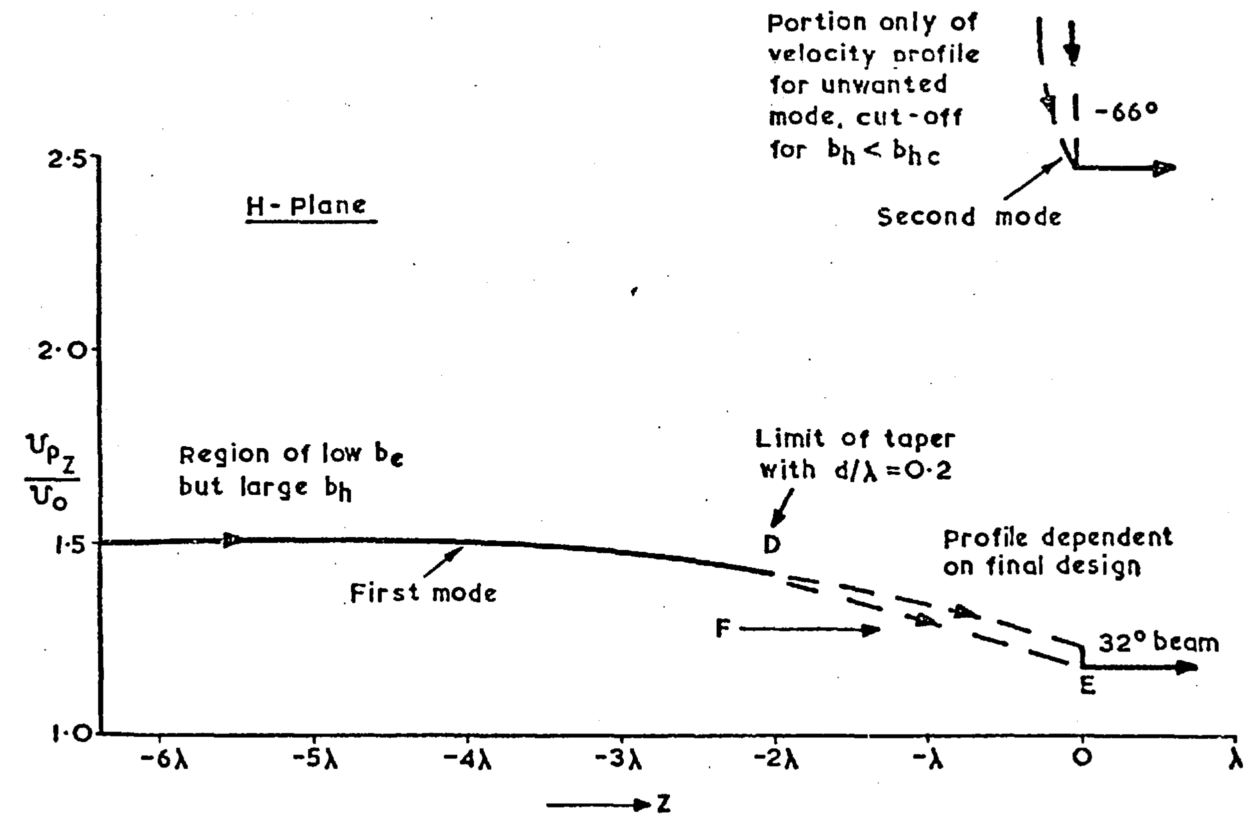

Fig.3.35b H-plane axial phase velocity profile, $\psi_h = 132^o$

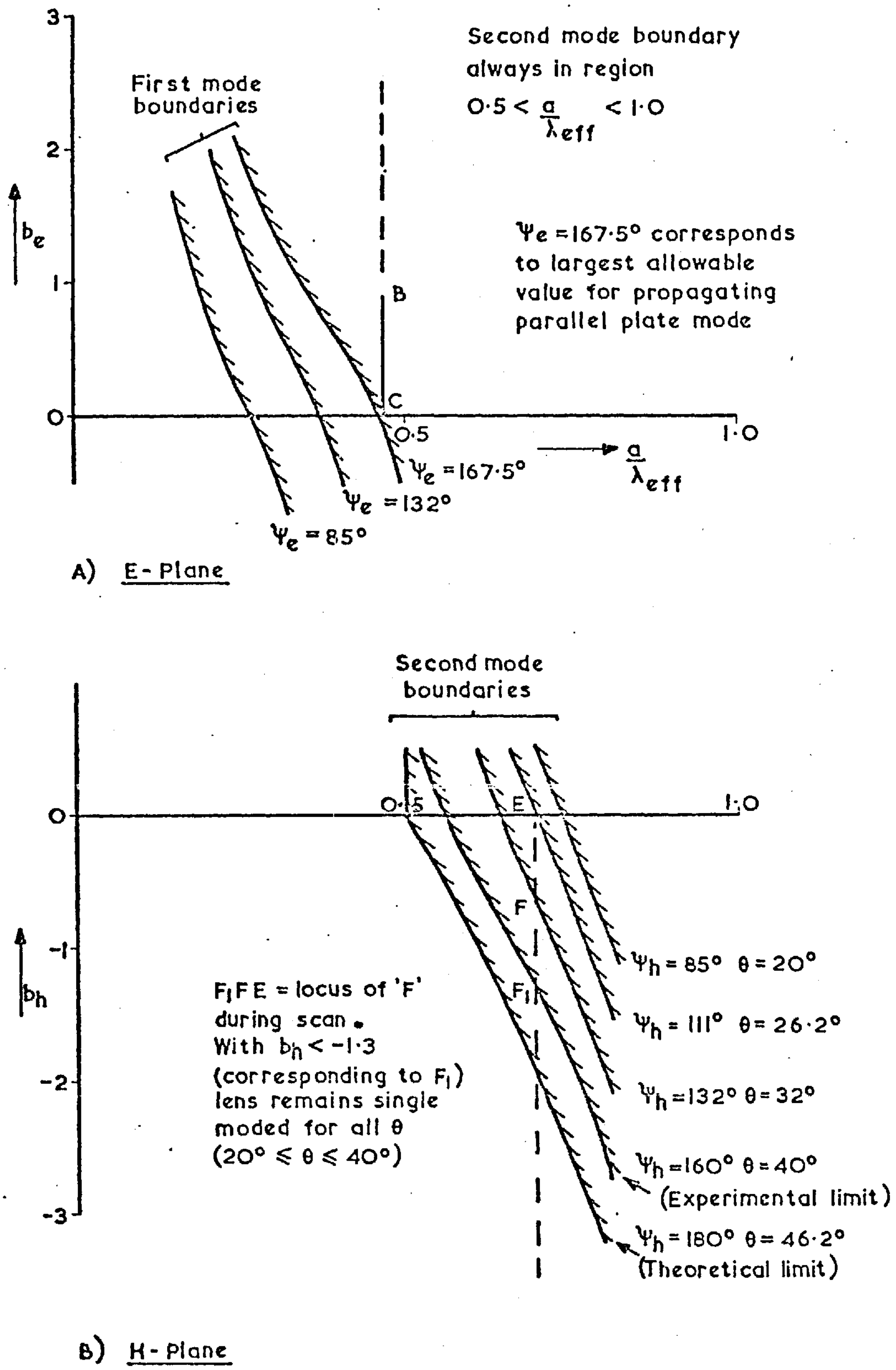

Fig. 3.36 Locus of the significant mode boundaries during scan

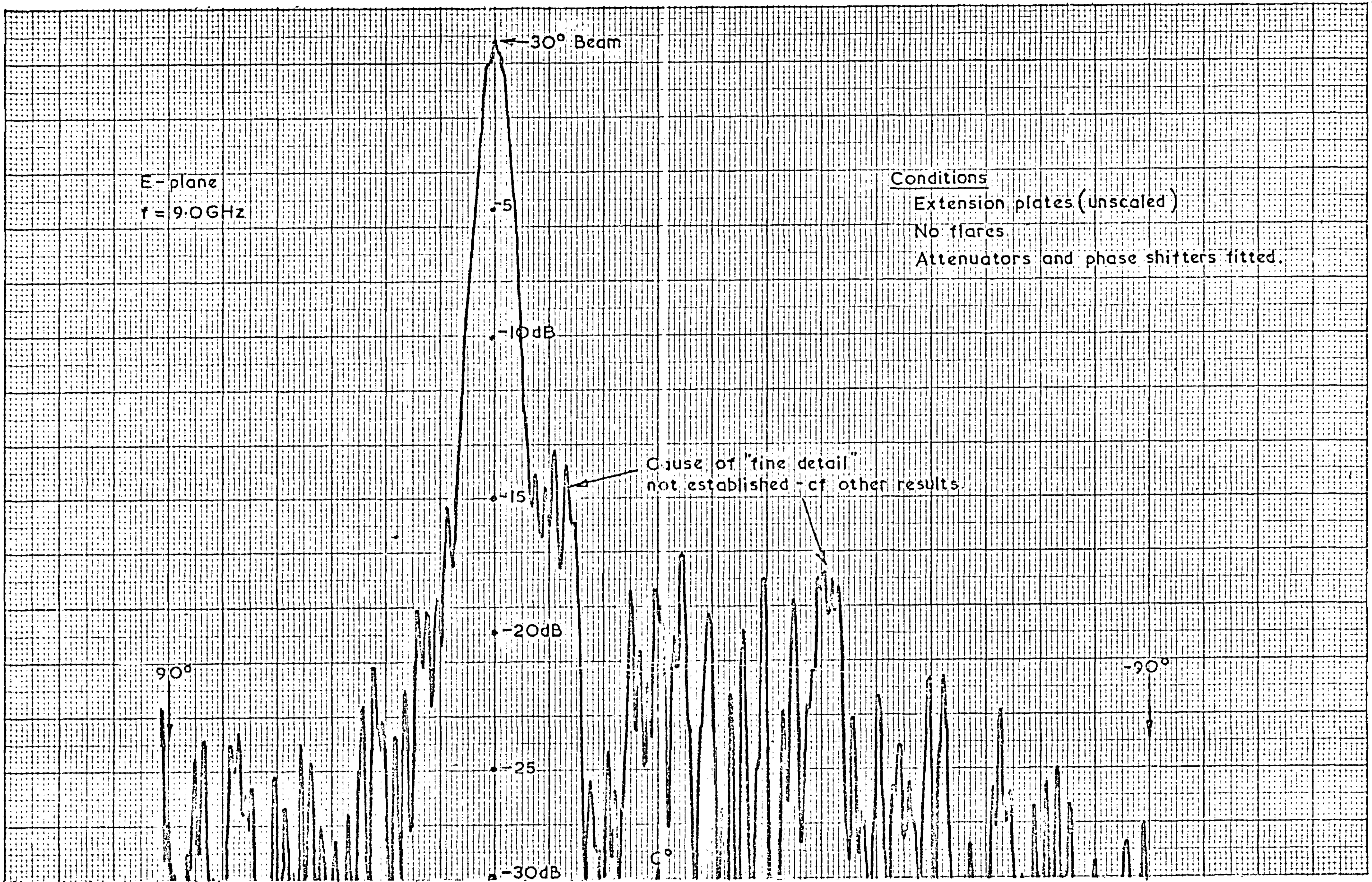

Fig. 3.37 Measured E-plane pattern for array with reactive element boundaries (30° main beam)

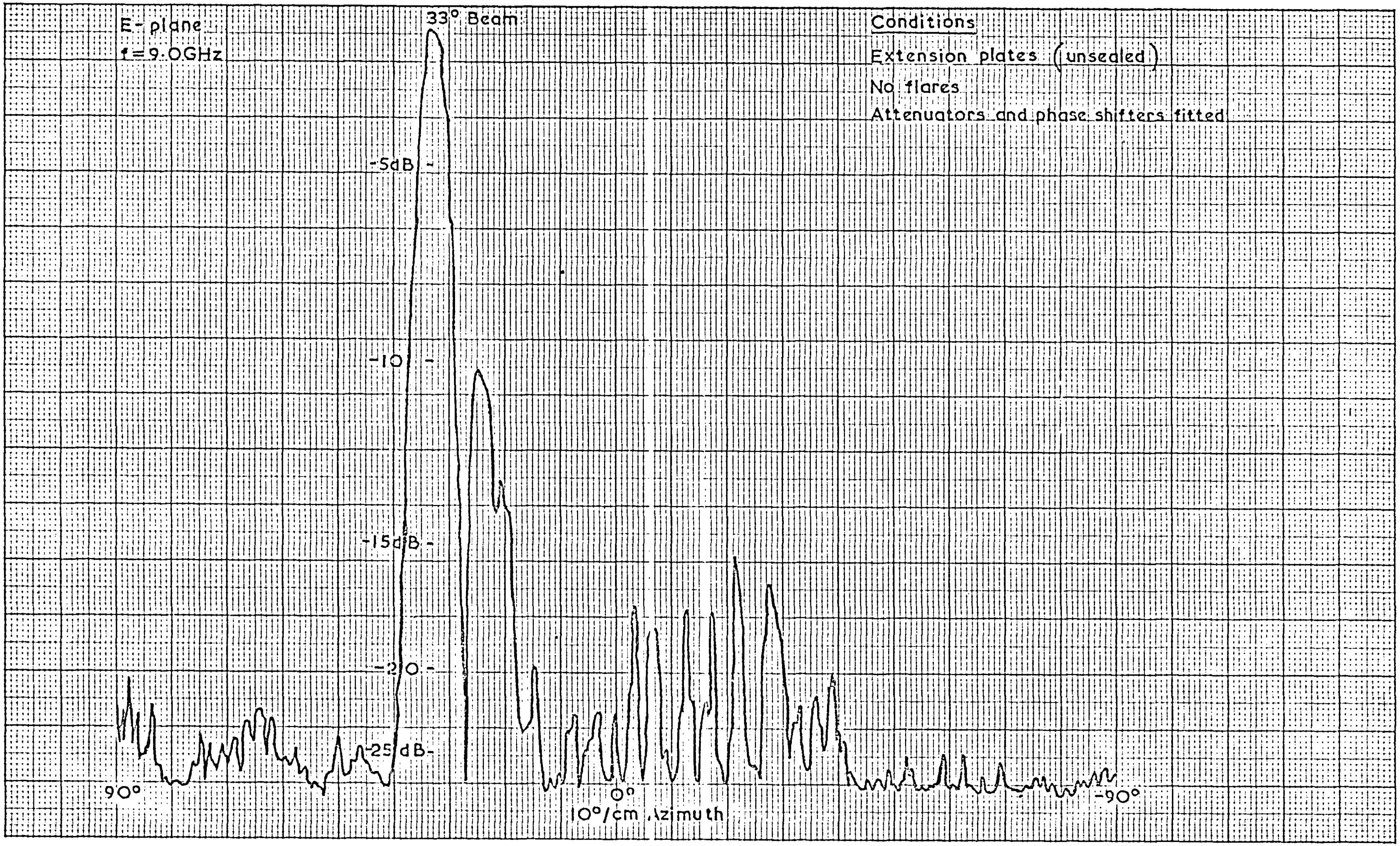

Fig. 3.38 Measured E-plane pattern for array with reactive element boundaries (33^o main beam)

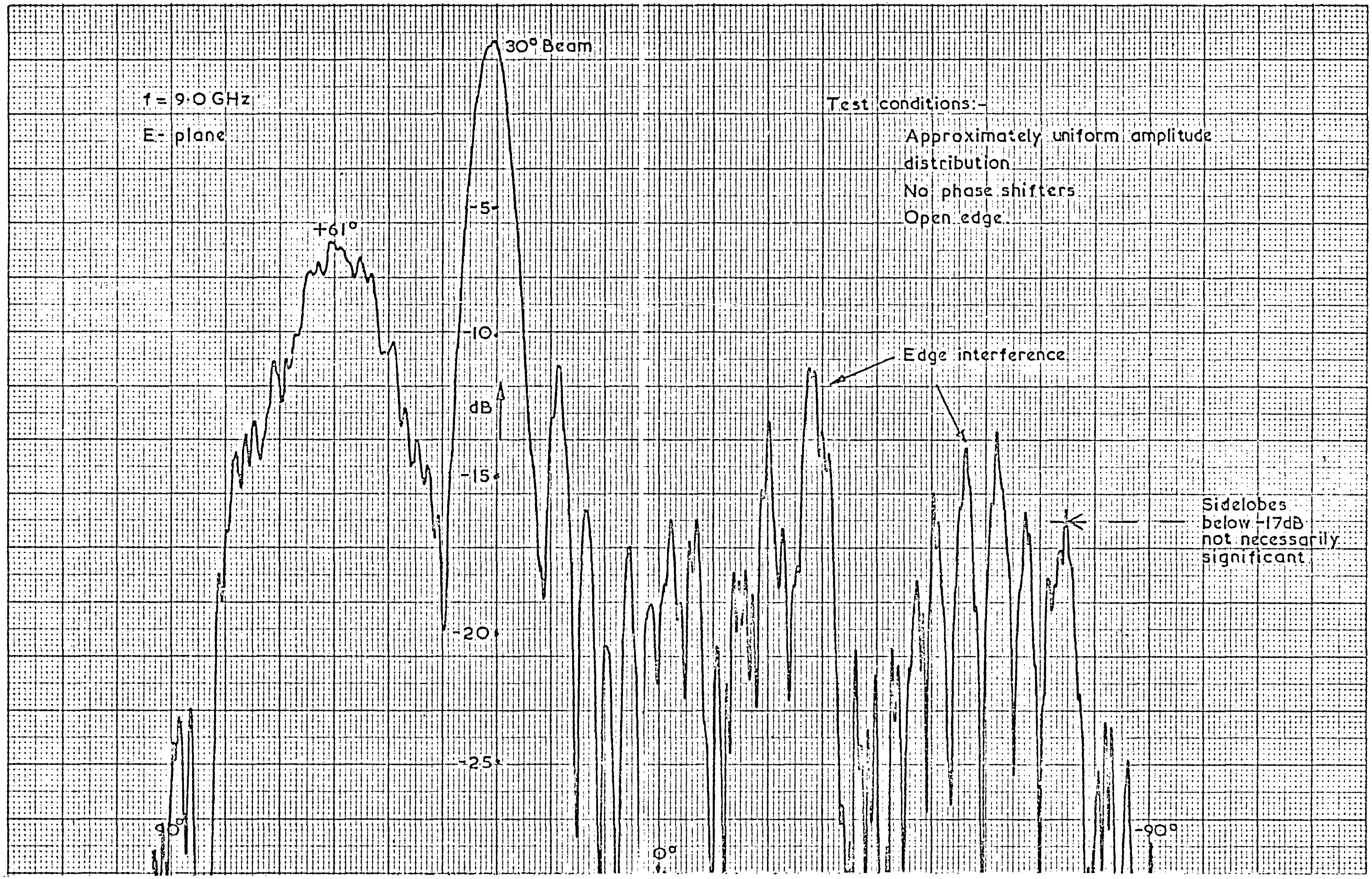

Fig.3.39 E-plane array pattern with uncompensated edge effects

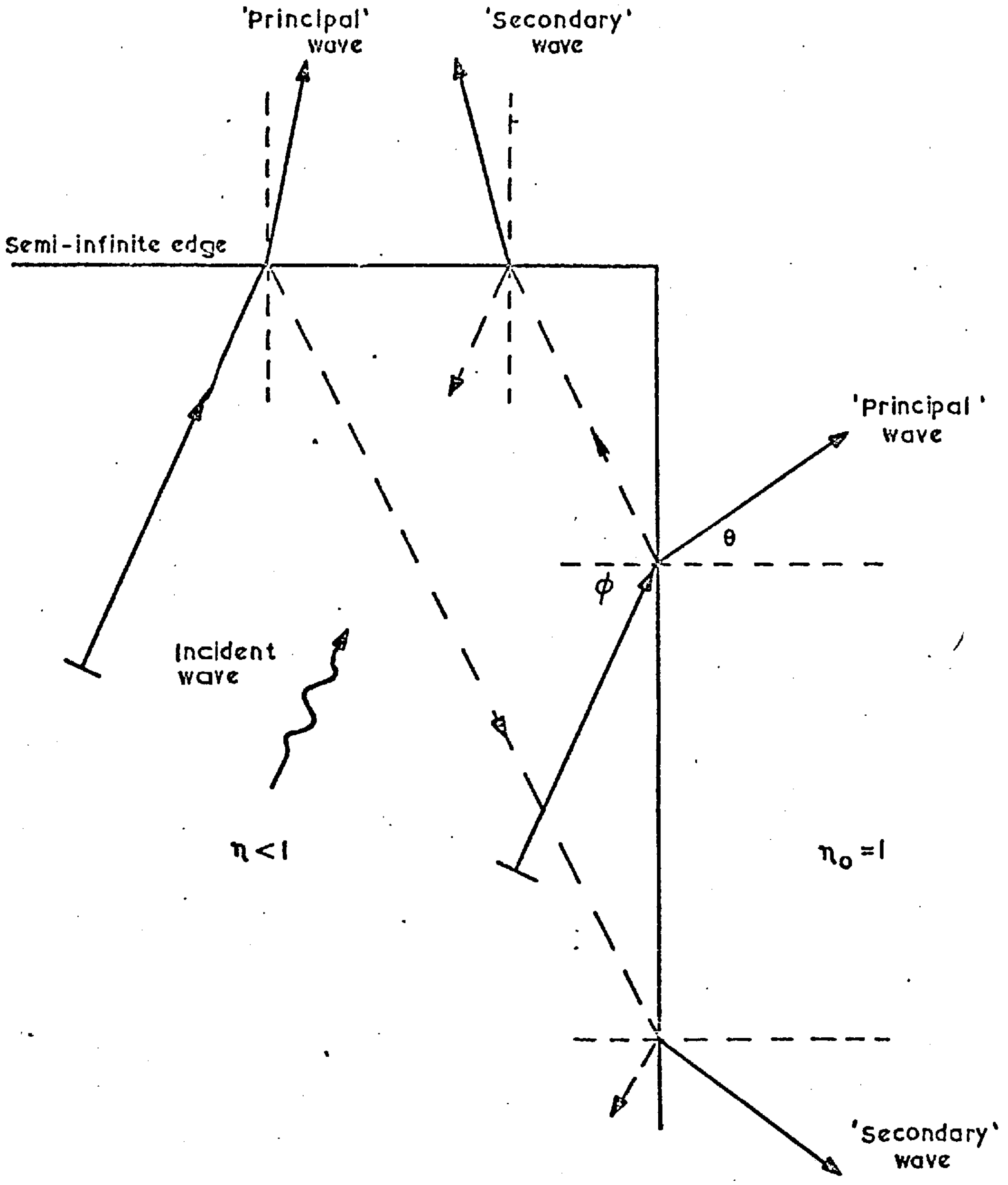

Fig. 3.40 Model for interpreting E-plane edge effects

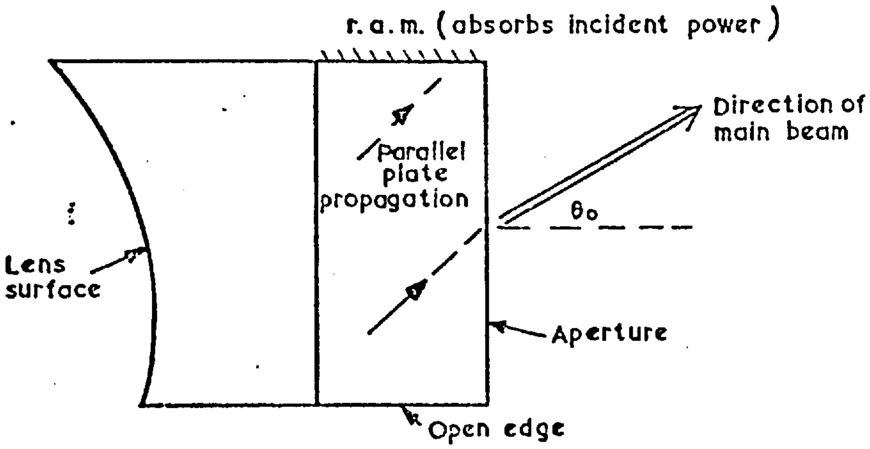

Fig. 3.41 Schematic showing position of r.a.m. to reduce pattern degradation

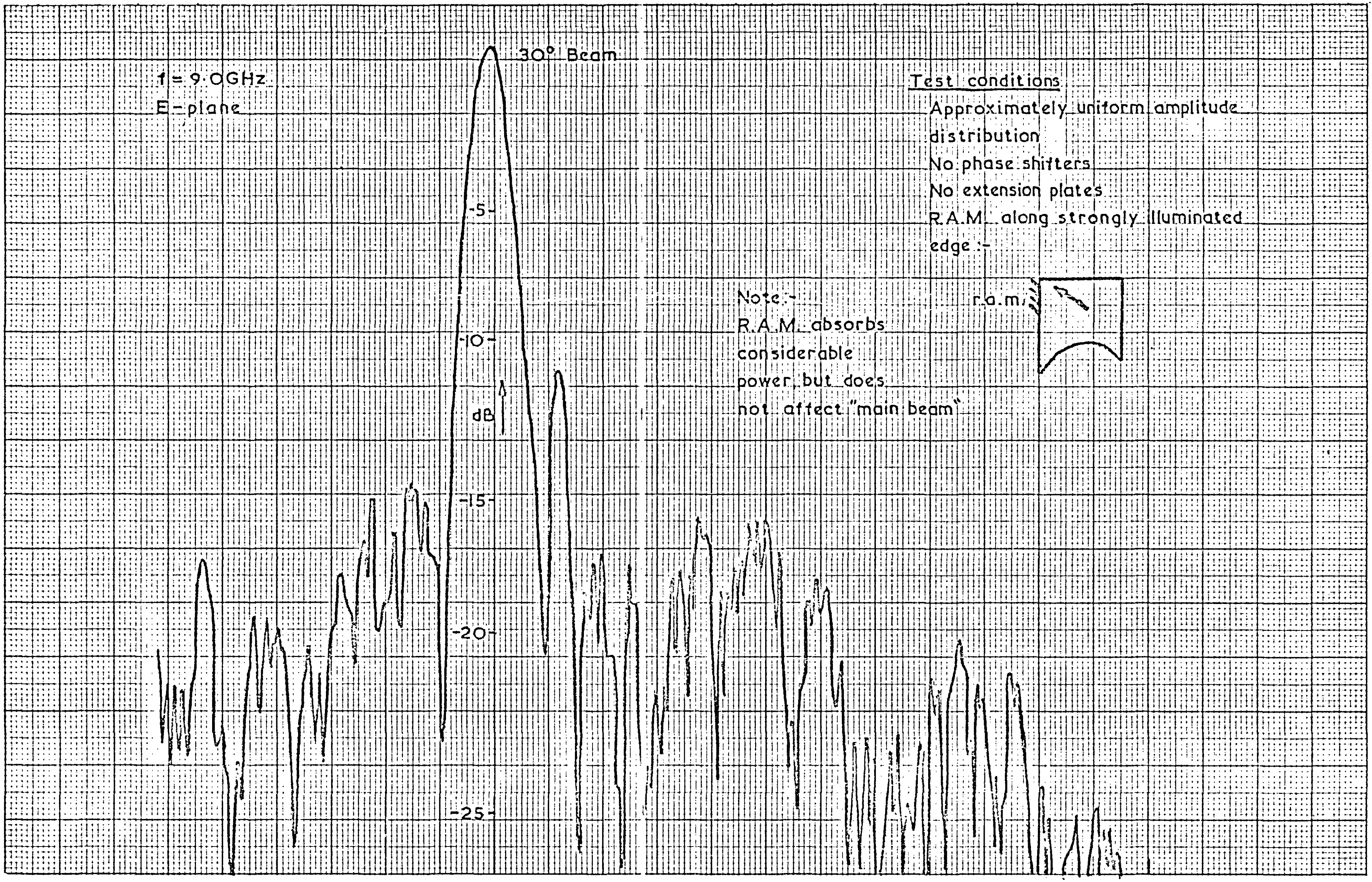

Fig.3.42 E-plane pattern, showing suppression of edge effects with r.a.m.

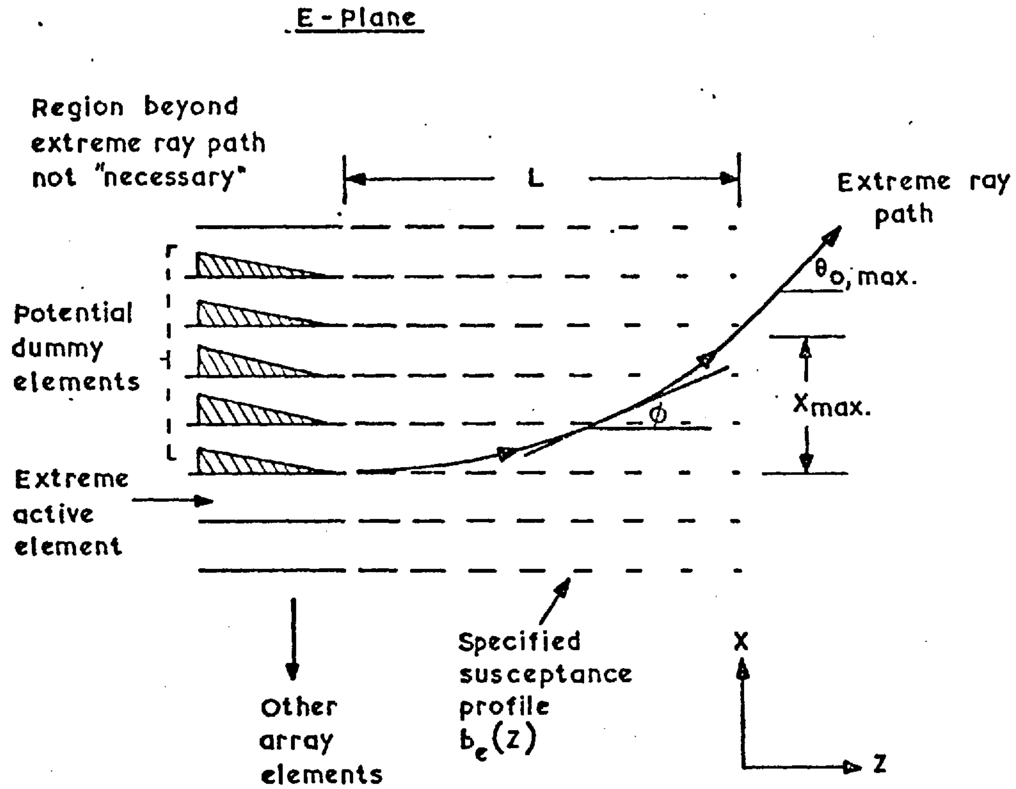

Fig. 3.43 Model for minimum number of dummy elements

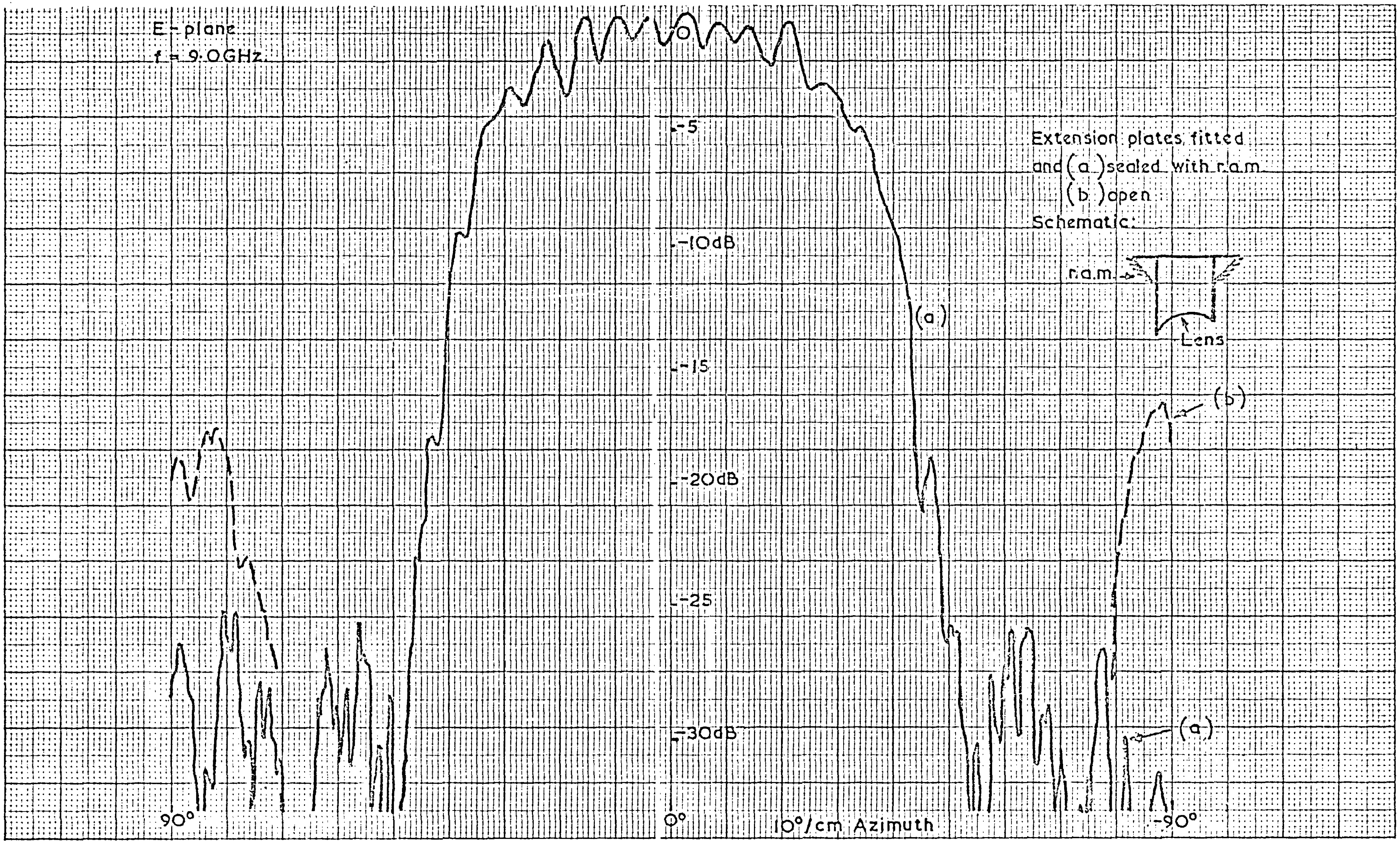

Fig. 3.44 E-plane centre element pattern for reactive boundary array

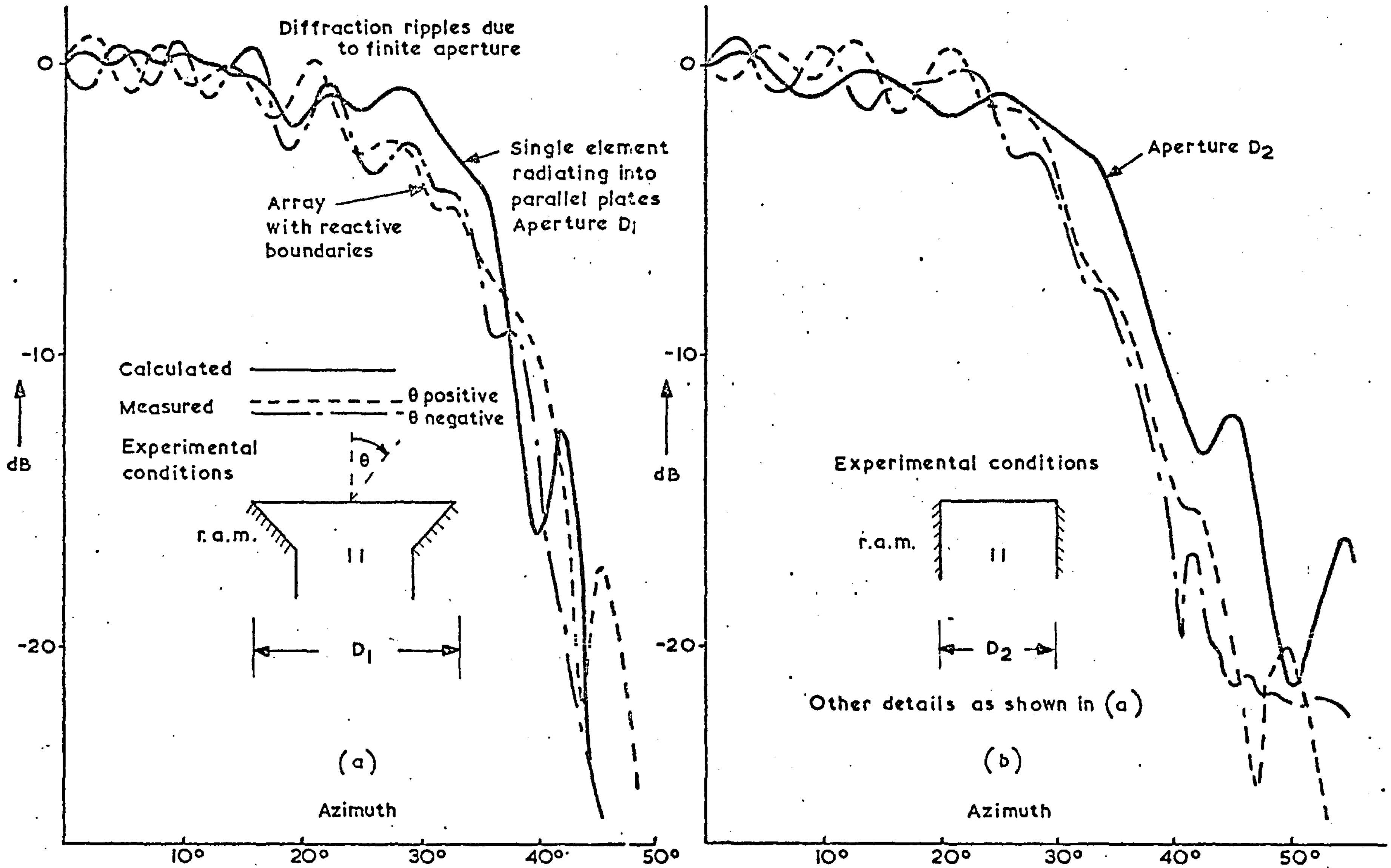

Fig.3.45 Comparison of centre element patterns with calculated patterns for dimensionally equivalent parallel-plate structures.

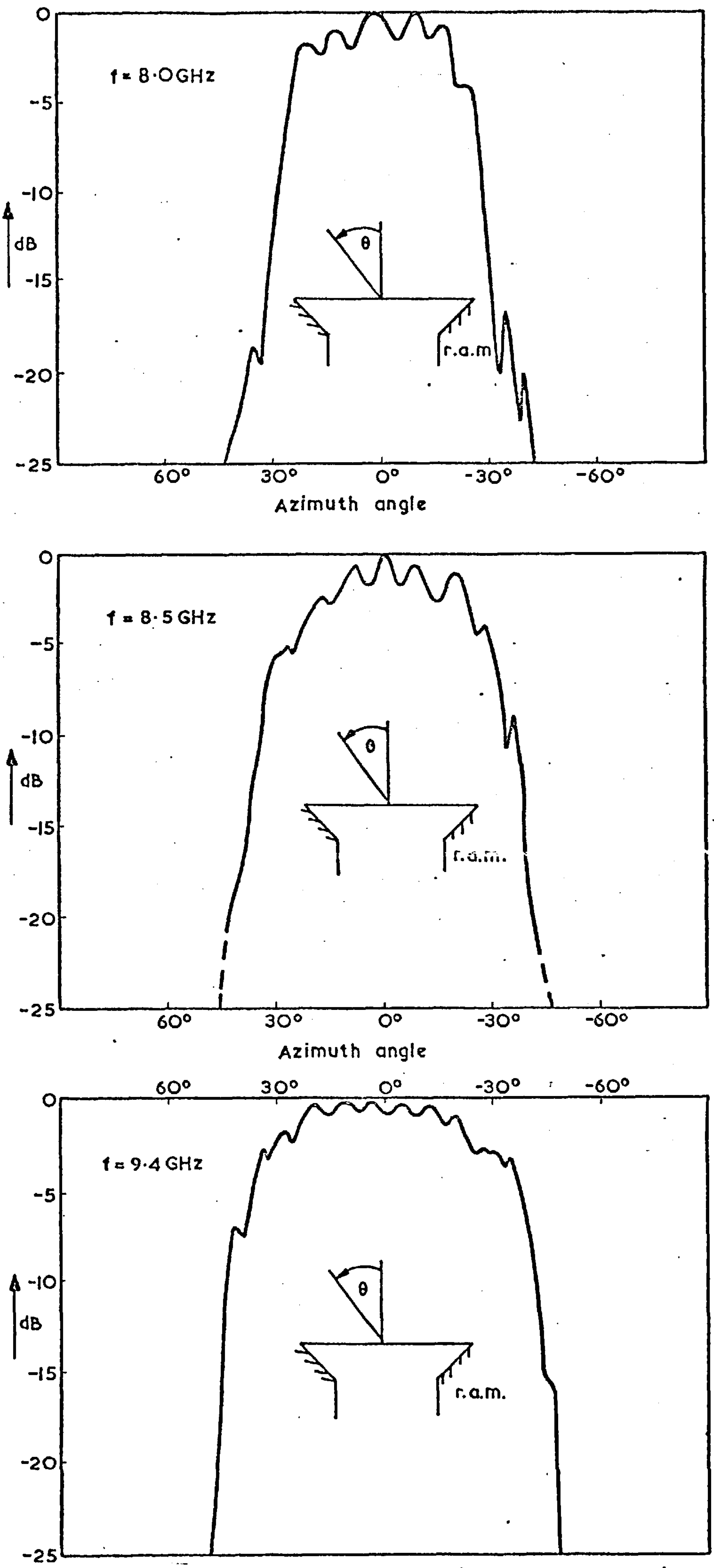

Fig.3.46 Measured centre element patterns at different frequencies

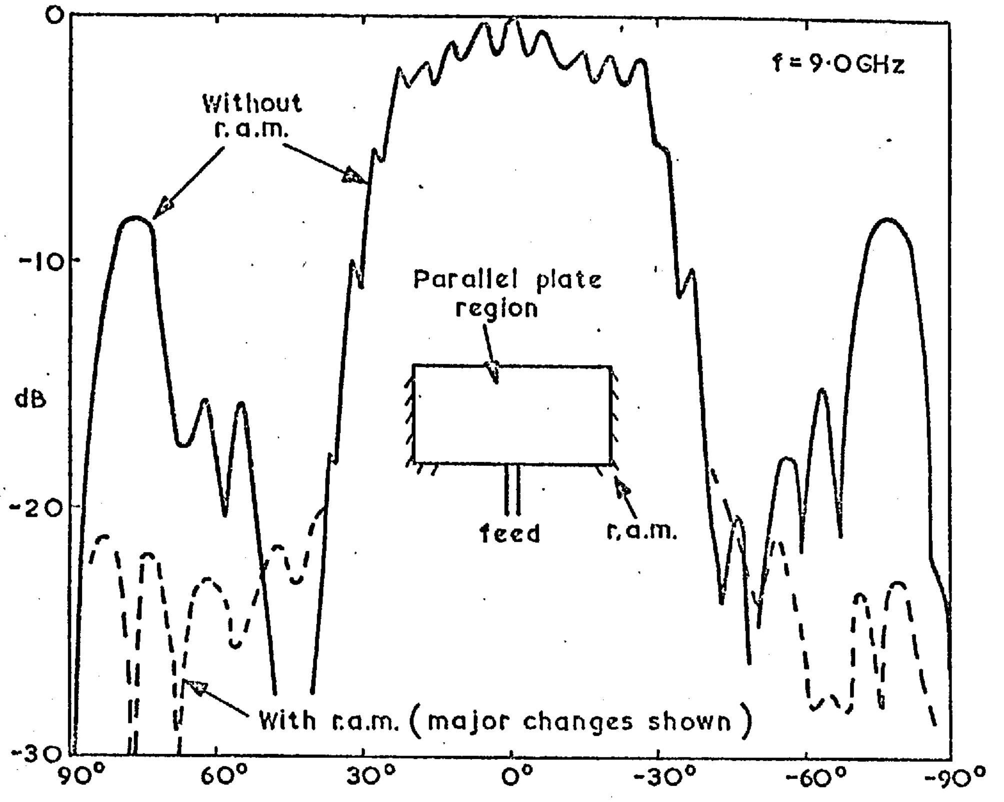

Fig. 3.47 E-plane edge effects in parallel plate structure

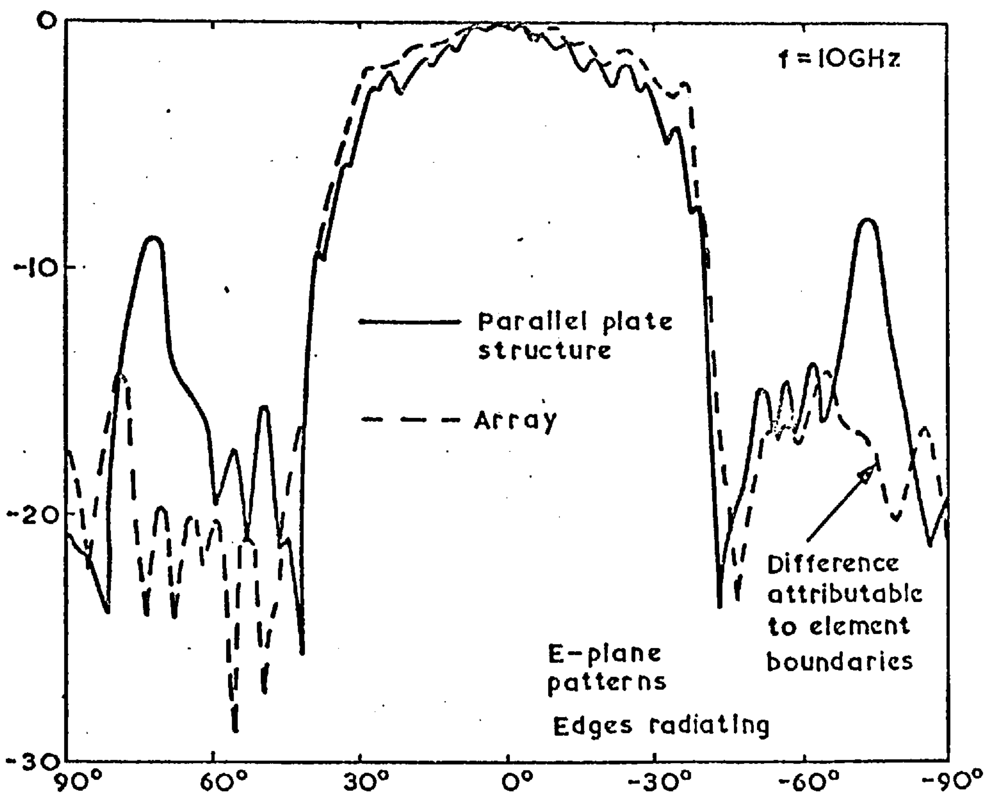

Fig.3.48 Comparison of edge radiation

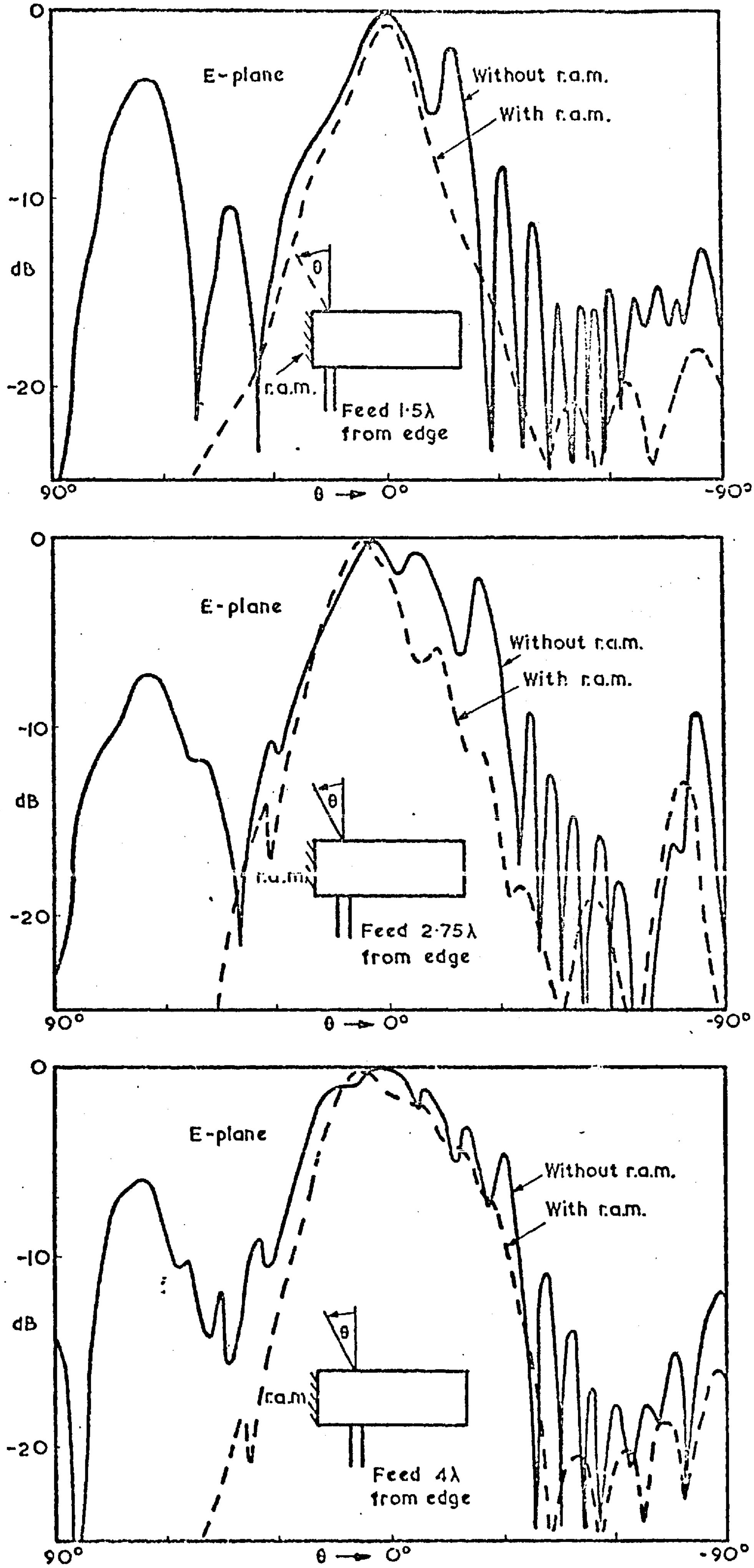

<u>Fig. 3.49</u> Edge element patterns with and without r.a.m. (Parallel plate dimensions = 15λ x 6λ x 0.67λ).

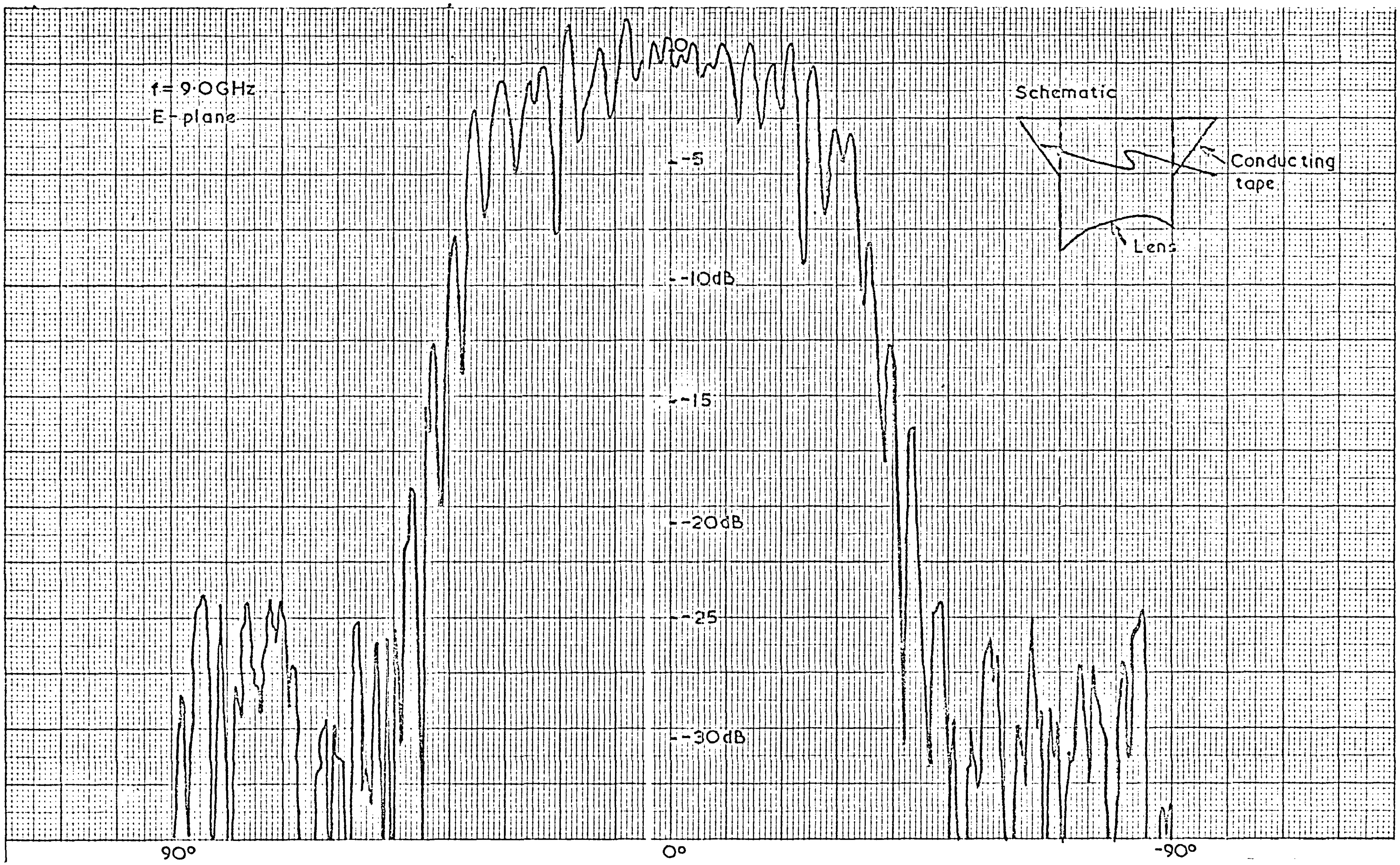

Fig. 3.50 Element pattern perturbed by resonance effects with edges sealed by conducting tape.

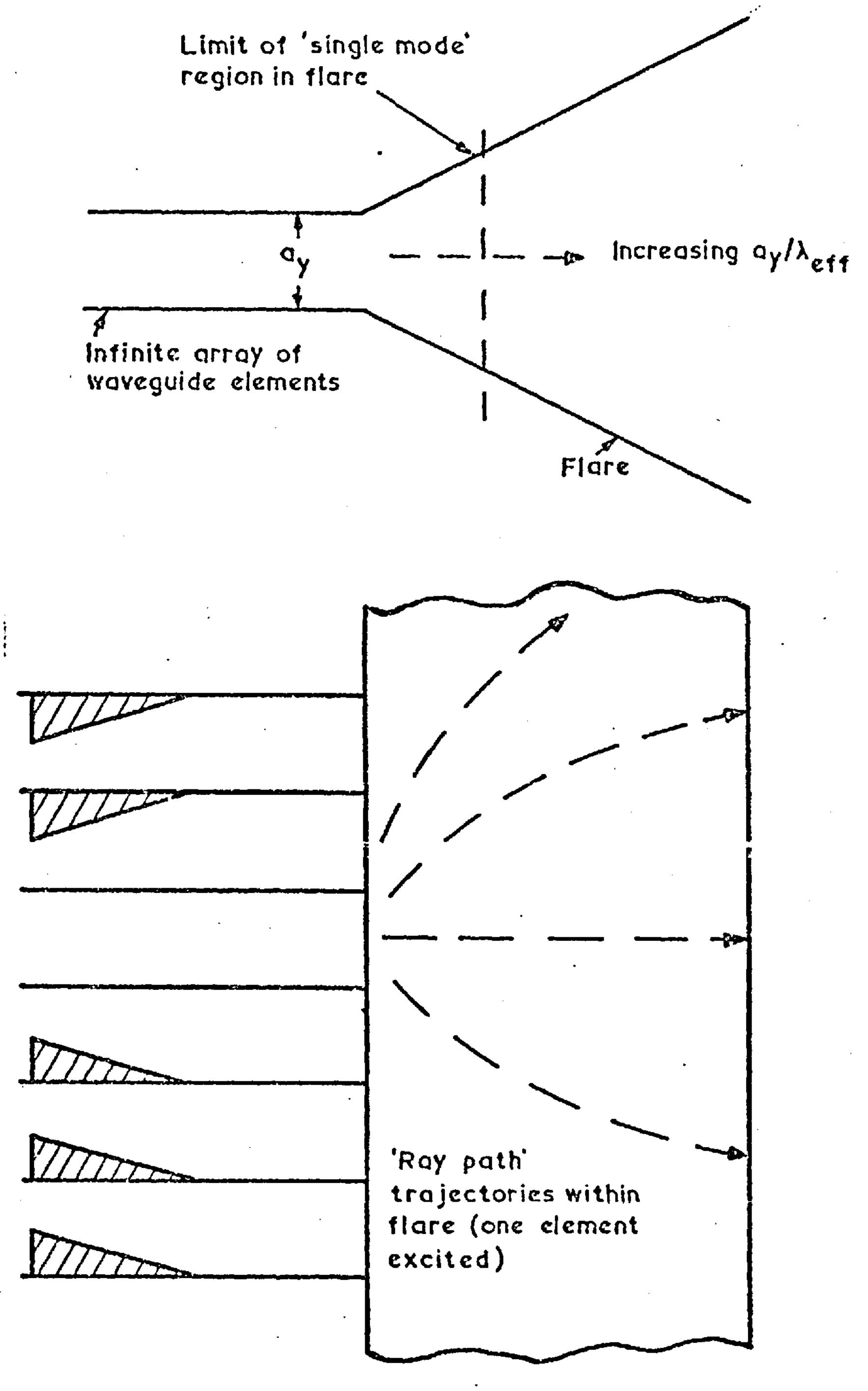

Fig. 3.51 Interpretation of flare action - with reference to grating wave suppression and edge effects.

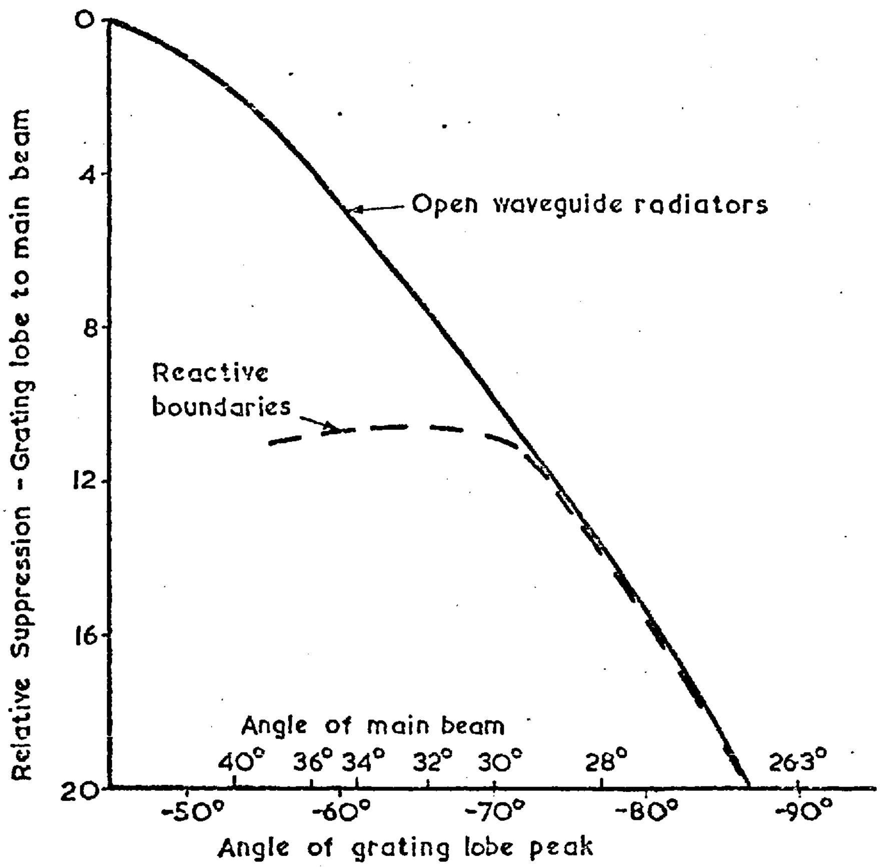

Fig. 3.52 Grating lobe suppression in H-plane for initial reactive boundaries

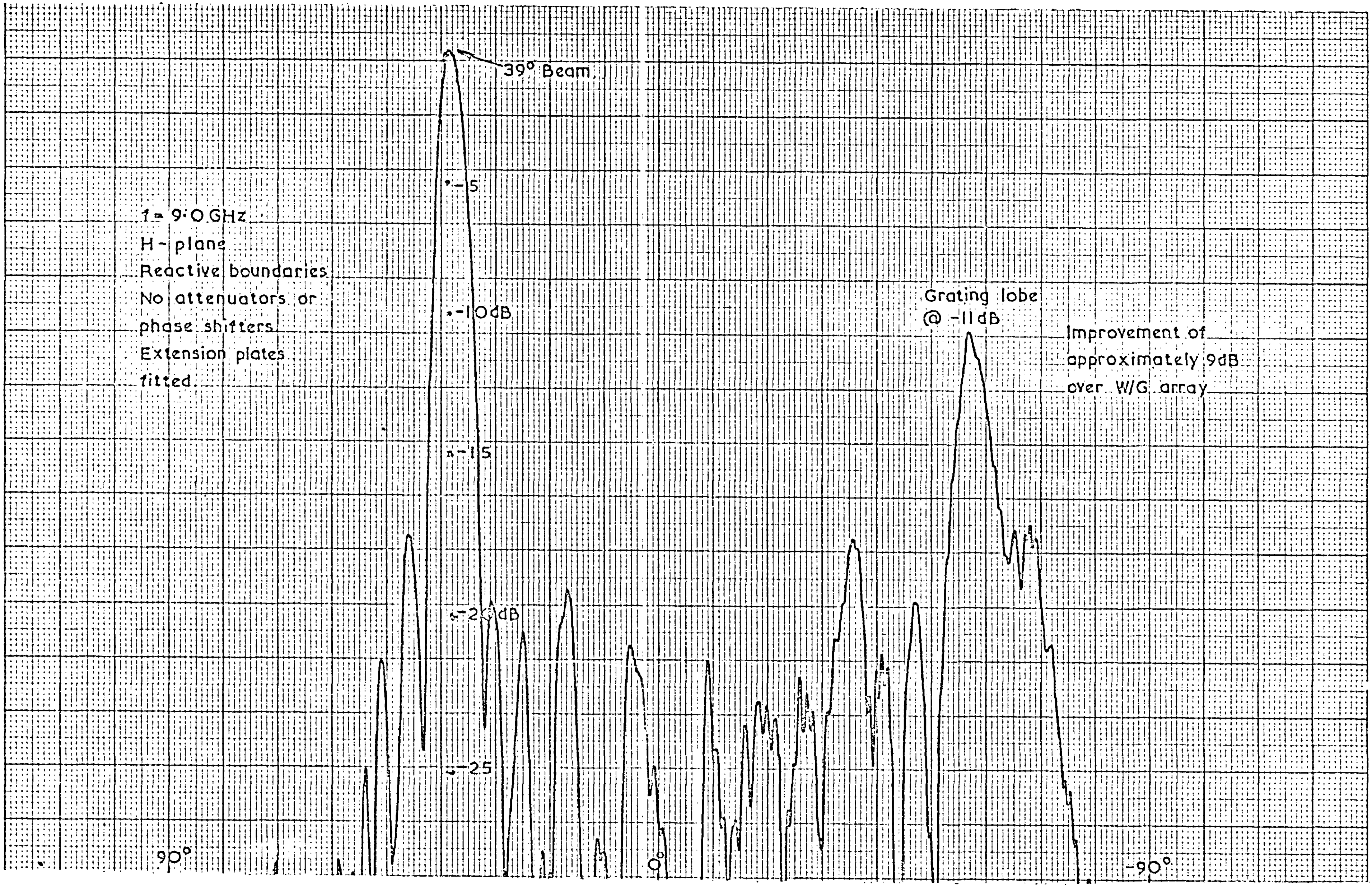

Fig.3.53 H-plane array pattern - reactive boundaries between elements.

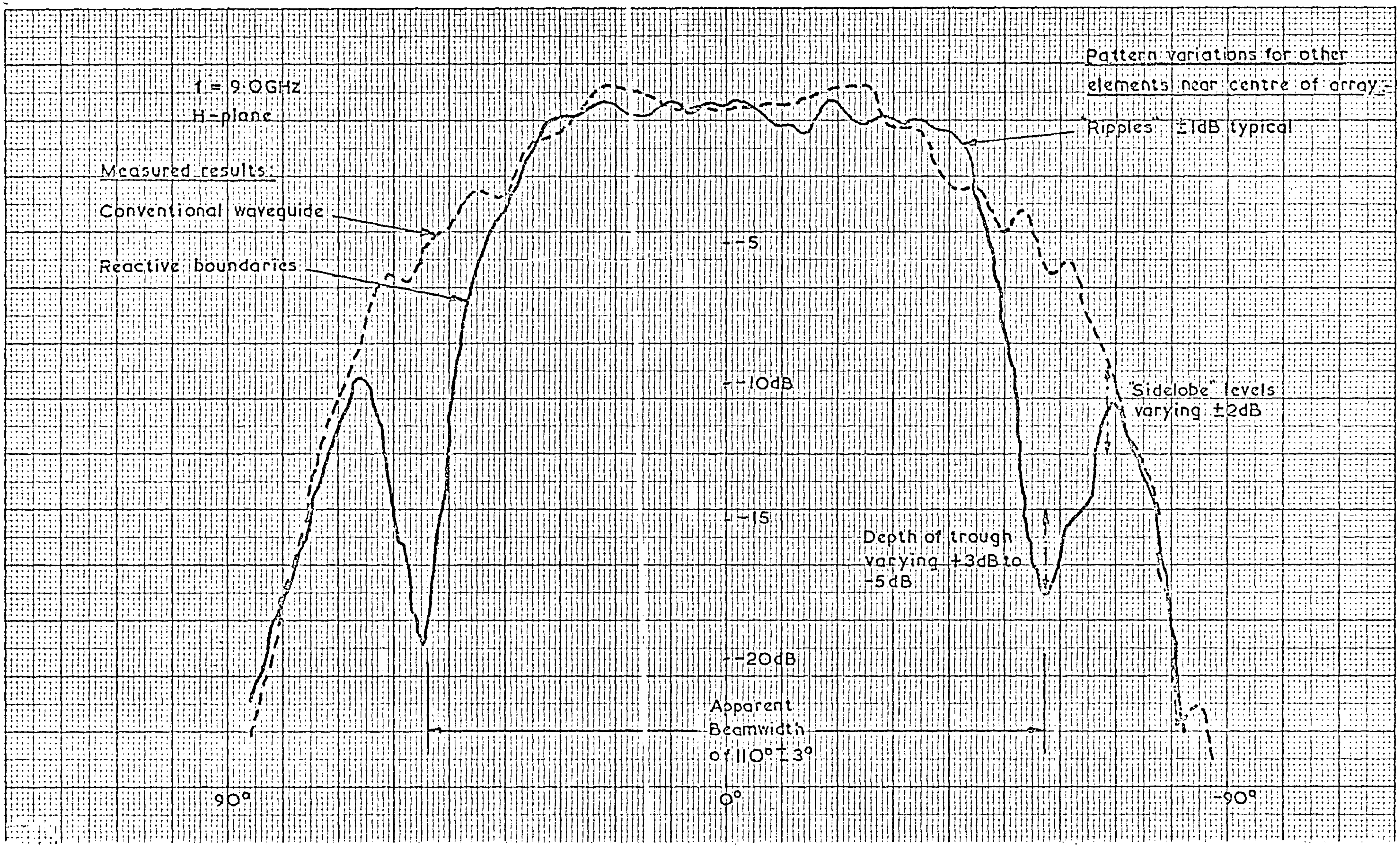

Fig. 3.54 Typical H-plane "centre" element pattern with reactive boundaries. (Result in Fig. 3.29 superimposed)

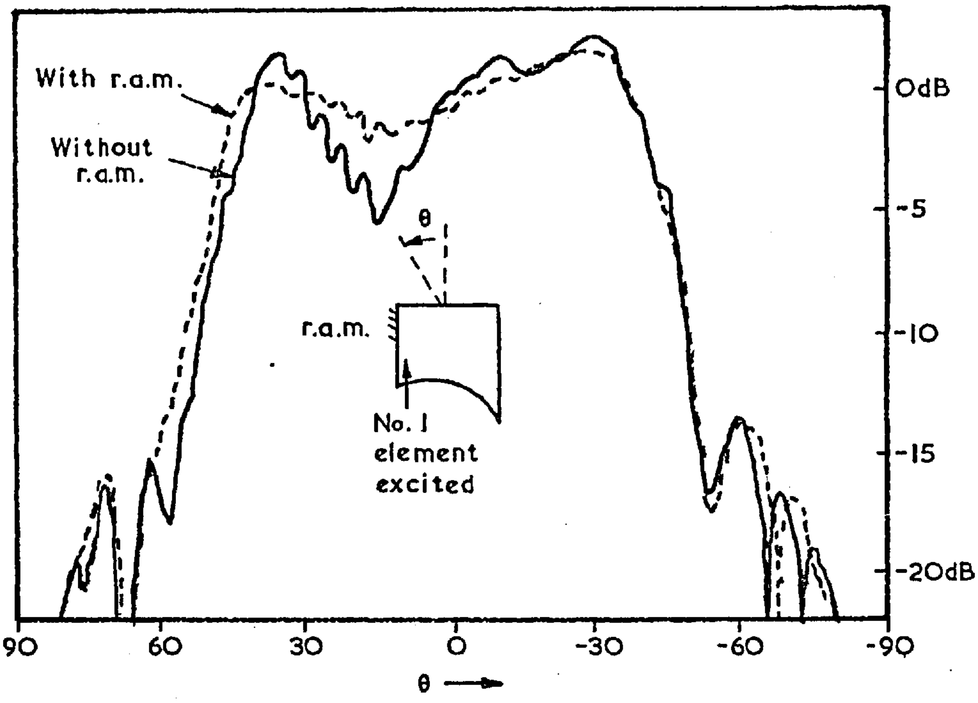

Fig. 3.55 H-plane patterns for the edge element with and without r.a.m. sealing the open edge - lens fitted with reactive boundaries

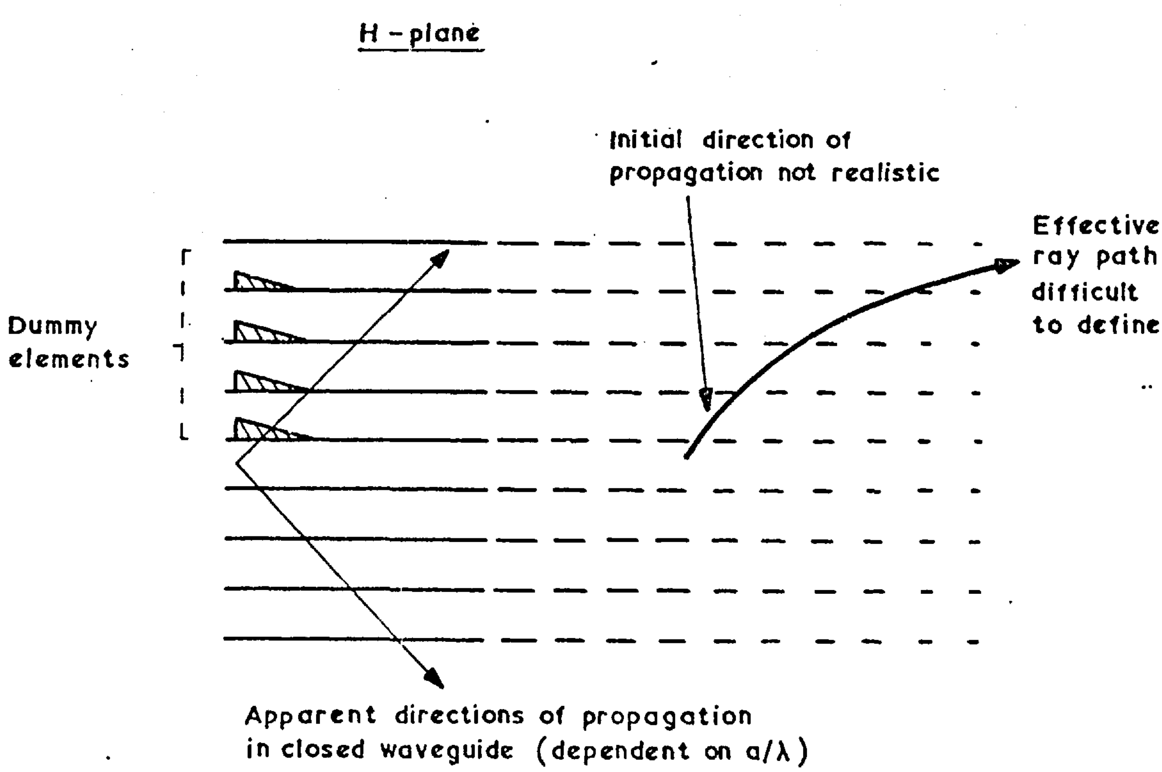

Fig. 3.56 Ray path anomaly in H-plane where $-b_h \Rightarrow \infty$

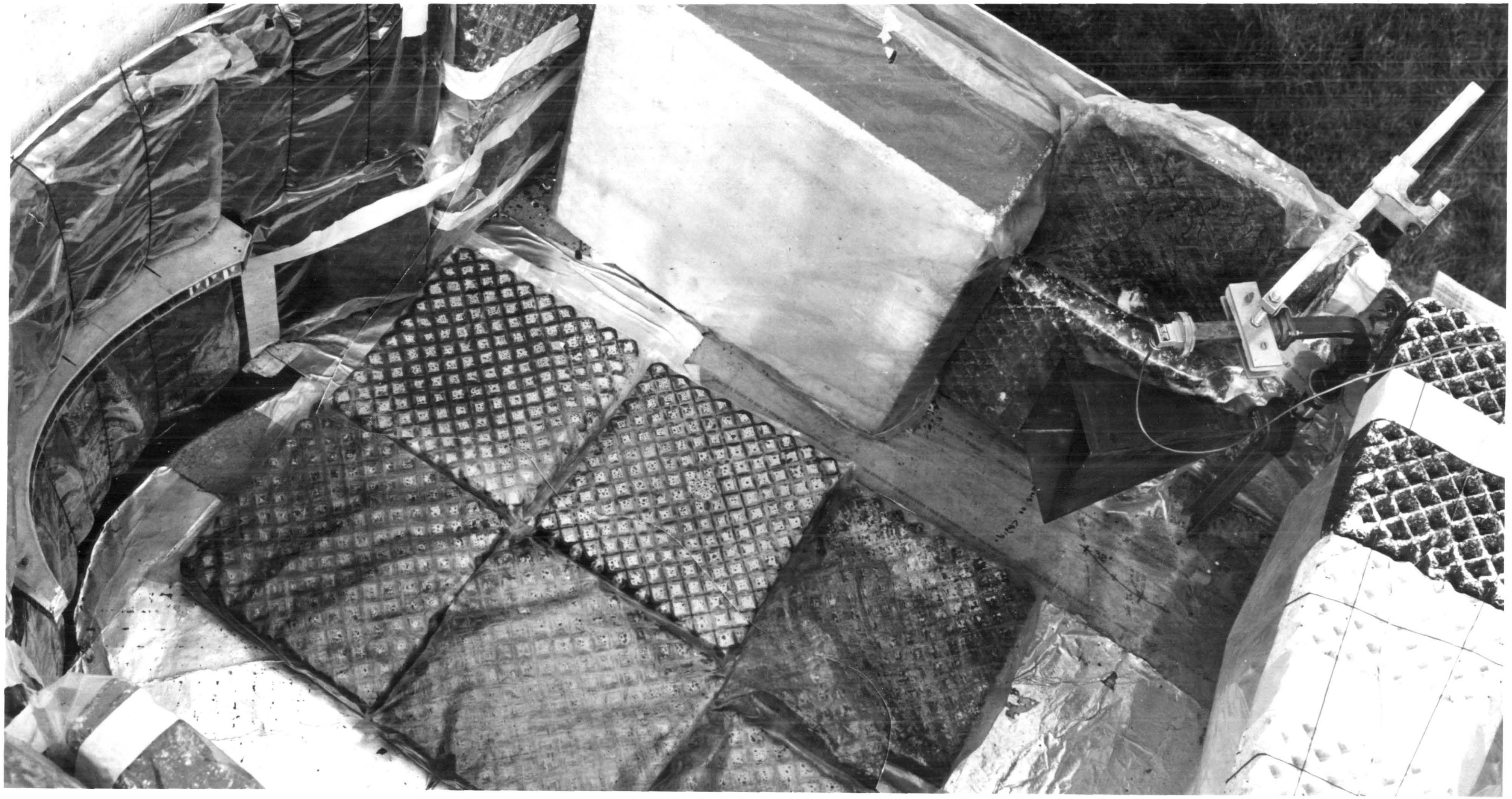

Fig.3.A1 R.F. sealed enclosure, showing disposition of lens, feed horn and "free space" blocks.

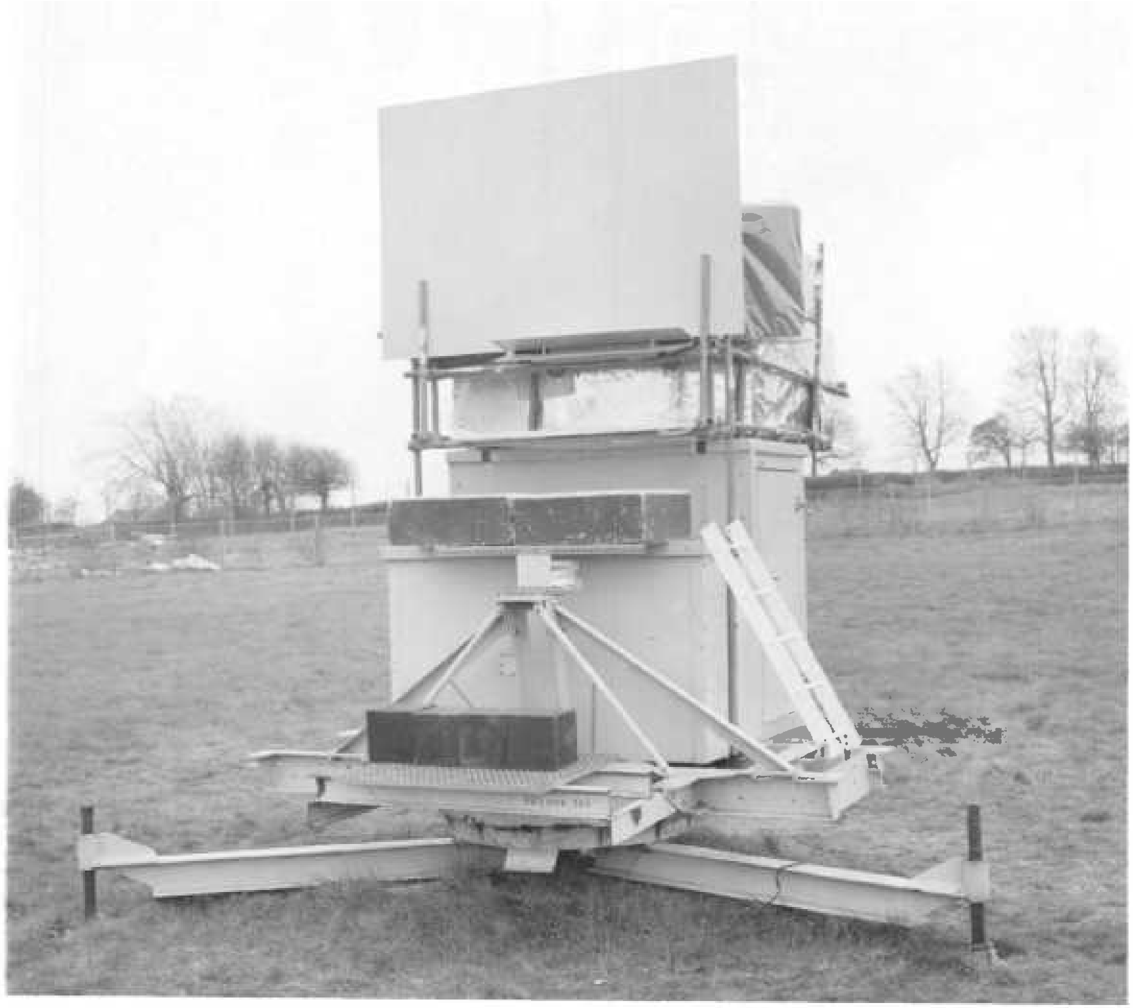

Fig.3.A2 View of lens and feed enclosure mounted on receiver cabin

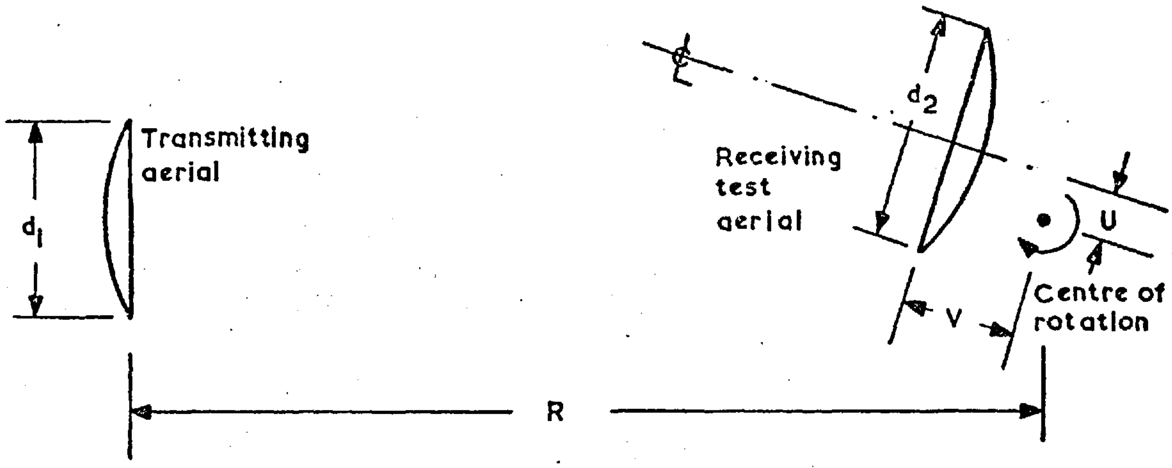

In the experimental system

$d_1 = 0{\cdot}9\,m$ $\quad$ $U = 0{\cdot}12m$

$d_2 = 0{\cdot}46m$ $\quad$ $V = 0{\cdot}1m$ (max.)

For $\lambda = 0{\cdot}033m$ $\quad$ $R_{min.} \Rightarrow 75m$

Fig. 3.A3 Aerial test site geometry (plan view)

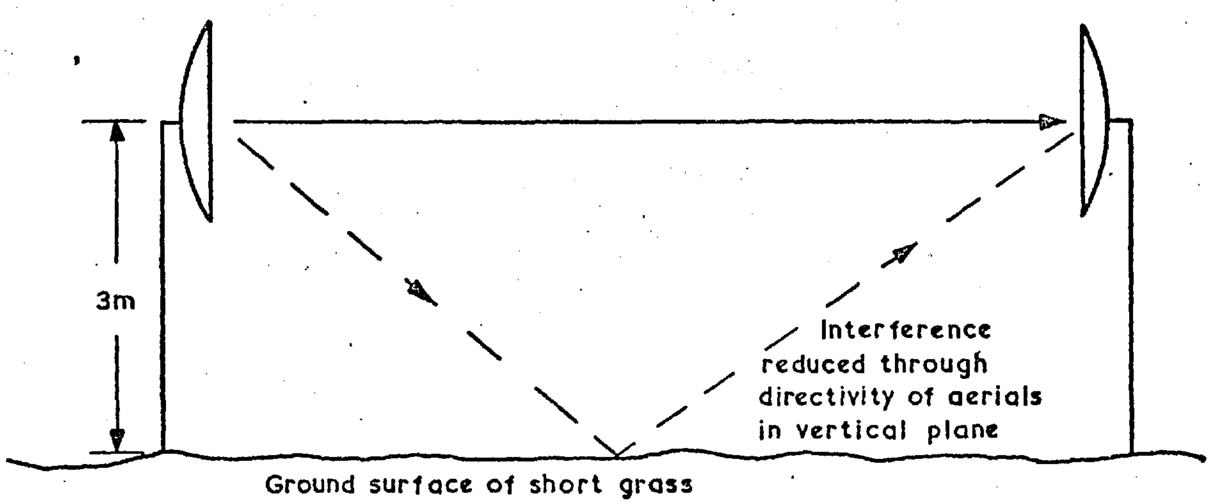

Fig. 3.A4 Aerial test site geometry (elevation view)

CHAPTER 4

CHARACTERISATION OF AN AXIAL SUSCEPTANCE DISCONTINUITY IN INFINITE ARRAY STRUCTURES

4.1. Introduction

In this chapter, the network properties of an infinite array structure with an axial susceptance discontinuity are derived. The analysis is an extension of Sections 2.2 and 2.5, in which the modes of propagation in a region with constant susceptance boundaries were defined. The same assumptions given in Section 2.1 are invoked, except of course for the presence of a line discontinuity in boundary susceptance. The unit cell geometry for either polarisation (i.e. E- or H- plane scan) is shown in Fig.4.1, with the axial co-ordinate (z) set to zero in the plane of the discontinuity. An exact solution of the boundary value problem defined by Fig.4.1 is obtained in the following sections, and expressed in the standard matrix form

$$[\underset{\sim}{b}] = [\underset{\sim}{S}]\ [\underset{\sim}{a}] \qquad \text{.... (1)}$$

where $[\underset{\sim}{a}]$ and $[\underset{\sim}{b}]$ characterise respectively the incident and reflected fields associated with each of the propagating nodes in the two regions $z < 0$ and $z > 0$;

and $[\underset{\sim}{S}]$ defines, in amplitude and phase, the reflection and transmission properties of the discontinuity.

Based on previous analyses and the intended application, (i.e. in array transitions with step discontinuities in susceptance), the following constraints can be placed on the parameters:

(i) The boundary susceptance is restricted to inductive values in the H-plane and capacitive values in the E-plane.

(ii) The magnitude of the susceptance is assumed larger in the region $z < 0$, corresponding to a discontinuity which, in the limit, becomes the aperture between a waveguide array and free space.

(iii) In the E-plane, it suffices to assume values of $a/\lambda < 0.5$ (cf.

(iii) contd.... Section 2.5.1). This ensures that only one propagating mode can exist either side of $z = 0$, and $[\underset{\sim}{a}]$ and $[\underset{\sim}{b}]$ become column matrices having two terms only.

(iv) In the H-plane, an element spacing in the range $0.5 < a/\lambda < 1.0$ is assumed. Consequently, at least one, and not more than two modes, can exist in either region. Three separate possibilities must be considered, corresponding to the potential number of dual moded regions (i.e. 0, 1, or 2).

In a cascade network with a series of discontinuities spaced less than a wavelength apart, it is also necessary to consider the effect of evanescent modes which are just cut-off. This involves an increase in the order of the scattering matrix. To illustrate this, one of the additional terms is calculated in Section 4.4.

The Wiener-Hopf technique is used throughout this chapter. This technique was originally applied by Carlson and Heins (70) to determine the properties of an interface between free space and an infinite array of uniformly-spaced parallel plates of infinitesimal thickness. Since that time, numerous problems in electromagnetic wave theory (and acoustics) have been solved using integral transform and analytic function theory. Many of these problems are described by Noble in a standard reference on Wiener-Hopf technique (90), which is also described or used in more recent engineering texts (94, 95, 96).

The boundary value problem represented by Fig.4.1 can be regarded as a generalisation of the problem considered by Carlson and Heins, and is idealy suited to analysis by the Wiener-Hopf technique. However, other methods of analysis could be applied, including the field matching technique first described by Berz (97), extended by Wu and Galindo (43) and now used as the basis of multi-mode techniques described in Section 1.2.4. In relation to Fig.4.1, this method requires the infinite series of eigenfunction fields in the regions $z < 0$ and $z > 0$ to be matched in the plane $z = 0$ with the incident mode specified (94). Using analytic function theory, exact solutions can be obtained in specific cases (e.g. 97, 43). By contrast with the normal restrictions on the Wiener-Hopf technique, this method can still be used to obtain approximate solutions (e.g. 81) when the unit cell dimensions either side of the discontinuity cannot be represented as an infinitely thin contour or edge. (Approximate methods for extending the Wiener-Hopf technique are discussed by Noble in Chapter 5 of reference 90.)

Where amplitude information will suffice, the problems considered in this chapter can also be analysed using momentum and energy conservation principles (98). The technique, which extends an earlier publication by Brown on the electromagnetic momentum concept applied to general "waveguide" discontinuities (99), yields numerical answers with considerably less analysis, and affords an independent check on the magnitude of terms in $[\underset{\sim}{S}]$ (eqn.(1)).

4.2. H-plane Wiener-Hopf Analysis

4.2.1. Preliminary Definitions

As an initial problem, consider an infinite array structure (with unit cell as shown in Fig.4.1) excited periodically by the incident H-plane mode (ϕ_{inc}) with remote sources at $z = -\infty$. The general solution in this unit cell of the array (where $-a/2 < x < a/2$) can then be written in the form:-

Total field = Incident field + Scattered field; i.e.

$$\phi(x,z) = \phi_{inc} + \int_{-\infty}^{\infty} dw.\ \exp(-jwz)\left[A(w)\exp(-jx\sqrt{k^2-w^2}) + B(w)\exp(jx\sqrt{k^2-w^2})\right] \quad \ldots. (2)$$

where the scattered field (ϕ_s) is expressed as an angular spectrum of plane waves in terms of the complex variable w. The Fourier integral given in eqn.(2) is defined if the portion of the integrand between square brackets is analytic in a strip about the real axis and tends to zero uniformly as $|\mathrm{Re}\ w| \to \infty$ (100). As a temporary expedient to ensure this condition, the standard assumption is made that the wavenumber k is complex, i.e.

$$k = k_1 - jk_2 \qquad .... (3)$$

where k_1 and k_2 are both positive real, and k_2 is small and can be set to zero at a later stage. In subsequent work, no complication arises through branch cuts associated with the isolated multi-valued function $(k^2-w^2)^{\frac{1}{2}}$, and the only branch of interest is defined by $\sqrt{k^2-w^2} = +k$ when $w = 0$ (see Fig.4.2a).

The functions A(w) and B(w) in eqn.(2) are unknown, while the incident field can be written as

$$\phi_{inc} = \left[\vec{A}_{1,n}\exp(-jx\sqrt{k^2-\beta^2_{1,n}}) + \vec{B}_{1,n}\exp(jx\sqrt{k^2-\beta^2_{1,n}})\right]\exp(-j\beta_{1,n}z) \qquad .... (4)$$

where the first and second subscripts specify the mode and the number of the reactive boundary region respectively;

the arrows indicate the axial (or z) direction of propagation,

and $\sqrt{k^2-\beta^2_{1,n}}$ is real, lies in the range $0 < a\sqrt{k^2-\beta^2_{1,n}} \leq \pi$, and satisfies the characteristic equation

$$K_{h,n}\frac{\sin(k_x a)}{k_x a} + \cos(k_x a) - \cos\psi_h = 0 \;\; (k_x=\sqrt{k^2-\beta^2_{1,n}}) \qquad .... (5a)$$

where $K_{h,n} = \pi.(a/\lambda).\,(-b_{h,n})$ .... (5b)

and $b_{h,n}$ is the boundary susceptance of the "n"th region (cf. Section 2.2). If the (complex) relation

$$k_x = \sqrt{k^2-w^2} \qquad .... (6)$$

is temporarily assumed for the branch defined above, then all points in the w plane are mapped by the region Re $k_x > 0$ with the branch cut chosen as shown in Fig.4.2a. For real values of k_x in the range

0 to ∞, the corresponding locus in the w plane is a hyperbola, which approaches the real and imaginary axes as $k_2 \to 0$ (see Fig.4.2b). All solutions of eqn.(5), and consequently all zeros of the complex function

$$F_n(w) = K_{h,n} \frac{\sin(a\sqrt{k^2-w^2})}{a\sqrt{k^2-w^2}} + \cos(a\sqrt{k^2-w^2}) - \cos\psi_h \qquad \text{.... (7)}$$

lie on this hyperbola (under the specified conditions on a/λ and $b_{h,n}$ - cf. Section 2.2). The value of k_2 is assumed sufficiently small to ensure that the distinction between real and imaginary roots in the w plane when $k_2 = 0$ can be preserved. Although $\beta_{1,n}$ does not quite fall on the real axis (see Fig.4.2), it remains valid to regard ϕ_{inc} as a propagating mode. Roots of eqn.(7) associated with evanescent modes are designated $j\xi_{i,n}$ below, with the subscript i corresponding to the range of the real variable k_x previously specified in Section 2.3 - i.e. $(i-1).\pi < k_x a \leqslant i\,\pi$.

4.2.2. Application of Boundary Conditions

The boundary conditions applied in Section 2.2 are relevant in the two regions $z < 0$ and $z > 0$. Over all z, $\phi(x,z)$ is continuous at $x = -a/2$ and $x = a/2$, and with periodic excitation, it follows that

$$\phi(-a/2+\delta,z) = \exp(j\psi_h).\phi(a/2-\delta,z) \quad \text{as } \delta \to 0 \qquad \text{.... (8)}$$

Substituting in eqn.(2), and setting $\delta = 0$,

$$\left[A(w)\exp(ja\sqrt{k^2-w^2}/2) + B(w)\exp(-ja\sqrt{k^2-w^2}/2)\right]$$

$$= \exp(j\psi_h)\left[A(w)\exp(-ja\sqrt{k^2-w^2}/2) + B(w)\exp(ja\sqrt{k^2-w^2}/2)\right] \qquad \text{.... (9)}$$

since $\phi_{inc}(-a/2,z) = \exp(j\psi_h).\phi_{inc}(a/2,z)$

.... (10)

and the equality of the integrals implies equality of the integrands. Using the results in Appendix 2A, the interdependence of $A(w)$ and $B(w)$ can be expressed in various forms, e.g.

$$B(w) = A(w)\,\frac{\sin\left[(a\sqrt{k^2-w^2} - \psi_h)/2\right]}{\sin\left[(a\sqrt{k^2-w^2} + \psi_h)/2\right]} \qquad \ldots.\ (11)$$

When $b_{h,n+1} = K_{h,n+1} = 0$, the function given by eqn. (11) has a pole when w is equal to each alternate root of eqn. (7). Consequently, the various modes obtained from eqn. (2) are specified below in terms of $A(w)$ if i is odd, and by $B(w)$ if i is even.

The second boundary condition must be applied separately in the regions $z < 0$ and $z > 0$. By comparison with eqns (8) and (9) in Chapter 2 and Appendix 2A, the required equation for all z is

$$\frac{1}{j\omega\mu}\left\{\left.\frac{\partial\phi}{\partial x}\right|_{x=-a/2+\delta} - \exp(j\psi_h)\cdot\left.\frac{\partial\phi}{\partial x}\right|_{x=a/2-\delta}\right\} = \frac{1}{jX_h}\,\phi\,\Big|_{x=-a/2}$$

$$\text{as } \delta \to 0 \qquad \ldots.\ (12)$$

where X_h must be specified as $X_{h,n}$ or $X_{h,n+1}$ as appropriate. For $z < 0$, ϕ_{inc} satisfies eqn (12), and the scattered field, after substitution and some algebraic simplification (cf. Appendix 2A,) can be shown to satisfy the condition

$$0 = \int_{-\infty}^{\infty} dw.\ \exp(-jwz)\left\{\frac{A(w).\ a\sqrt{k^2-w^2}.\ F_n(w)}{\sin[(a\sqrt{k^2-w^2} + \psi_h)/2]}\right\} \qquad \ldots.\ (13)$$

where $F_n(w)$ is given by eqn. (7). The function defined by this integral is proportional to the scattered field E_y along $x = a/2$, which must become asymptotic to an expression of the form $K_1 \exp(-j\beta_{1,n+1} z)$ as $z \to \infty$ (K_1 being independent of z). Consequently, it follows from standard transform theory (eg. 100) that

$$\frac{A(w).\ a\sqrt{k^2-w^2}.\ F_n(w)}{\sin[(a\sqrt{k^2-w^2}+\psi_h)/2]} = U(w)(\text{say}) \qquad \text{.... (14)}$$

is analytic in the region $\text{Im } w > \text{Im } \beta_{1,n+1}$.

For the region $z > 0$, ϕ_{inc} does not satisfy eqn.(12), and the condition to be satisfied by the total field can be reduced after substitution to

$$-\frac{\vec{A}_{1,n}\cdot a\sqrt{k^2-\beta^2_{1,n}}\cdot F_{n+1}(\beta_{1,n})\cdot \exp(-j\beta_{1,n}z)}{\sin[(a\sqrt{k^2-\beta^2_{1,n}}+\psi_h)/2]}$$

$$= \int_{-\infty}^{\infty} dw\ \exp(-jwz)\left\{\frac{A(w)\ .\ a\sqrt{k^2-w^2}\ .\ F_{n+1}(w)}{\sin[(a\sqrt{k^2-w^2}+\psi_h)/2]}\right\} \qquad \text{.... (15)}$$

The transform in the above equation has a pole at $w = \beta_{1,n}$ associated with the incident field. With partial factorisation to isolate this singularity, the remainder of the transform becomes analytic in a region $\text{Im } w < \text{Im} - \beta_{1,n}$, since the scattered field E_y along $x = a/2$ takes an asymptotic form $K_2 \exp(j\beta_{1,n}z)$ as $z \to -\infty$. This can be expressed by the equation

$$\frac{A(w)\ .\ a\sqrt{k^2-w^2}\ .\ F_{n+1}(w)}{\sin[(a\sqrt{k^2-w^2}+\psi_h)/2]} - \frac{C_h}{w-\beta_{1,n}} = L(w)(\text{say}) \qquad \text{.... (16)}$$

in the region $\text{Im}(w) < \text{Im} -\beta_{1,n}$, where C_h is independent of w. Closing the line integral on the R.H.S. of eqn. (15) in anticlockwise direction with a semicircle of infinite radius, the value of C_h is obtained immediately from the residue theorem, i.e.

$$C_h = \frac{1}{2\pi j}\cdot\frac{\vec{A}_{1,n}\cdot a\sqrt{k^2-\beta^2_{1,n}}\cdot F_{n+1}(\beta_{1,n})}{\sin[(a\sqrt{k^2-\beta^2_{1,n}}+\psi_h)/2]} \qquad \text{.... (17)}$$

By eliminating A(w) from eqns. (14) and (16), it is seen that the relation

$$U(w) \left[\frac{F_{n+1}(w)}{F_n(w)} \right] = L(w) + \frac{C_h}{w - \beta_{1,n}} \qquad \text{.... (18)}$$

is obtained which holds only in the common strip Im $\beta_{1,n+1}$ < Im w < Im − $\beta_{1,n}$.

4.2.3. Factorisation and Analytic Continuity

The sequence of analytical steps peculiar to "the Wiener-Hopf technique" must now be considered. To proceed with the analysis, it is first necessary to decompose the square-bracketed term in eqn. (18) into the form

$$\frac{F_{n+1}(w)}{F_n(w)} = \frac{F^+_{n+1}(w) \cdot F^-_{n+1}(w)}{F^+_n(w) \cdot F^-_n(w)} = \frac{F^+(w)}{F^-(w)} \qquad \text{.... (19)}$$

where the functions F^+ and F^- are analytic in upper and lower half-plane regions which include (at least part of) the common strip about the real axis. (This implies that individual functions, such as F^+_n, be analytic and non zero in their respective half planes). Since $F_{n+1}(w)$ and $F_n(w)$ are both even functions in w with simple zeros (cf. eqn. (7)), the required decomposition can be recognised immediately after applying the appropriate form of the Weierstrass factorisation theorem (101), viz

$$f_e(w) = f_e(0) \prod_{i=1}^{\infty} [1-(w/w_i)^2] \qquad \text{.... (20)}$$

where the roots are $\pm w_i$. (The following analysis does not apply in the special cases of second order roots, e.g. $b_h = \psi_h = 0$ see Section 4.2.5.) Assuming for illustrative purposes two propagating modes, the individual functions can then be expressed in the general form

$$F_n^{\pm}(w) = \left[F_n(0)\right]^{\frac{1}{2}} \cdot \exp\left[\mp\chi_n(w)\right] \cdot (1 \mp w/\beta_{1,n})\exp(\pm w/\zeta_{1,n}) \cdot$$

$$(1 \mp w/\beta_{2,n})\exp(\pm w/\zeta_{2,n}) \prod_{i=3}^{\infty} \left[(1 \mp jw/\xi_{i,n})\exp(\pm jw/\zeta_{i,n})\right] \qquad \ldots.(21)$$

where upper and lower signs go together. The exponential factors are required to ensure algebraic growth (and uniform convergence) in each half plane as $|w| \to \infty$ (see below). Normally in engineering problems, convergence is assured by setting $\zeta_{1,n} = \xi_{1,n}$ (eg. 43, 95) ; however, a more flexible choice is preferred in the present work, to simplify the specification of $[\chi_n(w) - \chi_{n+1}(w)]$.

As $i \to \infty$, the zeros $(\pm j\xi_{i,n})$ of $F_n(w)$ become independent of $K_{h,n}$. For any finite value of b_h, their asymptotic values can be found analytically from the equation

$$\cos(a\sqrt{k^2-w^2}) = \cos \psi_h \qquad \ldots. (22)$$

Assuming evanescent modes, it follows that

$$a\sqrt{k^2 + \xi_{1,n}^2} = (i-1)\pi + \psi_h \text{ if } i \text{ is odd} \qquad \ldots. (23a)$$

$$= i\,\pi - \psi_h \quad \text{if } i \text{ is even} \qquad \ldots. (23b)$$

$$\text{i.e.} \quad \xi_{i,n} \to \left.\begin{array}{ll} (\pi/a)i + (\psi_h - \pi)/a + O(i^{-1}) & \text{for } i \text{ odd} \\ (\pi/a)i + \psi_h/a + O(i^{-1}) & \text{for } i \text{ even} \end{array}\right\} i \to \infty \qquad \begin{array}{l} \ldots. (24a) \\ \ldots. (24b) \end{array}$$

Where $b_h = -\infty$, corresponding to the region $n = 0$ in Chapter 6, the zeros are given by

$$\xi_{i,0} \to \frac{\pi}{a}i + O(i^{-1}) \text{ as } i \to \infty \qquad \ldots. (25)$$

Therefore, for any value of b_h in the range $-\infty \leqslant b_h \leqslant 0$, the most significant term in these asymptotic forms is the same. By choosing

$$\zeta_{i,n} = \zeta_{i,n+1} \to \frac{\pi}{a}i + c + O(i^{-1}) \text{ as } i \to \infty \qquad \ldots. (26)$$

(where c is any constant) in the expressions for $F_{n+1}^{\pm}(w)/F_n^{\pm}(w)$, it follows from a result given by Noble (102) that $[\chi_n(w)-\chi_{n+1}(w)]$ should be set to zero to ensure algebraic growth in each half plane.

As a specific example, consider a junction between regions n and n + 1 with one and two propagating modes respectively. Using the results in the two preceding paragraphs, the functions $F^{\pm}(w)$ can be reduced to

$$F^{\pm}(w) = \left[\frac{F_{n+1}(0)}{F_n(0)}\right]^{\frac{1}{2}} \cdot \frac{(1 \mp w/\beta_{1,n+1})(1 \mp w/\beta_{2,n+1})}{(1 \mp w/\beta_{1,n})} \cdot \frac{\prod_{i=3}^{\infty}(1 \mp jw/\xi_{i,n+1})}{\prod_{i=2}^{\infty}(1 \mp jw/\xi_{i,n})} \quad \text{.... (27)}$$

These functions approach a constant value (i.e. $O(w^0)$) as $|w| \to \infty$ in their respective half planes of analyticity. The regions of analyticity correspond with those defined for L(w) and U(w).

Returning to eqn. (18), and substituting eqn. (19), the relation

$$U(w).F^{+}(w) = L(w)F^{-}(w) + \frac{C_h.F^{-}(w)}{w - \beta_{1,n}} \quad \text{.... (28)}$$

is obtained. The pole on the R.H.S. can be removed by subtracting the term $\frac{C_h\ F^{-}(\beta_{1,n})}{w - \beta_{1,n}}$ from both sides, giving the result

$$U(w).F^{+}(w) - \frac{C_h F^{-}(\beta_{1,n})}{w - \beta_{1,n}} = L(w).F^{-}(w) + \frac{C_h[F^{-}(w) - F^{-}(\beta_{1,n})]}{w - \beta_{1,n}} \quad \text{.... (29)}$$

This equation only applies in the region $\mathrm{Im}\ \beta_{1,n+1} < \mathrm{Im}(w) < \mathrm{Im} - \beta_{1,n}$, but the L.H.S. is analytic throughout the upper half plane, and the R.H.S. is analytic throughout the lower half plane. By the principles of analytic continuation, it therefore follows that both functions are equal to an entire function h(w) of finite order.

This function can be derived from the asymptotic relations between the fields (as $z \to 0$) and their transforms (as $|w| \to \infty$), sometimes known as the Abelian theorems (103). Specifically, if the behaviour of f(z) is known to be of the form cz^{ν} as $z \to 0^{+}$, then $F^{+}(w) \sim O(w^{-\nu-1})$ as $|w| \to \infty$ in the upper half plane. With this result, it is possible to put limits on the asymptotic behaviour of $U(w)$ in eqn. (29), which is the transform of a quantity proportional to the field E_y along $x = a/2$. For a conducting knife-edge at $z = 0$ (corresponding to one extreme where $b_{h,n} = -\infty$ and $b_{h,n+1} = 0$), the order of field singularity consistent with finite stored energy is $cz^{-\frac{1}{2}}$ as $z \to 0$ (104). For a vanishingly small discontinuity (corresponding to the other extreme where $b_{h,n} \to b_{h,n+1}$), the fields do not become infinite, and therefore take a form cz^0 as $z \to 0$. For the general discontinuity as defined by Fig. 4.1, it therefore follows that

$$E_y\Big|_{x=a/2} \sim cz^{\nu} \text{ as } z \to 0^+ \text{ with } -0.5 < \nu < 0 \qquad \ldots\ldots (30)$$

while $U(w) \sim O(w^{-\nu-1}) \to 0$ as $|w| \to \infty$, $\text{Im } w > \text{Im } \beta_{1,n+1}$ .... (31)

A term by term inspection of the L.H.S. of eqn. (29) now shows that the polynomial function $h(w)$ must be indentically equal to zero to comply with the known asymtotic behaviour of $U(w)$ and $F^{\pm}(w)$. [In the present example, it is now unnecessary to examine the asymptotic behaviour of the R.H.S. of eqn. (29) as $|w| \to \infty$ in the lower half plane, or to invoke the extended form of Louiville's theorem (cf. 105).] Substituting for $h(w)$ in eqn. (29),

$$U(w) = \frac{C_h}{w - \beta_{1,n}} \cdot \frac{F^-(\beta_{1,n})}{F^+(w)} \qquad \ldots\ldots (32)$$

and the required expression for $A(w)$ can be found directly from eqns. (14) and (19), viz

$$A(w) = \frac{\vec{A}_{1,n}}{2\pi j} \cdot \frac{\sqrt{k^2-\beta_{1,n}^2}}{\sqrt{k^2-w^2}} \cdot \frac{\sin\left[(a\sqrt{k^2-w^2} + \psi_h)/2\right]}{\sin\left[(a\sqrt{k^2-\beta_{1,n}^2} + \psi_h)/2\right]} \cdot$$

$$\frac{1}{w - \beta_{1,n}} \cdot \frac{F_{n+1}^+(\beta_{1,n})\, F_n^-(\beta_{1,n})}{F_{n+1}^+(w)\, F_n^-(w)} \qquad \ldots\ldots (33)$$

The form of this equation is sufficiently general in respect of w and the root ($\beta_{1,n}$) associated with a particular incident mode, to permit the corresponding relations for $A(w)$ (within a strip including $\text{Im } w = 0$) to be recognised without repeating the above analysis for other incident modes (see below).

4.2.4. Transmission and Reflection Coefficients

The amplitude and phase of any 'mode' in either region (i.e. $z < 0$ and $z > 0$) can be obtained by substituting eqn. (33) (together with eqn. (11)) in eqn. (2), and determining the residue associated with the appropriate pole of $A(w)$. In the region $z > 0$, the line integral is closed anticlockwise in the lower half plane, while for $z < 0$, it is closed clockwise in the upper half plane; in both cases, by a semicircle of infinite radius, which can be chosen to pass between the poles near the imaginary axis.

A simple check can be made on eqn. (33) by finding the scattered field in the region $z > 0$ introduced by the pole at $w = \beta_{1,n}$. By inspection, the result is $-\phi_{inc}$ as required, thereby removing this mode from the total field in the region $z > 0$.

The lowest order reflected mode, characterised by $\overleftarrow{A}_{1,n}$, is given by

$$\overleftarrow{A}_{1,n} = 2\pi j \,[\text{Residue associated with } A(w)\exp(-jx\sqrt{k^2-w^2})\exp(-jwz) \text{ at } w = -\beta_{1,n}] \qquad \ldots\ldots (34a)$$

$$= 2\pi j \lim_{w\to-\beta_{1,n}} \left[(w + \beta_{1,n}).A(w)\right] \qquad \ldots\ldots (34b)$$

i.e.

$$\frac{\overleftarrow{A}_{1,n}}{\overrightarrow{A}_{1,n}} = \lim_{w\to-\beta_{1,n}} \left[\frac{(w + \beta_{1,n})\, F^{+}_{n+1}(\beta_{1,n})\, F^{-}_{n}(\beta_{1,n})}{(w - \beta_{1,n})\, F^{+}_{n+1}(w)\, F^{-}_{n}(w)}\right] \qquad \ldots\ldots (34c)$$

(The remaining terms in $A(w)$ cancel with $w = -\beta_{1,n}$.)

If k_2 is set to zero, the amplitude of this reflection coefficient can be reduced to an expression involving only the real zeros $\beta_{i,n}$ and

$\beta_{i,n+1}$ of $F_n(w)$ and $F_{n+1}(w)$. Correspondingly, the phase depends on the imaginary zeros $j\xi_{i,n}$ and $j\xi_{i,n+1}$, and is equal to an infinite series of terms which converge as $i \to \infty$. Substituting appropriate expressions based on eqn. (21) in eqn. (34c), and assuming (as a specific example) one propagating mode in each region, the following result is obtained (Appendix 4A)

$$\frac{\overleftarrow{A}_{1,n}}{\vec{A}_{1,n}} = \frac{\beta_{1,n+1} - \beta_{1,n}}{\beta_{1,n+1} + \beta_{1,n}} \cdot \exp[j\{\pi + 2P_{2,2}(\beta_{1,n})\}] \qquad \text{.... (35)}$$

where $$P_{2,2}(u) = \sum_{i=2}^{\infty} \arctan\left[\frac{u}{\xi_{i,n}}\right] - \sum_{i=2}^{\infty} \arctan\left[\frac{u}{\xi_{i,n+1}}\right] \qquad \text{.... (36)}$$

The subscripts in $P_{2,2}(u)$ indicate the initial values of i in the two regions $z < 0$ and $z > 0$ respectively. Equation (35) defines the scattering matrix element S_{11} in eqn. (1) if the first element of the column matrix $[\underset{\sim}{a}]$ is $\vec{A}_{1,n}$.

The lowest order transmitted mode is characterised by

$$\vec{A}_{1,n+1} = -2\pi j \left\{ \lim_{w \to \beta_{1,n+1}} \left[(w - \beta_{1,n+1})\, A(w) \right] \right\} \qquad \text{.... (37)}$$

The corresponding transmission coefficient is then obtained from

$$\frac{\vec{A}_{1,n+1}}{\vec{A}_{1,n}} = - \frac{\sqrt{k^2-\beta_{1,n}^2}\ \sin[(a\sqrt{k^2-\beta_{1,n+1}^2} + \psi_h)/2]}{\sqrt{k^2-\beta_{1,n+1}^2}\ \sin[(a\sqrt{k^2-\beta_{1,n}^2} + \psi_h)/2]} \cdot$$

$$\lim_{w \to \beta_{1,n+1}} \left[\frac{(w - \beta_{1,n+1})\, F_{n+1}^{+}(\beta_{1,n})\, F^{-}(\beta_{1,n})}{(w - \beta_{1,n})\, F_{n+1}^{+}(w)\, F_n^{-}(w)} \right] \qquad \text{.... (38)}$$

The steps in the evaluation of the limit term in eqn. (38) are typical of the procedure when the scattering matrix element $S_{i'j'}$ is off diagonal (i.e. $i' \neq j'$). The amplitude can be expressed in closed form by utilising the derivatives $F_n'(w)$ of the unfactorised functions $F_n(w)$ when $k_2 = 0$. Appendix 4A illustrates the procedure for single moded regions, viz

$$\frac{\vec{A}_{1,n+1}}{\vec{A}_{1,n}} = \frac{\sqrt{k^2-\beta^2_{1,n}}}{\sqrt{k^2-\beta^2_{1,n+1}}} \cdot \frac{\sin\left[(a\sqrt{k^2-\beta^2_{1,n+1}} + \psi_h)/2\right]}{\sin\left[(a\sqrt{k^2-\beta^2_{1,n}} + \psi_h)/2\right]} \cdot \frac{2\sqrt{\beta_{1,n}\cdot\beta_{1,n+1}}}{\beta_{1,n+1} + \beta_{1,n}} \cdot$$

$$\sqrt{\frac{|F_{n+1}(\beta_{1,n})|}{|F_{n+1}'(\beta_{1,n+1})|} \cdot \frac{|F_n'(\beta_{1,n})|}{|F_n(\beta_{1,n+1})|}} \cdot \exp\left[j\{P_{2,2}(\beta_{1,n}) - P_{2,2}(\beta_{1,n+1})\}\right] \quad \text{.... (39)}$$

If $\vec{A}_{1,n+1}$ is regarded as the second element of the column matrix $[\underset{\sim}{a}]$, then eqn.(39) defines the term S_{21} in the 2 X 2 scattering matrix for propagating modes.

With proper normalisation of the incident fields and k_2 set to zero, it follows from standard network theory that the remaining two terms S_{12} and S_{22} in a 2 X 2 matrix can be obtained without further analysis of the junction. Under conditions of dual-moded propagation, however, it is essential to consider more than one incident mode to define all the elements in the corresponding scattering matrix. Consequently, as relations equivalent to eqn. (33) can be readily deduced for any incident mode, it is convenient for numerical purposes to retain unnormalised fields. The interrelationships afforded by reciprocity and power conservation can then be utilised to check the final results. Proceeding on this basis, all terms in the various H-plane scattering matrices (tabulated in Appendix 4B) can be found by noting the following modifications to eqn. (33):-

(i) For mode incidence from the R.H.S. in Fig. 4.1, say $\vec{A}_{1,n+1}$

$\vec{A}_{1,n}$ becomes $-\vec{A}_{1,n+1}$

and $\beta_{1,n}$ becomes $-\beta_{1,n+1}$

$$\text{i.e.}\quad A(w) = \frac{-\hat{A}_{1,n+1}}{2\pi j} \cdot \frac{\sqrt{k^2-\beta^2_{1,n+1}}}{\sqrt{k^2-w^2}} \cdot \frac{\sin[(a\sqrt{k^2-w^2} + \psi_h)/2]}{\sin[(a\sqrt{k^2-\beta^2_{1,n+1}} + \psi_h)/2]} \cdot$$

$$\frac{1}{w + \beta_{1,n+1}} \cdot \frac{F^+_{n+1}(-\beta_{1,n+1})\, F^-_n(-\beta_{1,n+1})}{F^+_{n+1}(w)\, F^-_n(w)} \qquad \ldots.\ (40)$$

(The change of sign occurs because the pole associated with the incident mode now lies in the upper half plane.)

(ii) For elements of the scattering matrix involving second modes in either region, characterisation by B(w) is achieved by substituting eqn. (11), which applies for any incident mode, with $w = \beta_{i,n}$ or $-\beta_{i,n+1}$ as appropriate. For example, if the second transmitted mode is required with dominant mode incidence from the L.H.S., then

A(w) becomes B(w) in eqn.(33).

while $\sin[(a\sqrt{k^2-w^2} + \psi_h)/2]$ becomes $\sin[(a\sqrt{k^2-w^2} - \psi_h)/2]$. .... (41)

(iii) Combinations of (i) and (ii) can be adopted as appropriate. The overall pattern can be easily recognised by studying the terms in the 4 X 4 matrix in Appendix 4B.

(For computational purposes, it should be remembered, of course, that the roots β_i and ξ_i are not constant (unless $b_h = -\infty$), but remain functionally dependent on ψ_h.)

4.2.5. Discussion of Results

The individual terms in the scattering matrices are consistent with the qualitative predictions in Chapters 2 and 3. In particular, it is clear that the two principal objectives of the design technique - viz the minimisation of reflected power for impedance matching, and the reduction of forward scattered power in the second mode for element pattern control - can be maintained with small discontinuities in boundary susceptance, i.e. with $\beta_{1,n} = \beta_{1,n+1} - \delta$ where $\delta \to 0$. The use of these results, within a cascade network constrained by the number of discontinuities and the extreme values of $b_h (b_{h,o} = -\infty,\ b_{h,m} = 0)$, is examined further in Chapter 6.

The scattering elements obtained for the 2 X 2 and 3 X 3 matrices in Appendix 4B can be checked against the results obtained by Wu and Galindo (eqn. (11) of reference 43) in the limiting case of a waveguide array radiating into free space. A term by term comparison suggests two possible discrepancies in phase. The first arises from the presence of a term $\exp[-jau(\ln 2)/\pi]$ (in a function analogous to $P_{2,2}(u)$ in eqn. (35)), which does not occur in the present work. However, this difference is only superficial, and can be clarified by modifying the factorised expressions for the function

$$\frac{F_m(w)}{F_o(w)} = \frac{\cos(a\sqrt{k^2-w^2}) - \cos\psi_h}{\dfrac{\sin(a\sqrt{k^2-w^2})}{a\sqrt{k^2-w^2}}} \qquad \text{.... (42)}$$

(For the present discussion, it suffices to have one propagating mode in each region.) If the function $F_m(w)$ is now factorised into two sets of "essentially imaginary" roots, i.e.

$$a\sqrt{k^2+\alpha_{i,m}^2} = 2\pi(i-1) + \psi_h \quad (i = 2,3,4 \ldots) \qquad \text{.... (43a)}$$

$$a\sqrt{k^2+\eta_{i,m}^2} = 2\pi(i-1) - \psi_h \quad (i = 2,3,4 \ldots)$$

while $F_O(w)$ is factorised as before, i.e. in terms of

$$a\sqrt{k^2+\xi_{i,O}^2} = \pi(i-1) \qquad (i = 2,3,4 \ldots) \qquad \text{.... (43c)}$$

it can be shown (using the procedures outlined in Section 4.2.3) that $[\chi_O(w) - \chi_m(w)]$ does not disappear, but becomes $[jaw(\ln 2)/\pi]$. Consequently,

$$\frac{F_m^+(w)}{F_0^+(w)} = \frac{[F_m(0)]^{\frac{1}{2}}}{[F_0(0)]^{\frac{1}{2}}} \cdot \exp[-jaw(\ln 2)/\pi] \cdot \frac{(1 - w/\beta_{1,m})}{(1 - w/\beta_{1,o})} \cdot$$

$$\prod_{i=2}^{\infty} \left[\frac{(1 - jw/\alpha_{i,m})(1 - jw/\eta_{i,m})}{(1 - jw/\xi_{i,o})} \right] \quad \ldots. (44)$$

The complete set of roots $\alpha_{i,m}$ and $\eta_{i,m}$ is equivalent, of course, to a complete set $\xi_{i,m}$ consistent with eqn. (21), but different phase results are obtained in the evaluation of residues (cf. Section 4.2.4) (with w = a real quantity) unless the additional term $\exp[-jaw(\ln 2/\pi]$ is included. Mathematically, the first of the two "discrepancies" is therefore a direct consequence of the relation implied by eqn. (44), viz

$$\prod_{i=2}^{I} \left[\frac{(1 - jw/\alpha_{i,m})(1 - jw/\mu_{i,m})}{(1 - jw/\xi_{i,m})} \right] \to \exp[+jaw(\ln 2)/\pi] \text{ as } I \to \infty. \quad \ldots. (45)$$

When estimating $P_{2,2}(u)$ numerically, no confusion can occur if all cases (including those where $b_h = -\infty$ or 0) are considered in the manner outlined in Section 4.2.4.

The second discrepancy concerns the sign of the transmission coefficients S_{21} and S_{31}. The results given by Wu and Galindo include a phase term $\exp(j\pi)$ which does not arise, for example, after substitution in the expression for S_{21} given by eqn. (39). To resolve this genuine discrepancy, experimental checks were made using the phased-array waveguide simulator described in Chapter 5. The measurements confirmed (to within 10^o) the phase as defined by eqn. (39) and in Appendix 4B. Wu and Galindo state that their expressions for the reflection and transmission coefficients, which are not derived in published work in the case of the H-plane scan, are "referred to E_y", as in the present work. However, the use of Hertzian vectors to describe the total field in reference 43 could be significant. With the geometry as shown in Fig. 3.17, a Hertzian vector TE_x and H_x differ only by constant factor for scanning in the quasi-E plane, which is the case analysed step by step in reference 43. However, if the fields are then described by a TM_y Hertzian vector for an H-plane scan, it is readily shown that the "constant of proportionality" with E_y takes different signs for scattered modes in the regions $z < 0$ and $z > 0$. It is conceivable that this difference may not have been allowed for in references 43 and 4 (pp 134-135).

The disposition of roots in the w-plane for a particular value of a/λ - say 0.707 - can be appreciated by reference to Fig. 4.3, which shows the calculated roots for the waveguide and free space regions. The roots corresponding to any particular value of b_h lie on the loci as shown, which in turn "stretch" or "contract" as ψ_h is varied. Whilst this representation has qualitative merit (particularly in relation to Chapter 2) it is inadequate of course as a general method of specifying the roots. For this task, and the subsequent calculation of the scattering matrix elements in the general case of an H-plane susceptance discontinuity, a numerical analysis is required. Using the computer programme described in the next section, (augmented by numerical tables of power flow) confirmation of power conservation is readily obtained. (A straight-forward analytical proof can also be developed, although the algebra is quite cumbersome in the case of a 4 X 4 matrix. The amplitudes of $S_{i'j'}$ in a 3 X 3 matrix have been obtained independently using momentum principles (98).) Finally, it should be noted that the occurrence of phase terms $\exp(j\pi)$

in the elements of the scattering matrices is such that the relationship between the arguments expected from reciprocity is preserved, viz

$$\arg S_{i'j'} = \arg S_{j'i'} \; ; \; i' \neq j' \qquad \ldots. \; (46)$$

4.3. Numerical Calculations of $[\underset{\sim}{S}]$ in H-plane

A computer programme which calculates all terms in the appropriate scattering matrix was written in fortran and run on the Honeywell Mk II Time Sharing System. The programme affords the normal flexibility expected for numerical purposes, with all the significant variables read from a data file. These included the analytical parameters a/λ, $\psi_{h,min}$, $\Delta\psi_h$, $\psi_{h,max}$, $b_{h,n}$ and $b_{h,n+1}$, together with the numerical variables "CONERR" (which governs the maximum error in the iterative process of estimating β_i and ξ_i) and "NUM" (which specifies the number of roots included in the calculation of the arguments). A simple decision process ensures that the correct form of $[\underset{\sim}{S}]$ is chosen for any particular set of parameters, with the appropriate terms in the 4 X 4 matrix output set to zero when modes become evanescent (see next section). The main programme is constructed in a standard manner around three subroutines. One of these finds the real or imaginary 'i'th root of the general characteristic equation (i.e. $F_n(w_i) = 0$), while the others calculate the amplitude and phase of the scattering matrix elements ($S_{i'j'}$) according to the number of real roots.

The efficiency of the subroutine which calculates the roots, and the number of times it is called by the main programme (i.e. 2 X NUM) are the key factors in the control of computing time. Setting CONERR = 10^{-4} and NUM = 30, and estimating roots according to the criterion

$$|F_n(w_i)| < i \times \text{CONERR} \qquad \ldots. \; (47)$$

the scattering matrix elements $S_{i'j'}$ could be calculated in amplitude and phase to $\pm$ 0.001 and $\pm$ 0.1° respectively for all finite b_h, and $5^\circ < \psi_h < 175^\circ$. This accuracy and range can be regarded as a combination of extreme cases, with the relaxation condition on the accuracy of higher roots (expn.(47)) not specified in an optimum manner (see below). Using Newton's rule (106) with an automatic reset if the estimate goes out of range, 250 to 800 loops were required to calculate 30 roots in each region. A series of tests revealed that approximately 1000 loops can be executed for 0.15 CRU'S (Computer Resource Units), with the number of iterations for one root lying in the range 3 to 15.

The number of roots can be reduced substantially when the susceptance discontinuity becomes small. For example, with susceptances $b_{h,n} = -0.83$ and $b_{h,n+1} = -0.4$, only 8 roots are required to preserve the computational accuracy quoted above. A smaller saving can be made by relaxing the value of CONERR, which controls the amplitude accuracy of terms $S_{i'j'}$ under various conditions - e.g. when $\beta_{1,n}$ and $\beta_{1,n+1}$ lie close together. For the determination of phase, the imaginary roots can be found satisfactorily with CONERR $\sim 10^{-3}$. The relaxation condition introduced by expn.(47) takes account of this in a very simple way. However, as the convergence in the vicinity of a root becomes quadratic using Newton's rule, the overall number of iterations is not significantly reduced. Computational time for the other two subroutines, executed once for any set of parameters, is approximately 0.04 CRU's.

The accuracy of the computer programme was tested initially by setting $b_{h,n}$ to a large value, and $b_{h,n+1}$ to zero. This enabled a comparison to be made with results published by Wu and Galindo for a waveguide array (43). The continuous curves for the amplitude and phase of S_{11} in Fig. 4.4 ($b_{h,n} = -1000$) cannot be distinguished from those in references 4 and 43, which are therefore not shown as separate results. Some of the computational features discussed in the preceding two paragraphs are conveniently illustrated by Fig. 4.4. The large discontinuity in susceptance makes it necessary to take NUM = 30 to ensure the convergence of $P_{2,2}(\beta_{1,n})$. With $b_{h,n} = 20$, a considerable difference in amplitude is also apparent, particularly when ψ_h is small. The choice of a relatively small value of a/λ (0.5714) has accentuated this effect, which is due to a quite significant relative difference in the roots when $b_{h,n} = -20$ and -1000.

Figures 4.5 to 4.7 illustrate principal trends in two of the matrix elements of most interest in cascaded networks (see Chapter 6). The element spacing of $a/\lambda = 0.695$ has been adopted as a value more typical of the element spacing which might be used for sectoral scanning to $\theta_{o,max} \sim 35^{\circ}$. In all these figures the discontinuities in the amplitude or phase derivatives can be linked with the occurrence of an additional propagating mode as ψ_h is increased. The figures provide the numerical values for the design examples considered in Chapter 6, and some of their important features are more appropriately discussed in that context.

4.4. Evanescent Modes

The total field in the region of a discontinuity includes contributions from all the poles of $A(w)$, - i.e. the two infinite sets of evanescent modes (eqn.(33)). These are the poles $w = j\xi_{i,n}$ in the region $z < 0$, and $w = -j\xi_{i,n+1}$ for $z > 0$. With the movement of roots in a multi-section transition during scan (see Fig. 4.3), it is evident that the field associated with the second mode should be considered, at planes within a wavelength of the discontinuity, as the corresponding root approaches the real axis.

The various analytical solutions can again be derived from eqn.(33). As an example, consider a structure which supports one propagating mode in the region $z < 0$, and two propagating modes for $z > 0$. The non-propagating mode $\overleftarrow{B}_{2,n}$ caused by the incident mode $\vec{A}_{1,n}$ is given by

$$\frac{\overleftarrow{B}_{2,n}}{\vec{A}_{1,n}} = \frac{\sqrt{k^2-\beta^2_{1,n}}}{\sqrt{k^2+\xi^2_{2,n}}} \cdot \frac{\sin[(a\sqrt{k^2+\xi^2_{2,n}} - \psi_h)/2]}{\sin[(a\sqrt{k^2-\beta^2_{1,n}} + \psi_h)/2]}$$

$$\lim_{w\to j\xi_{2,n}} \left\{ \frac{(w - j\xi_{2,n})\ F^+_{n+1}(\beta_{1,n})\ F^-_n(\beta_{1,n})}{(w-\beta_{1,n})\ F^+_{n+1}(w)\ F^-_n(w)} \right\} \quad \text{.... (47)}$$

The phase is readily reduced to the form

$$\text{Argument} = P_{3,3}(\beta_{1,n}) - \sum_{i=1}^{2} \left\{\arctan(\xi_{2,n}/\beta_{i,n+1})\right\} + \arctan(\xi_{2,n}/\beta_{1,n}) \quad \text{.... (48)}$$

However, the amplitude does not reduce into a compact expression when the pole lies on the imaginary axis, as revealed by substitution along lines similar to Appendix 4A. The term

$$\lim_{w\to j\xi_{2,n}} \left|\frac{(w - j\xi_{2,n})}{F^-_n(w)}\right| \text{ converges as } \left[\prod_i \left(1 - \frac{\xi_{2,n}a}{\pi i}\right)\right]^{-1} \quad \text{.... (49)}$$

which, in general, is a very slowly convergent function. As the evanescent mode is of network interest for a particular application, it is legitimate to utilise other conditions which would be satisfied by any practical design. Specifically, the evaluation of eqn.(47) would only be required in structures where any (isolated) susceptance discontinuity was small - say $b_{h,n} \sim -1$ and $\Delta b_h \sim 0.2$ to 0.4 (see Chapter 6). Under these conditions, $\xi_{i,n} \to \xi_{i,n+1}$ quite rapidly, and quotients of infinite products (which individually are slowly convergent) would exhibit satisfactory convergence for numerical purposes. It is therefore considered that an amplitude expression of the form

$$\frac{|\vec{B}_{2,n}|}{|\vec{A}_{1,n}|} = \frac{\sqrt{k^2-\beta_{1,n}^2}}{\sqrt{k^2+\xi_{2,n}^2}} \cdot \frac{\sin[(a\sqrt{k^2+\xi_{2,n}^2} - \psi_h)/2]}{\sin[(a\sqrt{k^2-\beta_{1,n}^2} + \psi_h)/2]} \cdot$$

$$\left\{ \sqrt{\frac{(\beta_{1,n+1} - \beta_{1,n})(\beta_{1,n} - \beta_{2,n+1})}{(\beta_{1,n+1} + \beta_{1,n})(\beta_{1,n} + \beta_{2,n+1})}} \cdot \sqrt{\frac{2\beta_{1,n} \left| F_{n+1}(\beta_{1,n}).F_n'(\beta_{1,n}) \right|}{(\beta_{1,n}^2 + \xi_{1,n}^2)}} \right\} \cdot$$

$$\left\{ \frac{\beta_{1,n}\cdot\xi_{2,n}}{\beta_{1,n+1}\cdot\beta_{2,n+1}} \cdot \sqrt{\frac{(\beta_{1,n+1}^2 + \xi_{2,n}^2)(\beta_{2,n+1}^2 + \xi_{2,n}^2)}{(\beta_{1,n}^2 + \xi_{2,n}^2)}} \cdot \frac{1}{|F_{n+1}(\xi_{2,n})|} \cdot \right.$$

$$\left. \prod_{i=3}^{\infty} \frac{\left[1 - \frac{\xi_{2,n}}{\xi_{i,n+1}}\right]}{\left[1 - \frac{\xi_{2,n}}{\xi_{i,n}}\right]} \right\} \qquad \text{.... (50)}$$

could be obtained accurately with 20 to 30 roots in the infinite product. This result (derived from eqn.(47)) has been partitioned by the larger brackets to indicate how the factors

$$\left| F_{n+1}^{+}(\beta_{1,n}).F_n^{-}(\beta_{1,n}) / (j\xi_{2,n} - \beta_{1,n}) \right|$$

and $$\lim_{w\to j\xi_{2,n}} \left| (w - j\xi_{2,n}) / [F_{n+1}^{+}(w).F_n^{-}(w)] \right|$$

have been expressed. The second of these factors has also been multiplied in its numerator and denominator by $F_{n+1}(\xi_{2,n})$.

The remaining terms in a 4 X 4 scattering matrix, which would probably suffice in all practical designs (because the next mode associated with $w = -j\xi_{3,n+1}$ would attenuate rapidly in the z direction) can be obtained in a corresponding form to eqn.(50).

4.5. E-plane Wiener-Hopf Analysis

As in Chapter 2, the E-plane analysis is given in summarised form.

With the incident field H_y in the reference unit cell given by

$$\phi_{inc} = \left[\vec{C}_{1,n}\exp(-jx\sqrt{k^2-\beta^2_{1,n}}) + \vec{D}_{1,n}\exp(jx\sqrt{k^2-\beta^2_{1,n}})\right]\exp(-j\beta_{1,n}z) \quad \ldots. (51)$$

the complete solution can be written as

$$\phi(x,z) = \phi_{inc} + \int_{-\infty}^{\infty} dw \,.\, \exp(-jwz)\left[C(w)\exp(-jx\sqrt{k^2-w^2}) + D(w)\exp(jx\sqrt{k^2-w^2})\right] \quad \ldots. (52)$$

In eqn.(51), it is reasonable to assume that $\beta_{1,n}$ is "essentially real" (corresponding to a propagating mode when $k_2 \to 0$) although it does not follow automatically that a propagating wave will form in the region $z > 0$ with $a/\lambda < 0.5$ (cf. E-plane mode chart Fig. 2.23). The boundary conditions are

$$\left.\frac{\partial\phi}{\partial x}\right|_{x=a/2-\delta} = \exp(-j\psi_e)\left.\frac{\partial\phi}{\partial x}\right|_{x=-a/2+\delta} \quad \text{for all } z \quad \ldots. (53)$$

and
$$\exp(-j\psi_e)\,.\,\phi\big|_{x=-a/2+\delta} - \phi\big|_{x=a/2-\delta} = \frac{-1}{\omega\varepsilon X_e}\left.\frac{\partial\phi}{\partial x}\right|_{x=a/2-\delta} \quad \ldots. (54)$$

in the separate regions $z < 0$ and $z > 0$ (designated by subscripts n and n + 1), with $\delta \to 0$ in both equations. As in the H-plane, these boundary conditions can be interpreted as constraints on the transforms - viz

$$\frac{D(w)}{C(w)} = \frac{\sin[(\psi_e - a\sqrt{k^2-w^2})/2]}{\sin[(\psi_e + a\sqrt{k^2-w^2})/2]} \quad \ldots. (55)$$

$$\frac{C(w)\,.\,G_n(w)}{\sin[(\psi_e + a\sqrt{k^2-w^2})/2]} = U(w) \text{ (say)} \quad \ldots. (56)$$

in a region of analyticity defined by Im $w >$ Im $\beta_{1,n+1}$

and
$$\frac{C(w)\,.\,G_{n+1}(w)}{\sin[(\psi_e + a\sqrt{k^2-w^2})/2]} - \frac{C_e}{w-\beta_{1,n}} = L(w) \text{ (say)} \quad \ldots. (57)$$

in a region of analyticity defined by Im $w <$ -Im $\beta_{1,n}$

where $G_n(w) = K_e(a\sqrt{k^2-w^2})\ \sin(a\sqrt{k^2-w^2}) + \cos(a\sqrt{k^2-w^2}) - \cos\psi_e$

$$\ldots\ldots (58)$$

and $$C_e = \frac{\vec{C}_{1,n} \cdot G_{n+1}(\beta_{1,n})}{\sin[(\psi_e + a\sqrt{k^2-\beta^2_{1,n}})/2]} \quad \ldots\ldots (59)$$

Following through the Weiner-Hopf procedure, an equation for $C(w)$ equivalent to eqn. (33) for $A(w)$ can be obtained which holds in the common strip of analyticity defined by eqns.(56) and (57), and is given by

$$C(w) = \frac{\vec{C}_{1,n}}{2\pi j} \cdot \frac{\sin[(\psi_e + a\sqrt{k^2-w^2})/2]}{\sin[(\psi_e + a\sqrt{k^2-\beta^2_{1,n}})/2]} \cdot \frac{1}{(w - \beta_{1,n})} \cdot \frac{G^+_{n+1}(\beta_{1,n}) \cdot G^-_n(\beta_{1,n})}{G^+_{n+1}(w) \cdot G^-_n(w)}$$

$$\ldots\ldots (60)$$

where $$G^{\pm}_n(w) = [G_n(0)]^{\frac{1}{2}}(1 + w/\beta_{1,n}) \cdot \prod_{i=2}^{\infty}\left[(1 + jw/\xi_{i,n})\exp(\pm jw/\zeta_{i,n})\right] \quad \ldots\ldots (61)$$

with $\xi^2_{i,n}$ and $\zeta^2_{i,n} \to \{[(i-1)\pi/a]^2 - k^2\}$ as $i \to \infty$, if $b_e > 0$. .... (62)

(where $b_e = 0$, the roots correspond to the values obtained from eqn.(23).)

Excluding the condition $\psi_e = 0$ (when the E-plane array is perfectly matched for any capacitive value of b_e, $\beta_{1,n} = \beta_{1,n+1}$ and $\xi_{i,n} = \xi_{i,n+1}$) the reflection and transmission coefficients can be obtained as before from the residue theorem after closing the line integral defining ϕ_s around the upper and lower half planes respectively. The complete scattering matrix, assuming that the mode characterised by $\vec{C}_{1,n+1}$ remains propagating, is given in Appendix 4C. The junction properties when $\vec{C}_{1,n+1}$ is cut-off are not of practical importance in the present work, although the various formulae can obviously be obtained from eqn.(60).

With $b_{e,n} = +\infty$ and $b_{e,n+1} = 0$, the transmission and reflection coefficients in Appendix 4C are again consistent with the results obtained by Wu and Galindo, after allowing for the different methods of factorisation (cf. Section 4.2.5). The even function $G_0(w)$, obtained within the waveguide feed where $b_{e,o} = \infty$, is given by

$$G_0(w) = (a\sqrt{k^2-w^2})\ \sin(a\sqrt{k^2-w^2}) \qquad \text{.... (63)}$$

For engineering purposes, a computer programme is required for the general susceptance discontinuity. Several features of the scattering matrix are discussed in Chapter 6.

APPENDIX 4A

The following summary illustrates the derivation of scattering matrix elements. A single propagating mode is assumed in each region. Reflection coefficients can be recognised simply by expanding the appropriate product expression. Taking eqn. (34c) in the text as an example,

$$\frac{\overleftarrow{A}_{1,n}}{\overrightarrow{A}_{1,n}} = \lim_{w\to-\beta_{1,n}} \left\{ \frac{(w + \beta_{1,n})(1 - \beta_{1,n}/\beta_{1,n+1})(1 + \beta_{1,n}/\beta_{1,n})}{(w - \beta_{1,n})(1 - w/\beta_{1,n+1})(1 + w/\beta_{1,n})} \cdot \prod_{i=2}^{\infty} \left[\frac{(1 - j\beta_{1,n}/\xi_{i,n+1})(1 + j\beta_{1,n}/\xi_{i,n})}{(1 - jw/\xi_{i,n+1})(1 + jw/\xi_{i,n})}\right] \right\}$$

$$= -\left\{\frac{\beta_{1,n+1} - \beta_{1,n}}{\beta_{1,n+1} + \beta_{1,n}}\right\} \prod_{i=2}^{\infty} \left[\frac{(1 - j\beta_{1,n}/\xi_{i,n+1})(1 + j\beta_{1,n}/\xi_{i,n})}{(1 + j\beta_{1,n}/\xi_{i,n+1})(1 - j\beta_{1,n}/\xi_{i,n})}\right]$$

The infinite product has unit magnitude, and an argument given by

$$2P_{2,2}(\beta_{1,n}) = 2 \sum_{i=2}^{\infty} [\arctan(\beta_{1,n}/\xi_{i,n}) - \arctan(\beta_{1,n}/\xi_{i,n+1})]$$

as stated in the text.

Elements $S_{i'j'}$ $(i' \neq j')$ cannot be reduced in such an elementary fashion. Consider an expansion of the limit given in eqn. (38) of the text, viz

$$\lim_{w\to\beta_{1,n+1}} \left\{ \frac{(w - \beta_{1,n+1})(1 - \beta_{1,n}/\beta_{1,n+1})(1 + \beta_{1,n}/\beta_{1,n})}{(w - \beta_{1,n})(1 - w/\beta_{1,n+1})(1 + w/\beta_{1,n})} \cdot \prod_{i=2}^{\infty} \left[\frac{(1 - j\beta_{1,n}/\xi_{i,n+1})(1 + j\beta_{1,n}/\xi_{i,n})}{(1 - jw/\xi_{i,n+1})(1 + jw/\xi_{i,n})}\right] \right\}$$

The argument of S_{21} can be obtained immediately from this expression (apart from the negative sign in eqn. (38)). However, the infinite product form of the amplitude can be reduced further by taking the square root of terms such as

$$\left| \lim_{w\to\beta_{1,n+1}} \left[\frac{w - \beta_{1,n+1}}{F^{+}_{n+1}(w)}\right]^2 \right|$$

$$\lim_{w\to\beta_{1,n+1}} \left\{ \frac{\left|(w - \beta_{1,n+1})^2\right|}{\left|F_{n+1}(0)(1 - w/\beta_{1,n+1})^2\right| \left| \prod_{i=2}^{\infty} \left[(1 - jw/\xi_{i,n+1})\exp(jw/\xi_{i,n+1})\right]^2 \right|} \right\} \quad \ldots. \text{(A1)}$$

If $\beta_{1,n+1}$ and $\xi_{i,n+1}$ are real, then factors

$(1 - j\beta_{1,n+1}/\xi_{i,n+1})$ are equal in magnitude to $(1 + j\beta_{1,n+1}/\xi_{i,n+1})$. Consequently, by multiplying through by $(1 + w/\beta_{1,n+1})$, the R.H.S. of eqn. (A1) becomes

$$\lim_{w\to\beta_{1,n+1}} \left|\frac{w - \beta_{1,n+1}}{F_{n+1}(w)}\right| . \left|-2\beta_{1,n+1}\right| = \frac{2\beta_{1,n+1}}{\left|F'_{n+1}(\beta_{1,n+1})\right|} \quad \ldots. \text{(A2)}$$

Similarly, it can be shown that

$$\left|\left[F^{-}_{n}(\beta_{1,n})\right]^2\right| = 2\beta_{1,n} \left|F'_{n}(\beta_{1,n})\right| \quad \ldots. \text{(A3)}$$

$$\left|\left[F^{+}_{n+1}(\beta_{1,n})\right]^2\right| = \frac{\beta_{1,n+1} - \beta_{1,n}}{\beta_{1,n+1} + \beta_{1,n}} \left|F_{n+1}(\beta_{1,n})\right| \quad \ldots. \text{(A4)}$$

$$\lim_{w\to\beta_{1,n+1}} \left|\frac{1}{\left[F^{-}_{n}(w)\right]^2}\right| = \frac{\beta_{1,n+1} - \beta_{1,n}}{\beta_{1,n+1} + \beta_{1,n}} . \frac{1}{\left|F_{n}(\beta_{1,n+1})\right|} \quad \ldots. \text{(A5)}$$

Combining equations (A2) to (A5) in eqn. (38) of text, the amplitude given in eqn. (39) of the text is obtained.

The extension of this technique is straight forward when more than one mode propagates in either region. For example, if region n + 1 is dual-moded, then

$$\lim_{w\to\beta_{1,n+1}} \left| \left[\frac{w - \beta_{1,n+1}}{F^{+}_{n+1}(w)}\right]^2 \right| = \frac{2\beta_{1,n+1}}{\left|F_{n+1}(\beta_{1,n+1})\right|} . \frac{\beta_{1,n+1} + \beta_{2,n+1}}{\beta_{1,n+1} - \beta_{2,n+1}}$$

The following results are obtained for the H-plane scattering matrix, by taking the appropriate expressions for A(w) and B(w) (as defined in the text), and evaluating the residues associated with each propagating mode (as illustrated in Appendix 4A).

(i) For one propagating mode in each region,

$$\begin{bmatrix} \overleftarrow{A}_{1,n} \\ \overrightarrow{A}_{1,n+1} \end{bmatrix} = \begin{bmatrix} S_{11} & S_{12} \\ S_{21} & S_{22} \end{bmatrix} \begin{bmatrix} \overrightarrow{A}_{1,n} \\ \overleftarrow{A}_{1,n+1} \end{bmatrix} ;$$

where

$$S_{11} = \frac{\beta_{1,n+1} - \beta_{1,n}}{\beta_{1,n+1} + \beta_{1,n}} \cdot \exp[j\{\pi + 2P_{2,2}(\beta_{1,n})\}]$$

$$S_{22} = \frac{\beta_{1,n+1} - \beta_{1,n}}{\beta_{1,n+1} + \beta_{1,n}} \cdot \exp[-j2P_{2,2}(\beta_{1,n+1})]$$

$$S_{21} = \left\{\sqrt{\frac{k^2 - \beta_{1,n}^2}{k^2 - \beta_{1,n+1}^2}} \cdot \frac{\sin[(a\sqrt{k^2 - \beta_{1,n+1}^2} + \psi_h)/2]}{\sin[(a\sqrt{k^2 - \beta_{1,n}^2} + \psi_h)/2]} \cdot \sqrt{\left|\frac{F_n'(\beta_{1,n})\,F_{n+1}(\beta_{1,n})}{F_n(\beta_{1,n+1})\,F_{n+1}'(\beta_{1,n+1})}\right|}\right\}$$

$$\left\{\frac{2\sqrt{\beta_{1,n}\beta_{1,n+1}}}{\beta_{1,n} + \beta_{1,n+1}}\right\} \cdot \exp[j\{P_{2,2}(\beta_{1,n}) - P_{2,2}(\beta_{1,n+1})\}]$$

$$= \{U_{21}\} \cdot \{V_{21}\} \cdot \exp[j\alpha_{21}] \quad \text{(say)}$$

where U_{21} is the first set of terms bracketed $\{\ \}$

and V_{21} is the second set of terms bracketed $\{\ \}$

then

$$S_{12} = \frac{1}{U_{21}} \cdot V_{21} \cdot \exp[j\alpha_{21}]$$

(ii) For one propagating mode in the region $z < 0$ and two propagating modes in the region $z > 0$,

$$\begin{bmatrix} \overleftarrow{A}_{1,n} \\ \overrightarrow{A}_{1,n+1} \\ \overrightarrow{B}_{2,n+1} \end{bmatrix} = \begin{bmatrix} S_{11} & S_{12} & S_{13} \\ S_{21} & S_{22} & S_{23} \\ S_{31} & S_{32} & S_{33} \end{bmatrix} \begin{bmatrix} \overrightarrow{A}_{1,n} \\ \overleftarrow{A}_{1,n+1} \\ \overleftarrow{B}_{2,n+1} \end{bmatrix} ;$$

where

$$S_{11} = \frac{(\beta_{1,n+1} - \beta_{1,n})}{(\beta_{1,n+1} + \beta_{1,n})} \cdot \frac{(\beta_{1,n} - \beta_{2,n+1})}{(\beta_{1,n} + \beta_{2,n+1})} \cdot \exp\left[j\, 2\, P_{2,3}(\beta_{1,n})\right]$$

$$S_{12} = \left\{ \sqrt{\frac{k^2 - \beta_{1,n+1}^2}{k^2 - \beta_{1,n}^2}} \cdot \frac{\sin[(a\sqrt{k^2 - \beta_{1,n}^2} + \psi_h)/2]}{\sin[(a\sqrt{k^2 - \beta_{1,n+1}^2} + \psi_h)/2]} \cdot \sqrt{\left| \frac{F_n(\beta_{1,n+1})\, F'_{n+1}(\beta_{1,n+1})}{F'_n(\beta_{1,n})\, F_{n+1}(\beta_{1,n})} \right|} \right\} \cdot$$

$$\left\{ \frac{2\sqrt{\beta_{1,n}\, \beta_{1,n+1}}}{\beta_{1,n} + \beta_{1,n+1}} \sqrt{\frac{(\beta_{1,n+1} + \beta_{2,n+1})(\beta_{1,n} - \beta_{2,n+1})}{(\beta_{1,n+1} - \beta_{2,n+1})(\beta_{1,n} + \beta_{2,n+1})}} \right\} \exp\left[j\{P_{2,3}(\beta_{1,n}) - P_{2,3}(\beta_{1,n+1})\}\right]$$

$$= \{U_{12}\}\{V_{12}\} \exp[j\alpha_{12}] \qquad \textit{(say)}$$

then

$$S_{21} = \frac{1}{U_{12}} \cdot V_{12} \exp[j\alpha_{12}]$$

$$S_{13} = \left\{ \sqrt{\frac{k^2 - \beta_{2,n+1}^2}{k^2 - \beta_{1,n}^2}} \cdot \frac{\sin[(a\sqrt{k^2 - \beta_{1,n}^2} + \psi_h)/2]}{\sin[(a\sqrt{k^2 - \beta_{2,n+1}^2} - \psi_h)/2]} \cdot \sqrt{\left| \frac{F_n(\beta_{2,n+1})\, F'_{n+1}(\beta_{2,n+1})}{F'_n(\beta_{1,n})\, F_{n+1}(\beta_{1,n})} \right|} \right\} \cdot$$

$$\cdot \left\{ \frac{2\sqrt{\beta_{1,n}\, \beta_{2,n+1}}}{\beta_{1,n} + \beta_{2,n+1}} \cdot \sqrt{\frac{(\beta_{1,n+1} + \beta_{2,n+1})(\beta_{1,n+1} - \beta_{1,n})}{(\beta_{1,n+1} - \beta_{2,n+1})(\beta_{1,n+1} + \beta_{1,n})}} \right\} \exp\left[j\{P_{2,3}(\beta_{1,n}) - P_{2,3}(\beta_{2,n+1})\}\right]$$

$$= \{U_{13}\}\{V_{13}\} \exp[j\alpha_{13}]$$

then

$$S_{31} = \frac{1}{U_{13}} \cdot V_{13} \exp[j\alpha_{13}]$$

$$S_{22} = \frac{(\beta_{1,n+1} + \beta_{2,n+1})}{(\beta_{1,n+1} - \beta_{2,n+1})} \cdot \frac{(\beta_{1,n+1} - \beta_{1,n})}{(\beta_{1,n+1} + \beta_{1,n})} \cdot \exp\left[j\{\pi - 2P_{2,3}(\beta_{1,n+1})\}\right]$$

$$S_{23} = \left\{ \sqrt{\frac{k^2 - \beta_{2,n+1}^2}{k^2 - \beta_{1,n+1}^2}} \cdot \frac{\sin[(a\sqrt{k^2 - \beta_{1,n+1}^2} + \psi_h)/2]}{\sin[(a\sqrt{k^2 - \beta_{2,n+1}^2} - \psi_h)/2]} \cdot \sqrt{\left| \frac{F_n(\beta_{2,n+1})\, F'_{n+1}(\beta_{2,n+1})}{F_n(\beta_{1,n+1})\, F'_{n+1}(\beta_{1,n+1})} \right|} \right\} \cdot$$

$$\left\{ \frac{2\sqrt{\beta_{1,n+1}\, \beta_{2,n+1}}}{\beta_{1,n+1} - \beta_{2,n+1}} \cdot \sqrt{\frac{(\beta_{1,n+1} - \beta_{1,n})(\beta_{1,n} - \beta_{2,n+1})}{(\beta_{1,n+1} + \beta_{1,n})(\beta_{1,n} + \beta_{2,n+1})}} \right\} \exp\left[j\{-P_{2,3}(\beta_{1,n+1}) - P_{2,3}(\beta_{2,n+1})\}\right]$$

$$= \{U_{23}\}\{V_{23}\} \exp[j\alpha_{23}]$$

then

$$S_{32} = \frac{1}{U_{23}} \cdot V_{23} \exp[j\alpha_{23}]$$

$$S_{33} = \frac{\beta_{1,n+1} + \beta_{2,n+1}}{\beta_{1,n+1} - \beta_{2,n+1}} \cdot \frac{\beta_{1,n} - \beta_{2,n+1}}{\beta_{1,n} + \beta_{2,n+1}} \cdot \exp\left[j\left\{\pi - 2P_{2,3}(\beta_{2,n+1})\right\}\right]$$

(iii) For two propagating modes in each region,

$$\begin{bmatrix} \overleftarrow{A}_{1,n} \\ \overrightarrow{A}_{1,n+1} \\ \overleftarrow{B}_{2,n} \\ \overrightarrow{B}_{2,n+1} \end{bmatrix} = \begin{bmatrix} S_{11} & S_{12} & S_{13} & S_{14} \\ S_{21} & S_{22} & S_{23} & S_{24} \\ S_{31} & S_{32} & S_{33} & S_{34} \\ S_{41} & S_{42} & S_{43} & S_{44} \end{bmatrix} \begin{bmatrix} \overrightarrow{A}_{1,n} \\ \overleftarrow{A}_{1,n+1} \\ \overrightarrow{B}_{2,n} \\ \overleftarrow{B}_{2,n+1} \end{bmatrix};$$

where

$$S_{11} = \frac{(\beta_{1,n+1} - \beta_{1,n})}{(\beta_{1,n+1} + \beta_{1,n})} \cdot \frac{(\beta_{1,n} - \beta_{2,n+1})(\beta_{1,n} + \beta_{2,n})}{(\beta_{1,n} + \beta_{2,n+1})(\beta_{1,n} - \beta_{2,n})} \cdot \exp\left[j\left\{\pi + 2P_{3,3}(\beta_{1,n})\right\}\right]$$

$$S_{12} = \left\{\sqrt{\frac{k^2 - \beta_{1,n+1}^2}{k^2 - \beta_{1,n}^2}} \cdot \frac{\sin\left[(a\sqrt{k^2 - \beta_{1,n}^2} + \psi_h)/2\right]}{\sin\left[(a\sqrt{k^2 - \beta_{1,n+1}^2} + \psi_h)/2\right]} \cdot \sqrt{\left|\frac{F_n(\beta_{1,n+1}) \cdot F'_{n+1}(\beta_{1,n+1})}{F'_n(\beta_{1,n}) \cdot F_{n+1}(\beta_{1,n})}\right|}\right\}$$

$$\cdot \left\{\frac{2\sqrt{\beta_{1,n}\beta_{1,n+1}}}{\beta_{1,n} + \beta_{1,n+1}} \cdot \sqrt{\frac{(\beta_{1,n+1} + \beta_{2,n+1})(\beta_{1,n+1} - \beta_{1,n})(\beta_{1,n} - \beta_{2,n+1})(\beta_{1,n} + \beta_{2,n})}{(\beta_{1,n+1} - \beta_{2,n+1})(\beta_{1,n+1} + \beta_{1,n})(\beta_{1,n} + \beta_{2,n+1})(\beta_{1,n} - \beta_{2,n})}}\right\}$$

$$\cdot \exp\left[j\left\{P_{3,3}(\beta_{1,n}) - P_{3,3}(\beta_{1,n+1})\right\}\right]$$

$$= \left\{U_{12}\right\} \cdot \left\{V_{12}\right\} \cdot \exp\left[j\alpha_{12}\right]$$

then

$$S_{21} = \frac{1}{U_{12}} \cdot V_{12} \cdot \exp\left[j\alpha_{12}\right]$$

$$S_{13} = \left\{\sqrt{\frac{k^2 - \beta_{2,n}^2}{k^2 - \beta_{1,n}^2}} \cdot \frac{\sin\left[(a\sqrt{k^2 - \beta_{1,n}^2} + \psi_h)/2\right]}{\sin\left[(a\sqrt{k^2 - \beta_{2,n}^2} - \psi_h)/2\right]} \cdot \sqrt{\left|\frac{F_{n+1}(\beta_{2,n})\, F'_n(\beta_{2,n})}{F_{n+1}(\beta_{1,n})\, F'_n(\beta_{1,n})}\right|}\right.$$

$$\cdot \left\{\frac{2\sqrt{\beta_{1,n} \cdot \beta_{2,n}}}{\beta_{1,n} - \beta_{2,n}} \sqrt{\frac{(\beta_{1,n+1} - \beta_{1,n})(\beta_{1,n+1} - \beta_{2,n})(\beta_{1,n} - \beta_{2,n})(\beta_{2,n+1} - \beta_{2,n})}{(\beta_{1,n+1} + \beta_{1,n})(\beta_{1,n+1} + \beta_{2,n})(\beta_{1,n} + \beta_{2,n})(\beta_{2,n+1} + \beta_{2,n})}}\right\}$$

$$\cdot \exp\left[j\left\{P_{3,3}(\beta_{2,n}) + P_{3,3}(\beta_{1,n})\right\}\right]$$

$$= \{ U_{13} \} \cdot \{ V_{13} \} \quad \exp\left[j \alpha_{13} \right]$$

then

$$S_{31} = \frac{1}{U_{13}} \cdot V_{13} \quad \exp\left[j \alpha_{13} \right]$$

$$S_{14} = \left\{ \sqrt{\frac{k^2 - \beta_{2,n+1}^2}{k^2 - \beta_{1,n}^2}} \cdot \frac{\sin\left[\left(a\sqrt{k^2 - \beta_{1,n}^2} + \psi_h\right)/2 \right]}{\sin\left[\left(a\sqrt{k^2 - \beta_{2,n+1}^2} - \psi_h\right)/2 \right]} \cdot \sqrt{\left| \frac{F_n(\beta_{2,n+1})\, F'_{n+1}(\beta_{2,n+1})}{F'_n(\beta_{1,n})\, F_{n+1}(\beta_{1,n})} \right|} \right\}$$

$$\cdot \left\{ \frac{2\sqrt{\beta_{1,n} \cdot \beta_{2,n+1}}}{\beta_{1,n} + \beta_{2,n+1}} \cdot \sqrt{\frac{(\beta_{1,n+1} + \beta_{2,n+1})(\beta_{2,n+1} - \beta_{2,n})}{(\beta_{1,n+1} - \beta_{2,n+1})(\beta_{2,n+1} + \beta_{2,n})}} \right.$$

$$\left. \cdot \sqrt{\frac{(\beta_{1,n} + \beta_{2,n})(\beta_{1,n+1} - \beta_{1,n})}{(\beta_{1,n} - \beta_{2,n})(\beta_{1,n+1} + \beta_{1,n})}} \right\}$$

$$\cdot \exp\left[j \{ P_{3,3}(\beta_{1,n}) - P_{3,3}(\beta_{2,n+1}) \} \right]$$

$$= \{ U_{14} \} \cdot \{ V_{14} \} \cdot \exp\left[j \alpha_{14} \right]$$

then

$$S_{41} = \frac{1}{U_{14}} \cdot V_{14} \cdot \exp\left[j \alpha_{14} \right]$$

$$S_{22} = \frac{(\beta_{1,n+1} + \beta_{2,n+1})(\beta_{1,n+1} - \beta_{1,n})(\beta_{1,n+1} - \beta_{2,n})}{(\beta_{1,n+1} - \beta_{2,n+1})(\beta_{1,n+1} + \beta_{1,n})(\beta_{1,n+1} + \beta_{2,n})} \cdot \exp\left[-2j\, P_{3,3}(\beta_{1,n+1}) \right]$$

$$S_{23} = \left\{ \sqrt{\frac{k^2 - \beta_{2,n}^2}{k^2 - \beta_{1,n+1}^2}} \cdot \frac{\sin\left[\left(a\sqrt{k^2 - \beta_{1,n+1}^2} + \psi_h\right)/2 \right]}{\sin\left[\left(a\sqrt{k^2 - \beta_{2,n}^2} - \psi_h\right)/2 \right]} \sqrt{\left| \frac{F_{n+1}(\beta_{2,n})\, F'_n(\beta_{2,n})}{F'_{n+1}(\beta_{1,n+1})\, F_n(\beta_{1,n+1})} \right|} \right\}$$

$$\cdot \left\{ \frac{2\sqrt{\beta_{2,n} \cdot \beta_{1,n+1}}}{\beta_{2,n} + \beta_{1,n+1}} \cdot \sqrt{\frac{(\beta_{1,n+1} + \beta_{2,n+1})(\beta_{1,n+1} - \beta_{1,n})}{(\beta_{1,n+1} - \beta_{2,n+1})(\beta_{1,n+1} + \beta_{1,n})}} \right.$$

$$\left. \cdot \sqrt{\frac{(\beta_{1,n} + \beta_{2,n})(\beta_{2,n+1} - \beta_{2,n})}{(\beta_{1,n} - \beta_{2,n})(\beta_{2,n+1} + \beta_{2,n})}} \right\}$$

$$\cdot \exp\left[j \{ \pi + P_{3,3}(\beta_{2,n}) - P_{3,3}(\beta_{1,n+1}) \} \right]$$

i.e.

$$S_{23} = \{ U_{23} \} \cdot \{ V_{23} \} \cdot \exp[j\alpha_{23}]$$

then

$$S_{32} = \frac{1}{U_{23}} \cdot V_{23} \exp[j\alpha_{23}]$$

$$S_{24} = \left\{ \sqrt{\frac{k^2 - \beta^2_{2,n+1}}{k^2 - \beta^2_{1,n+1}}} \cdot \frac{\sin[(a\sqrt{k^2 - \beta^2_{1,n+1}} + \psi_h)/2]}{\sin[(a\sqrt{k^2 - \beta^2_{2,n+1}} - \psi_h)/2]} \sqrt{\left| \frac{F'_{n+1}(\beta_{2,n+1}) F_n(\beta_{2,n+1})}{F'_{n+1}(\beta_{1,n+1}) F_n(\beta_{1,n+1})} \right|} \right\}$$

$$\cdot \left\{ \frac{2\sqrt{\beta_{1,n+1}\beta_{2,n+1}}}{\beta_{1,n+1} - \beta_{2,n+1}} \cdot \sqrt{\frac{(\beta_{1,n+1} - \beta_{1,n})(\beta_{1,n+1} - \beta_{2,n})(\beta_{1,n} - \beta_{2,n+1})(\beta_{2,n+1} - \beta_{2,n})}{(\beta_{1,n+1} + \beta_{1,n})(\beta_{1,n+1} + \beta_{2,n})(\beta_{1,n} + \beta_{2,n+1})(\beta_{2,n+1} - \beta_{2,n})}} \right\}$$

$$\cdot \exp[j\{\pi - P_{3,3}(\beta_{1,n+1}) - P_{3,3}(\beta_{2,n+1})\}]$$

$$= \{ U_{24} \} \cdot \{ V_{24} \} \cdot \exp[j\alpha_{24}]$$

then

$$S_{42} = \frac{1}{U_{24}} \cdot V_{24} \cdot \exp[j\alpha_{24}]$$

$$S_{33} = \frac{(\beta_{1,n+1} - \beta_{2,n})(\beta_{2,n+1} - \beta_{2,n})(\beta_{1,n} + \beta_{2,n})}{(\beta_{1,n+1} + \beta_{2,n})(\beta_{2,n+1} + \beta_{2,n})(\beta_{1,n} - \beta_{2,n})} \cdot \exp[j\{\pi + 2P_{3,3}(\beta_{2,n})\}]$$

$$S_{34} = \left\{ \sqrt{\frac{k^2 - \beta^2_{2,n+1}}{k^2 - \beta^2_{2,n}}} \cdot \frac{\sin[(a\sqrt{k^2 - \beta^2_{2,n}} - \psi_h)/2]}{\sin[(a\sqrt{k^2 - \beta^2_{2,n+1}} - \psi_h)/2]} \sqrt{\left| \frac{F_n(\beta_{2,n+1}) F'_{n+1}(\beta_{2,n+1})}{F'_n(\beta_{2,n}) F_{n+1}(\beta_{2,n})} \right|} \right\}$$

$$\cdot \left\{ \frac{2\sqrt{\beta_{2,n} \cdot \beta_{2,n+1}}}{\beta_{2,n} + \beta_{2,n+1}} \sqrt{\frac{(\beta_{1,n+1} + \beta_{2,n+1})(\beta_{1,n} - \beta_{2,n+1})(\beta_{1,n} + \beta_{2,n})(\beta_{1,n+1} - \beta_{2,n})}{(\beta_{1,n+1} - \beta_{2,n+1})(\beta_{1,n} + \beta_{2,n+1})(\beta_{1,n} - \beta_{2,n})(\beta_{1,n+1} + \beta_{2,n})}} \right\}$$

$$\cdot \exp[j\{ P_{3,3}(\beta_{2,n}) - P_{3,3}(\beta_{2,n+1}) \}]$$

$$= \{ U_{34} \} \{ V_{34} \} \cdot \exp[j\alpha_{34}]$$

then

$$S_{43} = \frac{1}{\sqcup_{34}} \cdot V_{34} \cdot \exp\left[j\alpha_{34}\right]$$

and

$$S_{44} = \frac{(\beta_{1,n+1} + \beta_{2,n+1})(\beta_{1,n} - \beta_{2,n+1})(\beta_{2,n+1} - \beta_{2,n})}{(\beta_{1,n+1} - \beta_{2,n+1})(\beta_{1,n} + \beta_{2,n+1})(\beta_{2,n+1} + \beta_{2,n})} \cdot \exp\left[-j\,P_{3,3}(\beta_{2,n+1})\right]$$

APPENDIX 4C

The 2 X 2 scattering matrix in the E-plane is given by

$$\begin{bmatrix} \overleftarrow{C}_{1,n} \\ \overrightarrow{C}_{1,n+1} \end{bmatrix} = \begin{bmatrix} S_{11} & S_{12} \\ S_{21} & S_{22} \end{bmatrix} \begin{bmatrix} \overrightarrow{C}_{1,n} \\ \overleftarrow{C}_{1,n+1} \end{bmatrix}$$

where $S_{11} = \dfrac{\beta_{1,n} - \beta_{1,n+1}}{\beta_{1,n} + \beta_{1,n+1}} \cdot \exp[j2P_{2,2}(\beta_{1,n})]$

$$S_{22} = \frac{\beta_{1,n} - \beta_{1,n+1}}{\beta_{1,n} + \beta_{1,n+1}} \cdot \exp[j\{\pi - 2P_{2,2}(\beta_{1,n+1})\}]$$

$$S_{21} = \left\{\frac{\sin[(\psi_e + a\sqrt{k^2-\beta^2_{1,n+1}})/2]}{\sin[(\psi_e + a\sqrt{k^2-\beta^2_{1,n}})/2]} \cdot \sqrt{\left|\frac{G_{n+1}(\beta_{1,n})G'_n(\beta_{1,n})}{G'_{n+1}(\beta_{1,n+1})G_n(\beta_{1,n+1})}\right|}\right\}$$

$$\cdot\left\{\frac{2\sqrt{\beta_{1,n}\beta_{1,n+1}}}{\beta_{1,n} + \beta_{1,n+1}}\right\} \exp[j\{P_{2,2}(\beta_{1,n}) - P_{2,2}(\beta_{1,n+1})\}]$$

$$= \{U_{21}\}\{V_{21}\} \exp[j\alpha_{21}] \quad \text{say}$$

then $S_{12} = \dfrac{1}{U_{21}} \cdot V_{21} \cdot \exp[j\alpha_{21}]$

Note that

$$|S_{11}| \cdot |S_{22}| = 1 - |S_{21}| \cdot |S_{12}|$$

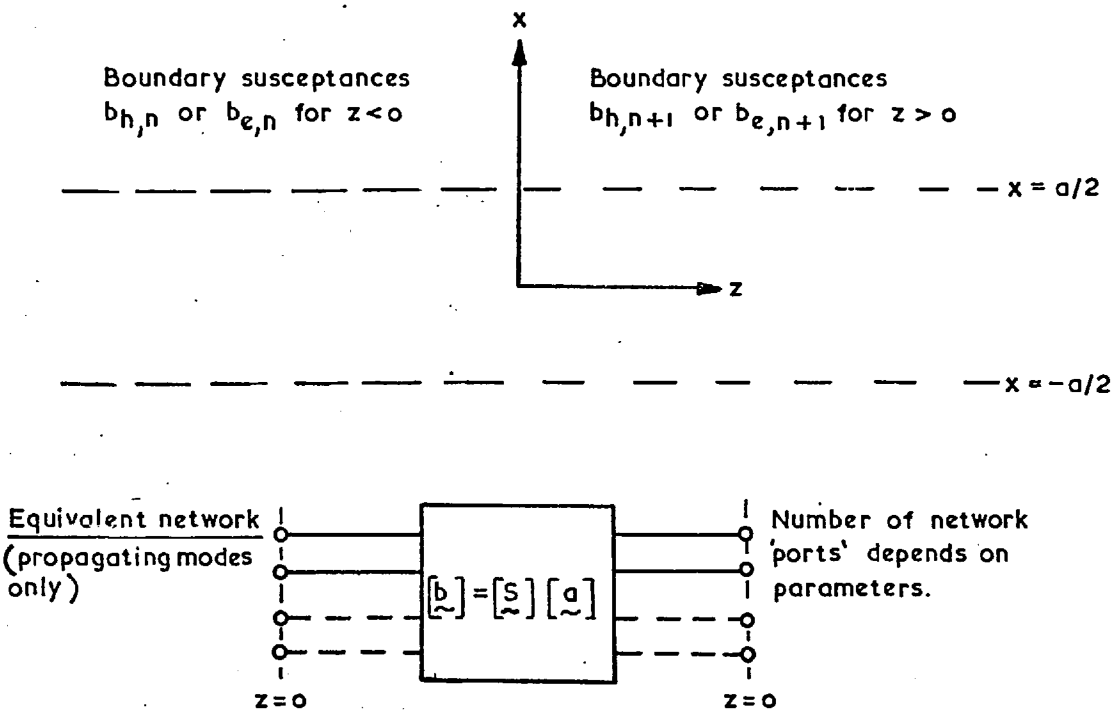

In H-plane: E_y continuous across boundaries.

H_z discontinuity across boundaries $\propto b_h$.

In E-plane: E_z continuous across boundaries.

H_y discontinuity across boundaries $\propto b_e$.

Fig. 4.1 Reduced boundary value problem in a periodically excited infinite array structure.

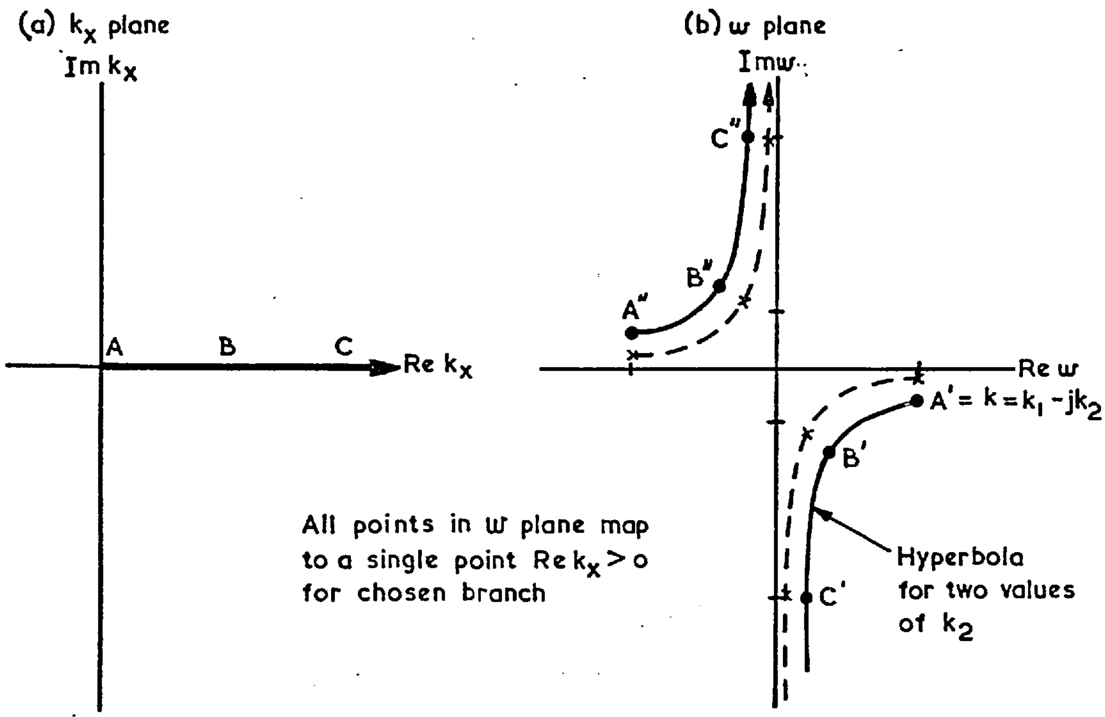

Fig. 4.2 Loci in w plane corresponding to line ABC in k_x plane, as a function of k_2.

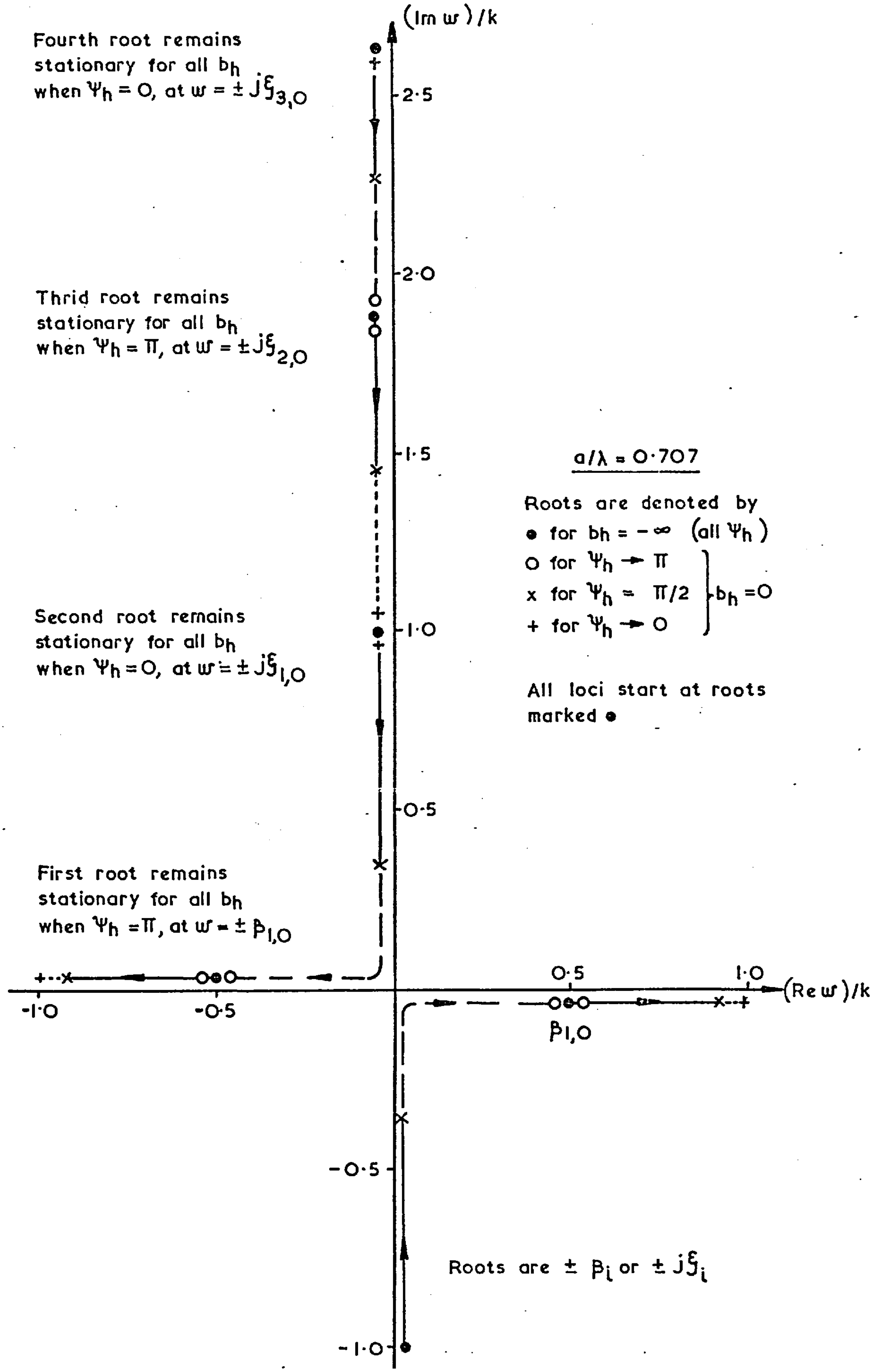

Fig. 4.3 Limits of root loci in w-plane determined by waveguide to free space discontinuity (Roots offset from axes for clarity)

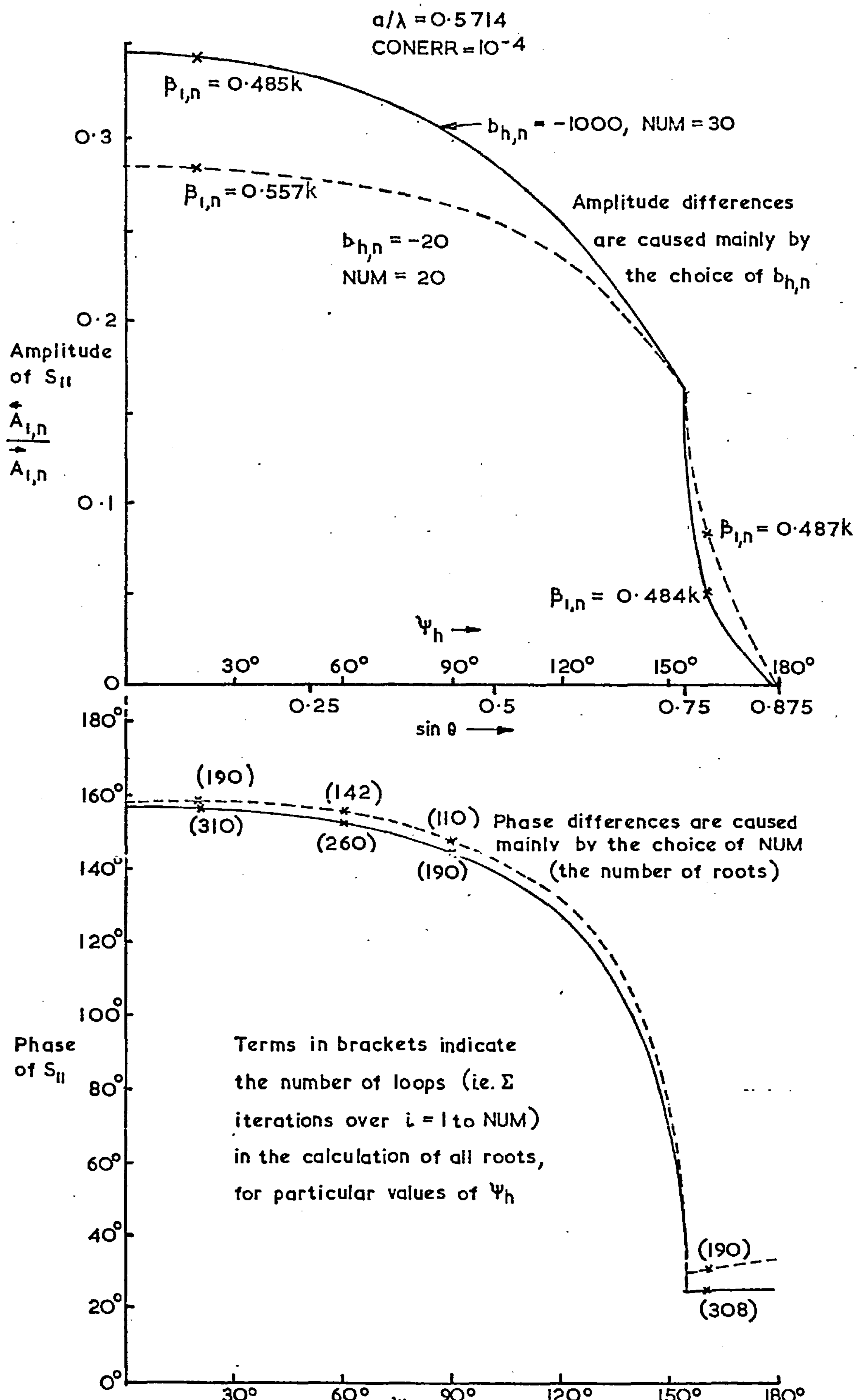

Fig. 4.4 Calculated H-plane reflection coefficients for finite susceptance to free space discontinuity (i.e. $b_{h,n+1}=0$). The continuous curves are indistinguishable from the results for a waveguide array as given by Wu and Galindo (references 4,43).

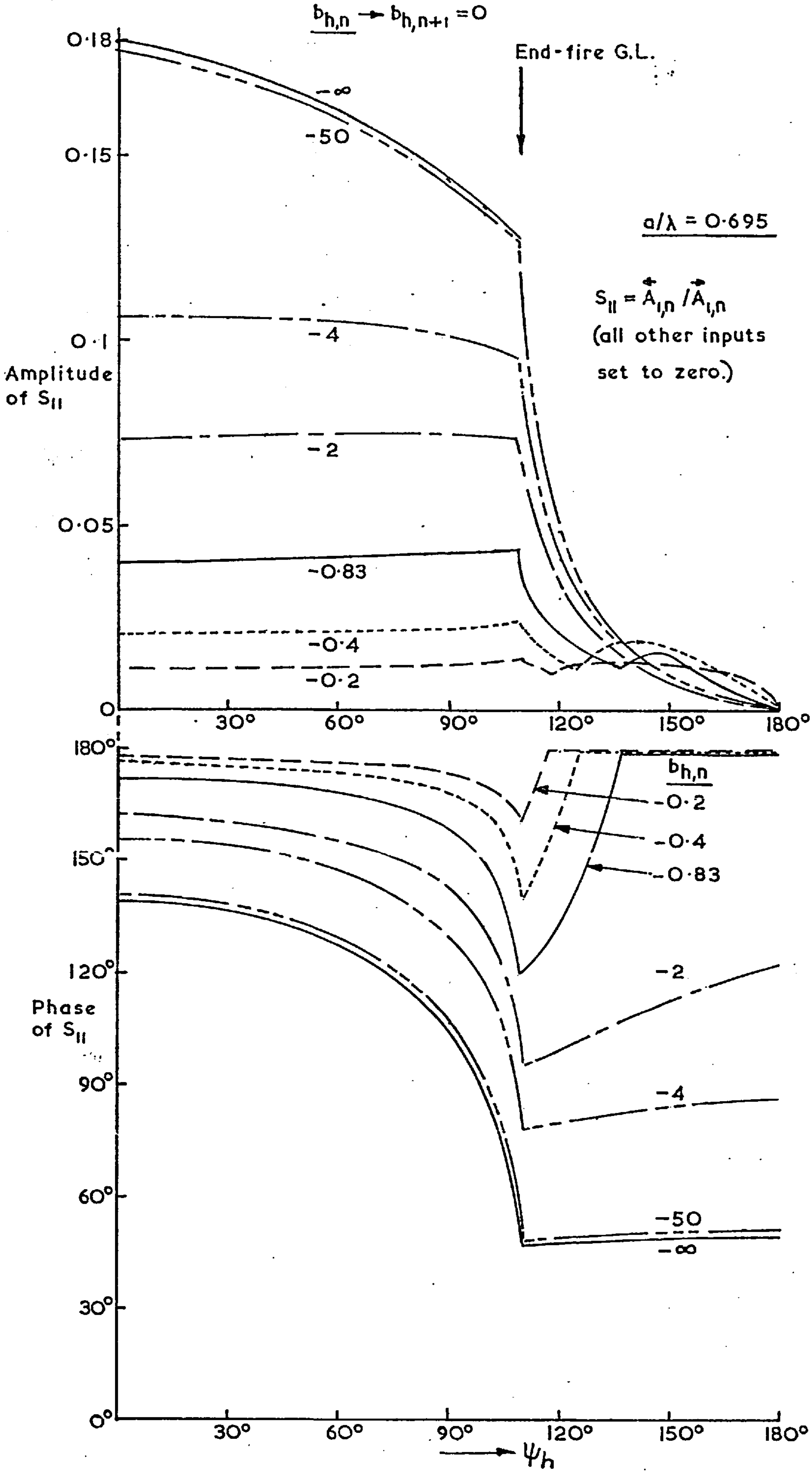

Fig. 4.5 Dominant mode reflection coefficient for junction $b_{h,n}$ to $b_{h,n+1} = 0$ (free space), with $a/\lambda = 0.695$.

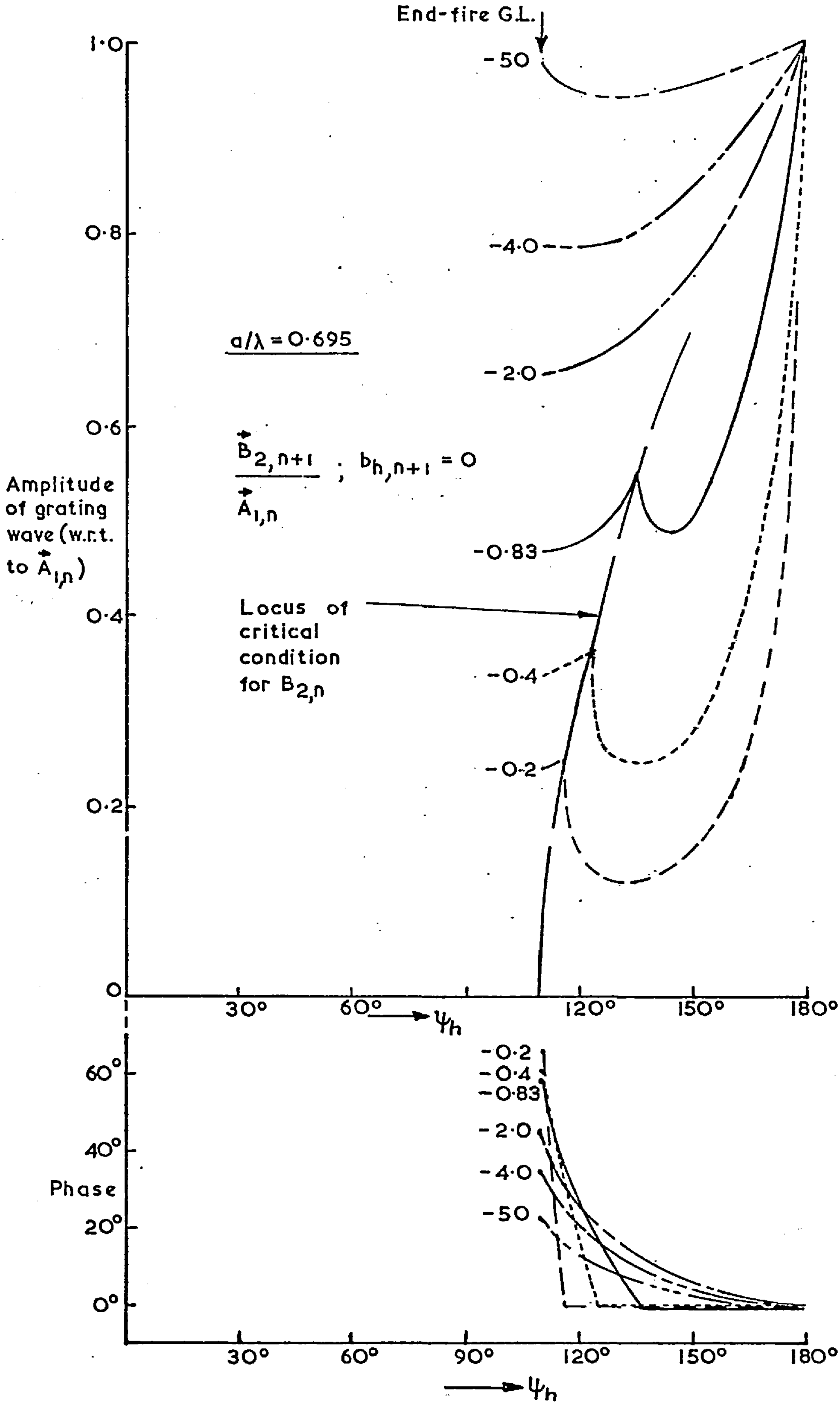

Fig. 4.6 Calculated amplitude and phase of $\vec{B}_{2,n+1}/\vec{A}_{1,n}$ for finite susceptance to free space junction discontinuities, $a/\lambda = 0.695$.

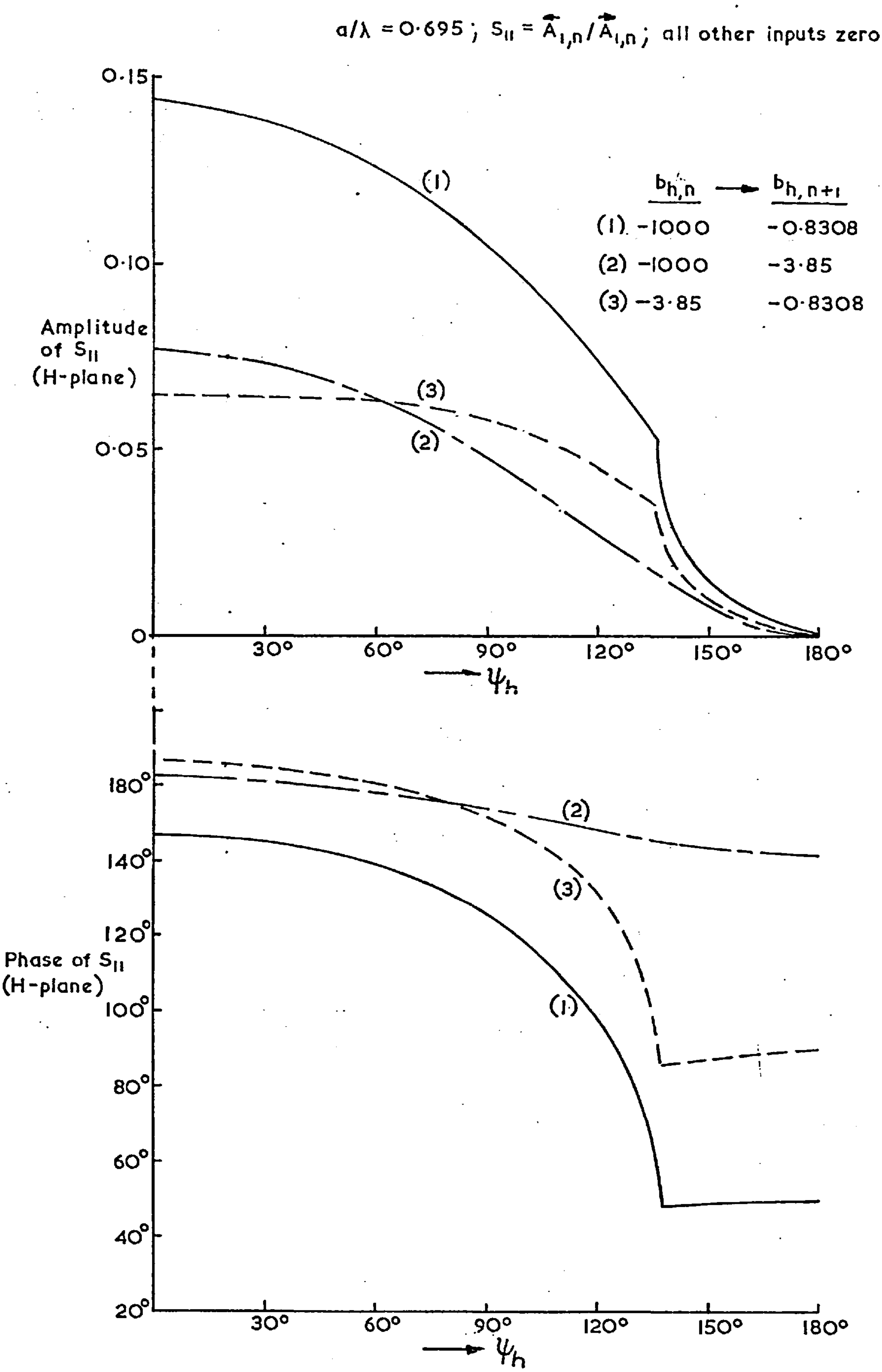

Fig. 4.7 Amplitude and phase of the dominant mode reflection coefficient (S_{11}) for H-plane susceptance discontinuities ($a/\lambda = 0.695$)

CHAPTER 5

H-PLANE MEASUREMENTS USING AN INFINITE-ARRAY WAVEGUIDE SIMULATOR

5.1. Introduction

The experimental investigation described in this chapter was undertaken to examine two related topics, viz

(i) the limitations imposed by the periodic character of practical reactive boundaries,

and

(ii) the requirement for small susceptances in the H-plane.

These topics were highlighted in Chapter 3 (Section 3.7.2, para.(ii)) as basic problems affecting element pattern control in the H-plane. The work described in this chapter makes use of the theoretical results derived in Chapter 4, and provides the experimental justification for proceeding with the analysis of multi-section transitions (in Chapter 6).

The one and a half element C-band waveguide simulator shown in Fig.5.1 was developed as the primary experimental apparatus. Its transmission and reflection properties are equivalent to those of an infinite array with element phasing $\psi_h = 120^\circ$. The design and calibration of the experimental equipment are summarised in Section 5.2. A comparison of theoretical and measured grating wave suppression for a waveguide array shows agreement to within 1% at all frequencies.

Subsequently, it is established that the grating wave suppression offered by realisable H-plane boundaries is affected adversely by axial Floquet modes. Performance consistent with the theoretical results obtained in Chapter 4 can be achieved when the boundary periodicity (i.e. d/λ in Figs.3.31 to 3.33) is small in relation to the element separation (a/λ). The experimental results indicate that d/a should not exceed a value of 0.25 if satisfactory agreement with theory is required.

This restriction magnifies the practical difficulties in obtaining small inductive susceptances near the array aperture (cf. Section 3.5.2).

In the case of boundaries formed from uniformly spaced conducting posts, the cross-sectional radii required to achieve values of $b_h \sim -1$ become quite unrealistic. However, a dielectric substrate providing mechanical support offers the additional advantage (mainly because of its shunt capacitance) of more realistic conductor dimensions. It is shown that the properties of conducting grids printed on low loss dielectrics such as alumina can be predicted accurately from the separately known results for the inductance of the grid and the capacitance of the dielectric sheet. Boundaries of this construction must remain inductive overall to prevent slow wave propagation within an H-plane array transition. A bandwidth penalty is incurred as the thickness of the dielectric substrate is increased.

5.2. Design and Calibration of the Waveguide Simulator

Recourse to simulation techniques in closed waveguide structures was considered necessary to clarify some of the major problems revealed by the feasibility study with the lens. As indicated in Section 3.1, simulation of an infinite array environment by imaging a small number of elements in the walls of a waveguide is a standard experimental technique (64).

The principal concepts behind the technique were first published in 1965 by Hannan and Balfour (62), and have been noted in the introduction to Chapter 3. For the one and a half element simulator shown in Fig.5.1, it suffices to consider an infinite array excited by two sets of coherent generators with phasings for the "r"th element given by $2\pi r/3$ and $(\pi - 2\pi r)/3$. As shown in Fig.5.2, this excitation guarantees a null field on the planes $x = a/2$ and $-a$ for all values of boundary susceptance b_h. Consequently, the presence of conducting boundaries at these two planes does not perturb the fields associated with propagating or evanescent modes of the infinite array. This property permits the reflection and transmission coefficients, for $\psi_h = 120^\circ$, to be determined from measurements within the resulting closed structure. The two "mainbeams" and the two "grating waves" become the TE_{10} and TE_{20} modes respectively across the $1\frac{1}{2}$ element aperture $x = -a$ to $x = a/2$ (see Fig.5.2).

The principal experimental requirements and their influence on the design can be summarised as follows:-

(i) By contrast with the lens, the simulator was conceived as a precision device, affording a direct and accurate comparison between theory and experiment. With the automatic elimination of edge effects, this objective was achieved by electroforming all waveguide components and ensuring high standards of mechanical assembly.

(ii) With interest in the H-plane centred on element pattern control, dual mode operation in the region beyond the aperture was essential. A "looking out" type simulator (equivalent to a transmitting array (64)) was therefore chosen to avoid any requirement for higher-order mode launchers. With the "half" element cut-off in an initial region of infinite boundary susceptance, excitation of the simulator could be achieved quite simply, by applying the TE_{10} mode to the "complete" element.

(iii) To enhance the flexibility of the simulator, the array portion was constructed in two parts separating along the element boundary (i.e. $x = -a/2$ in Fig.5.2). The disassembled feed is shown in Fig.5.3. The axial flanges, machined from copper bars as matching pairs, were held in contact with their respective mandrels during the subsequent copper deposition process to become integral parts of the final electroformed components. For measurements taken under infinite array conditions, the reactive boundary structures could then be clamped accurately by these flanges in the manner indicated by Fig.5.3. (As an aid to electricl continuity, a very thin film of semi-fluid silver resin was applied to the flanges prior to each assembly of the feed section.)

(iv) To permit greater design freedom without sacrificing accuracy, the element boundaries were chemically milled from 0.25mm beryllium copper sheets (see Figs.5.1 and 5.3). Working to modern commercial standards, this double-sided etching process could provide conducting "posts" of approximately hexagonal cross-section (see Fig.5.4). A dimensional accuracy of 0.025mm was maintained during manufacture, which was consistent with assembly requirements.

The restriction to a single scan condition (corresponding to $\psi_h = 120^{\circ}$ at any frequency) was the most obvious limitation of the one and a half element simulator (cf. Section 3.1). However, the additional complexity and expense of a set of "looking in" type simulators (64) or a multi-element "looking out" type simulator (107), for examining more than one scan condition, could not be justified. [It should be noted that a relatively large number of elements would be needed in a multi-element structure to examine two or three scan conditions with a visible grating wave. Furthermore, as the novel approach described by Gustincic (107) - involving the measurement of N coupling coefficients in an N element simulator - only yields information about the active reflection coefficient, simultaneous excitation of all elements remains a basic requirement when measuring the relative grating wave suppression.]

An element separation of 47.78mm (which includes an allowance of 0.25mm for the thickness of the element boundary) was adopted to provide a normal flange connection with a WR12 waveguide bench. Some of the resulting characteristics of the simulator are summarised by Fig.5.5, including the main beam and grating wave angles as a function of frequency and the theoretical limits of dual beam radiation (viz $4.19\text{GHz} < f < 6.3\text{GHz}$). [In practice, accurate measurements could not be obtained at the lower end of this band, where the TE_{20} mode was increasingly difficult to terminate in a broadband load of reasonable length (see below).]

The measurement of the main beam and grating wave amplitudes was accomplished with a single probe connected to the test channel of a network analyser. The probe was inserted sequentially in each of three equispaced transverse locations affording positional accuracies, i.e. in plan and in depth of penetration, of 0.02mm (Fig.5.1). Care was taken in the design of the probe to prevent any significant disturbance of the fields within the simulator. (Field perturbations could not be detected experimentally.) The measuring technique enabled a phasor diagram to be constructed showing the amplitude and phase of the TE_{20} mode relative to the TE_{10} mode in the plane of the probe locations. As shown in Fig.5.6, this "three probe technique" provided redundant data, which could then be used to monitor the measuring accuracy. The probes were sufficiently remote from the aperture plane discontinuity to ensure that evanescent grating waves (i.e. the TE_{no} modes, $n > 3$) had become insignificant. With all flanges dowelled to preserve the alignment of the waveguide walls, no cross-mode coupling within a 400mm length of the simulator guide could be detected.

For the evaluation of boundary structures, single mode conditions were maintained within the array feed to minimise the number of parameters affecting performance. This lead to an upper limit on frequency dictated by the critical susceptance for the second mode, i.e.

$$b_{hc} = 2 \left\{ \frac{\cos(2\pi a/\lambda) + 0.5}{\sin(2\pi a/\lambda)} \right\} \qquad \text{.... (1)}$$

which is plotted in Fig.5.7 for a = 47.78mm. Working within this limit, the expected amplitude of the grating wave relative to the main beam was given by

$$\left| \frac{\vec{B}_{2,1}}{\vec{A}_{2,1}} \right| = \sqrt{\frac{(\beta^2_{1,1} - \beta^2_{1,0})}{(\beta^2_{1,0} - \beta^2_{2,1})}} \qquad \text{.... (2)}$$

with the regions either side of the aperture designated by subscripts 0 and 1. This simple expression can be obtained from the 3 X 3 scattering matrix given in Appendix 4B, as the ratio of $|S_{31}/S_{21}|$. It is derived in Appendix 5A.

An alternative form of eqn.(2) can be obtained by noting that

$$\beta^2_{1,1} = k^2 - (\psi_h/a)^2 \qquad \text{.... (3a)}$$

$$\beta^2_{2,1} = k^2 - [(2\pi-\psi_h)/a]^2 \qquad \text{.... (3b)}$$

and $$(\beta_{1,0}a)^2 = (ka)^2 - (k_x a)^2_1 \qquad \text{.... (3c)}$$

where $(k_x a)_1$ is the dominant mode solution of the H-plane characteristic equation (eqn.(14), Chapter 2) within the feed region. Substituting in eqn.(2), it immediately follows that

$$\left|\frac{\vec{B}_{2,1}}{\vec{A}_{1,1}}\right| = \sqrt{\frac{(k_x a)^2_1 - \psi_h{}^2}{(2\pi-\psi_h)^2 - (k_x a)^2_1}} \qquad \text{.... (4)}$$

In Fig.5.8, the theoretical relationships between the element boundary susceptance b_h, $(k_x a)_1$, and $|\vec{B}_{2,1}/\vec{A}_{1,1}|$ are given for a frequency of 4.375GHz. At any other frequency within the limits defined in Fig.5.7, it is necessary (in general) to recalculate $(k_x a)_1$, to find $|\vec{B}_{2,1}/\vec{A}_{1,1}|$. However, for boundary structures with b_h proportional to frequency, e.g. the parallel wire grid, with $r \ll d \ll \lambda$ (cf. eqn.(16), Chapter 3) and

$$b_h \approx -\frac{\lambda}{d}\left[\ln\left(\frac{d}{2\pi r}\right)\right]^{-1}, \qquad \text{.... (5)}$$

$(k_x a)_1$ is independent of frequency and the ratio $|\vec{B}_{2,1}/\vec{A}_{1,1}|$ remains constant. For a conventional waveguide array, $(k_x a)_1 = \pi$, and the relative amplitude of the grating wave is simply $\sqrt{5/7}$ (0.845) for $\psi_h = 2\pi/3$.

Preliminary calibration tests at 3.95GHz (i.e. a frequency below TE_{20} mode cut-off) indicated that the fields detected at the probe locations were consistent with single mode theory to an "accuracy" of $\pm$0.05dB in amplitude and $\pm 1^{\circ}$ in phase - i.e. to limits within the specified resolution of the network analyser. Overall calibration of the simulator for subsequent measurement of $|\vec{B}_{2,1}/\vec{A}_{1,1}|$ was then accomplished using a set of waveguide element boundaries. The results are given in Fig.5.9 for the frequency range 4.25GHz to 4.7GHz. Apart from the close agreement between theory and measurement, the significant feature of Fig.5.9 is the complication caused by the imperfect TE_{20} mode termination at frequencies below 4.4GHz. The dotted regions of "experimental uncertainty" correspond to the peak amplitude and phase fluctuations observed at probe positions 1 and 3 (see Fig.5.6) during sliding load tests. [The combination load developed for this purpose is shown in Fig.5.1. Its TE_{10} V.S.W.R. was less than 1.01 at all frequencies, for any relative setting of the two wedges.] At 4.25GHz, the TE_{20} reflection coefficient was sufficiently small (i.e. < 0.15) to ensure that the coupling between $\overleftarrow{B}_{2,1}$ and $\vec{A}_{1,1}$ at the aperture remained undetectable. Using the sliding load technique, it was therefore possible to extend the frequency range from f = 4.4GHz to approximately 4.25GHz by estimating the "mean" value of the vector field at probes 1 and 3. Below 4.25GHz, however, the wavelength of the TE_{20} mode became too long to observe the extremes of amplitude and phase with the total available length of overmoded guide.

The sliding load technique has been utilised where necessary to obtain the simulator results given in the next section.

5.3. The Effects of Element Boundary Periodicity

Prior to the simulator tests with periodic boundary structures, chemically milled samples were produced which could be characterised in a WR12 waveguide bench. The two configurations examined initially are sketched in Fig.5.10, and are identified below as "parallel-post" or "inclined-post" structures.

In the case of the parallel-post structures, slotted-line measurements of network susceptance were undertaken for calibration purposes.

Batches of cross-guide septa with d = 23.77mm and 11.88mm (i.e. constrained as indicated in Fig.5.10) were tested at discrete frequencies between 4GHz and 5GHz, and the results compared with the theoretical values for cylindrical posts of radius r = 0.12mm (cf. eqns.(16) and (17) Chapter 3). With f = 4.375GHz, the measured spread in the "far field" susceptances (b_h) was less than 4%, as indicated by the following table:-

d/λ	Measured values (Upper and lower) (limits for batches of 6)	Theoretical value
0.347	-0.80 to -0.84	-0.82
0.173	-2.10 to -2.23	-2.14

Referring to Fig.5.11, it is seen that these (typical) results corresponded to an effective tolerance of $\pm$0.02mm on the radii of cylindrical posts, and confirmed the accuracy of the chemical milling process.

Similar tests with "inclined post" septa indicated that the susceptance became smaller (for posts of constant average separation and "radius") as the angle of inclination of the posts θ_p in Fig.5.10 was increased in relation to the incident electric field. For example, at 4.375GHz, the variation in average b_h for "two-post" septa (d/λ = 0.347) was as follows:-

θ_p	b_h	
0^o	-0.82	
14^o	-0.74	
28^o	-0.65	
40^o	∿-0.35	Measurements made with 0.25mm dia. copper wire clamped between flanges
45^o	∿-0.15	

On the assumption that the unknown susceptance of inclined cylindrical wire gratings, with

$$b_h = F(\lambda/d,\ d/r,\ \theta',\ \theta_p,\ \lambda/d_p), \qquad \dots . (6)$$

might approximate to a relation of the form

$$b_h = -\frac{\lambda}{d} \cdot \left[\ln \frac{d}{2\pi r_{eff}}\right]^{-1} \qquad \dots\dots (7)$$

with d and $d_p << \lambda$, $\theta_p < 45^o$, and $r << d$, it was found that a meaningful effective radius (r_{eff}) could be defined to account for all the experimental results. Over the frequency range 4GHz to 5GHz, and for septa with d = 23.77mm and 11.88mm, the various results corresponded with the characteristics of parallel post gratings (for each value of d) as shown in Fig.5.12. The condition preventing an overlap of the wires i.e.

$$d/2 > d_p \tan \theta_p \qquad \dots\dots (8)$$

was observed in all the samples evaluated.

As a final series of tests, it was confirmed that the properties of an individual septum (with $d/\lambda < 1/2$) were not affected by the presence of adjacent septa spaced at intervals corresponding to the element spacing within the simulated array (cf. reference 42).

Parallel and inclined post structures with d = 11.42mm and 22.84mm respectively were chosen for evaluation as element boundaries within the simulator (see Fig.5.1). Integral multiples of d for the parallel post structure could then be achieved by removing the relatively fine wires as appropriate from some of the available samples. Detailed experimental results are given in Figs.5.13 and 5.14.

The principal effect of element boundary periodicity can be deduced from the following table, which compares the experimental values of $|\vec{B}_{2,1}/\vec{A}_{1,1}|$ with theoretical predictions based on eqn.(2) and Fig.5.8.

Frequency = 4.375GHz			$\lvert\vec{B}_{2,1}/\vec{A}_{1,1}\rvert$	
DESCRIPTION OF ELEMENT BOUNDARY				
Structure	(Network) Susceptance (b_h)	d/λ	Measured	Theoretical
1) Conducting sheet	$-\infty$	0	0.845	0.845
2) Parallel post	-2.22	0.167	0.66	0.65
3) " "	-0.85	0.333	0.55	0.48
4) " "	-0.44	0.5	0.51	0.37
5) Inclined post (θ_p=25°)	∿-0.67	0.333	0.51	0.44
6) Inclined post (θ_p=37°)	∿-0.58	0.333	0.48	0.42

(For cases (3) to (6), an iterative procedure has been adopted to obtain b_h and $(k_x a)_1$. For cases (5) and (6), the values of r_{eff} are based on Fig.5.12.)

A discrepancy increasing sharply for $d/\lambda > 1/6$ is evident between results in the last two columns. Its explanation lies in the approximate representation of the boundary structures as "uniform current sheets", a concept which ignores the space harmonics necessarily associated with any *axial* periodicity. Its implications are therefore fundamental for reactive boundary transitions providing element pattern control.

Two aspects of periodic structure behaviour must be distinguished at this point. The first concerns the propagation characteristics within a region of constant boundary susceptance (cf. Chapter 2). The introduction of axial periodicity (e.g. through a two dimensional structure of parallel posts equivalent to an artificial dielectric) does not invalidate the modal properties identified in Chapter 2 if an effective susceptance b_h can be defined and the boundaries remain decoupled. (These conditions could be satisfied with relatively large values of d/λ (∿0.5), as shown in Section 3.5.2.) As evidence of this, it was found during the simulator tests that the upper frequency limit for single mode propagation could be predicted accurately from Fig.5.7, provided an iterative process was adopted to find b_h. However, the "fields" associated with an axially propagating mode under these conditions can not be considered an accurate approximation to the total field, except for a very narrow strip down the centre of each element. This is nevertheless sufficient to define properties normally associated with (single moded) artificial dielectrics, such as wave impedance and propagation velocity (cf. references 42, 44).

The second aspect, which embraces the problem highlighted by the table above, concerns the properties of a susceptance discontinuity in which the axial periodicity of the boundaries is simultaneously modified. In this respect, the interface between a region of finite susceptance and free space poses a severe but crucial test for the theory given in Chapter 4. The axial space harmonics (or Floquet modes) associated with each element boundary become part of the total aperture field, and consequently affect the grating wave suppression adversely. Their amplitudes can only be contained by reducing d/λ (88). Since the achievement of element pattern control is the ultimate objective, it follows from the experimental results given in Figs.5.13 and 5.14 that d/λ must be small (by comparison with a/λ) in the vicinity of the aperture. The close agreement between the experimental and calculated values for $|\vec{B}_{2,1}/\vec{A}_{1,1}|$ when $d/\lambda = 1/6$ indicates that a maximum value of approximately 0.25 for d/a is acceptable (cf. further results given in next section).

The requirement to keep d/λ small was recognised in Chapter 3, but the reasons given did not emphasise directly the basic restriction now evident. In the light of Fig.5.13, for instance, it is clear that the element boundaries in the modified lens (Fig.3.9) were fundamentally unsuitable near the aperture, where "d/λ" increased to ~0.4. The use of "longer tapers" affording definition of the "susceptance profile" (by iterative calculations near the aperture), would not have ensured the desired pattern control. Further clarification is provided by re-examining the expressions for the susceptance of parallel-wire grids (88), viz

$$b_h = \frac{-\lambda}{d}\left[\ln\left(\frac{d}{2\pi r}\right) + \tfrac{1}{2}\{f(\theta') + f(-\theta')\}\right]^{-1} \quad \ldots.\ (8)$$

where $$f(\theta') = \sum_{n=1}^{\infty} \frac{1}{n}\, n\lambda/d\{(\sin\theta' + n\lambda/d)^2 - 1\}^{-\frac{1}{2}} - 1 \quad \ldots.\ (9)$$

In earlier work, emphasis was placed on the need to minimise variations in $f(\theta')$ with element phasing. From eqn.(9), this requirement (which was not observed in the boundaries designed for the lens) is equivalent to keeping $\lambda/d >> \sin\theta'$ (or $d/\lambda << 1$) and ensuring that $f(\theta') \to 0$. Under this condition, the amplitude of the "n"th space harmonic, which is also proportional to the term

$$(\pi/d)\{(\sin\theta' + n\lambda/d)^2 - 1\}^{-\frac{1}{2}},\ (n=\pm1,\pm2,\cdots) \quad \ldots.\ (10)$$

is automatically contained. Physically, of course, the space harmonics cannot be *eliminated* with this form of element boundary structure, since the observed "reactance" is a direct consequence of the energy stored in their fields. The sense in which the array problems created by transverse periodicity have been replaced by similar problems in the axial direction appears to be an inherent limitation. The engineering potential of the proposal outlined in Section 2.4 is therefore dependent on utilising the greater design freedom available in the axial direction.

To conclude this section, it should be noted that the experimental results given in Fig.5.13 (particularly for the larger values of d) could be predicted more accurately. For example, the analytical technique developed by Brown and Seeley (108) to explain the phase of reflected and transmitted waves at the surface of an artificial dielectric could be extended. For the two dimensional array of parallel posts shown in Fig.5.15a, an equivalent circuit of *transverse* coupling networks, interconnected by a number of transmission lines, could be formulated (Fig.5.15b). Assuming $a/\lambda \sim 0.7$ and $d/\lambda \sim 0.3$, a minimum of three transmission lines would probably be needed in the analysis, with the coupling networks characterised accordingly as "6 ports". Independent "modes of propagation" in the periodic structure, equal to the number of transmission lines assumed (109), could then be obtained. Finally, the transmission and reflection coefficients at the interface could be deduced by a field matching technique if the same number of free space modes were assumed. (This approach becomes impractical-and unnecessary, of course - when the recommended constraint on d/a is observed.)

5.4. Boundary Structures with Small Inductive Susceptance

The problem of realising small values for b_h is magnified by the restriction on d/λ discussed above. In the case of parallel post structures, the required radii become quite unrealistic. For example, if $d/\lambda = 1/6$, a radius of $10^{-6}.d$ is required to obtain a susceptance (b_h) of -0.5. For the element boundaries considered in the previous section, this radius would be only 0.5 microns. (With $d/\lambda = 0.1$, the corresponding radius would be 5×10^{-4} microns!)

The "wire" size adopted in the chemically milled samples was a compromise between the requirement for low susceptances and the constraints imposed by manufacturing accuracies and mechanical handling. For this reason, the inclined wire structures were developed as part of an initial programme to achieve smaller susceptances. The results given in the previous section suggest that this approach has genuine merit, but insufficient to overcome the problem indicated above.

The basic need for additional parameters in the design of low susceptance boundaries led to a series of tests with sheets of alumina in parallel with the cross-guide septa as shown in Fig.5.16. By using a material with a high dielectric constant, the possibility of achieving smaller values of (inductive) susceptance with highly localised fields was created.

To interpret the experimental results, the network properties of a dielectric sheet (thickness t) are required. For the propagation directions defined in Fig.5.17a, it is shown in reference 110 that the normalised input impedance (Z_{in}) at the air-dielectric interface is given by

$$Z_{in} = \frac{Z[1 + jZ\tan\{kt(\varepsilon_r - \sin^2\theta')^{\frac{1}{2}}\}]}{Z + j\tan\{kt(\varepsilon_r - \sin^2\theta')^{\frac{1}{2}}\}} \qquad \ldots. (11)$$

$$\text{where} \quad Z = \frac{\cos\theta'}{(\varepsilon_r - \sin^2\theta')^{\frac{1}{2}}} \qquad \ldots. (12)$$

If $\varepsilon_r \gg 1$ and $kt(\varepsilon_r - \sin^2\theta')^{\frac{1}{2}}$ is small, it follows that

$$Z \ll 1$$

$$\text{and} \quad Z_{in} \approx \frac{Z}{Z + jkt(\varepsilon_r - \sin^2\theta')^{\frac{1}{2}}} \qquad \ldots. (13)$$

$$\text{i.e.} \quad Z_{in} \approx \frac{\{\cos\theta'/jkt(\varepsilon_r - \sin^2\theta')\}}{1 + \{\cos\theta'/jkt(\varepsilon_r - \sin^2\theta')\}} \qquad \ldots. (14)$$

A comparison of this expression with the equivalent circuit in Fig.5.17b indicates that the (unnormalised) susceptance (B_c) of a thin dielectric sheet with $\varepsilon_r \gg 1$ is accurately approximated by

$$B_c = \sqrt{\frac{\varepsilon_o}{\mu_o}} \cdot kt(\varepsilon_r - \sin^2\theta') \qquad \ldots. (15)$$

This value was confirmed experimentally in waveguide tests to within 5% for alumina ($\varepsilon_r = 9.8$) of thicknesses 0.62mm, 1.25mm and 1.87mm, despite the systematic error introduced by mechanical clearances around the walls.

The tests with alumina sheets and inductive septa mounted together in the waveguide cross-section revealed that the net susceptance (b_h) was approximately equal to the sum of the individual susceptances of isolated inductive and capacitive structures, as indicated by the following experimental results.

NORMALISED SUSCEPTANCES (f = 4.375GHz)

Inductive septa in isolation	Dielectric sheet in isolation	Inductive septa and dielectric sheet mounted together
-0.80	+0.53	-0.26
-0.80	+1.07	+0.28
-2.20	+1.07	-1.12

With $d/\lambda \ll 1$ for the inductive grid, and $\varepsilon_r \gg 1$ for the thin capacitive sheet, a simplified expression for the normalised susceptance of such structures is obtained from eqns.(3) and (15), viz

$$b_h \simeq -\frac{\lambda}{d}\left[\ln\left(\frac{d}{2\,r}\right)\right]^{-1} + 2\pi\cdot\frac{t}{\lambda}\cdot\varepsilon_r \qquad \text{.... (16)}$$

Whilst the separability of the inductive and capacitive contributions is not based on a rigorous analysis (e.g. by variational techniques (111)), the experimental validity of similar formulations has been demonstrated for thin film bolometers (112). The assumption of a thin dielectric sheet is obviously important.

In simulator tests, an improvement in grating wave suppression consistent with the calculated reduction in susceptance was obtained. The experimental results are given in Fig.5.18, while the following table highlights the agreement with predicted values of $|\vec{B}_{2,1}/\vec{A}_{1,1}|$ for small values of d/λ.

	DESCRIPTION OF ELEMENT BOUNDARIES				$\lvert\vec{B}_{2,1}/\vec{A}_{1,1}\rvert$	
	d/λ	f (GHz)	Thickness of alumina (t) in mm	b_h (calculated values)	Calculated	Measured
1)	0.167	4.375	0.62	-1.68	0.60	0.61
2)	0.167	4.375	1.25	-1.15	0.53	0.55
3)	0.167	4.375	1.87	-0.62	0.43	0.44
4)	0.332	4.35	0.62	-0.34	0.32	0.44
5)	0.326	4.275	0.62	-0.18	0.23	0.34

(Cases (1) to (4) refer to "parallel-post" boundaries, whilst case (5) refers to an "inclined-post" boundary.)

The excellent agreement between theoretical and experimental values of $|\vec{B}_{2,1}/\vec{A}_{1,1}|$ for boundaries with tightly coupled reactive fields (cases (1) to (3) above with $d/\lambda = 0.167$) is significant for two reasons.

(1) With an experimental verification of the theory given in Chapter 4, the analysis of a cascade network of "constant susceptance regions" can be undertaken in the knowledge that element boundary structures which accurately approximate this behaviour are realisable. In particular, the theoretical requirement for small inductive susceptances (which is established in Chapter 6) can be fulfilled (see following paragraphs).

(2) The technical justification is provided for the future development of inductive grids printed on dielectric substrates. In the first instance, the problems arising from this logical extension of the work described above would relate to manufacturing technology - e.g. the provision of an electrically satisfactory method of supporting the substrates within an array configuration. The implicit similarities with microstrip technology should be noted.

The principal advantages afforded by printed circuit technology include:-

(i) the design freedom required to obtain a complete range of inductive susceptances (in particular, values of $b_h > -1$) with small d/λ;

(ii) the ability to specify much smaller radii for the conducting posts (e.g. 0.01mm) without serious problems due to manufacturing tolerances;

(iii) the mechanical support provided by the substrates for the very fine conductors;

(iv) the possibility of economic batch production, especially when constant values of susceptance are required for a "reactively-stepped" transition.

The features (i) and (ii) above are interrelated, and provide some control of the inherent frequency limitations which are illustrated by the numerical examples given in Fig.5.19. For example, the retention of a broad band capability (say > 10%) depends on the use of very fine conducting tracks and thin dielectric sheets, since obvious limits are imposed if b_h becomes too large at frequencies below f_o, or capacitive at frequencies above f_o. Further numerical and experimental work is required to explore these limitations in more detail.

APPENDIX 5A

The theoretical expressions for the elements $S_{i'j'}$ of the scattering matrices given in Appendices 4B and 4C can be simplified when the region (n + 1) is free space. In the following derivation, attention is focussed on the terms S_{31} and S_{21} of the 3 X 3 H-plane matrix, to show how eqn.(2) in Chapter 5 is obtained. As in the text, the two regions are designated below by subscripts 0 and 1.

Referring to Appendix 4B, it is seen that the following substitutions will be required

$$\sqrt{k^2-\beta^2_{1,1}} \rightarrow \psi_h/a \qquad \text{....(A1)}$$

$$\sqrt{k^2-\beta^2_{2,1}} \rightarrow (2\pi - \psi_h)/a \qquad \text{....(A2)}$$

$$\sin\left[(a\sqrt{k^2-\beta^2_{1,1}} - \psi_h)/2\right] \rightarrow \sin(\psi_h) \qquad \text{....(A3)}$$

$$\sin\left[(a\sqrt{k^2-\beta^2_{2,1}} - \psi_h)/2\right] \rightarrow -\sin(\psi_h) \qquad \text{....(A4)}$$

$$|F_0(\beta_{1,1})| \rightarrow K_{h,0}\cdot \sin(\psi_h)/\psi_h \qquad \text{....(A5)}$$

$$|F_0(\beta_{1,2})| \rightarrow K_{h,0}\cdot \sin(\psi_h)/(2\pi - \psi_h) \qquad \text{....(A6)}$$

$$|F_1'(\beta_{1,1})| \rightarrow a\beta_{1,1}\cdot \sin(\psi_h)/\psi_h \qquad \text{....(A7)}$$

$$|F_1'(\beta_{2,1})| \rightarrow a\beta_{2,1}\cdot \sin(\psi_h)/(2\pi - \psi_h) \qquad \text{....(A8)}$$

It is convenient to reduce the lengthy analytical expressions for S_{31} and S_{21} (in the case of a 3 X 3 matrix) by considering the two ratios U_{12}/U_{13} and V_{13}/V_{12}. Substituting in accordance with eqns. (A1) to (A8) as required, and omitting factors which cancel analytically:-

$$\frac{\{U_{12}\}}{\{U_{13}\}} \rightarrow \frac{\psi_h/a}{(2\pi-\psi_h)a}\cdot\frac{-\sin(\psi_h)}{\sin(\psi_h)}\cdot\sqrt{\frac{K_{h,o}\sin(\psi_h)/\psi_h \quad a\beta_{1,1}\sin(\psi_h)/\psi_h}{K_{h,o}\sin(\psi_h)/(2\pi-\psi_h) \quad a\beta_{2,1}\sin(\psi_h)/(2\pi-\psi_h)}}$$

i.e $$\frac{\{U_{1,2}\}}{\{U_{1,3}\}} = \sqrt{\frac{\beta_{1,1}}{\beta_{2,1}}} \qquad \text{....(A9)}$$

and $$\frac{\{V_{1,3}\}}{\{V_{1,2}\}} \rightarrow \sqrt{\frac{\beta_{2,1}}{\beta_{1,1}}} \cdot \frac{(\beta_{1,0}+\beta_{1,0})}{(\beta_{1,0}+\beta_{2,1})} \cdot \sqrt{\frac{(\beta_{1,1} - \beta_{1,0})(\beta_{1,0} + \beta_{2,1})}{(\beta_{1,1} + \beta_{1,0})(\beta_{1,0} - \beta_{2,1})}}$$

$$= \sqrt{\frac{\beta_{2,1}}{\beta_{1,1}} \cdot \frac{(\beta^2_{1,1} - \beta^2_{1,0})}{(\beta^2_{1,0} \quad \beta^2_{2,1})}} \qquad \text{...(A10)}$$

The result given as eqn.(2) in the text follows directly from eqns.(A9) and (A10).

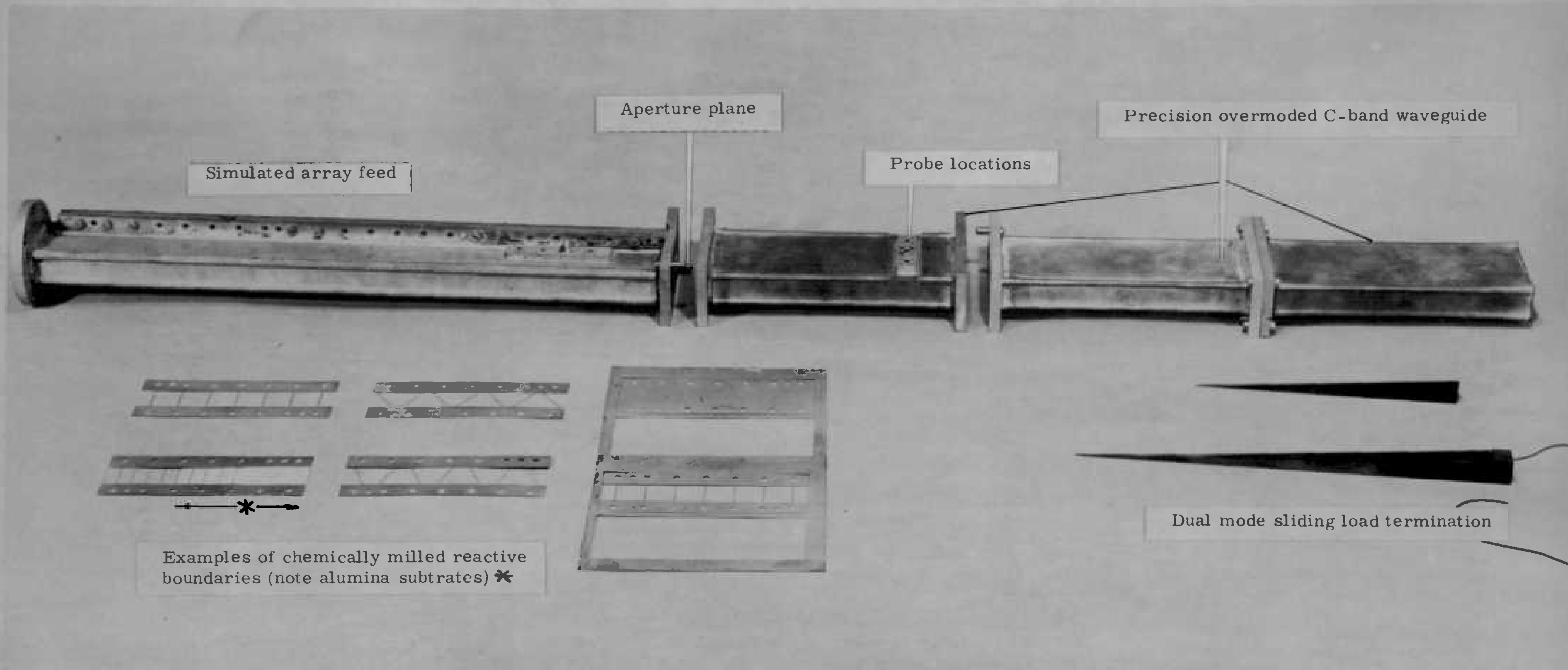

Fig. 5.1 Complete $1\frac{1}{2}$ element phased array simulator (overall length ≈ 1.25m)

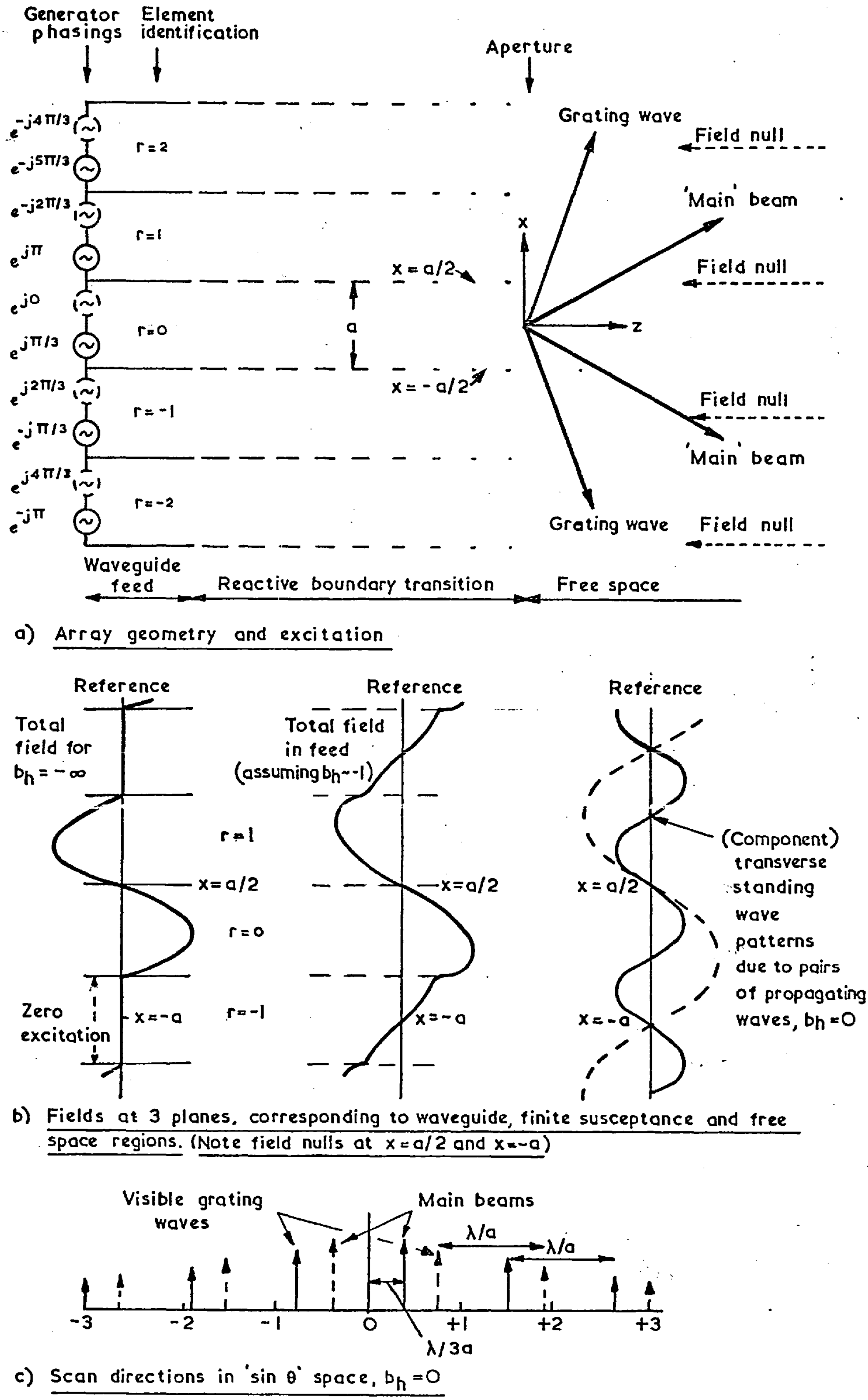

Fig.5.2 Portion of an infinite array structure excited by two sets of generators. The element phasings have been chosen to ensure field nulls at x = a/2 and x = -a, for all values of z.

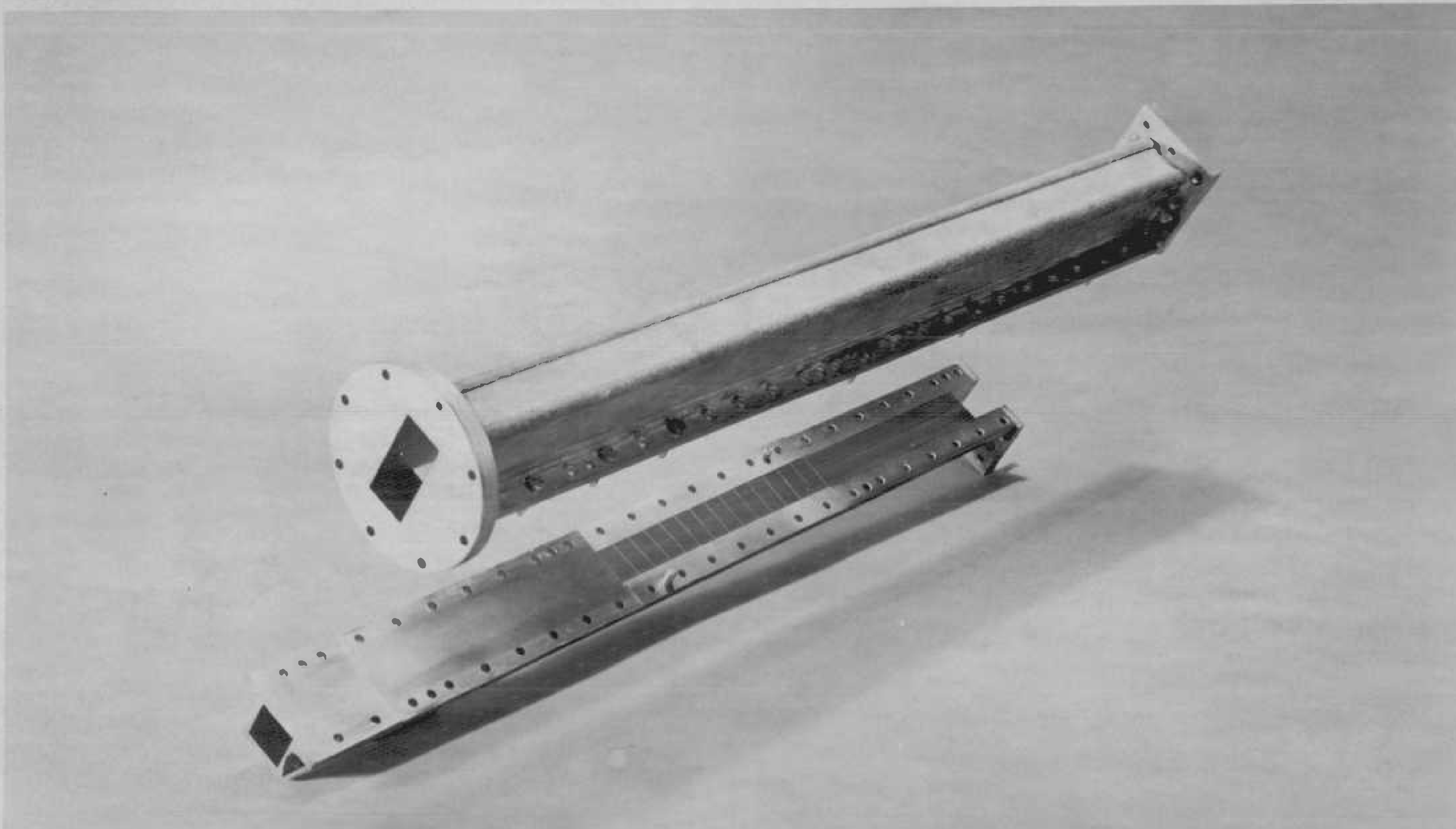

Fig. 5.3 Disassembled $1\frac{1}{2}$ element simulator feed

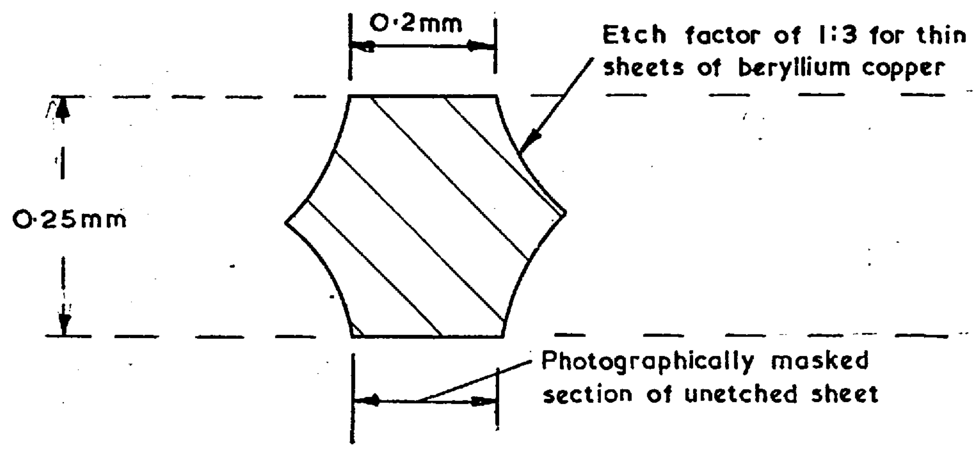

Fig.5.4 Cross-section detail of "posts" in reactive grids formed by chemical milling techniques

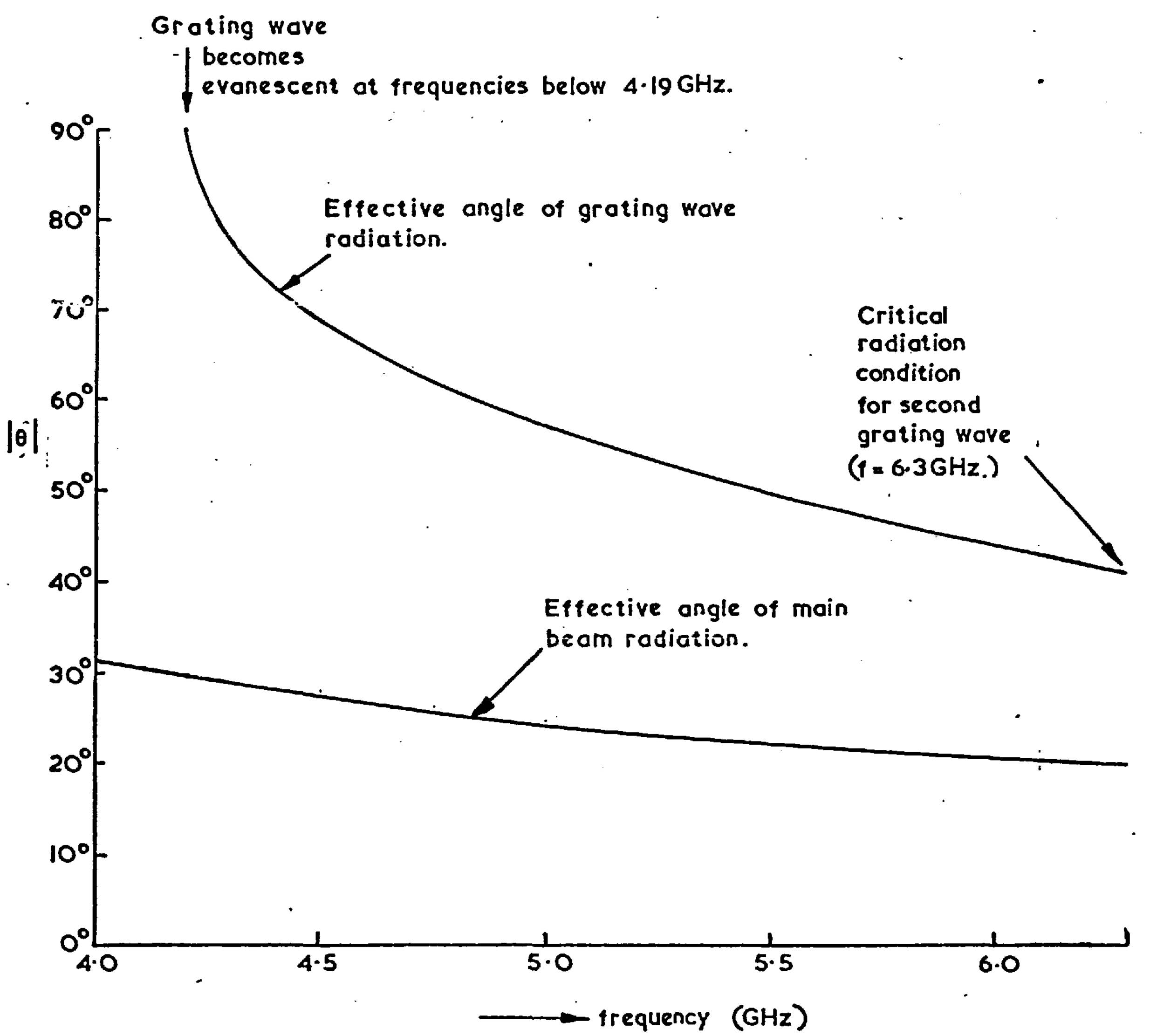

Fig.5.5 Radiation characteristics of an infinite array with $\psi_h = 120^{\circ}$ and a = 47.7mm

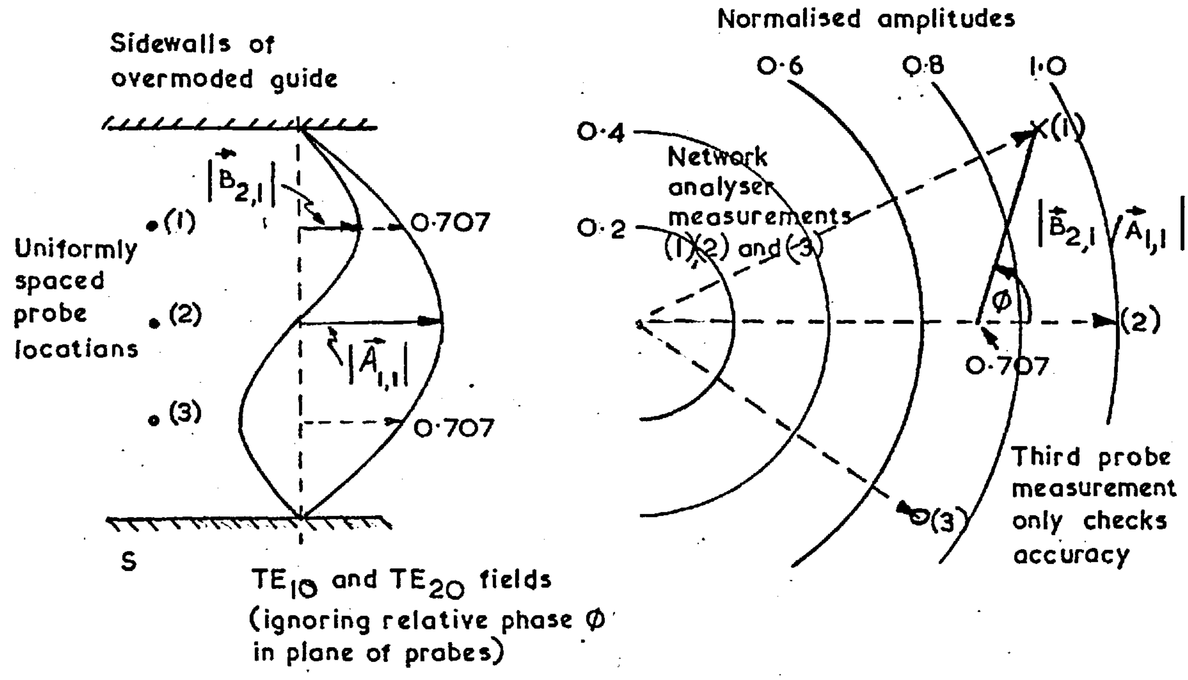

Fig.5.6 Probe positions in over-moded guide and the method adopted for recording results

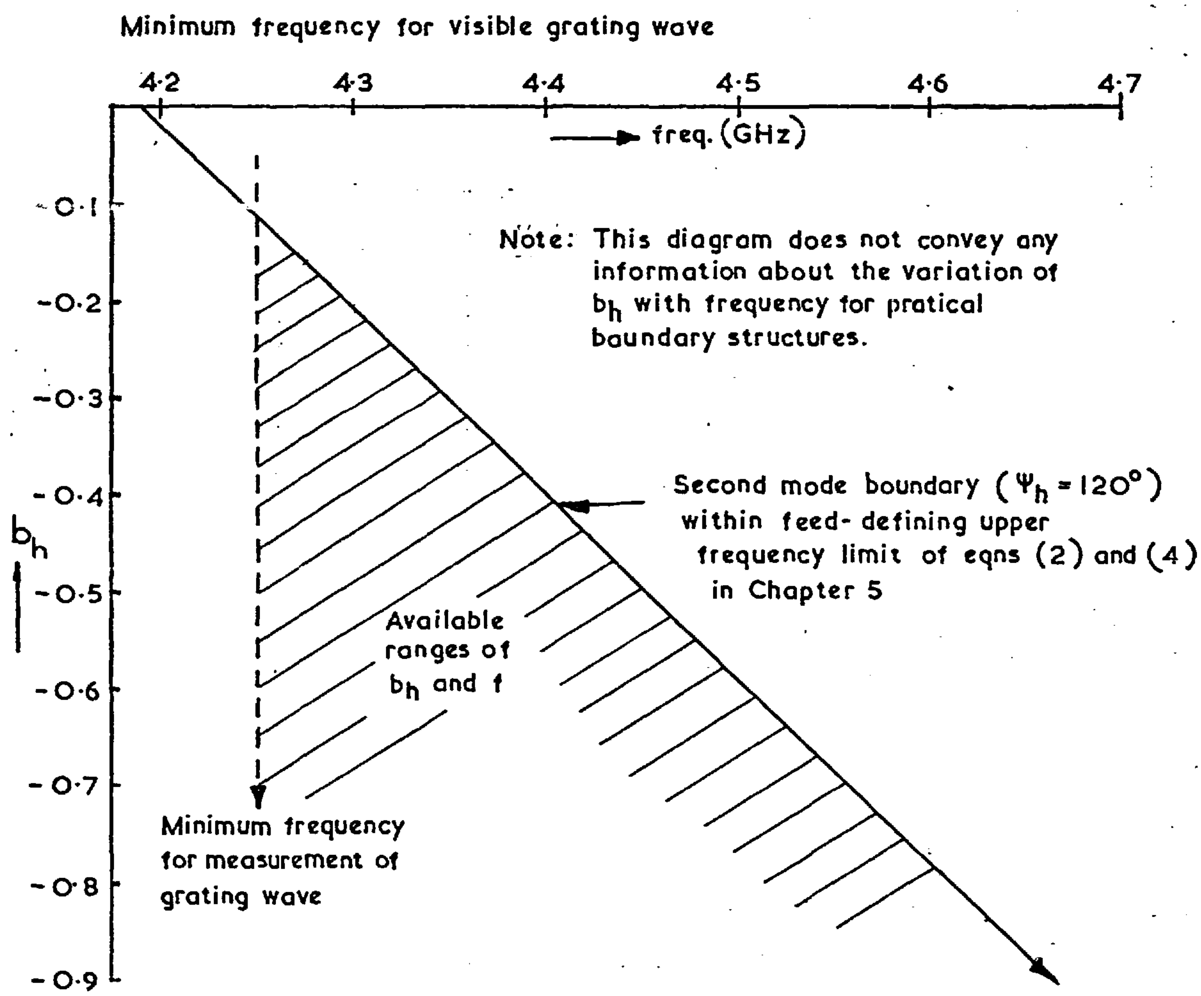

Fig.5.7 Modified mode chart showing the range of boundary susceptances and frequencies available for simulator measurements, assuming a single-moded feed and a visible grating wave (ψ_h = 120°)

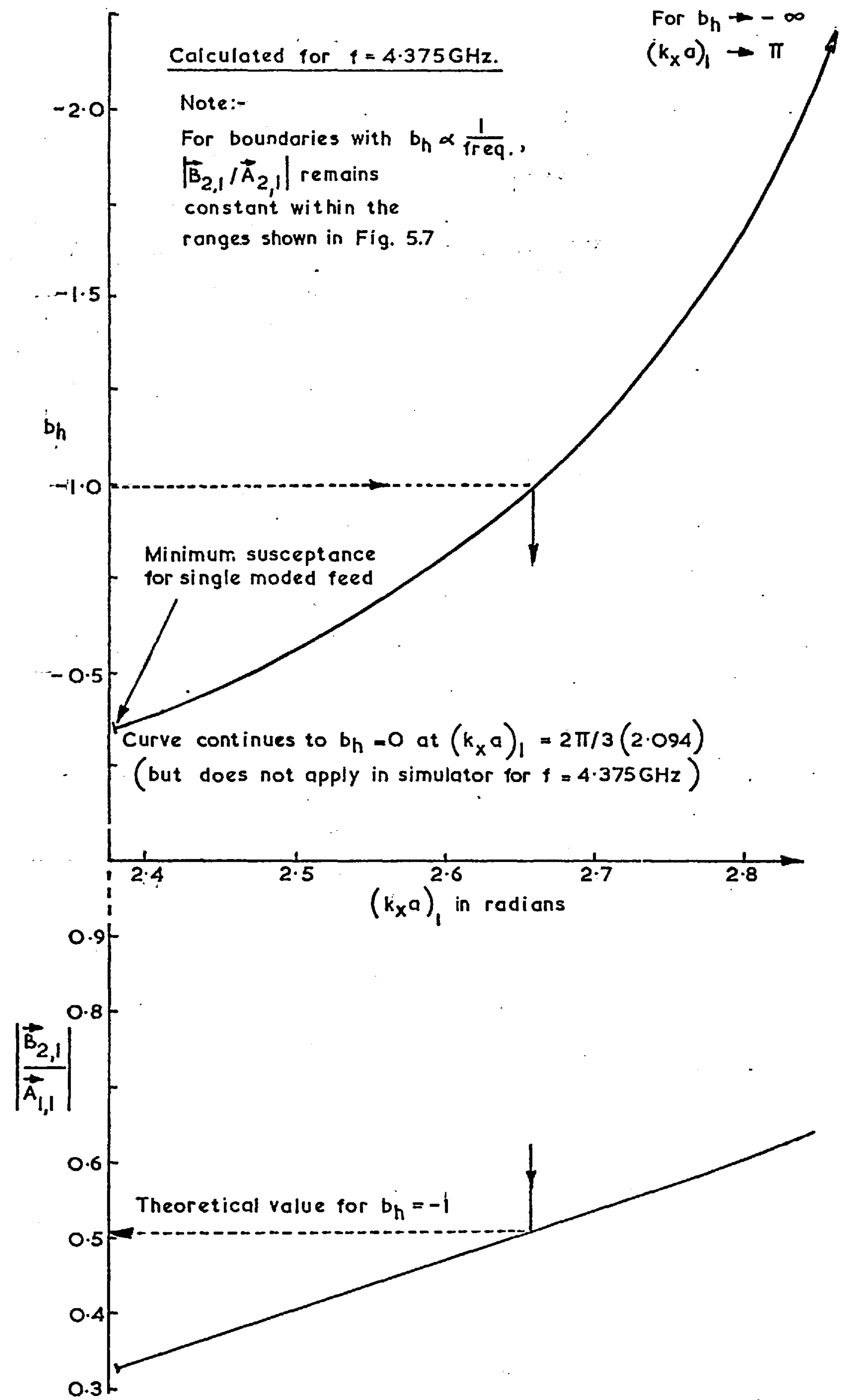

Fig.5.8 Theoretical properties of simulator relating boundary susceptance within feed to wave amplitudes in free space.

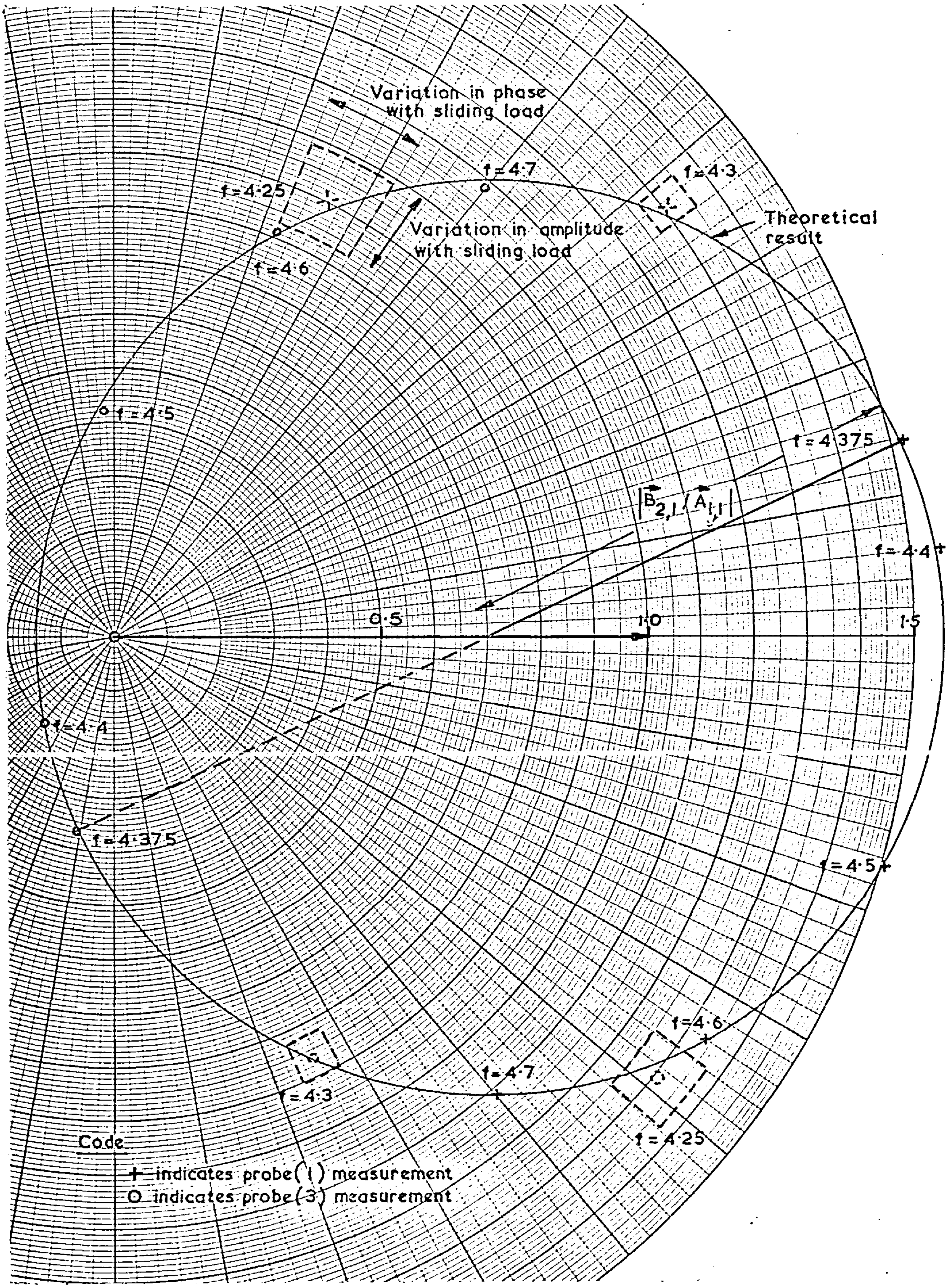

Fig.5.9 Calibration of simulator, using element boundaries with infinite susceptance (Theoretical result for $|\vec{B}_{2,1}/\vec{A}_{1,1}| = \sqrt{5/7}$ for all frequencies shown).

a) Parallel-post structure

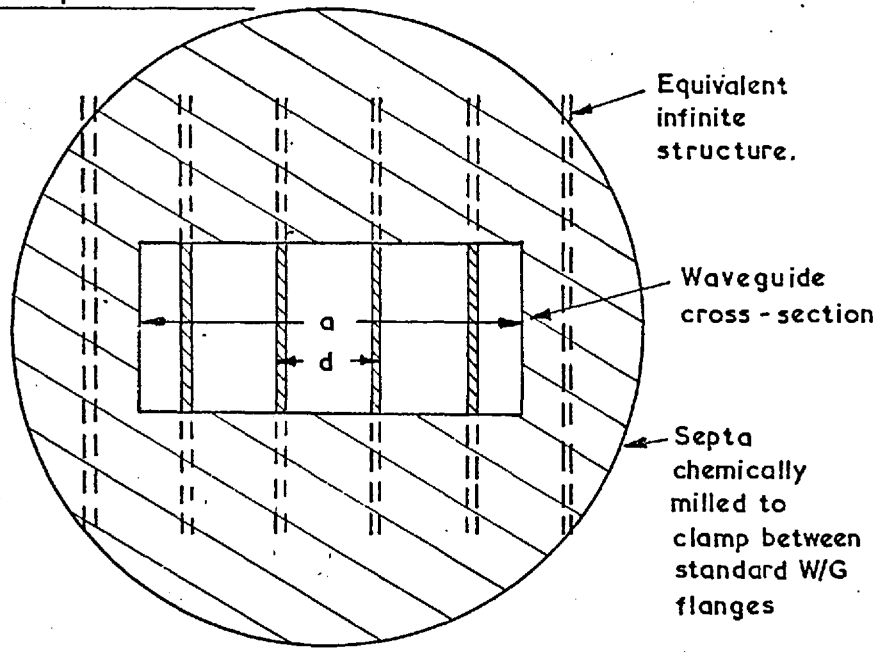

b) Inclined post structure

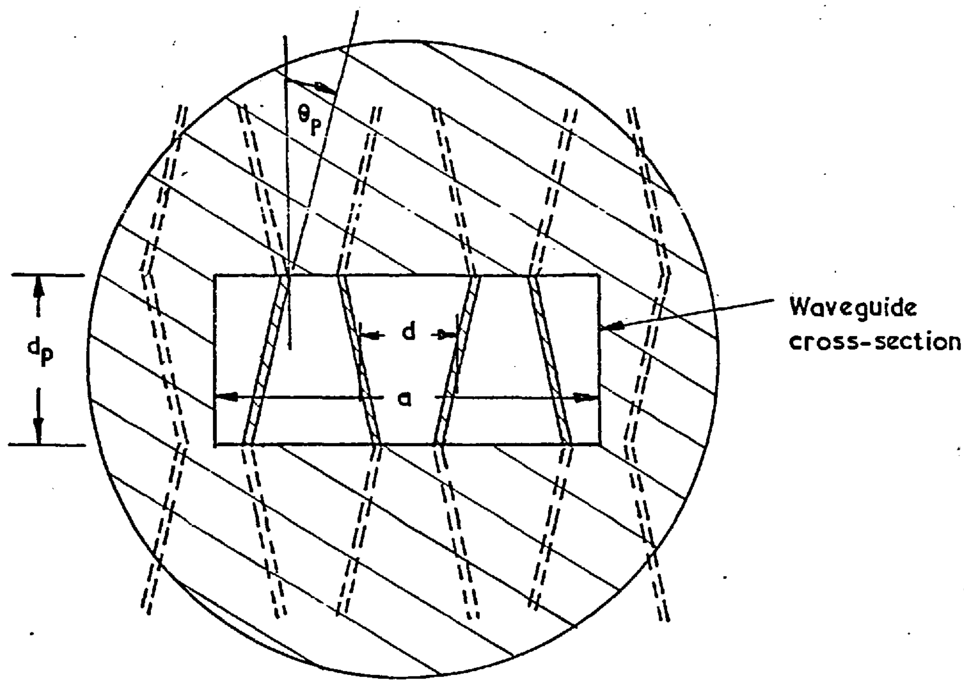

In both cases, $\theta' = \arcsin\left(\lambda/2a\right)$, in the following equivalent problem:-

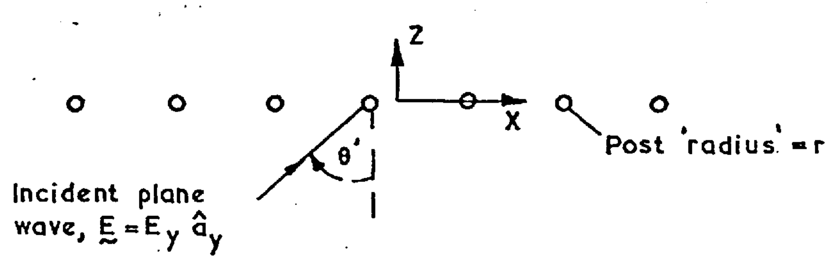

Fig.5.10 Details of cross-guide chemically-milled septa developed to characterise element boundaries

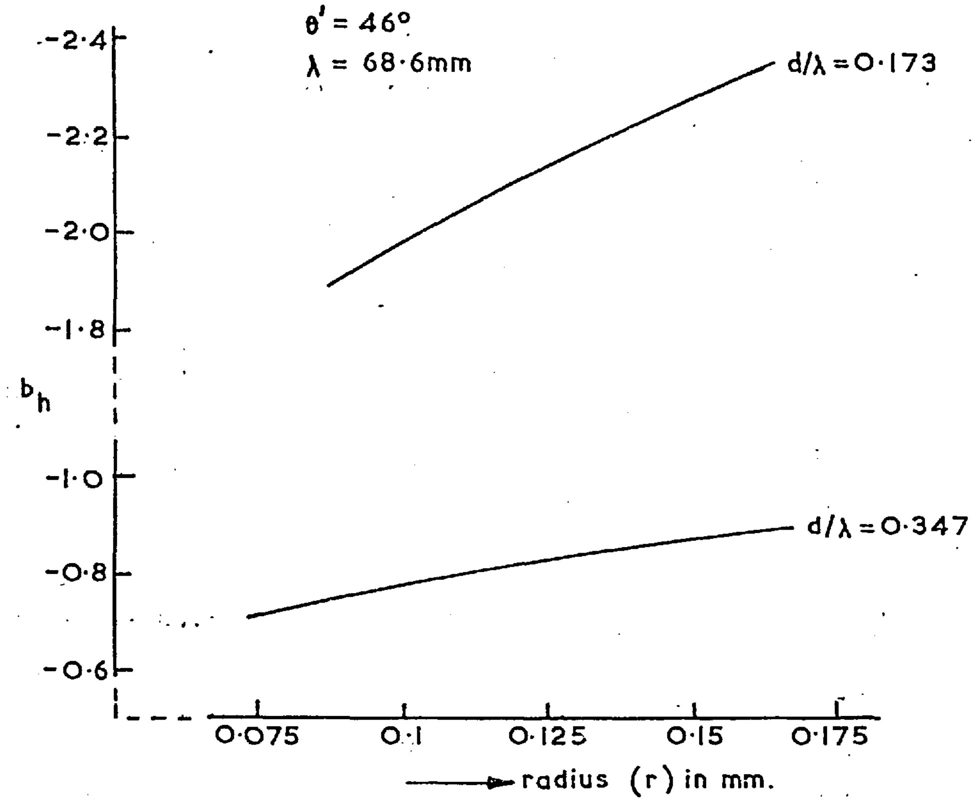

Fig.5.11 Calculated susceptance b_h of parallel wire grids, for wires of cylindrical cross-section

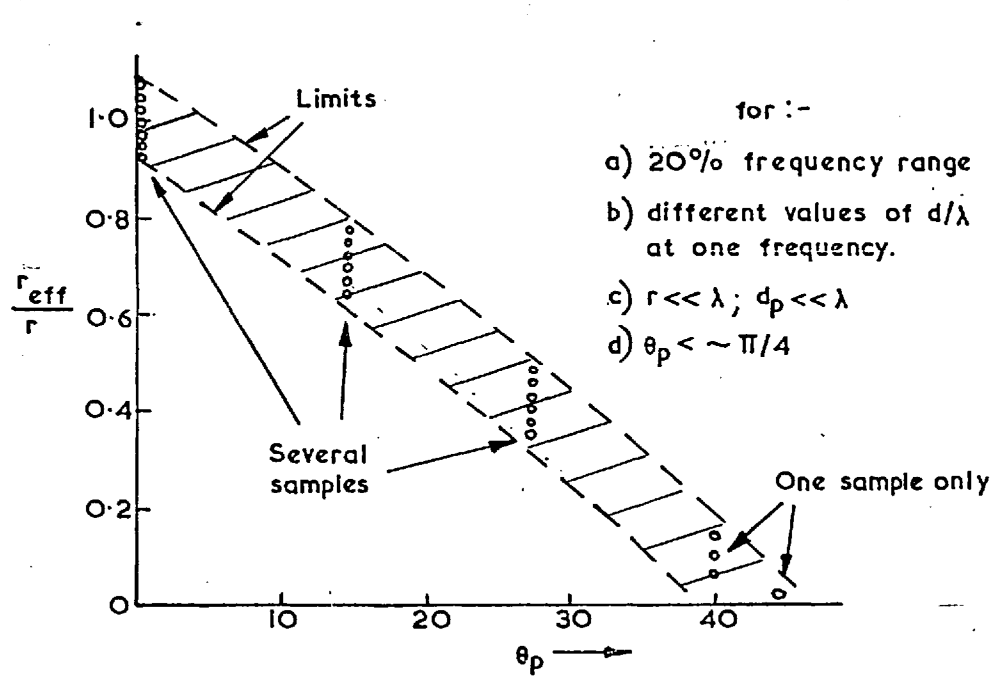

Fig.5.12 Experimental interpretation of results for inclined wire gratings as a function of θ_p, with r = 0.12mm, d_p = 22.2mm

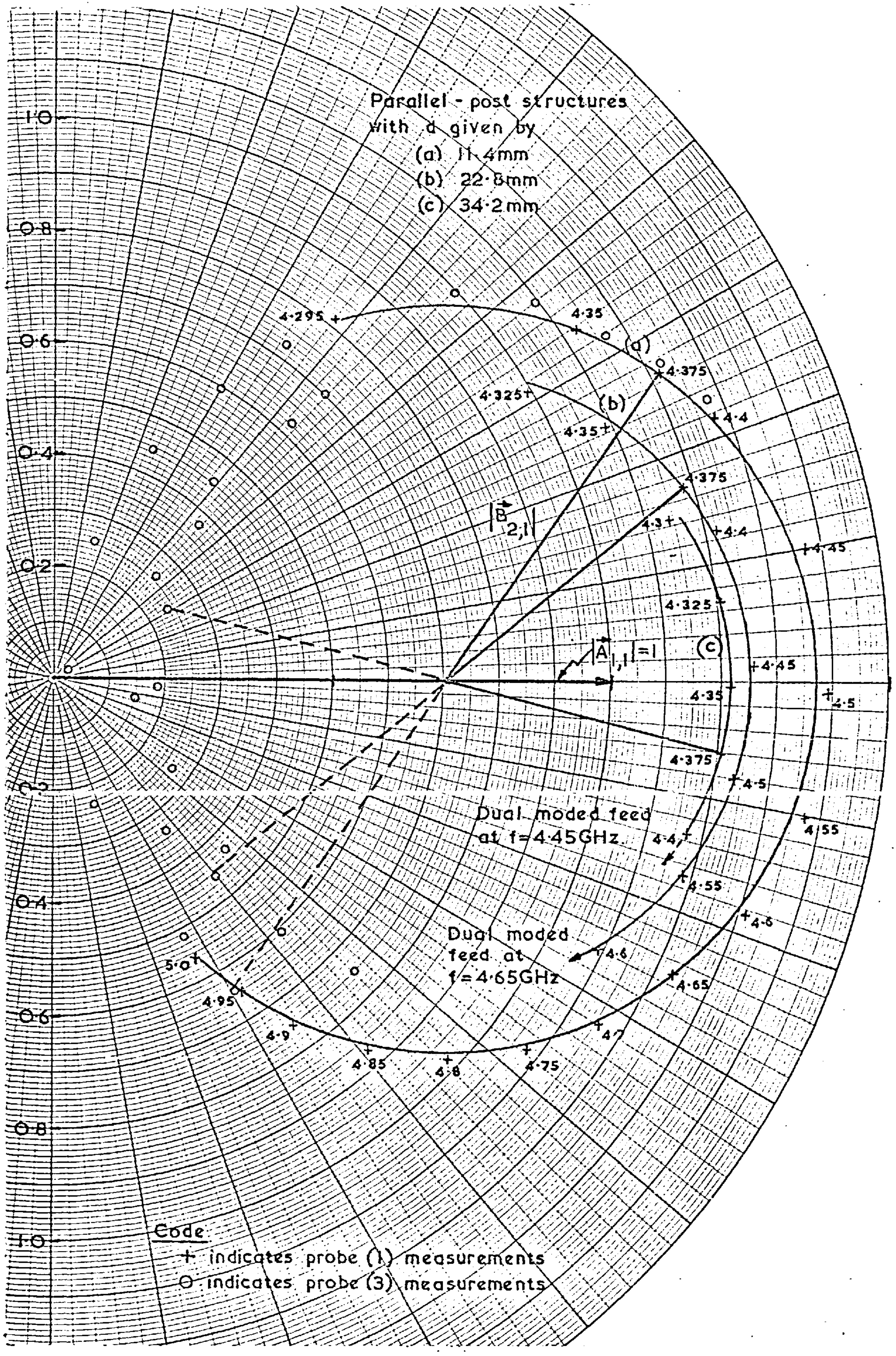

Fig.5.13 Simulator results for parallel post boundary structures (Numbers indicate frequency in GHz)

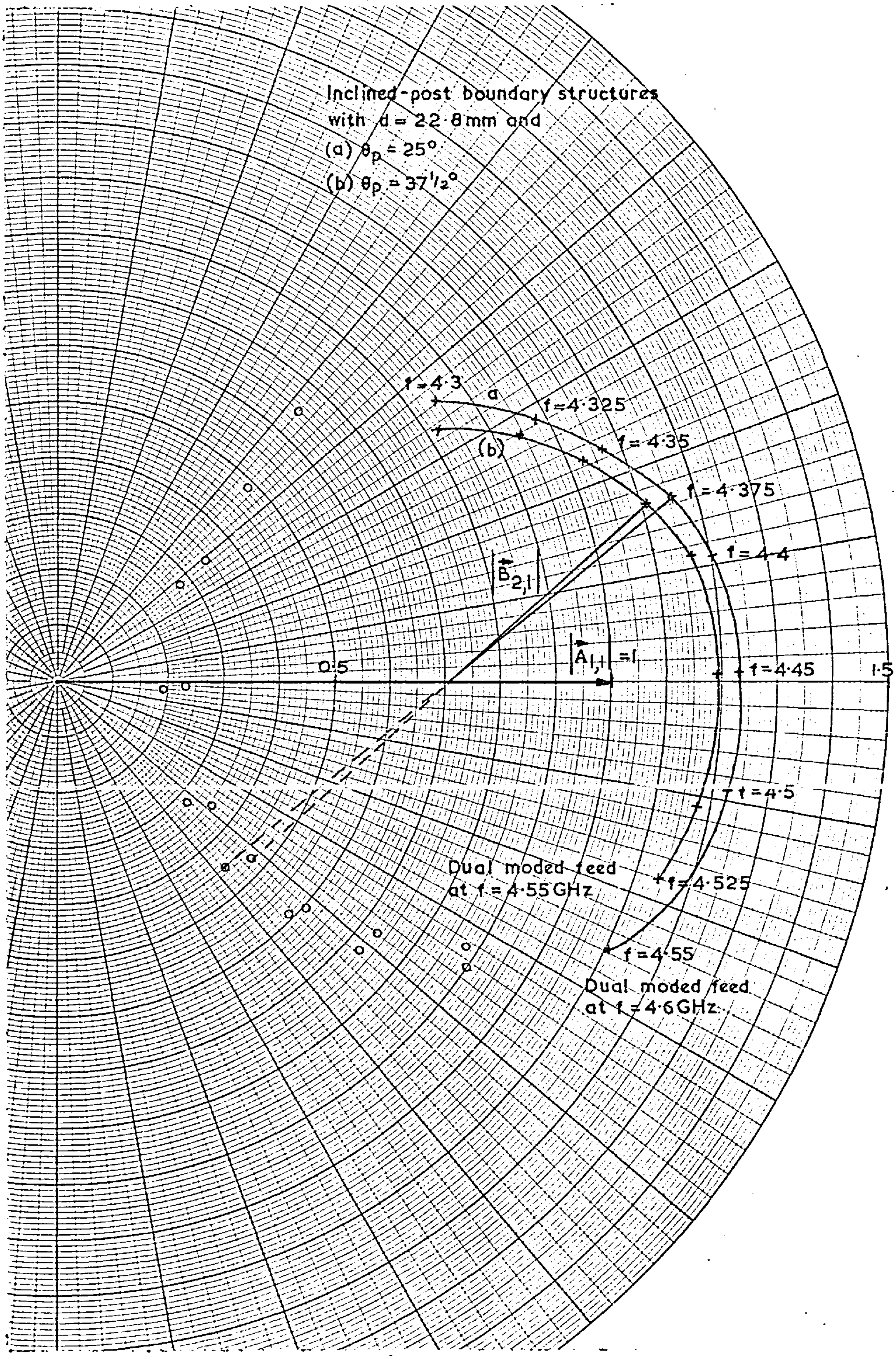

Fig.5.14 Simulator results for inclined post boundary structures

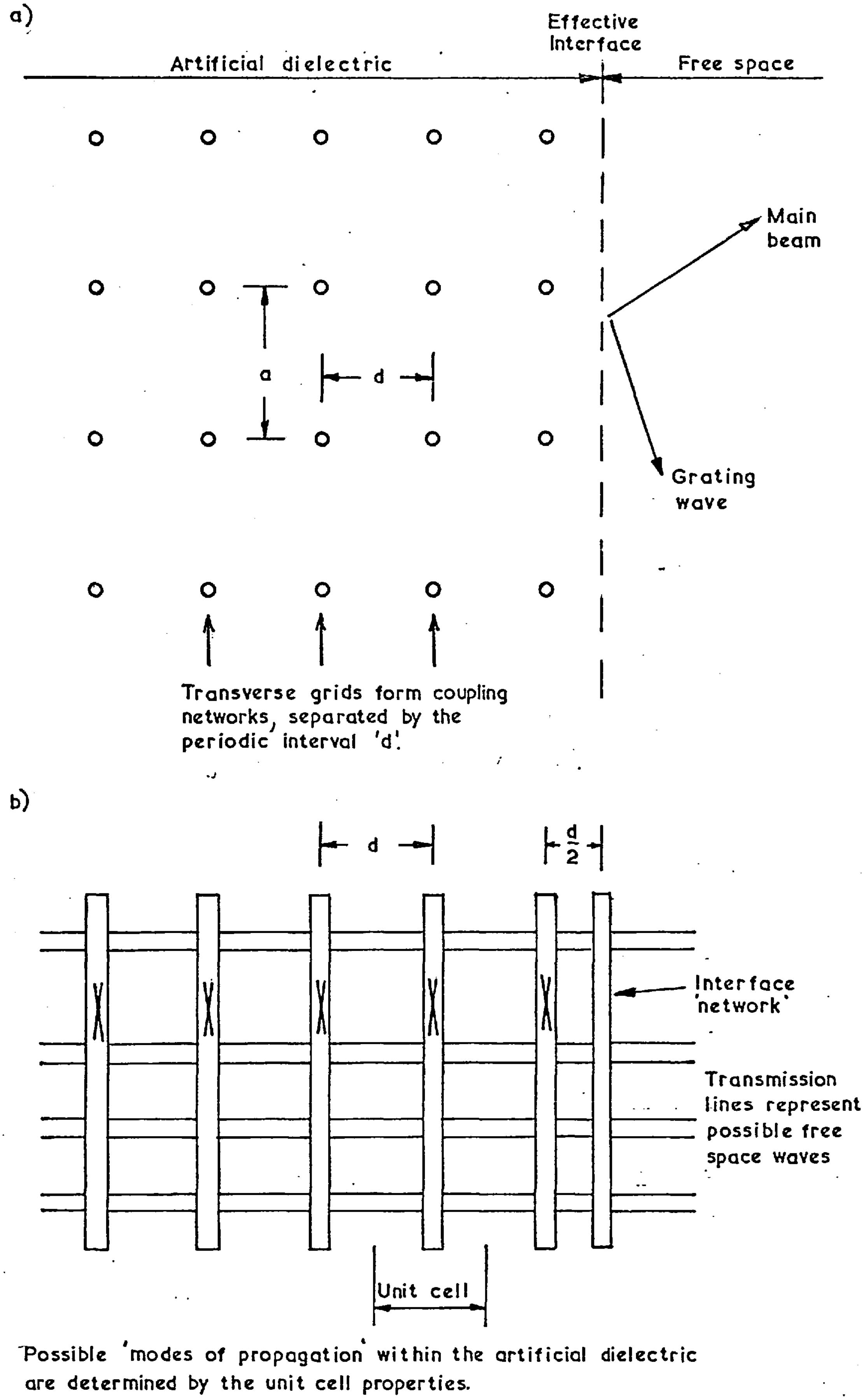

Fig.5.15 Model for analysing the simulator performance when d becomes large (say d/a > 0.5) (reference 108).

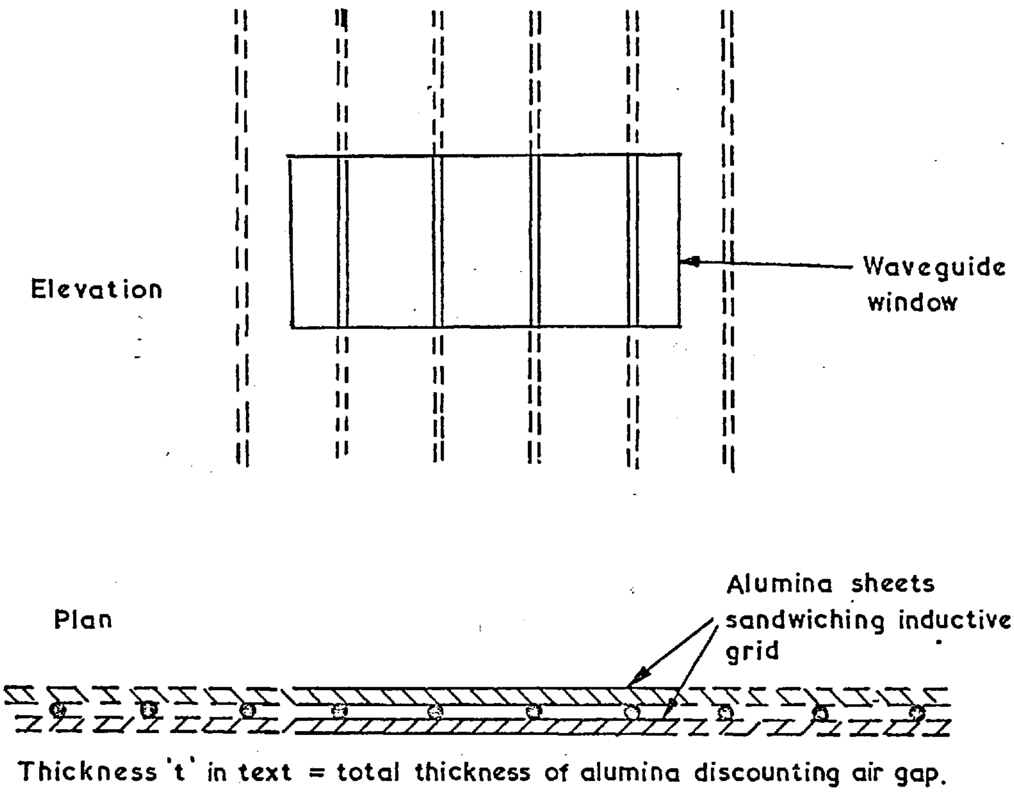

Fig.5.16 Arrangement of dielectric sheets and periodic grids for the evaluation of low susceptance boundaries

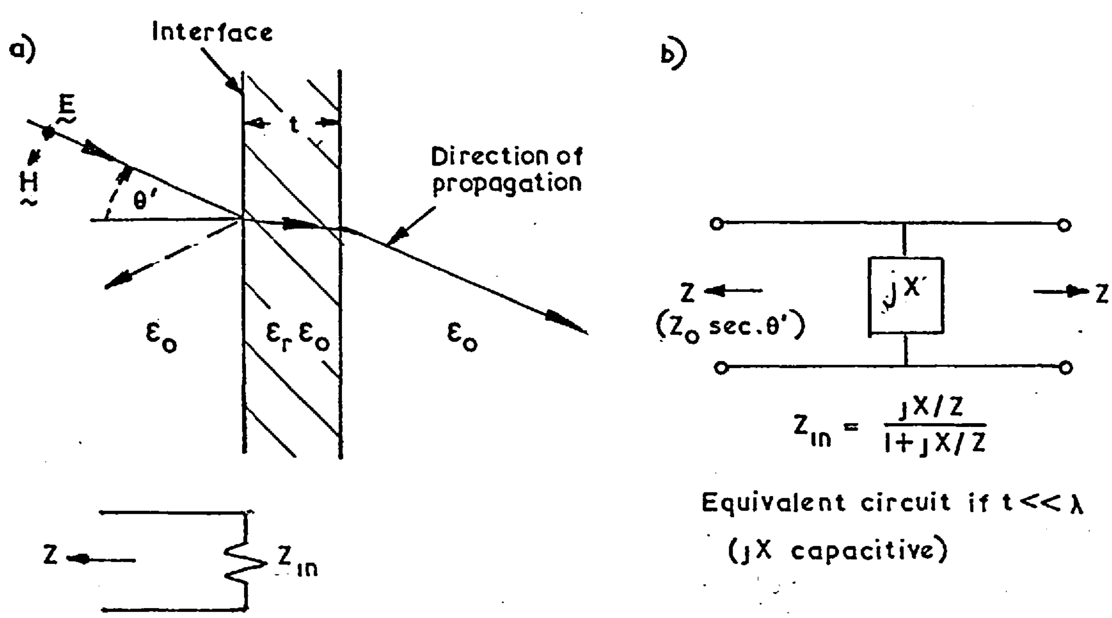

Fig.5.17 Plane wave transmission through an infinite dielectric sheet of thickness t, and an equivalent circuit for small t/λ.

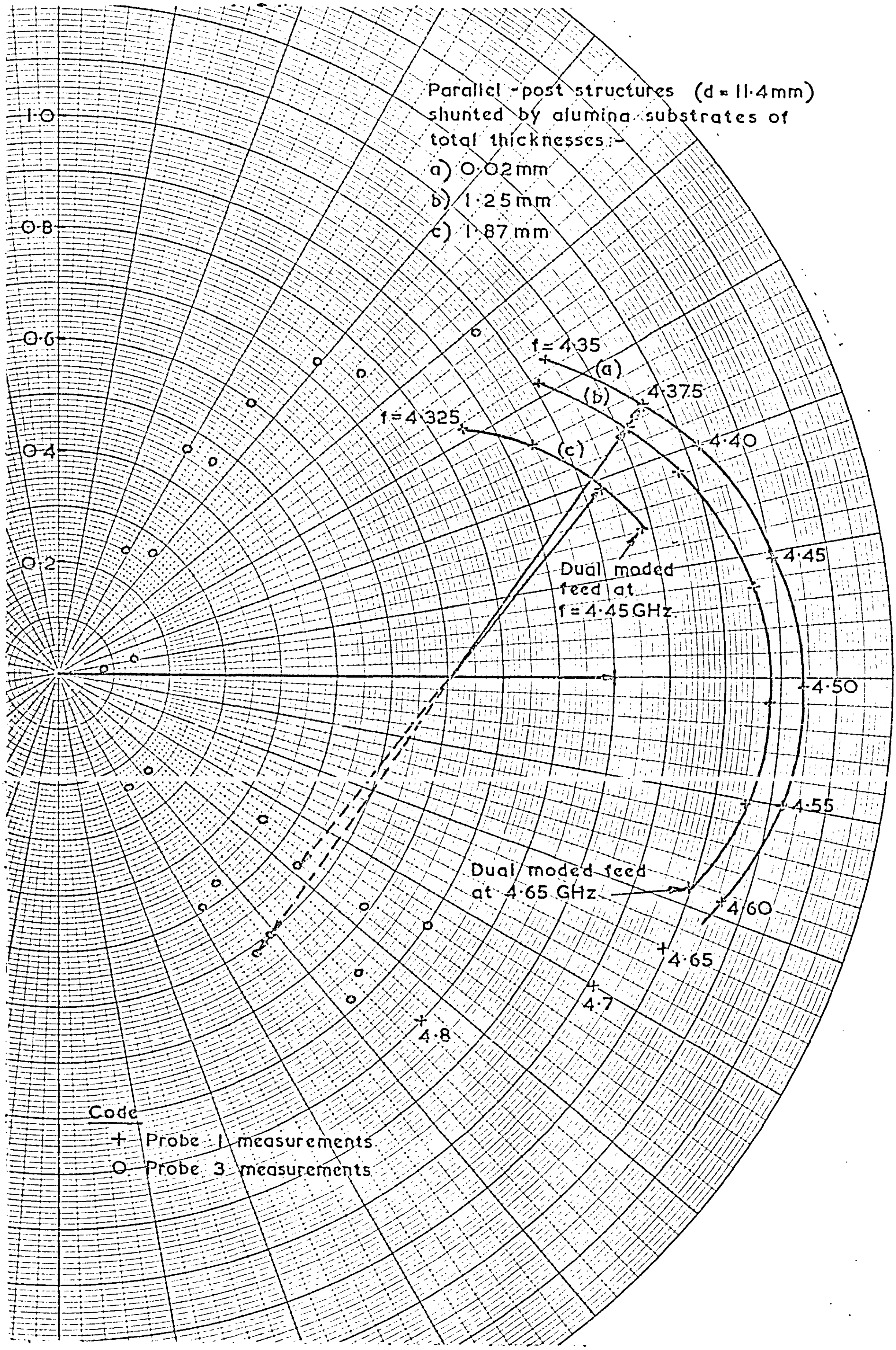

Fig.5.18 Simulator results for parallel post structures shunted by alumina substrates

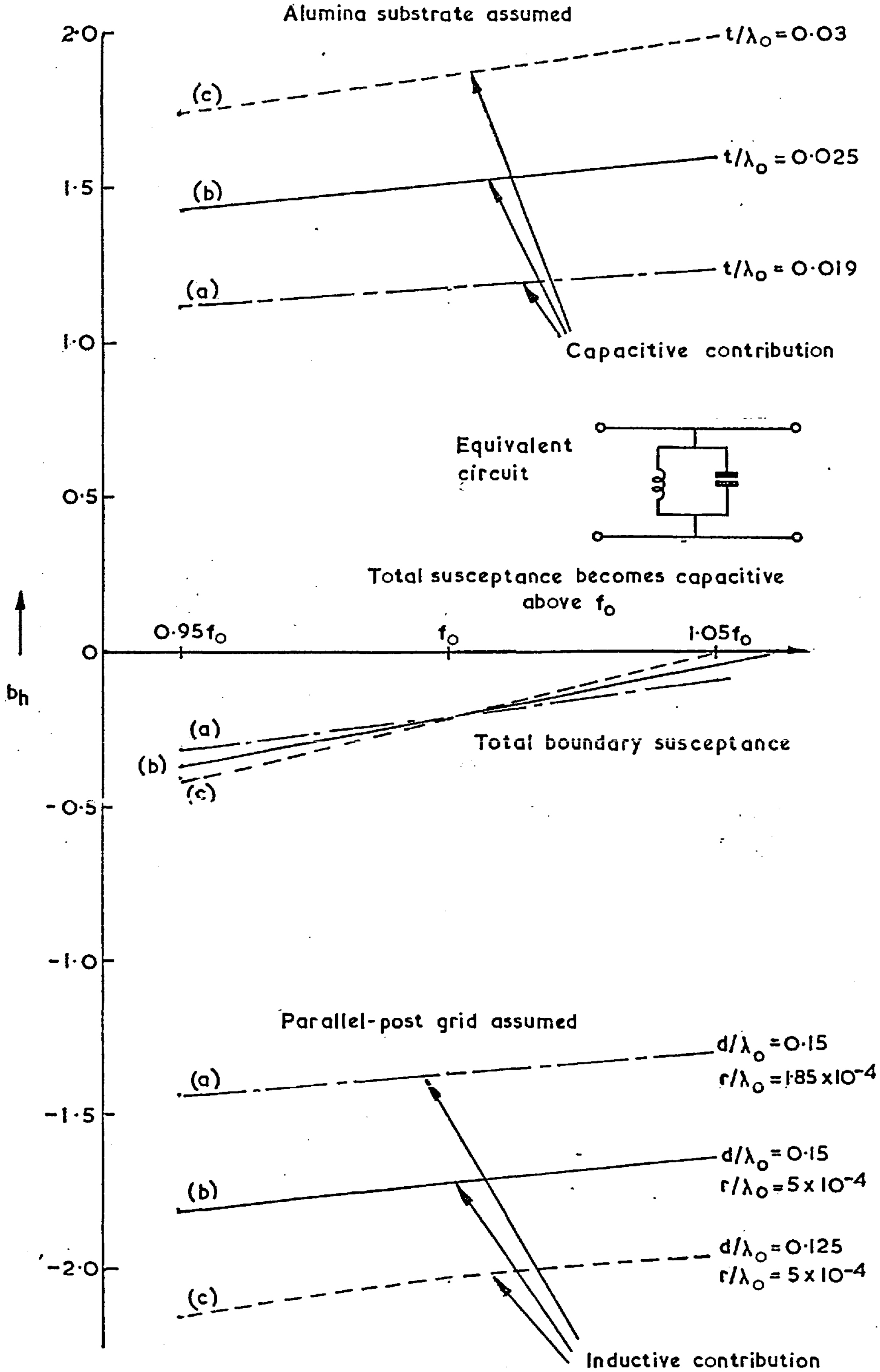

Fig.5.19 Variation of boundary susceptance with frequency for different printed circuit designs, assuming a requirement for $b_h = -0.2$ at f_o.

CHAPTER 6

DESIGN PROCEDURES FOR MULTI-SECTION INFINITE ARRAY TRANSITIONS

6.1 Introduction

The purpose of this chapter is to outline general design techniques for E- and H-plane multi-section transition structures. Each section is assumed to consist of a constant susceptance region, with the same ideal characteristics ascribed to the boundary structures as in Chapters 2 and 4. The susceptances form a monotonic sequence in either polarisation (i.e. $b_{h,n} < b_{h,n+1}$ in the H-plane, and $b_{e,n} > b_{e,n+1}$ in the E-plane) with limit values - $b_{h,o} = b_{e,o} = \infty$ and $b_{h,m} = b_{e,m} = 0$. (As in Chapter 4, the second subscript indicates the number of the susceptance region, i.e. $m = 0,1,2, \ldots,m-1, m$, where m is finite.) Although an infinite array is assumed in the analyses, a numerical procedure is outlined for estimating the number of dummy elements required in a practical (finite) array. Analytical and numerical results are given for single-section transitions, while for structures of 2 or more sections, numerical optimisation techniques are recommended. The economic feasibility of applying published "parameter optimisation" strategies is established (e.g. 113).

The proposed technique can be split into two distinct parts. The first requires that the results developed in Chapters 2 and 4 be organised so that an objective function U (which can be some feature of the element pattern, the active reflection coefficient, or a consistent combination of both) is expressed in terms of the design parameters. These are the boundary susceptance and length of each section, and (in principle at least) the element spacing. In all cases considered, this objective function is chosen to be the maximum deviation of the response from "ideal" behaviour *when the maximum scan angle is specified to be less than the theoretical limit.* (It must be emphasised that this concept of "ideal" behaviour is not identical with that of Hannan (8), which can be regarded as the extreme case when the maximum scan angle and the theoretical limit are equal. Nevertheless, a close and flexible relationship is preserved by the present formulation which is a natural consequence of constraining the transition to a finite length.) The second part requires an optimisation strategy (executed on a high speed computer) to choose suitably constrained parameters which minimise the value of the objective function - i.e. parameters which minimise deviation of the response from the (still unattainable) "ideal" response. For example, in the case of an inhomogeneous multi-section waveguide transformer, such a "minimax" strategy leads to an equi-ripple, minimum V.S.W.R. response over a specified bandwidth (114). The basic similarities between the design problems for these transformers and arrays with reactive element boundaries have already been noted in Section 2.3.2.

Several features peculiar to the multi-section array structure appear to preclude the possibility of extending this analogy to cover approximate methods of design, which are often satisfactory for waveguide transformers (e.g.115,116). Approximate analytical techniques depend on a simplifying relationship; for instance, in Riblet's model (116), it is assumed that the relative impedance of two waveguides of slightly different widths is constant over the design bandwidth. In addition, all theoretical models assume that a first-order correction for "non-ideal" transmission line junctions is sufficient to account for the effective shunt susceptance at each discontinuity. It is considered that the effective "impedance variations" in any reactive boundary section operating near a cut-off condition, and the corresponding changes in the arguments of the affected scattering matrix elements, could not be handled realistically with these transmission line concepts. (The H-plane results given in Figs. 4.4 to 4.7 illustrate how the phase of terms $S_{i'j'}$ vary quite rapidly with element phasing in the vicinity of a cut-off condition. A similar effect is evident in the E-plane (see following section).) Approximate techniques are most likely to help in setting initial values in the numerical optimisation.

6.2. Formulation of Objective Functions

Retaining the operating conditions which were recommended in Chapter 2 during the study of mode charts (Figs. 2.11 and 2.23), the E- and H-plane element spacings can be taken to be $0 < a/\lambda_{eff} < 0.5$ and $0.5 < a/\lambda < 1.0$ respectively. The multi-section E-plane structure, which then corresponds to a cascade series of two port networks (Fig. 6.1), is considered first.

The E-plane problem can be approached from either of two equivalent viewpoints. Assuming the network shown in Fig. 6.1 to be lossless, it follows directly that maximum power transfer into the free space wave (characterised by $\vec{C}_{1,m}$) would be achieved if the insertion loss were zero over the required scanning range $0 < \psi_e < \psi_{e,max}$, where $\psi_{e,max}$ is less than the theoretical limit $2\pi\ a/\lambda_{eff}$. Alternatively, this same "ideal" requirement can be deduced from the previously observed limitations of an E-plane waveguide array (Chapter 3) and the impedance matching problems at large scan angles. The variation of $|R_a(\psi_e)|$ for a waveguide array with $a/\lambda_{eff} < 0.5$ takes the form shown in Fig. 6.2 (c.f. 43). For the cascade network, it is first necessary to evaluate $|\overleftarrow{C}_{1,0}/\vec{C}_{1,0}|$ within the range $0 < \psi_e < \psi_{e,max}$. The objective function U can then be defined as $|\overleftarrow{C}_{1,0}/\vec{C}_{1,0}|_{max}$. As shown subsequently, the choice of $\psi_{e,max}$ imposes fundamental restrictions on the potential performance of an optimised transition.

Before continuing with a formal derivation of U, it is important to recall that the other performance characteristic of major interest in this thesis, viz the control of the radiation patterns to avoid grating lobes, is readily achieved with conventional rectangular waveguides in the E-plane using parallel plates and flares (as discussed in Chapter 3). The element spacing notation a/λ_{eff} is intended to emphasise that the actual free-space element separation (a/λ) can exceed 0.5. For rectangular waveguides, a/λ_{eff} tends to 0.5 as the critical condition for the TE_{11} mode is approached. Square waveguide elements can be successfully operated with a/λ just less than 0.707, (i.e. $a/\lambda_{eff} < 0.5$) and the corresponding sectoral coverage, beyond the parallel plate region, approaches $\pm 45^{\circ}$. Whilst this coverage can be easily reduced by operating with a smaller element spacing (e.g using standard rectangular waveguide) it can not exceed 45° (within a single moded structure with thin walls) unless the height of the elements is gradually increased within the transition structure (cf. eqn.(12) in Chapter 3 and the E-plane mode charts (Figs. 2.23 and 3.34a)). This corresponds to placing the reactive boundaries between diverging plates - i.e. in an appropriate flare (cf. Sections 3.4 and 3.6.1). It should also be noted that the matching problem between parallel plate structures and free space becomes more serious as the required sectoral coverage is reduced, since the parallel plate region must be operated nearer to the TE mode cut-off condition. These additional aspects in the design of practical linear arrays are not included in the following analysis.

Following standard practice, the junction characteristics given in Appendix 4C, viz

$$\begin{bmatrix} \overleftarrow{C}_{1,n} \\ \overrightarrow{C}_{1,n+1} \end{bmatrix} = \begin{bmatrix} S_{11} & S_{12} \\ S_{21} & S_{22} \end{bmatrix} \begin{bmatrix} \overrightarrow{C}_{1,n} \\ \overleftarrow{C}_{1,n+1} \end{bmatrix} \qquad \ldots.(1)$$

can be expressed in the form of a transmission matrix, with

$$\begin{bmatrix} \overrightarrow{C}_{1,n} \\ \overleftarrow{C}_{1,n} \end{bmatrix} = \frac{1}{S_{21}} \begin{bmatrix} 1 & -S_{22} \\ S_{11} & (S_{21}S_{12}-S_{11}S_{22}) \end{bmatrix} \begin{bmatrix} \overrightarrow{C}_{1,n+1} \\ \overleftarrow{C}_{1,n+1} \end{bmatrix} . \qquad \ldots.(2)$$

Since only the first mode is encountered in the E-plane, the subscript 1 in terms $C_{1,n}$ etc. can be dropped at this stage for simplicity. Furthermore, to distinguish the various junctions, eqn.(1) can also be rewritten in the form (cf. Appendix 4C)

$$\begin{bmatrix} \overleftarrow{C}_n \\ \overrightarrow{C}_{n+1} \end{bmatrix} = \begin{bmatrix} \rho_n.\exp(j\alpha_n') & \frac{1}{U_n}\sqrt{1-\rho_n^2}.\exp\{j(\alpha_n'+\alpha_n'')/2\} \\ U_n\sqrt{1-\rho_n^2}.\exp\{j(\alpha_n'+\alpha_n'')/2\} & -\rho_n.\exp(j\alpha_n'') \end{bmatrix} \begin{bmatrix} \overrightarrow{C}_n \\ \overleftarrow{C}_{n+1} \end{bmatrix} \quad ...(3)$$

where ρ_n = magnitude of the term S_{11} (i.e. the reflection coefficient)

$\alpha_n' = P_{2,2}(\beta_{1,n})$

$\alpha_n'' = P_{2,2}(\beta_{1,n+1})$

and U_n = the real factor U appearing in Appendix 4C, and does not equal unity because the fields (described by C_n and C_{n+1}) are not normalised in terms of power flow (cf. Section 4.2.4).

The reference plane for the fields $\overrightarrow{C}_n$ and $\overleftarrow{C}_n$ can be moved from z_n to $z_n - d_n$ by the matrix equation

$$\begin{bmatrix} \overrightarrow{C}_n' \\ \overleftarrow{C}_n' \end{bmatrix} = \begin{bmatrix} \exp(j\beta_n d_n) & 0 \\ 0 & \exp(-j\beta_n d_n) \end{bmatrix} \begin{bmatrix} \overrightarrow{C}_n \\ \overleftarrow{C}_n \end{bmatrix} \quad .... (4)$$

reading β_n for $\beta_{1,n}$. Combining eqns. (3) and (4), the effective transmission properties for a single section of the structure (see Fig. 6.3) can be written as

$$\begin{bmatrix} \overrightarrow{C}_n' \\ \overleftarrow{C}_n' \end{bmatrix} = \frac{\exp\{-j(\alpha_n'+\alpha_n'')/2\}}{U_n\sqrt{1-\rho_n^2}} \begin{bmatrix} \exp(j\beta_n d_n) & \rho_n\exp\{j(\alpha_n''+\beta_n d_n)\} \\ \rho_n\exp\{j(\alpha_n'-\beta_n d_n)\} & \exp\{j(\alpha_n'+\alpha_n''-\beta_n d_n)\} \end{bmatrix} \begin{bmatrix} \overrightarrow{C}_{n+1} \\ \overleftarrow{C}_{n+1} \end{bmatrix}$$

$$.... (5)$$

or more compactly as

$$\left[\underset{\sim}{C}_n'\right] = \left[\underset{\sim}{T}\right]_n \left[\underset{\sim}{C}_{n+1}\right] \quad .... (6)$$

For the network in Fig. 6.1, the fields $\left[\underset{\sim}{C}_o\right]$ are then related to $\left[\underset{\sim}{C}_m\right]$ by a correctly ordered sequence of matrix multiplications implicit in the relation

$$\left[\underset{\sim}{C}_o\right] = \left\{\prod_{n=o}^{m-1} \left[\underset{\sim}{T}\right]_n\right\} \left[\underset{\sim}{C}_m\right] \qquad \ldots. (7)$$

i.e. $$\begin{bmatrix} \vec{C}_o \\ \overleftarrow{C}_o \end{bmatrix} = \begin{bmatrix} T_{11} & T_{12} \\ T_{21} & T_{22} \end{bmatrix} \begin{bmatrix} \vec{C}_m \\ \overleftarrow{C}_m \end{bmatrix} \qquad \ldots. (8)$$

In transmission, $\overleftarrow{C}_m = 0$, and the active reflection coefficient $R_a(\psi_e)$ is given by

$$R_a(\psi_e) = \frac{\overleftarrow{C}_o}{\vec{C}_o} = \frac{T_{21}}{T_{11}} \qquad \ldots. (9)$$

The objective function U can then be expressed in terms of the design parameters (Φ_e) as

$U(\Phi_e) = \max |R_a(\psi_e)|$

where

Φ_e is the string $\left[a, d_1, b_{e,1}, \ldots., d_n, b_{e,n}, \ldots., d_{m-1}, b_{e,m-1}\right]$ .... (10)

The normal interrelationship between a/λ_{eff} and ψ_e for scanning over a specified sector $\pm\theta_{o,max}$ could be regarded as a design constraint. The parameters in eqn.(10) do not include $b_{e,m}$ and $b_{e,o}$, which are fixed, or d_o, which does not affect U in a lossless structure. The degrees of freedom afforded by this formulation are examined numerically for m = 2 in Section 6.3 and in Section 6.4 when m > 2.

The H-plane design task is more complicated than the E-plane problem. The equivalent cascade network in Fig. 6.4 illustrates that the number of "ports" at junctions near the aperture is a function of

ψ_h, with 2, 3 or 4 modes to be considered. To resolve this variable condition, all junctions could be represented as 4 ports, but this is unnecessary for regions where the second mode is always cut-off and of negligible amplitude at very short distances from the junction (as in the E-plane). By selecting a value for the element spacing in advance (using, for instance, the numerical results given in the next section as a guide to a "realistic" value within the range $(1 + \sin\theta_{o,max})^{-1} < a/\lambda < (2\sin\theta_{o,max})^{-1}$), the design task can be split into two parts. This division can be made by calculating the critical susceptance for the second mode at the maximum scan angle, with the relation derived in Section 2.2.2, viz

$$b_{hc} = 2\left\{\frac{\cos(2\pi a/\lambda) - \cos(\psi_{h,max})}{\sin(2\pi a/\lambda)}\right\} \quad \text{.... (11)}$$

and including a section with this susceptance in the transition, (say the "i"th section). Then the purpose of sections 1, 2, ... i-1, which constitute a network of 2 ports, is to maximise the power incident on the (i + 1)th section. This defines a partial objective which is analogous in principle to that in the E-plane, but simpler to achieve in practice, as shown in the next section. An inspection of the 2 X 2 scattering matrix given in Appendix 4B reveals that it can be written in a similar form to eqn. (3) above, except for a sign reversal on terms S_{11} and S_{22}. Consequently, a set of equations equivalent to eqns.(4) to (9) can again be obtained, and the corresponding objective U can be expressed in terms of the parameters (Φ_{h1}) as

$$U(\Phi_{h1}) = \max|R_a(\psi_h)|\,;\ \text{where}\ \Phi_{h1} = [d_1, b_{h,1}, d_2, b_{h,2}, \cdots\, d_{i-1}, b_{h,i-1}] \quad \text{.... (12)}$$

For the cascaded regions (i+1, i+2, ..., m-1), the simultaneous operational requirements for element pattern control and high radiation efficiency lead in principle to the dual task of minimising $\vec{B}_{2,m}$ and $\overleftarrow{A}_{1,i}$. Fortunately, the constraints on the design ensure that $\overleftarrow{A}_{1,i}$ remains small for any choice of parameters $b_{h,n}$ and d_n $(i - 1 < n < m - 1)$ and less than an upper limit which can be estimated readily (see next section). It is therefore considered practical to utilise all the degrees of freedom to achieve optimum grating lobe suppression, through an objective function given by

$$U \propto \max \left[\frac{\text{Power radiated in the grating lobe}}{\text{Power radiated in the main beam}}\right] \quad \text{.... (13a)}$$

$$\propto \max \left[\frac{|\vec{B}_{2,m}|^2 \ \beta_{2,m}^2}{|\vec{A}_{1,m}|^2 \ \beta_{1,m}^2}\right] \quad \text{.... (13b)}$$

i.e.

$$U = \max \frac{|\vec{B}_{2,m}| \ \beta_{2,m}}{|\vec{A}_{1,m}| \ \beta_{1,m}} \quad \text{.... (13c)}$$

within the range $2\pi(1 - a/\lambda) \leq \psi_h \leq \psi_{h,max}$ (where $\psi_{h,max} = 2\pi \ a/\lambda \sin \theta_{o,max}$ and the parameters are $b_{h,i+1}, d_{i+1}, b_{h,i+2}, \ldots, b_{h,m-1}, d_{m-1}$.) Relation (13b) is derived from (13a) through the equations for power flow in any mode (eqn.(34), Chapter 2 with $\vec{B}_{1,m} = \vec{A}_{2,m} = 0$) and the dependence of $g_e(\theta)$ on the power transmission coefficients (eg. eqn.(8), Chapter 3).

The element pattern for a waveguide array with $a/\lambda = 0.695$ (Fig. 6.5) indicates the two angular sectors of interest for symmetrical scanning about broadside. For relative grating lobe suppression exceeding 20dB, it is clear from Fig. 6.5 that most of the improvement (on a "dB scale") afforded by reactive boundaries must come from a reduction in the numerator on the RHS of eqn.(13c) rather than any significant increase in the denominator. (The improvement in main beam power must be less than 3dB, and would typically be < 2dB). It could therefore be argued that an adequate objective function would be

$$U = \max \quad |B_{2,m}| \ \beta_{2,m} \quad \text{.... (14)}$$

[The incident power prevented by a transition structure from radiating in the grating lobe is retained automatically within the main beam assuming that $\overleftarrow{A}_{1,i}$ remains negligible.] The distinction between eqns.(13c) and (14) would become significant only during the final stages of parameter optimisation with a "minimax" strategy. Equation (14) would lead to an essentially equi-ripple element pattern in the region $\arcsin[(\lambda/a)-\sin\theta_{o,max}] < |\theta| < \pi/2$, whereas the result using eqn.(13c) would include an effective compensation for the gain reduction caused by aperture projection.

The 4 port network equations in Appendix 4B for a single junction, given by

$$[\overleftarrow{A}_{1,n}, \overrightarrow{A}_{1,n+1}, \overleftarrow{B}_{2,n}, \overrightarrow{B}_{2,n+1}]^t$$
$$= [S]_n \, [\overrightarrow{A}_{1,n}, \overleftarrow{A}_{1,n+1}, \overrightarrow{B}_{2,n}, \overleftarrow{B}_{2,n+1}]^t \qquad \ldots. (15)$$

(where the superscript t indicates the transpose) can be rearranged in the form

$$[\overrightarrow{A}_{1,n}, \overleftarrow{A}_{1,n}, \overrightarrow{B}_{2,n}, \overleftarrow{B}_{2,n}]^t$$
$$= [\underset{\sim}{T}]_n \, [\overrightarrow{A}_{1,n+1}, \overleftarrow{A}_{1,n+1}, \overrightarrow{B}_{2,n+1}, \overleftarrow{B}_{2,n+1}]^t \qquad \ldots. (16)$$

Due to the different formulae for terms $S_{i',j'}$ when the mode denoted by $B_{2,n}$ is cut-off, this transmission matrix is most conveniently obtained by standard computer subroutines. (The lengthy analytical expressions for the elements of this matrix are not needed in following sections, and are therefore not given.) The reference plane for the column matrix $[\overrightarrow{A}_{1,n}, \overleftarrow{A}_{1,n}, \overrightarrow{B}_{2,n}, \overleftarrow{B}_{2,n}]^t$ can be referred to the preceding junction by premultiplying eqn. (16) by the diagonal matrix

$$\begin{bmatrix} \exp(j\beta_{1,n}d_n) & & & 0 \\ & \exp(-j\beta_{1,n}d_n) & & \\ & & \exp(\gamma_{2,n}d_n) & \\ 0 & & & \exp(-\gamma_{2,n}d_n) \end{bmatrix}$$

where $\gamma_{2,n} = j\beta_{2,n}$ or $\xi_{2,n}$ as appropriate, and the result, corresponding to the transmission properties of a single section, has the general form

$$[\vec{A}'_{1,n}\ ,\ \overleftarrow{A}'_{1,n}\ ,\ \overleftarrow{B}'_{2,n}\ ,\ \overleftarrow{B}'_{2,n}]^t = [\underset{\sim}{T}']_n\ [\vec{A}_{1,n+1}\ ,\ \overleftarrow{A}_{1,n+1}\ ,\ \vec{B}_{2,n+1}\ ,\ \overleftarrow{B}_{2,n+1}]^t \quad \text{.... (17)}$$

The overall transmission matrix relating the fields in "i"th section and in free space is then given by the ordered product

$$[\underset{\sim}{T}'] = \prod_{n=i}^{m-1} [T']_n \quad \text{.... (18)}$$

Reverting to a scattering matrix format with

$$[\overleftarrow{A}'_{1,i}\ ,\ \vec{A}_{1,m}\ ,\ \overleftarrow{B}'_{2,i}\ ,\ \vec{B}_{2,m}]^t = [\underset{\sim}{S}']\ [\vec{A}'_{1,i}\ ,\ \overleftarrow{A}_{1,m}\ ,\ \vec{B}'_{2,i}\ ,\ \overleftarrow{B}_{2,m}]^t \quad \text{.... (19)}$$

and noting that $\overleftarrow{A}_{1,m} = \vec{B}_{2,i} = \overleftarrow{B}_{2,m} = 0$ (in a transmitting array), the objective function defined by eqn.(13c) can be accurately approximated by the relation

$$U(\Phi_{h2}) = \max \frac{|S'_{41}| \cdot \beta_{2,m}}{|S'_{21}| \cdot \beta_{1,m}};\ \text{where } \Phi_{h2} = [d_{i+1}, b_{h,i+1} \cdots d_{m-1}, b_{h,m-1}] \quad \text{....(20)}$$

.... (20)

over the range $2\pi(1 - a/\lambda) < \psi_h < \psi_{h,max}$ as already indicated. (S'_{41} and S'_{21} are elements of the matrix defined in eqn.(19)). The approximation arises by ignoring the incident power variations in the "i"th region when $U(\Phi_{h1})$ is not identically zero.

An optimisation approach based on eqns.(12) and (20) does not include the length of the "i"th section (i.e. the section chosen to give single moded propagation at $\psi_{h,max}$) as a design parameter. As a simple solution, it would be adequate to choose d_i so that the evanescent fields at its 2 junctions are not interacting. For larger values of a/λ (say $a/\lambda > 0.75$), it might be considered sufficient to let $i = 1$, and simply choose d_i to reduce the small reflection "losses" between the waveguide feed and the region i + 1. The numerical examples given in the following section provide the necessary background for estimating the acceptability of the latter approach.

6.3. Single - Section Transitions

The performance of single-section transitions can be considered without recourse to numerical optimisation strategies. The results given below provide some initial guidelines for estimating the number of sections which would be needed to meet performance specifications on impedance matching and grating lobe suppression. In the H-plane, the term "single-section" is strictly inappropriate, since the final structure would contain 3 regions of finite susceptance. However, by selecting $b_{h,2}$ in accordance with eqn.(11), the partitioned structure can be analysed readily as 2 "single-section" transitions, with parameters $b_{h,1}$ and d_1 in one case, and $b_{h,3}$ and d_3 in the other. The E-plane matching problem is again examined first (Fig. 6.6), for a single value of a/λ_{eff}.

Taking a/λ_{eff} as 0.45, the maximum value of ψ_e to avoid complete internal reflection at the array aperture is 162° (or $2\pi.a/\lambda_{eff}$). In Fig. 6.7, an auxiliary axis is included which shows the equivalent scan angle θ_o in free space when this array consists of square waveguide elements ($a/\lambda = 0.673$) and parallel plates extending a finite distance beyond the "aperture" formed by the waveguide elements. The value chosen for a/λ_{eff} is considered typical of the range which might be adopted in practice.

For the one-section transition, the active reflection coefficient can be expressed as

$$R_a(\psi_e) = \frac{S_{11}^f \exp(j\beta_1 d_1) + S_{11}^a (S_{21}^f S_{12}^f - S_{11}^f S_{22}^f)\exp(-j\beta_1 d_1)}{\exp(j\beta_1 d_1) - S_{11}^a S_{22}^f \exp(-j\beta_1 d_1)} \quad \text{.... (21)}$$

where the terms are defined in Fig. 6.6. Using the properties of the junctions expressed by eqn. (3), the degrees of freedom afforded by $b_{e,1}$ and d_1 can be utilised by setting eqn. (21) to zero at some specified element phasing ψ_e'. The two conditions to be satisfied are given by

$$|S_{11}^a| = |S_{11}^f| \quad \text{.... (22)}$$

$$2\ \beta_1 d_1 = \pi + \arg(S_{11}^a) + \arg(-S_{22}^f) \quad \text{.... (23)}$$

These equations are analogous with the junction-compensated requirements for quarter-wavelength impedance matching of waveguide transformers at a single frequency.

Reference to Appendix 4C shows that the relation between β_0, β_1 and β_2 at ψ_e' is specified by the first of the two conditions (eqn. (22)), with

$$\beta_1^2 = \beta_0\beta_2 \text{ at } \psi_e = \psi_e' \quad \text{.... (24)}$$

where $\beta_0 = k$ .... (25a)

and $\beta_2 = k\left[1-\left(\frac{\psi_e'}{2\pi}\cdot\frac{\lambda_{eff}}{a}\right)^2\right]^{\frac{1}{2}}$ .... (25b)

The appropriate value of $b_{e,1}$ is then obtained from the characteristic E-plane equation as

$$b_{e,1} = 2\frac{\left[\cos(a\sqrt{k^2-\beta_1^2}) - \cos(\psi_e')\right]}{\sin(a\sqrt{k^2-\beta_1^2})} \quad \text{.... (26)}$$

The length of the section can be chosen after the arguments of the complex terms S_{11}^a and S_{22}^f have been calculated for junctions with susceptance discontinuities of $b_{e,o}$ to $b_{e,1}$ and $b_{e,1}$ to $b_{e,2}$.

This design procedure has been carried out (using 8 roots to estimate the phase of the scattering matrix elements and a modern desk calculator) with $\psi_e' = 135^{\circ}$ and $a/\lambda_{eff} = 0.45$, to illustrate the predicted improvement in performance. As implied by the results in Fig. 6.7, the required value of $b_{e,1}$ becomes 1.275. The curves labelled (2) and (3) in Fig. 6.7 have been obtained at values of $\psi_e = 30^{\circ}, 90^{\circ}, 120^{\circ}, 135^{\circ}, 155^{\circ}$ and (for curve (2)) 180°. (The active reflection coefficient for the waveguide array (labelled (1) in Fig. 6.7) is given in reference 43, and provided a convenient check on numerical accuracy.)

Figures 6.8a and b show the variation with ψ_e of two of the principal terms affecting $R_a(\psi_e)$ as defined in eqn.(21). The argument of $-S^f_{22}$ varies less than $\pm$ 5° from $[-\arg(S^f_{11})]$ over the full range of ψ_e, and the resulting "junction phase effects" (Fig. 6.7) contribute to an increase in $|R_a(\psi_e)|$ where $\psi_e < 120^{\circ}$ or $> 135^{\circ}$. The relatively small deviation of $\beta_1 d_1$ from the quarterwavelength condition at values of $\psi_e > 135^{\circ}$ tends to preserve the required phase conditions for impedance matching, with the main limitation arising from the rapid increase in $|S^a_{11}|$ as $\psi_e \to 162^{\circ}$, as shown by Fig. 6.7. The net improvement afforded by this design is shown in Fig. 6.9.

The significance of ψ_e' as the basic "optimisation" parameter should be noted. To achieve a better radiation efficiency with the single-section transition at values of ψ_e between 150° and 162°, a larger value of ψ_e' must be adopted. For example, choosing ψ_e' as 155°, the required susceptance is reduced from the previous value of 1.275 to 0.53, while the length of the section is increased by approximately 40%. The major consequences can be appreciated without calculating the junction phase effects, since the amplitudes of S^a_{11} and S^f_{11} diverge rapidly at values of ψ_e below 155°, and the variation in electrical path length $\beta_1 d_1$ is more pronounced than in Fig. 6.8b. These trends are illustrated in Fig. 6.10, from which it can be predicted that the improvement at $\psi_e = 90^{\circ}$ due to the presence of the transition would be quite negligible. Nevertheless, it could be considered that the resulting variation in $|R_a(\psi_e)|$, which must be constrained as shown in Fig. 6.11, is preferable to that obtained in Fig. 6.9 with $\psi_e' = 135^{\circ}$. The design choice afforded by ψ_e' is therefore clarified. By choosing a value of ψ_e' close to the cut-off condition (i.e. 162° in the present example), the control over $|R_a(\psi_e)|$ is confined to a narrower range (or "band") of scan angles, but is more significant in terms of the improvement in radiation efficiency at ψ_e' as indicated by Figs. 6.9 and 6.11. This effect is comparable with the design options for wide angle matching of radomes consisting of sandwiched dielectric sheets or a single dielectric loaded with periodic metal gratings (52).

Turning to the H-plane problem, the principles outlined in the previous section are applied to an array with $a/\lambda = 0.695$, which is required to scan to $\sin\theta_{o,max} = \pm 0.55$. This element spacing and maximum scan angle correspond to a condition lying between the operating limits examined in Chapter 1 - i.e.

$$\frac{a}{\lambda} < \frac{1}{1 + \sin\theta_{o,max}} \qquad \text{.... (27a)}$$

for grating waves to remain evanescent, and

$$\frac{a}{\lambda} < \frac{1}{2\sin\theta_{o,max}} \qquad \text{.... (27b)}$$

for an element phasing of π radians (see Fig. 1.7). The significance of specifying both $\theta_{o,max}$ and a/λ in advance is examined in Section 6.3. For the purpose of the following example, it is sufficient that a/λ and $\theta_{o,max}$ should lie between the two conditions given by expns. (27a) & (27b).

With $\psi_{h,max} = 137.5^{\circ}$, the critical susceptance for the second mode becomes $- 0.83$ on substitution in eqn.(11). This defines the susceptance of the "i"th section, i.e. with i = 2, $b_{h,2} = - 0.83$. The two remaining parts of the design can be undertaken using, in part, the results given in Figs. 4.5 to 4.7. As the impedance matching section can be designed in a manner equivalent to the technique already discussed above, the detailed procedure is not repeated. The active mismatch between the waveguide feed and a region with $b_h = - 0.83$ (in the absence of any intermediate region) is indicated by the curve labelled (1) in Fig. 4.7. By contrast with the E-plane problem, the "insertion loss" over all ψ_h would be quite small (< 0.1dB) without any matching section. Applying conditions equivalent to those given in eqns.(22) to (26), a zero of reflection between regions 0 and 2 can be achieved at $\psi_h = 60^{\circ}$ with a "junction-corrected" quarter wavelength section when $b_{h,1} = - 3.85$ (see curves labelled (2) and (3) in Fig. 4.7). The variation in $\beta_{1,1}d_1$ and the phase correction for junction effects over the required range of ψ_h are shown in Fig. 6.12, from which it can be established that the insertion loss is reduced to a negligible level for any element phasing, with the maximum value of $\overleftarrow{A}_{1,0}/\overrightarrow{A}_{1,0}(\overleftarrow{A}_{1,2} = 0)$ being 0.025 at $\psi_{h,max}$ (Fig. 6.13).

In the light of this result, it is difficult to foresee any engineering requirement for more than one matching section when a/λ exceeds a value of about 0.6. [The initial problem, as defined in Fig. 4.7 by curve (1) for $a/\lambda = 0.695$, becomes smaller as a/λ increases.] However, a multi-section matching transition might be justified if the element spacing were required to be in the range $0.5 < a/\lambda < 0.55$ (say), in which event, the problem of grating-wave radiation would be trivial.

For the second part of the design, an initial qualitative assessment suggests that an element pattern zero could be achieved in the grating wave section when region 3 is approximately half a wavelength for the first mode ($\vec{A}_{1,3}$). This conclusion is obtained by assuming that the forward scattered second mode ($\vec{B}_{2,3}$), generated at the discontinuity between regions 2 and 3, is relatively small in amplitude and sufficiently close to cut-off for its wavelength to be significantly larger than that of the dominant mode $\vec{A}_{1,3}$. Ignoring all secondary and higher order reflections within the transition, an element pattern zero can be introduced when the *additional* forward scattered second mode generated at the aperture discontinuity (i.e. between regions 3 and 4) is equal in ámplitude and out of phase with the transmitted component of $\vec{B}_{2,3}$. This principle is represented schematically by the series of "phasor" diagrams given in Fig. 6.14, where the scattering matrix superscripts "f" and "a" are reintroduced for reference below.

A detailed examination of computed 4 port scattering matrices for susceptance discontinuities with $\Delta b_h \sim 0.3$ to 0.5 and $a/\lambda = 0.695$ reveals that this qualitative assessment is realistic over a satisfactory range of ψ_h. The grating wave can then be approximated by the expression

$$\vec{B}_{2,4} = S^f_{41}S^a_{43}\exp(-j\beta_{2,3}d_3) + S^f_{21}S^a_{41}\exp(j\beta_{1,3}d_3) \qquad \ldots. \ (28)$$

and the resultant uncertainty estimated subsequently. For $\vec{B}_{2,4}$ to vanish at a particular angle $\theta' = \arcsin[(\lambda/a)(1 - \psi_h'/2\pi)]$, it is necessary to find a combination of $b_{h,3}$ and d_3 which renders

$$|S^f_{41}||S^a_{43}| = |S^f_{21}||S^a_{41}| \qquad \ldots. \ (29a)$$

and $\arg(S^f_{41}) + \arg(S^a_{43}) - \arg(S^f_{21} - \arg(S^a_{41}) = \pi - (\beta_{1,3}-\beta_{2,3})d_3$ ....(29b)

for the element phasing ψ_h'. Whilst the degrees of freedom are sufficient to satisfy these two conditions, the selection of a value $b_{h,3}$ to fulfil eqn.(29a) is extremely complicated on an analytical basis, which can be confirmed by inspecting the amplitude expressions given in Appendix 4B for individual terms $S_{i'j'}$. To overcome this difficulty, the ratios $|S^f_{41}/S^f_{21}|$ and $|S^a_{41}/S^a_{43}|$ can be calculated as functions of the potential susceptance of region 3 for the proposed element phasing ψ_h'. In the present example, ψ_h' is taken as 132.5^o, which is slightly less than $\psi'_{h,max}$ (137.5^o), for which the conventional grating wave problem is most serious (Fig. 6.5). From Fig. 6.15, it can be seen that the susceptance $b_{h,3}$ should be -0.4 to satisfy eqn. (29a). With the susceptances $b_{h,2}$, $b_{h,3}$ and $b_{h,4}$ all defined, the junction phase effects included in eqn. (29b) can be obtained, and the second parameter (d_3) specified.

The amplitude and phase of S^f_{41} and S^a_{43} are shown in Fig. 6.16, where the significant variation in the amplitude of S^a_{43} (for $\psi_h < \psi_{h,max}$) can be attributed to the relative difference between $\beta_{2,3}$ and $\beta_{2,4}$ as $\beta_{23} \to 0$. By contrast, the smaller relative differences between the dominant mode roots $\beta_{1,2}$, $\beta_{1,3}$ and $\beta_{1,4}$ ensure that terms such as S^a_{21} and S^f_{21} are approximately unity (and positive real). Over the range of element phasing now of interest (i.e. $109.7^o < \psi_h < 137.5^o$), the term S^f_{21} remains equal to 1.01 ± 0.01 in amplitude and 0 ± 0.5^o in phase. Consequently, the term $S^f_{21}\ S^a_{41}$, as a function of ψ_h, is effectively given by the computed result in Fig. 4.6 with $b_{h,n} = -0.4$. In combination with the phase information in Fig. 6.16, the required value of d_3 becomes $0.87\lambda_o$, which makes $\beta_{1,3}d_3$ equal to 252^o at ψ_h'.

The resulting variation in the amplitude of eqn.(28) is the crucial factor in terms of grating wave suppression at all angles. and Fig. 6.17 shows the control afforded by the single-section transition assuming eqn.(28). The effective limits on ψ_h should be noted in Fig. 6.17. For values of $\psi_h > \psi_{h,max}$, the assumption that $B_{2,2}$ remains evanescent is invalidated. Conversely, at $\psi_h = 121.5^{\circ}$, the mode $B_{2,3}$ becomes evanescent, and the exponent $-j\beta_{2,3}d_3$ in eqn.(28) must be replaced by $-\xi_{2,3}d_3$, with a corresponding adjustment in the expression for S^f_{41}.

The element pattern produced by an overall transition with the above design of regions of 1,2 and 3 is shown in Fig. 6.18 and labelled (1). The dotted portions indicate the spatial sectors where some uncertainty exists due to the effects just described. A comparison with the corresponding pattern for a waveguide array (labelled (2) in Fig. 6.18) shows that the minimum grating wave suppression has been improved from - 6.7dB to around - 19dB. The third result in Fig. 6.18 indicates the performance afforded by a transition which remains single moded at $\psi_{h,max}$ - i.e. $b_{h,m-1}$ is determined by eqn.(11) - when the maximum available power is incident on the aperture. Such a transition is accurately approximated by the above design with region 3 omitted. It is clear from this set of numerical results that the net grating wave suppression is achieved partially by the action of the single moded regions (which reduce the mean fluctuations of the periodic incident fields in a fully operative array - cf. Fig. 2.7) and partially by the dual moded region 3. However, the results confirm that the presence of the latter region (or more generally, several dual moded regions) is an essential theoretical requirement if useful grating wave suppression (say > 20dB) is desired over a significant spatial sector (e.g. $60^{\circ} < |\theta| < 90^{\circ}$). For a specified maximum scan angle $\theta_{o,max}$, the partial contribution to the grating wave suppression from the single moded regions decreases as a/λ increases.

Three other features of the main result in Fig. 6.18 require further comment. As the minimum grating wave suppression is possibly the most significant characteristic, the uncertainty associated with the "sidelobe peak" justifies first consideration. The three dotted lines shown around $\theta \sim 75^{\circ}$ correspond to the results when

(i) the evanescent mode $B_{2,3}$ is ignored, which leads to an optimistic estimate of the minimum grating wave suppression;

(ii) the term S^{f}_{41} in eqn.(28) is approximated in amplitude and phase by its cut-off value, which gives a pessimistic result;

(iii) an "estimate" is made which notes the effective constraint imposed by the pattern labelled (3), where grating wave suppression is sacrificed by omitting region 3.

Whilst it is apparent that the effects of evanescent modes should be included in any general computer formulation for a multi-section transition, the net uncertainty of less than 1dB does not warrant the additional calculation in the present example.

The second feature to note is the significance of ψ_h' as the essential design parameter in a "single-section" transition. As the grating wave suppression at $\psi_{h,max}$ is approoimately -24dB in the present case with $\psi_h' = 132.5^{\circ}$, it follows that a slightly smaller value of ψ_h' (possibly 130°) would be a better design choice. With a very small reduction in the magnitude of $b_{h,3}$, the "sidelobe peak" could then be reduced at the expense of an increase in grating wave radiation at $\psi_{h,max}$, and minimum grating wave suppression of 20dB might be achieved after optimisation. However, the result in Fig. 6.18 is sufficiently close to the single section optimum to provide the required guidelines about performance.

The third effect to be noted is the slight improvement in radiation efficiency afforded by the inclusion of the impedance matching region, which is only evident over the range $0 < |\theta| < 26.2^{\circ}$ (the angle for an end-fire grating wave). As already suggested, it could be sufficient to design the H-plane transition without this intermediate section, particularly for larger values of a/λ.

To complete this discussion, it is appropriate to review the principal assumptions in the above derivation.

(i) The question of radiation efficiency with one or more dual moded regions has not been considered explicitly. For the design outlined above, the dominant mode reflection coefficients between regions 2 and 3, and 3 and 4, remain < 0.025 for all ψ_h (cf. Fig. 4.5). Although the reflected "waves" tend to add in phase, the insertion loss remains negligible and approximately equal (at least over the range $\psi_h < \psi_{h,max}$) to the loss when region 3 is omitted - i.e. for the susceptance discontinuity $b_{h,i}$ to $b_{h,m}$.

(ii) Several assumptions are implicit in eqn.(28) and its schematic interpretation in Fig. 6.14. With only one section, these can be checked for each of the intercoupling possibilities at the two discontinuities. However, in a transition with more than one dual moded region or with ψ_h closer to 180°, it would be essential to adopt the formally correct approach defined by eqns. (15) to (19). This also obviates the necessity to check on the effects of multiple reflections as a mode approaches cut-off, when the electrical path lengths and certain affected elements $S_{i'j'}$ of the terminating junctions vary rapidly.

6.4. Extension to Multi-Section Transitions

Utilising a high-speed digital computer, it is evident that the performance of a multi-section transition can be analysed accurately, and in principle, optimised by adjustment of the design parameters. The feasibility of the second step is discussed below in the context of potential engineering specifications, with the formal requirements being to minimise the appropriate objective functions given in Section 6.2.

By analogy with the performance options in the design of multi-section filters, it is necessary to define the term "optimisation" more precisely. This can be done by utilising the concepts of a "forbidden band" and "rates of cut-off" which affect the design of Tchebyscheff equi-ripple networks (117). The well-known trade-off between passband ripple and stopband attenuation has a direct parallel in the design of E-and H-plane transitions with a given number of sections. The theoretical "ideal" for each of the latter, and the practical possibilities afforded by a 3 section transition, are sketched schematically in Fig. 6.19. For the E-plane array, an increasing performance penalty must be accepted within the operating section as the maximum scan angle converges on the limit defined by $\psi_e = 2\pi\, a/\lambda_{eff}$. In the H-plane, the minimum grating wave suppression is reduced as the desired coverage (or the element spacing) is increased. As shown in Fig. 6.19, the optimum results need not exhibit zeros, and the interval between the ripple "peaks" would be weighted by the initial waveguide problem.

The number of sections which might be incorporated in a practical structure is a key factor affecting the feasibility of any numerical optimisation strategy. In the light of the theoretical results for single-section transitions, the importance of tolerances and ohmic losses in practical arrays, and the desirability of containing the overall length (normal to the aperture), it is considered that the number of sections should be restricted to around 3 or 4. In the E-plane, the final choice could depend on the conductor losses associated with the reactive boundary currents, since there would seem little point in a structure which provided impedance matching, but attenuated more power over much of the scan sector, than would otherwise have been reflected. In the H-plane, the deciding factor could be the required tolerances, since mode coupling within each dual-moded section has been neglected. For either polarisation, these individual factors are governed by the physical form of the reactive boundaries.

The principal factors governing the feasibility of an optimisation procedure include:-

(i) the potential improvement in performance over an "unoptimised" design with the same number of sections,

(ii) the accuracy of "built-in" assumptions;

(iii) the ability to initialise parameter values realistically;

(iv) the unit cost of computing the function to be optimised;

(v) the number of parameters in the network;

(vi) the consequences of any parameter constraints; and

(vii) the availability of efficient optimisation strategies.

Some of these factors are interrelated, but a general conclusion can be reached in relation to the present requirements by considering each of the above in turn. In the following assessment, constant reference is made to the set of papers by Bandler (114,118) and Bandler and Macdonald (113).

(i) For inhomogeneous waveguide transformers, Bandler has shown that the optimised performance represents a significant improvement over that obtained from recognised approximate techniques. One example compares the response of an optimised 3 section transformer with that of a 5-section transformer designed by Matthaei, Young and Jones (49). Assuming a maximum V.S.W.R.

of 1.04, the optimised design yields an increased bandwidth despite the smaller number of sections. For reactive boundary transitions, it is considered that the "optimisation" of performance would be an essential economic requirement in a large array. In particular, any reduction in the number of sections (say from 3 to 2) afforded by optimisation routines would be of considerable importance.

The reasons for bypassing approximate analytical techniques have already been discussed in Section 6.1.

(ii) In the design of inhomogeneous waveguide networks, the junction effects are specified approximately (114). The validity of the theoretical results is enhanced by keeping discontinuities small. In a reactive boundary transition, any approximation is a consequence of the non-ideal boundaries. The achievement of effective susceptances $b_{e,n}$ or $b_{h,n}$ which remain constant with element phasing is a basic requirement to ensure agreement between theory and practice.

(iii) The initialisation of parameters is one of the more difficult problems, especially in the case of the dual moded H-plane transition. However, the single section results provide certain basic guidelines about section lengths and probable susceptance values. The optimisation strategies considered under (vii) rely directly on numerical search procedures and have been run with "poor engineering estimates" as initial values without serious cost penalties (see (vii)).

(iv) The unit cost of estimating any of the objective functions given in Section 6.1 is inseparably tied to the time required to characterise the junctions and perform the matrix manipulations for a particular value of element phasing. With the many opportunities to utilise current or stored values of variables (such as the roots of the characteristic functions), it is considered that the average time required to execute these steps for a 3 section dual-moded H-plane transition should be quite acceptable with efficient programming - possibly about 0.1 CRU's on the Honeywell Mk II System.

(v) With 3 sections, it should be practical to "optimise" all 6 network parameters with a reasonable number of objective function evaluations (say $< 10^3$). Apart from Bandler's examples of 6 parameter optimisation of microwave networks (requiring 1200 to 1300 function evaluations for 5 figure definition of parameter values) related experience on other problems (119) suggests that significant improvements in performance can be obtained before computing costs exceed benefits. With multi-section transitions, the selection of realistic termination criteria, based on design tolerances for b_n and d_n, would help to reduce the number of function evaluations required. For programme development and initial testing, it could be sensible to choose fixed values of susceptances and to allow variations only in the length of sections. (This would introduce a major saving, since the junctions would only need to be characterised once for each value of ψ.)

(vi) With sensible initial values (as distinct from "good estimates") and search intervals, it is considered that the parameter constraints should not introduce any complications during optimisation. For example, any attempt to make $b_{h,n} > b_{h,n+1}$ would cause a deterioration in performance. Similarly, the variation of electrical path lengths with element phasing represents in general a performance penalty which can only be contained by shortening the section lengths. Quarter wavelength sections are therefore better than three-quarter wavelength sections for impedance matching. It might be practical to use an essentially unconstrained strategy during optimisation, with occasional monitoring to check on current parameter values.

(vii) The choice of numerical strategies which are efficient (in terms of convergence) is the most important factor in the present assessment. Bandler and Macdonald emphasise that a "minimax" formulation gives rise, in general, to discontinuous partial derivatives of the objective function with respect to the network parameters. The optimum set of parameters can then be difficult (or impossible) to obtain with gradient search routines, such as the classical steepest descent method. The use of direct pattern search techniques becomes practical under these conditions. Two subroutines, designated "Razor Search" and "Ripple Search", were developed by Bandler and Macdonald to exploit this possibility, and are described in reference 113 through detailed flowcharts.

Whilst it is unnecessary to be committed to these particular routines, the two tasks which they perform would be essential in any alternative minimax strategy. The "Razor Search" subroutine is a modified version of multi-dimensional pattern search, which evaluates the consequences of perturbing the network parameters on the objective function. The "Ripple Search" subroutine is used to define the unimodal regions of the network response in terms of one variable - e.g. frequency or (for the present purpose) element phasing, and to find the objective function without close fixed-interval sampling. These concepts are illustrated in Fig. 6.20.

Some simplification of these strategies should be possible to satisfy the present engineering requirements. For instance, it would be unnecessary to specify U to an accuracy which affords

5 figure definition of the design parameters. Consequently, the smooth peaks of the ripple pattern shown in Fig.6.20 could probably be estimated to a sufficient accuracy by interpolation rather than direct search strategies, such as the Fibonnacci scheme used by Bandler and Macdonald.

Overall, it is considered that numerical optimisation of multi-section transitions, along the lines discussed above and in Section 6.2, is both feasible and desirable.

6.5 Control of Edge Effects with Dummy Elements

Although the preceding analysis is based on the "infinite array" concept, the proposed form of the transition and method of design create new tools for specifying the required number of dummy elements in finite arrays. Assuming a multi-section transition has been designed, a relatively straight forward use of superposition principles would enable the aperture fields associated with a single waveguide element to be derived. The technique could replace the approximate E-plane method investigated in Chapter 3 for estimating a suitable number of dummy elements. (The previous method was not satisfactory for H-plane transition structures.)

The principle is summarised schematically in Fig.6.21, and is applicable to either polarisation. By introducing a set of 2n signal generators in each waveguide feed, with periodic element phasings given by

$$\psi = 0,\ \pm\pi/n,\ \pm 2\pi/n,\ \pm 3\pi/n,\ \ldots\ldots,\ \pm(n-1)\pi/n,\ \pi \qquad \ldots.(30)$$

the net excitation of the (2n - 1) waveguide elements either side of the reference element is zero. The total aperture field at any point (x, 0) on the aperture could be estimated by summing all the "significant" free space modes (roots $\beta_{1,m}$, $\beta_{2,m}$ or $-j\xi_{2,m}$ and the set $-j\xi_{i,m}$, $i = 3,4$) for each value of ψ in eqn.(30). If the analysis assumed only the propagating mode(s) in region (m - 1), the number of grating waves to be considered would be restricted to those of amplitude (at $z = 0$) comparable with the first evanescent mode in region $(m - 1)$ "incident" on the aperture discontinuity. The number of modes to be considered would be governed by the susceptance discontinuity in the aperture plane.

With a suitably large number of generators, the total field at elements $r \sim \pm n/2$ would tend to vanish, while the total field between these limits could be sampled along the x-axis to predict the amplitude and phase distributions due to a single element. This technique would have practical engineering value, rather than any theoretical significance as a method for predicting the aperture fields required to fulfil Hannan's proposals (8).

The changes in the element pattern caused by the gradual elimination of elements could be estimated by Fourier transform techniques, by assuming that all power not reaching the aperture was absorbed (eg. by r.a.m.). This information could then be utilised to assess the number of dummy elements required. It should be noted that the above procedure would not require extensive additional programming.

The same principle would enable the mutual coupling between the waveguide elements to be determined (eg. in the E-plane, where $a/\lambda_{eff} < 0.5$ and coupling is unavoidable).

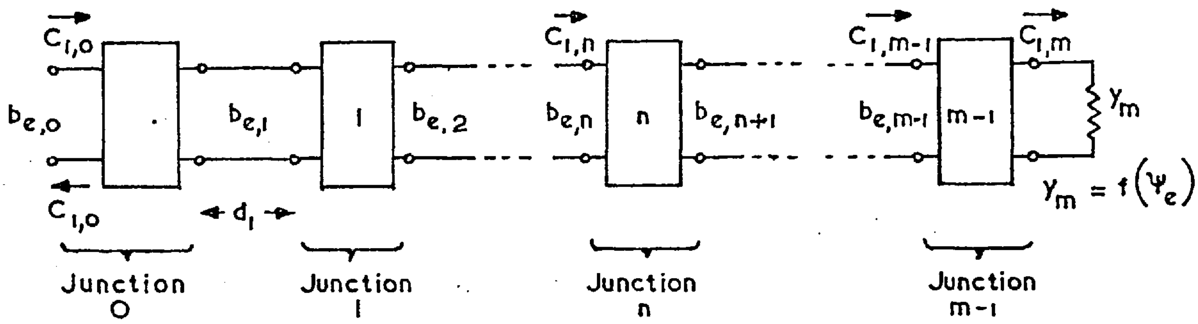

Fig. 6.1 Equivalent cascade network for E-plane multi-section transition

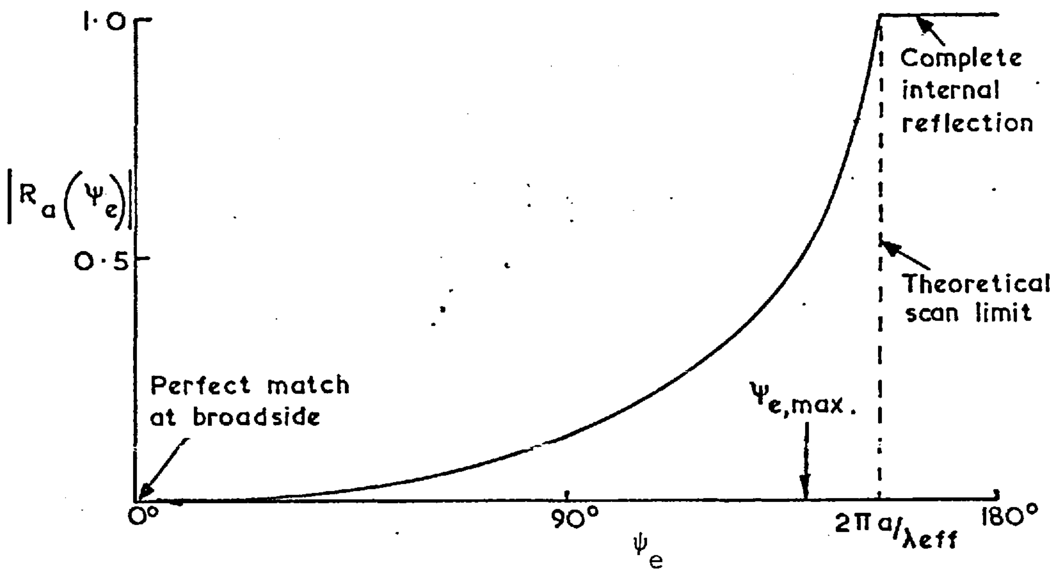

Fig. 6.2 Major features of the impedance-matching problem for an E-plane waveguide array

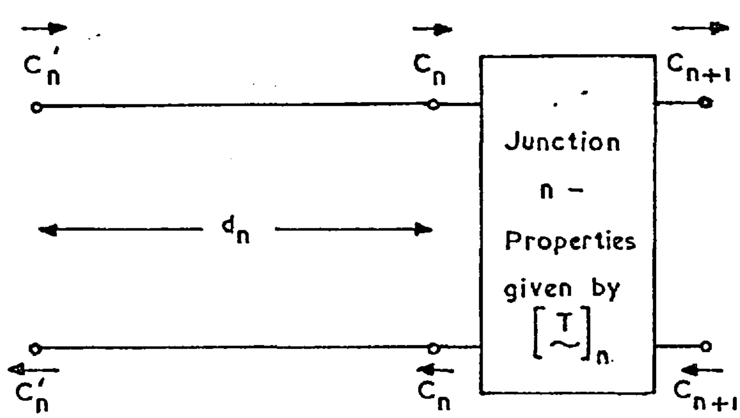

Fig. 6.3 One section of the two-port cascade network in Fig. 6.1 (first mode subscript ommitted)

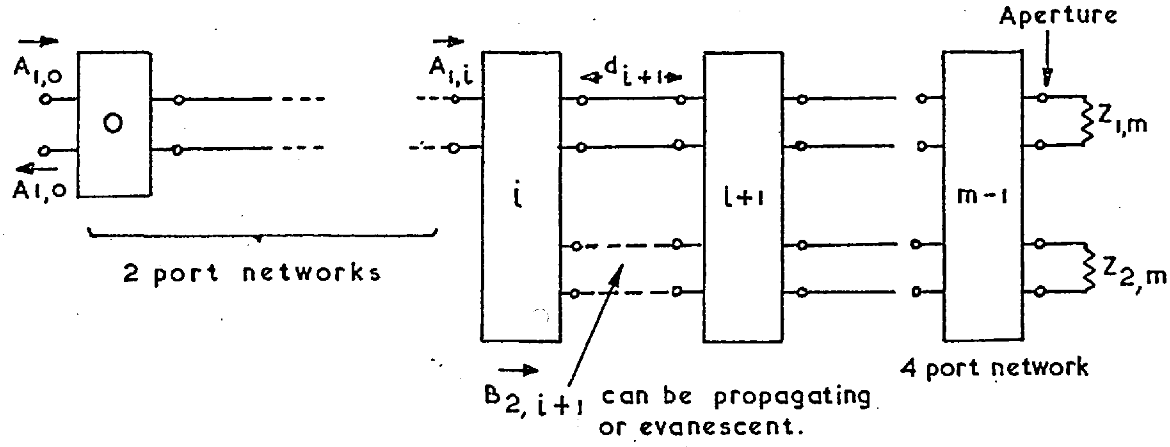

Fig. 6.4 Equivalent cascade network for H-plane multi-section transition

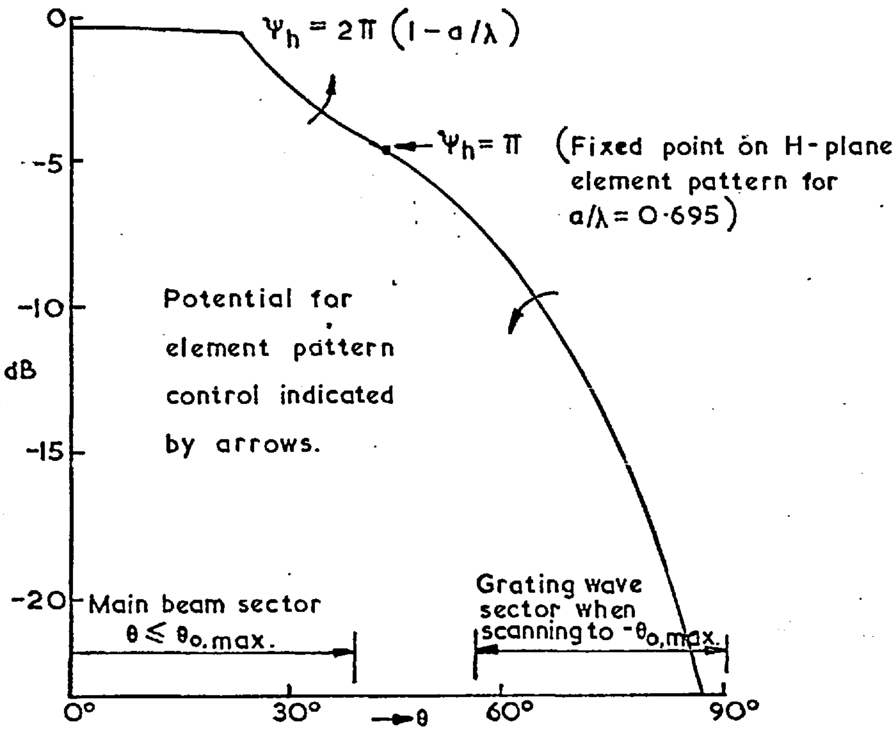

Fig. 6.5 Symmetrical portion of the H-plane element pattern for a waveguide array (a/λ = 0.695)

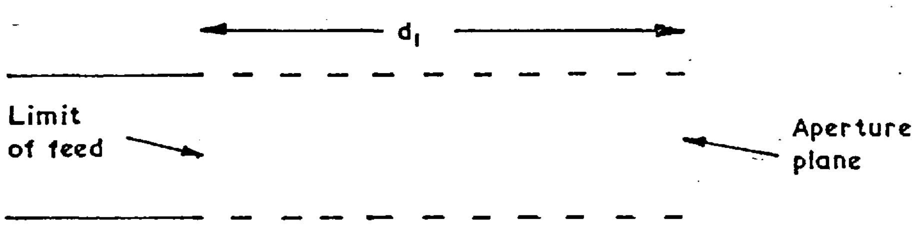

$$[\underset{\sim}{S}]^f = \begin{bmatrix} S^f_{11} & S^f_{12} \\ S^f_{21} & S^f_{22} \end{bmatrix} \qquad [\underset{\sim}{S}]^a = \begin{bmatrix} S^a_{11} & S^a_{12} \\ S^a_{21} & S^a_{22} \end{bmatrix}$$

Fig. 6.6 Single-section transition - showing the notation used to distinguish the two junctions

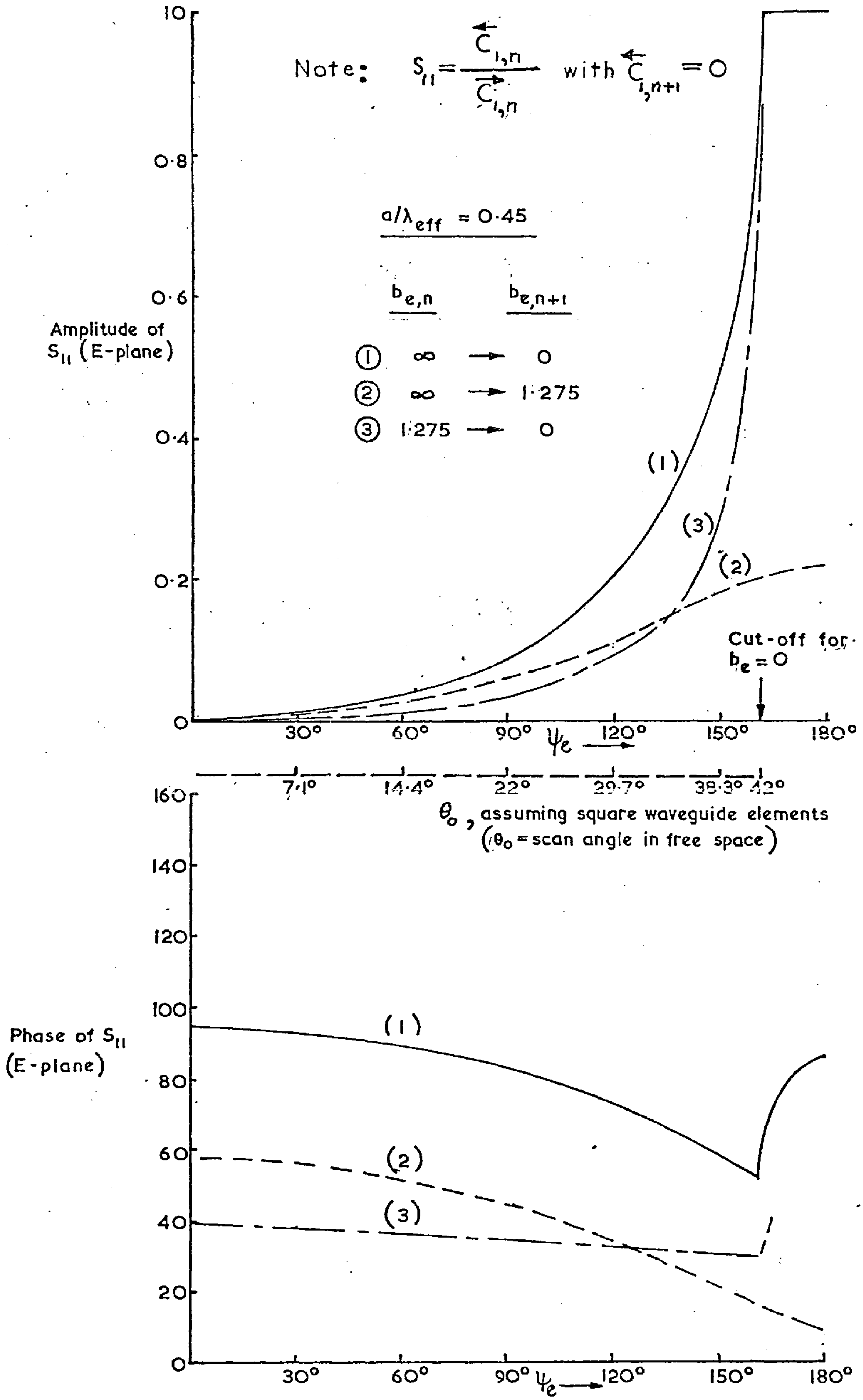

Fig. 6.7 Calculated amplitude and phase of "reflection coefficients" (S_{11}) in E-plane for $a/\lambda_{eff} = 0.45$

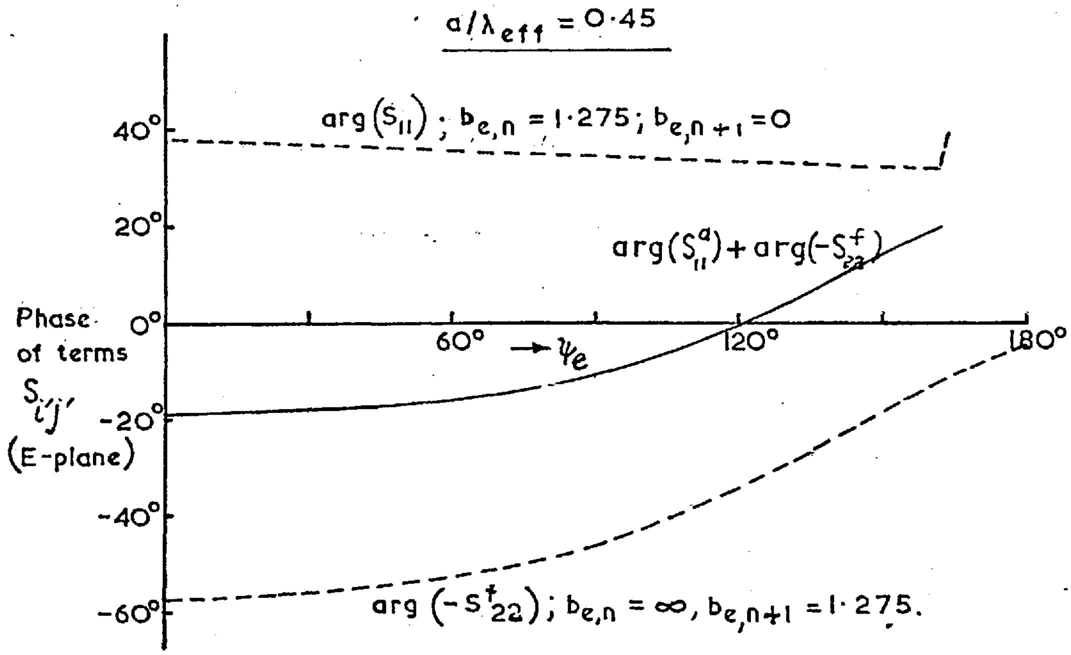

Fig. 6.8a "Junction" phase effects for E-plane susceptance discontinuities ($a/\lambda_{eff} = 0.4$)

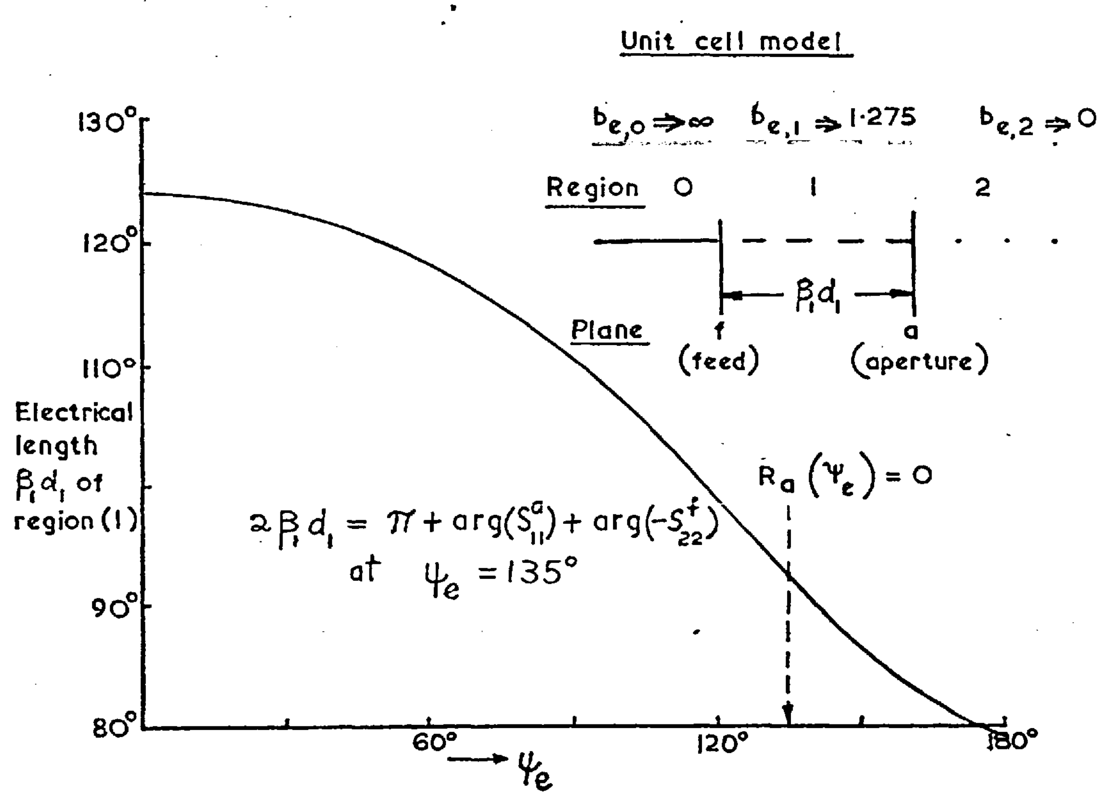

Fig. 6.8b Variation of junction-corrected "quarter wavelength" section $\beta_{1,1}d_1$ with element phasing ($a/\lambda_{eff} = 0.45$)

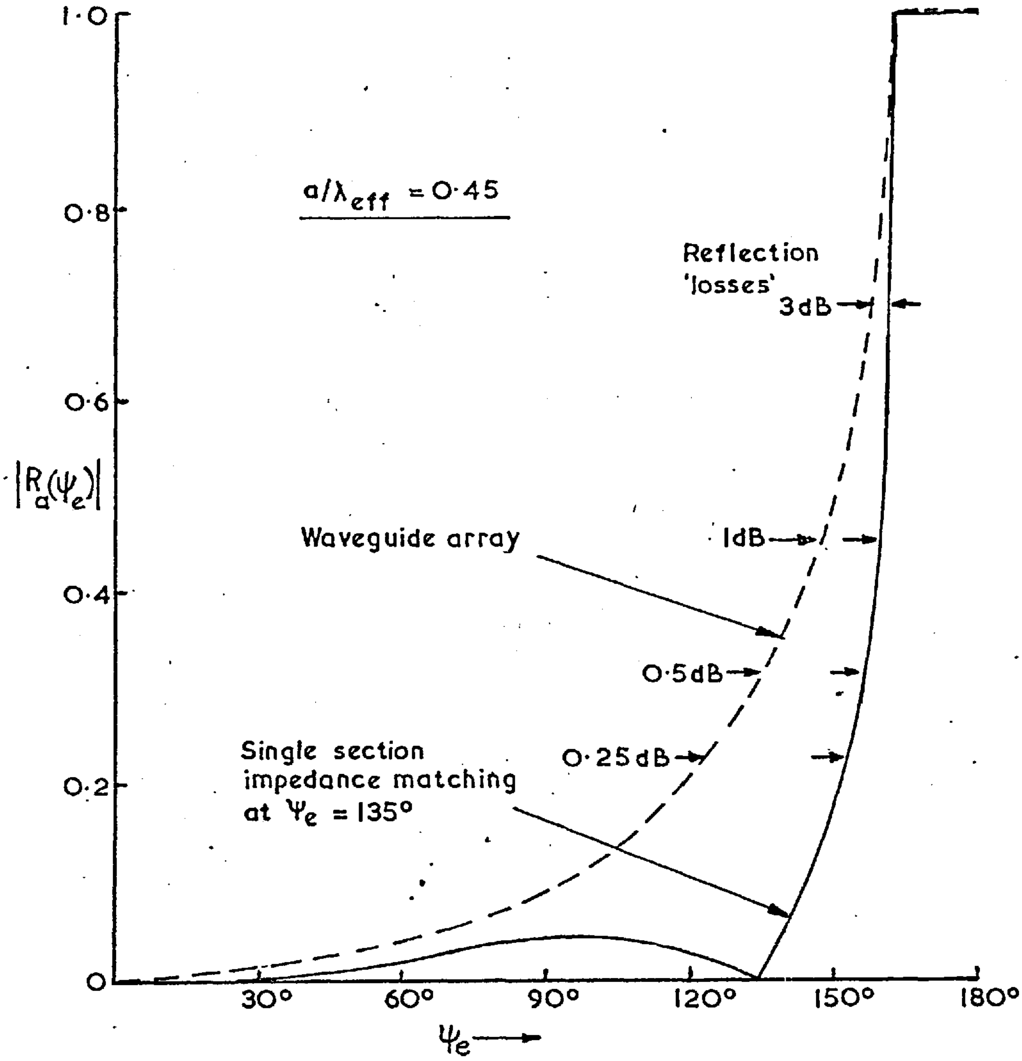

Fig. 6.9 Active reflection coefficient for an E-plane array with and without a single-section finite susceptance transition (a/λ_{eff} = 0.45)

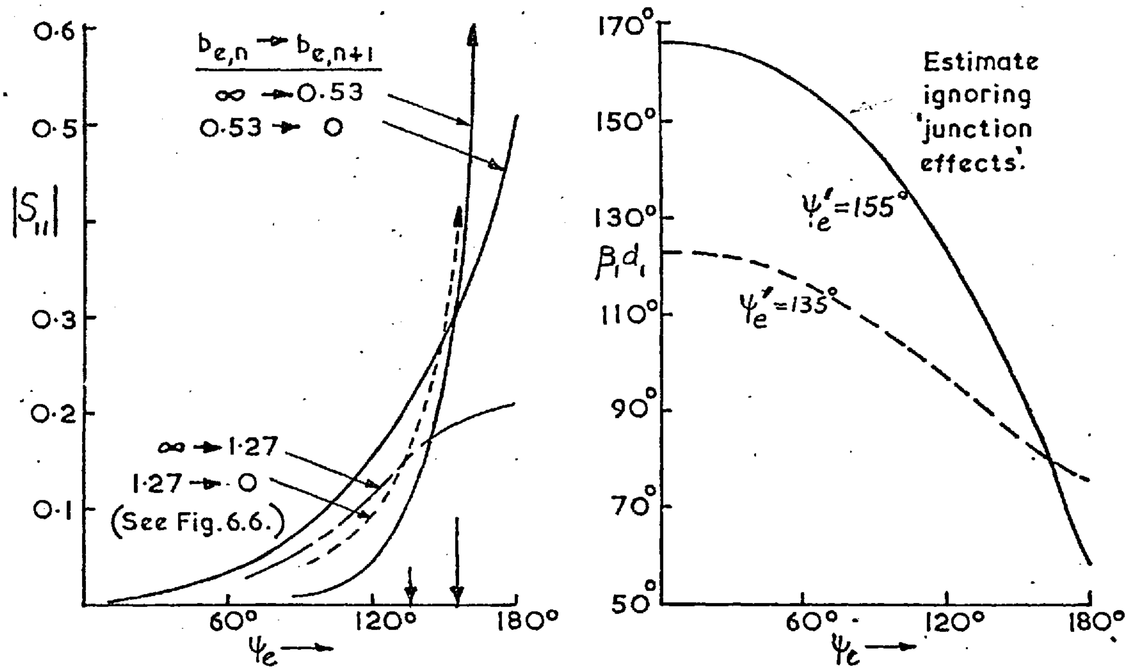

Fig. 6.10 Dependence of terms $|S^a_{11}|$, $|S^f_{11}|$ and $\beta_1 d_1$ on the choice of ψ_e' for single-section transitions.

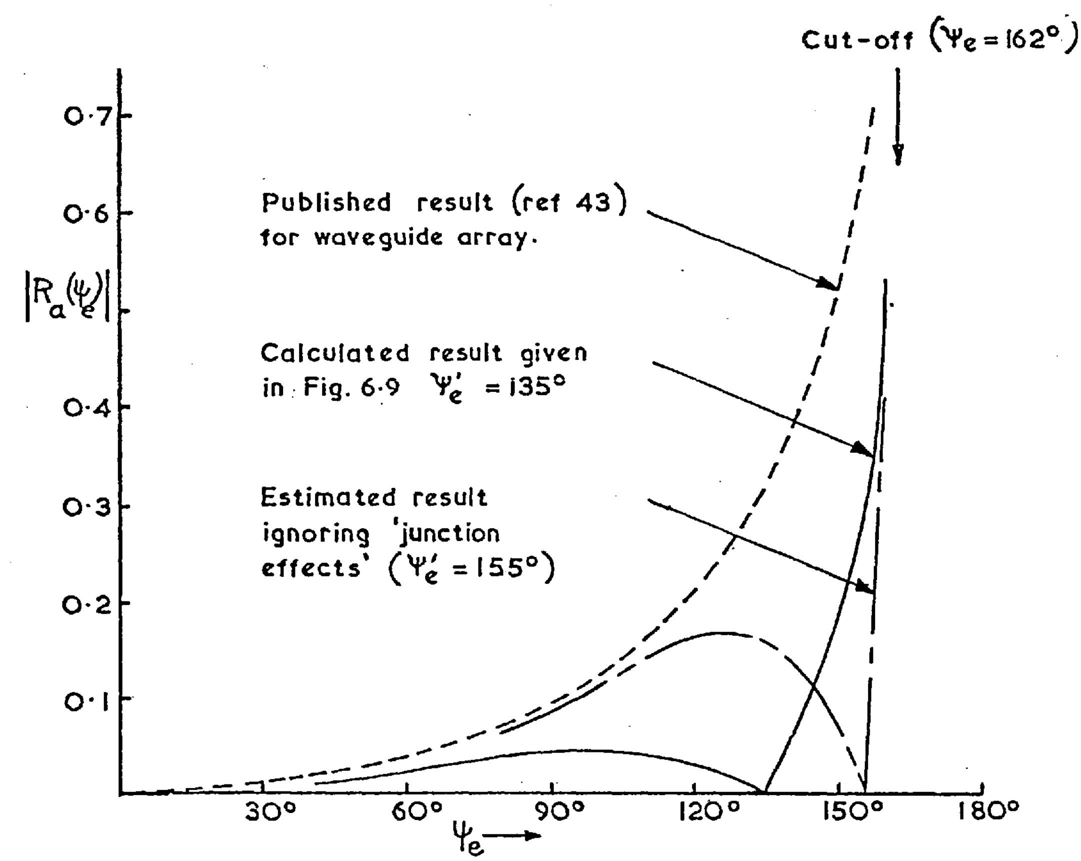

Fig. 6.11 Estimated variation in performance by setting $\psi_e' = 155°$ in place of $\psi_e' = 135°$, for a single-section transition.

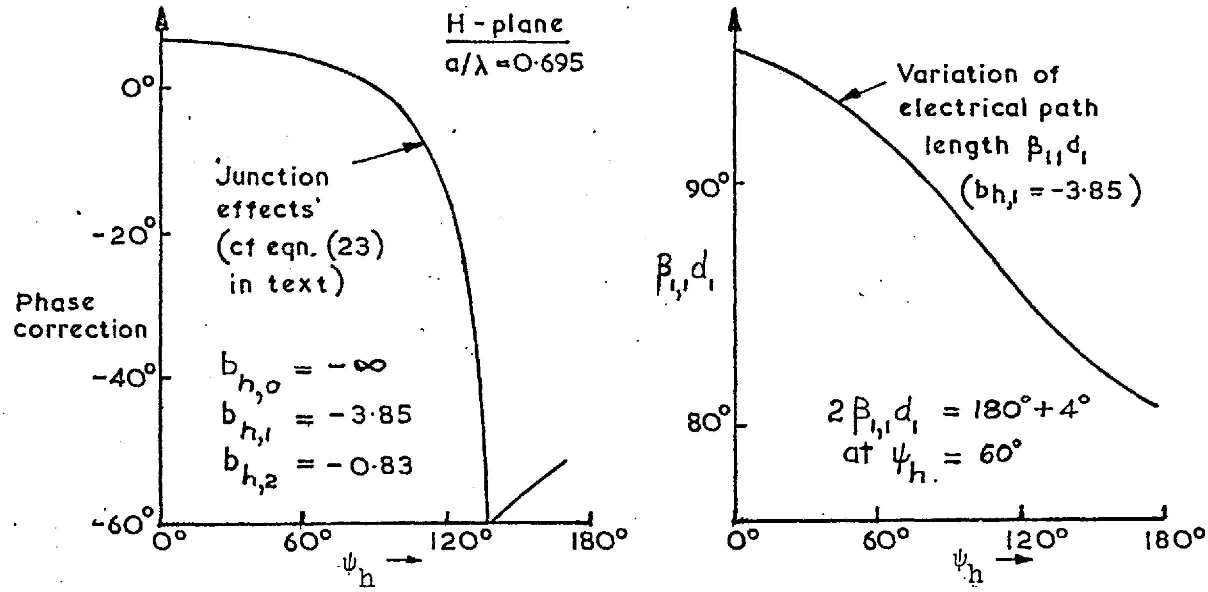

Fig. 6.12 Junction effects and variation of electrical path length for "quarter wavelength" single section impedance matching in H-plane (a/λ = 0.695).

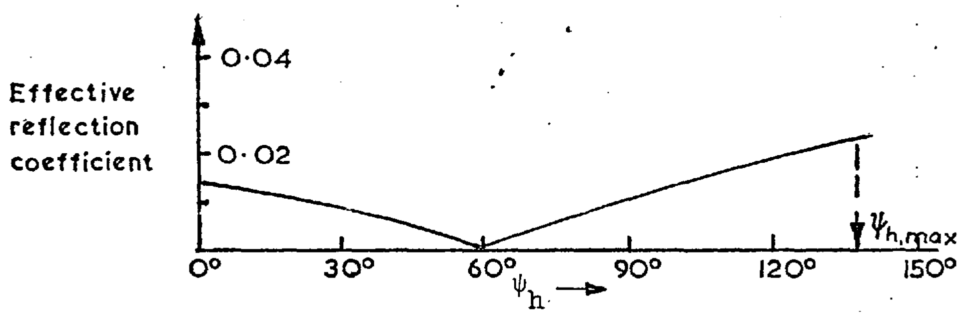

Fig. 6.13 Variation of "active reflection coefficient" for a single-section H-plane transition, assuming $\overleftarrow{A}_{1,2} = 0$ (i.e. ignoring reflections within the dual-moded section).

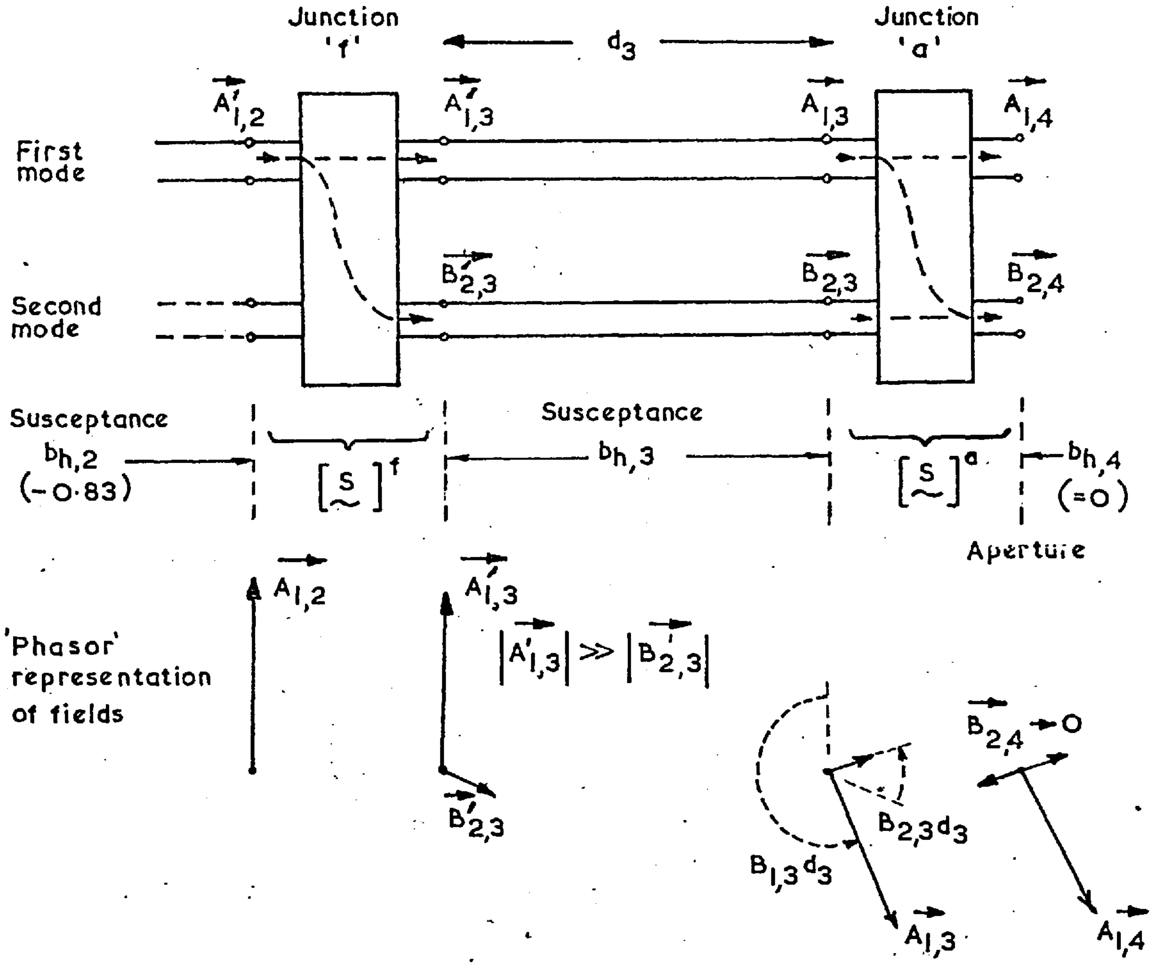

Fig. 6.14 Equivalent network and schematic interpretation of the control of grating wave radiation ($\vec{B}_{2,4}$) afforded by a single section dual-moded transition. To a first-order approximation, the two junctions behave as directional couplers.

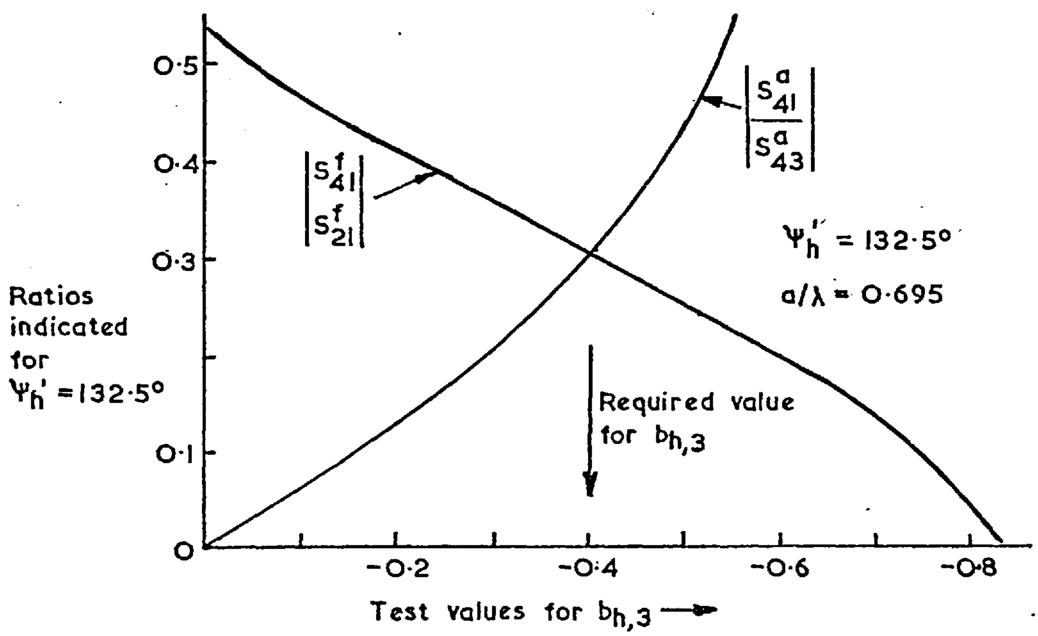

Fig. 6.15 Numerically calculated ratios $|S^f_{41}/S^f_{21}|$ and $|S^a_{41}/S^a_{43}|$ as defined by Fig. 6.14 and eqn.(15), for $b_{h,2} = -0.83$, $b_{h,4} = 0$ and $\psi_h' = 132.5^o$

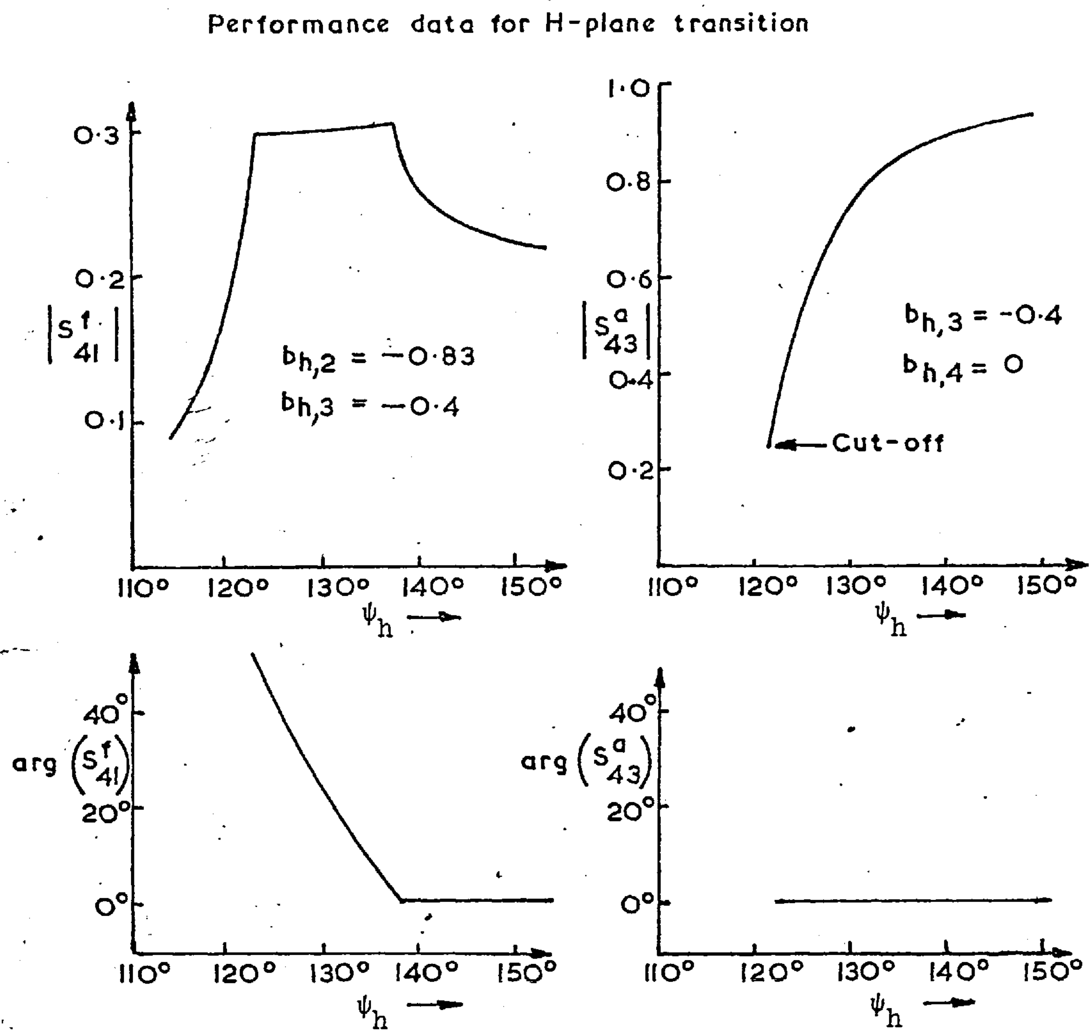

Fig. 6.16 Scattering matrix elements S^f_{41} and S^a_{43} for the "single-section" H-plane transition, $b_{h,2} = -0.83$, $b_{h,3} = -0.4$ and $b_{h,4} = 0$.

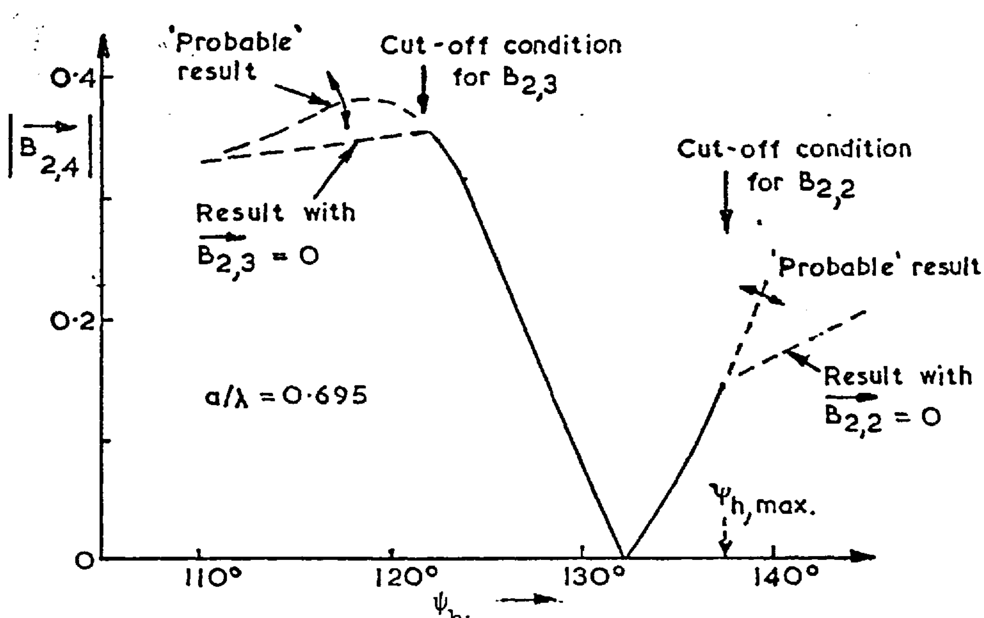

Fig. 6.17 Amplitude of grating wave ($\vec{B}_{2,4}$) with a "single-section" dual-moded transition for element pattern control.

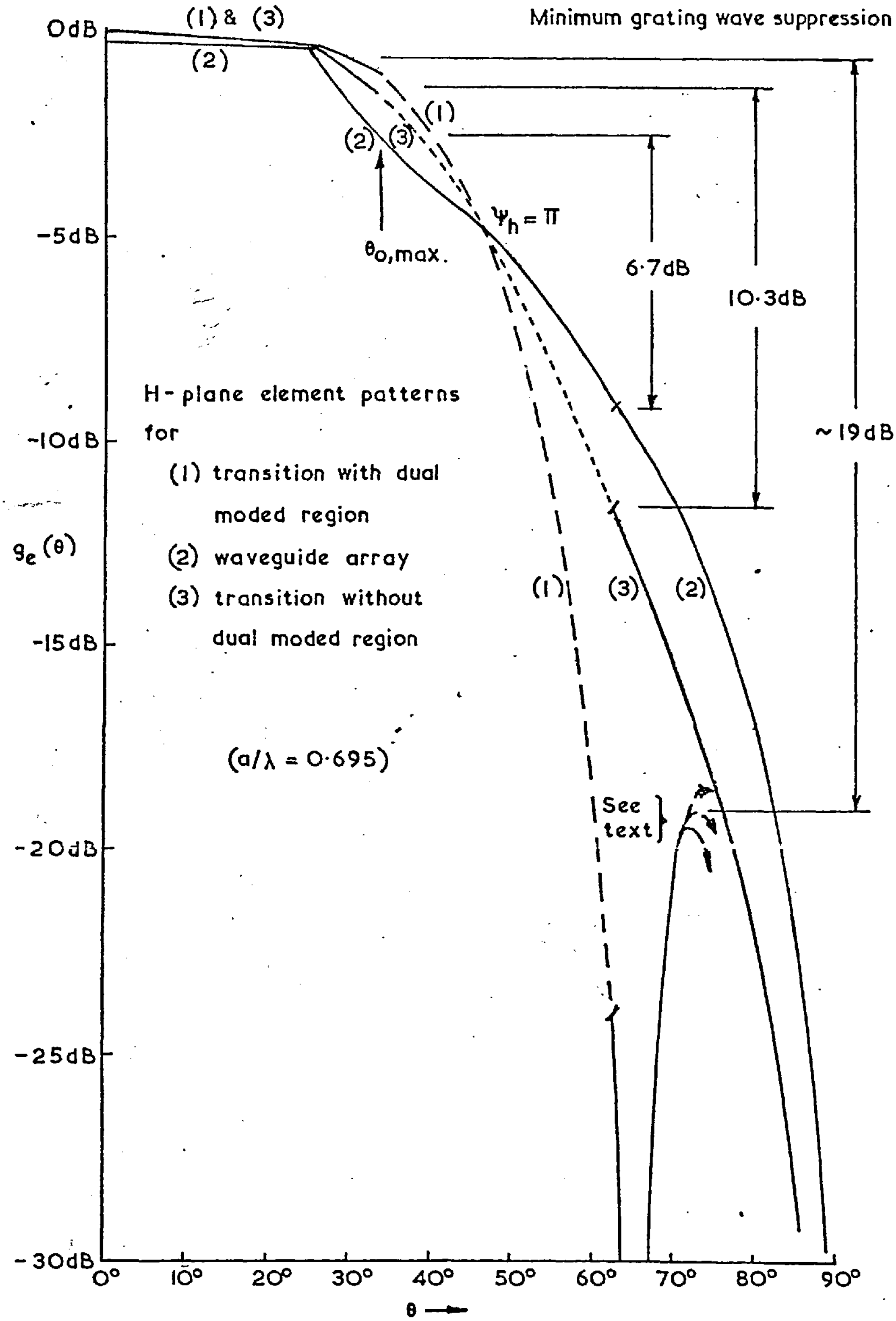

Fig. 6.18 Comparison of calculated H-plane element patterns $a/\lambda = 0.695$, $\theta_{o,max} = 33.5^{o}$

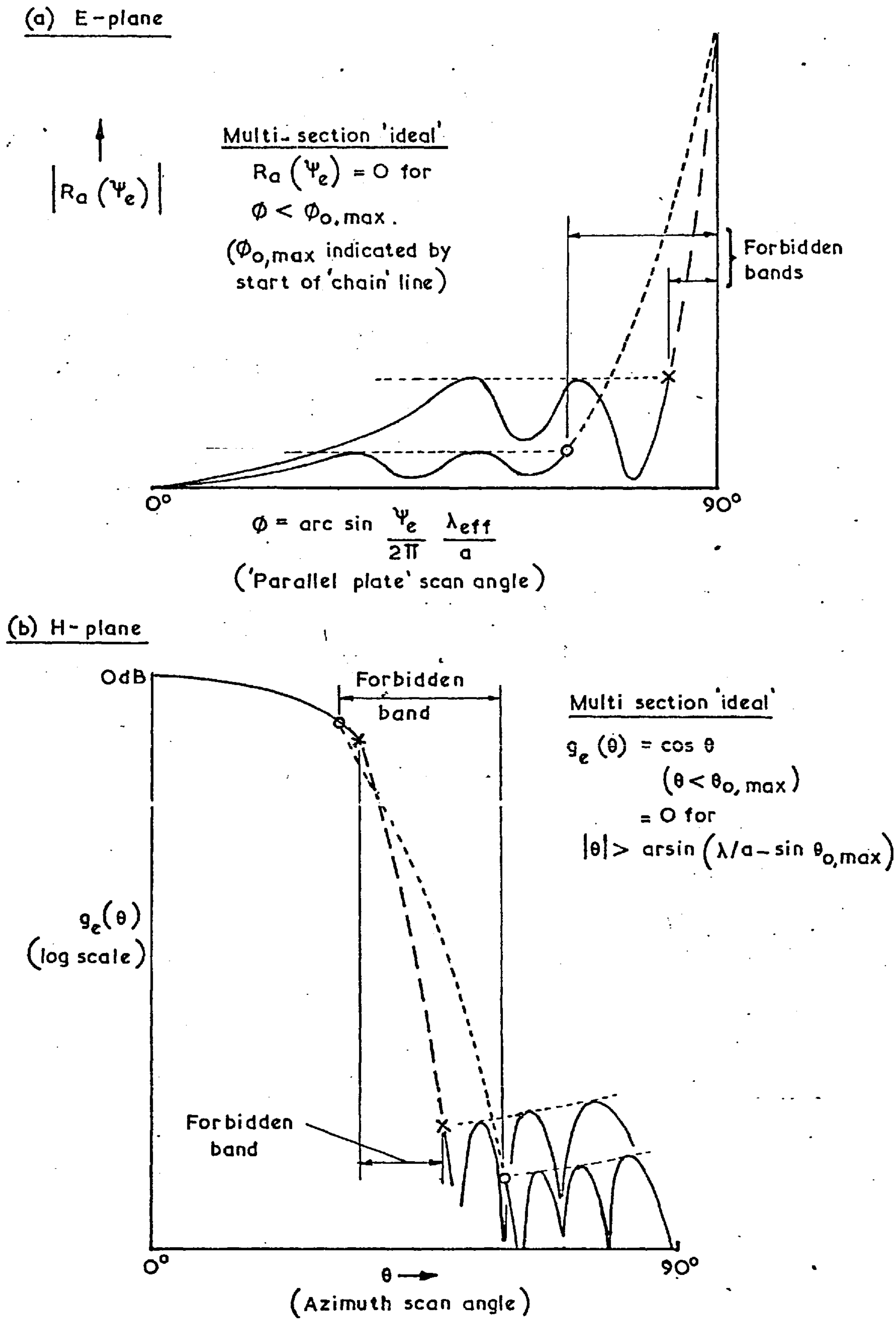

Fig. 6.19 Concepts of "optimum" and "ideal" behaviour for multi-section transitions. For a given number of sections, the objective function is degraded as the "forbidden band" is reduced.

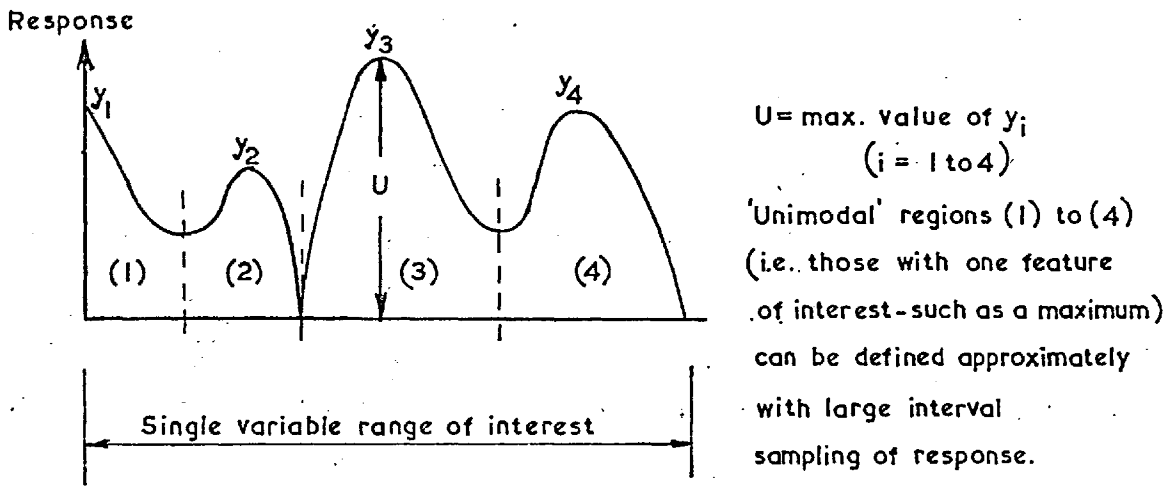

Fig. 6.20 Typical example of a response function arising during numerical optimisation. "Ripple Search" finds U (and monitors significant changes in unimodal regions);"Razor Search" reduces U.

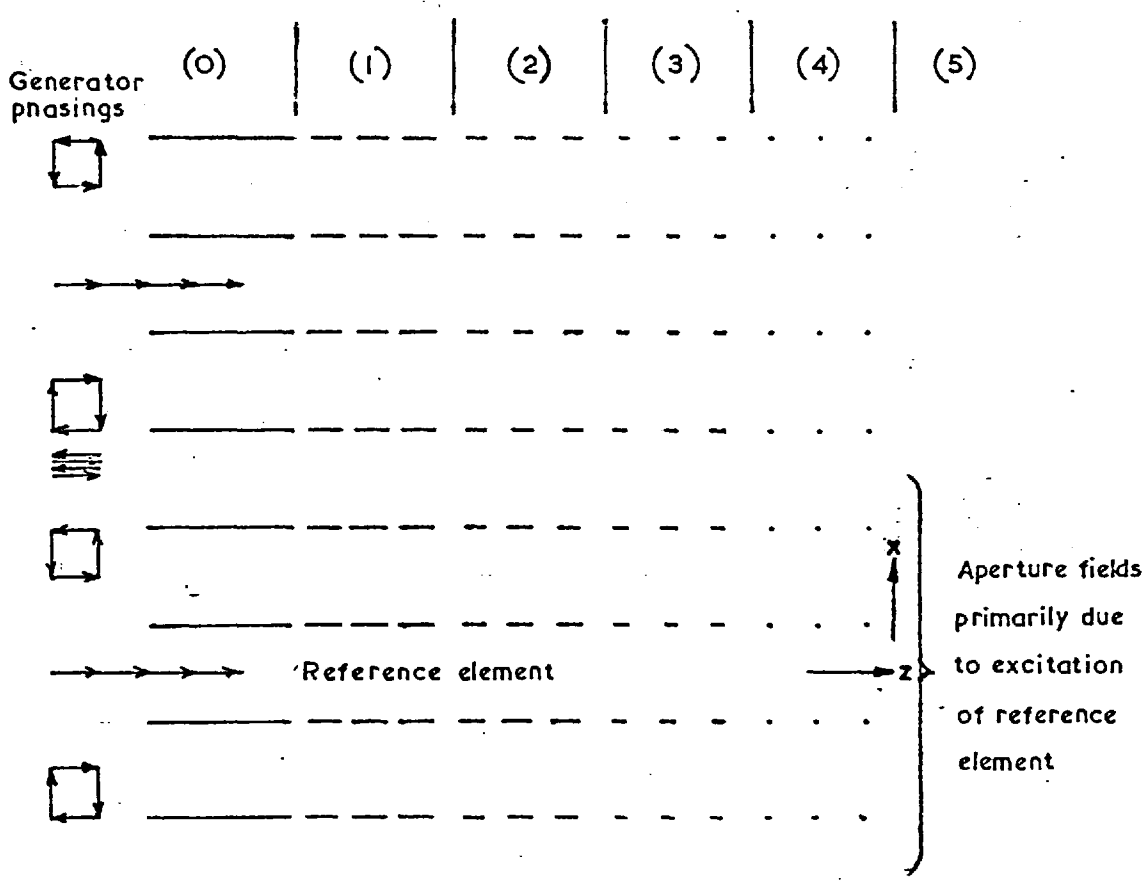

Fig. 6.21. Periodic excitation required to estimate the aperture field distribution for a single element in a multi-section transition (2n = 4 for illustrative purposes)

CHAPTER 7

CONCLUSIONS

A new technique for controlling the performance limitations of array antennas (in particular, electronically scanned arrays) has been described. The central principle is the elimination of the abrupt discontinuity in boundary conditions which occurs at the aperture surface of conventional waveguide arrays, by inserting reactive surfaces. Control of the grating lobe amplitude and of the impedance mismatch between the guides and freespace in linear arrays has been demonstrated. The problems for E- and H-plane polarisation are essentially complementary, in the sense that impedance matching is more difficult to achieve in the E-plane whereas control of the grating wave amplitude is more difficult in the H-plane. In both polarisations, the potential saving in the number of elements needed in a sectorally scanned array is a major advantage.

The technique has been presented at two levels, with an initial emphasis (in Chapters 2 and 3) on the underlying principles, and a subsequent emphasis (in Chapters 4, 5 and 6) on practical design details. In Chapter 2, it is shown that theoretically ideal performance, as specified by Hannan, could be obtained with infinitely-long "reactive current sheets" forming extensions to the conducting sidewalls between adjacent elements. The susceptance of these current sheets must be tapered monotonically from an infinite value, corresponding to perfectly conducting walls, to a zero value, corresponding to free space. As demonstrated by the experimental results given in Chapter 3, the periodic character of realizable reactive structures imposes restrictions in addition to those created by the requirement for a transition region of finite length. The principal parameters in shaping the E-plane element pattern are also defined in Chapter 3. In particular, it is shown that grating waves can be eliminated by introducing a parallel-plate region (beyond the array aperture) which reduces the effective element separation to a value $a/\lambda_{eff} < 0.5$.

Chapters 4 to 6 lay the foundations for a practical design procedure. Retaining the concept of boundary susceptance as a unifying parameter, the network properties of E- and H-plane array structures with an axial reactance discontinuity are obtained. The performance possibilities for multi-section transitions (with each section characterised by a constant boundary susceptance and an axial length) are then established by analysing the equivalent cascade network. Calculated results for simple transitions providing impedance matching and grating wave suppression are given, and indicate the possibility of operating with a/λ approaching $(2 \sin \theta_{o,max})^{-1}$ in the H-plane, and with $\psi_{e,max}$ approaching $2\pi a/\lambda_{eff}$ in the E-plane. Numerical search strategies are required to optimise the performance of transitions in which more than one constant-susceptance region must be considered at any time. The theoretical work is supported by an experimental evaluation of structures which achieve the small boundary susceptances required for H-plane arrays. Encouraging results are demonstrated for structures consisting of conducting grids in parallel with a low-loss dielectric such as alumina, which could be manufactured by printed circuit techniques.

Further developments may be envisaged. For engineering applications, a programme is required to achieve boundary structures which could be incorporated in linear arrays with multi-section optimised transitions. Questions concerning bandwidth, tolerances, conduction losses, power handling and mechanical strength will arise during such a programme. Complementing this activity, several topics have been identified which warrant further research. These include the possibility of extending the principle to planar arrays (as indicated in Section 2.7.1), the definition of the aperture field distribution for a "theoretically ideal element" (Section 2.4.1), a detailed analysis of the mutual coupling between elements (Section 2.6.2) and a more detailed analysis of edge radiation in finite array structures (Sections 3.6 and 6.5).

REFERENCES

1. Proc. IEEE, Vol. 56, No. 11, November 1968, Special Issue on Electronic Scanning. (Reference works published in 1968 and earlier.)

2. Knittel, G.H., *Design of Radiating Elements for Large Planar Arrays: Accomplishments and Remaining Challenges,* Microwave Jnl., Vol. 15, September 1972. (Special issue of *Microwave Journal,* with 4 review papers on aspects of phased array design.)

3. Hansen, R.C., Editor, *Microwave Scanning Antennas,* Vol. II, *Array theory and Practice,* Academic Press, New York, 1966. (Reference works published in 1965 and earlier.)

4. Amitay, N., V. Galindo and C.P. Wu, *Theory and Analysis of Phased Array Antennas,* Wiley-Interscience, New York, 1972. (Reference works published in 1969 and earlier.)

5. Oliner, A.A. and G.H. Knittel, Editors, *Phased-Array Antennas,* Artech House: Dedham, MA, 1972 (Proceedings of the 1970 Phased-Array Antenna Symposium. Reference works published in 1970 and earlier.)

NOTE:- (Specific references contained in 1-5 are given below where appropriate.)

6. Wu, C.P., *Analysis of Finite Parallel Plate Waveguide Arrays,* 1968 IEEE G-AP International Symposium Program and Digest, pp.124-133, September 1968.

7. Diamond, B.L., *Small Arrays - Their Analysis and Their Use for the Design of Array Elements,* 1970 Phased Array Symposium, Polytechnic Institute of Brooklyn. (Ibid 5, pp.127-131.)

8. Hannan, P.W., *The Element Gain Paradox for a Phased-Array Antenna,* IEEE Trans. Ant. and Prop., Vol. AP-12, pp. 423-433, July 1964.

9. Kahn, W.K. and W. Wasylkiwskyj, *Theory of Coupling, Radiation and Scattering by Antennas,* Proc. Symp. on Generalized Networks, Vol. 16, Brooklyn, N.Y.: Polytechnic Press, 1966, pp. 83-114.

10. Wasylkiwskyj, W. and W.K. Kahn, *Theory of mutual coupling among minimum - scattering antennas,* IEEE Trans. Ant. and Prop., Vol. AP-18, pp. 204-216, March 1970.

11. Wasylkiwskyj, W. and W.K. Kahn, *Scattering properties and Mutual Coupling of Antennas with Prescribed Radiation Patterns,* IEEE Trans. Ant. and Prop., Vol. AP-18, pp. 741-752, November 1970.

12. Wasylkiwskyj, W. and W.K. Kahn, *Infinite Arrays of Sub-Array Antennas,* 1970 Phased-Array Symposium, Polytechnic Institute of Brooklyn. (Ibid 5, pp. 83-90.)

13. Montgomery, C.G., R.H. Dicke and E.M. Purcell, *Principles of Microwave Circuits,* M.I.T. Rad. Lab. Series, Vol. 8. New York: McGraw-Hill, 1948, pp. 317-333.

14. Kahn, W.K. and H. Kurss, *Minimum Scattering Antennas,* IEEE Trans. Ant. and Prop., Vol. AP-13, pp. 671-675, September 1965.

15. Jamieson, A.R., *Aperture Antennas,* Ph. D. thesis, Univ. of Canterbury, Christchurch, New Zealand, 1970.

16. Oliner, A.A., *Surface Wave Effects and Blindness in Phased-Array Antennas,* 1970 Phased Array Symposium, Polytechnic Institute of Brooklyn. (Ibid 5, pp. 107-112.)

17. Diamond, B.L., *A Generalised Approach to the Analysis of Infinite Planar Arrays,* Proc. IEEE, Vol. 56, pp. 1837-1851, November 1968.

18. Ehlenberger, A.G., L. Schwartzman and L. Topper, *Design Criteria for Linearly Polarised Waveguide Arrays,* Proc. IEEE, Vol. 56, pp. 1861-1872, November 1968.

19. Hansen, R.C., *Microwave Scanning Antennas,* Vol. 1, Van Nostrand, 1964. Chapter 1, pp. 10-11.

20. Hannan, P.W., *A Proof that a Phased-Array Antenna can be Impedance Matched for all Scan Angles,* Radio Science, Vol. 2, pp. 361-369, March 1967.

21. Wheeler, H.A., *The Grating-Lobe Series for the Impedance Variation in Planar Phased-Array Antennas,* IEEE Trans. Ant. and Prop., Vol. AP-14, pp. 707-714, November 1966.

22. Stark, L., *Radiation Impedance of a Dipole in an Infinite Planar Phased Array,* Radio Science, Vol. 2, pp. 361-377, March 1966.

23. Farrell, G.F., Jr. and D.H. Kuhn, *Mutual Coupling in Infinite Planar Arrays of Rectangular Waveguide Horns,* IEEE Trans. Ant. and Prop., Vol. AP-16, pp. 405-414, July 1968.

24. Galindo, V. and C.P. Wu, *Dielectric Loaded and Covered Rectangular Waveguide Phased Array,* Bell System Tech. Jnl., Vol. 47, pp. 93-116, January 1968.

25. Mailloux, R.J., *Reduction of Mutual Coupling Using Perfectly Conducting Fences,* IEEE Trans. Ant. and Prop., AP-19, pp. 166-173, March 1971.

26. Lee, S.W. and W.R. Jones, *On the Suppression of Radiation Nulls and Broadband Impedance Matching of Rectangular Waveguide Phased Arrays,* IEEE Trans. Ant. and Prop., Vol. AP-19, pp. 41-51, January 1971.

27. Diamond, B.L. and G.H. Knittel, *A New Procedure for the Design of a Waveguide Element for a Phased Array Antenna,* 1970 Phased Array Symposium, Polytechnic Institute of Brooklyn (Ibid 5, pp. 149-156).

28. Hsiao, J.K., *Analysis of Interleaved Arrays of Waveguide Elements,* IEEE Trans. Ant. and Prop., Vol. AP-19, pp. 729-735, November 1971.

29. Tsandoulas, G.N., *Wideband Limitations of Waveguide Arrays,* Microwave Jnl., Vol. 15, pp. 49-56, September 1972.

30. Cox, R.M. and W.E. Rupp, *Circularly Polarised Phased Array Antenna Element,* IEEE Trans. Ant. and Prop., Vol. AP-18, pp. 804-806, November 1970.

31. Amitay, N., J.S. Cook, R.G. Pecina and C.P. Wu, *On Mutual Coupling and Matching Conditions in Large Planar Phased Arrays,* IEEE G-AP International Symposium Digest, pp. 150-156, 1964.

32. Varon, D. and G.I. Zysman, *On the Mismatch of Electronically Steerable Phased-Array Antennas,* Radio Science, Vol. 3, pp. 487-489, May 1968.

33. Varon, D. and G.I. Zysman, *Some Properties and Limitations of Electronically Steerable Phased-Array Antennas,* Bell Systems Tech. Jnl., Vol. 46, pp. 1561-1586, September 1967.

34. Fano, R.M., *Theoretical Limitations on the Broadband Matching of Arbitrary Impedances,*Jnl.Franklin Institute, No. 249, pp. 57-83 and 139-154, 1950.

35. Phelan, H.R. and J.L. Harrison, *Phased Array Costs Cut by New Radiating Elements,* Microwaves, Vol. 12, pp. 40-43, January, 1973.

36. Hannan, P.W., D.S. Lerner and G.H. Knittel, *Impedance Matching a Phased-Array Antenna Over Wide Scan Angles by Connecting Circuits,* IEEE Trans. Ant. and Prop., AP-13, pp. 28-34, January 1965.

37. Amitay, N., *Improvement of Planar Array Match by Compensation Through Contiguous Element Coupling,* IEEE Trans. Ant. and Prop., Vol. AP-14, pp. 580-586, September 1966.

38. Amitay, N., R.G. Pecina and C.P. Wu., *Radiation Properties of Large Planar Arrays,* Bell Systems Tech. Jnl., Monograph 5047, February 1965.

39. Arredondo, G.A., P.E. Butzien and R.W. Humes, *The Design of a Wide Band Wide Scan-Angle Waveguide Radiating Element,* 1970 Phased Array Symposium, Polytechnic Institute of Brooklyn (Ibid 5, pp. 173-177).

40. Wheeler, H.A. *Simple Relations Derived from a Phased-Array Antenna Made of an Infinite Current Sheet,* IEEE Trans. Ant. and Prop., Vol. AP-13, pp. 506-514, July 1965.

41. Bryant, G.H., *Propagation in corrugated waveguides,* Proc. IEE , Vol. 116, pp. 203-213, February 1969.

42. Brown, J., *Artificial Dielectrics having Refractive Indices less than Unity,* Proc. IEE , Vol. 100, Pt. 4, pp. 51-62, 1953.

43. Wu, C.P. and V. Galindo, *Properties of a Phased Array of Rectangular Waveguides with Thin Walls.* IEEE Trans. Ant. and Prop., Vol. AP-14, pp. 163-173, March 1966.

44. Collin, R.E., *Field Theory of Guided Waves,* McGraw-Hill, New York, 1961. Chapter 9, pp. 375-379.

45. Ibid 44, Chapter 11, pp. 454-461.

46. Ibid 44, Chapter 5, pp. 177-178.

47. Ibid 44, Chapter 5, pp. 204-205.

48. Jasik, H. (Ed), *Antenna Engineering Handbook,* McGray-Hill, 1961. Chapter 31, pp. 17-20.

49. Matthaei, G.L., L. Young and E.M.T. Jones, *Microwave Filters, Impedance-Matching Networks and Coupling Structures,* McGraw-Hill, 1964 Chapter 6, p. 257.

50. Southworth, G.C., *Principles and Applications of Waveguide Transmission,* Van Nostrand, 1950, pp. 269-275.

51. Klopfenstein, R.W., *A Transmission Line Taper of Improved Design,* Proc. IRE, Vol. 44, pp. 31-35, January 1956.

52. Carne, A. and Brown, J., *Theory of Reflections From Rodded-Type Artificial Dielectric,* Proc. IEE, Vol. 106, Pt. B, pp. 107-115, March 1959.

53. Ibid 44, Chapter 12.

54. Brown, J. and W. Jackson, *The Properties of Artificial Dielectrics at Centimetre Wavelengths,* Proc. IEE, Vol. 102, Pt. B, pp. 11-16, January 1955.

55. Brown, J., *A Theoretical Study of Some Artificial Dielectrics,* Ph.D. thesis, University of London, 1954.

56. Ibid 44, p. 541.

57. Miles, J., *The Reduction of Three-Dimensional Electromagnetic Problems,* Jnl. of Applied Physics, Vol. 23, p. 372, 1952.

58. Sangster, A.J., *A Variational Analysis of Waveguide Coupling,* M.Sc. thesis, Univ. of Aberdeen, 1964.

59. Sommers, J.E., *Measurements of the Effects of Mutual Coupling on Waveguide Horn Phased Arrays,* R.R.E. Memorandum No. 2668, Royal Radar Establishment, Malvern, U.K., July 1971.

60. Blasi, E.A. and R.S. Eliott, *Scanning Antenna Arrays of Discrete Elements,* IRE Trans. Ant. and Prop., Vol. AP-7, p. 435, July 1959.

61. Oliner, A.A. and R.G. Malech, *Mutual Coupling in Finite Scanning Arrays,* Ibid 4, Chapter IV, pp. 339-342.

62. Hannan, P.W. and M.A. Balfour, *Simulation of a Phased Array Antenna in a Waveguide,* IEEE Trans. Ant. and Prop., Vol. AP-13, pp. 342-353, May 1965.

63. Gregorwich, W.S., A. Hessel and G.H. Knittel, *A Waveguide Simulator Study of a Blindness Effect in a Phased Array,* Microwave Jnl., Vol. 14, pp. 37-41, September 1971.

64. Wheeler, H.A., *A Survey of the Simulator Technique for Designing a Radiating Element,* 1970 Phased Array-Antenna Symposium, Polytechnic Institute of Brooklyn, (Ibid 5, pp. 132-148).

65 Milne K., *Studies of the Wide Angle Scanning Properties of Microwave Lens Aerials,* Ph. D. thesis, University of London, 1951.

66. Brown, J., *Microwave Lens,* Methuen & Co., London, 1953.

67. Sengupta, D.L. and R.E. Hiatt, *Radar Handbook,* (Editor: M.I. Skolnik) Chapter 10, McGraw-Hill, 1970.

68. De Size, L. K., and J. F. Ramsay, *Reflecting Systems,* Ibid 19, Chapter 2, pp. 141-143.

69. Whitehead, E. A. N., *The Theory of Parallel Plate Media for Microwave Lenses,* Proc. IEE , Vol. 98, Pt. III, pp. 133-140, January 1951.

70. Carlson, J.E., and A. E. Heins, *The Reflection of an Electromagnetic Plane Wave by an Infinite Set of Plates,* Qtrly. of App. Maths., Vol. IV, pp. 313-329, January 1947 (Part 1); and Vol. V., pp. 82-88, April 1947 (Part II).

71. Muehldorf, E. I., *The Phase Centre of Horn Antennas,* IEEE Trans. Ant. and Prop., Vol. AP-18, pp. 753-760, November 1970.

72. Plessey Company: Data Sheets for P-10 Polyurethane Foam.

73. Rubin, R., *Antenna Measurements,* Ibid 48, Chapter 34.

74. Worthington, H.R., *Technique of Microwave Measurements,* (Editor C. G. Montgomery), Chapter 15, M.I.T. Rad. Lab. Series, No.11, McGraw Hill, 1950.

75. Hollis, J. S., T. J. Lyon and L. Clayton (Editors), *Microwave Antenna Measurements,* Chapter 14, Scientific Atlanta Inc., U.S.A., July 1970.

76. Ibid 19, pp. 30-33.

77. Milne, K., *The Effects of Phase Errors on Simple Aperture Illuminations,* Proceedings of a Conference on Centimetric Aerials for Marine Navigation Radar, June 1950. H.M.S.O. London, 1952.

78. Ibid 48, Chapter 2 , pp. 36-41.

79. Skolnik, M.I., *Antenna Theory,* (Editors R. E. Collin and F. J. Zucker), Vol. 1, McGraw Hill, 1969. Chapter 6, pp. 227-233.

80. Miles, G. R. and A. J. T. Whitaker., *Computed Radiation Patterns of a Step-Phased Array,* R.R.E. Technical Note, No. 735, Royal Radar Establishment, Malvern, U.K., March 1969.

81. Galindo, V. and C. P. Wu., *Numerical Solutions for an Infinite Phased Array of Rectangular Waveguides with Thick Walls,* IEEE Trans. Ant. and Prop., Vol. AP-14, pp. 149-158, March 1966.

82. Lee, S. W., N. Wong and R. Tang., *Analysis of Infinite Planar Array of Rectangular Waveguides by Generalised Scattering Matrix Approach,* 1970 Phased-Array Antenna Symposium, Polytechnic Institute of Brooklyn, (Ibid 5, pp. 91-106).

83. Edelberg, S. and A. A. Oliner., *Mutual Coupling Effects in Large Antenna Arrays: Part 1 - Slot Arrays,* IRE Trans. Ant. and Prop., Vol. AP-8, pp. 286-297, May 1960.

84. Ibid 4, Chapter 8, pp. 347-370.

85. Chappas, C., Private Communication (through Imperial College).

86. Galindo, V. and C. P. Wu., *On the Asymptotic Decay of Coupling for Infinite Phased Arrays*, Proc. IEEE., Vol. 56, pp. 163-173, November 1968.

87. Marcuvitz, N. (Editor), *Waveguide Handbook*, Chapter 5, M.I.T. Rad. Lab. Series, McGraw-Hill, 1951.

88. Macfarlane, G. G., *Surface Impedance of an Infinite Parallel-Wire Grid at Oblique Angles of Incidence*, Jnl. IEE, Vol. 93, Pt. 111A, pp. 1523-1527, October 1946.

89. Wasylkiwskyj, W., *On the Transmission Coefficient of an Infinite Grating of Parallel, Perfectly Conducting Circular Cylinders*, IEEE Trans. Ant. and Prop., AP-19, pp. 704-708, September 1971.

90. Noble, B., *Methods Based on the Wiener-Hopf Technique for the Solution of Partial Differential Equations*, Pergamon Press, 1958.

91. Plessey Company: Data Sheets for Microwave Absorbent Materials.

92. Wood, C., Private Communication (within Plessey Company).

93. Ibid 90, Chapter 3, pp. 105-110.

94. Ibid 44, Chapter 10, pp. 421-430.

95. Roos, B. W., *Analytic Functions and Distributions in Physics and Engineering*, J. Wiley and Sons, 1969. Chapters 1 and 3.

96. King, R. W. P., and C. W. Harrison, *Antennas and Waves : A Modern Approach*, M.I.T. Press, 1969, Chapter 3, Section 3.9, pp. 201-224.

97. Berz, F., *Reflection and Refraction of Microwaves at a Set of Metallic Plates*, Proc. IEE, Vol. 98, Pt.III, pp. 47-55, January 1951.

98. Brown, J., Private Communication.

99. Brown, J., *Electromagnetic Momentum associated with Waveguide Modes*, Proc. IEE, Vol. 113, pp. 27-34, January, 1966.

100. Ibid 90, Chapter 1, p. 12.

101. Ibid 90, Chapter 1, pp. 14-15 and p. 40.

102. Ibid 90, Chapter 3, p. 128.

103. Ibid 90, Chapter 1, p. 36.

104. Ibid 44, Chapter 1, pp. 18-20.

105. Ibid 90, Chapter 1, pp. 37-38.

106. Kreysig, E., *Advanced Engineering Mathematics*, Wiley, 1962, pp. 29-30.

107. Gustincic, J.J., *The Determination of Active Array Impedance with Multielement Waveguide Simulators*, IEEE, Trans. Ant. and Prop., Vol. AP-20, pp. 589-595, September 1972.

108. Brown, J. and J.S. Seeley, *The Fields associated with an Interface between Free Space and an Artificial Dielectric*, Proc. IEE, Vol. 105, Pt. C, pp. 465-471, September, 1958 (Monograph 300R).

109. Brown, J. *Propagation in Coupled Transmission Line Systems*, Quart. Jnl. Mechanics and Applied Maths., Vol. 11, Pt. 2, pp. 235-243, 1958.

110. Ibid 44, Chapter 3, pp. 87-90.

111. Ibid 44, Chapter 8, pp. 314-367.

112. Brown, J., *Reactive effects in transverse-film bolometers in rectangular waveguides*, Proc. IEE, Vol. 110, pp. 77-78, January 1963.

113. Bandler, J.W. and P.A. Macdonald, *Optimisation of Microwave Networks by Razor Search*, IEEE Trans. Microwave Theory and Techniques, Vol. MTT-17, pp. 552-562, August 1969.

114. Bandler, J.W., *Computer Optimisation of Inhomogeneous Waveguide Transformers*, IEEE Trans. Microwave Theory and Techniques, Vol. MTT-17, pp. 563-571, August 1969.

115. Young, L., *Inhomogeneous Quarter-wave Transformers*, Mitrowave Jnl., Vol. 5, pp. 84-89, February 1962.

116. Riblet, H.J., *A General Design Procedure for Quarter-Wavelength Inhomogeneous Impedance Transformers having approximately Equal-ripple Performance*, IEEE Trans. Microwave Theory and Techniques, Vol. MTT-10, pp. 339-359, September 1962.

117. Ibid 49, Chapter 4, pp. 83-162.

118. Bandler, J.W. *Optimisation Methods for Computer-aided Design*, IEEE Trans. Microwave Theory and Techniques, Vol. MTT-17. pp. 533-552, August 1969.

119. Wigmore, C., Private Communication (within Plessey Company).

120. Tamir, T., *Antenna Theory*,(Editors R.E. Collin and F.J. Zucker), Vol. II, McGraw Hill, 1969. Chapter 20, pp. 259-297.